

The Arctic Climate System

This second edition brings this definitive book completely up to date with the many advances in our understanding of Arctic climate since the first edition was published in 2005. The book has also been extensively reorganized to weave issues of Arctic change throughout the text, rather than confining them to a single chapter.

This book is the first to provide an integrated assessment of the Arctic climate system, recognizing that a true understanding of how the Arctic functions lies in appreciating the interactions and linkages among its various components. It begins with a historical perspective, addressing the early exploration of the Arctic, the growth of systematic observations, and the advent of the modern research era. This is followed by a discussion of the basic physical and climatic characteristics of the Arctic. Later chapters address atmospheric and ocean energy budgets, atmospheric circulation, the surface energy budget, the hydrologic budget, atmosphere–ocean–sea ice interactions, and regional climate regimes. Modeling is an important tool in Arctic climate research and is accorded its own chapter. Following a review of past climates (paleoclimates), the book closes with a brief assessment of the Arctic’s uncertain future. Though targeted mainly at advanced students and researchers, this book is accessible to anyone with an interest in the Arctic and a basic understanding of climate science.

Cambridge Atmospheric and Space Science Series

Editors: A. J. Dessler, J.T. Houghton, and M. J. Rycroft

This series of upper-level texts and research monographs covers the physics and chemistry of different regions of the Earth’s atmosphere, from the troposphere and stratosphere, up through the ionosphere and magnetosphere, and out to the interplanetary medium.

MARK C. SERREZE is the director of the National Snow and Ice Data Center (NSIDC), part of the Cooperative Institute for Environmental Sciences (CIRES) at the University of Colorado, Boulder. He is also a Fellow of CIRES and a professor in the Department of Geography. His Arctic research interests are wide-ranging and include atmosphere–sea ice interactions, synoptic climatology, hydroclimatology, boundary layer problems, numerical weather prediction, and climate change. Dr. Serreze has conducted fieldwork in the Canadian Arctic on sea ice and ice caps, and on the Alaskan tundra.

ROGER G. BARRY is a Distinguished Professor of Geography Emeritus at the University of Colorado, Boulder, and the former director of NSIDC. He was recently the director of the International CLIVAR Project Office at the National Oceanography Centre in Southampton, United Kingdom. He has written more than 250 research papers, and his books include *Mountain Weather and Climate* (Third Edition, 2008); *Atmosphere, Weather and Climate* (Ninth Edition, 2009, with Richard Chorley); *Synoptic Climatology: Methods and Applications* (1973, with A. H. Perry); *Synoptic and Dynamic Climatology* (2001, with Andrew Carleton); and *The Global Cryosphere: Past, Present and Future* (2011, with Thian Gan). In 1999, Dr. Barry was elected a Fellow of the American Geophysical Union in recognition of his contributions to research in climatology and cryospheric science. In 2009–2010 he spent nine months on a Humboldt Fellowship at the Glaciology Commission in Munich.

Cambridge Atmospheric and Space Science Series

EDITORS

Alexander J. Dessler

John T. Houghton

Michael J. Rycroft

TITLES IN PRINT IN THIS SERIES

M. H. Rees

Physics and chemistry of the upper atmosphere

R. Daley

Atmosphere data analysis

J. K. Hargreaves

The solar-terrestrial environment

J. R. Garratt

The atmosphere boundary layer

S. Sazhin

Whistler-mode waves in a hot plasma

S. P. Gary

Theory of space plasma microinstabilities

I. N. James

Introduction to circulating atmospheres

T. I. Gombosi

Gaskinetic theory

M. Walt

Introduction to geomagnetically trapped radiation

B. A. Kagan

Ocean-atmosphere interaction and climate modelling

D. Hastings and H. Garrett

Spacecraft-environment interactions

J. C. King and J. Turner

Antarctic meteorology and climatology

T. E. Cravens

Physics of solar system plasmas

J. F. Lemaire and K. I. Gringauz

The Earth's plasmasphere

T. I. Gombosi

Physics of space environment

J. Green

Atmospheric dynamics

G. E. Thomas and K. Stamnes

Radiative transfer in the atmosphere and ocean

I. G. Enting

Inverse problems in atmospheric constituent transport

R. D. Hunsucker and J. K. Hargreaves

The high-latitude ionosphere and its effects on radio propagation

N. Meyer-Vernet

Basics of the solar wind

V. Y. Trakhtengerts and M. J. Rycroft

Whistler and Alfvén mode cyclotron masers in space

R.W. Schunk and A. F. Nagy

Ionospheres: Physics, plasma physics, and chemistry

Second Edition

The Arctic Climate System

Second Edition

Mark C. Serreze

University of Colorado at Boulder

Roger G. Barry

University of Colorado at Boulder



CAMBRIDGE
UNIVERSITY PRESS

32 Avenue of the Americas, New York, NY 10013-2473, USA

Cambridge University Press is part of the University of Cambridge.

It furthers the University's mission by disseminating knowledge in the pursuit of education, learning, and research at the highest international levels of excellence.

www.cambridge.org

Information on this title: www.cambridge.org/9781107037175

© Mark C. Serreze and Roger G. Barry 2005, 2014

This publication is in copyright. Subject to statutory exception and to the provisions of relevant collective licensing agreements, no reproduction of any part may take place without the written permission of Cambridge University Press.

First published 2005

Second edition 2014

Printed in the United States of America

A catalog record for this publication is available from the British Library.

Library of Congress Cataloging in Publication data

Serreze, Mark C., author.

The Arctic climate system / Mark C. Serreze, University of Colorado at Boulder, Roger G. Barry, University of Colorado at Boulder. – Second edition.

pages cm – (Cambridge atmospheric and space science series)

Includes bibliographical references and index.

ISBN 978-1-107-03717-5 (hardback)

1. Arctic regions – Climate. 2. Climatology – Arctic regions. I. Barry, Roger G. (Roger Graham), 1935– author. II. Title.

QC994.8.S475 2014

551.6911'3-dc23 2013047705

ISBN 978-1-107-03717-5 Hardback

Cambridge University Press has no responsibility for the persistence or accuracy of URLs for external or third-party Internet Web sites referred to in this publication and does not guarantee that any content on such Web sites is, or will remain, accurate or appropriate.

Contents

Preface	<i>page</i>	ix
Acknowledgments		xi
List of Acronyms		xiii
List of Selected Web Sites		xix
1.	The Evolution of Knowledge about the Arctic and Its Climate	1
2.	Physical Characteristics and Basic Climatic Features	23
3.	The Basic Atmospheric and Ocean Energy Budgets	65
4.	The Atmospheric Circulation	85
5.	Energy Exchanges at the Surface	138
6.	Precipitation, Net Precipitation, and River Discharge	177
7.	Arctic Ocean–Sea Ice–Climate Interactions	209
8.	Climate Regimes of the Arctic	249
9.	Modeling the Arctic Climate System	273
10.	Arctic Paleoclimates	311
11.	The Uncertain Future	343
	References	353
	Index	397
	Color plate section follows page 172.	

Preface

This book provides the reader with an overview of the Arctic climate system, its links with the global climate system, and the pronounced environmental changes unfolding in the region. It begins with a historical perspective, addressing the early exploration of the Arctic, the growth of systematic observations, and the advent of the modern research era. This is followed by a discussion of the basic physical and climatic characteristics of the Arctic. Later chapters address atmospheric and ocean energy budgets, atmospheric circulation, the surface energy budget, the hydrologic budget, atmosphere–ocean–sea ice interactions, and regional climate regimes. Modeling is an important tool in Arctic climate research and is accorded its own chapter. Following a review of past climates (paleoclimates), the book closes with a brief assessment of uncertainties in the Arctic’s future.

Arctic science has advanced greatly since the first edition of this book was published in 2005. This is reflected in extensive updates to much of the material. Change has become such an integral part of the Arctic climate system that it can no longer be largely relegated to a single chapter. As such, this second edition weaves issues of Arctic change throughout the text. In turn, based on the first author’s use of this textbook in the classroom, some less useful or dated material has been removed, and the presentation of some topics has been changed, hopefully for the better. While this book is targeted at advanced undergraduate and graduate students, the material should be accessible to anyone with an interest in the Arctic and a basic understanding of climate science. The text contains numerous illustrations to help the reader and extensive references to research papers on specific topics.

Acknowledgments

This book would not have been possible without the help of many people. Our deepest appreciation for NSIDC contributions to the first edition goes to Mary Jo Brodzik, Nancy Geiger-Wooten, Terry Haran, Ken Knowles, Miranda Lavrakas, and Naomi Saliman. To our reviewers of the first edition – Todd Arbetter, Yarrow Axford, David Bromwich, John Cassano, Richard Lammers, Amanda Lynch, Drew Slater, and John Walsh – all of you were instrumental in helping improve the content, presentation, and rigor of the text. Jeff Key provided figures specifically for this book, as did Andy Barrett, Ken Fowler, Richard Lammers, Jim Maslanik, Jamie Morison, Ignatius Rigor, Julianne Stroeve, and Hengchun Ye. A host of colleagues took time from their busy schedules to answer questions and provide guidance. The list includes Terry Chapin, Clara Deser, Jennifer Francis, Jim Hurrell, Dave McGuire, Walt Meier, Giff Miller, Anne Nolin, Jim Overland, Ola Persson, Gavin Schmidt, Kevin Trenberth, and Tingjun Zhang. Writing the second edition of the textbook involved not just many updates and changes in presentation but a major reorganization to better reflect the central issue of climate change in the Arctic. For their help, as well as their patience, we thank the entire NSIDC crew, but especially Andy Barrett, Cindy Brekke, Erika Lenz, Kevin Schaefer, Drew Slater, Julianne Stroeve, and Natasha Vizcarra. Without the unfailing support of our spouses, Susan and Eileen, we would both be lost. Thanks are also due to the National Science Foundation, the National Oceanic and Atmospheric Administration, and the National Aeronautics and Space Administration. Finally, without the enthusiasm of Ray Bradley, Mark Serreze might have never become interested in Arctic climate science.

Acronyms

AAAS	American Association for the Advancement of Science
ACSYS	Arctic Climate System Study
AGCM	Atmospheric Global Climate Model (or General Circulation Model)
AGU	American Geophysical Union
AMO	Atlantic Multi-decadal Oscillation
AMOC	Atlantic Meridional Overturning Circulation
AMS	American Meteorological Society
AMSR	Advanced Microwave Sounding Radiometer
AO	Arctic Oscillation
AOGCM	Atmosphere-Ocean Global Climate Model (or General Circulation Model)
AOMIP	Arctic Model Intercomparison Project
AON	Arctic Observing Network
APP	Arctic Polar Pathfinder
AR4	IPCC Fourth Assessment report
AR5	IPCC Fifth Assessment report
ARCMIP	Arctic Regional Climate Model Intercomparison Project
ARCSS	Arctic System Science program
ARCSyM	Arctic Regional Climate System Model
ASOF	Arctic-Subarctic Ocean Fluxes program
ASR	Arctic System Reanalysis
AVHRR	Advanced Very High Resolution Radiometer
AWS	Automatic Weather Station
BOREAS	Boreal Ecosystem-Atmosphere Study
CCN	Cloud Condensation Nuclei

CESM	Community Earth System Model
CFC	Chlorofluorocarbon
CFSR	Climate Forecast System Reanalysis
CHAMP	Community-Wide Hydrologic Analysis and Modeling Program
CHASM	Chameleon Surface Model
CISK	Conditional Instability of the Second Kind
CLASS	Canadian Land Surface Scheme
CliC	Climate and Cryosphere project
CLM	Community Land Model
CMIP	Coupled Model Intercomparison Project
CRYSYS	Cryosphere System in Canada program
CSAS	Changing Seasonality in the Arctic System
CTD	Conductivity Temperature Density (sensor)
DA	Arctic Dipole Anomaly
DEWLINE	Distant Early Warning Line
DMSP	Defense Meteorological Satellite Program
D-O	Dansgaard-Oeschger (cycle)
DU	Dobson Unit
ECMWF	European Centre for Medium Range Weather Forecasts
ELA	Equilibrium Line Altitude
ENSO	El-Niño Southern Oscillation
EOF	Empirical Orthogonal Function
EP	Eliassen-Palm(flux)
ERA-15	ECMWF 15-year reanalysis project
ERA-40	ECMWF 40-year reanalysis project
ERA-Interim	ECMWF Interim reanalysis project
ERBE	Earth Radiation Budget Experiment
ESMR	Electrically Scanning Microwave Radiometer
ET	Evapotranspiration
FAMOS	Forum for Arctic Modeling and Observational Synthesis
FYI	First-year Ice
GCM	Global Climate Model (or General Circulation Model)
GC-Net	Greenland Climate Network
GEWEX	Global Energy and Water Exchanges project
GIN	Greenland-Iceland-Norwegian sea
GISP2	Greenland Ice Sheet Project 2
GPP	Gross Primary Production
GRACE	Gravity Recovery and Climate Experiment
GRIP	Greenland Ice Core Project
GSA	Great Salinity Anomaly
HARC	Human Dimensions of the Arctic
HIRHAM	A combination of High Resolution Limited Area Model and ECHAM4
HR	Heterotrophic Respiration

HTM	Holocene Thermal Maximum
IABP	International Arctic Buoy Program
ICESat	Ice, Cloud and Land Elevation Satellite
ICOADS	International Comprehensive Ocean Atmosphere Data Set
IPA	International Permafrost Association
IPCC	Intergovernmental Panel on Climate Change
IPY	International Polar Year
IRD	Ice Rafted Detritus
ISCCP	International Satellite Cloud Climatology Project
LAI	Land Atmosphere Ice Interactions program
LGM	Last Glacial Maximum
LIA	Little Ice Age
LSM	Land Surface Model
MERRA	Modern Era Retrospective Analysis for Research and Applications
MIP	Model Intercomparison Project
MIS	Marine Isotope Stage
MM5	Pennsylvania State University/NCAR Fifth-Generation Regional Model
MODIS	Moderate Resolution Imaging Spectro-Radiometer
MYI	Multiyear Ice
NADW	North Atlantic Deepwater
NAM	Northern Annular Mode
NAO	North Atlantic Oscillation
NASA	National Aeronautics and Space Administration
NCAR	National Center for Atmospheric Research
NCEP	National Centers for Environmental Prediction
NDVI	Normalized Difference Vegetation Index
NEE	Net Ecosystem Exchange
NEEM	North Greenland Eemian Ice Drilling (ice core)
NEP	Net Ecosystem Production
NIC	National Ice Center
NOAA	National Oceanic and Atmospheric Administration
NP	North Pole (drifting station program)
NPP	Net Primary Production
NSF	National Science Foundation
NSIDC	National Snow and Ice Data Center
NWP	Numerical Weather Prediction
OAI	Ocean Atmosphere Ice Interactions program
PACTS	Pan-Arctic Cycles, Transitions and Sustainability program
PARCA	Program for Arctic Regional Climate Assessment
PARCS	Paleo-Environmental Arctic Studies program
PC	Principal Component
PCF	Permafrost Carbon feedback

PCMDI	Program for Climate Model Diagnosis and Intercomparison
PDF	Probability Density Function
PDO	Pacific Decadal Oscillation
P-ET	Precipitation minus Evapotranspiration
PILPS	Project for Intercomparison of Land Surface Parameterization Schemes
PIOMAS	Pan-Arctic Ice Ocean Modeling and Assimilation System
PIZ	Perennial Ice Zone
PNA	Pacific North America (teleconnection pattern)
PSC	Polar Stratospheric Cloud
PV	Potential Vorticity
PW	Petawatt
QBO	Quasi-Biennial Oscillation
RACMO	Regional Atmospheric Climate Model
RBL	Radiative Boundary Layer
RCP	Representative Concentration Pathway
SAR	Synthetic Aperture Radar
SAT	Surface Air Temperature
SCICEX	Submarine Arctic Science Program
SCM	Single Column Model
SEARCH	Study of Environmental Arctic Change
SHEBA	Surface Heat Budget of the Arctic Ocean
SiBCASA	Simple Biosphere/Carnegie-Ames-Stanford Approach (model)
SIC	Sea Ice Concentration
SIZ	Seasonal Ice Zone
SLP	Sea Level Pressure
SMMR	Scanning Multichannel Microwave Radiometer
SMOW	Standard Mean Ocean Water
SSM/I	Special Sensor Microwave/Imager
SSMIS	Special Sensor Microwave Imager Sounder
SST	Sea Surface Temperature
SZA	Solar Zenith Angle
TEM	Transformed Eulerian Mean
TEM	Terrestrial Ecosystem Model
TFP	Thermal Front Parameter
THC	Thermohaline Circulation
TIROS	Television Infrared Observation Satellite
TOA	Top of Atmosphere
TOMS	Total Ozone Mapping Spectrometer
TOVS	TIROS Operational Vertical Spectrometer
TPDS	Transpolar Drift Stream
UHI	Urban Heat Island
ULS	Upward Looking Sonar
VEINS	Variability of Exchanges in the Northern Seas

VHRR	Very High Resolution Radiometer
VIC	Variable Infiltration Capacity Model
WCRP	World Climate Research Programme
WISHE	Wind-Induced Surface Heat Exchange
WRF	Weather Research and Forecasting
YD	Younger Dryas

Selected Web Sites

Alfred Wegner Institute

<http://www.awi.de/en>

Arctic Centre, University of Lapland

<http://www.arcticcentre.org/>

Arctic Research Consortium of the United States (ARCUS)

<http://www.arcus.org/>

Byrd Polar Research Center, Ohio State University

<http://www-bprc.mps.ohio-state.edu/>

Canadian Ice Service

<http://ice-glaces.ec.gc.ca/>

Climate Diagnostics Center, NOAA

<http://www.cdc.noaa.gov/>

Cold Regions Research and Engineering Laboratory (CRREL)

<http://www.crrel.usace.army.mil/>

Cooperative Institute for Arctic Research (CIFAR), University of Alaska

<http://www.cifar.uaf.edu/>

CRYSYS – CRYosphere SYstem in Canada

<http://www.ccin.ca/home/>

European Centre for Medium Range Weather Forecasts (ECMWF)

<http://www.ecmwf.int/>

Geophysical Institute (GI), University of Alaska

<http://www.gi.alaska.edu/snowice/>

Institute of Arctic and Alpine Research (INSTAAR), University of Colorado

<http://instaar.colorado.edu/>

- Intergovernmental Panel on Climate Change (IPCC)
<http://www.ipcc.ch/>
- International Arctic Buoy Program (IABP)
<http://iabp.apl.washington.edu/>
- International Arctic Research Center (IARC), University of Alaska
<http://www.iarc.uaf.edu/>
- National Center for Atmospheric Research (NCAR)
<http://ncar.ucar.edu/>
- National Ice Center (NIC), NOAA
<http://www.natice.noaa.gov/>
- National Snow and Ice Data Center (NSIDC), University of Colorado
<http://www.nsidc.org/>
- NOAA Arctic Climate Research
<http://www.arctic.noaa.gov/arp/resources.html>
- Norsk Polarinstitut
<http://www.npolar.no/no/>
- Polar Science Center, University of Washington
<http://psc.apl.washington.edu/>
- Scott Polar Research Institute
<http://www.spri.cam.ac.uk/>
- World Climate Research Programme (WCRP) Climate and Cryosphere (CliC) Program
<http://www.climate-cryosphere.org/>

1

The Evolution of Knowledge about the Arctic and Its Climate

Overview

The land of the midnight sun has enchanted humankind for centuries. Rarely does a visitor to this unique and storied region leave without impressions that last a lifetime. Whether it is images of immense glaciers, the shifting pack ice under steel-gray skies, the Aurora Borealis, or bountiful wildlife grazing treeless, windswept tundra, the Arctic, even today, evokes images of a largely wild and untamed place. For many, the Arctic is as much a feeling as it is a region. Those with even a passing knowledge of it are familiar with the spirit of adventure – humans against nature – that drove some of the early exploration of the region. But the history of Arctic exploration and discovery is much more than Robert Peary’s glorified, albeit doubtful, conquest of the pole. The expeditions of Vitus Bering, John Franklin, Martin Frobisher, Henry Hudson, Fridjof Nansen, George Nares, Otto Sverdrup, Alfred Wegner, and others variously reflected nationalism, the shifting economic significance of the region, and scientific inquiry. Many of the geographic place names in the Arctic honor these explorers (Figure 1.1). To appreciate our present understanding of the Arctic, we need to step back and review some of this rich history over the past four or five centuries, recognizing, of course, that there have been indigenous populations in the Arctic for thousands of years.

1.1 Historical Exploration

In the sixteenth century, the Arctic came to be seen by the nations of northern Europe as a potential route to China. Three possible routes were considered: directly across

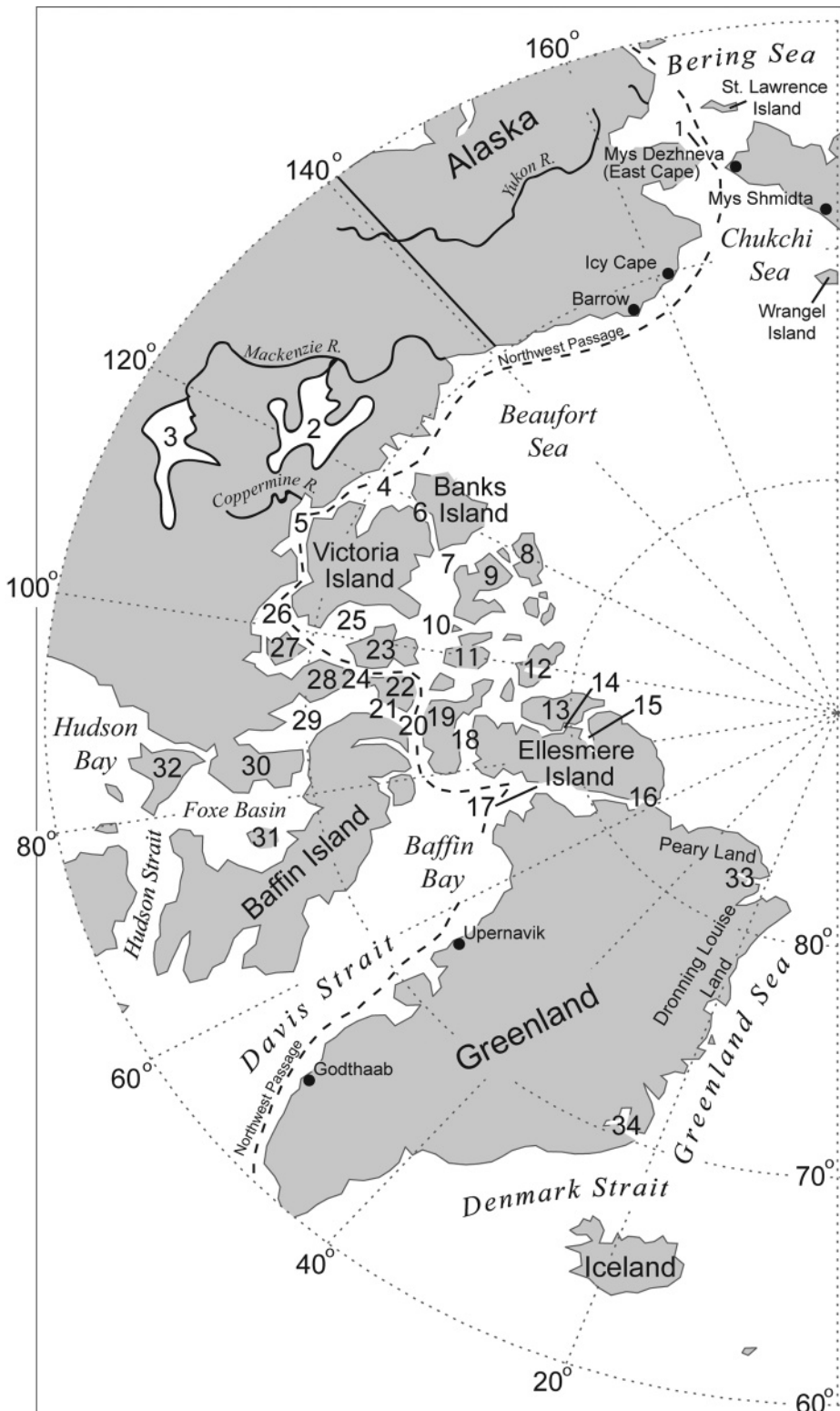
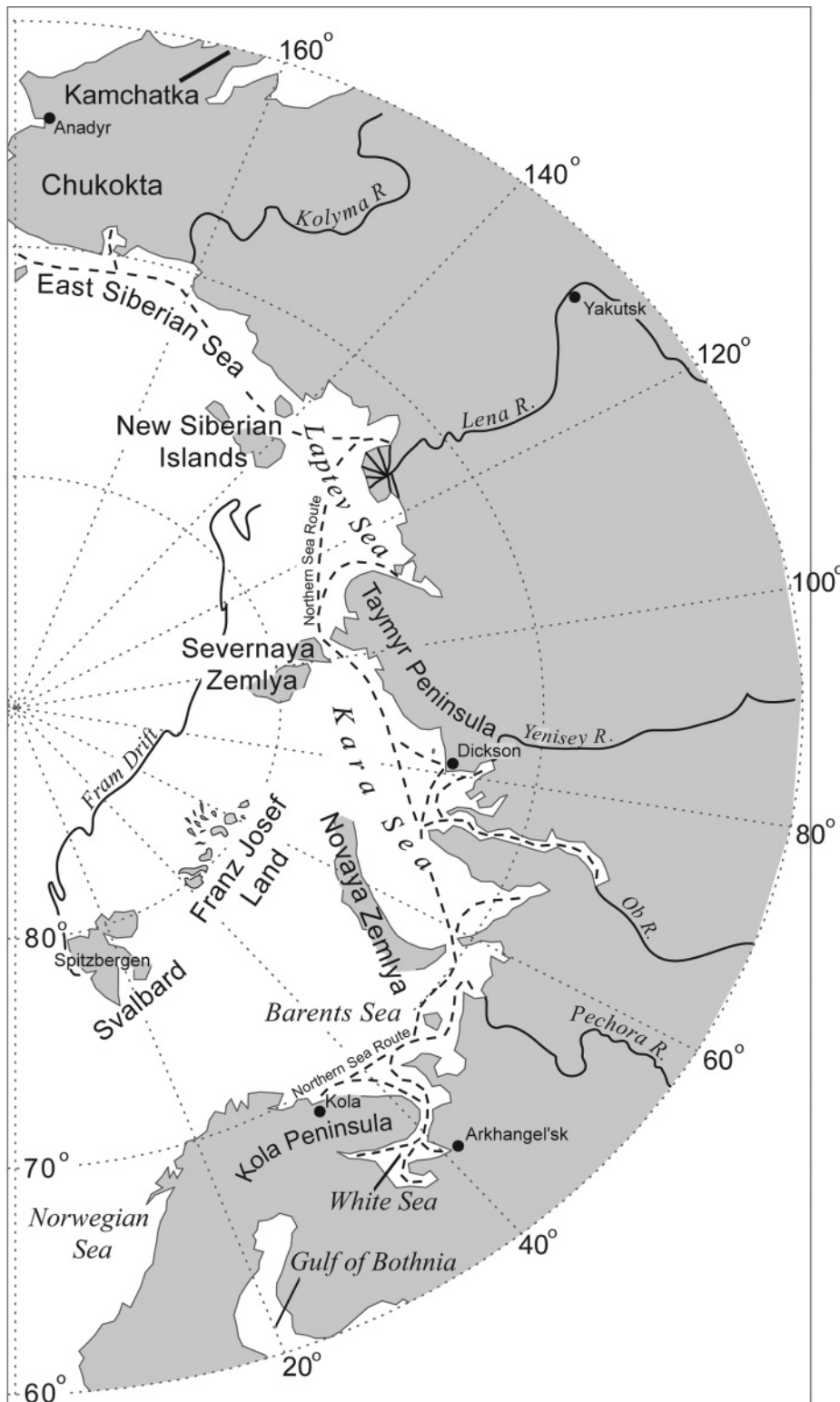


Figure 1.1. Geographic place names of the Arctic with special reference to early exploration of the region. 1. Bering Strait, 2. Great Bear Lake, 3. Great Slave Lake, 4. Admunsen Gulf, 5. Coronation Gulf, 6. Prince of Wales Strait, 7. M'Clure Strait, 8. Prince Patrick Island, 9. Melville Island, 10. Melville Sound, 11. Bathurst Island, 12. Ellef and Admiralty Islands, 13. Axel Heiberg Island, 14. Eureka Sound, 15. Greeley Fiord, 16. Lady Franklin



Bay, 17. Smith Sound, 18. Jones Sound, 19. Devon Island, 20. Lancaster Sound, 21. Prince Regent's Inlet, 22. Somerset Island, 23. Prince of Wales Island, 24. Bellot Strait, 25. M'Clintock Channel, 26. Queen Maud Gulf, 27. King William Island, 28. Boothia Peninsula, 29. Gulf of Boothia, 30. Melville Peninsula, 31. Prince Charles Island, 32. Southampton Island, 33. Independence Fiord, 34. Scoresby Sound (courtesy of M. Lavrakas, NSIDC, Boulder, CO).

the Arctic Ocean, through the Northwest Passage (from the Davis Strait, through the channels of the Canadian Arctic Archipelago, and then along the coast of Alaska), and through the Northeast Passage (along the Eurasian coast, also known as the Northern Sea Route) (Figure 1.1). Although the motives of the explorers and their backers were sometimes complex, the promise of a shortcut to the mythical riches of the Orient deluded European traders and financiers for almost three centuries (Saladin d'Anglure, 1984). Arctic geography, as represented by early cartographers, was a mixture of myth and hypothesis. Most charts identified the northern ocean as the *Mare Glaciale*, or *congelatum* (frozen ocean). Prevailing views ingrained from maps like those drafted by Nicolo Zeno (1558) and Gerhard Mercator (1569 and 1595), arguably hindered the incorporation of observations from early explorers such as Martin Frobisher (1576–1578) and John Davis (1585–1587) (Wallis, 1984).

Knowledge gained from subsequent expeditions complemented reports from fishermen, whale and walrus hunters, traders of the Hudson's Bay and English Muscovy companies, as well as Dutch and Russian merchants in the Northeast Passage (Mirny, 1934; Kirwan, 1962; Armstrong, 1984). According to W. Barr (1991), Russia had a trade route from the White Sea to Western Europe by AD 1500. In the 1550s to 1580s, the English Company of Merchant Adventurers mounted expeditions in search of a Northeast Passage (Mansir, 1989). After Richard Chancellor reached the White Sea in 1553, trading through the Muscovy Company soon followed (Okhuizen, 1995). Europeans soon “discovered” Novaya Zemlya and an open passage to the Kara Sea. The name Novaya Zemlya (“new land”) was already in use by the local coastal inhabitants, although it then referred only to the southern island. Its origin is uncertain, according to Bulatov and Popov (1996).

Between 1565 and 1584, the Dutch White Sea Trading Company under Oliver Brunei established a station on the Kola Peninsula. Traveling overland, Brunei then reached the Ob River. Already by this time Russian fishing vessels were sailing east of the Pechora river into the Kara Sea. During subsequent Dutch expeditions, ships, led by Willem Barents, sailed into an ice-free Kara Sea in 1594. In 1596, they discovered Spitzbergen and sailed along its west coast beyond 80°N. Unfortunately, their ship was beset by ice off Novaya Zemlya and they were obliged to over-winter on the northeast coast at Ice Haven. A group of hardy survivors reached Kola in small boats in the summer of 1597 (De Veer, 1876). The remnants of their hut and possessions were found in 1781.

Henry Hudson also sailed northward to the west of Spitzbergen in 1607, reaching 80.38°N, a latitude that was not exceeded until 1773. In 1609–1610, he discovered and explored Hudson Bay until the crew mutinied and he and a number of others were cast adrift. Despite this setback, the discoveries made by Hudson and his successors led to the establishment of the Hudson's Bay Company in London in 1670. In 1616, William Baffin followed the west coast of Greenland and worked through pack ice to Melville Bay and the entrance to Smith Sound. On his southward voyage, he sighted both Jones Sound and Lancaster Sound opening westward. Regrettably, Baffin's map and tables were discarded by Samuel Purchas, a successor

to the Elizabethan naval chronicler Richard Hakluyt, so that even Baffin Bay did not appear on many English maps of the early nineteenth century.

On the Asian side of the Arctic, Russian traders had explored the Laptev Sea coast by the mid-seventeenth century (Barr, 1991) and reached the Sea of Okhotsk by traveling overland. A Cossack group traveled to the Kolyma River in 1644 and then sailed down it. In 1648, their boats rounded the East Cape (referred to as Mys Dezhneva on Russian charts, after Semyon Dezhnev, a leader of the expedition) reaching the Anadyr River, but these accomplishments were unknown until an account was located in Yakutsk by G. Mueller, during Bering's overland journey to Kamchatka in 1725 (Fisher, 1984). A map of Siberia compiled by the Dutch cartographer N. Witsen (dated 1687) drew on many Russian sources and provided a wealth of detail on western Siberia (Okhuizen, 1995). However, his account of the eastern limit of the Asian coast indicates uncertainty and lack of knowledge of the Cossack expedition. A chart included by Witsen depicted a sea ice limit at about 75°N in the Barents Sea in the year 1676, apparently based on a voyage by an English expedition under John Wood.

Russian exploration of the Arctic began to be nationally organized under Peter the Great. In 1725, Vitus Bering, a native-born navigator in the service of the Russian Navy, was appointed to find a Northeast Passage to the Pacific Ocean. G.F. Mueller was a German working in the new Russian Academy of Sciences established by Peter the Great. In reporting on Dezhnev's explorations in northeast Siberia, Mueller recognized that climatic and ice conditions rendered the Northeast Passage impractical as a trade route. Bering's expedition traveled overland from Yakutsk to the Sea of Okhotsk. Subsequently, he circumnavigated Kamchatka, reaching the Gulf of Anadyr, St. Lawrence Island, and the fog-shrouded Bering Strait (the narrow, shallow channel separating Asia and Alaska). He sailed through the Bering Strait without sighting Alaska, but in 1732, one of his vessels sailed off the coast of Alaska near Nome (Barr, 1991). Between 1733 and 1743, nearly 1,000 men participated in the Great Northern Expedition to explore the possibility of a Northern Sea Route. Their goal was to chart the north coast of Siberia in five sectors: from Archangel'sk to the Ob River, and then east to the Yenisey River, the Taymyr Peninsula, the Lena River, and the Anadyr River. Members of Bering's team included S. Chelyuskin (who reached Asia's most northerly point) K.P. Laptev and D.Y. Laptev. Occasionally, as in 1737, the explorations were favored by mild summer weather, but commonly sea ice and fogs hampered them. Indeed, the severe ice conditions led to the abandonment of interest in the sea route.

Russian mapping of the Asian-Arctic coast was well advanced by the mid-eighteenth century. However, for Europeans and North Americans, the fact that Asia and North America are separated by the Bering Strait was only established later by James Cook. In 1778, Cook sailed into the Chukchi Sea, reaching Mys Shmidtta. This encouraged the Russians to explore Chukotka (eastern Siberia) with land parties in the late eighteenth century. During 1820–1823, surveys were made by F. Anzhu of the New Siberian Islands and by F. Wrangel of the north coast of Chukotka. The

latter also tried unsuccessfully to reach the land offshore (Wrangel Island) that is now named after him.

Knowledge of the North American Arctic lagged far behind that of northern Eurasia. In northwestern Canada, the combined interests of commercial and mining opportunities, as well as company sovereignty, led to land expeditions mounted by the Hudson's Bay Company northwestward from Churchill. Samuel Hearne crossed overland to the Arctic coast at the mouth of the Coppermine River on his third attempt in 1771–1772. The UK Royal Society aided in scientific investigations, and Dymond and Wales (1770) published meteorological observations made at Prince Wales's Port (Churchill), on the coast of Hudson Bay in 1768. Trading posts also kept records of the freeze-up of the ice (Catchpole and Faurer, 1983). In 1789, Alexander Mackenzie, a fur trader, reached the delta of the river named after him, but the rest of the North American Arctic coast remained largely unknown until the 1850s.

In the late eighteenth century, recurring fanciful notions of an open polar sea led to several attempts to sail northward to find it (Wright, 1953). In 1764–1765, M.V. Lomonosov sailed north from Svalbard with little success, and in 1773, C. Phipps made a similar unsuccessful attempt in the same area, using two Royal Navy ships equipped with ice-strengthened bows and bottoms. Phipps's chart shows the location and nature of the marginal ice zone north of Svalbard during July–August 1773 (Savours, 1984). In 1818, John Barrow prepared a chronology of early voyages of discovery. It includes many reports of ships encountering sea ice and icebergs. Barrow (1818) also observed that conditions were generally colder on the eastern as opposed to the western coasts of continents and islands. He accepted the views of Martin Frobisher, John Davis, and others that the central Arctic Ocean was deep and thus ice-free. William Scoresby Jr., a British whaling captain, made regular visits to northern waters in the early nineteenth century. Encouraged by contacts with scientists of the day, he made observations of ocean temperature, meteorological phenomena, atmospheric refraction, ice conditions, and snow crystals (Scoresby, 1820; McConnell, 1986). In one paper he rejected the notion of an open polar sea (Scoresby, 1811–1816). But after encountering much less ice than usual off the east coast of Greenland between 74°N and 80°N in 1817, he suggested that ice-free conditions might recur once every ten or twenty years (Martin, 1988).

Explorations of Otto von Kotzebue in Russian Alaska (1815–1818) and the imperial ukaz (decree) of 1821, claiming the western North American Arctic as Russian, led to concern and objections by the British and U.S. governments. This prompted new explorations of northwest Canada by the British Navy. John Franklin, accompanied by several scientifically trained explorers, made overland journeys from Hudson Bay to the Arctic in 1819–1822 and 1825–1827. The discovery of coal formations and fossiliferous limestone along the Mackenzie River, indicative of warmer past climates, added to nineteenth-century controversy over climatic change. John Richardson reported the existence of permanently frozen ground (permafrost) and encouraged the Hudson's Bay Company to begin taking ground temperature measurements. The first results, available in 1841, and similar observations made by

Baer (1838) in Siberia, led to acceptance of the reality of such frozen ground. The Franklin expeditions made meteorological observations at Fort Franklin on Great Bear Lake in 1825–1827 (Franklin, 1828). George Back and Richard King kept records at Fort Reliance on Great Slave Lake during 1833–1835. A compilation of the meteorological observations that were made on thirty-six Arctic expeditions undertaken between 1819 and 1858 are listed in a special report (Meteorological Council, 1879–1888/Part 4 1885). The British Admiralty and Royal Society ensured that John Ross's 1818 expedition to search for the Northwest Passage also carried out geomagnetic, meteorological, and oceanographic observations (Levere, 1993). The first deliberate over-wintering in the Arctic took place at Winter Harbour, Melville Island, during William Parry's first expedition in 1819–1820. Again, observations of magnetic and meteorological conditions were recorded, as well as of wildlife (Parry, 1821). The expedition reached longitude 113.80° W, before being stopped by ice at the entrance to the M'Clure Strait. A decade later, John Ross and his nephew James were forced to over-winter at Felix Harbour on Boothia Peninsula, where they collected meteorological and magnetic data (Ross, 1835).

Russian interest in its Alaskan Territory waned in the 1860s. This was attributable to its remoteness, the small number of settlers, and the control Russia had gained in 1860 of areas on the Pacific coast of northeast Asia, including the site of Vladivostok (Vaughan, 1999). Financial problems finally resulted in its sale to the United States in 1867. The purchase price of \$7.2 million amounted to about two cents per acre. The purchase, initiated by Secretary of State William T. Seward, was criticized in some corners ("Seward's Folly"), but was in hindsight a bargain. Although American whalers were already operating in Alaskan waters and there was some inland exploration, there was little serious scientific interest in Alaska until well into the twentieth century, apart from the International Polar Year station set up at Barrow (Ray, 1885).

Scientific measurements made by the British Navy received careful attention following the publication of an Admiralty Manual (Herschel, 1851). It outlined requirements for observations in the physical and natural sciences, including meteorology and hydrography, to be made at least four times daily, and every two hours during voyages of discovery. Regular meteorological observations and weather reports began in many countries in the 1850s.

In 1848, the first of many searches began for Sir John Franklin and his crew, who had set out in 1845 in the ships *Erebus* and *Terror* to conquer the Northwest Passage but failed to emerge in the Pacific. The searches were in no small part owing to urging of the English Admiralty by Franklin's wife. Clues to the fate of Franklin and his men were finally provided by the discovery of relics and gravesites on Beechey Island, where it appears the crew over-wintered in 1845–1846. While surveying for the Hudson's Bay Company, Dr. John Rae was told by Inuit hunters that the ships had become icebound and that Franklin's men tried to reach safety on foot but had succumbed to cold, some resorting to cannibalism. Victorian English society was repulsed by the suggestion of cannibalism, and Rae was vilified. Studies conducted during the 1980s and onward conclude that crew most likely died from a combination

of starvation, bad weather, scurvy, botulism, and lead poisoning (canned goods at the time were sealed with lead solder, and the ship's water distillation system may have had lead-soldered joints). In a belated vindication of Rae's report, the bones of some of the crew discovered on King William Island were found to bear distinct blade cut marks. Franklin's grave remains undiscovered.

During 1850–1855, R. Collinson and R. M'Clure searched Amundsen Gulf, Coronation Gulf, Victoria Island, and Banks Island, confirming the existence of a Northwest Passage via Melville Sound, reached thirty years earlier by Parry. These expeditions also made numerous scientific observations (Meteorological Council, 1879–1888; Levere, 1993). C. Schott, for example, analyzed the records of McClintock (1862) in Baffin Bay and Prince Regent's Inlet. An American expedition led by Elisha Kane searched the West Coast of Greenland northward to Smith Sound during 1853–1855. Weather records were maintained at 78.62°N, 70.67°W from September 1853 through April 1855 (Kane, 1856). The book also includes monthly mean isotherm charts for Baffin Bay prepared by C. Schott using Kane's observations and earlier charts of H. Dove. Kane also espoused the recurring notion of an open polar sea, perhaps based on his observations of the North Water polynya in Smith Sound (Dunbar and Dunbar, 1972).

In 1822, William Scoresby, Jr. followed the east coast of Greenland from 72°N southward to 69°N, while his father explored the extensive sound named after him. In 1820–1830, W. Graah of the Royal Danish Navy traveled northward along the East Coast to 65°N using native boats (umiaks). However, he was stopped by heavy ice. East Greenland was then neglected until 1869 when Karl Koldewey in the *Germania* over-wintered at Pendulum Island (74.5°N). The next spring they reached 77°N on a sledging trip. Between 1879 and 1900, Danish Navy expeditions completed mapping of the East Coast of Greenland and studied the ice conditions (Ryder, 1896).

The margins of the Greenland Ice Sheet were visited once or twice in the eighteenth century, but no serious attempt to visit the interior was made until Nordenskiold traveled inland near Godthaab in 1870. Soon after, Norwegian and Danish geologists observed high rates of glacier motion compared with glaciers in the Alps, arousing scientific interest. Nordenskiold made another unsuccessful attempt to cross Greenland in 1883. Finally, in 1888, Nansen, Sverdrup, and four companions skied and sledged westward across the ice at about latitude 64°N, eventually reaching Godthaab. In 1892, Robert Peary traveled northeastward from Smith Sound, crossing the northern part of the ice sheet and finding ice-free Peary Land. He also reached the head of Independence Fiord and wrongly concluded that he was at the shore of the East Greenland Sea. This incorrect conclusion had tragic consequences for members of a subsequent Danish expedition in 1906.

In the 1860s and 1870s, Arctic exploration was dominated by attempts to reach the pole. Among notable expeditions are those of Charles Hall who explored Baffin Island and Melville Peninsula. In 1871, he took the steamer *Polaris* up Smith Sound to 82.18°N and explored ice-free North Greenland. Hall's work in Ellesmere Island was followed by the British Arctic Expedition of 1875–1876 under George

Nares. In the vessel *Alert* he rounded the north tip of Ellesmere Island, halting at Floeberg Beach (82.27°N) as the sea began to freeze. The name “floeberg” refers to ice blocks rafted up onto the beach by onshore winds (Gadbois and Laverdiere, 1954). Sledging trips conducted in the spring over the hummocked and ridged sea ice demonstrated the fallacy of the open polar sea. Indeed, the expedition coined the phrase “paleocrystic sea” (Levere, 1993).

Robert Peary’s claim to have attained the Pole across this irregular and chaotic sea ice surface with Matthew Henson in April 1909 remains in doubt. While some historians are of the view that he either did reach the pole or honestly thought that he had, others feel that he deliberately exaggerated his accomplishments. Issues contributing to doubt include the lack of clear documentation of navigation and the implausible travel speed claimed during the last part of the journey. The first undisputed attainment of the pole was by Roald Amundsen in 1926, the explorer who is perhaps better known for reaching the South Pole in 1911.

During 1898–1902, Otto Sverdrup in the *Fram*, accompanied by cartographer Lt. Isachsen, made discoveries of new land in the northwestern part of the Canadian Arctic Archipelago by sailing along Jones Sound and then traveling overland. Axel Heiberg Island, Ellef Ringnes and Amund Ringnes islands, Eureka Sound, and Greely Fiord were all added to the map. Henrik Mohn (1907) summarized the meteorological observations from the expedition. In 1903, Amundsen (Figure 1.2) sailed the *Gjøa* from Norway into Lancaster Sound. After spending two winters near King William Island, he reached the Mackenzie delta in August 1905, finally achieving the Northwest Passage. The remaining blank spaces on the maps of the Canadian Arctic Archipelago were now being filled in. In 1914, the American “Crocker Land” Expedition led by Donald MacMillan showed that Peary’s “Crocker Land” northwest of Ellesmere Island was an illusion. Apparently, Peary was confused by the towering effect of a superior mirage (fata morgana). Oddly, a Rand McNally Atlas from the late 1940s owned by the first author of the present volume shows Crocker Land as a mapped feature.

Vilhjalmar Stefansson’s Canadian Arctic Expedition of 1913–1918 focused on the Beaufort Sea, Banks Island, Prince Patrick, and Borden and Meighen islands in the northwest of the Canadian Arctic Archipelago. This added considerably to the known extent of Canadian territory. The mapping of northeast Greenland was completed by the Danmark Expedition in 1906–1908, with surveyor J.P. Koch and Alfred Wegener, and by the Thule Expeditions led by K. Rasmussen in 1912 and 1916–1917. A notable discovery was the mountainous ice-free (nunatak) region of Dronning Louise Land (ca. $76.0\text{--}77.3^{\circ}\text{N}$, $23\text{--}26^{\circ}\text{W}$) inland from the coast near modern Dansmarkhavn. In 1913, Koch and Wegener set out from there to cross the widest part of the ice sheet, barely making it to Upernivik on the west coast.

A new scientific direction in the exploration of the Arctic Ocean began with the voyages of the *Tegetthoff* in the Eurasian Arctic in 1871 and 1872–1874. Pursuing a suggestion of the German geographer August Petermann that the northeastward flow of warm Atlantic water might reduce the ice cover in the eastern Arctic, two Austrian scientists, Lt. Karl Weyprecht and Lt. J. Payer, found little ice off Novaya



Figure 1.2. Roald Amundsen, the first to conquer the Northwest Passage (and the first to reach the South Pole) (From “The South Pole”, Volume II, Library Call Number M82.1/99 A529s., libr0351, Treasures of the NOAA Library Collection, by Mr. Steve Nicklas, NOS, NGS).

Zemlya in 1871. The following year, they were less fortunate and the ship drifted northwestward in the ice. In August 1873, they discovered Franz Josef Land and were obliged to over-winter. The ship was abandoned and they were rescued in a small boat off Novaya Zemlya in August 1874. They advanced a new hypothesis that Franz Josef Land pointed to a landmass over the North Pole. This same idea led Lt. George De Long to explore the East Siberian Sea in the vicinity of Wrangel Island. However, his ship, the *Jeanette*, became trapped in the ice in September 1879 and drifted northwestward before being crushed north of the New Siberian Islands in June 1881. Only three members of the crew survived. Three years later a remarkable find was made of some wreckage from the *Jeanette* on the southwest coast of Greenland. Professor Henrik Mohn proposed that the Arctic ice, drifting under the influence of winds and ocean currents, must have transported them. Nils Nordenskiold finally conquered the Northeast Passage in 1878–1879. The steam-powered *Vega* became beset in late September off the North Cape and could not proceed into the Bering Strait until July 20, 1879. Nevertheless, the feasibility of the Northern Sea Route had been established.

The first polar icebreaker, the *Yermak*, was built for the Russian navy in Newcastle, England in 1898. After sustaining some damage in heavy ice off Svalbard in 1899, it was operated mainly in the Baltic Sea (Barr, 1991). Two small icebreakers were

built to facilitate the survey of the Siberian coast by the Russian Arctic Ocean Hydrographic Expedition during 1910–1915. In 1913, the surprising discovery was made of the Severnaya Zemlya archipelago, which was not mapped until 1930–1932 by G.A. Ushakov (Vaughan, 1999). In the 1920s, following the Russian Bolshevik Revolution, the Kara Sea began to be exploited by cargo ships supported by ice-breakers. This accelerated in 1932 after the formation of the Northern Sea Route Directorate, which also took over administration of the Russian Arctic islands and the Asiatic part of the Soviet Union north of 62°N (Gakkel and Chernenko, 1959; Belov, 1969; Armstrong, 1952, 1995).

1.2 The Beginning of Systematic Observations

The modern basis of Arctic science, and meteorology in particular, was the outcome of Karl Weypricht's suggestion for an International Polar Expedition. Planning began at a conference in Hamburg in 1879, with eleven nations pledging support. Weyprecht died in 1881, but the First International Polar Year (IPY) was mounted in 1882–1883. Barr (1985) provides a detailed account of the various national expeditions. Figure 1.3 shows the distribution of the twelve principal stations established in the North Polar Region. Unfortunately, the Dutch expedition bound for Dikson at the mouth of the Yenisey River became beset by ice in the Kara Sea. An auxiliary program of observations, supervised by the physicist K.R. Koch (1891) was carried out at six Moravian Mission stations along the Labrador coast. Important contributions to polar science were made during the IPY (e.g. Dawson, 1886; von Neumayer and Boergen, 1886), but the widely spaced stations made it hard to use the data for meteorological studies. Moreover, the drama of Adolphus Greely's tragic expedition to Lady Franklin Bay, Ellesmere Island, and his expedition's "farthest north" (83.40°N on the North Greenland coast) tended to overshadow the IPY's scientific achievements. After relief ships had failed to reach his camp at Ft. Conger, Greely followed strict orders to retreat down the coast. Winter overtook his party. Of twenty-six men, only seven (including Greely) lived to see the relief ship in June 1884. Some of the meteorological records nevertheless survived (Greely, 1896).

The drift of the Norwegian vessel *Fram* across the Arctic Ocean from the New Siberian Islands to Spitzbergen was a bold new direction in Arctic exploration. The discovery on the coasts of Greenland of wreckage from the *Jeanette* and finds of Siberian driftwood, gave Fridtjof Nansen (Figure 1.4) the idea of utilizing the drift of the *Fram*. Despite widespread criticism by leading polar explorers, his views were vindicated and the successful voyage represented a major advance in knowledge of ice motion and Arctic Ocean circulation. Instead of being crushed, the specially designed vessel was lifted up by the ice and, in this way, drifted with the ice for most of its journey, September 1893 through August 1896 (Nansen, 1898). Mohn (1905) published the meteorological results of the expedition, and these data are now included on a CD-ROM (Arctic Climatology Project, 2000). Nansen and H. Johansen left the ship on March 14, 1895 and traveled over the ice to 86.23° N

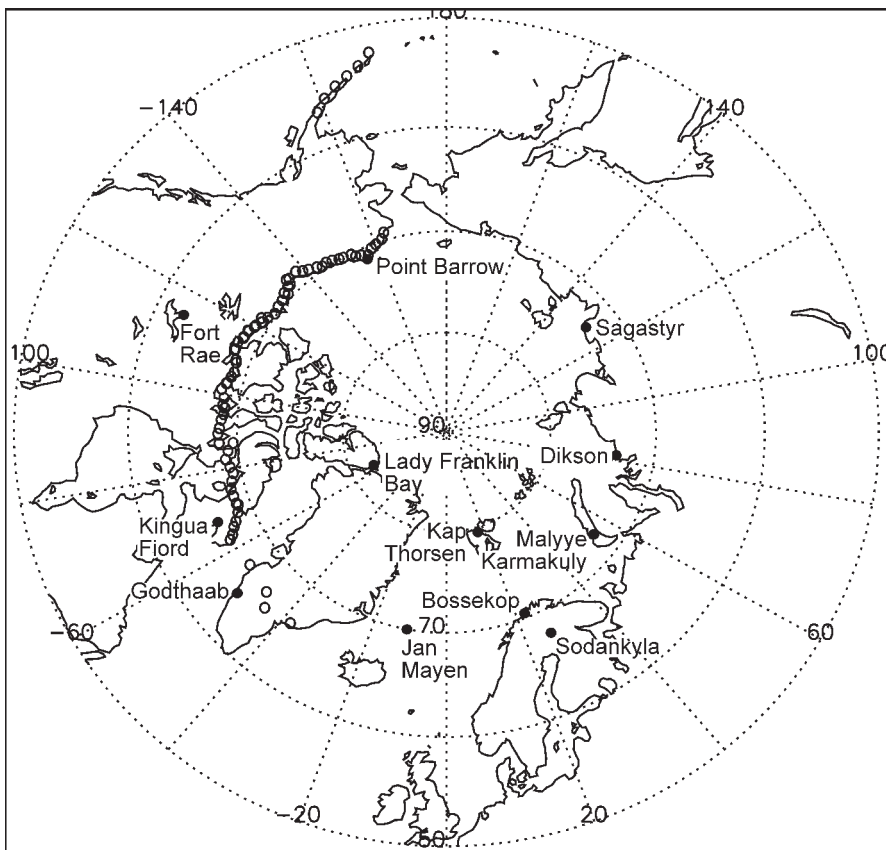


Figure 1.3. Distribution of the 12 principal stations established during the first International Polar Year (IPY) (solid circles) and the Defense Early Warning Line (DEWLINE) stations (open circles). The DEWLINE network was installed during 1957–1959. Weather records were collected for more than 30 years (courtesy of M. Lavrakas, NSIDC, Boulder, CO).

before being forced to head south to Franz Josef Land. Meteorological observations were made in Franz Josef Land by the Ziegler expedition of 1903–1905 (Fleming, 1907).

Icebergs in the Labrador Current became a major concern for shipping after the sinking of the *Titanic* in 1912. As a result, the International Ice Patrol Service was established to document and count icebergs drifting southward. Oceanographic and sea ice conditions in the Davis Strait and the Labrador Sea were also first studied in detail by U.S. Coast Guard expeditions between 1928 and 1935 (Smith, Soule, and Mosby, 1937).

The 1910s and 1920s witnessed the advent of Arctic exploration by aircraft and airship. Regular airborne reconnaissance of ice conditions in the Kara Sea began in the Soviet Union in 1924. This was later extended to the entire Russian Arctic for mapping sea ice conditions (Borodachev and Shil'nikov, 2002). Important oceanographic and meteorological observations were collected by the *Maud* Expedition

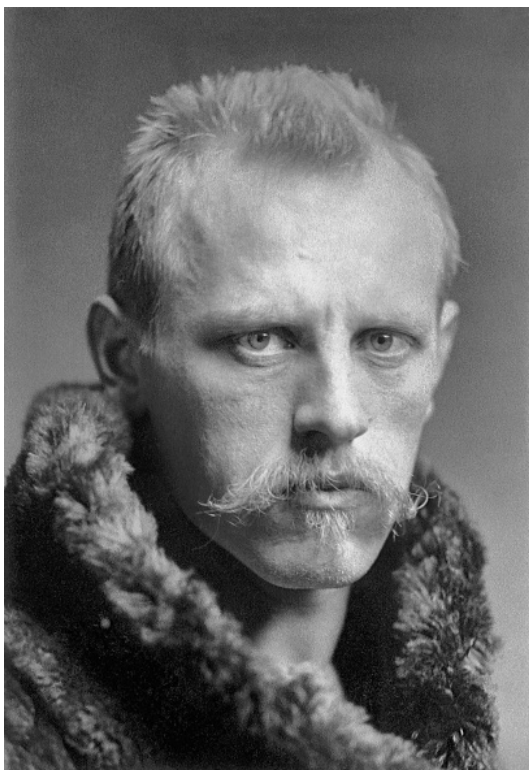


Figure 1.4. Fridjof Nansen (George Grantham Bain Collection, Library of Congress).

(1918–1925) under Harald Sverdrup. Meteorological data from the *Maud* are readily available (Arctic Climatology Project, 2000). The first serious attempt to explore the Arctic Ocean beneath the sea ice was made by Sir Hubert Wilkins and H. Sverdrup in 1931. They reached 82.25°N, north of Spitzbergen, before storms and damage to the primitive diving equipment forced their return.

In the 1930s, meteorological studies were carried out on the Greenland Ice Sheet. In support of their work, the British Arctic Air Route Expedition led by Gino Watkins (1932) had two aircraft equipped for ice or water landings. An ice cap weather station (67.1°N, 41.8°W, 2,440 m) was manned from September 1930 to May 1931 (Mirrless, 1934). Because of blizzards and supply problems, A. Courtauld operated the station on his own from December to March and he was trapped inside the shelter from late March until the beginning of May 1931. At the same time, a German expedition under Alfred Wegener, established the station Eismitte (70.9°N, 40.7°W, 3,000 m) near the crest of the ice sheet. The records were analyzed and interpreted by F. Loewe (1936), who supervised the measurements. Ice thickness measurements suggested for the first time that the bedrock of Greenland was a saucer-shaped depression.

A Second International Polar Year was conducted in 1932–1933, fifty years after the first, with ninety-four Arctic meteorological stations in operation (Laursen, 1959). However, World War II prevented much of the data from being published and

fully analyzed. The plan to archive the data at the Danish Meteorological Institute was apparently never fulfilled, although the synoptic maps were finally completed in London in 1950 (Laursen, 1982). In the summer of 1932, the Russian icebreaker *Sibiryakov* completed the Northern Sea Route from Arkhangelsk to the Far East in a single season (Barr, 1978). Another major prewar milestone was the establishment by aircraft of the *North Pole 1* station under Ivan Papanin. This was the first of the Soviet Union's Arctic Ocean drifting stations (the North Pole Drifting Station program). Utilizing the experiences of Long, Nansen, and the scientists from the *Chelyuskin*, which sank in the Chukchi Sea in February 1934, the four-man ice camp drifted from 89.4°N, 78.7°E in May 1937 to 70°N, 20°E in February 1938, carrying out meteorological and oceanographic measurements. Also during 1937–1939, there was an unplanned drift of the icebreaker *Georgy Sedov* after becoming beset in the northern Laptev Sea. The *Georgy Sedov* drifted for 812 days in a more northerly trajectory than that taken by the *Fram*.

One of the last epic "firsts" was the two-way completion of the Northwest Passage by the tiny Royal Canadian Mounted Police vessel *St. Roch*. The vessel sailed east–west via the Bellot Strait between the Boothia Peninsula and Somerset Island during 1940–1942 and west–east via the Prince of Wales Strait, Melville Sound, and Lancaster Sound in the summer of 1944. A demonstration of commercial possibilities for the passage was made by the transits of the nuclear-powered U.S. tanker *Manhattan* in 1969 and 1970, but regular commercial usage of the passage is still unrealized.

1.3 The Modern Era

World War II demonstrated the strategic importance of the Arctic seas, Greenland, and Alaska. Germany established a number of clandestine weather stations in Spitzbergen and East Greenland during 1940–1945 (Blyth, 1951; Selinger and Glen, 1983), and the U.S.A. established air bases in West Greenland. Strategic concerns were reinforced with the advent of the Cold War. Between 1947 and 1950, the Canadian and U.S. governments established five weather stations in the Canadian Arctic Archipelago and the network was further enhanced by the opening of the chain of Distant Early Warning Line (DEWLINE) stations from the Davis Strait to northern Alaska in 1957 (Figure 1.3). The DEWLINE was intended to give early warning of a nuclear attack by the Soviet Union via strategic bombers (the shortest route to North America is across the Arctic Ocean). The Soviet Union resumed the North Pole drifting station program in 1950, with the North Pole (NP) 2 station. The NP program operated continuously until July 1991, ending with station NP-31 (Romanov, Konstantinov, and Kornilov, 2000). It resumed during 2003–2004 with NP-32 and NP-33. NP-39 was established in October 2011. The next in the series, NP-40, was evacuated in June 2013 because of break up of the ice floe that it was located on. The meteorological data from the NP 1–31 stations, U.S. drifting stations (Sater, 1968), and other Soviet era Arctic data are assembled on CD-ROMs

(NSIDC, 1996; Arctic Climatology Project, 2000) that continue to be widely used. The U.S. Air Force established the ice island station T-3 in March 1952 through the initiative of J. Fletcher. L. Koenig and his colleagues (1952) recognized ice islands such as T-3 as fragments that break off the Ward Hunt ice shelf of northern Ellesmere Island (Hattersley-Smith, Crary, and Christie, 1955). These may circulate for many years in the Beaufort Sea gyre (Montgomery, 1952). Most of the Russian NP stations have been on thick ice floes rather than ice islands such as T-3.

There were new glaciological and meteorological expeditions on the Greenland Ice Sheet. Notable ones include the 1948–1951 Expeditions Polaires Francaises led by P.E. Victor in southern and central Greenland and the British North Greenland Expedition of 1952–1954. The former expedition operated Station Centrale at 70.9°N, 40.6°W (2993 m) during 1949–1950 near the site of Eismitte, while the latter established Northice at 78.1°N, 38.5°W (2343 m). Also, the Arctic Institute of North America sponsored studies on the Barnes and Penny ice caps of Baffin Island in the early 1950s (Orvig, 1954).

Following World War II, it was decided to hold an International Geophysical Year, July 1957 to December 1958. Considerable emphasis was put on Antarctic observations that had not previously been possible, but some specific programs were carried out in the Arctic. For example, McGill University operated the first station in the interior of the Canadian Arctic Archipelago at Lake Hazen, Ellesmere Island (Jackson, 1959a). Soviet scientific expeditions were mounted to study the glacial meteorology of the ice caps of Franz Josef Land (Krenke, 1961).

In the mid-1970s, the Defense Research Board of Canada supported further work on Ellesmere Island (Hattersley-Smith, 1974). Exploration for oil and gas off the north coast of Alaska led to intensive studies of the near-shore marine environment. The Offshore Continental Shelf Environmental Assessment Project resulted in numerous publications which added much to our knowledge of near-shore sea ice, ocean, and climate conditions. The British Trans-Arctic Expedition of 1968–1969 led by Wally Herbert, with glaciologist Roy (Fritz) Koerner, provided valuable information on Arctic Ocean ice conditions (Koerner, 1970).

The first submarine transect under the Arctic sea ice cover, from north of Alaska, along longitude 155°W to the Pole, and then to the Fram Strait, was carried out in August 1958 by the U.S. nuclear submarine *Nautilus*. It was in large part a display of Cold-War power. A repeat cruise was undertaken by the *USS Queenfish* in August 1970, but the detailed sonar data on sea ice drafts from the two cruises were not available to the scientific community until 1986, when they were analyzed for a doctoral dissertation by A.S. McLaren (1989), former commander of the *Queenfish*. The first submarine to surface at the North Pole was the *USS Skate* in 1959.

The Submarine Arctic Science Program, SCICEX, was launched in 1994. SCICEX is a federal interagency collaboration among the U.S. Navy, research agencies, and the marine research community to use nuclear-powered submarines for scientific studies of the Arctic Ocean. After a test voyage in 1993, in which civilian scientists joined Navy personnel, five dedicated science cruises took place between 1995 and 1999. Since then, there have been Science Accommodation Missions, facilitated by

the U.S Arctic Submarine Lab, during which some time is set aside for the collection of unclassified scientific data (e.g., hydrographic and ice thickness data) during otherwise classified missions.

Information on surface air pressure, air temperature, and ice drift in the central Arctic Ocean was greatly augmented by the inauguration in 1979 of the Arctic Ocean Buoy Program by the University of Washington, Seattle. In 1991, this became the International Arctic Buoy Program (IABP) and involves cooperation between many nations. Initially, around twenty buoys were deployed, mainly from airdrops; but in the 1990s, the number rose to more than thirty operating at any time. Data are relayed via satellite in near-real time to the Global Telecommunications System. Newer technologies include drifting buoys that can measure changes in ice thickness (mass balance buoys) and that carry thermistor strings.

Oceanographic data from the IAPB and submarines are complemented by programs maintaining arrays of upward looking moored sonar (to obtain ice draft), moored buoys recording temperature and salinity and other variables across the major Arctic straits, and CTD casts (conductivity, temperature, depth). An example of one of these programs is Arctic–Subarctic Ocean Flux Study (ASOF), an international effort with the objective of measuring and modeling variability in the fluxes of mass, heat, and salt between the Arctic Ocean and the subpolar seas. ASOF itself grew from the VEINS program (Variability of Exchanges in the Northern Seas).

The first deep ice core from the Greenland Ice Sheet was recovered in 1966 from a 1387-meter hole drilled to bedrock at Camp Century (71.2°N , 61.1°W , 1,885 m) (Dansgaard et al., 1971). For many years this provided the primary record of glacial and post-glacial climate through analysis of isotopic composition, trapped air bubbles, and other paleoclimate information. Additional cores were obtained from Greenland and from ice caps in the Canadian Arctic, but major advances in paleoclimate research followed the Greenland Ice Sheet Project 2 (GISP 2) and the European Greenland Ice Core Project (GRIP). Holes drilled between 1989 and 1993 provided more than 3,000 meters of ice core near Summit (72.6°N , 34.6°W) (Hammer et al., 1997). In 1999, U.S. and European agencies installed a new year-round atmospheric observatory at Summit, complementing a chain of automatic weather stations installed in the 1990s around the ice sheet (Steffen, Box, and Abdalati, 1996) and still maintained.

The breakup of the Soviet Union in 1991 dealt a blow to the Arctic research community. Through the 1970s and 1980s, there was continued growth in the network of surface stations in the Soviet Arctic providing information on temperature, precipitation, river discharge, and upper-air conditions. But following the breakup, economic realities forced the closure of many sites, as well as termination of the North Pole drifting station program (which, as discussed, has been reinitiated). Routine aircraft ice reconnaissance flights were also discontinued. In turn, cost-cutting in Canada during the 1990s led to the loss of stations and the replacement of others by automatic systems. Generally speaking, the most complete database of surface observations in the Arctic is for the 1960–1990 period.

In some respects, these losses have been balanced by improved satellite remote sensing capabilities. Routine Arctic coverage began in the early 1970s with the polar-orbiting U.S. Air Force Defense Meteorological Satellite Program (DMSP) system and the National Oceanographic and Atmospheric Administration's (NOAA) Television Infrared Observation Satellite (TIROS), carrying the Very High Resolution Radiometer (VHRR). The visible and infrared channels on these platforms provided for the first useful satellite-based assessments of sea ice extent and concentration and information on synoptic and sub-synoptic cloud systems. The late 1970s saw the first of an ongoing series of TIROS-N systems with the Advanced VHRR (AVHRR) and the TIROS Operational Vertical Spectrometer (TOVS). Data sets of cloud cover, surface radiation fluxes, and sea ice motion derived from AVHRR are finding wide use by the community. TOVS data are assimilated along with profiles from radiosondes (balloon-borne sounding instruments) and other data sources in numerical weather prediction models. Since 1999, as part of the National Aeronautics and Space Administration's (NASA) Earth Observing System (EOS), the Moderate Resolution Imaging Spectro-Radiometer (MODIS), flown on both the Aqua and Terra satellites, has provided high resolution coverage of clouds, snow and sea ice.

The advent of passive microwave sensors on NASA satellites, starting in 1973 with the Electrically Scanning Microwave Radiometer (ESMR), was significant in providing the ability to monitor sea ice conditions throughout the polar night and in the presence of cloud cover (which cannot be done with optical and infrared systems like MODIS). ESMR was superseded by the Scanning Multichannel Microwave Radiometer (SMMR) (launched in 1978), and with the launch of the DMSP F8 satellite in 1987, the first of the Special Sensor Microwave/Imager (SSM/I) series of sensors. With the launch of DMSP F16, SSM/I was superseded in 2005 by the Special Sensor Microwave Imager/Sounder (SSMIS). The combined SMMR, SSM/I and SSMIS records provide daily, continuously updated gridded fields of sea ice extent and concentration spanning more than thirty years. The passive microwave data are also used to assess surface melt over sea ice and ice sheets. Starting in 2002, the Advanced Microwave Sounding Radiometer E (AMSR-E) aboard the NASA Aqua satellite provided ice concentration data at a higher spatial resolution than SSM/I or SSMIS. Although AMSR-E failed in 2011, the Japan Aerospace Exploration Agency successfully launched the AMSR2 instrument in 2012. In the 1990s, European and Japanese research satellites carried synthetic aperture (active) radar (SAR) sensors. These provided high-resolution sea ice data, also with all-weather and polar darkness capability. In November 1995, Canada launched Radarsat, giving routine coverage of most of the Arctic.

From 2003 through 2009, NASA's Ice, Cloud and land Elevation Satellite (ICESat), carrying a laser altimeter system with the ability to detect variations in surface height, provided information on sea ice thickness and (through time changes in height) ice sheet mass balance. ICESat-2, with advanced capabilities, is scheduled for launch in 2017. Operation IceBridge, a series of aircraft missions carrying a suite of sensors, is spanning the gap between ICESat and ICESat-2. CryoSat-2,

a European Space Agency satellite launched in April 2010, uses a radar altimeter system to provide information on ice sea ice thickness and ice sheets. The earlier CryoSat-1 satellite failed to reach orbit. A highly successful NASA mission called GRACE (Gravity Recovery and Climate Experiment), launched in 2002, is making detailed measurements of the earth's gravity field; one of its notable achievements is assessing changes in the mass balance of the earth's ice sheets through time changes in the regional gravity field.

The growth in dedicated Arctic research by the United States and other countries has also helped to offset some of the data losses in Russia and Canada. Starting in the early 1990s, the Arctic System Science (ARCSS) program of the U.S National Science Foundation (NSF) has supported a series of focused projects. These have included Land Atmosphere Ice Interactions (LAII); Ocean/Atmosphere/Ice Interactions (OAI); Paleo-environmental Arctic Studies (PARCS); Human Dimensions of the Arctic System (HARC); the Community-wide Hydrologic Analysis and Modeling Program (CHAMP); Pan-Arctic Cycles, Transitions and Sustainability (PACTS); and the Changing Seasonality in the Arctic System (CSAS). ARCSS has funded large field efforts, such as the Surface Heat Budget of the Arctic Ocean (SHEBA) experiment in 1997–1998 in the Beaufort Sea. In 2000, a “North Pole Environmental Observatory” program was initiated. Properties of the ocean and ice, as well as meteorological and drift characteristics are being observed.

Major international efforts include the ASOF program, the Boreal Ecosystem-Atmosphere Study (BOREAS) and CRYSYS (CRYosphere SYStem in Canada), which developed capabilities to monitor and understand regional and large-scale variations in cryospheric variables of importance to Canada and to improve understanding of the role of the cryosphere in the climate system. The World Climate Research Programme (WCRP) has promoted international coordination of Arctic research through the Global Energy and Water Exchanges project (GEWEX), the Arctic Climate System Study (ACSYS), and its successor, the Climate and Cryosphere (CliC) program. A major activity in 2007–2009 was the Third International Polar Year (IPY) that involved sixty nations and more than 50,000 scientists, students, educators, residents, and support staff. The Third IPY encompassed 228 projects, more than half of them in the Arctic. Main areas of focus were polar ice sheet science, sea ice vulnerability and connections to society, marine ecosystems, marine carbon cycling and ocean acidification, polar atmospheric observations and lower latitude impacts, and terrestrial earth systems and permafrost including carbon reservoirs. A large Canadian IPY effort, the Circumpolar Flaw Lead System Study, involved the research icebreaker CCGS Amundsen being frozen into a flaw lead.

In the late 1990s, NSF launched the Study of Environmental Arctic Change (SEARCH). SEARCH subsequently found support from other U.S. agencies, and had a European counterpart called SEARCH for DAMOCLES (Developing Arctic Modeling and Observing Capabilities for Long-Term Environmental Studies), which ended in 2010. The Arctic Observing Network (AON) is closely linked to SEARCH and represented the major U.S. Arctic contribution to the Third IPY. Many AON projects are still ongoing; a major challenge now being faced is designing and

implementing a sustainable network to monitor and understand emerging changes in the Arctic system.

The Arctic community has greatly benefited from an explosive growth in numerical modeling. The models range widely from single-column models, designed to examine processes such as sea ice growth and melt at a particular site, to regional models of the ice-ocean system, to fully coupled (ice-ocean-atmosphere) global models. Models are being constantly updated and improved in terms of resolution and processes treated. As this book was being written, there was considerable focus on evaluating simulations contained in the Coupled Model Intercomparison Project (CMIP5) archive that were used in the Intergovernmental Panel on Climate Change (IPCC) fifth assessment report. This follows on the heels of CMIP3, which archived output from models used in the fourth IPCC report.

An important area in modeling is data assimilation. Data assimilation can be thought of as an optimal blending of models and observations. It recognizes that both data and models are imperfect, but when blended with appropriate physical constraints, they can provide valuable products. Data assimilation is a central element of numerical weather prediction. Atmospheric reanalyses are a key need in reliable modern Arctic research. Atmosphere reanalyses are retrospective forms of numerical weather prediction in which historical observations (from radiosondes, satellites, aircraft, and other sources) are ingested into a numerical weather model to provide gridded analyses (typically every six hours) spanning many years of atmospheric pressure heights, winds, humidity, and other variables, as well as forecasts of variables such as precipitation. The best known first generation reanalysis is the National Centers for Environmental Prediction/National Center for Atmospheric Research (NCEP/NCAR) reanalysis project (Kalnay et al., 1996) which is still in operation. Outputs based on NCEP/NCAR are available back to 1948. ERA-40 represents a second generation atmospheric reanalysis developed by the European Centre for Medium Range Weather Forecasts (ECMWF). Third-generation atmospheric reanalyses include the NASA Modern Era Retrospective-Analysis for Research and Applications (MERRA) (Rienecker et al., 2011), the National Oceanic and Atmospheric Administration CFSR (Climate Forecast System Reanalysis) (Saha et al., 2010) and ERA-Interim, also referred to as ERA-I (Dee et al., 2011). The Twentieth Century Reanalysis uses surface pressure observations only to construct atmospheric fields as far back as 1871 (Compo et al., 2011).

1.4 The Changing Arctic System

Arctic research over the past two decades has increasingly focused on assessing and understanding major environmental changes unfolding in the region, which encompass the oceans, land, and atmosphere. Whereas Arctic change was largely reserved for the final chapter in the first edition of this textbook, this structure is no longer tenable – change is now such a dominant part of the Arctic Climate System that it now must be addressed throughout the book. Here, we only briefly set the stage.

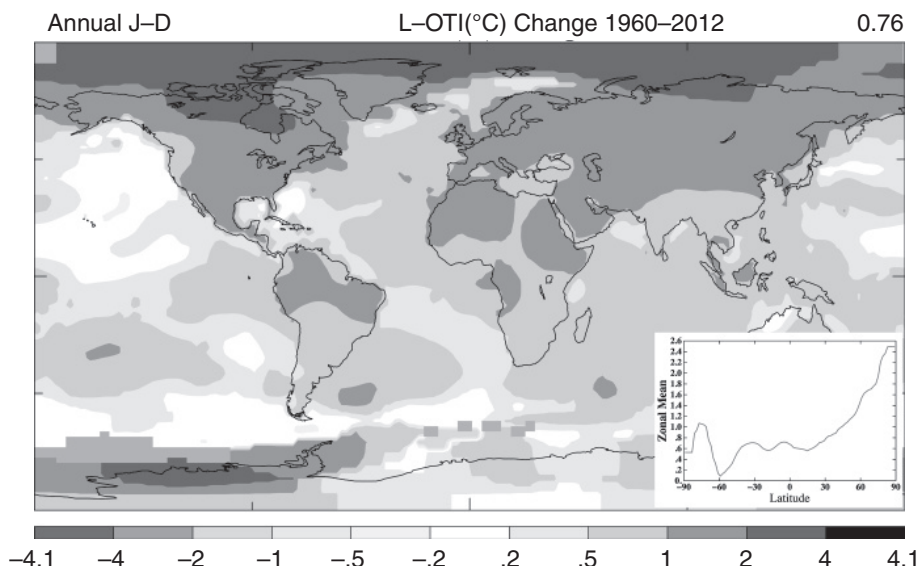


Figure 1.5. Linear trends in annual averages surface air temperature over the 1960–2012 period. The inset shows linear trends averaged by latitude. The larger trends over the Arctic region (Arctic amplification) are obvious (based on the National Aeronautics and Space Administration Goddard Institute for Space Sciences [NASA GISS] temperature analysis) (<http://data.giss.nasa.gov/gistemp>). (See plate section for color version.)

It is well-known that the globe as a whole is warming; the upward trend in surface air temperature over the past fifty years has been especially strong in the Arctic (Figure 1.5), with the strongest trends in autumn and winter. As assessed over the satellite passive microwave record (1979 to present), sea ice extent shows downward linear trends in all months, the largest (12 percent per decade) at the end of the melt season in September (Figure 1.6). The temperature of the intermediate-depth (150–900 m) Atlantic water of the Arctic Ocean has increased in recent decades (Polyakov et al., 2010). Data from marine sediments indicate that the Atlantic inflow is now the warmest of the past 2,000 years (Spielhagen et al., 2011). The mass balance of the Greenland Ice Sheet has shown accelerating mass loss, contributing to sea level rise (e.g., Rignot and Kanagaratnam, 2006; Rignot et al., 2008; Jiang, Dixon, and Wdowinski, 2010; Shepherd et al., 2012). Satellite data show that the extent of seasonal surface melt over the Greenland Ice Sheet is increasing (Tedesco et al., 2010). As a consequence of Arctic warming, growth of alder, willow, and dwarf birch shrubs has increased in northern Alaska over the past fifty years. Satellite-derived vegetation indices also suggest this is occurring in western Canada, Scandinavia, and parts of Russia (Tape, Sturm, and Racine, 2006). As demonstrated by increasing values of the satellite-derived Normalized Difference Vegetation Index (NDVI), which represents the fraction of photosynthetically active radiation absorbed by the plant canopy, the Arctic tundra is greening (Bhatt et al., 2010). Permafrost temperatures that have been monitored since the middle of the twentieth century exhibit a general pattern of warming in Alaska, northwest Canada,

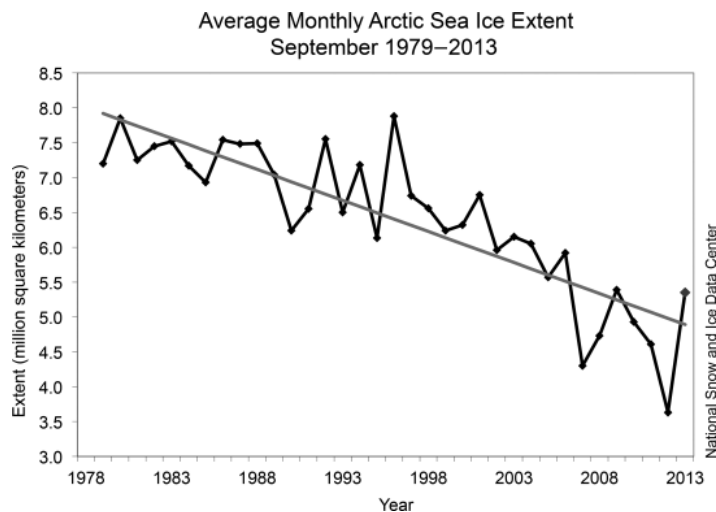


Figure 1.6. Time series and linear trend in September Arctic sea ice extent over the 1979–2013 period (from NSIDC, Boulder, CO). (See plate section for color version.)

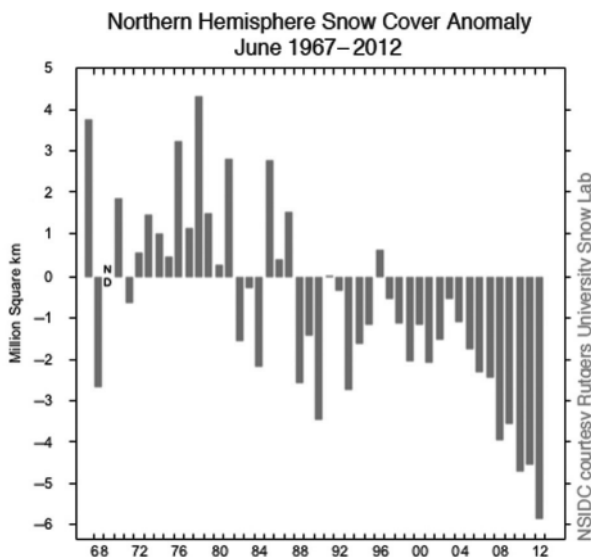


Figure 1.7. Anomalies in satellite-derived snow cover extent for the Northern Hemisphere over the 1967–2012 period (from NSIDC, courtesy Rutgers University Snow Laboratory). (See plate section for color version.)

and Siberia (e.g., Romanovsky et al., 2010a; Romanovsky, Smith, and Christiansen, 2010b), but with large variability from region to region and for different parts of the records. In some areas, permafrost is thawing. Northern Hemisphere snow cover extent is decreasing during May and June (when snow cover is mainly located in the Arctic) (Derkzen and Brown, 2012) (Figure 1.7).

The changing Arctic climate system is leading to countless impacts and human responses (ACIA, 2005). Changing sea ice and snow cover conditions affect the ability of indigenous peoples to hunt marine and land mammals and to herd

reindeer, for example. Shrinking sea ice is increasing marine access to the Arctic Ocean and will enable exploration for oil, gas, and other mineral resources, as well as increased tourism, creating economic benefits but also increasing risks for environmental damage. These changes are accompanied by strategic implications for Canada, Denmark, Norway, Russia, and the United States, in particular. A major concern is to improve maritime infrastructure, including aids to navigation, port facilities, icebreaking escort, ship tracking, oil spill prevention and response, environmental monitoring, and search and rescue capabilities. With regard to navigation, it is important to recognize that only about 10 percent of the Arctic has adequate hydrographic charts.

Where will Arctic research go in the twenty-first century? Given current trends, we will see continued emphasis on better elucidating the role of the Arctic in global climate variability and change, and in elucidating the regional impacts of change within the Arctic. A major lesson learned over the past thirty years or so is that while the Arctic is a major player in global climate, fully understanding its role requires that we come to grips with the intimate couplings between its atmosphere, land, and ocean. Although achieving this goal must draw in part from better synthesis of observations, the community must also capitalize on the growing capabilities of models and satellite remote sensing. An equally fundamental requirement is capturing the interest of bright and inquisitive new minds and bringing them into the field of Arctic climate science. If the present textbook helps in this regard, the authors will consider themselves to have made a contribution.

Focus Questions and Exercises

- 1) How could international collaboration in Arctic research be strengthened?
What are the impediments to collaboration?
- 2) Describe the major issues that may determine whether the Northwest Passage or Northern Sea Route become viable options for commercial ship travel between the Atlantic and Pacific Oceans.
- 3) Why should climate change in the Arctic be of concern to residents of middle latitudes?

2

Physical Characteristics and Basic Climatic Features

Overview

The Arctic climate system is characterized by its low thermal energy state and intimate couplings between the atmosphere, the ocean, and the land. This makes the Arctic a challenging and fascinating region to study. But given the complex nature of the Arctic climate system, where does one start in describing it? The necessary basic foundation is provided in the present chapter through an overview of some of the basic physical characteristics of the Arctic.

The most formal definition of the Arctic is the region north of the Arctic Circle (66.5°N). When defined in this way, its most fundamental characteristic is continuous summer daylight and its absence during the polar night, the duration of each depending on latitude. Figure 2.1 shows the changes in day length with latitude and time of year. For the extreme case of the North pole, the sun is above the horizon for six months between the spring and autumn equinoxes and below the horizon for the remaining six months. In more common usage, the Arctic does not have strict geographical boundaries. Arctic conditions (e.g., extreme winter cold or the presence of permafrost) may be found well south of the Arctic Circle. The terms Arctic and North Polar Region are sometimes used interchangeably.

The geography of the North Polar Region is in striking contrast to its southern counterpart. The Arctic Ocean occupies most of the area north of latitude 70°N . Apart from the sector between 20°E and 20°W , it is almost entirely surrounded by the landmasses of Eurasia and North America. Throughout the year, much of the Arctic Ocean is covered by

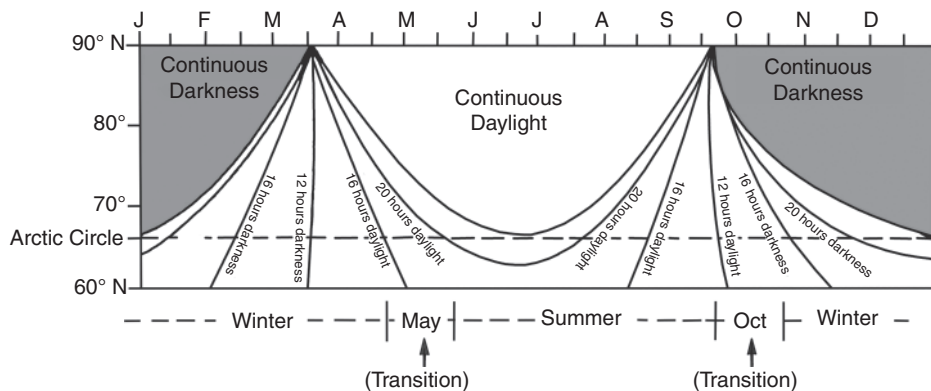


Figure 2.1. Duration of daylight and darkness from 60° to 90° N (from Central Intelligence Agency Polar Regions Atlas, 1978, by permission of United States Government).

floating sea ice. Both the sea ice cover and land areas of the Arctic are snow covered for most of the year. Permanent land ice does not occupy a large area outside of Greenland. Sub-polar ice caps and glaciers are found mainly in the mountainous parts of the Siberian and Canadian archipelagos, and in Svalbard and Iceland. However, most of the lands are underlain by permafrost (perennially frozen ground), some of which is rich in ground ice. Based on broad latitudinal, climatic, and biological characteristics, the Arctic land surface is sometimes broken down into the High Arctic and the Low Arctic. The land surface in the High Arctic is often characterized as polar desert, an extreme form of tundra. In the Low Arctic, the tundra commonly includes shrub vegetation of birch and willow. Large areas are covered by lakes and wetlands.

Surface air temperatures (SATs, approximately 2 m above the surface) exhibit remarkable regional and seasonal variability. January mean SATs of less than -40°C characterize parts of Siberia. Over the central Arctic Ocean, winter temperatures are somewhat moderated by heat fluxes through the ice cover. January mean values of -25°C to -32°C are typical. By sharp contrast, January temperatures around Iceland are near the freezing mark, manifesting the warm, open ocean waters and atmospheric heat transports associated with the North Atlantic cyclone track. During July, mean values over snow-free land surfaces are typically 10°C to 20°C . Over the central Arctic Ocean, the presence of a melting ice surface keeps summer temperatures close to zero. Mean annual precipitation ranges widely, from less than 200 mm over parts of the Canadian Arctic Archipelago to well more than 1,000 mm in parts of the Atlantic sector. Land areas exhibit a general summer precipitation maximum, whereas the Atlantic sector exhibits a cold-season maximum. The Arctic is a very cloudy place. Over the Atlantic sector, there is approximately 80 percent

cloud cover throughout the year. For the central Arctic Ocean, mean summer values of about 80 percent compare to winter values of typically 60 percent. Much of the summer cloud cover comprises low-level stratus.

2.1 The Arctic Ocean

2.1.1 Definition and Bathymetry

The Arctic Ocean covers an area of 14 million km² according to J. Welsh and his colleagues (1986). But definitions of the Arctic Ocean and its various seas have tended to be somewhat imprecise and/or arbitrary. Definition can be important, however, in terms of determining the freshwater runoff from the Arctic lands into the ocean and its effects on ocean salinity. Russian sources commonly divide the Arctic Ocean into several climatic regions. Figure 2.2 provides a breakdown from Russian sources based more on geographic boundaries. In general usage, the term Arctic Ocean would exclude at least the Bering and Greenland Seas, as well as the Labrador Sea and Baffin Bay. The term “central Arctic Ocean” is very common in the literature. A reasonable definition of the central Arctic Ocean is the region north of all land areas that is covered year-round by sea ice (reviewed in the discussion that follows). This is similar to the Russian term *Severnogo Ledovitnogo Okean* (northern ice-covered ocean).

The Arctic Ocean has limited connection to the world oceans (Figure 2.3) and is therefore sometimes referred to as a Mediterranean-type sea. Depths vary greatly. The narrow and shallow Bering Strait (separating Alaska from Russia) connects the Arctic Ocean to the Pacific Ocean. The deeper Greenland and Norwegian seas link it to the North Atlantic Ocean. There are also shallow passageways, with sills 85–140 m deep, through the Canadian Arctic Archipelago to Baffin Bay and the Labrador Sea. The central Arctic Ocean comprises two major deep basins of more than 3,000 m depth – the Amerasian (or Canada) and Eurasian basins, separated by the Lomonosov Ridge.

Off most of North America, the continental shelf is narrow. In sharp contrast, off Eurasia there is a series of broad shallow shelf seas – from west to east, the Barents, Kara, Laptev, East Siberian and Chukchi seas. Almost half of the Arctic Ocean is underlain by continental shelves (Johnson, Pogrebinsky, and Macnab, 1994). Water depths are in the range of 120–230 m in the eastern Kara Sea, but only 20–30 m in the Laptev Sea and the East Siberian Sea (Danilov, 2000).

2.1.2 The Sea Ice Cover

The surface of the Arctic Ocean is characterized by its floating cover of sea ice. The processes of sea ice growth, melt, circulation, and variability are discussed at length in Chapter 7. As will become clear in the next few chapters, the sea ice cover is intimately coupled with the atmospheric energy budget, the atmospheric

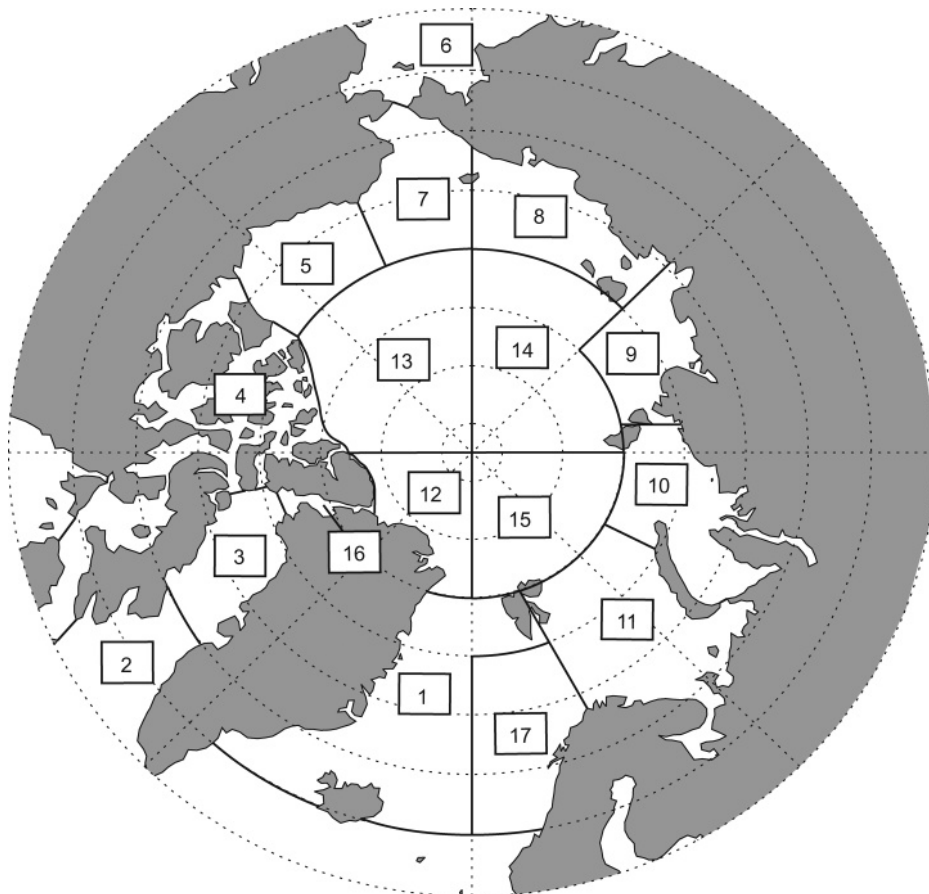


Figure 2.2. Definition of Arctic seas, based on Russian sources (from Welsh et al., 1986). 1. Greenland Sea, 2. Labrador Sea, 3. Baffin Bay, 4. Canadian Arctic Archipelago, 5. Beaufort Sea, 6. Bering Sea, 7. Chukchi Sea, 8. East Siberian Sea, 9. Laptev Sea, 10. Kara Sea, 11. Barents Sea, 12. Greenland Arctic Basin, 13. North American Arctic Basin, 14. Russian Arctic Basin, 15. European Arctic Basin, 16. Kane Basin, 17. Norwegian Sea (from Welsh et al., 1986, by permission of United States Government).

circulation, the surface energy budget and the hydrologic budget. Accordingly, we introduce some basic aspects of sea ice processes and Arctic oceanography here.

The Northern Hemisphere sea ice cover, the bulk of which lies within the Arctic Ocean, ranges in extent from upwards of 15 million km² in March to about a third of that value in September, the end of the melt season. Extent is generally defined as regions with an ice concentration (i.e., a fractional ice cover) of at least 15 percent. There is large variability in extent from year to year, largest in the summer months. As introduced in Chapter 1, analysis of the satellite record (1979 to present) documents negative linear trends in extent for all months, strongest for September. Mean ice extent for March and September, based on the 1979–2001 period, is shown in Figure 2.4. During winter, ice extent in the Arctic Ocean is largely constrained by the surrounding landmasses and in the Greenland, Norwegian, and Barents seas

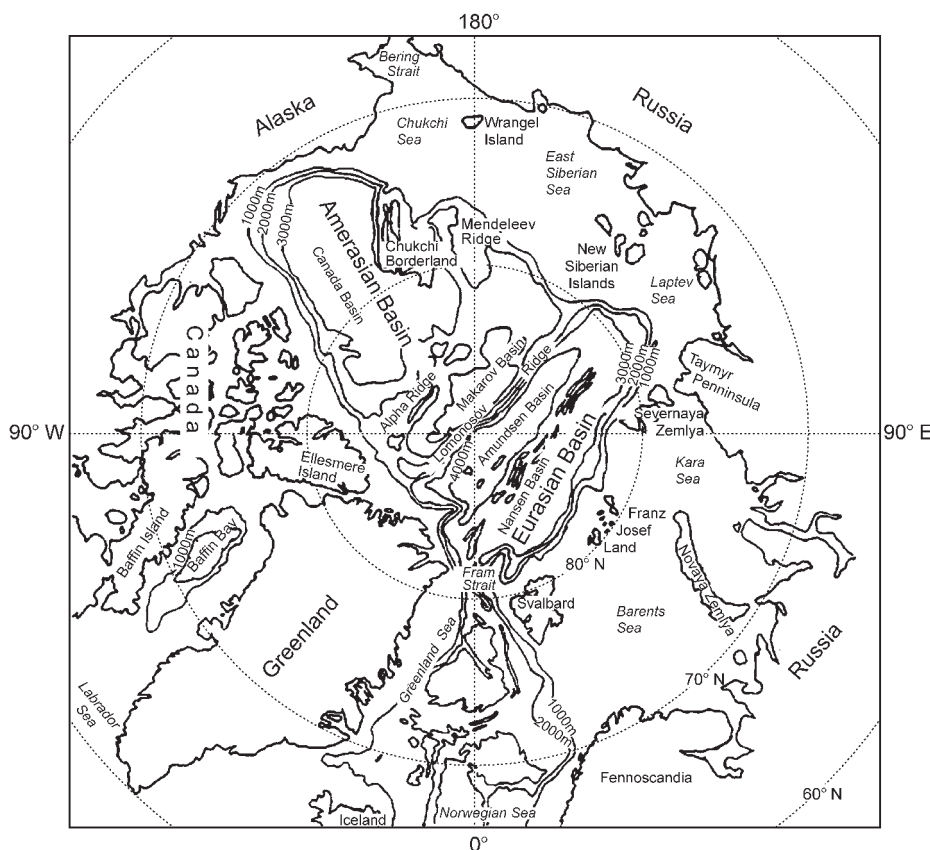


Figure 2.3. Bathymetry of the Arctic Ocean and major geographical features (adapted from Clark and Grantz, 2002, by permission of AGU).

(hereafter termed “the Atlantic sector”) by relatively warm ocean waters that discourage ice formation.

The sea ice cover is not a featureless slab, but consists of individual ice floes ranging from a few meters to many kilometers across. Floes are separated by roughly linear openings, known as leads, and irregularly shaped openings known as polynyas. Typical winter ice concentrations over the central Arctic Ocean are 98–99 percent, compared to 85–95 percent during late summer. During winter, leads generally quickly refreeze to form areas of new, thin ice. Ice concentrations decrease near the sea ice/open ocean margins. Figure 2.5 shows a typical summer sea ice field over the central Arctic Ocean based on MODIS satellite imagery. Figure 2.6 shows another summer scene that captures the transition from sea ice to open ocean waters (termed “the marginal ice zone”). Note how the sea ice margin ranges from rather sharp to very diffuse. The image clearly shows numerous large individual floes, as well as polynyas.

Apart from areas of landfast ice along coasts (ice locked to the shoreline), the sea ice cover is almost constantly in motion. This is because of the influence of wind

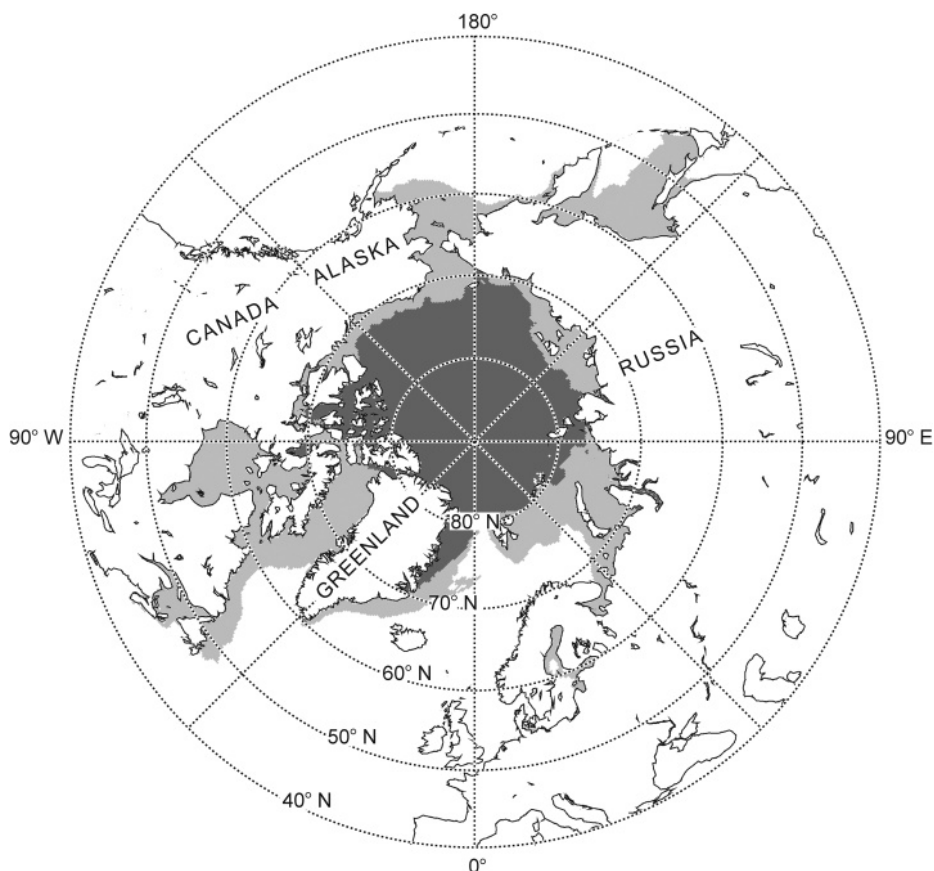


Figure 2.4. Mean sea ice extent for March (all shaded areas) and September (dark shading), based on data from the Special Sensor Microwave/Imager (SSM/I) over the 1979–2001 period. SSM/I has a nominal resolution of 25 km (courtesy of K. Knowles, NSIDC, Boulder, CO).

stress on the upper surface of the sea ice cover, water stress on the lower surface of the ice, floe-to-floe interactions, and ocean tilt (see Chapter 7 for discussion of the sea ice momentum budget). Ice motion varies strongly from day to day, largely in response to variations in the wind field. Leads and polynyas in the pack ice are largely the result of differential ice motion. Divergent (spreading) ice motion acts to reduce the ice concentration; convergent motion increases it. Convergent motion can force one floe to ride over another, a process known as rafting, producing thicker deformed ice characterized by ridges and corresponding underwater keels. Much of the ice cover consists of deformed ice.

Thermodynamic ice growth occurs at the bottom of the ice cover (the ice–interfacce), but melt can occur at both the top and bottom. During autumn, the marginal seas and openings in the pack ice refreeze, forming new ice that thickens during the

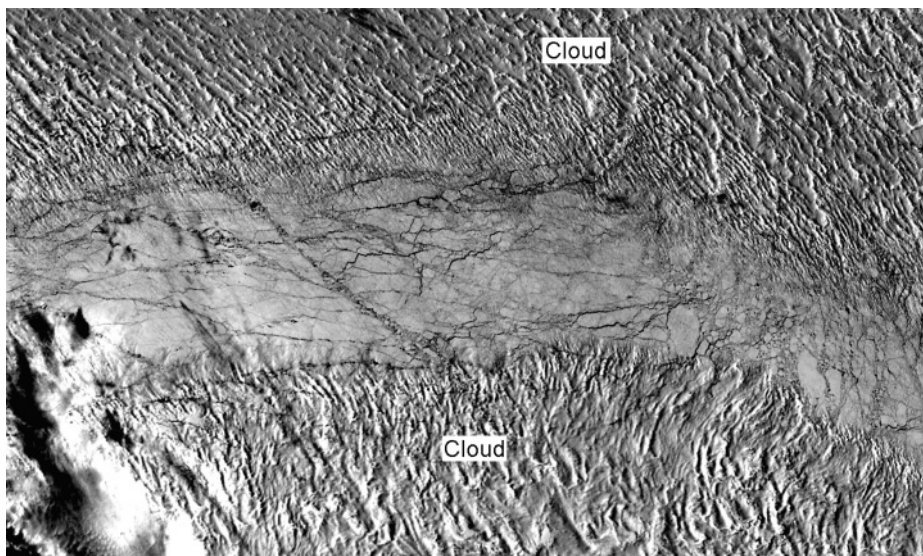


Figure 2.5. Sea ice field for the central Arctic Ocean for July 6, 2001, based on visible-band Moderate Resolution Imaging Spectroradiometer (MODIS) imagery. The horizontal resolution is about 250 m. The image is about 376 km by 226 km. The “strip” in the middle of the image shows a typical configuration of leads in the sea ice cover. At the top and bottom of the image, cloud cover masks the surface, a pervasive problem in the Arctic with respect to visible and infrared-band systems. Passive microwave sensors like SSM/I and SSMIS have all-weather capability and can monitor sea ice conditions during polar darkness, but at a relatively coarse spatial resolution (courtesy of T. Haran, NSIDC, Boulder, CO).

winter to become first-year ice. New ice thickens at a rate of between 3 and 10 cm per day for SATs between about -10°C and -30°C (Maykut, 1986). However, the rate decreases by an order of magnitude as the ice thickens from 10 to 60 cm. The reason is that the thermodynamic growth rate depends strongly on the temperature gradient in the ice – as the ice becomes thicker, the gradient becomes smaller, and it therefore becomes harder to conduct heat upward through the ice. Nearly half of the ice area is accounted for by deformed ice that persists through the summer, becoming second-year ice. If it survives another melt season, it becomes third-year ice, and so on. Any ice two years or older is termed multiyear ice. Ice thicknesses across the Arctic are extremely variable. Undeformed first-year ice at the end of winter ranges from a thin veneer to about 2 m thick. Multiyear ice is typically thicker, averaging perhaps 3.5–4.5 m but sometimes much more; but ridging can also result in very thick first-year ice. In general, the thickest ice is found off the Canadian Arctic Archipelago and northern Greenland (mean values of 6–7 m). Except when very young, sea ice is essentially fresh water – as ice forms, brine is rejected. For first-year ice thicker than 1 m, a salinity of 2–6 psu (dimensionless practical salinity units) is typical. Salinities are considerably lower for multiyear ice.

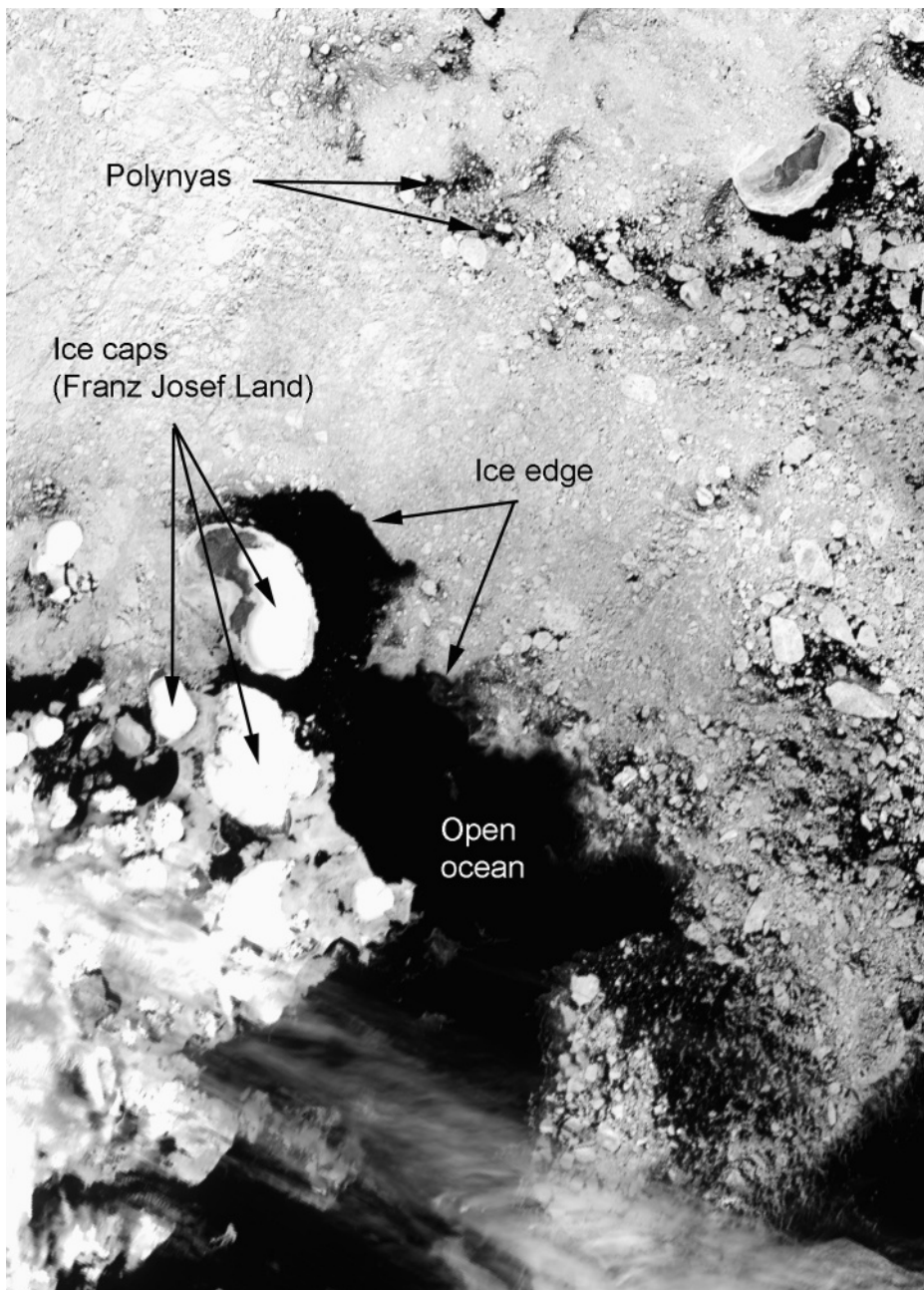


Figure 2.6. Sea ice field in the Barents Sea near Franz Josef Land (see Figure 2.3) for July 6, 2001, based on visible-band Moderate Resolution Imaging Spectroradiometer (MODIS) imagery. The horizontal resolution is about 250 m. The image is about 526 km by 376 km. The scene shows the transition from high ice concentration to open ocean waters (the marginal ice zone). Note the large individual ice floes and polynyas on the right-hand side of the image and the ice caps on the islands of Franz Josef Land (courtesy of T. Haran, NSIDC, Boulder, CO).

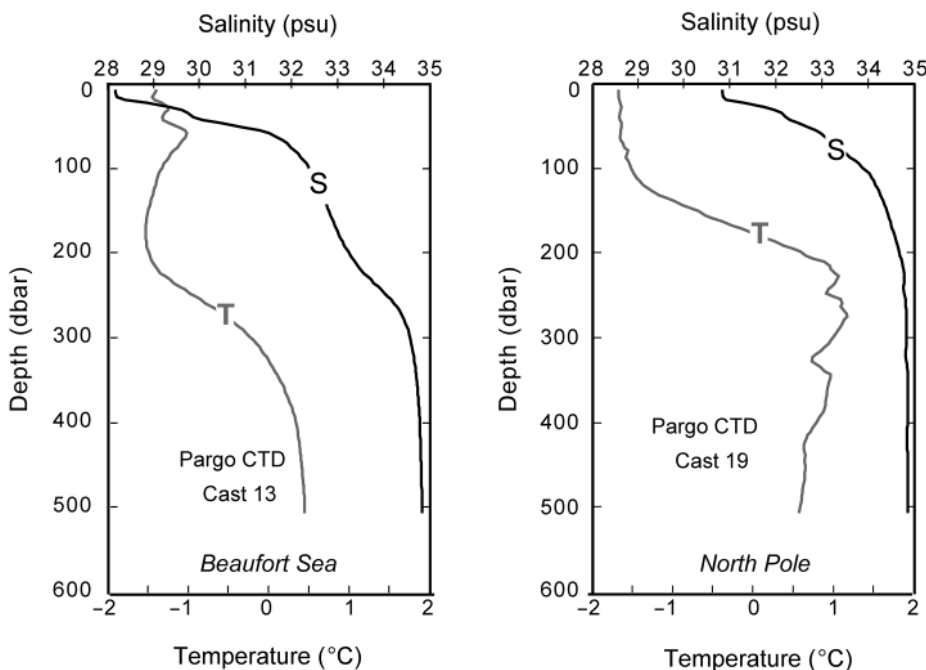


Figure 2.7. Temperature and salinity profiles for the Beaufort Sea and near the North Pole. The y-axis is depth in decibars (dbar), which closely approximates depth in meters (courtesy of J. Morison, Polar Science Center, University of Washington, Seattle, WA).

2.1.3 Physical Oceanography

Figure 2.7 shows typical vertical profiles of temperature and salinity for the Beaufort Sea (north of Alaska, see Figure 2.2) and near the North Pole, collected during the August–September 1993 cruise of the submarine *USS Pargo*. Although the two profiles show some obvious differences, which will be addressed shortly, several common features stand out. Note first the existence of a low salinity surface layer. In these two examples, surface salinities are about 28 psu (Beaufort Sea) and 31 psu (near the Pole). Standard ocean water is around 35 psu. Temperatures in the surface layer are near the salinity-adjusted freezing point (salt in solution depresses the freezing point to below 0°C). The region below the surface layer, extending to about 200–300 m depth is characterized by a rapid increase in salinity. This is attended by an increase in temperature to maximum (and above-freezing) values at around 300–500 m depth. Although temperature falls off at greater water depths, from about 400 m downward (not shown) salinity stays fairly uniform at 34.5–35.0 psu.

The layer of rapid salinity increase is termed a “halocline.” The layer of rapid temperature increase is termed a “thermocline.” Over most of the global ocean, a stable upper-ocean stratification (less dense water at the top) is maintained by higher water temperatures closer to the surface. However, at the low water temperatures found in the Arctic Ocean, the density stratification is determined not by

temperature, but by the vertical profile of salinity – lower salinity means lower density. Consequently, the halocline is associated with a strong increase in density with depth, known as a “pycnocline.” As density increases strongly with depth, the upper Arctic Ocean is very stably stratified, which inhibits vertical mixing. The importance of the strong “cold Arctic halocline” – so-called because of the associated low temperatures – cannot be overstressed. As will be examined further in Chapter 7, the fresh surface layer and limited vertical mixing with the warmer waters below is the key feature of the Arctic Ocean that – along with low winter air temperatures – allows sea ice to form readily.

Maintenance of the fresh, low-density surface layer (and, in turn, the cold Arctic halocline) is in large part determined by river input. The importance of this river inflow is demonstrated by the fact that the Arctic Ocean contains only about 1 percent of the global volume of seawater, yet it receives about 11 percent of the world’s river flow, which peaks in June because of melt of the terrestrial snowpack (see Chapter 6). The Eurasian drainages of the Ob, Yenisey, and Lena, along with the Mackenzie River in Canada, supply two-thirds of the total river discharge. Figure 2.8 gives the boundaries of the Arctic terrestrial drainage and these four major individual watersheds. The Arctic drainage, which extends well into middle latitudes, is defined in the figure as all areas draining into the Arctic Ocean as well as into Hudson Bay, James Bay, the Hudson Strait, the Bering Strait, and the northern Bering Sea. The influence of river inflow is immediately evident in the map of mean surface salinity for summer (Figure 2.9). The freshwater discharged by the major rivers during early summer gives rise to very low salinity values along the Siberian continental shelves and near the Mackenzie delta; this fresh water in turn mixes outward to impact much of the central Arctic Ocean. The contrast with the winter mean surface salinity field when river discharge is small (Figure 2.10) is obvious.

Another contributor to the fresh, low-density surface layer is the influx of relatively low salinity waters from the Pacific Ocean into the Arctic Ocean through the Bering Strait. It is the influence of closer proximity to river runoff and Pacific-derived waters that gives rise to the lower surface salinities in the Beaufort Sea example in Figure 2.7. A further significant contribution to the fresh surface layer is made by net precipitation (precipitation less evaporation) over the Arctic Ocean itself. The salinity of the surface layer is also influenced by the growth and melt of the sea ice cover. As sea ice forms, brine is rejected. Although this brine rejection explains why the sea ice itself is quite fresh, the density of the underlying surface water layer increases as does the depth of vertical mixing. By contrast, as ice melts in summer, the surface layer becomes fresher, and vertical mixing is inhibited.

Understanding the observed vertical ocean structure also requires us to consider the inflow of Atlantic-derived waters. Figure 2.11 is a simple schematic of the mean surface and deep ocean currents in the Arctic Ocean. First, it is necessary to provide a brief word on the surface currents, setting the stage for more detailed investigations in Chapter 7. Immediately obvious is the surface/near surface flow entering the

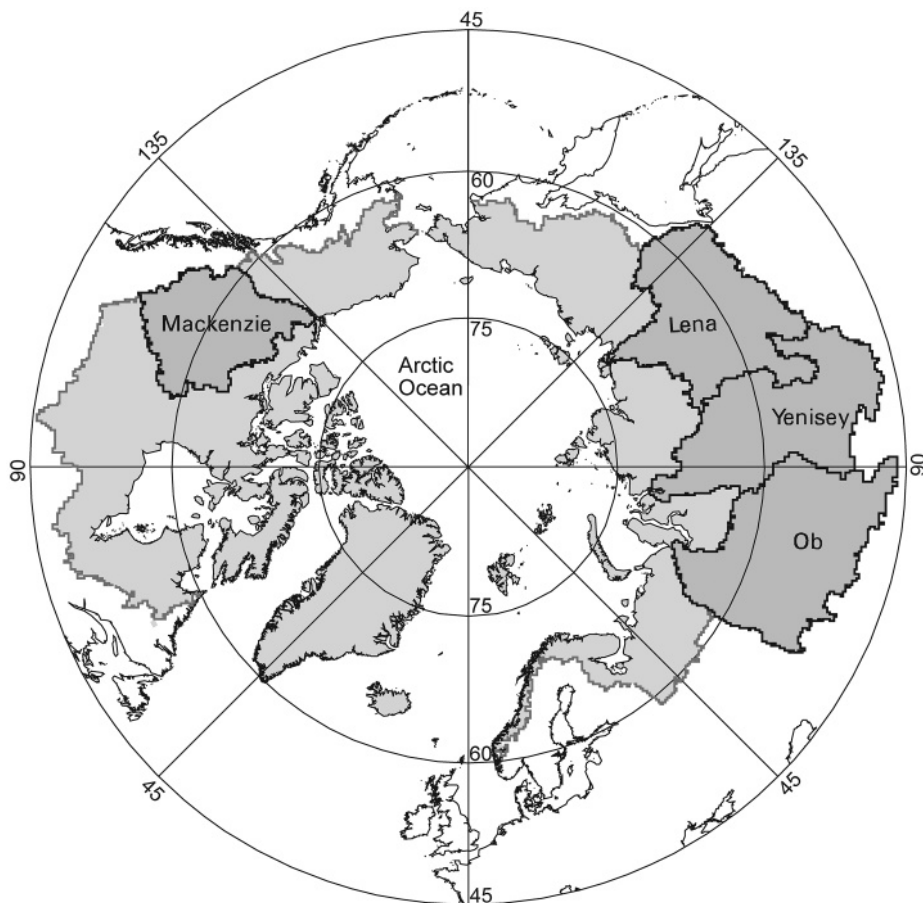


Figure 2.8. The Arctic terrestrial drainage (all shaded regions) and its four largest individual watersheds (darker shading) (courtesy of A. Barrett, NSIDC, Boulder, CO).

Arctic Ocean from the Bering Strait. Note also the clockwise motion of the upper ocean (and hence the overlying sea ice cover) within and north of the Beaufort Sea, known as the Beaufort Gyre, and the motion from the Siberian shelves, across the pole and through the Fram Strait, known as the Transpolar Drift Stream. South of the Fram Strait, this becomes the East Greenland Current, which extends to a considerable depth. The temperature maximum layer at about 300–500 m depth seen in the profiles in Figure 2.7 manifests the inflow of warm Atlantic-derived waters. This Atlantic inflow is provided by two branches, one west of Spitzbergen (the West Spitzbergen Current) and one through the Barents Sea (the Barents Sea Branch). Atlantic water sinks below the Arctic surface layer in the northern Barents Sea. The temperature maximum layer is known as the Atlantic Layer. The stronger temperature maximum in the North Pole example of Figure 2.7 manifests the stronger influence of Atlantic-derived waters in this area. Note also from Figure 2.11 how the deep ocean currents in the Arctic Ocean are closely allied with the bottom topography.

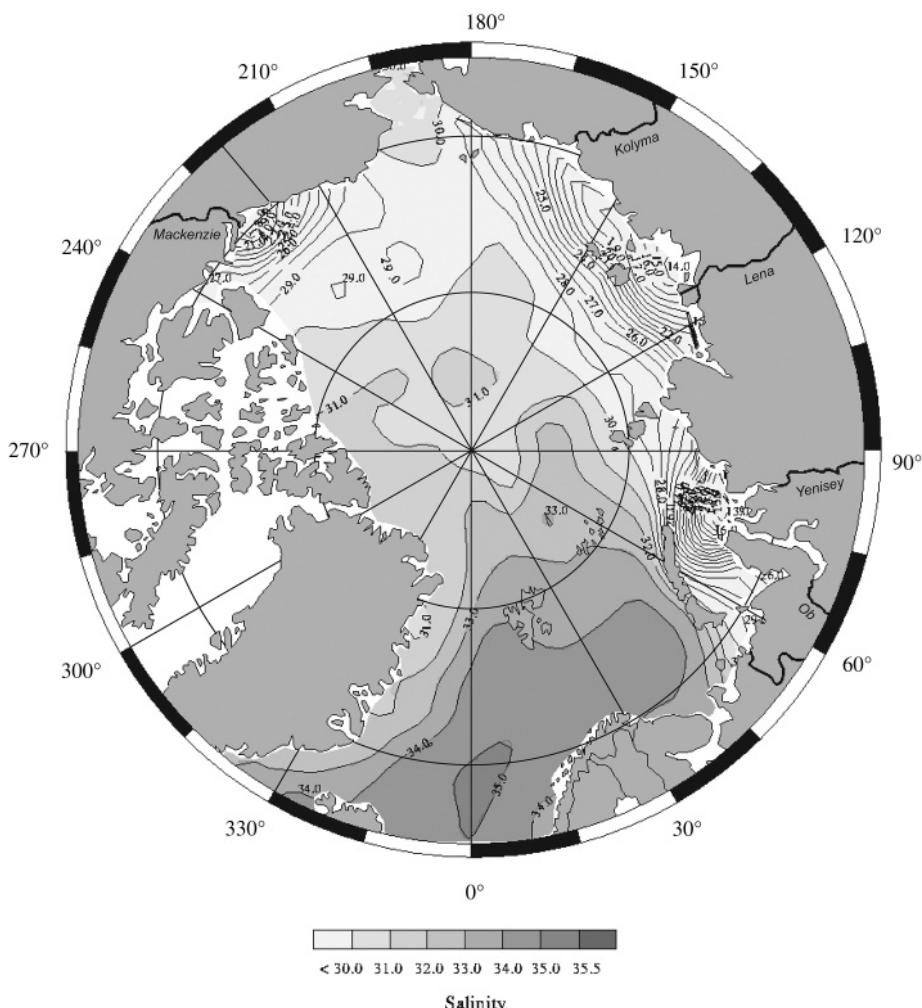


Figure 2.9. Mean surface salinity (psu) for summer (adapted from Arctic Climatology Project, 1998, by permission of NSIDC, Boulder, CO).

Given the great importance of freshwater in the Arctic Ocean, efforts have been made to quantify its major sources, sinks, and storage terms (e.g., Aagaard and Carmack, 1989). Figure 2.12 depicts annual freshwater fluxes and stores relative to a reference salinity of 34.8 psu (taken as the average salinity of the Arctic Ocean), based on a variety of atmospheric, terrestrial, and oceanic data sources, each with their own sources of error. Volumetric freshwater fluxes (F_{FW}) can be related to total volumetric water fluxes (F_T) and the observed salinity (S) of the water associated with the flux as:

$$F_{FW} = F_T (1 - S/34.8) \quad (2.1)$$

Hence if the total water flux has a salinity less than the reference value, the flux has a positive freshwater component. If the salinity of the water flux is higher than

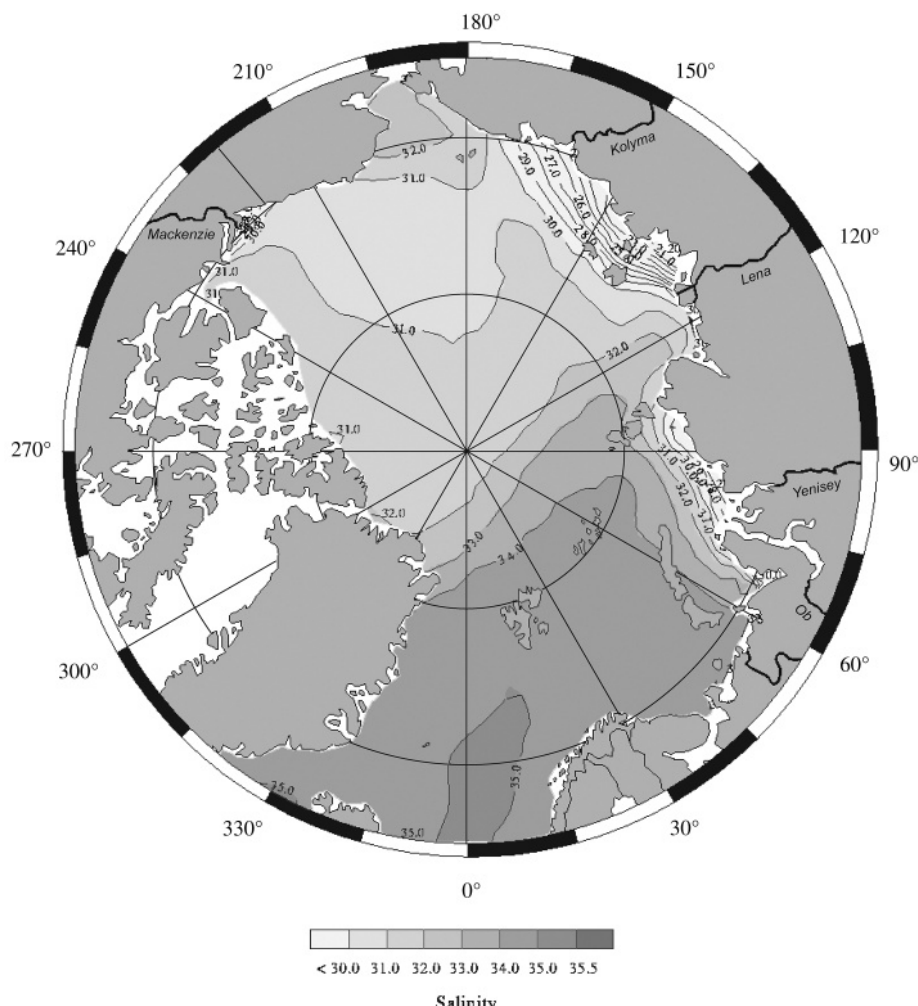


Figure 2.10. Mean surface salinity (psu) for winter (adapted from Arctic Climatology Project, 1997, by permission of NSIDC, Boulder, CO).

the reference salinity, it has a negative freshwater component. The same basic idea holds for calculating freshwater storages, ST, where in this case the salinity S refers to the salinity of the storage term in question:

$$ST_{FW} = ST_T (1 - S/34.8) \quad (2.2)$$

Focusing on the major terms, river runoff to the Arctic Ocean, representing net precipitation over the terrestrial Arctic drainage, is estimated at about $3,200 \text{ km}^3$. Note that the terrestrial drainage is much larger in area than the Arctic Ocean that it empties into. Although the Arctic Ocean gains about $3,300 \text{ km}^3$ of freshwater from precipitation over the ocean itself, this is partly countered by evaporation, leaving an oceanic net precipitation input of about $2,000 \text{ km}^3$. As the atmosphere loses water through the excess of precipitation over evaporation over both

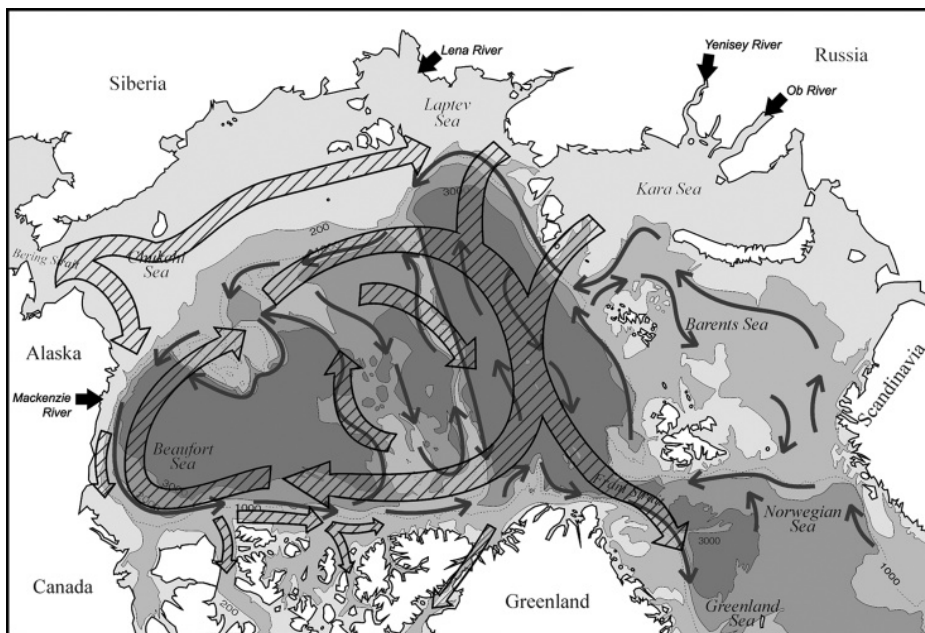


Figure 2.11. Major surface (hatched arrows) and deep currents (thin black arrows) of the Arctic Ocean, along with the locations of discharge from the four largest Arctic-draining rivers (Ob, Yenisey, Lena, and Mackenzie). Shading corresponds to bathymetry (courtesy of G. Holloway, Institute of Ocean Sciences, Sidney, BC).

the oceanic and terrestrial domains, there must be a compensating convergence of water vapor into the atmospheric domain, estimated at about $4,900 \text{ km}^3$. The inflow of low-salinity water through the Bering Strait is estimated at $2,500 \text{ km}^3$. The major outflows of freshwater from the ocean are through the Fram Strait, both as sea ice and as fairly low-salinity liquid water (less than the 34.8 reference), and through the channels of the Canadian Arctic Archipelago as low-salinity liquid water. There are a number of smaller terms, some of which are not shown in the schematic. Note that while the Barents Sea Branch and the West Spitzbergen Current represent water inflows to the Arctic, in the framework of the freshwater balance adopted here, they count as freshwater sinks because the mean salinity of these inflows is higher than the adopted reference salinity. Although there is no reason that the freshwater budget is ever in a steady state, the oceanic imbalance of 700 km^3 , is within the error bounds of the data sources and hence indistinguishable from zero. Note that the terrestrial budget is also not closed. On the basis of the ratio between storage and inputs, freshwater in the Arctic Ocean has a mean residence time of about a decade. This is understood in that annual freshwater input, while large ($8,500 \text{ km}^3$), is an order of magnitude smaller than oceanic freshwater storage of $84,000 \text{ km}^3$. Freshwater in the atmosphere, as water vapor, has a residence time of only about a week.

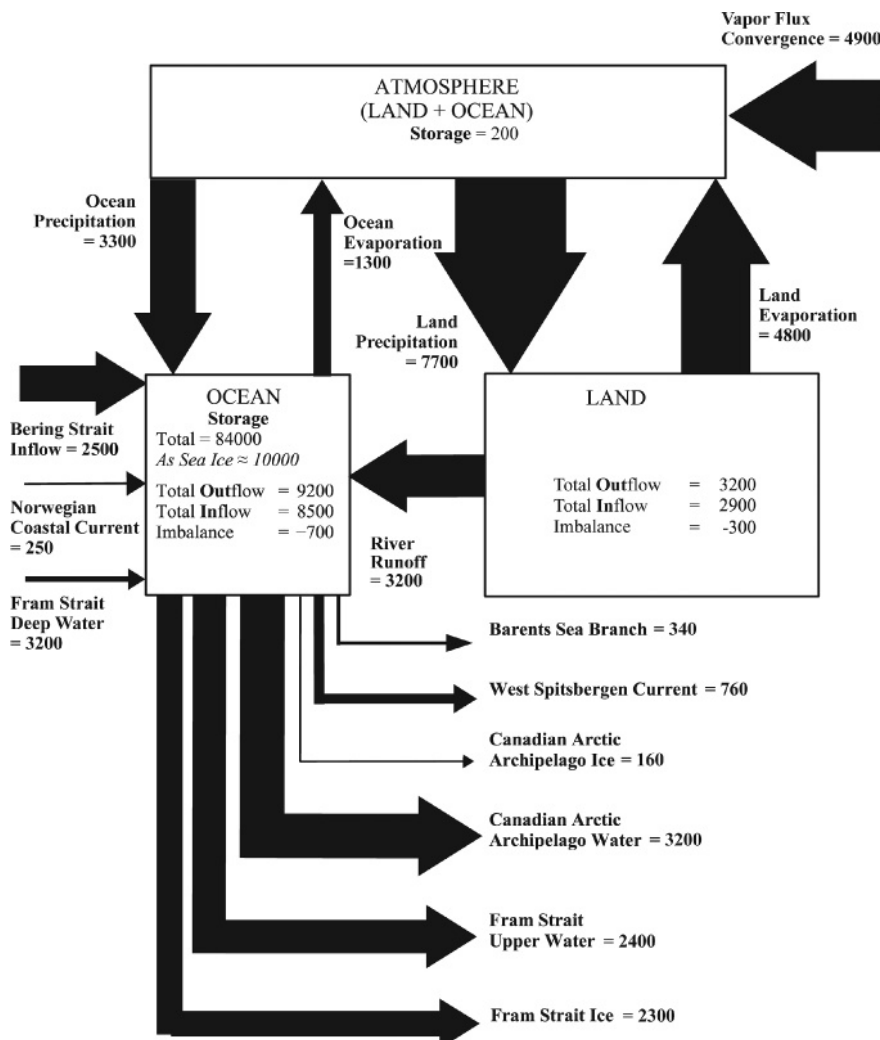


Figure 2.12. Annual mean freshwater budget of the Arctic, relative to a reference salinity of 34.8 psu. The atmospheric box combines the land domain (the Arctic terrestrial drainage) and the ocean domain. The boxes for land and ocean are sized proportional to their areas. Transports are in units of km^3 per year. Stores are in km^3 . The width of the arrows is proportional to the size of the transports (from Serreze et al., 2006, by permission of AGU).

2.2 The Arctic Lands

2.2.1 Topography and Permanent Ice Masses

The physiography of the Arctic lands is summarized in Figure 2.13. Much of the Arctic land area is low lying, especially western and central Siberia, the western part of the Canadian Arctic Archipelago and coastal Alaska. Mountains and high

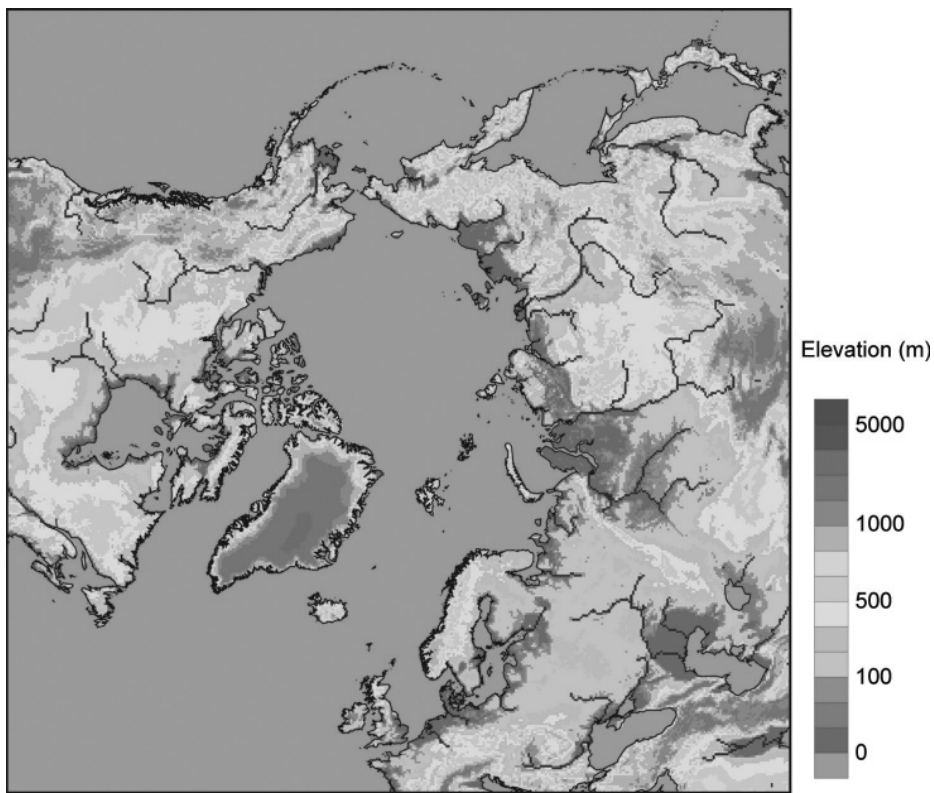


Figure 2.13. Physiography of the Arctic lands, showing topography and major river systems (courtesy of R. Lammers, University of New Hampshire, Durham, NH). (See plate section for color version.)

plateaus are prominent in the eastern Canadian Arctic, coastal regions bordering the Greenland Ice Sheet, interior Alaska, northeastern Siberia, and Scandinavia. The highest mountain north of the Arctic Circle is Gunnbjorns Fjaeld (86.92°N , 29.87°W), which rises to 3,800 m some 80 km inland from the East Greenland coast in Knud Rasmussen Land. In eastern Baffin Island there are peaks exceeding 2,100 m, but, in general, the dissected plateaus are around 1,500–1,800 m elevation. On Devon and Ellesmere islands, ice caps rise to 1,900–2,000 m. In northern Alaska, the Brooks Range rises to 1,500–3,000 m. The higher peaks in the more massive subarctic Alaska Range typically exceed 3,000 m. The Alaska Range contains Denali (Mount McKinley), the highest mountain in North America, with an elevation of 6,194 m. There are numerous mountain ranges in northeastern Siberia. There are several north-south mountain ranges east of the Lena River. From the Arctic Circle at $140\text{--}145^{\circ}\text{E}$, the Momsky-Chersky ranges, with peaks rising to 2,500–3,100 m, stretch southeastward. The Okhotsk-Kolyma mountain ranges of Chukhotka rise to 1,800–2,100 m.

Of the permanent ice masses (glaciers, ice caps, and ice sheets), the Greenland Ice Sheet is the most prominent and is by far the largest ice mass of the Northern

Table 2.1 Major Arctic ice caps

Name/Region	Surface area (10^3 km^3)
Devon Is.	16.6
Ellesmere Is.	77.2
Axel Heiberg Is.	12.6
Barnes (Baffin Is.)	6.0
Penny (Baffin Is.)	6.0
Iceland	11.3
West Spitzbergen	36.6
Northeast Land	14
Franz Josef Land	13.7
Novaya Zemlya	23.6
Severnaya Zemlya	18.3
Greenland Ice Sheet	1710
Greenland glaciers/ice caps	48.6

Sources: From Field (1975); Govorukha (1988); and Williams and Ferringo (2002).

Hemisphere. The ice sheet covers an area of 1.71 million km^2 , and contains an ice volume of $2.93 \times 10^6 \text{ km}^3$ (Bamber, Layberry, and Gogineni, 2001), which if completely melted is equivalent to a sea level rise of about 7 m. There is a central dome rising to 3,200 m elevation and a subsidiary dome in Southern Greenland. A detailed map is provided at Figure 8.1. The dimensions of the other Arctic ice caps are insignificant by comparison (see Table 2.1), although they exert an influence on the local climate conditions. Paralleling the pattern for the Greenland Ice Sheet (see Chapter 8), the net mass balance of most Arctic ice caps and glaciers has turned negative (Dyurgerov and Meier, 1997)

Based on data through the middle 1990s, approximately 40 percent of the surface of the Greenland Ice Sheet saw surface melt during summer (Abdalati and Steffen, 1997). However, both the areal extent of surface melt and melt intensity show general upward trends over the past several decades (Tedesco et al., 2010). For several days in early July 2012, nearly the entire ice sheet experienced a brief period of surface melt, including the summit. Although this was the first time in the satellite record that the summit has seen melt, there is evidence in ice core data of similar events occurring several times over the past few thousand years. This is again discussed in more detail in Chapter 8.

In sharp contrast to the Antarctic, there are only a few small ice shelves (floating shelves of glacier ice connected to the shore) in the Arctic. Until fairly recently, the Ward Hunt Shelf extended about 100 km along the north coast of Ellesmere Island (Jeffries, 1992; Mueller, Vincent, and Jeffries, 2003). It was up to 20 km wide, occupied three fiords and was 40–50 m thick. Since the early 1900s, however, its size has been greatly reduced and there have been many calving events leading to the formation of ice islands that may drift around the Arctic Ocean for many years. An

example from a calving event prior to the recent breakup is the ice island T-3 (also known as Fletcher's Ice Island), which was used as a platform for meteorological surveys and ocean research between 1952 and 1978.

2.2.2 Land Cover

The Arctic lands are commonly subdivided into the High Arctic and the Low Arctic based on broad climatic, geographical, and biological grounds (Bliss, 1997), but many ecologists recognize five subzones (Walker et al., 2002). As a general statement, the High Arctic is characterized by more severe environmental conditions than the Low Arctic, reflected in the type and distribution of vegetation.

Land in the High Arctic is generally characterized by tundra, a Finnish term for treeless upland. More generally, tundra refers to the treeless regions north of the Arctic tree line. The most extreme High Arctic tundra landscape falls under the category of polar desert, which implies both cold and a lack of moisture. Good examples are provided by the Canadian Arctic Archipelago and Peary Land in northeast Greenland. The concept of polar desert was introduced by the German geographer S. Passarge (1920). Subsequently, the term has been applied in a geo-botanical context by V. Alexandrova (1970). Figure 2.14 shows the extent of polar desert as interpreted by R. Charlier (1969). E. Korotkevich (1972) includes ice caps and the Greenland Ice Sheet in the polar desert category.

Field studies of polar desert sites on 10 islands in the Canadian Arctic Archipelago showed only 2–3 percent plant cover (Bliss, 1997). The brief summers are relatively warm, but scant moisture permits only a few cushion-form plants, mosses, and lichens to grow in niches with favorable microclimates, particularly at sites where snow banks provide melt water. In these favored areas, which occupy about 3–5 percent of the landscape, about 25–35 percent of the surface is typically vegetated. Vegetation is suppressed under semi-permanent snow banks. As discussed by J. Ives (1962), for north-central Baffin Island, it is possible that the limited cover of lichens and vascular plants is attributable to the widespread presence of snow banks during the Little Ice Age (150–400 years ago).

Much of the polar and sub-polar desert surface is covered with fell fields (*felsenmeier*), comprising gravel and angular blocks derived from freeze-thaw splitting of the bedrock. As the first author can attest, such fell fields should be climbed only with extreme caution. Stones and fine sediments are often organized as patterned ground. This may consist of stone circles and ice-wedge polygons up to a few meters across, or stone stripes on sloping surfaces (French, 1996).

As for less extreme forms of tundra, in the North American Arctic, L.C. Bliss (1997) distinguishes wet meadow (graminoid-moss) tundra comprised of dwarf-shrub heaths and polar semi-deserts of cushion plants, cryptograms, and herbs. In northern Russia, the so-called typical tundra (Chernov and Matveyeva, 1997) is predominantly moss and lichen covered (polar semi-desert according to Bliss), with sedges and dwarf shrubs, and dry heaths. The vertical structure is about 20 cm in height.

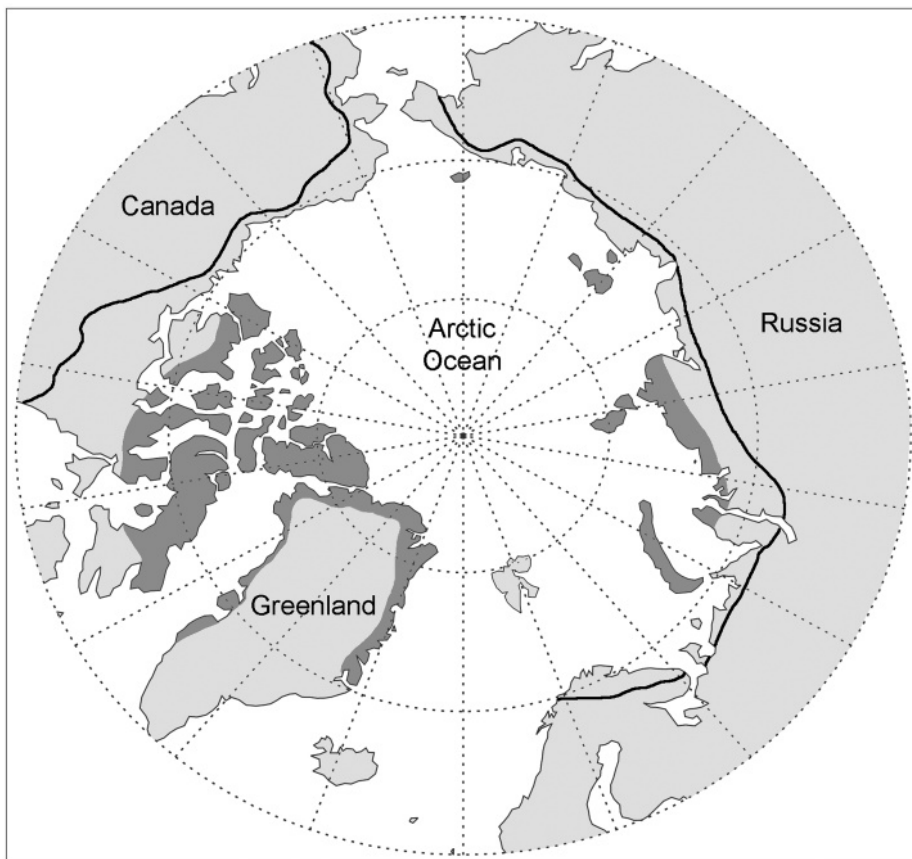


Figure 2.14. Distribution of Arctic polar desert (dark shading) and approximate southern limit of tundra (bold line) (adapted from Charlier, 1969, also see Webber, 1974, courtesy of N. Saliman, NSIDC, Boulder, CO).

In the Low Arctic of both northern continents, vegetation covers 80–100 percent of the surface. Shrubs are an important component, together with sedges and grasses. There is variety in the vertical structure. Several species of alder, birch, and willow in the tall shrub tundra reach 2–5 m height, whereas in low shrub tundra, dwarf birch and dwarf willow are only 40–60 cm high. Where the canopy is more open, heath and tussock species are widespread. At the southern margin of the Low Arctic tundra, there is a forest-tundra transition or ecotone. Tree “islands” and gallery forest are found along major watercourses such as the Mackenzie, Khatanga, and Lena rivers, extending to 71°N to 72°N. The forest-tundra ecotone is some 50–100 km wide. This is a result of the effects on the forest limit of climatic fluctuations over the past 4,000–5,000 years, and recurrent fires that destroy slow-growing lichens and mosses (Nichols, 1976; Elliott-Fisk, 1983). South of the ecotone is the boreal forest (or taiga, a Russian term).

As outlined in Chapter 1, in response to warming, the vegetation of the Arctic is changing, including greening of the tundra (as assessed from satellite data) and

increasing coverage of shrubs, a process known as shrubification (Mynemi et al., 1997; Sturm, Racine, and Tape, 2001; Zhou et al., 2001; Nemani et al., 2003; Tape et al., 2006; Bhatt et al., 2010).

2.2.3 Frozen Ground

Perennially frozen ground, known as permafrost, underlies nearly all of the Arctic land area. Permafrost is said to be present whenever ground temperatures are below freezing through two summer seasons. Ground ice need not be present, although in sediments ice may be present either in segregated form throughout, or as lenses and wedges (French, 1996). The upper part of the ground in permafrost regions, termed the active layer, thaws seasonally. The active layer depth depends on air temperature, vegetation cover, soil material, moisture content, and the amount of insulation provided by winter snow cover. In the Low Arctic the average active layer depth varies from 80–90 cm in the south to 50–60 cm in the north. Active layer depths are greater on heated slopes and in coarse-textured soils, and least in peat bogs (Chernov and Matveyeva, 1997).

In acting as an impermeable barrier, the presence of permafrost plays a major role in the hydrology of the Arctic. Following snowmelt, the ground becomes waterlogged unless there is sufficient topographic relief for drainage channels to form. Hence there are numerous shallow lakes. Permafrost is generally absent beneath large deep lakes, especially in the Sub-Arctic. As outlined in Chapter 6, in areas with sufficient drainage, the impermeable permafrost barrier fosters rapid channeling of precipitation and meltwater into streams, which impacts strongly on the seasonality of river discharge and evaporation rates.

Zones in which permafrost may be present account for 24 percent of the exposed Northern Hemisphere land surface (Zhang et al., 1999). However, the actual area underlain by permafrost is smaller if we take account of the fractional coverage of different permafrost zones (continuous = 90 to 100 percent; discontinuous = 50 to 90 percent; sporadic = 10 to 50 percent; isolated = less than 10 percent of the ground underlain by permafrost). On this basis, 12.8–17.8 percent of the exposed land surface is underlain by permafrost (Zhang et al., 2001). The area mapped as continuous permafrost represents 47 percent of the entire permafrost region of the Northern Hemisphere. In addition, there is frozen ground below much of the Greenland Ice Sheet and the sub-polar ice caps.

The Northern Hemisphere permafrost distribution, shown in simplified form in Figure 2.15, was compiled by the International Permafrost Association (IPA) (Brown et al., 1997). Permafrost is spatially continuous where the mean annual SAT is below approximately -7°C , and is discontinuous for an SAT of -1°C to -3°C . The permafrost thins toward the southern borders, near the -1°C SAT isotherm (Ives, 1974). In the zone of continuous permafrost, the thickness exceeds 600 m in northeastern Siberia and in northern Canada and Alaska. Extreme depths of 1,200–1,470 m are found in the Anabar Plateau of north-central Siberia ($72\text{--}73^{\circ}\text{N}$, 113°E) (Tumel, 2002). This is attributed to ice-free conditions through the Quaternary, low

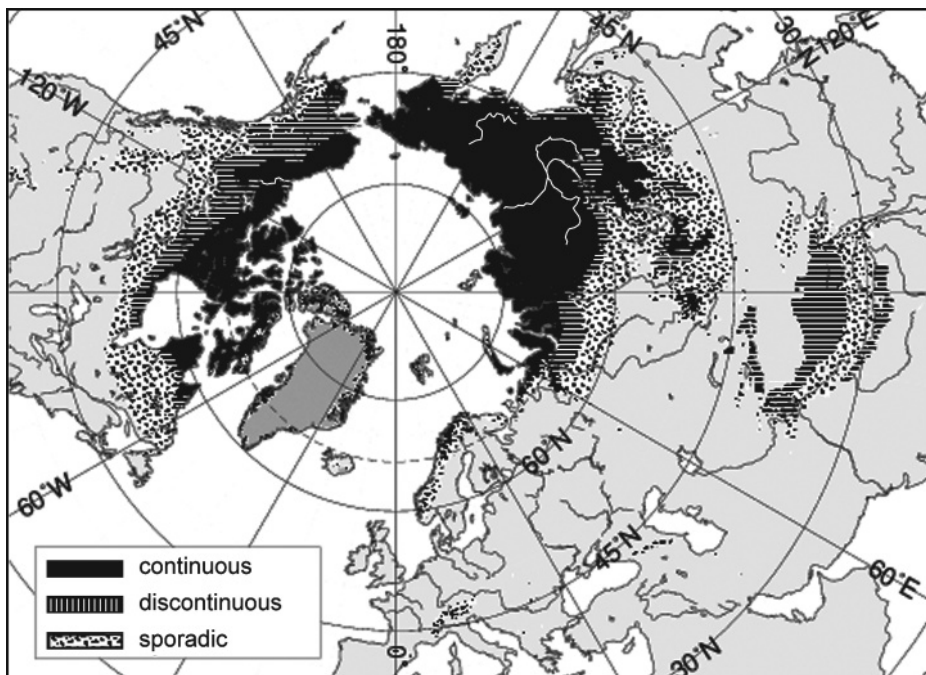


Figure 2.15. Northern Hemisphere permafrost distribution, simplified from the International Permafrost Association map. Black areas indicate continuous permafrost, striped areas indicate discontinuous permafrost, and stippled areas indicate sporadic permafrost (courtesy of C. Oelke, NSIDC, Boulder, CO).

geothermal heat fluxes and high bedrock conductivity. There is extensive discontinuous permafrost southward from the zone of continuous permafrost in Siberia and Canada, and also in northern Scandinavia. The typical thickness is approximately 50 m in the discontinuous zone, but only a few meters where the distribution is sporadic. Exposed treeless ridges and north-facing slopes are underlain by permafrost, whereas it may be absent in forested valleys, especially where there are large lakes. In general, the permafrost thins southward and becomes sporadic. Eventually it is found only in islands in favorable locations. Some of these permafrost islands may be relicts that are unstable under the present climate.

North of the Arctic coastline, there is a considerable zone of submarine permafrost underlying shallow sections of the continental shelf seas. This zone is extensive in the Barents, Kara, Laptev, and East Siberian seas, but is narrower in the Chukchi and Beaufort seas. These shelf areas were exposed during the glacial intervals of the Pleistocene (Chapter 10) when global sea level was lowered by 120–135 meters, and the mean winter air temperatures fell well below modern values. The modern occurrence and characteristics of submarine permafrost are determined by a number of factors. These include the water mass structure and vertical circulation, the absorption of solar radiation in summer when the coastal seas are ice-free, and the corresponding heat loss to the atmosphere in winter through polynyas and leads,

geothermal heat flow, the bottom water temperature, salinity and the freezing of bottom sediments by grounded landfast ice and grounded keels. Seaward of the submarine permafrost, there may also be a narrow zone of seasonally frozen submarine sediments. A. Gavrilov (2001) proposes that most submarine permafrost represents relic strata formed during glacial episodes of the late Pleistocene. The upper ice-rich strata would have been thermally abraded during sea level rises such as during the Holocene. In the Beaufort Sea, the permafrost upper boundary varies between the seabed and 100–150 m and its base may lie as deep as 600–900 m. In the Laptev Sea region where the terrestrial permafrost is 500–800 m thick, ice-bonded permafrost offshore is relic (Hubberten and Romanovskii, 2001). It is continuous to the –65 m water depth and discontinuous to –100 to –120 m depth. The maximum submarine permafrost thickness is about 500 m north of Kotelnaya Island.

The ice content of permafrost is difficult to determine quantitatively, owing to its spatial variability and the limited number of boreholes allowing for analysis. Only about 10 percent of the terrestrial permafrost area is “ice rich.” The IPA map shows that ice-rich permafrost, with an ice content of less than 20 percent by volume in the upper 10–20 m of the ground, is widespread in the coastal Siberian lowlands of Yamal (around the Ob estuary) and east of the Lena delta in Yakutia.

Permafrost temperatures have been monitored in Alaska, Russia, and Canada since the middle of twentieth century. These data document a general pattern of warming permafrost in Alaska, northwest Canada, and Siberia (e.g., Romanovsky et al., 2010a, 2010b) but with large variability from region to region and for different parts of the records. In some areas, permafrost is thawing. Permafrost degradation is of growing concern because of impacts on infrastructure (e.g., roads, runways) and because thaw may lead to the release of carbon stored in permafrost soils to the atmosphere (see Chapter 10).

Aufeis (German for “ice on top”), a special component of ground ice, represents layered ice that forms when surface water from springs and groundwater seepage freezes because of persistent low temperatures, or when rivers overflow their banks, sometimes as a result of ice jams. It usually melts out during summer and tends to occur in the same area year after year. Aufeis is also known as “overflow”, “icing,” and “naled” (a Russian term). Aufeis can be found throughout the Arctic. The total area of aufeis for all of northern Russia is estimated to be 128,000 km² (Kotlyakov, 1997). The largest single feature in northeastern Siberia (120 km²) extends for up to 26 km along the valley of the Momy River (Golubchikov, 1996). Aufeis accumulation can lead to blocked culverts and flooded roads.

2.2.4 Lakes

Lakes are an important element of the Arctic and subarctic landscape. G. Bonan (1995) estimates that water surfaces (including wet muskeg bogs and swamps) occupy up to 20–40 percent of the landscape in the glacial drift-covered lowlands of northern Canada and western Siberia (Figure 2.16). In northern Canada there are several lakes larger than 1,000 km² in area. Great Bear Lake (31,000 km²) and Great

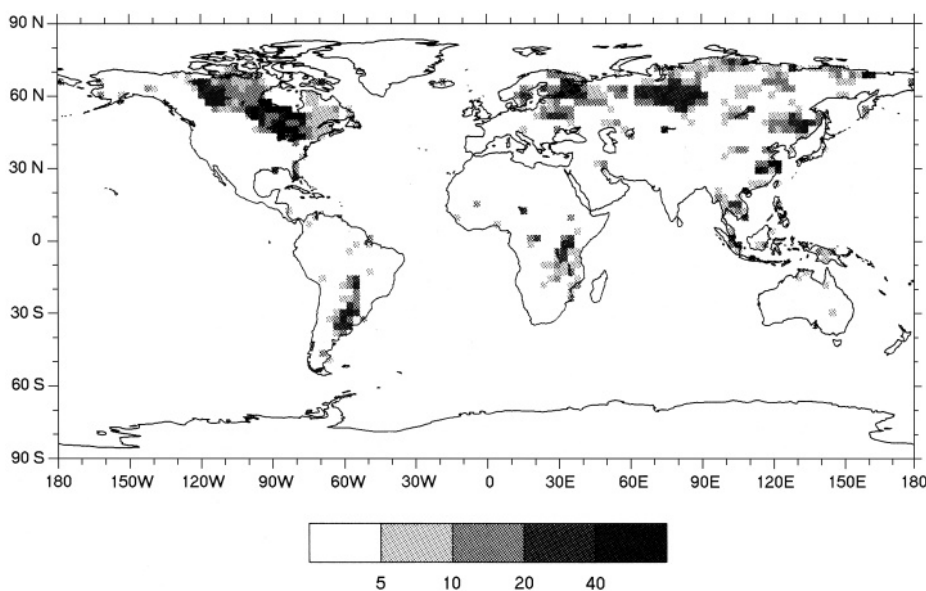


Figure 2.16. Percentage coverage of inland water (freshwater lakes and marshes) (from Bonan, 1995, by permission of AMS).

Slave Lake ($28,500 \text{ km}^2$) are by far the largest and both exceed 400 m in depth. By contrast, Lake Netilling on Baffin Island is just more than $5,000 \text{ km}^2$ and Lake Hazen on Ellesmere Island (81.5°N , 70°W) is 540 km^2 . In Finnish Lapland, the largest is Lake Inari (69°N , 27.5°E) at more than $1,000 \text{ km}^2$. There are few major lakes in the Russian Arctic. Lake Taymyr (74°N , 74°E) has an area of about $4,500 \text{ km}^2$. In the tundra areas of western Siberia and the Taymyr Peninsula, lakes are typically smaller than 0.3 km^2 , with a few larger than 50 km^2 . Here they represent 2–5 percent of the surface (Ananjeva, 2000); but in the coastal plain of northern Alaska, so-called thaw lakes form about 40 percent of the surface. In Greenland, the Arctic islands, and the mountains of Alaska and the Yukon (Post and Mayo, 1971), there are many ice-dammed lakes. Many of them periodically drain and subsequently refill. Hence they are ephemeral features of the landscape.

2.3 Basic Climatic Elements

2.3.1 Snow Cover

Most of the Arctic land and perennial sea ice surface has a snow cover for at least 6–8 months of the year. For a number of reasons snow cover is a key climatic variable: (1) its high albedo (reflectivity in solar wavelengths), typically 0.80 to 0.90 for new snow; (2) the insulating effect it has on the underlying tundra or sea ice; and (3) its role in storing precipitation over terrestrial regions, which is released as river discharge during spring and summer. As we have already seen, this impacts

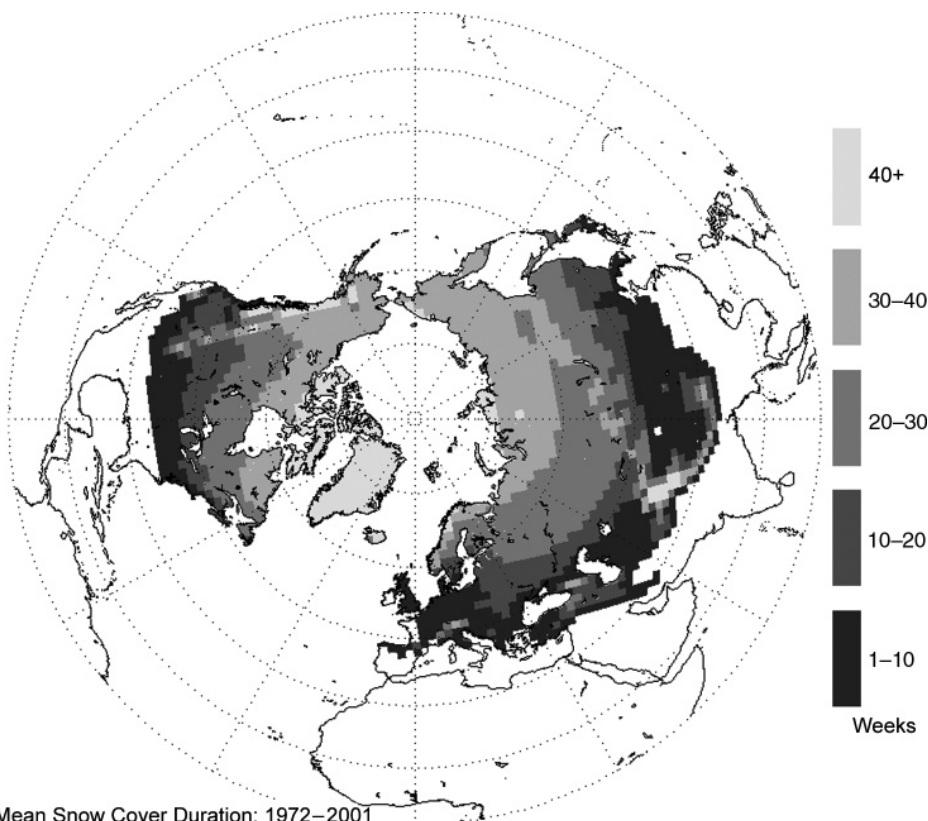


Figure 2.17. Average number of weeks of snow cover over the Northern Hemisphere, based on the NSIDC blended weekly product (courtesy of M.J. Brodzik, NSIDC, Boulder, CO).

strongly on the vertical density profile of the Arctic Ocean that in turn influences sea ice formation.

Figure 2.17 shows the generalized distribution of snow cover duration over the northern continents. The impact of latitude is obvious. In northern Canada, Alaska, and Asia, snow is typically present 30–40 weeks per year. Terrestrial snow cover classes have been developed according to climatic and vegetational zones, as well as on the basis of depth, duration, and density (e.g., Bilello, 1957; Benson, 1969). M. Sturm, J. Holmgren, and G. Liston, (1995) developed a classification for land that takes account of the stratigraphic and textural attributes of a snow pack. The classification has a number of categories of seasonal snow cover: tundra, taiga, maritime, alpine, prairie, and ephemeral. There is also a special class for highly variable mountain snow cover. Although several of the names follow earlier schemes based on climatic/vegetation zones, these designations do not require such geographical associations; only the relevant physical characteristics are considered (see Table 2.1 in Sturm et al., 1995). The classes were identified on the basis of a statistical analysis

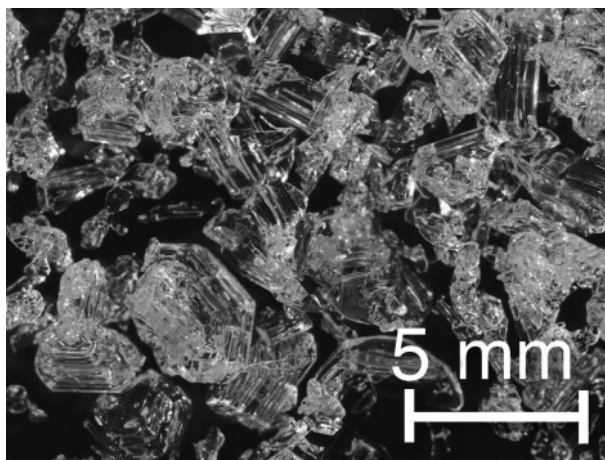


Figure 2.18. Depth hoar crystals collected from the base of a tundra snowpack on the North Slope of Alaska (courtesy of Kelly Elder, USDA Forest Service). (See plate section for color version.)

of field measurements and climatic data for Alaska. Five of the six classes are found in Alaska.

Tundra and taiga snow dominate most of the Arctic. Tundra snow is a thin, wind-blown snow, with typical maximum depths of around 750 mm and a bulk density of typically 380 kg m^{-3} . It consists of a basal layer of depth hoar, overlain by multiple wind slabs. Surface sastrugi are common. Depth hoar represents a low cohesion layer of large, faceted ice crystals at the base of a snowpack. Depth hoar forms when there is a strong vertical temperature gradient in the snowpack (temperature decreasing upward). This results in a vertical gradient in water vapor and hence an upward migration of water vapor within the snowpack. Water sublimates from existing ice crystals and desublimates (deposits) on others, resulting in large, faceted crystals (Figure 2.18). The combination of fairly thin winter snow covers and low winter air temperatures makes the Arctic an ideal place for depth hoar formation. Sastrugi refers to sharp, irregular ridges of snow formed from wind scour and deposition, aligned along the prevailing wind direction. Ridges typically range from perhaps 0.1 to 1 m in height, and from 0.5 to 10 m in length (Figure 2.19). Travel over a rough, irregular sastrugi surface can be difficult. Taiga snow is thin to moderately deep (300–1,200 mm) with a lower bulk density than tundra snow (260 kg m^{-3}). It is found in forest climates in which wind, initial snow density, and air temperature are all low.

Although there are a number of terrestrial snow depth data sets for Arctic land areas, they have limited spatial coverage. Figure 2.20 is an attempt to map the mean annual maximum snow depth for Eurasia, based on Russian data. Depending on the region, maximum snow depth tends to occur between February and early April. North of 60°N , maximum snow depths range from 300–800 mm. Assuming an average density value of about 300 kg m^{-3} across Eurasia yields maximum snow water equivalents of about 100 to 270 mm. On a local scale, the snow pack thickness varies considerably in relation to terrain and wind conditions. Surveys carried out



Figure 2.19. Sastrugi on the North Slope of Alaska (courtesy of Matthew Sturm, University of Alaska, Fairbanks, AK). (See plate section for color version.)

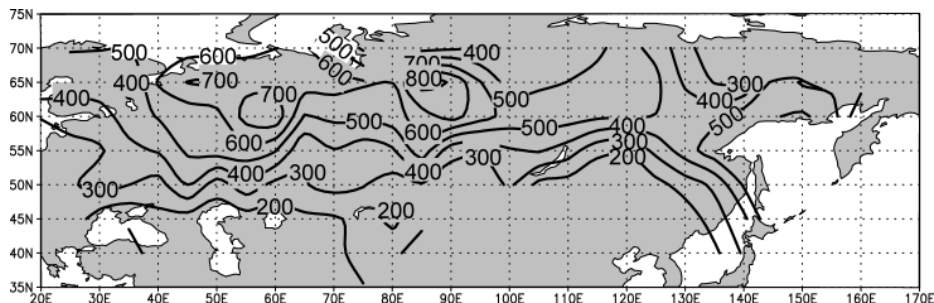


Figure 2.20. Maximum snow depth (mm) over Eurasia, compiled from Russian sources (courtesy of H. Ye, California State University, Los Angeles, CA).

over seven years in a small basin near Resolute Bay N.W.T. (Woo et al., 1983) show that gullies and valleys have the largest accumulations, and exposed hilltops have the smallest accumulations. This basic pattern tends to be maintained from year to year. Amounts on slopes are variable according to exposure to the prevailing wind and locally concave/convex surfaces. As just discussed, snow depth can be quite variable in regions of sastrugi. The snowmelt season on the tundra is typically brief, often lasting less than two weeks (Weller et al., 1972). When bare ground begins to appear, local heat advection from the warmer exposed surface accelerates the melt of the shrinking snow patches.

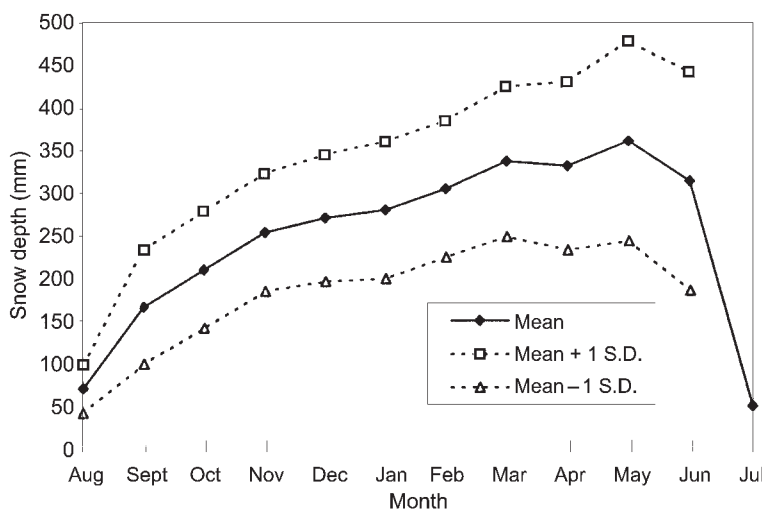


Figure 2.21. Mean annual cycle of snow depth (mm) and $+/-1$ standard deviation over the central Arctic Ocean based on NP data (from Colony et al., 1998, by permission of Cambridge University Press).

The NOAA snow chart climate data record allows for analysis of variability and trends in terrestrial Northern Hemisphere snow covered area back to 1967. As assessed for the 1967–2012 period, snow cover extent for winter and autumn has been variable. By sharp contrast, as introduced in Chapter 1 (Figure 1.7), snow cover extent for spring (when snow is mainly located in the Arctic) exhibits a pronounced downward trend; the trend is larger over Eurasia than over North America. Particularly large negative anomalies in spring extent characterize the last few years of the data record (Derksen and Brown, 2012).

Turning to the Arctic Ocean, snow depth data were collected by Russian scientists during airborne landings each spring between 1959 and 1988, under the *Sever* (“North”) program (Romanov, 1995). These records provide average snow thickness on the predominant sea ice type in the landing area, in sastrugi behind pressure ridges, and an average for the windward and lee side of hummocks (Colony, Radionov, and Tanis, 1998). More consistent spatial information has been derived from the snow survey lines at the Russian NP drifting stations between 1954 and 1991. These represent measurements from snow lines of 1 km length as well as at snow stakes installed at the meteorological station sites. Daily measurements were made at the stakes and once to three times monthly along the snowlines at 10 m intervals. Snow density along each line was sampled at every 100 m. Snow lines were chosen to be over flat ice.

The mean seasonal cycles in mean snow height (essentially equivalent to snow depth and hence treated as such here), snow density, and the $+/-1$ standard deviations based on grouping all available snow line data are reproduced in Figures 2.21 and 2.22. The distribution of snow depths in April is given in Figure 2.23. Snow depth is greatest in May, with a mean of about 350 mm. The onset of melt is

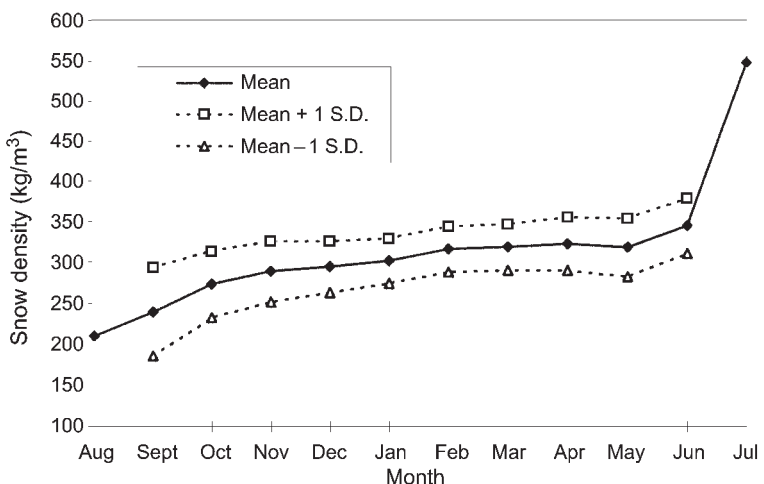


Figure 2.22. Mean annual cycle of snow density (kg m^{-3}) and $+/-1$ standard deviation over the central Arctic Ocean based on NP data (from Colony et al., 1998, by permission of Cambridge University Press).

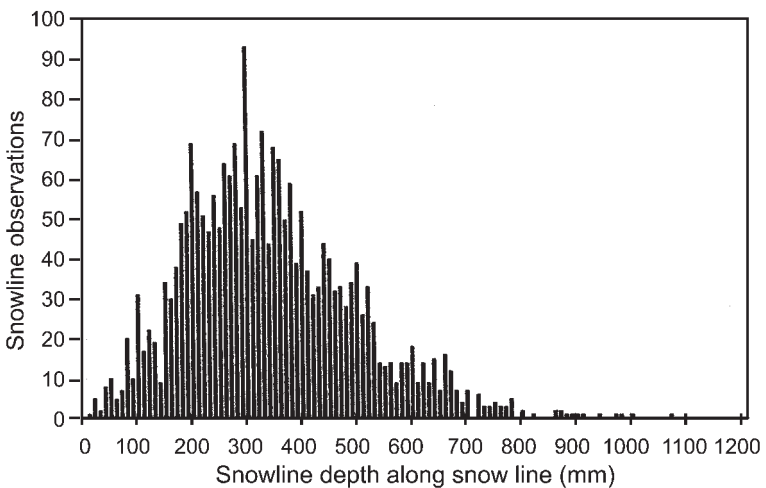


Figure 2.23. Distribution of snow depth (mm) over the central Arctic Ocean for April from NP data (from Colony et al., 1998, by permission of Cambridge University Press).

observed as a rapid decline in depth between June and July to a minimum of about 50 mm in August. The standard deviation of snow depth is fairly large and naturally increases with mean snow depth. This represents both spatial and year-to-year variability. During April, snow depths range from near zero to more than 1,000 mm, pointing to drifting and wind scour. As the snowlines are over flat ice, the standard deviation in snow depth is lower than would be obtained for regional averages that include rough ice. Considering the mean snow density and depth, the average water

equivalent during April and May is approximately 100–110 mm. Locally, the snow depth also depends on the ice age; when a lead forms in the ice in winter, new ice growth takes place. The snow then accumulates on the surface of the new ice from snowfall and drifting.

2.3.2 Snowline Altitude

The average climatic snowline is the elevation above which snow will survive the summer melt season. It is indicative of both snowfall and SAT, the latter especially in summer. It is around 1,200–1,400 m in Iceland and 700–900 m in Jan Mayen, decreasing northeastward. In Svalbard, it is only 200 m in western coastal regions, rising inland to 800 m (Koryakin, 1990). On Novaya Zemlya, it decreases from 400–600 m on the western, Barents Sea coast to 200–300 m on the eastern Kara Sea coast. On Severnaya Zemlya the snowline lies between 400 and 600 m, compared to Franz Josef Archipelago where it is about 250 m and on De Long Island in the New Siberian Islands where it lies at 300 m.

2.3.3 Temperature

I. Rigor, R. Colony, and S. Martin (2000) compiled maps of mean Arctic SAT based on blending data from coastal and inland stations with Arctic Ocean measurement from the NP stations and from the IABP. Since 1979, the IABP has maintained arrays of drifting buoys over the Arctic Ocean to provide records of surface pressure, ice drift, and SAT (see also Chapter 1, Section 1.3). As is evident from Figure 2.24, the annual cycle of SAT varies dramatically between inland continental sites and maritime and coastal regions.

Temperatures drop below the freezing point during the second half of August over most of the Arctic Ocean and by mid-September along the Arctic coast from Taymyr eastward to 120°W. January means near the North Pole are –32° to –33°C. The lowest winter SATs in the Northern Hemisphere are recorded in northeastern Siberia in association with the strong Siberian anticyclone (Chapter 4). Mean values of below –40°C are found in January. Locally (and not evident on the scale of Figure 2.24), topographic effects play a major role. “Cold air lakes” form during winter in basins and valleys. Verkhoyansk, located along the Yana River at 67°N, is notorious for its winter low temperatures. A. Hastings (1961) indicates that 60–70 percent of observed SATs here in January are below –40°C and mean annual minimum values of –62°C are recorded. In the lowlands west and southwest of Great Bear Lake, there is a corresponding area in which mean annual minima are –48°C or below. Despite the record low of –63°C recorded at Snag (62°N, 140°W) in the Yukon, there is a higher frequency of temperature readings below –40°C recorded at Eureka in Ellesmere Island. Also, based on the records during 1957–1958 at Lake Hazen, the interior valleys of Ellesmere Island may experience the longest periods of readings below –40°C in North America, as a result of the very light winds (Jackson, 1959a).

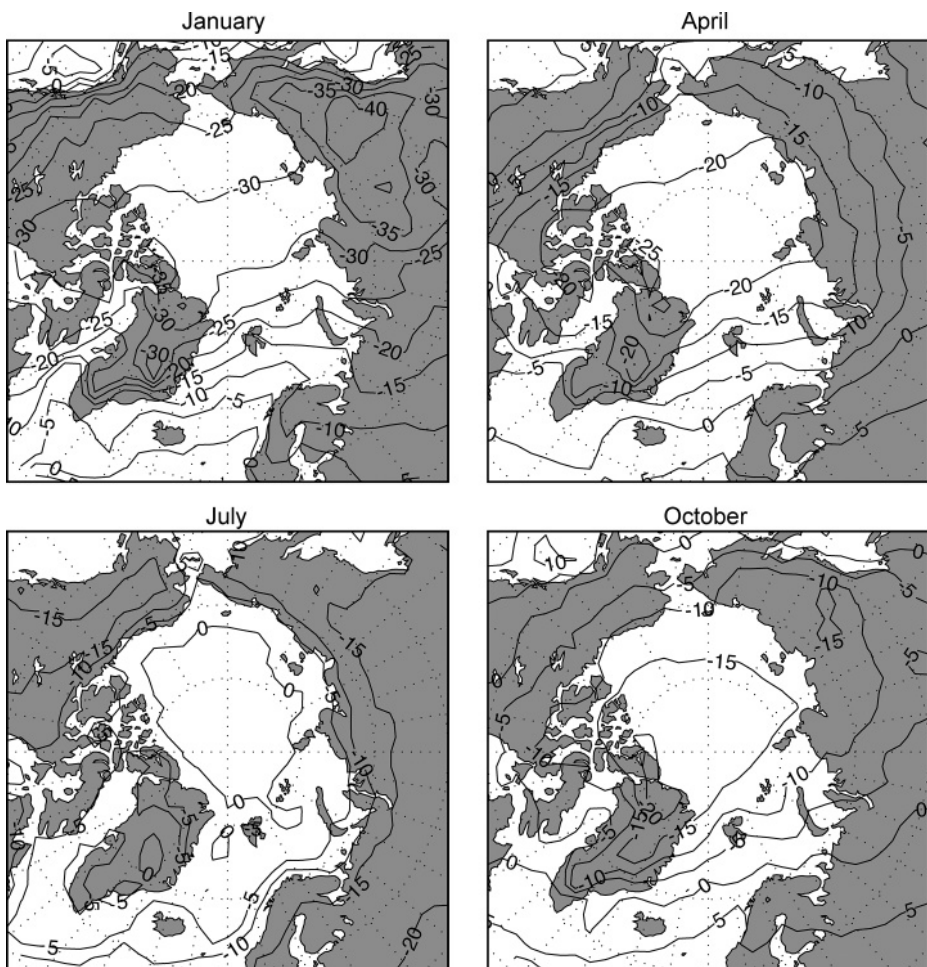


Figure 2.24. Mean surface air temperature ($^{\circ}\text{C}$) for January, April, July, and October (adapted and updated from Rigor et al., 2000, by permission of AMS).

Over the Arctic Ocean, the formation of leads and polynyas locally permits strong sensible and latent heat transfers into the atmospheric boundary layer. These prevent winter SATs over the Arctic Ocean from reaching the extremes observed in the interior of northeastern Siberia and northwest Canada. The importance of the downward longwave radiation flux, and hence cloud cover, on winter SAT variability over the central Arctic Ocean, is examined in Chapter 5. The highest winter values are observed in the Greenland-Barents and Chukchi Sea sectors. This pattern is largely established by the presence of open water that heats the overlying atmosphere; open water is itself maintained by the warm North Atlantic Current.

During spring (as shown in the April field), the Siberian surface “cold pole” has disappeared. The lowest temperatures are found over the Arctic Ocean and the Canadian Arctic Archipelago. The April pattern clearly shows the effects of the cold polar vortex (see Chapter 4), which extends throughout the troposphere and tends

to isolate the air within it from external sources of advection (Overland, Miletta Adams, and Bond, 1997).

Temperatures rise to the melting point over the coasts by the end of May and over most of the central Arctic Ocean by mid-June. The melt season over the central Arctic Ocean is about 60 days long, compared to about 100 days over the coastal sector from 90°E eastward to 120°W. July temperatures at the coast average about 5°C with a sharp rise inland over a distance of 10–20 km. Like spring, the lowest temperatures are found over the Canadian Arctic Archipelago.

The preceding discussion must be viewed with the understanding that over the past several decades, annual mean SATs over the Arctic as a whole have risen more strongly than for the Northern Hemisphere as a whole, with the warming most pronounced during autumn and winter over parts of the Arctic Ocean (Figure 1.5). Although it is generally accepted that this strong warming (termed “Arctic amplification”) in part manifests forcing by increased concentrations of atmospheric greenhouse gases, it appears that a suite of processes are at work, including (1) reductions in sea ice extent, leading to stronger summer heat gain in the ocean mixed layer, with this heat then released back to the atmosphere in autumn and winter; (2) changes in atmospheric circulation leading to an increased atmospheric heat flux convergence; (3) changes in cloud cover and water vapor; (4) increased concentrations of black carbon aerosols and soot on the snow cover; and (5) the strong static stability of the lower atmosphere (Serreze and Barry, 2011). These issues are expanded on in subsequent chapters.

A notable aspect of the Arctic atmosphere is the presence of strong low-level temperature inversions during winter (situations in which temperature increases rather than decreases with height). These surface or near-surface based features generally extend to about 1,200 m during January–March, with a temperature difference from the inversion base to top of typically 11°–12°C (Serreze, Kahl, and Schnell, 1992b). As examined in Chapter 5, the inversion layer tends to be maintained by an approximate radiative equilibrium associated with the different longwave emissivities of the surface (an approximate blackbody) and of the temperature maximum layer aloft (a selective emitter), with northward heat advection countering the outward radiation loss to space (Overland and Guest, 1991). Especially strong winter inversions are found inland in eastern Siberia and northwest Canada-Alaska in the deep intermontane basins and valleys that characterize these regions. From May through September, the Arctic is characterized by weaker, elevated inversions.

2.3.4 Humidity

Because of the low temperatures in the Arctic, especially during winter, the amount of moisture in the atmosphere is quite limited. Near the surface, mean specific humidity (the mass of water vapor per unit mass of air, including the water vapor) for winter as averaged for the region north of 70°N is only about 1 g kg^{-1} compared to about $3\text{--}4 \text{ g kg}^{-1}$ in summer. The total water column vapor (or precipitable water, the equivalent liquid depth of water vapor in an atmospheric column) between the surface and 300 hPa, averaged for 70–90°N, ranges from about 2.5 mm in January

to 14 mm in July (Serreze, Barry, and Walsh, 1995a). This compares to a global mean annual average of about 25 mm. Approximately 80 percent of the total water vapor in all months is concentrated between the surface and 700 hPa and 95 is percent below 500 hPa. During the summer half-year, the spatial pattern of precipitable water is primarily a function of latitude, whereas there is greater asymmetry in the winter half-year. Amounts are least over the Canadian sector and largest over the Norwegian Sea as a result of patterns of evaporation, the planetary wave structure, and associated vapor transports by synoptic-scale eddies. On average, the strongest moisture transports into the Arctic tend to be found near the prime meridian in association with the North Atlantic cyclone track (Chapter 6). As shown by J. Gyakum (2000), moisture transports associated with significant precipitation events over the Arctic drainage basins are often organized into well-defined “tropospheric rivers” (Zhu and Newell, 1998).

2.3.5 Aerosols and their Climate Effects

Aerosols (small liquid or solid particles in the air of either natural or anthropogenic origin) play a major yet still incompletely understood role in Arctic climate through their direct effects on scattering and absorption of solar radiation, through indirect effects by their influence on cloud albedo and lifetime, and, through aerosol deposition (soot on snow), the surface albedo. Natural aerosols include sea salt, dust and pollen, sulfate from volcanic eruptions, and black carbon from biomass burning. Anthropogenic aerosols include sulfate and black carbon from fossil fuel burning and other products from industrial activities.

Arctic explorers of the nineteenth century were surprised by the peculiar haze that could sometimes limit visibility. As reviewed by T. Garrett and L. Verzella (2008), the first formal recognition of what we now call Arctic haze can be traced to a paper published in *Science* by the Swedish geologist Erik Nordenskiold, who also remarked on “kryokonite,” a thin, dark layer distributed over ice that contained not only microscopic plants, but metallic iron, cobalt, and nickel. Although Nordenskiold attributed the mineral content to the deposition of cosmic dust, what he was actually looking at was the deposition of airborne particulates associated with smelting and coal combustion in industrial regions lying to the south. Fridjof Nansen came to this basic conclusion in 1882 after an evaluation of “ice dust” collected along the southeast coast of Greenland. Only much later did J. Mitchell (1957) draw widespread attention to the Arctic haze phenomenon on the basis of observations during the U.S. Air Force “Ptarmigan” series of aircraft weather reconnaissance missions.

As is now known, Arctic haze, which has seasonal peaks in late winter and spring, is attributed to soot, dust, and sulfate aerosols emitted by industrial complexes, especially those in northern Eurasia, which are then transported into the Arctic. Industrial plants in northern Russia located in the Kola Peninsula, Norilsk (nickel-copper smelting) and oil and gas exploitation in the Tyumen area, are all chemically identifiable sources within the Arctic Circle (Harris and Kahl, 1994).

However, there is still uncertainty regarding the relative contribution of different geopolitical contributions to Arctic pollution. It has been suggested that Southeast Asia may be a significant source of black carbon (soot) aerosols in the Arctic troposphere (Koch and Hansen, 2005).

The peak in Arctic haze in late winter and spring reflects both the nature of the atmospheric circulation that promotes transport from northern Eurasia and slow removal processes. Concentrations are spatially and temporally heterogeneous. For example, aerosol optical depth (a unitless measure of the cumulative depletion of radiation through the atmosphere by aerosols; a larger value means more depletion) measured from airborne sun photometer measurements during April 2009 in the European to the Alaskan Arctic, from subarctic latitudes, and near the North Pole ranged from about 0.12 to more than 0.35, with the aerosol haze concentrated within and just above the surface-based temperature inversion layer (Stone et al., 2010). Based on continuous measurements at the Koldewey station in Spitzbergen (79°N, 12°E), Arctic haze in spring was present 40 percent of the time, compared to less than 4 percent in summer (Herber et al., 2002). The lower frequency of haze events in summer reflects the greater efficiency of removal processes in this season (Bourgeois and Bey, 2011). Forest fires, which are more common in spring and summer, can also lead to substantial concentrations of climate-relevant aerosol species in the Arctic, including black carbon. C. Warneke and colleagues (2010) find that forest fires in Russia during spring can double the high Arctic atmospheric background aerosol concentrations that have built up during winter.

Globally, the direct climate effect of aerosols is cooling through the scattering of solar radiation. However, direct effects depend on the type of aerosol. In contrast to sulfate aerosols that cool, black carbon aerosols strongly absorb solar radiation and hence have a warming effect on the atmosphere. D. Shindell and G. Faluvegi (2009) argue that, because of a combination of cleaner combustion techniques in the United States and Europe but growing anthropogenic emissions from Asia, the Arctic now has more black carbon aerosols. Their modeling study suggests that this change has substantially contributed to the observed Arctic warming over the past three decades.

There are two known major aerosol indirect effects linked to cloud cover that revolve around the role of aerosols as cloud condensation nuclei (CCN). The first, known as the cloud-albedo or Twomey effect, says that an increase in CCN leads to more cloud droplets of smaller size, manifested as an increase in cloud albedo. The second is known as the life-time or Albrecht effect; that is, an increase in aerosol concentrations leads to more abundant and smaller droplets that take longer to grow to precipitable sizes through collisions, increasing cloud lifetime. For both of these indirect aerosol effects, impacts on cloud albedo compete with effects on cloud longwave emissivity and hence the downward longwave flux to the surface. C. Mauritzen et al., (2011) show that over the central Arctic when there are conditions with low aerosol concentrations, a small increase in aerosol loading can substantially enhance cloudiness, which warms the surface through enhancing the downward longwave radiation flux.

Coming full circle to early observations by Nordenskiold and Nansen, aerosol deposition on snow and ice surfaces reduces the surface albedo. Soot on snow linked to fossil burning appears to be a significant climate forcing in the Arctic (Hansen and Nazarenko, 2003) and may contribute to the observed strong decline in summer sea ice extent.

2.3.6 Clouds

Cloud cover has first order impacts on the Arctic surface radiation balance (see Chapter 5). Cloud microphysical and radiative properties are hence a vibrant area of research. This includes impacts of aerosol loading on cloud albedo and lifetime as discussed in the preceding section. Although much has been learned from modeling, remote sensing, and special observation programs (e.g., SHEBA, the Department of Energy Atmospheric Radiation Monitoring program, and IPY efforts), continuing problems are the paucity of accurate observational data on even cloud amounts over the Arctic and challenges in obtaining cloud information from satellite sensors.

Over the Arctic, one can observe many of the same generic low level (e.g., stratus, stratocumulus), middle level (e.g., altocumulus) and high level (e.g., cirrus) cloud types as seen in middle latitudes. At the very cold summer mesopause (roughly 85 km) noctilucent clouds form when temperatures fall to 190 K. They are composed of minute ice crystals through upwelling of trace amounts of water vapor. Despite the high latitude of the Arctic, convective cloud cover is common over Eurasian and Alaskan land areas during summer. Convective cloud cover is also frequent during winter over the Norwegian Sea – cold outbreaks from the north, when reaching the fairly warm, ice free waters off the Norwegian coast, result in destabilization of the air.

However, cloud classification can be problematic in the Arctic. J. Curry and her colleagues (1996) identify four “unusual” boundary layer cloud types over the Arctic Ocean, the first two falling into the general category of low-level, optically thin Arctic stratus: (1) extensive summertime boundary layer clouds with multiple layers; (2) mixed-phase (ice and water) boundary layer clouds during the transitional season; (3) low-level ice crystal clouds and “clear-sky” ice crystal precipitation (the latter often termed “diamond dust”) in stable wintertime boundary layers; and (4) wintertime ice crystal “plumes” emanating from open leads (Schnell et al., 1989). Measurements in the western Arctic during SHEBA (Intrieri and Shupe, 2004) show that true clear sky diamond dust occurs about 13 percent of the time during November through mid-May. However, the occurrence of diamond dust is often greatly over-reported (145 percent of the time) by observers, mainly during polar darkness. Lidar profiles showed that for nearly all these misreports, ice crystals were actually precipitating from clouds.

Overall, cloud cover is least extensive during winter and most extensive during summer. This seasonality is well expressed over the central Arctic Ocean and is primarily driven by the seasonality in low-level stratus. By comparison, the Atlantic

sector of the Arctic Ocean is quite cloudy for all months. Nevertheless, even mean monthly cloudiness is rather poorly quantified, perhaps only within 5–10 percent. As reviewed by Curry et al., (1996), there are several reasons for this unsatisfying state of affairs. Although cloud fraction (the part of the celestial dome covered by cloud) is a standard variable of synoptic weather reports, spatial coverage of observations is spotty and the measurement itself is somewhat subjective. The most comprehensive surface-based data set for the central Arctic Ocean is still from the Russian NP program. In addition, during the long polar night, cloud observations are difficult, especially under moonless skies. An analysis by C. Hahn, S. Warren, and J. London (1995) of Arctic Ocean cloud amounts observed in winter under moonlit and moonless conditions suggests an underestimate of total cloudiness by about 5 percent. There are a number of satellite-derived gridded data sets. For example, gridded satellite-derived estimates of cloud parameters (cloud amount, cloud top height, optical thickness, and so on) with global coverage are provided through the International Satellite Cloud Climatology Project (ISCCP) (Rossow and Schiffer, 1991). Gridded polar-specific cloud products from 1982 onward are provided as part of the AVHRR Polar Pathfinder effort (Maslanik et al., 1997). Cloud detection in both data sets is based on a combination of visible and infrared wavelength imagery. For example, the ISCCP-C1 (daily) and C2 (monthly) data sets for the polar regions are based on AVHRR data from channels 1 (0.58–0.68 μm, 1 μm = 10⁻⁶ m) and channels 4 (10.3 to 11.3 μm). The Arctic Polar Pathfinder (APP-x) effort includes cloud properties along with surface radiation fluxes and other variables on a daily basis (Key and Intrieri, 2000). Cloud fraction is also available from the MODIS sensor.

There are fundamental problems with satellite retrievals in high latitudes. In the visible wavelengths, clouds and the snow/ice surfaces have essentially the same reflectance, making cloud discrimination very difficult. Infrared measurements are limited by the fact that temperature differences between clouds and the surface are usually small. Because of the low-level temperature inversion, cloud tops may be warmer than the surface.

A. Schweiger and J. Key (1992) show a wide discrepancy between the annual cycle of total cloud amount in the Arctic reported by S. Warren and his colleagues (1988) from surface stations and from ISCCP-C2 data, although except for the central Arctic Ocean the basic spatial patterns are in general agreement. L. Wilson, J. Curry, and S. Ackerman (1993) suggested that some of the discrepancies in winter might be attributable to the frequent occurrence of ice crystals (diamond dust) in the atmosphere, which might be identified as low-level cirrus by the ISCCP algorithms. The ISCCP-C products have been superseded by the ISSCP-D series, which includes improvements to mitigate the problems found over polar surfaces. However, it has also been shown (Schweiger et al., 1999) that the ISCCP-D1 product still has significant problems and overestimates cloudiness in winter and summer compared with the NP observations. Moreover, the annual cycle of cloudiness is reversed from that observed at surface stations. In a more recent study, R. Eastman and S. Warren (2010b) find that interannual variability in cloud amounts

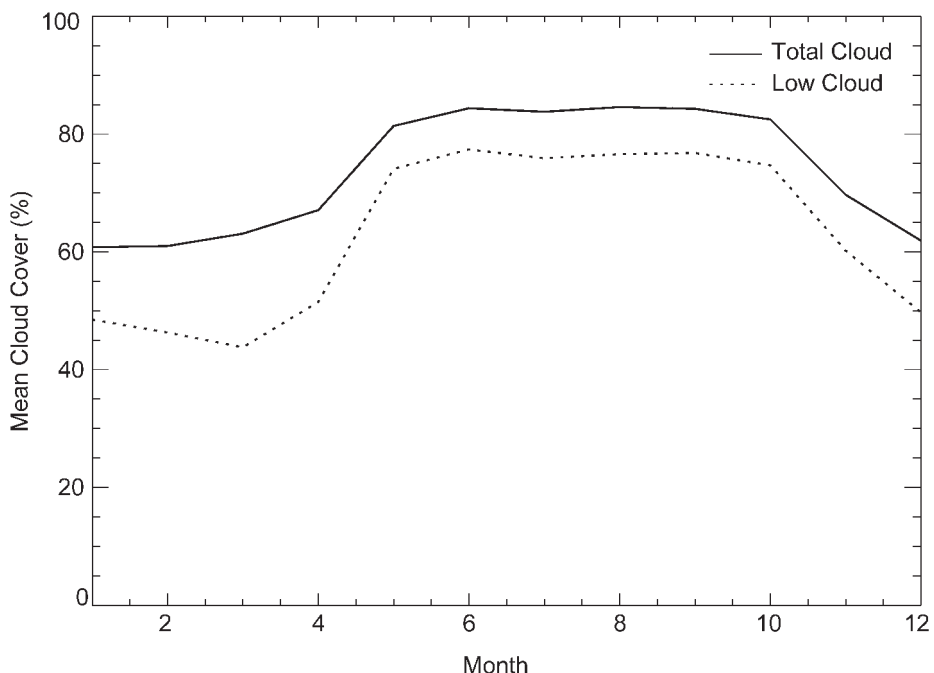


Figure 2.25. Mean annual cycle of cloud cover (total cloud and low cloud, in %) for the central Arctic Ocean based on ICOADS data through 1995 (by the authors).

based on surface observations and APP-x in general show poor agreement. A large negative trend in cloud cover in winter found in the APP-x data is not seen in the surface observations.

Figure 2.25 shows the mean annual cycle of cloudiness (percent cover) over the central Arctic Ocean based on surface observations from the International Comprehensive Ocean Atmosphere Data Set (ICOADS) through 1995. The ICOADS records for this region are from a combination of observations from the NP program and ship reports. No adjustments for moonlit versus moonless conditions or for ice crystal clouds are incorporated. Results are given for the percent of the celestial dome covered by clouds of all types (total cloud cover) and by only low cloud cover. During the winter months, there is typically about 60 percent total cloud cover, and about 45–50 percent low cloud cover. During summer, corresponding values are about 80 percent and 70 percent. Hence the annual cycle is largely driven by low-level (stratus) clouds. Note the abrupt increase in central Arctic Ocean cloud cover between May and June and the abrupt decline between October and November. These results are broadly consistent with those from other studies.

There has been considerable work addressing summer Arctic stratus. G. Herman and R. Goody (1976) envisioned the formation of summer stratus as an airmass modification process, whereby relatively warm and moist air of continental origin in an initially unsaturated airmass moves over the ice cover and condenses because of radiative and diffusive cooling to the colder surface and longwave emission to

space. Once the cloud becomes optically thick enough so that cloud top radiative cooling becomes large, turbulent kinetic energy is produced and vertical mixing occurs, producing more condensation because of adiabatic cooling. The subsequent study of J. Curry, E. Ebert, and G. Herman (1988) supports this basic view. The springtime increase in cloud cover takes place prior to the onset of widespread surface melting (Barry et al., 1987) implying that evaporation from the pack ice surface is not important. The observed persistence of the stratus is viewed in terms of the sluggishness of effective dissipating processes (e.g., precipitation, radiative heating, convective heating, synoptic activity). Several mechanisms have been proposed to account for the observed multiple layering, which are reviewed by Curry et al., (1996).

As pointed out by J. Beesley and R. Moritz (1999), for the central Arctic Ocean, there is a fairly sharp rise in the vapor flux convergence between May and June (Walsh et al., 1994; Serreze et al., 1995a; Cullather, Bromwich, and Serreze, 2000). This increase occurs about a month earlier than the sharp spring rise in the amount of Arctic stratus, hence casting Herman and Goody's (1976) interpretation into question. Based on results from a radiative-turbulent column model, Beesley and Moritz (1999) suggest that a more dominant role on the seasonality of low-level stratus is played by the temperature-dependent formation of atmospheric ice. Briefly, at temperatures below freezing, the saturation vapor pressure over ice is lower than over liquid water, such that ice particles grow at the expense of the liquid condensate. The concentration of ice crystals is smaller than that of CCN. Hence a given mass of frozen condensate is distributed among smaller numbers of larger nuclei that grow rapidly to precipitable sizes when the environment is supersaturated with respect to ice, disfavoring the development of stratus. As discussed by Beesley and Moritz (1999), this can be viewed as a "preemptive dissipation" of stratus during the cold season, as the process can prevent the humidity of clear air from reaching saturation with respect to liquid water. This idea is supported by numerous observations of ice crystal precipitation during the winter months. During summer, when temperatures are higher, the ice-crystal scavenging processes are less effective and stratus is more likely to form and persist.

Figure 2.26 provides the corresponding ICOADS-derived mean annual cycle in cloud cover for the Atlantic sector of the Arctic Ocean, taken as the region between 60°N to 65°N latitude and 40°W to 40°E longitude. Note in comparison to the central Arctic Ocean, the lack of seasonality in the means of both total and low cloud cover hover at about 85 percent and 75 percent, respectively. This manifests the persistence for all months in this region of frequent synoptic activity (see Chapter 4) and fairly high atmospheric humidity and temperatures.

The advantage of satellite data, of course, is the regular Arctic-wide coverage. Figure 2.27 provides mean fields of cloud cover (percent) for the four mid-season months based on the APP-x data set, which is considered to be improved over ISCCP-D. The fields are averaged for the years 1982 through 1999. To summarize: (1) cloud cover is rather extensive over most of the Arctic during all seasons; (2) lesser amounts are found over central Greenland, as the ice sheet extends above

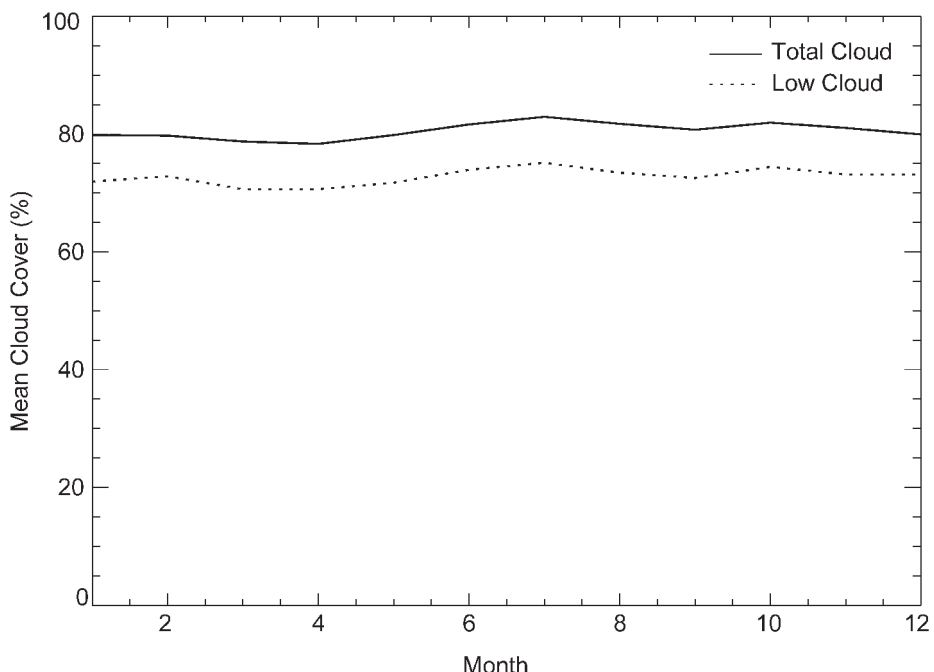


Figure 2.26. Mean annual cycle of cloud cover (total cloud and low cloud, in %) for the Atlantic sector of the Arctic Ocean based on ICOADS data through 1995 (by the authors).

much of the tropospheric water vapor; and (3) in accord with the surface-based ICOADS observations, cloud cover is particularly extensive in the Atlantic sector for all months.

Based on surface observations, Eastman and Warren (2010a) show a positive trend in Arctic Ocean cloud cover, linked to the observed decline in sea ice extent. The relationship, however, is complex. Whereas sea ice loss may promote more cloud cover, changes in cloud cover will also influence the ice cover. A key issue regarding the latter is the nature of the cloud radiative forcing. As already introduced, whereas clouds reduce the shortwave radiation flux to the surface, largely through their high albedo, they increase the longwave flux to the surface. It appears that, except in summer, the net effect of clouds is to warm the surface (the longwave effect wins), and the cloud changes identified by Warren and Eastman (2010a) appear to have a net warming effect. This finds support in the study of J. Francis and E. Hunter (2006) based on infrared sounding data from satellites. We return the issue of cloud radiative forcing in Chapter 5.

2.3.7 Precipitation

Arctic precipitation is another key climate variable, which, like cloud cover, is still inadequately determined. The density of observing stations is generally quite low,

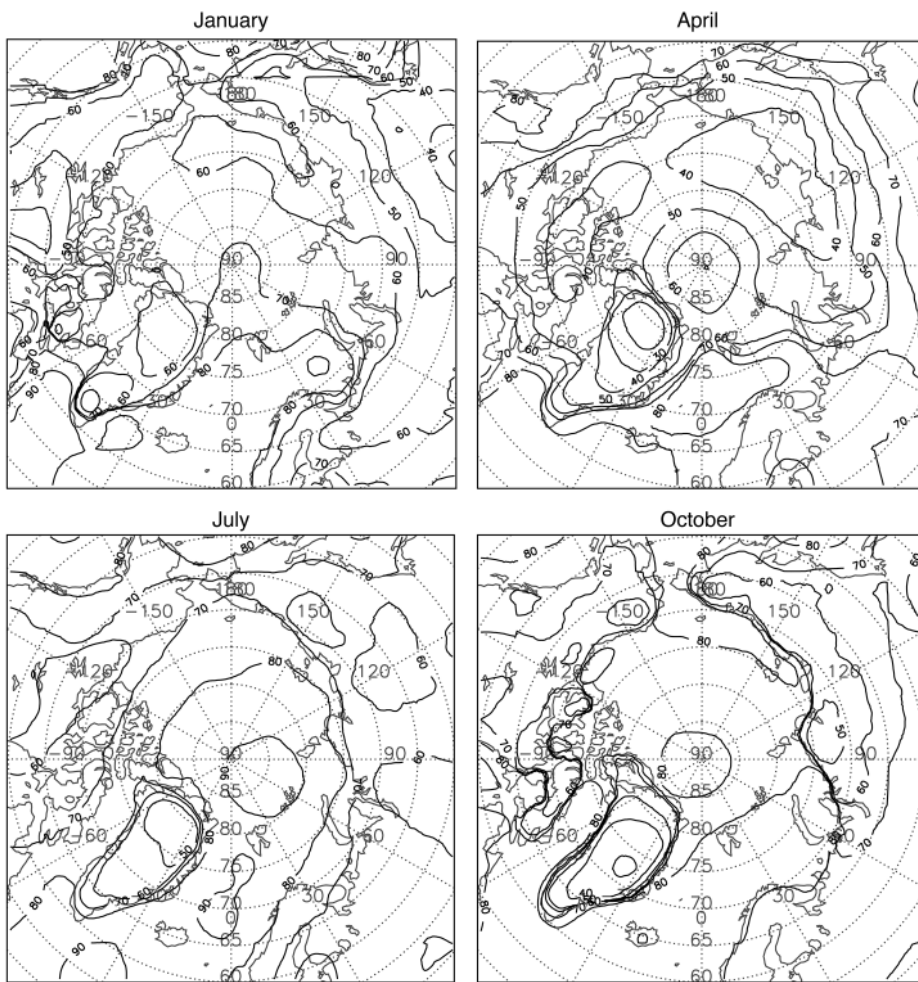


Figure 2.27. Mean cloud cover (%) from the APP-x data set (1982–1999) for: January, April, July, and October (courtesy of J. Key, NOAA, Madison, WI).

particularly over the Canadian Arctic Archipelago, the Greenland Ice Sheet and the Arctic Ocean, making it difficult to obtain accurate regional precipitation estimates. The station density problem has become more severe as fiscal constraints in Canada and Russia have led to the closure of many stations. In recognition of network deficiencies, various techniques have been explored to compile Arctic-specific data sets that make use of output from numerical weather prediction models (e.g., Chen, Bromwich, and Bai, 1997; Serreze, Clark, and Bromwich, 2003b). A number of gridded global data sets providing Arctic coverage have been developed based on satellite retrievals or blending satellite retrievals with station gauge data and numerical weather model output (e.g., Xie and Arkin, 1997; Huffman et al., 1997, Huffman et al., 2001). Arctic results, however, are of questionable value; although satellite retrievals are confounded by snow-covered surfaces, there is an ongoing

problem of gauge catch of solid precipitation. The latter issue primarily revolves around gauge under-catch of solid precipitation. The most important environmental variable influencing catch efficiency is wind speed (Yang et al., 2001). Different gauge and shield combinations have and continue to be used, which vary in catch efficiency, especially for high wind speeds. Errors can reach 50–100 percent in cold, windy environments such as the Arctic. This has created artificial discontinuities in cold-region precipitation within countries and across national borders.

Efforts have been made to provide data sets with bias adjustments, mostly with respect to monthly totals. D. Legates and C. Willmott (1990) provide a global gridded climatology. P. Groisman and colleagues (1991) and E. Mekis and W. Hogg (1999) provide adjusted monthly station data sets for the Former Soviet Union and Canada, respectively. Adjustments are generally climatological in that they represent constant multipliers to raw monthly precipitation totals. Corrections require information on gauge type, mean winds and site conditions. Yang (1999) performed daily corrections to the Russian NP records. Different data sets may also include adjustments for the neglect of trace amounts, as well as evaporation and wetting (moisture that sticks to the inside of the gauge after it is emptied). The neglect of trace precipitation can be important in the Arctic, as total precipitation amounts are low in many areas.

Figure 2.28 shows the pattern of mean annual precipitation across the Arctic. This is a best-guess attempt on our part, based on bias adjusted gauge data from several different data sources, bias-adjusted output from a numerical weather prediction mode, and satellite retrievals over open-ocean areas. Although annual precipitation totals for much of the Arctic are rather low, amounts vary widely. Totals of less than 200 mm are found over the Canadian Arctic Archipelago (polar desert) and the Beaufort Sea. Over the central Arctic Ocean, mean totals are around 300–400 mm. The largest amounts in the Arctic, exceeding 1,000 mm and locally much higher, are found over the Atlantic sector, southeast Greenland, and coastal Scandinavia. This is essentially a reflection of the northward extension of the primary North Atlantic cyclone track and Icelandic Low (Chapter 4), associated strong horizontal convergence of water vapor and local orographic uplift of moist air.

There is a strong seasonality in Arctic precipitation as well as liquid/solid contributions, which is addressed in Chapter 6 along with precipitation mechanisms. That chapter also provides a closer focus on Greenland. For the present, it is sufficient to state that for the Atlantic sector of the Arctic, precipitation has a cold season maximum and summer minimum, in accord with seasonality in the strength of the North Atlantic cyclone track. By contrast, most land areas and the central Arctic Ocean exhibit a summer maximum and cold season minimum. The summer maximum over land areas is strongly associated with surface evaporation. The summer maximum for the central Arctic Ocean, by contrast, is a response to the seasonal maximum in vapor flux convergence.

Nearly all of the current generation of global climate models project that Arctic precipitation will increase through the twenty-first century (see Chapter 11). Whether or not Arctic precipitation has exhibited a positive trend over recent decades remains

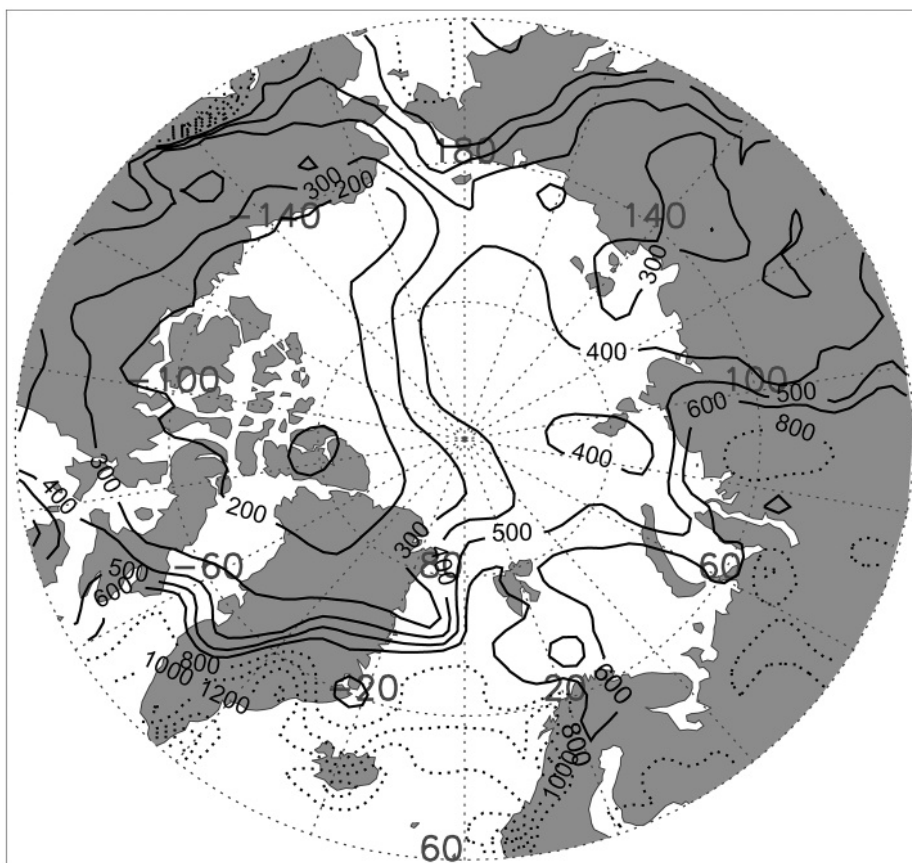


Figure 2.28. Mean annual precipitation (mm) based on available bias-adjusted data sources. Contour intervals are 100 mm (solid, for amounts up to 600 mm) and 200 mm (dotted, for amounts 800 mm and greater) (by the authors).

controversial, although observed increases in the discharge of Eurasian river draining into the Arctic indicates that it has, which is supported by recent work pointing to increases in net atmospheric vapor transport over the Eurasian drainages (Zhang et al., 2012). The issue ultimately boils down to a problem of detection using either sparse surface observations or data from satellite retrievals and atmospheric reanalyses, all of which have considerable sources of uncertainty.

2.3.8 Wind regime

Winds are relatively light in the central Arctic with mean annual speeds averaging $4\text{--}6 \text{ m s}^{-1}$. The NP observations show mean speeds of about 5 m s^{-1} year round. At locations in Severnaya Zemlya and Franz Josef Land, mean monthly wind speeds are only $6\text{--}7 \text{ m s}^{-1}$ in January (Borisov, 1975). In the Barents-Kara sea sector, cyclonic disturbances in winter bring higher wind speeds. The highest frequencies of strong winds ($>11 \text{ m s}^{-1}$) in winter are reported in the Barents Sea (>40 percent),

off Cape Farewell and southeastern Greenland (>40 percent) and in the Bering Sea (>30 percent).

At locations dominated by anticyclonic conditions and strong, persistent surface-based temperature inversions, winds are light. This is also true in sheltered valleys and coastal fiords. For example, in January 1958, the mean wind speed was 4.7 m s^{-1} at Alert, 5.1 m s^{-1} at Eureka, but only 1.3 m s^{-1} inland at Lake Hazen (Jackson, 1959b). At stations in the Canadian Arctic, mean wind speeds are typically less than in the Russian Arctic owing to the lower frequency of cyclone activity and calms are frequent. Nevertheless, when gales do occur, they may last several days and extreme wind speeds exceeding 45 m s^{-1} (hurricane strength) can occur on the east coast of Baffin Island. Katabatic winds over Greenland and Greenland tip jets are discussed in Chapter 8.

2.3.9 Blowing Snow

Despite the general predominance of light winds, blowing snow is a frequent phenomenon during the Arctic winter months. Winds greater than 5 m s^{-1} will begin to lift loose snow off the ground causing drifting snow and when it is raised to 1.8 m or more it is designated as blowing snow. This requires suspension of snow particles, which typically occurs with wind speeds greater than 15 m s^{-1} . It plays an important, yet still poorly quantified, role in sublimation of the snow cover (a direct change from solid to vapor phase), as snow grains in transport are more subject to this process. In the Barren Grounds of Canada, frequencies of blowing snow reach 15 percent or more in winter, but they may be twice as high on the Greenland ice cap.

Focus Questions and Exercises

- 1) Figure 2.24 shows spatial patterns of average Arctic surface air temperature for January, April, July, and October. Imagine a world in which all ocean areas poleward of 70°N were replaced by land (i.e., there is no longer an Arctic Ocean). Draw a new set of temperature maps for January, April, July, and October corresponding to this imaginary world and describe how and why they differ from those in Figure 2.24.
- 2) Why is annual average temperature and precipitation much lower at the South Pole than at the North Pole?
- 3) The Arctic is an ideal location for the development of large depth hoar crystals as the base of the snowpack. Explain why this is so.

3

The Basic Atmospheric and Ocean Energy Budgets

Overview

The fundamental role of the Arctic in the global climate system is to serve as the Northern Hemisphere “heat sink.” On an annual basis, net receipts of solar radiation in the Arctic are smaller than in equatorial regions. The atmosphere and ocean work to balance this differential radiative heating through poleward energy transports, with the atmosphere playing the primary role. Because of stronger differential radiative heating in winter, the atmospheric transports are largest at this time. The poleward transports into the Arctic region itself are maximized around the prime meridian and the date line. This reflects the location of the primary storm tracks and, in winter, strong surface heat fluxes from open water areas.

An instructive approach to understand the energetics of the Arctic heat sink is to consider the system from the perspective of its energy budget. The energy budget of a given column of air, extending from the surface to the top of the atmosphere, can be expressed in terms of four components: (1) the change in atmospheric energy storage composed of internal energy, potential energy, latent heat energy and kinetic energy, the last generally quite small; (2) the net radiation balance at the top of the atmosphere; (3) the net poleward transport of atmospheric energy by the atmospheric circulation; and (4) the net surface heat flux. The energy of a given underlying column extending, from the surface downward, if represented by ocean, is approximately represented by: (1) the change in ocean energy storage in terms of latent heat as floating sea ice and any overlying snow cover, and in the sensible heat of the ocean water; (2) the horizontal convergence of the oceanic sensible heat flux and the

horizontal divergence of the latent heat flux as sea ice; and (3) the net surface heat flux through which the atmosphere and ocean communicate. If the underlying column represents land, the situation is simpler. Here, the time changes in energy storage, primarily contained in the latent heat content of snow and ice and sensible heat in the soil column, is essentially balanced by the net surface flux.

We first consider conditions averaged over a simple polar cap domain, extending from 70°N to the pole. For long-term annual means, the change in atmospheric energy storage is approximately zero. This is not true, however, when we consider the annual cycle. The atmosphere gains energy during spring, but there is a loss in autumn. This is manifested in annual cycles of atmospheric temperature, humidity, and the height of atmospheric pressure surfaces. In winter, incoming solar radiation is negligible and there is a strong net radiation deficit at the top of the atmosphere driven by the longwave radiative losses. The net radiation deficit is mostly balanced by large poleward atmospheric energy transports, but also by a significant heat input from the underlying column to the atmosphere by the upward net surface flux. This is primarily represented by the growth of sea ice and the release of sensible heat stored in the ocean; for the polar cap as a whole, energy exchanges over land play a secondary role. The incoming solar flux is largest in summer, allied with a seasonal maximum in longwave loss to space. However, the net radiation balance at the top of the atmosphere is near zero in July. Compared to winter, the atmospheric transports are smaller. For July, this transport is approximately that which is needed to balance the downward (into the underlying column) net surface flux, largely associated with the melt of sea ice and sensible heat gain by the ocean. When attention is focused to an Arctic Ocean domain, we find that the ocean gains heat through both the horizontal convergence of oceanic heat transport and the export of sea ice out of the Arctic. Together, these support a small annual mean upward net surface heat flux, representing a heat source to the overlying atmosphere.

3.1 The Arctic and the Global Energy Budget

3.1.1 The Radiation Balance

Considered as a whole and for long-term annual means, and assuming a stationary climate, the earth is in a state of radiation balance, meaning that the net solar radiation at the top of the atmosphere (TOA) is balanced by the longwave radiation emitted to space:

$$R_{\text{top}} = (1-A) S\pi R^2 - \sigma T_e^4 4\pi R^2 = 0 \quad (3.1)$$

The first term on the right is the net TOA solar radiation flux, where S is the solar constant (1361.5 W m^{-2} at average earth-sun distance), A is the planetary albedo (approximately 0.3), and R is the radius of the earth (6371 km). Note that about 99.9 percent of the radiation emitted by the sun is in wavelengths of 0.15 to 4 μm with a peak intensity near 0.5 μm . Approximately 50 percent of the total emitted energy is within the visible spectrum (approximately 0.4–0.7 μm). The planetary albedo (A) differs from the surface albedo (α) (see Chapter 5) in that it includes the effects of scattering and absorption by clouds, aerosols and atmospheric gases, as well as the surface albedo. However, to a first order, absorbtion of solar radiation by the atmosphere itself is relatively small. Put differently, most of the solar radiation that is not scattered back to space by the atmosphere reaches the surface. Assuming a planetary albedo of 0.3, the net solar flux at the top of the atmosphere is about $1.220 \times 10^{17} \text{ J}$ per year of energy; division by the surface area of the planet ($4\pi R^2$) yields a radiation flux density of 239 W m^{-2} .

The second term on the right is the balancing longwave radiation emitted to space, where σ is the Stefan-Boltzman constant ($5.7 \times 10^{-8} \text{ W m}^{-2}\text{K}^{-4}$), and T_e is the effective radiation emission temperature of the earth, which is approximately 255 K. This longwave radiation is in wavelengths of about 4–300 μm , peaking at about 10 μm . In contrast to solar radiation, the atmosphere is semi-opaque with respect to longwave radiation. This effect is included in T_e . T_e depends on both the physical temperature and the longwave emissivity of the atmosphere and the surface considered as a whole. This emissivity is a measure of how efficiently the atmosphere and surface both absorb and emit longwave radiation. The surface is heated primarily through the absorption of solar radiation, and longwave radiation emitted toward the surface from the lower atmosphere. The atmosphere is heated primarily from the surface upward through vertical turbulent heat fluxes (sensible and latent heating) and longwave radiation exchanges. These longwave exchanges can be understood by considering an atmospheric column sliced into a series of thin slabs. Some of the radiation emitted from the surface is absorbed by the first slab above the surface (layer 1), heating that layer. Some of the radiation emitted by layer 1 is directed downward to the surface, while some is directed upward, some heating the next layer (layer 2), some heating higher layers (3,4,5, and so on) and some escaping to space. These layers in turn radiate both downward (to heat lower layers as well as the surface) or upward. Most of the longwave radiation emitted to space comes from the atmosphere. Direct emission to space from the surface occurs through various atmospheric “windows” (e.g., from 3–5 μm and from 8–14 μm , the former overlapping with the solar spectrum), within which atmospheric absorption is small.

Although approximate radiative balance ($R_{\text{top}} = 0$) holds for the earth as a whole, when zonal averages are examined (averages for different latitude circles), we find a strong latitudinal dependency of the net TOA solar flux: the equatorial regions receive more while the polar regions receive less. This uneven distribution of solar heating arises because the earth is a sphere. Solar radiation strikes the top of the atmosphere at a shallower (more grazing) angle in higher latitudes compared to lower latitudes. This basic pattern is in turn modified somewhat by latitudinal variations in

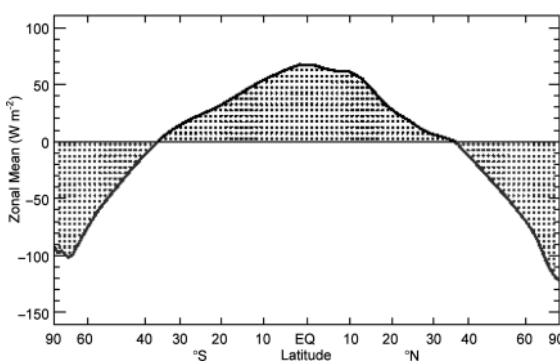


Figure 3.1. Zonal averages (averages by latitude) of the annual mean net radiation budget at the top of the atmosphere based on ERBE data (from Trenberth and Caron, 2001, by permission of AMS).

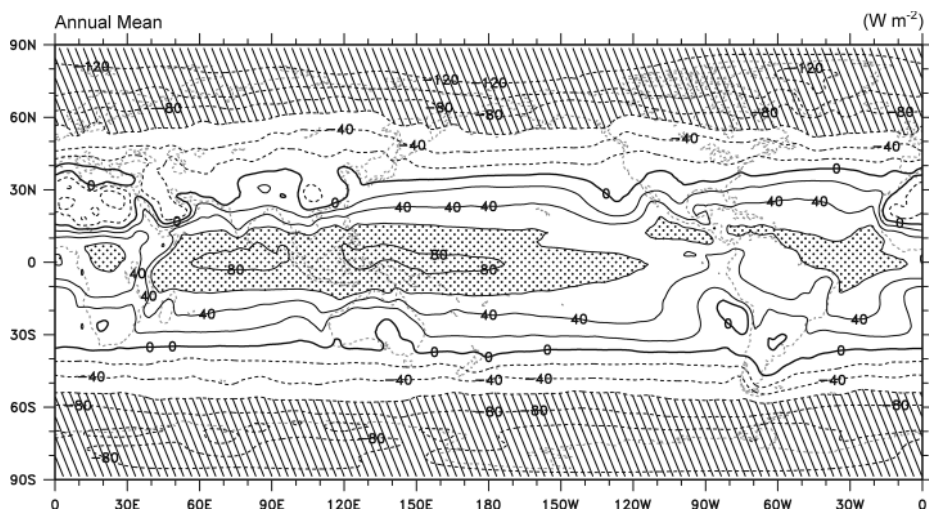


Figure 3.2. The global pattern of the annual mean net radiation budget at the top of the atmosphere based on ERBE data (from Trenberth et al., 2001, by permission of Springer-Verlag).

the planetary albedo. If radiation balance held at all latitudes, the latitudinal distribution of TOA outgoing longwave radiation would match that of the net TOA solar radiation. But this is not what is observed. Satellite data, such as from the Earth Radiation Budget Experiment (ERBE) (February 1985 through April 1989) and the follow-on CERES effort (Clouds and the Earth's Radiant Energy System) show that for annual averages, between about 38°N and 38°S, the earth receives more radiation than it emits to space (R_{top} is positive). Poleward of these latitudes, the earth emits more radiation than it receives (R_{top} is negative) (Figures 3.1 and 3.2).

3.1.2 Poleward Energy Transports

The implication of Figures 3.1 and 3.2 is that there must be poleward transports of energy by the atmosphere and oceans that warm the polar regions and cool the

equatorial regions. The uneven solar heating results in a decrease in tropospheric temperatures from south to north and a corresponding poleward decrease in the height of pressure surfaces, inducing a pressure gradient. The atmosphere works to reduce these gradients. In lower latitudes, where the Coriolis parameter is fairly small, the poleward atmospheric energy transport is associated with the thermally direct Hadley circulation cells. In the middle and higher latitudes, the time-mean tropospheric flow is primarily westerly (west to east), representing an approximate balance between the pressure gradient and Coriolis forces (geostrophic balance). The poleward energy transport is primarily accomplished via baroclinic eddies (associated with surface cyclones and anticyclones) and long waves that represent disturbances in the westerly flow. The differential solar heating also results in density gradients in the ocean, resulting in a net poleward transport of oceanic sensible heat, which plays a major role in low latitudes.

Estimates of the poleward transports by the atmosphere and ocean required to account for the TOA radiation imbalance shown in Figure 3.1 have been provided in numerous studies. The general approach has been to calculate the required transport from satellite-derived TOA radiation fluxes, the atmospheric transport from global reanalyses and then estimate the ocean transport as a residual. At present, direct estimates of ocean transport from ocean velocity and temperature are considered unreliable. Here we examine estimates of the annual mean atmospheric and ocean transports from the study of K. Trenberth and J. Caron (2001). They made use of the ERBE radiation data and atmospheric transports calculated from the NCEP/NCAR and ECMWF ERA-15 atmospheric reanalyses (see Chapter 9). Instead of obtaining the ocean transports as a residual, they used surface heat fluxes inferred from the atmospheric energy budget. Their estimates also contain adjustments for mass and energy balance. Details are provided in that paper and a companion study by Trenberth, Caron, and D. Stepaniak (2001).

The resulting estimates of the required annual transport and the atmospheric and oceanic contributions are given in Figure 3.3. The poleward ocean transport dominates only between 0° and 17°N. At 35°N, close to where the total peak transport occurs in both hemispheres, the atmospheric transport accounts for about 78 percent of the total in the Northern Hemisphere and 92 percent in the Southern Hemisphere. In general, a greater proportion of the required total transport is contributed by the atmosphere than the ocean as compared with older estimates.

Thermodynamically, the atmosphere can hence be viewed as the principal engine which pumps heat from equatorial sources to sinks in the Arctic and Antarctic. If there was no meridional energy exchange, the polar regions would be much colder, and the equatorial regions much warmer, than observed. Put differently, the polar regions, while certainly cold, are not nearly as cold as would be expected on the basis of their annual incoming solar radiation. Because the earth's rotational axis is inclined 23.5° with respect to its orbital plane, we experience seasonality in the latitudinal distribution of incoming (and net) solar radiation, expressed most strongly in the polar regions (see Figure 2.1 for effects on day length). During the winter of each hemisphere, the incoming solar radiation in the polar regions is small or zero,

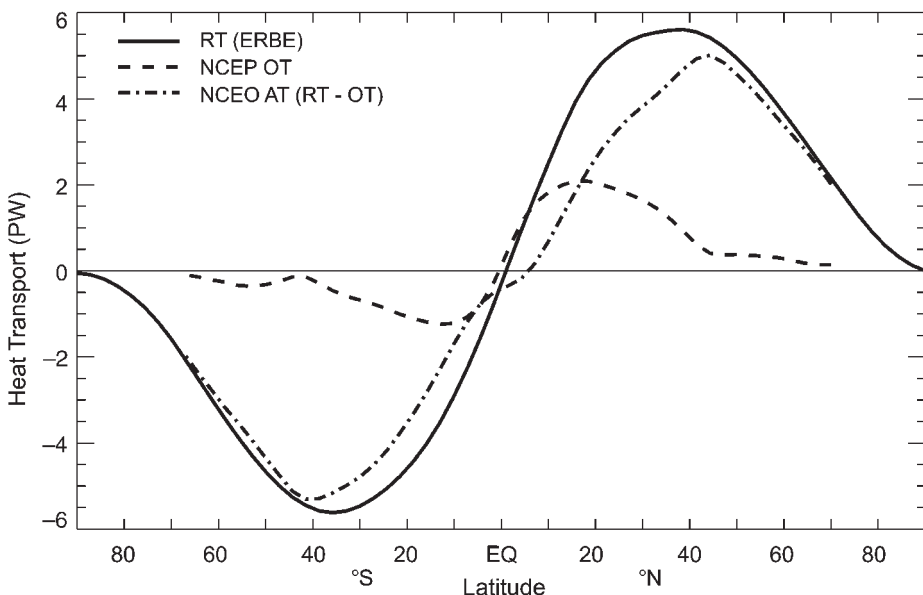


Figure 3.3. Zonal averages (averages by latitude) from the ERBE period of the mean annual energy transport required by the net radiation budget at the top of the atmosphere (RT), the total atmospheric transport (AT), and the ocean transport (OT). Units are petawatts (PW) (from Trenberth and Caron, 2001, by permission of AMS).

depending on the latitude. The temperature gradient between the equator and poles is therefore strongest, as is the poleward atmospheric transport. During summer, the solar declination is positive, and there is a more even latitudinal distribution of solar heating. This weakens the atmospheric temperature gradient, and the poleward atmospheric transport is correspondingly smaller (Figure 3.4).

3.2 The Terms of the Arctic Energy Budget

3.2.1 Overview

With the basic role of the Arctic in the global climate system established, focus turns to the energetics of the Arctic itself. Following the framework of past studies (Nakamura and Oort, 1988; Overland and Turet, 1994; Serreze et al., 2007) we consider the annual cycle of the energy budget of the Arctic atmosphere, viewed in terms of a column extending from the surface to the top of the atmosphere, and its connection with the energy budget of the underlying column, extending from the surface downward to a depth at which energy transfers can be assumed to be negligible. Figure 3.5 provides a schematic. After introducing the budget equations, we examine the situation for both a simplified polar cap, extending from 70–90°N, and for a domain representing the Arctic Ocean (Figure 3.6).

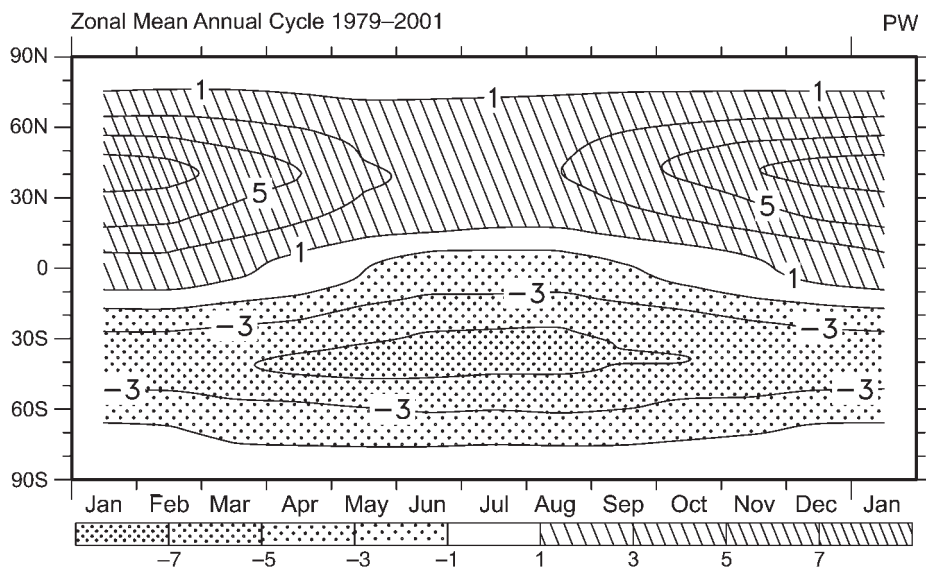


Figure 3.4. The zonal mean (averages by latitude) annual cycle of northward atmospheric energy transport, averaged for 1979–2001 (PW). Negative values in the Southern Hemisphere mean transport to the south (toward the South Pole) (from Trenberth and Stepaniak, 2003, by permission of AMS).

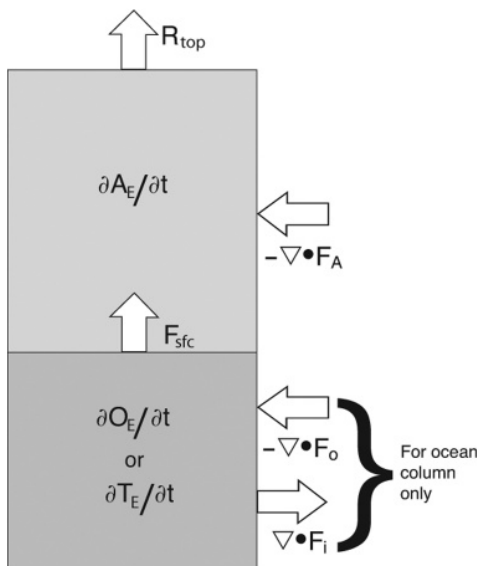


Figure 3.5. Schematic of the energy balance of an atmospheric column and underlying column, the latter representing either land or ocean. Terms are defined in the text (courtesy of N. Vizcarra, NSIDC, Boulder, CO).

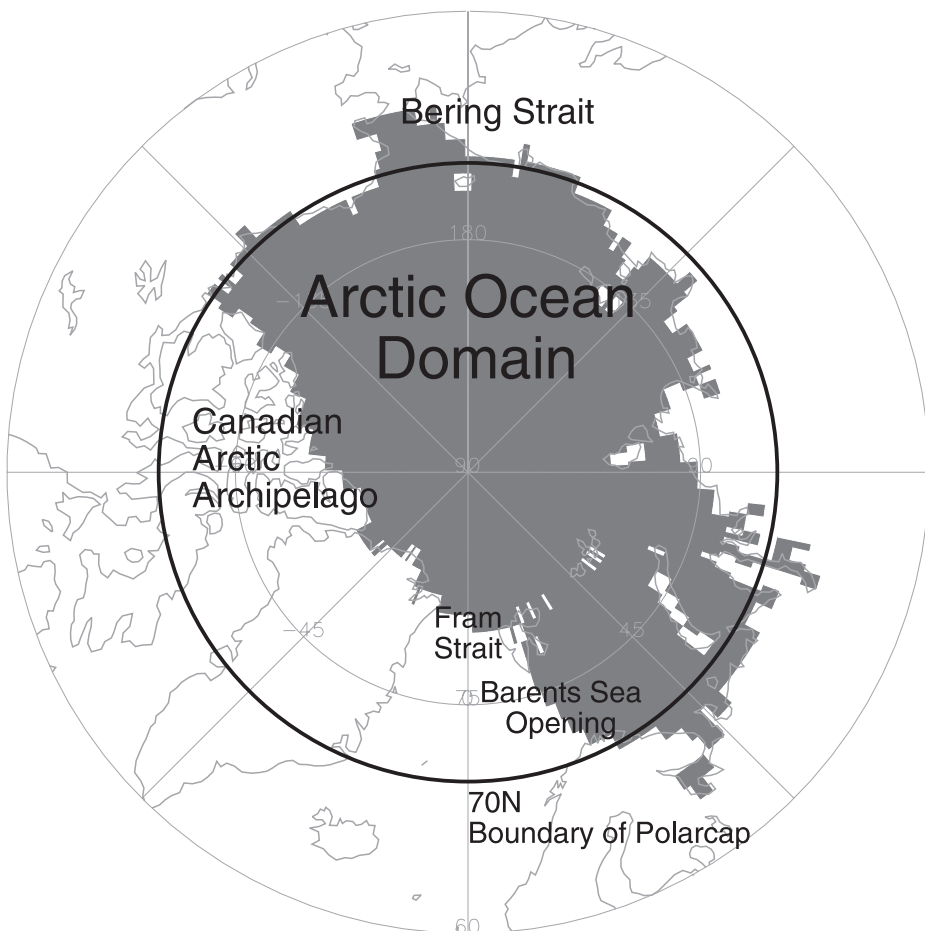


Figure 3.6. The polar cap domain (the region north of the 70°N circle) and the Arctic Ocean domain for which energy budgets are examined (from Serreze et al., 2007, by permission of AGU).

3.2.2 The Energy Budget Equations

The energy budget of any given atmospheric column is:

$$\partial A_E / \partial t = -\nabla \cdot F_A + R_{top} + F_{sfc} \quad (3.2)$$

which says that the time change in the storage of energy in the column ($\partial A_E / \partial t$) is represented by the sum of the convergence of the horizontal flux of atmospheric energy ($-\nabla \cdot F_A$), R_{top} , and the net surface heat flux (F_{sfc}). If the sum of the three terms on the right is positive, the atmospheric column gains energy. If their sum is negative, the atmospheric column loses energy. All units are in W m^{-2} . The basic question we are asking from Equation 3.2 is: what are the relative contributions of the net fluxes of energy into the sides, top, and bottom of the atmospheric column

and how do these vary seasonally to cause changes in the energy content of the atmospheric column?

Going through each of the terms on the right of Equation 3.2, the tendency in atmospheric energy storage is represented as:

$$\frac{\partial A_E}{\partial t} = \partial / \partial t 1/g \int_o^{ps} (c_p T + k + Lq + \Phi_s) dp \quad (3.3)$$

where p is pressure, T is temperature in Kelvin, c_p is the specific heat of the atmosphere at a constant pressure ($1005.7 \text{ J K}^{-1} \text{ kg}^{-1}$, $c_p T = c_v T + pV$, where c_v is the specific heat at constant column, and V is specific volume), k is kinetic energy, L is the latent heat of evaporation ($2.501 \times 10^6 \text{ J kg}^{-1}$), q is specific humidity (the ratio of the mass of water vapor in a sample to the total mass of air in a sample), g is gravitational acceleration (approximately 9.81 m s^{-2}), and Φ_s is the surface geopotential. The last is not a function of pressure (see Trenberth et al., 2001). Each of the terms in parentheses has units of Joules per kilogram (J kg^{-1}); that is, energy per unit mass. Vertical integration by dp and division by the gravitational acceleration yields units of J m^{-2} . Taking the tendency (the time change) in the storage results in the final desired units of W m^{-2} . Hence, atmospheric energy increases with a rise in the air temperature, a rise in moisture content and a rise in kinetic energy. The vertical integral of $c_p T$, which is the total enthalpy of the atmospheric column in question, contains both the internal energy and potential energy; if heat is added to the atmosphere, its temperature – and hence internal energy – increases, while at the same time, potential energy increases because the center of gravity of the atmosphere shifts upward (i.e., work is done). In the framework of Equation 3.3, liquid water is taken to be the zero latent heat state. This means that snowfall would appear as an energy gain in the atmosphere and an energy loss at the surface. The latent heat content of the atmosphere also ignores liquid water or ice in the atmosphere such as that contained in clouds.

As for the convergence of the horizontal flux of atmospheric energy,

$$-\nabla \bullet \mathbf{F}_A = -\nabla \bullet 1/g \int_o^{ps} (c_p T + \Phi + Lq + k) \mathbf{v} dp \quad (3.4)$$

Here, \mathbf{v} is the horizontal wind vector. This says that if more energy is being transported into the column by the horizontal wind than is being transported out of the column by the horizontal wind, then there is an energy flux convergence that contributes to an increase in the atmospheric energy storage. Conversely, if more energy is being transported out of the column by the horizontal wind than is being transported into the column by the horizontal wind, then there is an energy flux divergence (negative convergence) that contributes to a decrease in the atmospheric energy storage.

The final term in Equation 3.2, the net surface flux F_{sc} , is the net energy transfer between the atmospheric column and the underlying column. It is defined here as positive upward. If there is a net transfer of energy from the underlying column into the atmospheric column (a positive net surface flux), then this counts as an energy

gain by the atmospheric column and an equivalent loss by the underlying column. Conversely, if there is a net transfer of energy from the atmospheric column into the underlying column (a negative net surface flux), this counts as an energy loss from the atmospheric column and an equivalent gain by the underlying column. The net surface flux can be written as:

$$F_{\text{sfc}} = - (R_{\text{sfc}} + Q_H + Q_E) \quad (3.5)$$

where R_{sfc} is the net radiation at the surface (the sum of the net shortwave and net longwave radiation fluxes at the surface) and Q_H and Q_E are the turbulent sensible and latent heat fluxes. The terms on the right side of the equation (examined more closely in Chapter 5) are taken as positive downward; the minus sign is consistent with the convention that the net surface flux is positive upward (into the atmospheric column). Equation 3.5 is saying that, if the net radiation at the surface is not balanced with the turbulent fluxes, there must be an exchange of energy between the columns.

We now turn our attention to the energy budget of the underlying column, which could variously represent ocean with or without a floating sea ice cover (and an overlying snow cover), soil, soil with vegetation on the top (which may in turn be covered by snow), an ice sheet, or a glacier. If the column represents ocean, the following applies:

$$\partial O_E / \partial t = \partial / \partial t (L_i + S_o) = - F_{\text{sfc}} - \nabla \cdot \mathbf{F}_o + \nabla \cdot \mathbf{F}_i \quad (3.6)$$

which states that the tendency in energy storage in the ocean ($\partial O_E / \partial t$) is (approximately) represented by the sum of the tendency in latent heat storage in any floating sea ice and any overlying snow cover (L_i) and the tendency in sensible heat storage of the ocean water (S_o). The tendency in ocean energy storage is in turn equal to the sum of the negative of the net surface heat flux F_{sfc} , the horizontal convergence of the oceanic sensible heat flux (\mathbf{F}_o), and the horizontal divergence of the latent heat flux as sea ice (\mathbf{F}_i). The combination of the last two is the oceanic equivalent of the atmospheric flux convergence in Equation 3.2. A convergence (divergence) of oceanic heat into the polar cap domain acts to increase (or decrease) the heat content of the column. A given mass of ice has a lower energy content than a given mass of water at the same temperature. Assuming that a net export (or divergence) of sea ice from the column is replaced by the same mass of water at the same temperature, there is an effective increase in the heat content of the column. The sea ice terms in Equation 3.6 could include contributions by icebergs. Several small terms are ignored, including the sensible heat of the ice, sensible heat of the ice transport, kinetic energy changes in the ocean, and sensible heat transports associated with river discharge into the ocean.

A key point is that Equations 3.2 and 3.6 are linked through the net surface heat flux term. Reinforcing the previous discussion, it should be evident that if F_{sfc} is positive (a flux from the underlying column into the atmospheric column), this contributes to a loss of energy from the underlying column, which counts as a gain

of energy by the atmospheric column. If F_{sfc} is negative, it contributes to a loss of energy in the atmospheric column and a gain of energy in the underlying column.

Recall from Equation 3.5 that the net surface flux represents the sum of the net radiation at the surface and the turbulent sensible and latent heat fluxes. For an ocean column, the contribution of F_{sfc} to changes in heat storage is manifested in terms of ice melt, heat conduction, and absorption of solar radiation within the column (we can consider this as a bulk heating term). Regarding melt of snow or ice, a unit mass of liquid water at 0°C possesses a higher latent heat content than a unit mass of ice at the same temperature. Attaining the higher latent heat content requires an absorption of energy (e.g., surface net radiation directed downward), which, in the framework adopted here, counts as a heat loss from the atmospheric column. If temperature decreases from the surface downward into the underlying column, there will be a conduction of heat into the underlying column which again counts as a heat loss from the atmospheric column. If the temperature gradient is the reverse, the underlying column loses energy, which the atmospheric column gains. Sea ice growth is manifested in the conduction term. Ice growth, which occurs at the bottom ice, is associated with a latent heat release, which maintains a temperature gradient from the ice-ocean interface to the (colder) surface, and hence an upward conductive flux through the ice.

Solar radiation can penetrate to a considerable depth through liquid water and snow. Although some (or in the case of a snowpack, most) of this penetrating radiation will be scattered back out of the underlying column, that which is absorbed represents a heat gain. Absorption of solar radiation in low-albedo open water areas is a key part of seasonal heat gain in the upper part of the Arctic Ocean. Transmission of solar radiation through sea ice is highly variable, depending on the wavelength of the radiation, ice thickness, and the distribution of melt ponds and bare ice surface (Frey, Perovich, and Light, 2011).

More than 50 percent of the total solar radiation can be absorbed in the top 10 cm of ice. Essentially, all the ultraviolet and infrared radiation is absorbed in the upper 50 cm of ice.

If the underling column represents land (terrestrial, T; variously comprising soil, soil with vegetation on the top [which may in turn be covered by snow], an ice sheet or a glacier), the situation is simpler:

$$\partial T_E / \partial t = \partial / \partial t (L_T + S_T) = - F_{\text{sfc}} \quad (3.7)$$

where L_T and S_T are time changes in the terrestrial storage of latent heat and sensible heat. This would include latent heat storage in the form of ice (snow, glacier ice) and liquid water, sensible heat storage in the form of ice and liquid water, and sensible heat storage in the soil column. Because lateral heat transport divergences for a terrestrial column are small and can be ignored, the tendency in terrestrial heat storage is, to a good approximation, equal to the negative of the terrestrial net surface heat flux F_{sfc} . It is recognized, however, that lateral heat transports by rivers can be locally significant (Su et al., 2006).

The discussion that follows draws strongly on the study of Serreze et al. (2007), who examined the energy budgets for polar cap and Arctic Ocean domains (Figure 3.6) based on data from the ERA-40 and NCEP/NCAR reanalyses (see Chapter 9) for the 1979–2001 period, emphasizing the former product, along with satellite and oceanographic data compiled from a variety of sources. The reanalyses provide for gridded fields of atmospheric budget terms (data for each grid node representing a column); the atmospheric terms for each domain are based on averaging data over the nodes contained in each domain.

3.3 Energy Budget of the Polar Cap Domain

3.3.1 Understanding the Seasonal Cycle

Monthly atmospheric energy budget terms for the polar cap from ERA-40 are provided Table 3.1. We also make use of CERES satellite data for R_{top} and AVHRR data for planetary albedo during months with a significant solar flux. CERES can be viewed as a follow-on to the earlier ERBE (Wielicki et al., 1996). It must be stressed at this point that, although atmospheric reanalyses like ERA-40 provide for useful evaluations of the energy budget, even today, there is considerable uncertainty in some of the terms. For example, from Table 3.1, the monthly energy budget residual from ERA-40 (the sum of all of the budget terms; if the budget is closed, the sum is zero) can be as large as 24 W m^{-2} . The story is the largely the same for other atmosphere reanalysis. Mass correction errors applied to the atmosphere transports and errors in the surface fluxes needed to get F_{sfc} are known to be particularly problematic. Although, as seen from Table 3.1, there can be large differences in R_{top} between ERA-40 and the CERES satellite observations (although the latter are only for a short period, 2000–2005), satellite observations themselves have uncertainties.

With these caveats in mind, consider first the annual cycle in the rate of atmospheric energy storage of energy storage $\partial A_E / \partial t$, starting with August, which represents late summer. According to ERA-40, there is a loss of energy from the atmospheric column in this month of -17 W m^{-2} . The loss is at its maximum in September (-27 W m^{-2}), is roughly maintained in October (-22 W m^{-2}), then declines through the winter. It turns positive in February. The atmospheric energy gain increases during spring to a maximum of $+25 \text{ W m}^{-2}$ in April, and is slightly positive in July. The annual cycle in the atmospheric energy content can be readily seen in atmospheric variables averaged for the region north of 70°N , such as the mean height of the 300 hPa pressure surface (Figure 3.7) and the mean precipitable water (Figure 3.8) as evaluated from NCEP/NCAR data.

The annual cycle in the energy storage of the atmosphere is determined by the interactions of the three terms on the right of Equation 3.2. A useful starting point is to consider an idealized (but obviously unrealistic) polar cap for which there is no horizontal atmospheric heat flux convergence and no vertical heat transfers between the atmosphere and the underlying column ($-\nabla \cdot \mathbf{F}_A$ and F_{sfc} equal zero).

Table 3.1 Monthly and annual mean components of the atmospheric energy budget of the north polar cap domain

Month	Fluxes and Storage Changes (W m^{-2})					
	$\partial A_E / \partial t$	^a R_{top}	$-\nabla \cdot F_A$	F_{sfcc}	^b Plan. Albedo	^c Res.
<i>January</i>	-2	-175	[-173]	108	56	-9
<i>February</i>	5	-171	[-169]	112	51	-13
<i>March</i>	12	-143	[-145]	110	40	0.71
<i>April</i>	25	-88	[-92]	92	17	0.66
<i>May</i>	21	-27	[-37]	66	-18	0.64
<i>June</i>	18	23	[18]	89	-70	0.54
<i>July</i>	1	11	[21]	94	-85	0.45
<i>August</i>	-17	-66	[-58]	98	-39	0.48
<i>September</i>	-27	-145	[-140]	106	17	0.55
<i>October</i>	-22	-183	[-180]	114	53	-
<i>November</i>	-11	-184	[-180]	105	55	-
<i>December</i>	-3	-178	[-174]	111	58	-
Mean	0	-110	[-109]	100	11	-1

^a Values in brackets are from CERES for the 2000–2005 period, from Porter et al. (2010)

^b Planetary albedo from the AVHRR Polar Pathfinder Project

^c Energy budget residual in ERA-40 calculated as $R_{top} - \nabla \cdot F_A + F_{sfcc} - \partial A_E / \partial t$

Sources: From Serreze et al. (2007) and Porter et al. (2010).

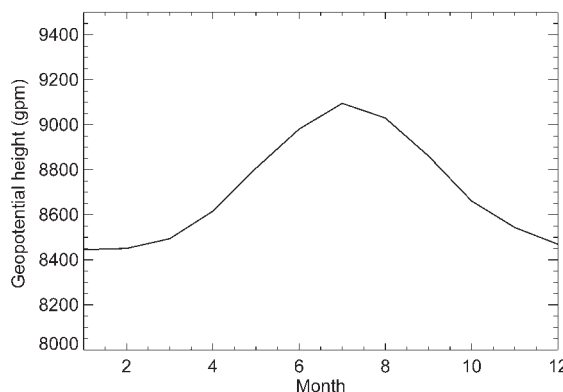


Figure 3.7. Mean annual cycle of 300 hPa geopotential height for the region 70–90°N. Results are based on NCEP/NCAR reanalysis data over the 1970–1999 period (by the authors).

Consider, in this simple model, the effects of the solar radiation flux on the atmospheric energy content. Solar radiation is the external energy source to the system. Remember that the atmosphere is approximately transparent to shortwave radiation but absorbs longwave radiation strongly outside the “atmospheric windows” (3–5 and 8–12 μm regions). Solar radiation heats the surface. The atmosphere is then heated from the bottom up by sensible and latent heat fluxes and the absorption of longwave radiation emitted by the surface. The system radiates longwave radiation into space. In radiative balance, the net solar radiation at the top of the

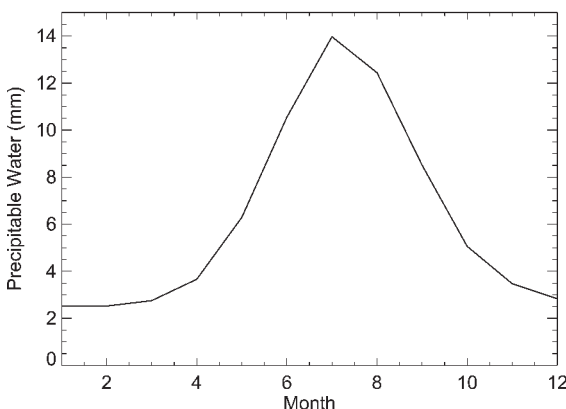


Figure 3.8. Mean annual cycle of precipitable water averaged for the region 70–90°N. Results are based on NCEP/NCAR reanalysis data over the 1979–2000 period (by the authors).

atmosphere must equal the longwave loss to space. With the assumption of radiative balance, the energy content of the atmosphere would follow the annual cycle of the solar radiation flux. The energy content would be largest in summer when the solar flux is strongest, and smallest in winter, with intermediate values during the shoulder seasons. The change in energy storage would be positive as the solar flux increases and negative as the solar flux decreases.

The observed annual cycle of the change in atmospheric energy storage bears qualitative resemblance to that expected from this simple model. The observed values are most positive in spring when the solar flux is increasing rapidly, and are most negative in autumn when the solar flux is decreasing rapidly. However, it is clear from the R_{top} values in Table 3.1, that – except for June and July – the system actually departs quite radically from radiative balance, with longwave loss to space exceeding the shortwave gain. The obvious explanation is that we have ignored $-\nabla \cdot F_A$ and F_{sfc} . We have furthermore ignored seasonality in the planetary albedo.

Consider autumn. The TOA net solar flux is small and becoming smaller, resulting in a decrease in the energy content of the atmosphere. The decline in the solar flux and hence the cooling of the atmospheric column is greater in higher as compared to middle latitudes. Hence the zonal mean temperature gradient in the atmosphere increases (temperatures decreasing to the north). This means that $-\nabla \cdot F_A$ increases, adding energy to the system to slow the cooling rate. As the atmosphere continues to cool, the net surface flux turns positive. The ocean loses sensible heat to the atmosphere. With continued cooling, sea ice forms, also releasing heat into the atmosphere to slow the cooling rate. Hence, although the atmosphere is cooling strongly in autumn, the braking effects of $-\nabla \cdot F_A$ and F_{sfc} mean that it cools at a slower rate than expected from the decline in the solar flux. While over land, the soil column is cooling and lakes and rivers are freezing, these effects on F_{sfc} for the polar cap are minor compared with the ocean heat losses (Serreze et al., 2007).

Autumn turns to winter. The atmosphere continues to lose energy, but as the winter solstice approaches, the rate slows. In part, this is because there is little change in the net solar flux (there is little solar radiation from October through February). The atmosphere is cold, but not becoming a great deal colder, so that although

$-\nabla \cdot \mathbf{F}_A$ is large, it is not changing much. F_{sfc} remains positive, primarily as sensible heat continues to leave the ocean reservoir and sea ice growth continues. The mean winter (December through February) surface flux 55 W m^{-2} includes the marginal seas, where values are comparatively high. Surface-based measurements by Maykut (1982) indicate that the upward flux over the central Arctic pack ice is closer to 21 W m^{-2} .

Spring approaches and the change in energy storage of the atmosphere turns positive, allied with an increase in the longwave loss to space. This is because of the growing input of solar radiation and the continued heat inputs by the surface flux. However, the effect of the higher solar declination is strongly offset by the high planetary albedo, largely owing to the extensive sea ice, snow cover, and clouds. But as the atmosphere warms, $-\nabla \cdot \mathbf{F}_A$ begins to decline. By April, the positive change in atmospheric energy storage attains its seasonal maximum owing in large part to the much stronger inputs of solar radiation, related to both the increase in solar declination and the first hints of a reduction in the planetary albedo. The strong energy gain of the atmosphere continues in May, but by June, when the solar input is largest, the rate of gain begins to decline. This occurs in part because of a weakening of the atmospheric circulation, and in part because of the net surface flux. By June, the snow and sea ice are melting, drawing heat from the atmospheric column. A large part of the solar input is also used to warm open water areas. The land surface also gains heat. In July, the change in atmospheric storage is close to zero, as is the TOA net radiation budget. For this month, the budget is determined by the opposing effects of the atmospheric transport and the net surface flux.

The planetary albedo is at its minimum in July and August. This primarily relates to the exposure of snow-free land, open ocean waters, and the removal of snow cover from the remaining sea ice cover. These influences outweigh the effects of the summer maximum in (highly reflective) cloud cover seen over most of the Arctic (see Chapter 2). The lower albedo of the sea ice cover does not result in sensible heating of the atmosphere (when melt is occurring, the skin temperature is fixed to the freezing point). By contrast, the stronger absorption of solar radiation by the sea ice promotes stronger ice melt, which represents a loss of energy in the atmospheric column.

As part of their earlier study, Nakamura and Oort (1988) compared the energy budgets for the north and south (Antarctic) polar caps. The annual cycles for the two polar caps, while similar in a qualitative sense, were found to differ markedly in the magnitude of the fluxes. Of interest is that the surface fluxes are much larger in the Arctic. In the Arctic, the seasonal variation in F_{sfc} was found to account for about 70 percent of the amplitude of the net radiation at the top of the atmosphere (R_{top}). What this means is that the ocean-cryosphere heat reservoir is as important as the atmospheric influx of energy from the middle latitudes in compensating for the radiation loss at the top of the atmosphere. In the Antarctic, the seasonal variation in the surface flux accounts for only a small fraction of the variation in R_{top} . As discussed by Nakamura and Oort (1988), the differences in budget terms between the two polar caps are not surprising given the radically different geography. Whereas the north polar cap is relatively flat and primary ocean covered, the south polar cap is a high-elevation, glacier-covered region.

3.3.2 Longitudinal Variations in Atmospheric Energy Fluxes

The term $-\nabla \cdot \mathbf{F}_A$ for the polar cap is identical to the meridional (north/south) component on the atmospheric energy flux averaged around the 70°N circle divided by the areas of the polar cap. As is evident in Figure 3.9, the convergence of atmospheric energy transport into the polar cap present in all months as shown in ERA-40 is the result of inflows along some longitudes being incompletely compensated by outflow along other longitudes, with the strength and relative importance of these inflows and outflows varying by season. In terms of total atmospheric energy transport (internal heat energy, potential energy, latent heat energy, and kinetic energy; top panel), there is a prominent region of poleward flow (contributing to flux convergence) centered at about 50°W. As shown in Chapter 4, this is just east of the axis of the mean 500 hPa eastern North American trough, pointing to contributions from the time mean flow and eddy transports associated with the North Atlantic storm track. These inflows are strongest in winter, at which time the North Atlantic storm track is most active. However, M. Tsukernik, T. Chase, and M. Serreze (2004) note that the longitude of this winter maximum corresponds roughly to the Norwegian Sea. This region is characterized by high convective heating rates associated with cold winter airmasses moving over open ocean waters. It appears that this regional heat source is an important contributor to the energy budget of the Arctic atmosphere.

To the west, centered at about 110°W, lies strong region of equatorward flow (contributing to flux divergence), also strongest in winter (discussed in Chapter 4), which is associated with the descending leg of the 500 hPa western North American ridge. Over Eurasia, centered at about 150°E, lies a region of inflow during the cold season, and weak outflow in summer. In winter, this longitude is just downstream of the East Asian trough. The trough weakens and shifts east in summer, helping to account for the outflows in this season. Finally, outflow dominates a broad region from about 30–90°E, with the longitude of the maximum varying by season. Hence, the peak in the flux convergence seen in winter (Table 3.1) is the net result of stronger inflows over some longitudes winning out over stronger outflows along other longitudes, with these inflow and outflows linked to large-scale features of the atmospheric circulation.

Interestingly, the convergence of latent heat energy, viewed by itself (bottom panel of Figure 3.9), peaks not in winter but in summer and early autumn (Serreze et al., 2007). The basic reason for this is that specific humidity is much higher at this time than in winter. This seasonal peak is primarily the result of strong moisture inflows in four regions, more than compensating for the strong outflows centered at about 110°W. The area of inflow at around 90°E is slightly east of the Urals trough. The area of summer inflow at about 165°W is just east of the East Asian trough. Prominent inflows at about 50°W and near the prime meridian are separated by a region of equatorward flow in summer, and weak poleward flow in the other seasons. This separation appears to be attributed to the Greenland Ice Sheet blocking the inflow of moisture (Serreze et al., 2007). Most of the moisture flow occurs at fairly low levels of the atmosphere (below 700 hPa, which is roughly 3000 m). At 70°N, the highest ice sheet elevations of about 2,900 m are found at about 35°W longitude.

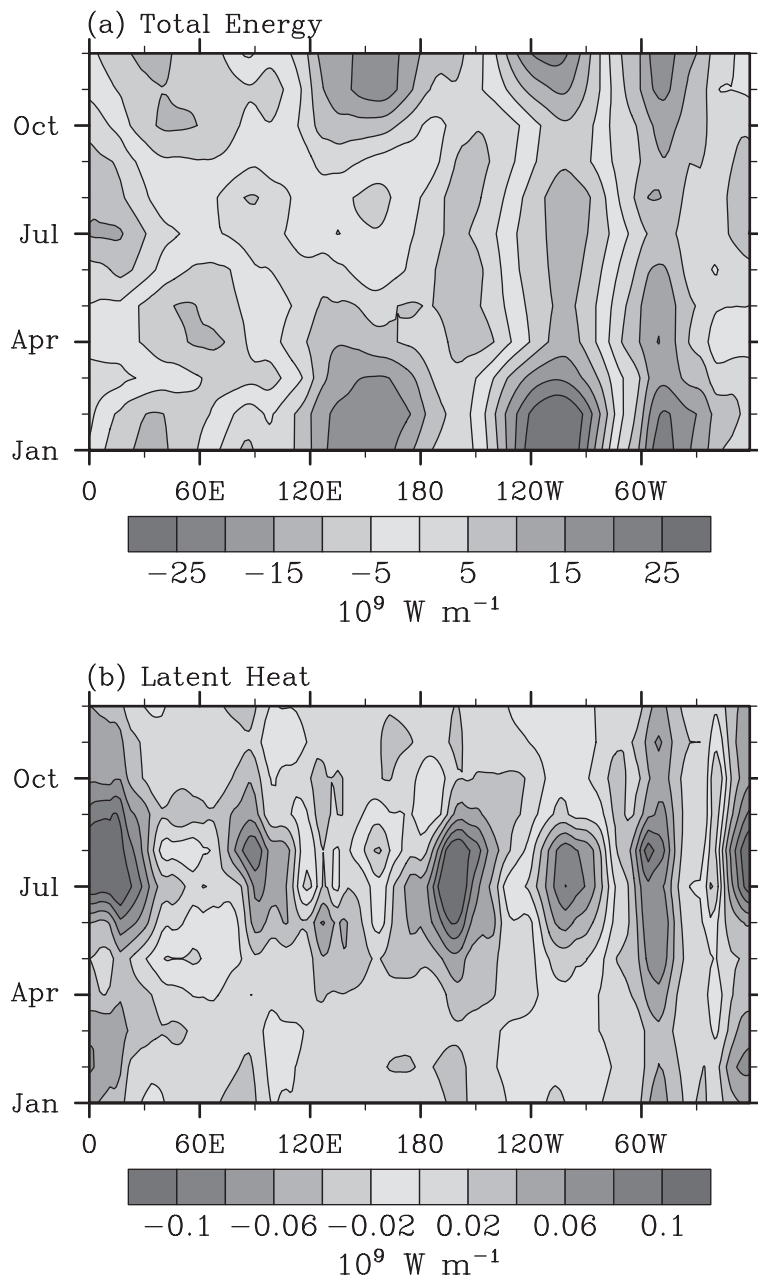


Figure 3.9. Annual cycle of the vertically integrated flow of: (a) total atmospheric energy; and (b) latent heat energy from ERA-40 across 70°N by longitude in units of Gigawatts per meter ($\text{GW m}^{-1} = 10^9 \text{ W m}^{-1}$) (from Serreze et al., 2007, by permission of AGU). (See plate section for color version.)

3.3.3 Understanding the Annual Mean

As shown in Table 3.1, in the annual mean, the change in atmosphere energy storage from ERA-40 is zero – the atmospheric energy that is gained through spring and summer is lost through autumn and winter. By contrast, the annual average net surface flux for the polar cap is positive, which together with the horizontal convergence of atmospheric energy essentially balances the net radiation budget at the top of the atmosphere. F_{sfc} over the terrestrial parts of the polar cap domain, for which lateral transfers of heat are small, should be close to zero in the annual mean; negative values through spring and summer (a heat gain by the subsurface column based on the sign convention adopted here) will be balanced by positive values through autumn and winter. The positive mean net surface flux shown in Table 3.1 must therefore manifest oceanic processes that provide a lateral heat source that allows the upward net surface flux to be maintained. Looking back to Equation 3.6 and examined in more detail shortly, this is represented by the combination the horizontal convergence of the oceanic sensible heat flux and the horizontal divergence of the latent heat flux as sea ice.

The insightful student will point out that the Arctic climate system is changing, which should be manifested in the energy budget terms. For example, there is no reason to expect that in the annual mean, there will be zero change atmospheric heat storage or a zero net surface heat flux over land (regarding the latter, recall from Chapter 2 that permafrost is warming over large parts of the Arctic). In response, one must remember that we are looking at fairly short records (ERA-40 ends in 2001) which are prone to error from a variety of sources.

With respect to linking the energy and freshwater budgets of the Arctic, recall from Chapter 2 that in the annual mean, the Arctic Ocean and its contributing terrestrial drainage are characterized by an excess of precipitation over evaporation – that is, P-E is positive. This is the same thing, but in different units, as saying that there is an annual mean convergence in the atmospheric transport of latent heat. The annual mean P-E averaged over the polar cap domain based on ERA-40 is 193 mm.

3.4 Energy Budget of the Arctic Ocean Domain

3.4.1 Understanding the Annual Cycle

Attention now turns to the irregularly shaped Arctic Ocean domain (Figure 3.6), for which we can explicitly examine the energy budget of the ocean and its link to the atmospheric budget. Recall from Equation 3.6 that change in ocean heat storage $\partial O_E / \partial t$ is determined by the sum of the vertical net surface flux F_{sfc} , the divergence of latent heat in the form of snow and sea ice $\nabla \cdot F_i$, and the oceanic convergence of sensible heat $-\nabla \cdot F_o$. The change in ocean heat storage can in turn be portioned into two major components: changes in sensible heat storage in the water (S_o), and the latent heat storage in snow and sea ice (L_i). Other terms, such as the change in the sensible heat of the sea ice and snow and the heat input by rivers draining into the Arctic Ocean, are small and can be ignored. Serreze et al. (2007) were able

Table 3.2. Monthly and annual mean energy budget terms for the Arctic Ocean domain

Mon.	Fluxes and Storage Changes									
	$\partial A_E / \partial t$	R_{top}	$-\nabla \cdot F_A$	F_{sfc}	$\partial O_E / \partial t$	S_o	$^a L_i$	$\nabla \cdot F_i$	$-\nabla \cdot F_o$	$^b Res.$
<i>Jan</i>	-4	-178	81	58	-52	-19	-33	3	3	-35
<i>Feb</i>	4	-175	91	53	-47	-16	-31	3	3	-35
<i>Mar</i>	12	-150	93	41	-34	-9	-25	4	3	-28
<i>Apr</i>	25	-96	72	20	-14	6	-20	4	2	-29
<i>May</i>	20	-37	44	-14	18	27	-9	3	2	-27
<i>Jun</i>	19	16	79	-75	79	40	40	3	2	1
<i>Jul</i>	2	10	91	-100	105	35	69	2	3	-1
<i>Aug</i>	-17	-68	92	-45	50	11	39	1	3	-4
<i>Sep</i>	-28	-150	95	18	-13	-5	-8	2	3	-9
<i>Oct</i>	-22	-186	97	58	-52	-4	-48	3	3	-9
<i>Nov</i>	-11	-186	85	59	-53	-29	-25	3	3	-31
<i>Dec</i>	2	-180	90	59	-52	-37	-15	4	3	-33
<i>Mean</i>	0	-115	84	11	-5	0	-5	3	3	-20

^a L_i is calculated as the difference between the measured terms $\partial O_E / \partial t$ and S_o

^b The residual is calculated as $R_{top} - \nabla \cdot F_A + F_{sfc} - \partial O_E / \partial t$

Source: From Serreze et al. (2007).

to assemble estimates of the major terms of the ocean energy budget except L_i , which they obtained as a residual. The divergence of latent heat as snow and ice was based on the Fram Strait sea ice export using data from Vinje, N. Nordlund, and A. Kvarnbekk (1998) and the oceanic convergence of sensible heat was estimated based on output from an ice-ocean model. The latter term represents the sum of heat transports through the Fram Strait, the Barents Sea opening, the Bering Strait, and the Canadian Arctic Archipelago. Sub-annual information on modeled heat flux was only archived as seasonal means, so for the annual cycle, the seasonal means were repeated for each month within a season. Changes in oceanic sensible heat storage were calculated from the University of Washington Polar Science Center Hydrographic Climatology data set. Terms of the atmospheric budget were again based on ERA-40 data. Monthly budget terms provided in Table 3.2, must again be viewed with the caveat of imbalances related to uncertainties in all of the budget terms. For example, assuming a steady state, the tendency in annual mean oceanic heat storage, such as that of the atmospheric heat storage, should be approximately zero. However, the results in Table 3.2 indicate a mean annual loss of oceanic heat of 5 W m^{-2} . Serreze et al. (2007) argue that this is primarily attributed to the net surface flux from ERA-40 (11 W m^{-2}) being too large; based on comparisons with other datasets, a value of 6 W m^{-2} is likely closer to the truth.

Like the polar cap, there is a clear annual cycle in atmospheric energy storage, with large changes in the shoulder seasons, and small changes in mid-summer (July) and during the winter months. However, as a result of the highly irregular shape of

the Arctic Ocean domain, and uncertainties in the data, there is no clear seasonality in the convergence of atmospheric energy transport. Notably, the July atmospheric transport is larger than for January.

Compared to the atmospheric transports, the horizontal ocean flux terms are small. Looking back to Chapter 2, we are led to conclude that, although the ice export through the Fram Strait is extremely important for the freshwater budget of the Arctic Ocean (it represents a primary sink), it has only a small influence on the heat budget of the ocean. Because of the smallness of the ocean transport terms, the annual cycle in total ocean heat storage is essentially determined by the net surface flux. However, it is these small ocean transport terms that maintain the upward net surface flux in the annual mean that is also seen for the polar cap domain (Table 3.1).

The summer gain in oceanic sensible heat is largest in June and July, and the loss is largest in November and December. Ice melt (positive L_i) occurs from June through August and is largest in July when it is about twice as big as the sensible heat gain. The strongest ice growth (negative L_i) is indicated for October, followed by a decline between November and December, and then another peak in January and February. The autumn peak is expected; there is ample open water in which new ice can grow. The second peak is somewhat puzzling. As argued by Serreze et al. (2007), part of the explanation is again an issue with the data, specifically, difficulties in calculating the storage changes in ocean sensible heat content from the hydrographic data and uncertainties in the ERA-40 net surface heat fluxes. However, the pattern is physically consistent with delayed ice growth in the warmer parts of the Arctic Ocean domain, specifically, in the Barents Sea region. The Barents Sea region is characterized by strong autumn and winter cooling and strong summer heating of the upper ocean via the net surface flux. However, autumn cooling of the water column in this region is delayed because of oceanic heat transport through the Barents Sea opening (the Barents Sea Branch of the Atlantic inflow). Hence, even as the surface waters cool, the ocean circulation keeps bringing heat into the region. The water column then cools strongly between November and December. However, there is still enough heat storage to prevent much ice growth until January and February.

Focus Questions and Exercises

- 1) The earth's axial tilt is 23.5° . Imagine a world in which the axial tilt is instead 27.5° . Describe, qualitatively, how the seasonal cycles in components of energy budgets of the Arctic atmosphere and ocean will differ from the case with a 23.5° axial tilt.
- 2) Compare and contrast, qualitatively, the seasonal cycles of the major components of the energy budget of the atmosphere for the north polar cap (the region poleward of 70°N) with what you would expect to see for the south polar cap (the region poleward of 70°S).
- 3) The vertically integrated horizontal convergence of water vapor into the Arctic region counts as a heat gain by the atmosphere. Why?

The Atmospheric Circulation

Overview

Some aspects of the atmospheric circulation of the Arctic were introduced in Chapters 2 and 3. The present chapter begins with a historical perspective. We then make use of data from the NCEP/NCAR reanalysis to provide a top-down analysis, starting with the stratosphere and moving to the tropopause, the troposphere, and the surface. The focus is largely on the mean state, aspects of seasonality, and important modes of large-scale atmospheric variability.

The stratospheric circulation during winter is dominated by a strong polar cyclonic vortex; along its margin is the polar night jet. The polar night jet decays through spring, to be replaced in summer by a weak circum-Arctic easterly flow. The winter vortex sometimes rapidly breaks down because of sudden stratospheric warmings, the effects of which can impact the troposphere and the surface. At 500 hPa, a circumpolar vortex is present year-round. The vortex is strongly asymmetric during winter, with major troughs over eastern North America and eastern Asia, and a weaker trough over western Asia. A prominent ridge is located over western North America. The lowest winter pressure heights at 500 hPa are found over the Canadian Arctic Archipelago. This asymmetry is related to orography, large-scale land-ocean distributions, and radiative forcing. The mid-tropospheric vortex weakens during spring and summer and becomes more symmetric than its winter counterpart.

The mean winter circulation at sea level has three prominent features: the Icelandic Low off the east coast of southern Greenland, the Aleutian Low south of Alaska, and the Siberian High in central Eurasia. The mean

Icelandic and Aleutian lows are maintained largely by their position downstream of the major mid-tropospheric stationary troughs, surface heating contrasts, and regional cyclone development (cyclogenesis). The winter Siberian High is a low-level feature driven by radiative cooling. The Icelandic and Aleutian lows are much weaker during summer and the Siberian high is replaced by mean low pressure. Weak low pressure also characterizes the central Arctic Ocean in summer, contrasting with a pronounced high over the Beaufort Sea in spring.

Winter cyclone activity on the Pacific side of the Arctic is most common in the vicinity of the Aleutian Low. By comparison, there is an extension of the North Atlantic cyclone track (of which the Icelandic Low is part of) deep into the Arctic. Cyclogenesis and large cyclone deepening rates are common, in part because of lee-side development along the southeast coast of Greenland and enhanced baroclinicity (strong horizontal temperature gradients) along the sea ice boundary. Bifurcation (splitting) of existing cyclones approaching Greenland from the south is also common. Because of the strong eddy activity and relatively warm, open water, the Atlantic sector is a primary pathway for transport of atmospheric energy into the Arctic (Chapter 3). Winter also sees a high frequency of mesoscale Polar Lows over open water areas of the marginal seas where convective activity is favored. While the Atlantic cyclone track weakens in summer, cyclone activity increases over land areas and the central Arctic Ocean.

A relative maximum in frontal frequencies is found during summer along northern Eurasia from about 60–70°N, best expressed over the eastern half of the continent. A similar relative maximum is found over Alaska, which although best expressed in summer, is present year-round. These features arise from strong differential heating between the Arctic Ocean and snow-free land. Orography appears to sharpen the baroclinicity. The regions of maximum summer frontal frequency correspond to preferred areas of cyclogenesis.

One of the most important large-scale modes of atmospheric variability affecting the Arctic is the North Atlantic Oscillation (NAO), which describes covariation in the strengths of the Icelandic Low and the Azores High to the south. The NAO can be viewed as the Atlantic-side component of the Arctic Oscillation (AO), also known as the Northern Annular Mode (NAM), which describes a shift of atmospheric mass between the Arctic and mid-latitudes, associated with strengthening and weakening of the circumpolar vortex. When there is less mass than normal in the Arctic and more mass than normal in middle latitudes, the AO is in its positive mode; in the reverse situation, the AO is in its negative mode. The NAO and AO are present year-round but vary in their seasonal structure. The AO and NAO have broadly had similar impacts on Arctic climate, including pronounced influences on SAT and (as

explored in Chapter 6), precipitation, not only over the Atlantic side of the Arctic strongly influenced by the Icelandic Low, but extending across large areas of the northern high latitudes. As explored in Chapter 7, The NAO and AO also have pronounced influences on the sea ice circulation, sea concentration, and extent. Recently, some attention has been paid to the Arctic Dipole Anomaly (DA), with centers of action over the northern Beaufort Sea and the Kara Sea, associated with an anomalous wind pattern that strongly affects sea ice conditions. Other patterns with prominent expression in the Arctic include the Pacific North American (PNA) teleconnection and the Pacific Decadal Oscillation (PDO), the latter strongly influencing the climate of Alaska.

4.1 Historical Perspective

The major “centers of action” in the Northern Hemisphere circulation – the Azores and Pacific highs, the subpolar Icelandic and Aleutian lows, and the Siberian High – had been identified in the 1880s by Teisserene de Bort. By 1920, the Bergen School of Meteorology (founded by Professor Vilhelm Bjerknes and colleagues in 1917) had developed pioneering ideas on the characteristics of extratropical cyclones. The nature of the general circulation of the atmosphere was interpreted in terms of a three-cell model by Bjerknes, Carl Rossby, and others. This model includes thermally direct Hadley cells in low latitudes, thermally indirect Ferrell cells in middle latitudes, and thermally direct cells in high latitudes, separated by the subtropical and polar front jet streams. Inroads were being made on the nature of climate variability. In 1932, Sir Gilbert Walker and E.W. Bliss (1932) published a landmark paper demonstrating that the North Atlantic Oscillation, reflecting covariability in the strengths of the Icelandic Low and Azores High, is a key atmospheric teleconnection (large-scale model of atmospheric variability) in the Northern Hemisphere, with impacts on the climates of northeastern North America and northern Europe.

However, a clear understanding of the Arctic circulation lagged behind. The earliest views of the Arctic’s atmospheric circulation can be attributed to H. von Helmholtz (1888), who argued that the Arctic was dominated by a more-or-less permanent anticyclone beneath a tropospheric vortex, a view that prevailed well into the twentieth century. His basic thinking was developed by W. Hobbs (1910, 1926) in his glacial anticyclone theory and further elaborated in a later paper (Hobbs, 1945) that focused on the perceived existence of a “Greenland glacial anticyclone” – a persistent anticyclone over the Greenland Ice Sheet having strong impacts on middle latitude weather. From today’s perspective, Hobbs’ papers provide for an amusing read.

Given the dearth of observations, misconception regarding the circulation north of the subpolar centers of action is not surprising. It was not until the 1940s and early 1950s that data were sufficient to make more definitive conclusions. Sea level pressure (SLP) analyses in the U.S. Historical Weather Map Series produced during

World War II contained strong positive biases away from the North Atlantic sector prior to the 1930s. Smaller errors are apparent up to 1939. As noted by P. Jones (1987), these maps were prepared by relatively untrained analysts, who tended to extrapolate into the data-poor Arctic with the concept of an Arctic high pressure cell still in mind.

While the glacial anticyclone paradigm was seemingly put to rest in papers by H. Dorsey (1945), F. Matthes (1946), and Matthes and A. Belmont (1946), Hobbs continued to argue for the Greenland glacial anticyclone for several more years (Hobbs, 1948). Even in the early 1950s, some studies depicted cyclone activity as largely restricted to the periphery of the Arctic Ocean (e.g., Pettersen, 1950). This view may have been influenced by Sverdrup's (1933) observations during the *Maud* Expedition (1918–1925) of the frequent passage of cyclones along the fringes of the Arctic Ocean. In a book chapter on Arctic climate published in 1958, F.K. Hare makes use of S. Pettersen's (1950) map, which for both winter and summer depicts most of the Arctic Ocean as a “Quiet Zone of Minimum Cyclonic Activity.” For summer, Hare provides the following description:

The quiet central zone in summer coincides fairly closely with the permanent pack ice of the Arctic Sea. Although a few frontal cyclones appear to cross it, the prevailing state is one of monotonously slack and ill-defined circulation, appropriate enough to what is certainly the world's largest quasi-homogeneous surface. Only along the flanks does cyclonic cloud and rainfall become at all common. (Hare, 1958, p. 69)

But an epiphany soon followed. The emergence in North America of more modern views of the Arctic circulation appears in the work of research groups at McGill University led by Hare (Wilson, 1958; Hare and Orvig, 1958) and at the University of Washington led by R. J. Reed (Keegan, 1958; Reed and Kunkel, 1960; Reed, 1962). These studies showed that while anticyclones are common and often persistent features, they are by no means permanent. It was also realized that cyclones can be found anywhere in the Arctic and in all seasons.

In the Soviet Union, by contrast, a relatively modern view had already been formulated in 1945 by B. Dzerzeevskii (1945). This study, remarkable both for its insight and in recognition of what must have been difficult wartime working conditions, was based on data from the icebreaker *Sedov*, the first Soviet drifting ice station, NP-1, and other observations. Dzerzeevskii correctly concluded that cyclone activity was common over the central Arctic Ocean during summer.

Turning to jet streams, fronts, and airmasses, conceptual models of the general circulation through the 1950s and 1960s presented in studies such as those by E. Palmén (1951), F. Defant and H. Taba (1957) and Palmén and C. Newton (1969) featured a two-front structure associated with the subtropical and polar front jet streams. This model can be traced back to the pioneering work by Bjerknes, Rossby and others described earlier. In the 1950s, however, the Canadian Meteorological Service adopted a three-front, three-jet stream, four-airmass model (Anderson,

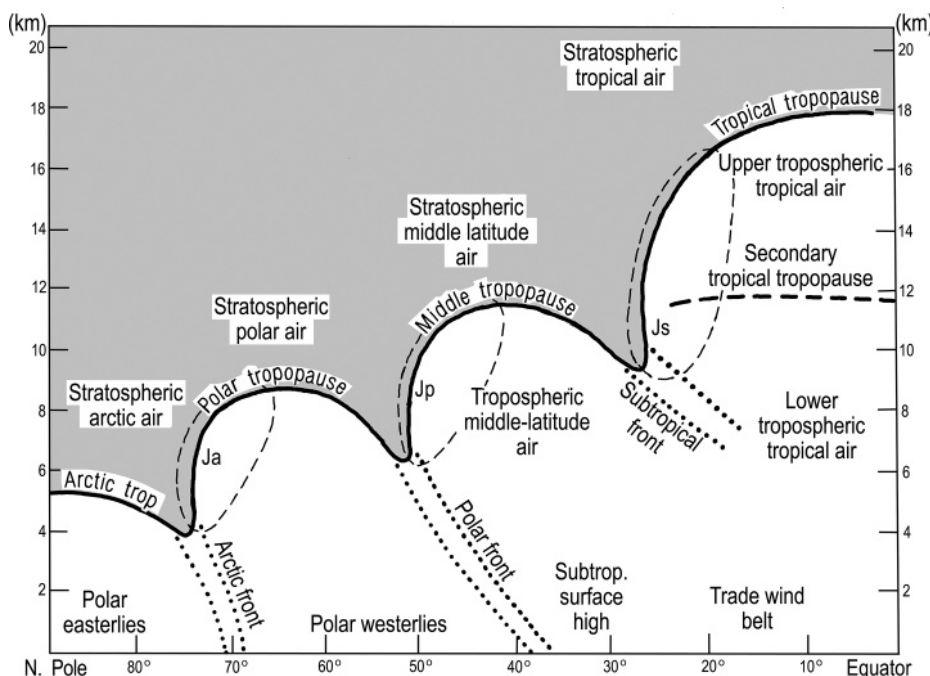


Figure 4.1. The meridional structure of the tropopause. The potential vorticity discontinuity tropopause is shown by heavy solid lines, with the stratosphere shaded. The primary frontal zones are bounded by heavy dotted lines. The 40 m s^{-1} isotach (thin dashed line) encircles the cores of the primary jet streams (Ja, Arctic; Jp, Polar; Js, Subtropical). The secondary (thermal) tropopause is indicated by the heavy dashed line. Major tropospheric and stratospheric airmasses, tropopause surfaces, and selected wind systems are labeled. Cross sections at any given time along any given longitude may differ greatly from this idealized model (from Shapiro et al., 1987b, by permission of AMS).

Boville, and McClellen, 1955; Penner, 1955; Galloway, 1958; McIntyre, 1958). Operational analyses were made by frontal contour charts showing the location of fronts at the 1,000-, 700- and 500-hPa levels. The northernmost fronts represented “Arctic fronts.” These analyses served as the basis for numerous climate studies.

M. Serreze, A. Lynch, and M. Clark (2001) provide a summary of some of the evolving thought regarding high latitude fronts. Arctic fronts were very much evident in vertical cross sections presented in early synoptic atlases (Boville, MacFarlane, and Steiner, 1959). More modern studies using aircraft data collected during the winter season under the Arctic Gas and Aerosol Program (Shapiro et al., 1984; Shapiro, 1985; Raatz et al., 1985; Shapiro, Hampel, and Krueger, 1987b) left little doubt regarding the reality of separate Arctic jet streams. These and other observations were used by Shapiro et al. (1987b) in a “revised” three-front model (Figure 4.1), which harks back to the Canadian scheme.

Some early studies of Arctic fronts include those of Reed (1960) using Northern Hemisphere weather maps; R. Bryson (1966) using streamlines and air mass analysis for North America; and R. Barry (1967), who as a young and enthusiastic researcher examined the preferred location of Arctic fronts over North America for January, April, July, and October using the Canadian frontal analyses. In a study for Eurasia, S. Krebs and Barry (1970) took a somewhat different approach of plotting the northernmost frontal boundaries depicted on Northern Hemisphere daily synoptic weather maps for July 1952–1956 to determine the median location, as well as the quartiles and outer deciles of the latitudinal distribution of fronts in relation to the forest (the tundra ecotone). They also analyzed the latitudinal gradient of 1,000–500 hPa thickness.

In the Canadian three-front model, Arctic fronts were objectively differentiated from polar fronts. But what if one instead plotted on a map the location of all fronts over some time period? Would one find geographically-preferred regions of high-latitude frontal activity separate from the major locus of polar fronts? That this is indeed the case finds its origins in the remarkable study of Dzerdzevskii (1945) and a subsequent paper by R. Reed and B. Kunkel (1960). The latter study was based on fronts plotted on summer (June–August) sea level pressure analyses for the 1952–1956 period. It revealed a belt of high frontal frequencies extending along the northern shores of Siberia and Alaska and southeastward across Canada. Reed and Kunkel argued that low frontal frequencies over Kamchatka and the high frequencies off Japan “make it abundantly clear that the polar front remains separate from, and well to the south of, the Arctic frontal zone” (p. 496). Their analysis of winter frontal frequencies failed to show a separate high-latitude feature. Consequently, the Arctic frontal zone as a geographical feature was considered to exist in summer only, in agreement with Dzerdzevskii (1945). We will return to the problem of the Arctic frontal zone later.

Investigation of stratospheric dynamics only became possible around 1960 when a sufficient number of sounding balloon ascents began to reach the 25 hPa level (~25 km) and higher on a routine basis. The first detailed characterizations of the circulation in the Arctic stratosphere were prepared by the Arctic Meteorology Research Group at McGill University (Hare, 1960a, 1960b, 1961) and the Institute of Meteorology at the Free University of Berlin under R. Scherhag (1960). R. Murgatroyd (1969) presents an early overview of stratospheric structure and dynamics based on balloon and rocket data. Efforts were intensified through the Climatic Impacts Assessment Program in the United States in the 1970s, owing to the need to assess the effects of supersonic aircraft on the stratosphere (Reiter, 1975). From the late 1970s onward, the availability of data from satellite sounders has greatly augmented our knowledge of the structure and composition of the stratosphere and the problem of stratospheric ozone depletion. In the past decade, it has become increasingly recognized that the circulations of the stratosphere and troposphere are intimately connected, and that these connections may be an important component of Arctic climate variability.

4.2 The Stratospheric Circulation

4.2.1 Mean Thermal Structure

The Arctic stratosphere extends upward from about 10 km to 40–50 km altitude. It is a very dry, statically stable region in which ozone dominates the absorption of solar ultraviolet radiation and emission of infrared radiation. In the troposphere (the region between the stratosphere and the surface, which contains about 80 percent of the atmospheric mass), the mean thermal structure is maintained by an approximate balance between infrared radiative cooling to space, surface radiative heating, and the subsequent vertical transport of sensible and latent heat by turbulent processes; and large-scale horizontal heat transport by synoptic-scale disturbances. The dominance of surface radiative heating results in surface and tropospheric temperatures that are highest in the equatorial regions and decrease toward the poles. As the troposphere is heated primarily from the surface and rising air cools, there is also a rapid decrease in temperature with altitude (however, the potential temperature – the temperature that an air parcel would have if raised or lowered to the 1000 hPa surface – increases with height). There are of course prominent seasonal and regional departures, such as strong low-level temperature inversions in the Arctic during winter (Chapter 5). By contrast, for mean conditions in the stratosphere, the infrared cooling to space is balanced primarily by radiative heating owing to absorption of ultraviolet radiation by ozone. As a result of ozone absorption, the mean temperature increases upward in the stratosphere (hence potential temperature increases strongly with height, meaning very stable conditions). Above roughly 50 km, we enter the mesosphere, where temperature again decreases with height because of reduced ozone absorption. In the stratosphere above about 30 hPa (roughly 25 km), the temperature decreases from the summer pole to the winter pole, in qualitative accord with radiative equilibrium conditions (in June, total solar radiation at the top of the atmosphere is greatest at the North Pole and least at the South Pole). Winter temperatures at around 30 km in the Arctic are below -70°C , whereas in midsummer – with twenty-four-hour sunlight – they exceed -40°C (Andrews, Holton, and Leovy, 1987). However, in the lower stratosphere, the temperature is strongly influenced by upper-tropospheric processes. This region is characterized by a mean temperature minimum at the equator and maxima at the summer pole and in the mid-latitudes of the winter hemisphere (Holton, 1992).

4.2.2 Mean Circulation and Dynamics

Figure 4.2 provides mean geopotential height fields at the 30 hPa level for the four mid-season months. In winter, as illustrated by January, the height field points to strong westerlies in the middle and upper stratosphere flowing around a deep cold vortex. Above 40 km (3 hPa, not shown), there is a polar night westerly jet stream in mid-latitudes. Peak mean zonal winds of 80 m s^{-1} actually occur around 60–70 km

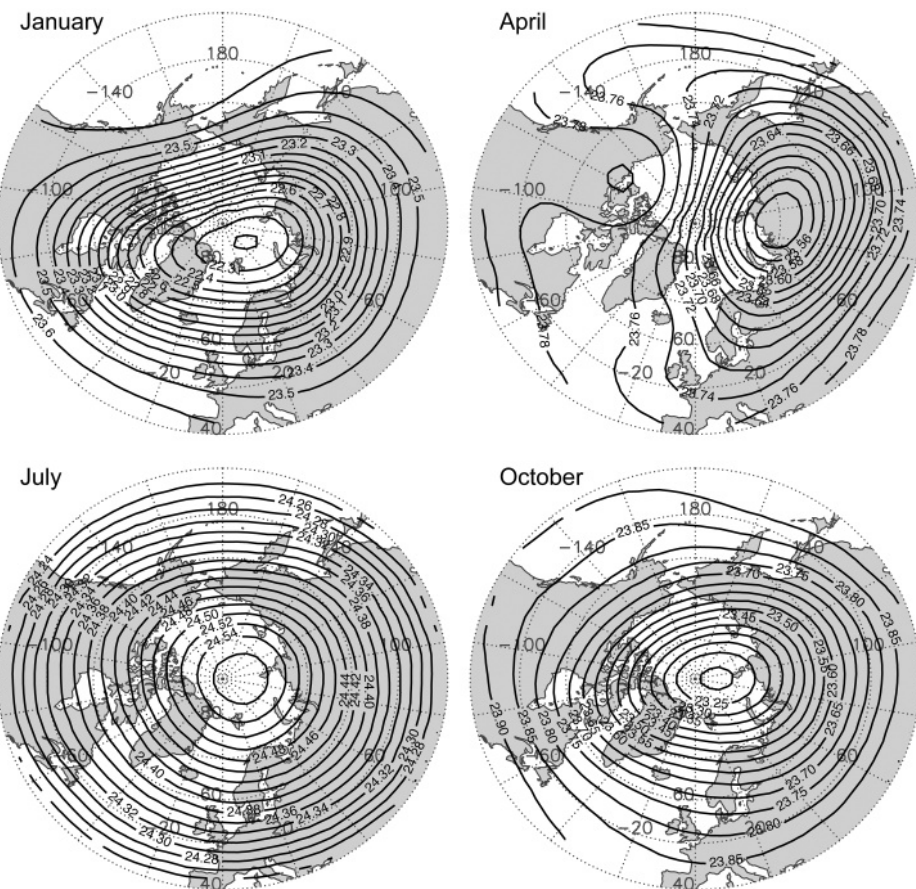


Figure 4.2. Fields of mean 30 hPa geopotential height (gpm) for the four mid-season months over the 1970–1999 period, based on NCEP/NCAR data (by the authors).

altitude (0.3 – 0.1 hPa). The winter mean stratospheric vortex is broadly symmetric, but less so than its Antarctic counterpart. There are troughs over eastern Asia and eastern North America and a weak ridge located over western North America. In spring, illustrated by the April field, the vortex center has shifted well off the pole to north-central Eurasia. In summer and above about 20 km (as seen in the July field), the cyclonic vortex has broken down. There is polar easterly flow around a highly symmetric warm polar anticyclone. Summer sees an easterly jet of about 60 m s^{-1} at 0.1 hPa located around $50\text{--}60^\circ\text{N}$. The October field illustrates the transition back toward winter conditions.

If there were no transports arising from the breaking of atmospheric waves propagating upward from the troposphere, the zonal mean temperature of the stratosphere would relax to a radiatively determined state, with the temperature distribution corresponding to an annually varying thermal equilibrium that follows the annual cycle in solar heating. The circulation would hence represent a zonal-mean zonal flow in balance with the meridional temperature gradient (a thermal wind balance), with

essentially no meridional or vertical circulation and no stratosphere-troposphere exchange (Holton, 1992; Andrews et al., 1987). As just discussed, the existence of a westerly vortex in winter and an easterly vortex in summer is qualitatively that expected from radiative equilibrium, but the winter season actually shows considerable departures from the radiatively determined state. In the 30–60 km region, the decrease in temperature from the winter pole to the summer pole is much smaller than the radiatively determined gradient. This is attributed to eddy transports that drive the flow away from a state of radiative balance. By contrast, the departure from radiative equilibrium in summer is small, implying a reduction in transports.

In the troposphere, these eddy transports are largely associated with traveling, synoptic-scale waves (which we associate with migrating cyclones and anticyclones at the surface). By contrast, winter transports in the stratosphere are associated with the long planetary waves, especially wavenumbers 1 and 2, which can penetrate into the stratosphere under certain conditions. Wavenumber refers to the number of atmospheric waves around a latitude circle. For any given day, Fourier Transform methods can be used to break down the total circulation at a given level in the atmosphere with respect to the relative contributions of long planetary waves (low wavenumbers), which move only slowly or remain stationary with respect to the earth's surface, and shorter traveling waves (higher wavenumbers). A strong wavenumber 2 component, for example, would have a pronounced expression of two ridges and two troughs, each separated by 180° longitude. If we look at the circulation on a typical winter day, we find that, whereas the troposphere has a strong contribution from the higher wavenumbers, the circulation of the stratosphere is more symmetric, indicating that the shorter waves are not readily penetrating into the stratosphere. For long time averages, the effects of the shorter waves cancel out. But even with such time averaging, the winter circulation of the stratosphere (Figure 4.2) is more symmetric than that of the troposphere (compare with Figure 4.7, described later). At 60°N, the mean January field in Figure 4.2 shows strong contributions from wavenumbers 1 and 2. This can be related to the impacts of orography and land – sea thermal contrasts (Pawson and Kubitz, 1996).

While a full explanation is beyond the scope of this textbook (see Holton, 1992, for further reading), it can be shown that waves will penetrate (vertically propagate) into the stratosphere provided that the zonal-mean wind is positive (the wind averaged around a latitude circle blows from west to east) but less than a critical value that depends strongly on the length of the waves. The longer the wave (i.e., the lower the wavenumber), the stronger the zonal wind can be and still that allows for vertical propagation. Because the zonal wind tends to be at a maximum near the tropopause in middle and high latitudes (much lower in altitude than the winter stratospheric jet), the shorter waves in winter tend to be “trapped” in the troposphere. In summer, the zonal-mean zonal winds in the stratosphere are negative (easterly, see the July field in Figure 4.2). There can be no vertical propagation of waves in these conditions. This is consistent with the fact that the summer stratospheric circulation is highly symmetric with a thermal structure close to that expected from radiative equilibrium.

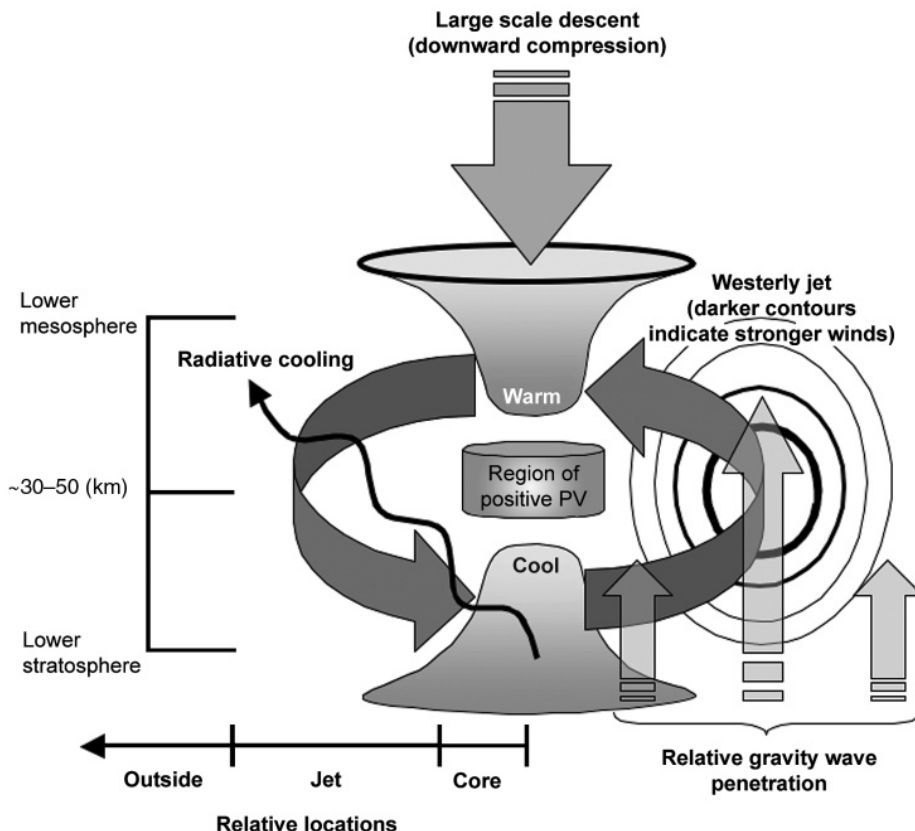


Figure 4.3. Schematic of the configuration of the winter stratospheric polar vortex as diagnosed from a hypothetical positive region of PV (i.e., a potential vorticity anomaly). The positive columnar region of PV is at the center of the vortex. Note the strong jet surrounding the region of PV, which weakens as one goes into the quasi-stationary core or outside the vortex altogether. Transparent, upward arrows conceptualize relative gravity wave activity (from Gerrard et al., 2002, by permission of AGU).

The typical thermal structure of the winter stratosphere features low temperatures in the vortex core of the lower stratosphere that increase outward from the axis of rotation. Conversely, there are high temperatures in the vortex core of the upper stratosphere and lower mesosphere that decrease outward. This is illustrated schematically in Figure 4.3. This vertical change in the temperature structure is attributed to warming through large-scale subsidence in the mesosphere and radiative cooling in the lower stratosphere during the polar night (Gerrard et al., 2002). The stratospheric jet maximum is located at the level of the temperature transition region in the vertical (10 to 1 hPa). Positive potential vorticity (PV) anomalies are found in the vortex core at the level of the thermal transition zone, with a cold trough below and warm dome above. The vortex winds, which are formed between the two thermal regimes, circulate around the core. Potential vorticity represents the specific volume (volume per unit mass of air) times the scalar product of the absolute

vorticity (the sum of relative and planetary vorticity) and the gradient of potential temperature. The PV maximum shown in Figure 4.3 arises from the low density of the air at stratospheric levels (specific volume is large), the strong increase of potential temperature with height (strong stability) and the positive absolute vorticity.

4.2.3 Sudden Stratospheric Warmings

An important aspect of variability in the stratospheric circulation is sudden stratospheric warmings. Scherhag (1960) first noted these in the 1950s and they were subsequently found to be a characteristic late winter phenomenon (Hare, 1961; Wilson and Godson, 1962, 1963; Labitzke, 1968, 1981). V. Limpasuvan, D. Thompson, and D. Hartmann (2004) provide a valuable composite analysis of the lifecycle of sudden stratospheric warming events in the Northern Hemisphere from the Transformed Eulerian Mean (TEM) framework. The reader is referred to that paper and extensive references therein for details.

The TEM framework is very useful for diagnosing the influence of eddies on the zonal mean circulation. It is useful to first consider the TEM framework in the context of the troposphere. Briefly, tropospheric eddies transport heat poleward. This acts to reduce the zonal mean temperature gradient in the extratropics and hence the strength of the zonal mean winds. Eddies also transport westerly zonal momentum poleward, tending to increase the zonal mean winds in the extratropics. In the TEM framework, the net effect of these processes at a given latitude can be expressed in terms of the divergence of the Eliassen-Palm (EP) flux. The EP flux has vertical and meridional components. The vertical component of the EP flux is related to the strength of the meridional eddy temperature flux ($\bar{v}'T'$) while the meridional component is related to strength of the eddy momentum flux ($\bar{u}'v'$), where the primes indicate departures from the zonal mean and the overbars indicate the zonal mean.

For long-term mean winter conditions, through much of the depth of the atmosphere and north of about 30°N, the EP flux divergence is negative (i.e., convergent). It can be shown that EP flux convergence represents a westward force on the zonal wind – that is, it induces slowing of the winds (Holton, 1992). In a steady state condition, the zonal wind and temperature are constant. Slowing of the zonal mean wind by the EP flux convergence is balanced by the effects of a residual circulation in the meridional plane that is in a thermally direct sense (clockwise as viewed in a mean cross section with the North Pole to the right). This residual circulation (which is part of the total zonal mean meridional circulation) is highly efficient in maintaining thermal wind balance in large-scale atmospheric motions and keeping the ageostrophic flow small in comparison with the geostrophic flow. The Coriolis force on the residual poleward meridional wind speeds up the zonal winds aloft. The Coriolis force on the residual equatorward wind reduces the zonal winds near the surface where the EP flux is divergent. Through continuity, there must be attendant vertical motions. A residual downward motion (adiabatic warming) balances radiative cooling in higher latitudes while upward motion (adiabatic cooling) in lower latitudes balances radiative warming. Departures from the steady state, seen

as time changes in the zonal wind and temperature, arise from imbalances between the EP flux divergence/convergence and associated residual circulations. The EP flux divergence pattern is weaker in summer.

The mean circulation and thermal structure of the winter stratosphere examined earlier can be similarly understood from the presence of mean EP flux convergence and meridional plane circulations associated with the upward propagation of planetary waves. In the extratropics, for example, eddy forcing maintains the observed stratospheric temperature above its radiative equilibrium. Hence there is net radiative cooling that is balanced by downward motion (adiabatic warming) associated with the residual circulation. In the tropics, the temperature is below radiative equilibrium, consistent with upward motion (adiabatic cooling). In turn, sudden stratospheric warmings (which, as the name implies, are transient events) can be understood from the anomalous upward propagation of planetary waves.

As outlined by Limpasuvan et al. (2004), when an anomalous vertically propagating planetary wave enters the stratosphere, it imparts an anomalous EP flux convergence. The decelerated westerly flow is brought back toward balance by the Coriolis force acting on the poleward mean residual flow anomaly. This induces adiabatic temperature changes that also try to bring the flow back to balance. Through continuity, the poleward mean meridional flow across the axis of the EP flux forcing requires sinking motion (adiabatic warming) below and poleward of the forcing region. In turn, there is rising motion (adiabatic warming) below and equatorward of the forcing region. These meridional-plane circulations quickly weaken the meridional temperature gradient, and give rise to rapid high-latitude stratospheric warming.

In extreme cases, stratospheric temperatures can rise 50K and the circumpolar vortex can reverse to easterly flow over the span of a few days. The presence of vertically propagating waves, while necessary for sudden stratospheric warmings, is not a sufficient condition. It appears that the stratospheric flow needs to be “preconditioned,” such that wave activity is focused toward the polar vortex. The preconditioning occurs when the vortex is poleward of its climatological position (Limpasuvan et al., 2004).

Figure 4.4 illustrates changes in 10 hPa temperature associated with a major warming event that took place between late December 1984 and early January 1985. Temperature fields are given for five-day averages from December 17–21, 1984, December 27–31, 1984, and January 6–10, 1985. These are identified by K. Kodera and M. Chiba (1995) as representing, respectively, the prewarming, warming, and postwarming phases of the event. The prewarming stage shows a vortex center located well off the pole over the Norwegian Sea, with minimum temperatures of about -72°C . During the warming phase, the vortex breaks down into four centers. The postwarming phase shows additional breakdown. The contrast in high latitude (e.g., north of 70°N) temperatures between the prewarming and the postwarming phases is readily apparent. Between the warming and postwarming phases, the stratospheric zonal-mean zonal winds reversed at 70°N (Kodera and Chiba, 1995).

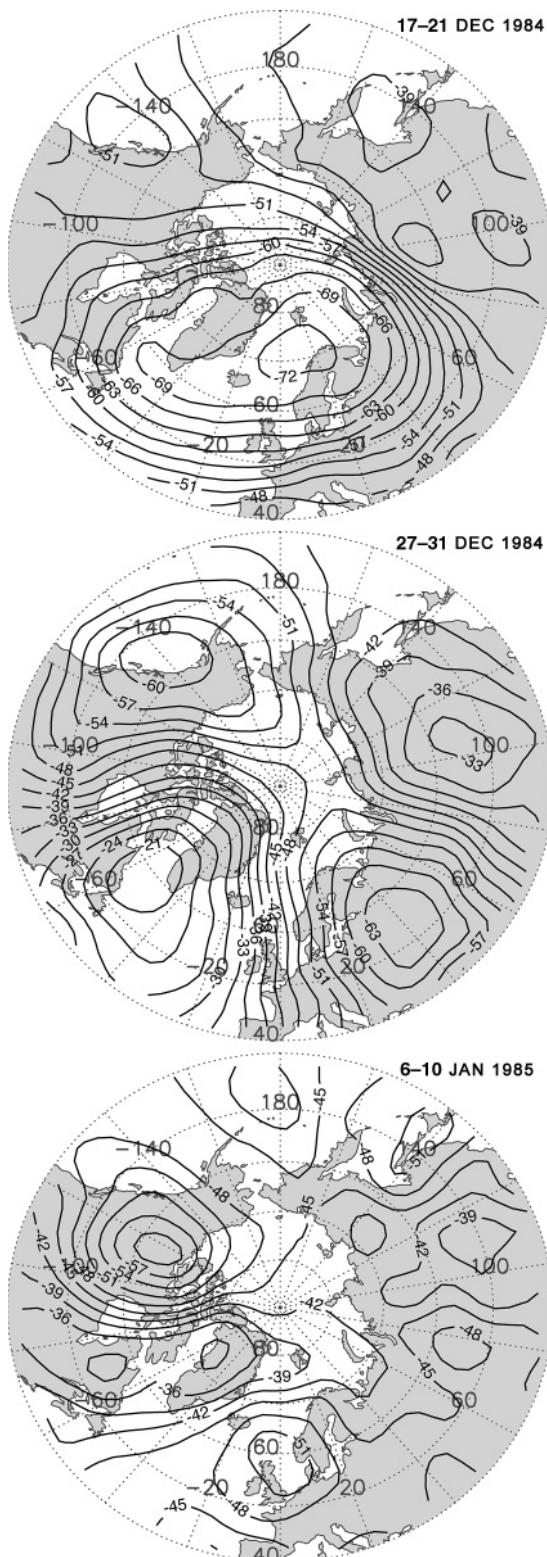


Figure 4.4. The change of 10 hPa temperatures ($^{\circ}$ C) associated with a sudden stratospheric warming event that occurred during late December 1984 through early January 1985. The plots give mean temperatures for the prewarming (December 17–21), warming (December 27–31), and postwarming (January 6–10) phases as identified by Kodera and Chiba (1995). Results are based on the NCEP/NCAR reanalysis (by the authors).

There is mounting evidence that sudden stratospheric warmings can have pronounced effects on the circulation of the troposphere and surface. Various mechanisms have been offered (Baldwin and Dunkerton, 1999, 2001; Hartmann et al., 2000; Ambaum and Hoskins, 2002; Perlitz and Harnik, 2003). Although they are still being elucidated, the point to be emphasized is the apparent existence of two-way coupling – while upward propagation of planetary waves influences the stratospheric circulation, changes in the stratospheric circulation can influence the troposphere and surface, for example, by changing the conditions for vertical propagation of waves. M. Baldwin and T. Dunkerton (2001) find that the surface signature of downward propagating anomalies strongly resembles the surface signature of the Northern Annular Mode (also referred to as the Arctic Oscillation), a mode of atmospheric variability that has pronounced impacts on Arctic climate (Section 4.7.2).

4.2.4 Ozone Characteristics

Ozone measurements can provide three types of information. The first is the total ozone in an atmospheric column. This is measured with the Dobson spectrophotometer, which compares the solar radiation at a wavelength where ozone absorption occurs with that in another wavelength where such effects are absent. Second is the spatial pattern of total ozone. This is determined by satellite sounders such as NASA's Total Ozone Mapping Spectrometer (TOMS) aboard Nimbus-7, Meteor-3 and ADEOS (Advanced Earth Observing Satellite). Third is the vertical distribution of ozone. This can be measured by chemical soundings of the stratosphere, by passive microwave limb sounding from satellites, or calculated at the surface using the Umkehr method. The last method determines the effect of solar zenith angle on the scattering of solar radiation.

The annual cycle of mean ozone column totals is shown in Figure 4.5 for two periods: 1964–1980 and 1984–1993. There is a strong annual cycle in high latitudes with values exceeding 400 DU (Dobson units = milli-atmosphere centimeters, or mm column depth at standard temperature and pressure) in late winter and spring. This compares to 300 DU in September. The late-winter to spring maximum is a result of strong poleward transports of ozone by the mean residual meridional plane circulation. However, winter variability is largely attributed to disturbances in the circulation.

The recurrent stratospheric “ozone hole” that develops over Antarctica each spring is well-known. This occurs because of photochemical catalytic reactions during the return of sunlight in September and October (austral spring). The main agents involved in such ozone destruction are chlorofluorocarbons (CFCs). If chlorine atoms are freed, a catalytic chain reaction can occur (Chartrand, de Grandpere, and McConnell, 1999). It has been shown that a reactive chlorine compound, chlorine monoxide (ClO), can be liberated from a reservoir species (such as hydrochloric acid or chlorine nitrate) through heterogeneous reactions in polar stratospheric clouds (PSCs). PSCs or nacreous (mother-of-pearl) clouds form at about 20–30 km

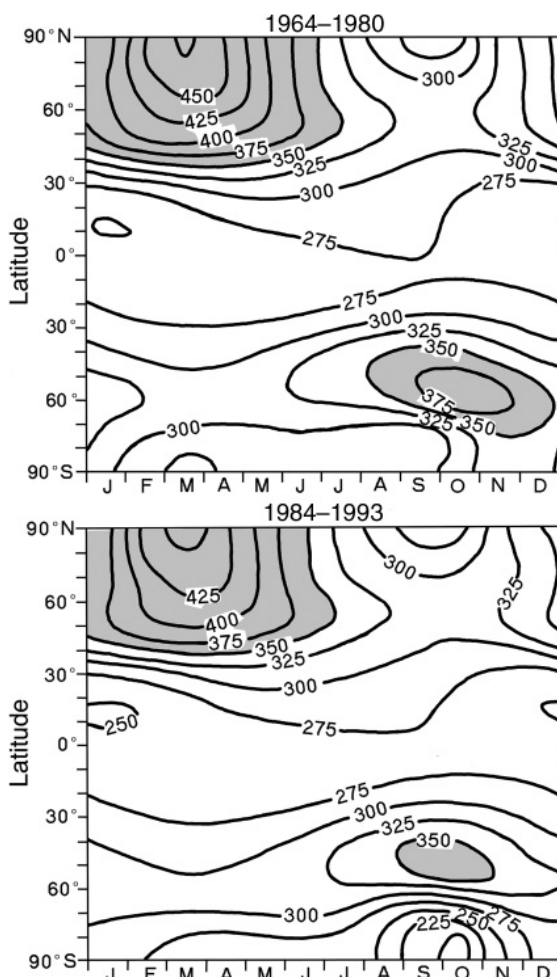


Figure 4.5. Mean column ozone totals (Dobson units) by month versus latitude for 1964–1980 and 1984–1993 (from Bojkov and Fiolotov, 1995, by permission of AGU).

altitude when temperatures fall below 195K. These clouds may be spectacularly observed when the sun is near or just below the horizon. The odd nitrogen absorbed by the cloud particles (nitric acid hydrates and water ice) allows reactions that lead to catalytic destruction of ozone. A bromine compound, BrO, can trigger similar catalytic reactions. Although the Montreal Protocol, which entered into force in 1989, phased out the production of CFCs, it will be decades until the ozone hole heals. In the Arctic stratosphere, the low temperatures associated with ozone destruction are less frequent than in the Antarctic but may still occur during about two months in a normal winter (Levi, 1992), and “mini” ozone holes have been observed (Solomon, 1999). One can see a reduction in total column ozone between the earlier and later periods plotted in Figure 4.5. The largest Arctic ozone loss ever observed occurred in 2011. For the first time in the record, the ozone destruction was comparable to that in the Antarctic ozone hole (Manney et al., 2011). The event was a result of unusually low stratospheric temperatures.

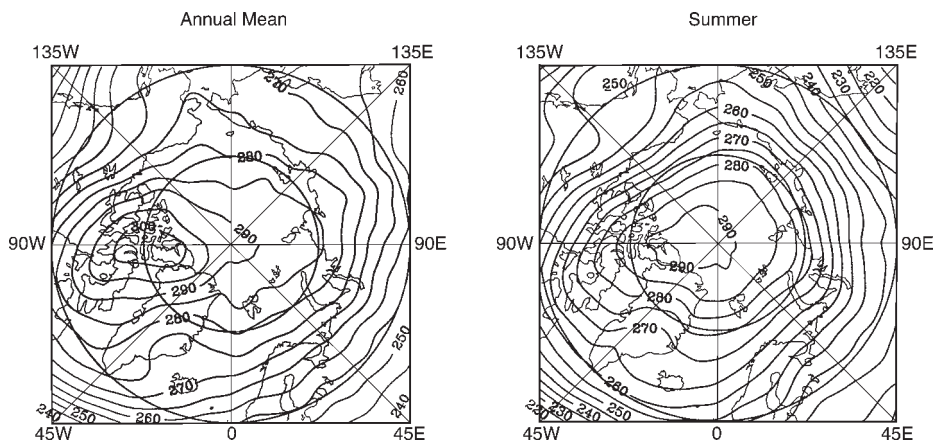


Figure 4.6. The annual mean and summer (June–August) tropopause pressure (hPa) based on the lapse rate definition derived from ECMWF data for 1200 UTC, 1979–1993 (adapted from Hoinka, 1998, by permission of AMS).

4.3 The Arctic Tropopause

4.3.1 Definition

The tropopause is the transition between the troposphere and stratosphere (see Figure 4.1). The tropopause can be defined on both thermal and dynamic criteria. The thermal definition is based on the lapse rate. The standard World Meteorological Organization definition of the tropopause is the lowest level above 500 hPa where the vertical temperature gradient decreases to less than or equal to $2^{\circ}\text{C km}^{-1}$ (provided that the average gradient in the upper 2 km layer is $<2^{\circ}\text{C km}^{-1}$). The existence of a nearly constant lapse rate in the troposphere and an isothermal lower stratosphere generally allows the tropopause to be distinguished in the Arctic even during the polar night (Highwood, Hoskins, and Berrisford, 2000). The dynamical criterion is based on an arbitrary threshold value of PV. K. Hoinka (1998) finds that the spatial pattern of tropopause heights based on the lapse rate criterion and on a value of 3.5 PV units ($\text{PVU} = 1.0 \times 10^{-6} \text{ m}^2 \text{ s}^{-1} \text{ K kg}^{-1}$) is generally similar.

4.3.2 Mean Characteristics

The lower boundary of the thermal tropopause at 85–90°N, based on soundings from the NP program for 1954–1991, has a minimum altitude of about 8.4 km in April and a maximum of 9.4 km in August (Nagurny, 1998). The mean thickness of the tropopause layer is only about 600 m over the Kara-Laptev seas in January, whereas in summer, it exceeds 1.6 km thickness in a belt from northern Norway to northern Novaya Zemlya and eastward to Wrangel Island (Makhover, 1983).

There is a secondary minimum (or maximum) in tropopause height in October (December–January). By contrast, the tropopause temperature shows a simple annual cycle with a minimum of -62°C in January and a maximum of -49°C in July, apparently following the annual cycle of temperature in the lower stratosphere as identified for the 100 hPa level (Wilson and Godson, 1963). E. J. Highwood et al. (2000) also point out that tropopause temperatures in winter are lower over the Eurasian sector and higher over the Canadian-Atlantic sector.

The existence of a double maximum/minimum in tropopause height (Gaigerov, 1967; Makhover, 1983), is attributed to several factors. The primary August maximum is attributed to the lag in the heating of the surrounding landmasses, while the secondary one in January is related to enhanced meridional heat transport by the planetary waves. The spring minimum is associated with the seasonal weakening of this transport. The autumn minimum relates to the cooling of the landmasses and a decrease in cyclone activity compared with late summer. Two patterns of the annual cycle in tropopause height are identified in different regions. Over North America and subarctic Siberia there is a simple annual wave (winter/summer – tropopause pressure maximum/minimum), whereas there is double wave (spring/autumn – maxima, summer/winter – minima) in the High Arctic, northern Europe, and western Siberia.

Figure 4.6 shows the spatial pattern of the mean thermally defined tropopause height (hPa) for 1979–1993 for the annual mean and summer. The first order pattern is that the Arctic tropopause is encountered lower in the atmosphere (i.e., at a higher pressure) than in lower latitudes. This is consistent with the schematic shown in Figure 4.1. The annual mean height field is nevertheless strongly eccentric near the Pole with a center of 280 hPa located over Devon-Ellesmere islands. In summer, the minimum extends from Ellesmere Island to the North Pole, and its average center is about 290 hPa (Hoinka, 1998). G. Zangl and K. Hoinka (2001) extended this work to examine the tropopause based on dynamic and thermodynamic criteria. Their January map is similar to the annual mean. Highwood et al. (2000) also obtain similar results

A key feature of the structure of the atmosphere in middle – high latitudes is the extent of tropopause folds. These are situated above strong baroclinic zones – associated with intense cyclones. In these regions, stratospheric air is extruded into the troposphere by intermittent folding of the tropopause (Danielsen, 1968). The associated mass removal of stratospheric air is maximized in late spring. The depression of the tropopause associated with the mean frontal zones is illustrated in Figure 4.1.

4.4 The Mid-Tropospheric Circulation

4.4.1 Mean Circulation

The primary feature of the mid-tropospheric (500 hPa) circulation in northern high latitudes is a well-developed cyclonic vortex during much of the year (Figure 4.7).

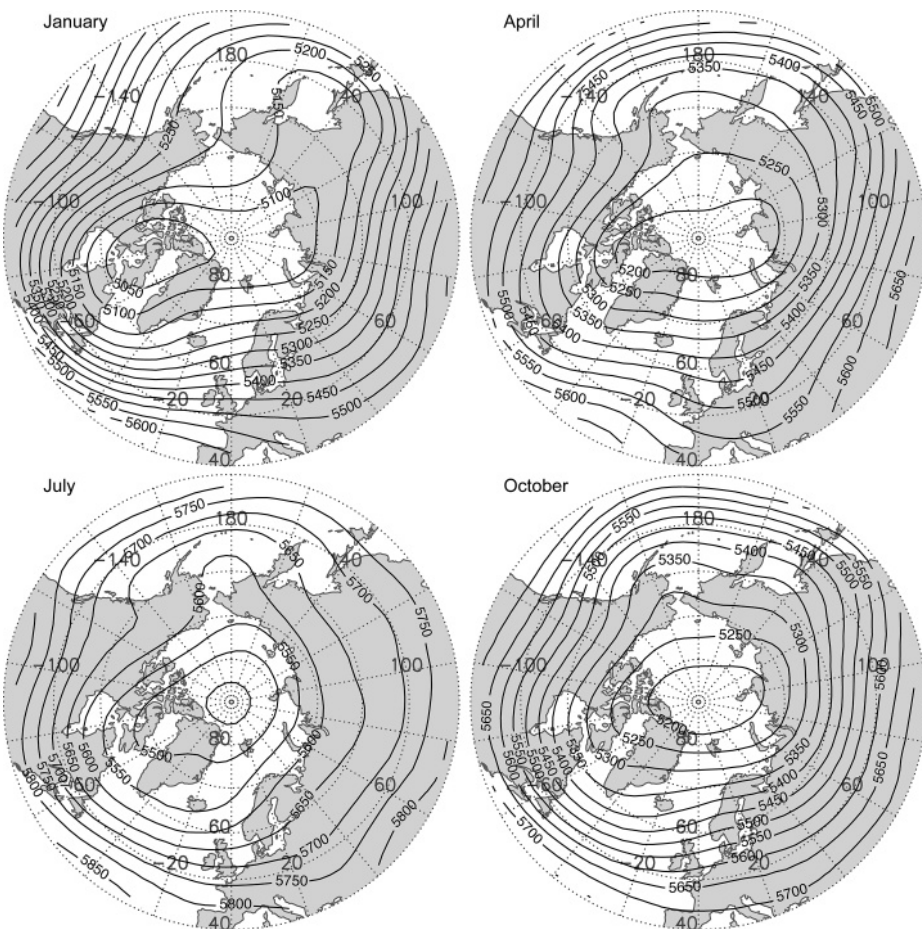


Figure 4.7. Fields of mean 500 hPa geopotential height (gpm) for the four mid-season months over the 1970–1999 period, based on NCEP/NCAR data (by the authors).

The winter vortex, as exemplified in the January field, is strongly asymmetrical. At 60°N, the mean flow is characterized by major troughs over eastern North America and eastern Asia and a weaker trough over western Asia (the Urals trough). A strong ridge is located over western North America, with much weaker ridges over the eastern Atlantic and central Asia. The lowest geopotential heights are found over the Canadian Arctic Archipelago. These features are related to dynamical forcing by orography (most importantly, the Rocky Mountains and the Himalayas disturb the circulation), thermal forcing associated with the large-scale land-ocean distribution (warm oceans versus cold land), and radiative forcing. From comparison with Figure 4.2, note the stronger winter asymmetry at 500 hPa as compared to the stratospheric vortex and the large relative shift in the vortex center. As discussed, the more symmetrical nature of the stratospheric winter vortex relates to the fact that only the long planetary waves can propagate up to high levels. In the fields shown in Figure 4.7, the shorter, traveling waves are averaged out. The resulting pattern of

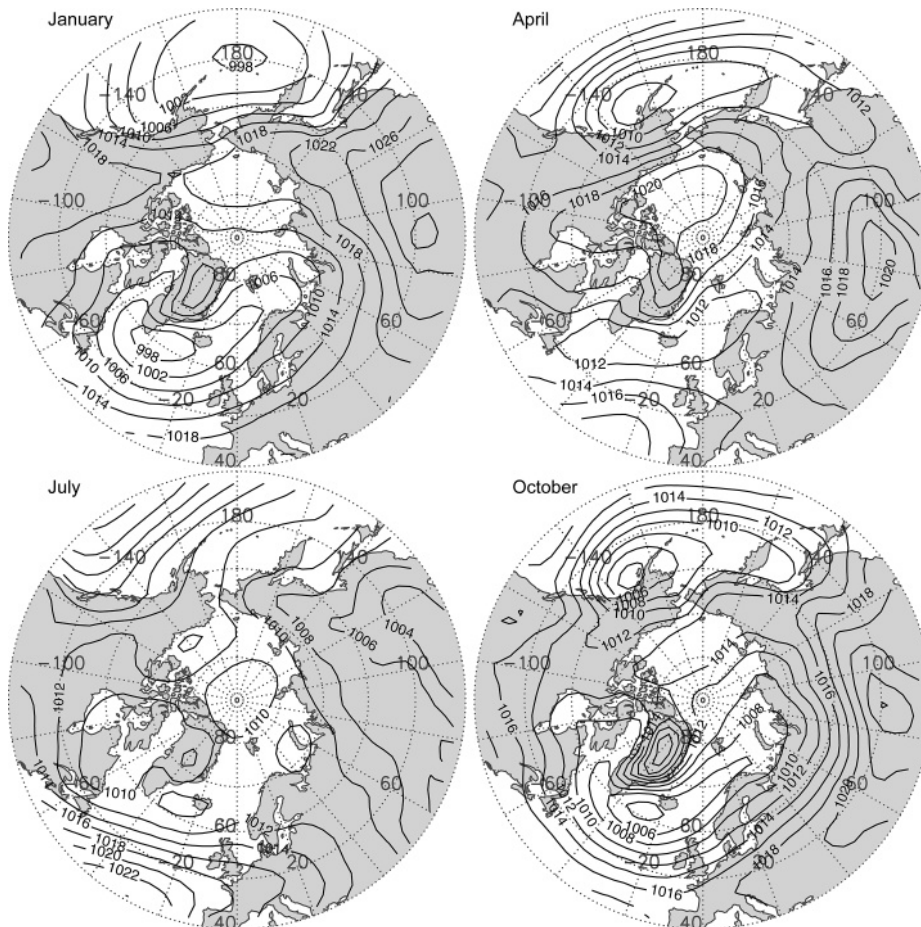


Figure 4.8. Mean sea level pressure (hPa) for the four mid-season months over the 1970–1999 period, based on NCEP/NCAR data (by the authors).

three troughs and three ridges that is fairly well expressed at about 60°N indicates that the total circulation at this latitude has a strong wavenumber 3 component. In summer, the 500 hPa vortex is much weaker in response to the more even latitudinal distribution of radiation and temperature. It is also more symmetric than its winter counterpart, with the lowest pressure heights centered over the pole.

4.4.2 Temperature Structure

The annual cycle of temperature in the middle troposphere shows a well-developed kernlose (or coreless) pattern. This refers to the observation that temperatures at 500 hPa, for example, seldom fall below -45°C in winter, despite a continued net radiative loss. This characteristic was originally noted in Antarctica. There, the mechanism seems to be a balance between outgoing longwave radiation, downward longwave radiation, and sensible heat flux from the top of the surface inversion

layer, although horizontal thermal advection by subpolar air masses has also been invoked (Van Loon, 1967). For the Arctic, T. Chase and colleagues (2002) propose that winter temperatures in the mid-troposphere are regulated by moist adiabatic ascent from airmasses in regular contact with high latitude open ocean regions, such as the Norwegian Sea. The idea is that airmasses move over such open water areas, where they are convectively heated. They then move over cold snow/ice surfaces. They cool from the bottom upward, albeit slowly. Before the cooling can significantly affect the mid-troposphere, the airmasses move over open ocean again, where they are rewarmed by convective heating. The proposed mechanism requires further investigation, but finds support in the subsequent study of M. Tsukernik et al. (2004), who identify the Norwegian Sea as a key region for convective warming (see also Chapter 3).

4.5 Surface and Near-Surface Circulation

4.5.1 Centers of Action

Fields of mean sea level pressure (SLP) for the four mid-season months are provided in Figure 4.8. The mean January circulation at sea level, representative of winter, is dominated by the three well-known subpolar “centers of action”: (1) the Siberian High over east-central Asia; (2) the Icelandic Low off the southeast coast of Greenland; and (3) the Aleutian Low in the North Pacific basin. The central Arctic Ocean appears as a saddle of relatively high pressures between the eastern Eurasian landmass and northwestern Canada.

The three centers of action are much weaker during April. The Aleutian Low exhibits a pronounced shift to the northeast, whereas the locus of the Siberian high has shifted slightly west. While the winter centers of action weaken, a closed high pressure cell develops over the Beaufort Sea. By July, the Aleutian Low has disappeared as a mean feature. The Icelandic Low is quite weak, and low pressures extend over the eastern Canadian Arctic. The Siberian High is replaced by a broad area of mean low pressure. An area of weak mean low pressure is also found near the pole in July. The mean October field illustrates the transition back to winter conditions.

The winter Siberian High is a cold, shallow anticyclone, driven largely by radiative cooling to space. The cold air is constrained by topography. The reality of some of the extreme high pressures reported in the region is open to question. This stems from difficulties in reducing station pressures recorded in upland valleys (where there are persistent cold air “lakes”) to sea level (Walker, 1967). But the existence of the anticyclone is not in dispute. Low 1,000- to 500-hPa thicknesses during winter are consistent with a cold anticyclone structure (Sahsamanoglou, Makrogiannis, and Kallimopolous, 1991) and cold highs regularly move eastward from the mean locus of the winter Siberian High (around 45–50°N, 90–110°E). The system periodically intensifies and gives rise to cold air outbreaks or surges over East Asia

Table 4.1. Mean and extreme monthly values (hPa) of the Siberian Anticyclone central pressure for November, January, and March (1873–1988)

	November	January	March
Maximum	1042.3	1048.5	1038.8
Mean	1032.7	1037.5	1031.1
Minimum	1027.2	1029.8	1024.9

Source: Based on Sahsamanoglou et al. (1991).

(Ding, 1990). Table 4.1 summarizes mean and extreme pressures under the Siberian High for November, January, and March. On average, the Siberian High is strongest in January and February. D. Walland and I. Simmonds (1997) suggest a negative (self-regulating) snow cover feedback in the vicinity of the winter Siberian High. They argue that cooling by an anomalously extensive snow cover strengthens the Siberian High, increasing the static stability of the lower troposphere. This results in decreased precipitation, limiting further advance of the snow field. Similarly, anomalously reduced snow cover weakens the Siberian High and decreases the static stability of the lower troposphere, encouraging increased precipitation and advance of the snow cover. Significant correlations have been found between anomalies of snow cover and the sea level pressure and height fields over the Arctic and North Atlantic (Cohen and Entekhabi, 1990; Cohen, Saito, and Entekhabi, 2001).

The winter Icelandic and Aleutian lows are complex features. In part, they manifest low-level thermal effects of the comparatively warm ocean bordering the ice margin and cold land. Surface pressures tend to be comparatively low over a warm surface as the overlying air is warmer, and hence less dense than over a cold surface. One of the observations that supports this idea is that isobars are roughly parallel to and more tightly crowded along the coastlines of Greenland and eastern Asia – Alaska, respectively (Wallace, 1983). Furthermore, both lows are located downstream of the major mid-tropospheric stationary troughs (Figure 4.7) where cyclogenesis is favored by upper-level divergence (see Barry and Carleton, 2001, pp. 459–461). They are hence part of the primary North Atlantic and North Pacific cyclone tracks, respectively. Finally, there are strong regional cyclone development processes associated with enhanced baroclinicity (strong horizontal temperature gradients along the sea ice margin) and the orographic effects of the southern Greenland Ice Sheet (discussed later). The winter Icelandic Low is part of a broad area of low pressure extending into the Barents and Kara seas. This feature reflects the thermal influences mentioned earlier and the penetration of cyclones northeastward into the Arctic Ocean.

As the latitudinal gradient of solar heating weakens in spring and summer, the general circulation also weakens. This is manifested in a weakening of the primary storm tracks and the low pressure centers of action. Springtime weakening of the Siberian High represents a general response to the increasing solar heating and loss of the snow cover. Development of a closed anticyclone off the Canadian Arctic

Archipelago in spring appears to reflect the infrequency of transient cyclones and the shift from eastern Siberia of the locus of lowest tropospheric temperatures.

The mean annual cycle of SLP varies across the Arctic. Based on a harmonic analysis using NCEP/NCAR data, R. Cullather and A. Lynch (2003) show that within the Atlantic sector, pressures tend to be highest in July and lowest in January. The area of the Siberian high is characterized by a February maximum and August minimum. By comparison, the Canada Basin/Laptev Sea region is dominated by a March maximum and September minimum. In an earlier effort, J. Walsh (1978) found that SLP averaged from 70–90°N exhibits a semi-annual cycle, with maxima in April and November, and minima in July and February. Cullather and Lynch (2003) examined this semi-annual cycle more closely and find it to be best expressed along the periphery of northern Greenland and extending to the pole. Their harmonic analysis depicts pressure maxima in May and November. Dynamically, this semiannual cycle can be related to seasonal variations in mass convergence as mass moves from Eurasia and into the Canadian Arctic Archipelago in spring and the reverse condition in autumn. The semiannual cycle exhibits pronounced interannual variability, associated with mass exchanges with the primary storm tracks in the north Atlantic and Pacific.

4.5.2 Cyclone Activity

Figure 4.9 depicts by season the frequency of extratropical cyclones north of 60°N over the 1970–1999 period. Figure 4.10 gives total counts of cyclogenesis (cyclone formation) events by season over the same period. Results are based on an algorithm applied to six-hour NCEP/NCAR SLP fields. Cyclones are identified using a series of search patterns, testing whether a grid-point SLP value is surrounded by grid point values at least 1 hPa higher than the central point being tested. Cyclones are tracked by comparing system positions on subsequent six-hour charts using a nearest-neighbor approach. Cyclogenesis is defined as the first appearance of a closed (1 hPa) isobar. Earlier versions of the algorithm based on twelve-hour pressure fields are described by Serreze (1995) and Serreze et al. (1997). X. Zhang et al. (2004) describe a broadly similar algorithm.

For cyclone frequency, cyclone occurrences in grid cells of 250 km over the thirty-year period were summed by season. The cell counts were then divided by the number of years. Hence, the plotted values represent system centers per season. For example, in any grid cell enclosed by the 3.0 contour, there is an average of at least three cyclone centers per season. For cyclogenesis, we simply summed events by grid cell over the thirty years. All maps have been heavily smoothed to improve clarity. Values over the Greenland Ice Sheet should be viewed with extreme caution owing to the problems of reducing pressures to sea level.

Building from previous discussion, winter cyclone activity is most prominent over the Atlantic side of the Arctic. This is consistent with the large atmospheric energy transports into the Arctic basin through this sector (Overland and Turet, 1994; Overland, Turet, and Oort, 1996; Serreze et al., 2007, see Figure 3.9).

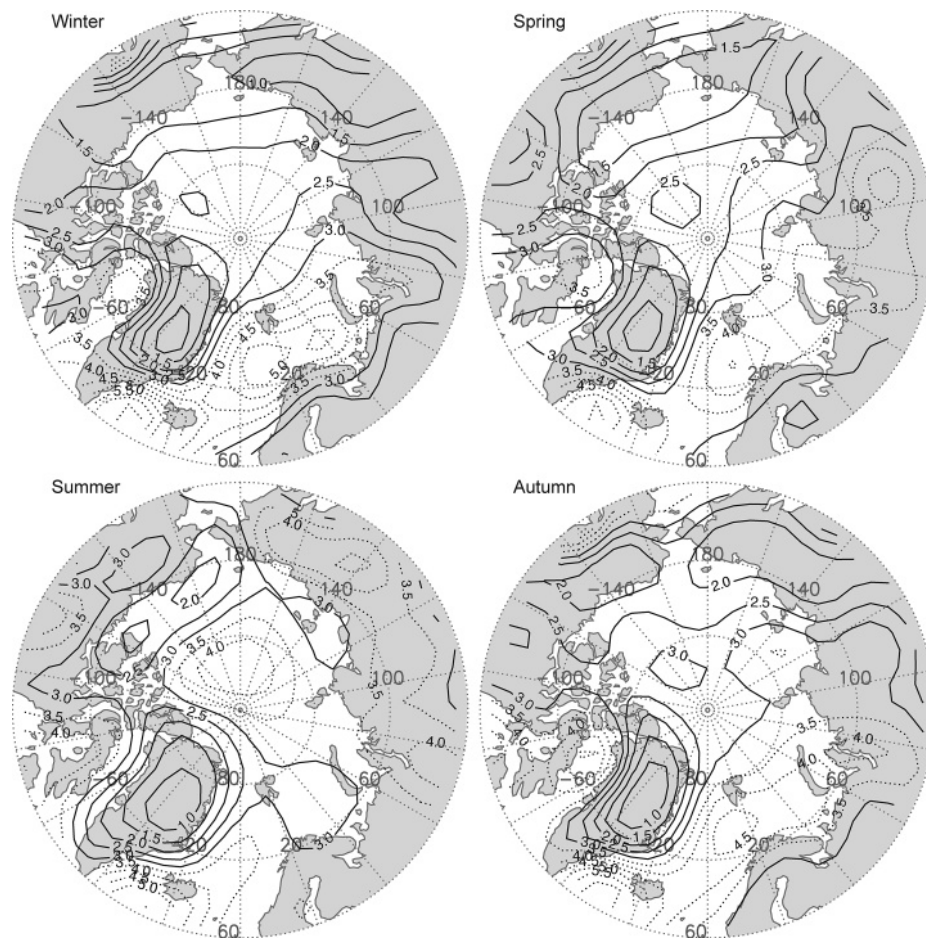


Figure 4.9. Cyclone frequency (cyclone passages per month) for winter, spring, summer, and autumn over the 1970–1999 period, based on NCEP/NCAR data (by the authors).

These cyclones take a northerly to easterly track. Activity peaks in the vicinity of the Icelandic Low. Another area of high cyclone frequencies is Baffin Bay. While cyclones are of course very common in the vicinity of the Aleutian Low, relatively few of these Pacific-side systems migrate into the Arctic. Relatively few closed lows are found over the central Greenland Ice Sheet. Zhang et al. (2004) provide similar results. In comparison to the early view of Pettersen (1950), based on limited data sources, it is clear that although winter cyclones over the central Arctic Ocean are infrequent in comparison to the Atlantic sector, they are by no means rare.

The winter Icelandic Low and the region extending into the Barents Sea is also a region of frequent cyclogenesis and system deepening (the deepening rate is a useful measure of cyclone intensification). The entire area is characterized by enhanced baroclinicity (strong temperature gradients). Rapid deepening of lows along the ice edge is frequently observed (Serreze, 1995; Serreze et al., 1997). Redevelopment of

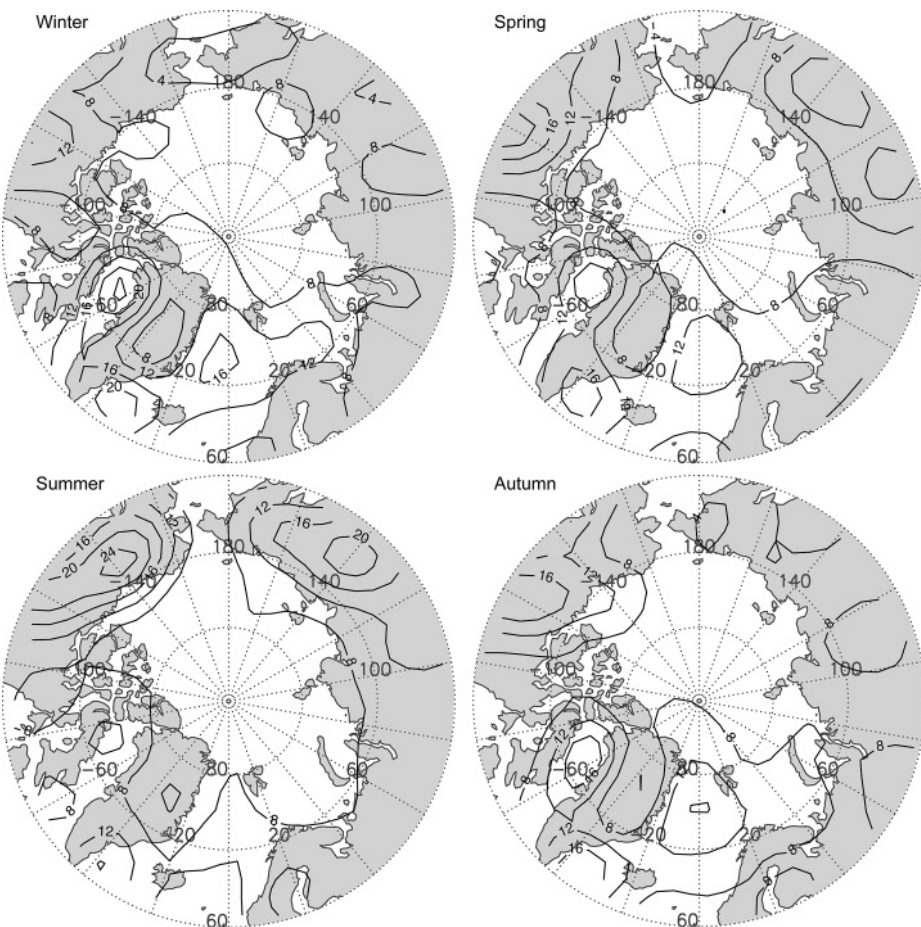


Figure 4.10. Cyclogenesis counts for winter, spring, summer, and autumn over the 1970–1999 period, based on NCEP/NCAR data (by the authors).

extratropical systems migrating from the south is common between Greenland and Iceland. Serreze et al. (1997) find that roughly half of all cyclones associated with the Icelandic Low form north of 55°N. Another interesting phenomenon is bifurcation (splitting) of lows moving in from the south and southwest by the high ice sheet barrier (elevations at about 64°N, near the southern tip of Greenland exceed 2,800 m, roughly the 700-hPa level), with one of the low pressure centers migrating poleward into Baffin Bay along the west coast of Greenland, with the other migrating poleward along the east coast of Greenland.

As shown by Tsukernik, Kindig, and Serreze (2007), strong deepening of cyclones in the Atlantic sector tends to occur in three preferred regions: (1) south of Greenland, at about 54°N; (2) near the locus of the mean Icelandic Low; and (3) just south of Svalbard. The area of preferred deepening south of Greenland is located in a region of maximum gradients in 500 hPa height just east of the axis of the mean eastern North American 500 hPa trough, where there tends to be positive vorticity

Table 4.2. Regional 12-h mean maximum deepening rates (hPa) of Arctic cyclones for different regions

Region	Max Deepening
	Winter (Summer)
Central Arctic Ocean	-1.5(-1.9)
Barents/Kara/Norw. Seas	-3.6(-2.3)
Greenland Sea/N. Atlantic	-6.8(-3.3)
Baffin Bay/Davis Strait	-3.2(-2.2)
Alaska/Canada	-0.8(-1.7)
Eurasia	-1.1(-1.8)

Source: Based on Serreze (1995).

advection increasing with height, promoting vertical motion and divergence. This region also lies just to the south of a strong gradient in sea surface temperature, associated with the contrast between the cold Labrador Current and the warmer North Atlantic Current. Given that winter cyclone counts are highest near the locus of the mean Icelandic Low, it follows naturally that this region appears as a maximum in the frequency of strong deepening. Lee-side cyclogenesis is common in this region (Kristjánsson and McInnes, 1999). The area of preferred deepening just south of Svalbard corresponds to the most northward penetration of open water in the Atlantic, in close proximity to very cold air over the Arctic Ocean.

Table 4.2 summarizes mean maximum twelve-hour deepening rates (hPa) of winter Arctic cyclones for several regions over the 1973–1992 period. These were compiled by finding the maximum twelve-hour deepening rate of all cyclones through their lifecycle, and then averaging those cases falling in each region. The much larger maximum deepening rates in the Greenland Sea/North Atlantic region (which includes the Icelandic Low) compared to land areas is readily apparent. In the Greenland Sea/North Atlantic, the lowest decile maximum deepening rate is -16.8 hPa over twelve hours, compared to only -6.1 hPa for the Central Arctic Ocean (not shown).

Whereas spring shows decreased vigor of the North Atlantic track both in terms of cyclone frequency and cyclogenesis, there is a deeper penetration of the track into Eurasia. It is important to note, however, how cyclogenesis increases over east/central Eurasia and northwestern Canada. The North Atlantic track is weakest during summer. Referring to Table 4.2, this is associated with much smaller maximum deepening rates, compared to winter. However, from Figures 4.9 and 4.10, we see: (1) a strong increase in cyclone activity over land areas, especially over eastern Eurasia; (2) an attendant seasonal maximum in cyclogenesis over land areas; and (3) a summer cyclone maximum over the central Arctic Ocean. Autumn illustrates the transition back toward winter conditions, with dominance of the North Atlantic track.

The summer cyclone maximum over the central Arctic Ocean was first noted by Dzerdzevskii (1945), then by Reed and Kunkel (1960), and much more recently

was the subject of a focused study (Serreze and Barrett, 2008). They find that the pattern is associated with the influx of lows generated over the Eurasian continent as well as cyclogenesis over the Arctic Ocean itself; very few enter from the North American continent. Cyclones migrating into the cyclone maximum region, along with those generated over the region itself, tend to track around the vortex and eventually occlude and dissipate within the region. The seasonal onset of the summer cyclone maximum is linked to an eastward shift in the Urals trough, development of a separate region of high-latitude baroclinicity, and migration of the 500-hPa vortex core near the pole. The latter two features are consistent with differential heating between the Arctic Ocean and snow-free land, an issue that is discussed shortly. However, the strength of the summer cyclone pattern is highly variable. When well-developed, the 500-hPa vortex is especially strong and symmetric about the pole. When poorly developed, the opposite pattern holds.

There have been a number of case studies of cyclone development processes over the Arctic Ocean. The series of papers by E. LeDrew (1984; 1988; 1989) is recommended. These studies made use of forms of the omega equation to diagnose the contributions of different mechanisms to the vertical motions in cyclones. As with mid-latitude systems, the effects of differential vorticity advection and temperature advection (see Holton, 1992) tend to dominate. Of particular interest, however, is the sometimes significant role of local heat sources in the Arctic basin (LeDrew, 1984).

4.5.3 Frontal Activity

Early studies of frontal activity in the Arctic, such as those of Reed and Kunkel (1960) and Barry (1967), were based on manual analysis. While extremely time consuming, manually depicted fronts always contain an element of subjectivity. With the advent of fast computers, thinking turned to the application of automated methods. T. Hewson (1998) provides a comprehensive review. Of the various methods that can be found in the literature, one that seems to work fairly well is a thermal front parameter (TFP). The TFP is defined as:

$$\text{TFP} = -\nabla|\nabla\tau| \bullet (\nabla\tau/|\nabla\tau|) \quad (4.1)$$

where τ is a thermodynamic variable. The TFP magnitude will be largest where there is a rapid change in the thermal gradient (the first term on the right) with a large component parallel to the direction of the (unitized) thermal gradient (the second term on the right). The minus sign places the frontal boundary on the warm-air side of the concentrated baroclinic zone (corresponding to a ridge line in the field of TFP). The simplest application is to define fronts based on ridge lines of TFP, with the requirement that the TFP exceed a selected threshold value. Further details and application of more robust approaches are described by Hewson (1998).

Serreze et al. (2001) used the TFP approach to assess frontal frequencies over a twenty-year period (1979–1998) for the region north of 30°N. The intent was to reexamine the concept introduced by Dzerdzevskii (1945) and Reed and Kunkel

(1960) of a “separate” summer Arctic frontal zone (Section 4.1). The study used six-hour, 850-hPa temperature fields from the NCEP/NCAR reanalysis.

Figure 4.11 shows derived frontal frequencies for winter and summer, expressed as the mean number of fronts per day (a frequency of 0.10 means a front was present on 10 percent of the days). Also shown are fields of the mean 850-hPa temperature gradient in K (100 km)⁻¹ based on the twenty-year period. The frontal analysis routine is inherently sensitive to strong temperature gradients in areas of extreme topography, the boundaries of high plateaus, and where there are strong land-ocean contrasts. Although it turns out that topography and land-ocean contrasts are important for understanding high-latitude frontal activity, this sensitivity can also cause problems. This issue was addressed simply by masking out known problem areas.

The winter frontal frequency field is rather noisy. High frequencies are found over most of North America except northeastern Canada, where the mean temperature gradient is weak. Note the band of high frequencies over the Atlantic basin that is associated with the eastern North American jet and its attendant storm track. There is an analogous feature (extending beyond the latitude bounds of the figure) over the Pacific basin that is associated with the East Asian jet and the Pacific storm track. From comparison with the mean temperature gradient field, one can see how the maxima in frontal frequency are placed on the warm side of these mean baroclinic zones. For example, the frontal zone over the Atlantic basin lies south of the maximum temperature gradient for this area. The winter gradient fields also exhibit features associated with topography and land/ocean contrasts. Consistent with the analysis of cyclone activity, there is a high frequency of fronts east and northeast of Greenland. There is separation between this area of frequent frontal activity and the relative maximum in fronts further south associated with the eastern North American jet. One could hence consider the area east and northeast of Greenland in the context of a separate wintertime Arctic frontal zone.

Spring (not shown) exhibits less frontal activity over the Atlantic basin, and northward migration of the Pacific basin feature. Frequencies are high over northwestern North America, with a general shift in activity toward the interior. A local maximum is found centered at about 65°N, which at the resolution of the NCEP/NCAR data is essentially colocated with the Brooks and Mackenzie ranges. There is some separation between the frontal activity over Alaska and that to the south in the Pacific basin.

In summer, the relative maximum in frontal frequencies over Alaska is well-expressed. Of particular interest is the development of a pronounced, zonally oriented band of high frontal frequencies over northern Eurasia, which essentially extends across the continent. Frontal frequencies are highest over eastern Eurasia, corresponding to the Yana, Indigirka and Kolyma valleys, which are bounded to the east, west and south by fairly high topography. The Eurasian and Alaskan features are broadly in agreement with the regions of high summer frontal frequency shown by Reed and Kunkel (1960), with the orientation of the Eurasian feature similar to the summer Arctic frontal zone plotted by Krebs and Barry (1970). The Eurasian and Alaskan frontal zones are associated with mean baroclinic zones

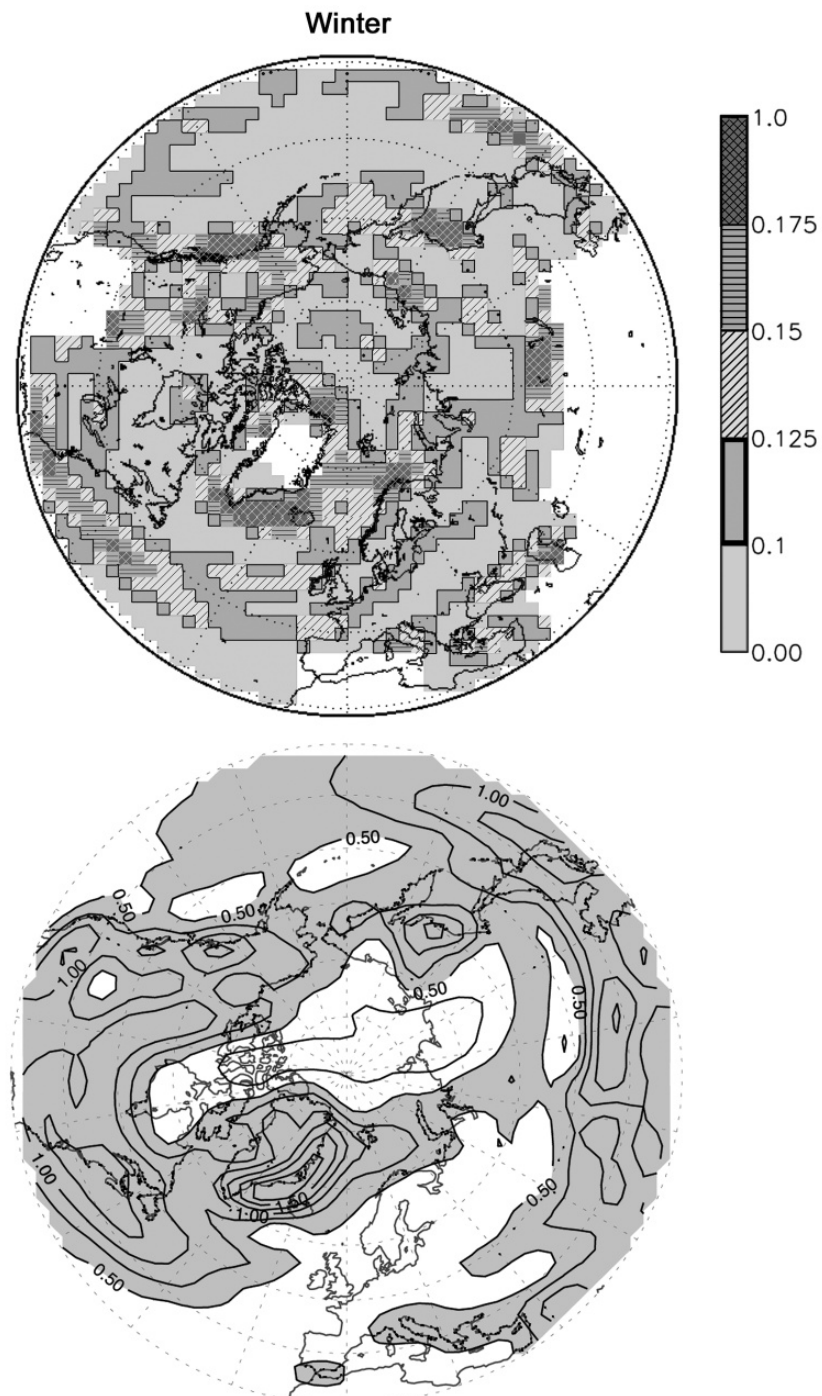


Figure 4.11. Frontal frequencies (top, fronts per day) and mean 850 hPa temperature gradients (bottom, K (100 km)^{-1}) for winter and summer. White areas in the frontal frequency maps represent regions with known problems related to extreme topography and surface heating. Areas where the mean temperature gradient exceeds $0.5 \text{ K (100 km)}^{-1}$ are shaded (adapted from Serreze et al., 2001, by permission of AMS).

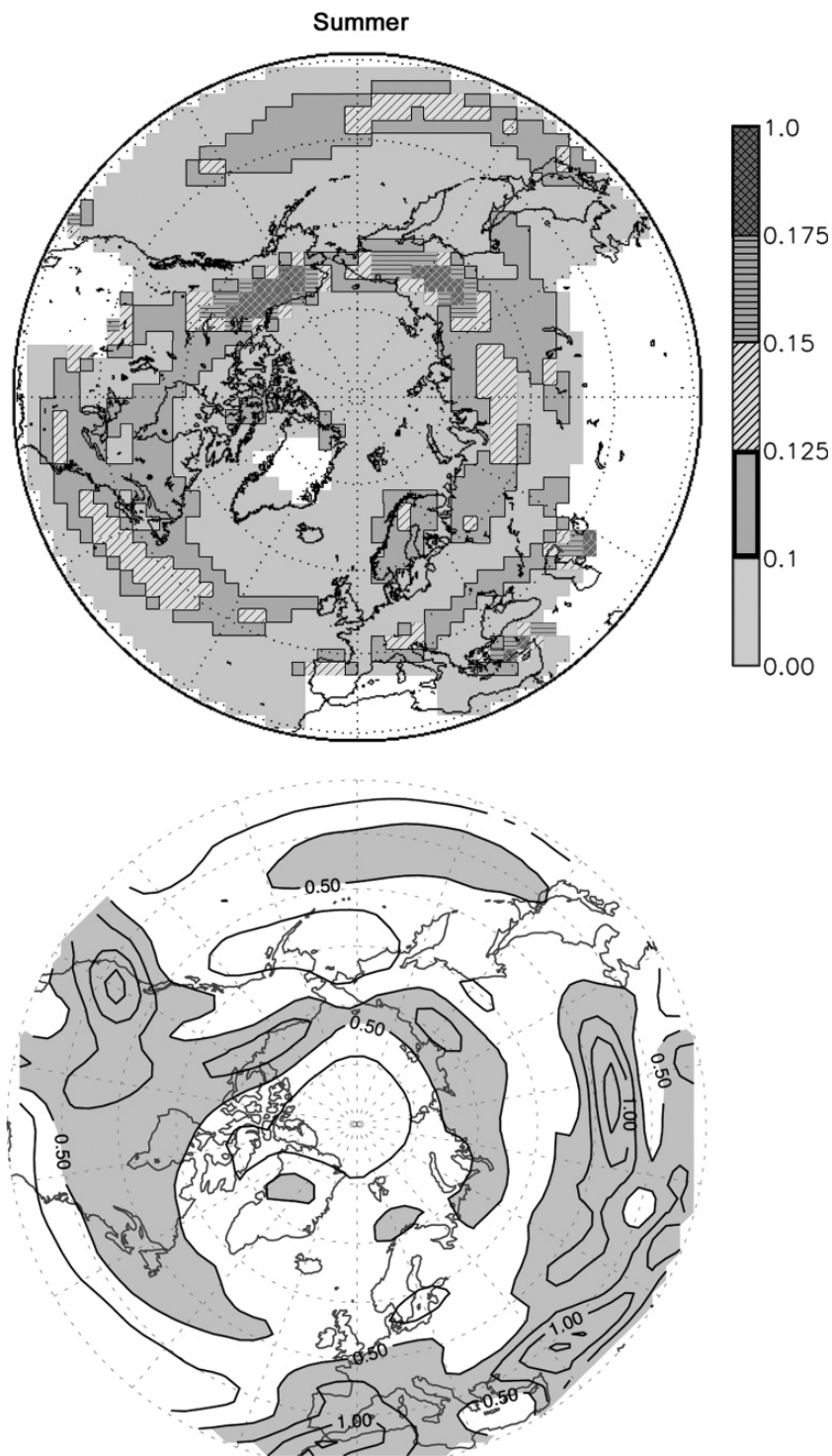


Figure 4.11. (Cont.)

aligned roughly along the Arctic Ocean coastline. Reed and Kunkel (1960) view the summer Arctic frontal zone in Eurasia as distinct from the region of high frontal frequencies in middle latitudes of the Pacific Basin. This separation is clearly captured in the automated frontal analysis. The well-defined Eurasian frontal zone seen in summer breaks down in autumn while the high-latitude feature over Alaska is still present in a weakened form. The Alaskan feature, best expressed in summer, hence persists throughout the year.

Development of the summer Arctic frontal zone is interpreted as a manifestation of: (1) differential heating between the Arctic Ocean and snow-free land; and (2) sharpening of the baroclinicity by coastal orography. These conclusions are drawn from the observation of that in summer, one sees development of a strong temperature gradient along the coast, and that the frontal zone is best pronounced where topography can “trap” the cold Arctic Ocean air. The differential heating link was first suggested by Dzerdzevskii (1945) and later by A. Kurashima (1968), and the concept of a topographic link can be traced back to Reed and Kunkel (1960). Additional support for topographic controls comes from the modeling study of A.H. Lynch, A.G. Slater, and M. Serreze (2001b) who examined frontal activity over Alaska. From comparisons between Figures 4.10 and 4.11, there is a close correspondence between the preferred areas of summer cyclogenesis over northeastern Eurasia and Alaska/Yukon and the relative maxima in summer frontal frequencies.

Vertical cross sections of the mean temperature gradient and winds throughout the troposphere provide further insight. Figure 4.12 shows cross sections at longitude 140°E. This longitude cuts through the region where the summer Eurasian frontal zone is best expressed. The zonal wind cross section for January shows a single jet with a core velocity of about 75 m s^{-1} . The tropospheric meridional temperature gradient is maximized at about 300 hPa (negative values meaning temperature decreases to the north). While bearing characteristics of the subtropical jet, the effects of statistical averaging with polar front jets are evident in the baroclinicity at lower levels and its extension to the north. Note the high-latitude baroclinicity at lower stratospheric levels, capturing the lower end of the polar night stratospheric jet discussed earlier. At this longitude, the Arctic frontal zone is best expressed during June. The June zonal wind cross section is dominated by a jet at about 35°N, about half as strong as that for winter. Note however, the development of a weaker, separate 300 hPa wind maximum (10 m s^{-1}) at 70°N. This can be associated with a distinct high-latitude baroclinic zone extending to 400 hPa, maximized at low levels close to the latitude of the Arctic Ocean coast.

The cross section in Figure 4.13 cuts through Alaska at longitude 140°W, where the high-latitude frontal zone is again well expressed. For January, a single jet (30 m s^{-1}) is found at about 30°N. The lower end of the stratospheric polar night jet is again seen at about 70°N. By sharp contrast, June reveals a subtropical jet at about 25°N, a polar jet at about 45°N, and a third Arctic jet at about 70°N. Similar to January, there is a fairly sharp, low-level baroclinic zone at high latitudes, but it is shifted north to about 70°N, again close to the latitude of the Arctic Ocean coast.

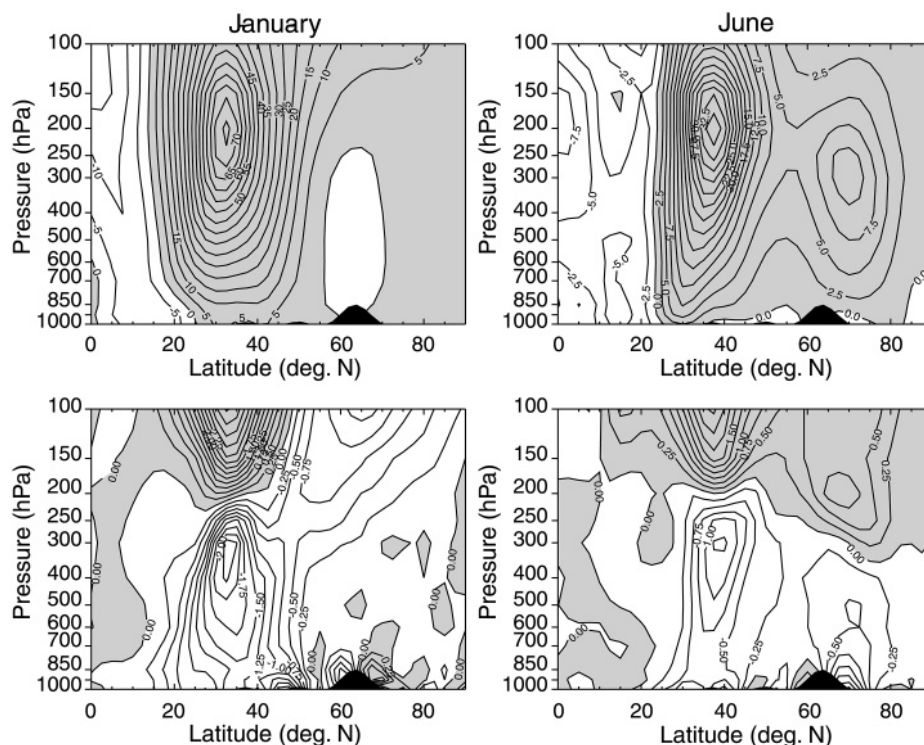


Figure 4.12. Mean zonal winds (m s^{-1}) (top panels) and meridional temperature gradient (K (100 km)^{-1}) (bottom panels) from the equator to the pole at 140°E for January and June. Positive values are shaded (from Serreze et al., 2001, by permission of AMS).

In eastern North America, the high-latitude summer frontal zone is not well expressed. At 80°W (not shown), both the winter and summer cross sections show a single jet. There is no evidence of a pronounced summer baroclinic zone along the Arctic coast. This follows in that the Canadian Arctic Archipelago is a heterogeneous landscape with a combination of land and ice-covered channels, acting to inhibit amplification of the baroclinicity such as seen along the Eurasian coast where the land/ocean boundary is well defined.

As first noted by Bryson (1966), the extent of Arctic air in summer, as represented by the median location of the Arctic front, also corresponds well with the northern limit of boreal forest. Barry (1967) confirmed this relationship for Canada west of Hudson Bay, but noted the existence of a broad forest-tundra ecotone over Labrador-Ungava. Krebs and Barry (1970) also demonstrated the close spatial association of the median location of the Arctic front over northern Eurasia in summer and the forest-tundra boundary. J. Larsen (1974) examined these ideas further for Canada. However, Hare (1968) pointed out that the relationships need not represent cause and effect – both the climatic and biotic patterns may be a consequence of atmospheric circulation conditions determined by radiative controls. This view

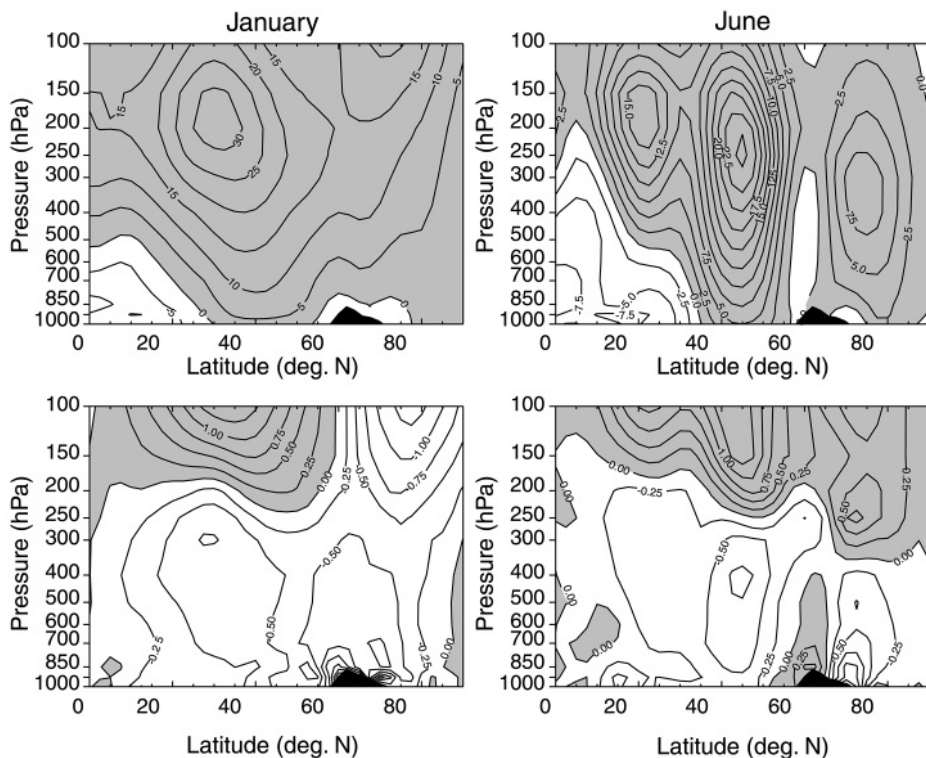


Figure 4.13. Mean zonal winds (m s^{-1}) (top panels) and meridional temperature gradient (K (100 km)^{-1}) (bottom panels) from the equator to the pole at 140°W for January and June. Positive values are shaded (from Serreze et al., 2001, by permission of AMS).

was explored further by Hare and J. Ritchie (1972) in an analysis of latitudinal radiational gradients.

Subsequently, R. Pielke and P. Vidale (1996) proposed that the forest/tundra boundary may itself help to determine the airmass contrasts and therefore the frontal location. Drawing on findings from BOREAS, they suggested that stronger heating of the boreal forest from its lower albedo is not compensated by an increase in transpiration, even with the larger leaf area index of the forest. The heterogeneity ("patchiness") of the boreal forest landscape gives rise to mesoscale circulations, which help to mix the heat upward, giving rise to a deep thermal contrast. Although a significant role of vegetation on regional and circumpolar climates on a range of time scales finds support in other studies (e.g., Bonan, Pollard, and Thompson, 1992; Bonan, Chapin, and Thompson, 1995; Foley et al., 1994; Lynch et al., 1999a), the available evidence as previously reviewed points to the treeline as primarily a response to the position of the Arctic frontal zone. North of the frontal zone, it is simply too cold for trees to grow in summer, although extreme winter temperature minima may be a further physiological control.

4.6 Polar Lows

4.6.1 Definition

Polar lows are intense maritime mesocyclones of typically 100–500 km in diameter. They may intensify rapidly, and surface winds speeds can sometimes reach hurricane force (Businger and Reed, 1989). They tend to be short lived, generally lasting only three to thirty-six hours. Polar Lows are the most intense category of the family of mesoscale cyclonic vortices found poleward of the main polar front, which are known generically as polar mesoscale cyclones. Polar Lows, which can present significant hazards to shipping, are also known as Arctic Instability Lows, comma clouds, and – in the Southern Hemisphere – Antarctic coastal vortices. In the north polar regions, Polar Lows are particularly common in the Nordic Seas, the Labrador Sea, the Bering Sea, the Gulf of Alaska, and the Sea of Japan. Hundreds of mesoscale lows can develop in these regions on an annual basis (Renfrew, 2003). Satellite images of two Polar Lows appear in Figures 4.14 and 4.15. The characteristics of Polar Lows have been examined in a number of studies. Papers by E. Rasmussen (1979), Shapiro, L. Fedor, and T. Hampel (1987a), S. Businger and R. Reed (1989), K. Emanuel and R. Rotunno (1989), S. Grønås and N. Kvamstø (1995) and A. Carleton (1996) are worth reading. Rasmussen and J. Turner (2002) provide a comprehensive assessment of Polar Lows while Renfrew (2003) provides a useful shorter review, which we draw from here.

4.6.2 Development Processes

As outlined by Renfrew (2003), Polar Lows develop over open water. When moving over land or the sea ice cover, they tend to rapidly dissipate. They can be thought of as “hybrid” systems, typically having features both baroclinic and convective in nature. A common feature of Polar Lows seen in satellite imagery is a spiral cloud (comma cloud) signature. Some systems develop a clear eye at the center similar to tropical cyclones (Figure 4.14). Generally, Polar Lows are warm-cored, and many have well-defined fronts as seen in extratropical, synoptic-scale lows. Purely baroclinic or topographically forced systems tend to remain fairly weak. Rapid intensification of an intense Polar Low seems to require some element of convection. The preferred areas for Polar Low development mentioned previously are those that are commonly subject to cold polar outbreaks, where cold continental air is advected over relatively warm open water – conditions favoring convection. Consequently, Polar Lows are essentially cold-season phenomena.

Two related mechanisms have been proposed to explain Polar Lows. The first is CISK (Conditional Instability of the Second Kind), which emphasizes the organization of cumulonimbus convection. An initial disturbance causes low level convergence and ascent, which in a conditionally unstable atmosphere, results in latent heat release through convection. The latent heat release leads to a drop in surface pressure, favoring more cyclonic relative vorticity, more low-level convergence and,

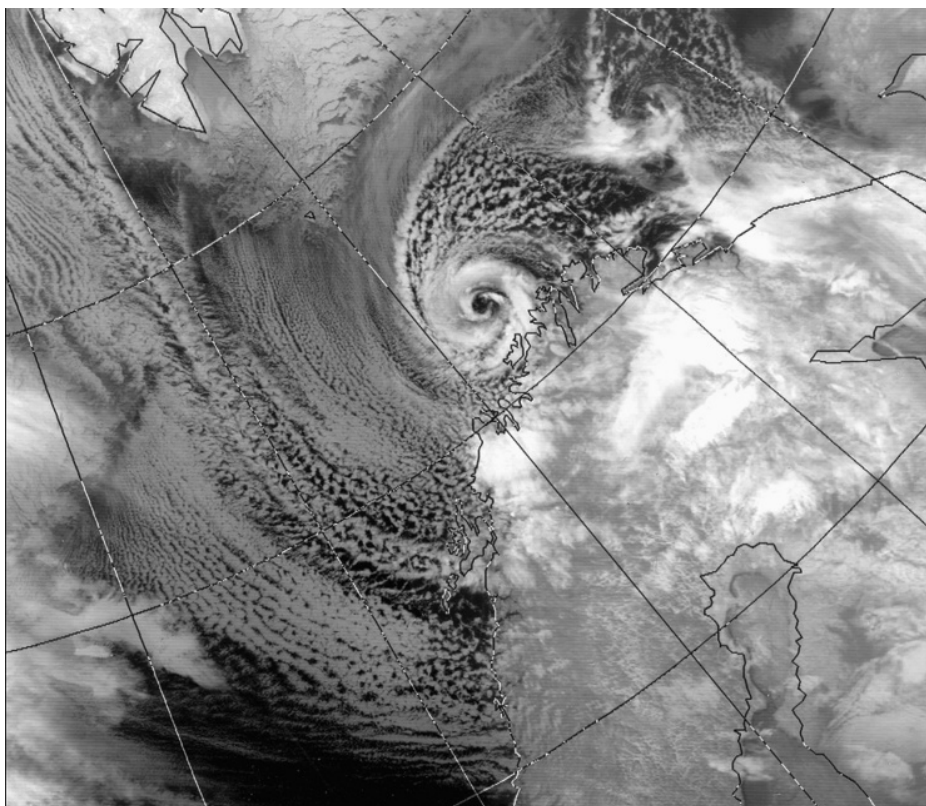


Figure 4.14. NOAA-9 image for February 27, 1987 of a Polar Low off the coast of northern Norway. Note the spiral cloud signature and central eye in this example (by permission of the NERC Satellite Receiving Station, University of Dundee, <http://www.sat.dundee.ac.uk/>).

through continuity, high-level divergence. The low-level convergence provides for a continued source of moisture and convective latent heat release – a feedback process that can lead to rapid development. It seems that cold polar outbreaks over open water in high latitudes can provide for the deep layer of conditional instability associated with the CISK process.

The second mechanism is known as WISHE (Wind Induced Surface Heat Exchange). WISHE is a feedback between the circulation and surface sensible and latent heat fluxes from the sea surface, with a stronger circulation giving rise to larger surface fluxes of heat, which are then redistributed aloft by convection, in turn strengthening the circulation. The feedback arises in that the surface heat fluxes are proportional to the wind speed – turn on the winds and the heat flux strengthens. The redistribution by convection results in a pressure drop, further strengthening the winds and hence the surface heat fluxes. WISHE can explain the growth of both tropical cyclones (hurricanes) and Polar Lows.

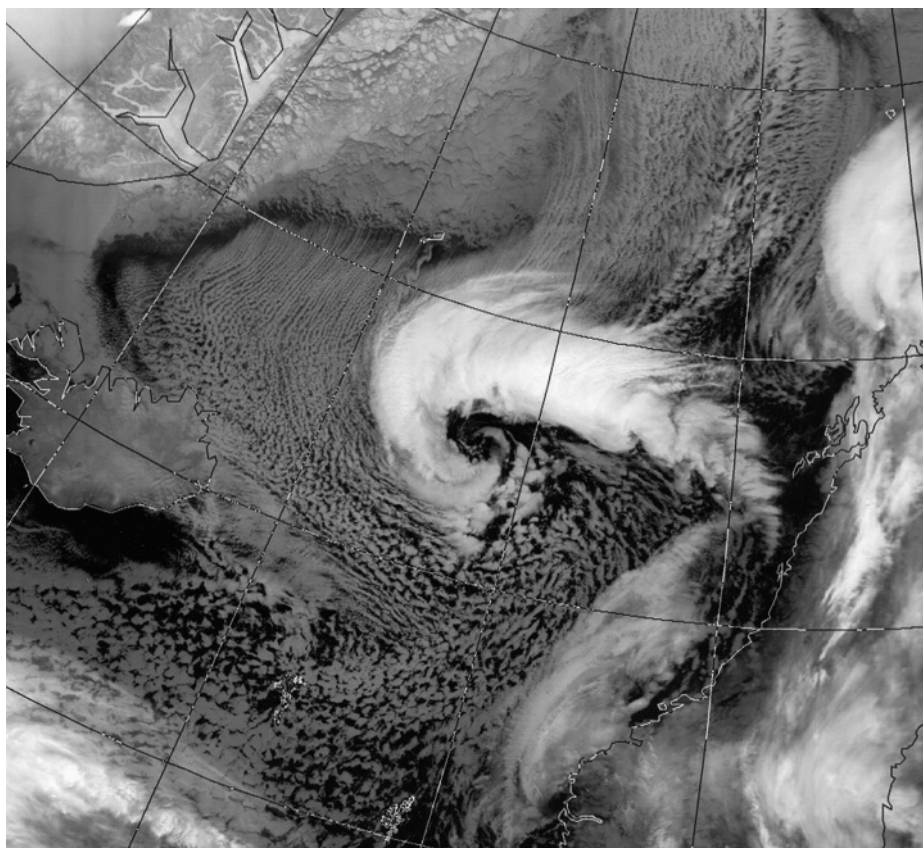


Figure 4.15. NOAA-12 image for January 19, 1998 of a Polar Low. Norway is on the right side of the image, with Iceland to the left side. Note the comma-shaped cloud band in this example (by permission of the NERC Satellite Receiving Station, University of Dundee, <http://www.sat.dundee.ac.uk/>).

In WISHE, the emphasis is placed on the surface fluxes as the primary growth-limiting process – the convection only serves to redistribute the heat. This contrasts with CISK, which emphasizes that the circulations amplify through their interaction with the convection itself. In the real world, however, the two mechanisms can be difficult to distinguish from each other. The common feature of both processes in Polar Low development, however, is that one needs an initial disturbance. The presence of some sort of baroclinic disturbance provides the key. Off East Greenland, mesocyclone development also appears to be forced by the effects of the ice sheet topography and low-level katabatic winds (Chapter 8). T. Klein and G. Heinemann (2002) show from simulations with a mesoscale model that channeling of the flow in the large valleys of east Greenland around Angmagssalik leads to convergence and cyclonic vorticity generation. This can be enhanced during strong katabatic events that supply cold air, augmenting low-level baroclinicity. These katabatic winds are themselves favored by the presence of a synoptic scale low in the Greenland Sea.

They propose that such synoptic support is important because the pure katabatic wind layer is only a few hundred meters deep. A positive feedback on the katabatic system can occur when a mesocyclone develops off the coast.

Numerical simulation of Polar Lows is still challenging. Renfrew (2003) also points out that polar mesocyclones, including Polar Lows, may play an important role in the high-latitude climate system through strong coupling of the atmosphere and ocean via air-sea heat exchange.

4.7 Modes of Atmospheric Variability Affecting the Arctic

4.7.1 The North Atlantic Oscillation (NAO)

The NAO has long been recognized as a major mode of atmospheric variability affecting the Arctic. The NAO describes the tendency for the Icelandic Low and Azores High, the two “centers of action” in the atmospheric circulation of the North Atlantic, to covary in strength. When the Icelandic Low is strong, the Azores High also tends to be strong; in this case, the NAO is in its positive phase. When the Icelandic Low and Azores High are both weak, the NAO is in its negative phase. In the negative phase, the Icelandic Low also tends to be shifted to the southwest. This covariability is associated with significant high-latitude signals in SAT, cyclone activity, moisture transport, precipitation, SSTs, and ocean heat transport; some of these impacts will be examined here while others will be addressed in subsequent chapters as appropriate. When its index is based on SLP anomalies between two fixed points (as has traditionally been the case [more on this shortly]), the NAO is best expressed during winter. Research has naturally focused on this season. As reviewed by H. van Loon and J. Rogers (1978), manifestations of the NAO have been recognized for centuries. For example, the missionary Hans Egede Saabye recorded in a diary kept in Greenland (1770–1778) that the Danes were well aware that when winters in Greenland were especially severe, the winters in Denmark tended to be mild, and vice-versa. Description of this temperature seesaw associated with the NAO can be found in writings throughout the nineteenth century.

The first formal description of the NAO is credited to Sir Gilbert Walker. In a paper with E.W. Bliss (Walker and Bliss, 1932), a selected set of highly correlated SAT, SLP, and precipitation time series at widely separated stations over eastern North America and Europe were combined to develop an NAO index. The same approach was used to identify the North Pacific Oscillation and the Southern Oscillation. Walker and Bliss described the NAO in terms of a tendency for sea level pressure to be low near Iceland in winter when it is high near the Azores and southwest Europe, attended by unusually high temperature in northwest Europe and low temperatures off the Labrador coast. When Iceland pressures are low (high), the NAO index is positive (negative). The NAO index is hence a measure of the meridional gradient in SLP over the north Atlantic, which can also be interpreted in terms of the strength of the mid-latitude westerly (west to east) winds.

Walker and Bliss 1932) suggested that a simpler index of the NAO could be based on the pressure difference between Iceland and the Azores (roughly representing the climatological centers of the Icelandic Low and Azores High). The utility of this simple index based on SLP at two fixed locations was confirmed by J. Wallace and D. Gutzler (1981) and has been widely adopted. There are a number of variants of the station-based NAO index using different stations and techniques. Most commonly it is based on the difference in standardized station SLP, the intent of the standardization being to reduce the dominance of the Iceland station. J. Rogers (1984) used Ponta Delgadas, Azores, and Akureyri, Iceland, whereas J. Hurrell (1995, 1996) used Lisbon, Portugal, and Stykkisholmur, Iceland. By contrast, van Loon and Rogers (1978) used an index based on the east-west contrast in SLP across the subpolar north Atlantic.

A disadvantage of an SLP-based index based on two stations is that it may not optimally capture the negative correlation between subtropical and subpolar SLP centers. For example, under the positive (negative) NAO mode, the Icelandic Low and Azores High are not just stronger (weaker), but exhibit poleward (equatorward) shifts. The centers of maximum anticorrelation also shift seasonally. In recognition, D. Portis et al. (2001) developed a seasonally and geographically varying “mobile” index of the NAO, defined as the difference between normalized SLP anomalies at the locations of maximum negative correlation between the subtropical and subpolar North Atlantic SLP. They found that the subtropical center shifts westward and northward into the central North Atlantic as the annual cycle passes through spring and summer. When tracked with their mobile NAO index, the NAO nodal correlations are only slightly weaker in the summer-half of the year as opposed to the winter half. Their index also shows that the NAO is strongest in March, followed by February and January.

Other investigations have made use of empirical orthogonal function (EOF) or rotated principal component (PC) analyses. These approaches have been applied variously to a North Atlantic domain or the Northern Hemisphere, using gridded SLP or tropospheric height fields (e.g., Trenberth and Paolino, 1980; Wallace and Gutzler, 1981; Barnston and Livezy, 1987; Thompson and Wallace, 1998, 2000; Hurrell et al., 2003). The NAO emerges very clearly as the leading mode of variability in the North Atlantic study of Trenberth and Paolino (1980), accounting for 34 percent of the variance in winter SLP. The first EOF from that study, reproduced in Figure 4.16, shows the dipole structure of the NAO. Similar results can be obtained through composite analysis of SLP fields for extremes of the NAO index. EOF or PC approaches are usually considered more robust than station-based indices in that they use information from the entire atmospheric field to extract the dominant modes of variability. On the other hand, from a practical viewpoint, individual station time series from which indices can be compiled are available for a longer time period than are gridded fields.

NAO time series for winter (December–March) through 2002, based on three different approaches using SLP data (station index, PC1 of the Atlantic sector, PC1 of the Northern Hemisphere) are presented in Figure 4.17. As mentioned, the advantage

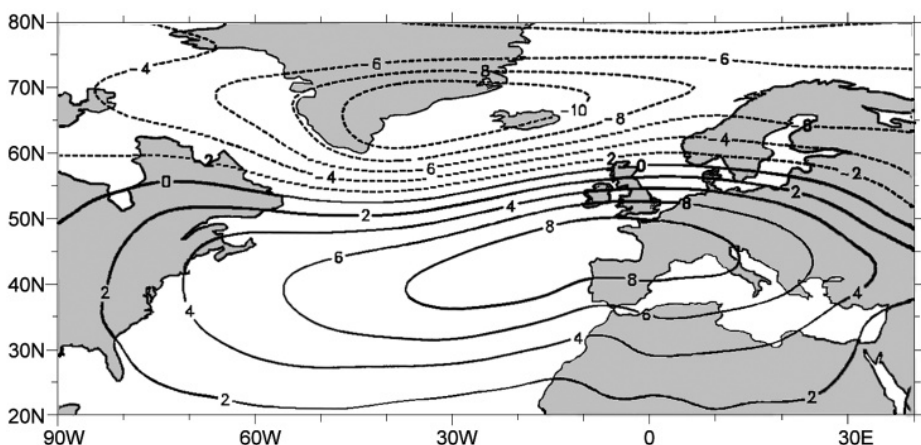


Figure 4.16. The first EOF of winter (December–March) sea level pressure for the North Atlantic sector over the 1899–1977 period, based on Trenberth and Paolino (1980) (from Dickson et al., 2000, by permission of AMS).

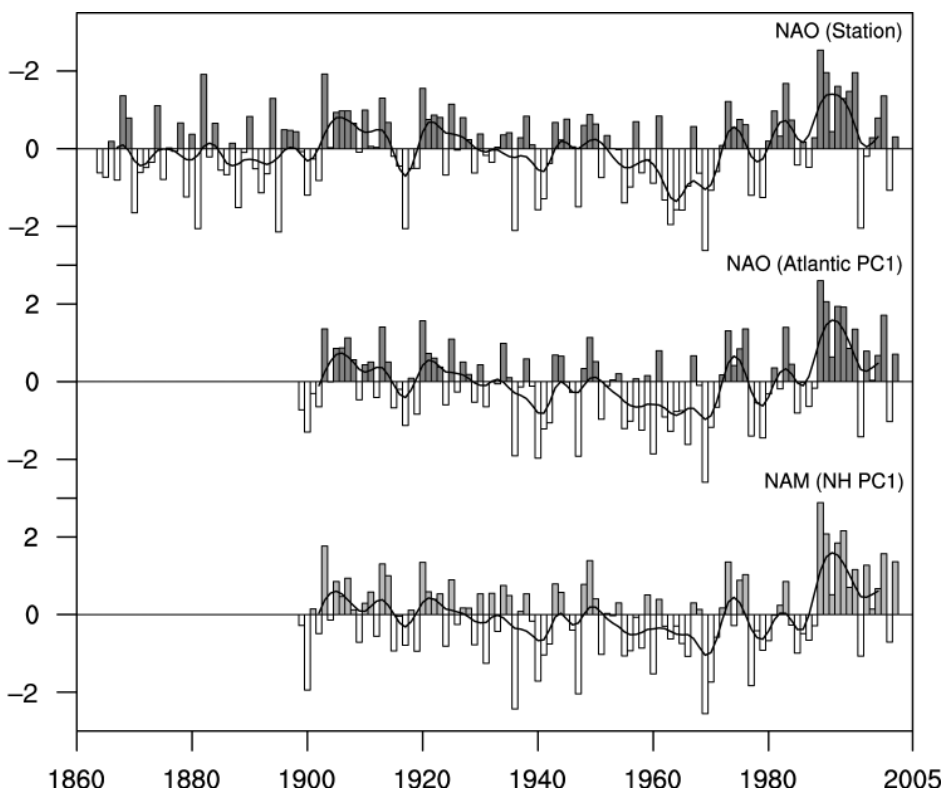


Figure 4.17. Normalized indices of the winter (December–March) NAO, based on the difference in normalized sea level pressure between Lisbon, Portugal and Stykkisholmur/Reykjavik, Iceland, PC1 of Atlantic sector sea level pressure ($20\text{--}70^\circ\text{N}$, $90^\circ\text{W}\text{--}40^\circ\text{E}$), and PC1 of Northern Hemisphere sea level pressure ($20\text{--}90^\circ\text{N}$). The latter time series is also known as the Arctic Oscillation or Northern Annular Mode. The heavy solid lines represent the indices smoothed to remove fluctuations with periods less than four years (from Hurrell et al., 2003, by permission of AGU).

of the station-based index (top panel) is that a longer record can be obtained (back to 1864). The time series structure from the three approaches is very similar for the period of overlap. As discussed shortly, the PC1 for the Northern Hemisphere has come to be known as the Arctic Oscillation or Northern Annular Mode.

Figure 4.18 shows SLP patterns, composite anomalies and composite differences for the region north of 50°N based on extremes of Hurrell's NAO index. Data are drawn for the years 1947–1996. Immediately evident is that the SLP signature, while strongest in the vicinity of the Icelandic Low (a maximum difference of 22 hPa between extreme positive and negative states), extends well into the Arctic Ocean. Over the pole, there is a composite difference of about 8 hPa. Building on previous discussion, the Icelandic Low, although weaker under the negative NAO/AO, is also shifted to the southwest. The low composite also shows a separate weak closed low over the Barents Sea.

Recall that one of the earliest-noted manifestations of the NAO/AO is the “seesaw” in SAT over Europe and northeastern North America. Under the positive mode, the SLP pattern associated with the strong Icelandic Low will tend to advect cold high latitude air over Greenland and eastern Canada, consistent with the tendency for negative temperature anomalies in these areas. By comparison, an opposing strong advection of warm lower-latitude air over northern Europe and Scandinavia is consistent with positive temperature anomalies in this area. Under the negative mode with a weak and southward-shifted Icelandic Low, winds over Greenland and eastern Canada are weaker (positive temperature anomalies). Winds over northern Europe and Scandinavia, while still southerly, are also much weaker than under the positive NAO mode, and have opposing temperature anomaly signals.

The map of correlations between the winter (November–February) NAO index and surface air temperatures (based on the NCEP/NCAR reanalysis) provided as Figure 4.19 reveals that the “seesaw” is just part of a larger-scale organization of anomalies; when the NAO is in its positive phase, temperatures tend to be below normal over a large area of the northern North Atlantic and northeastern North America, and above normal over a wide swath of northern Eurasia. The opposite pattern holds when the NAO is in its negative phase. Based on data through 1994, Hurrell (1996) concluded that the NAO accounts for 31 percent of the interannual variance of Northern Hemisphere extratropical temperatures over the past sixty years (through 1994) while the El-Nino Southern Oscillation (ENSO) accounts for 16 percent. The latter reflects the ENSO link with the strength of the Aleutian Low and amplitude of the downstream Pacific North America (PNA) mid-tropospheric wavetrain over North America that we will be briefly reviewing later.

It should come as no surprise that the NAO/AO is allied with pronounced signals in cyclone frequency. Serreze et al. (1997) inspected the NAO time series from 1966 through 1993. For each cold-season month (October through March), they extracted the seven years with the most positive and most negative NAO index values. For each month and seven-year period, they extracted records of cyclone events over the North Atlantic, using an automated detection and tracking algorithm applied to SLP fields. The positive minus negative NAO difference field in cyclone counts from

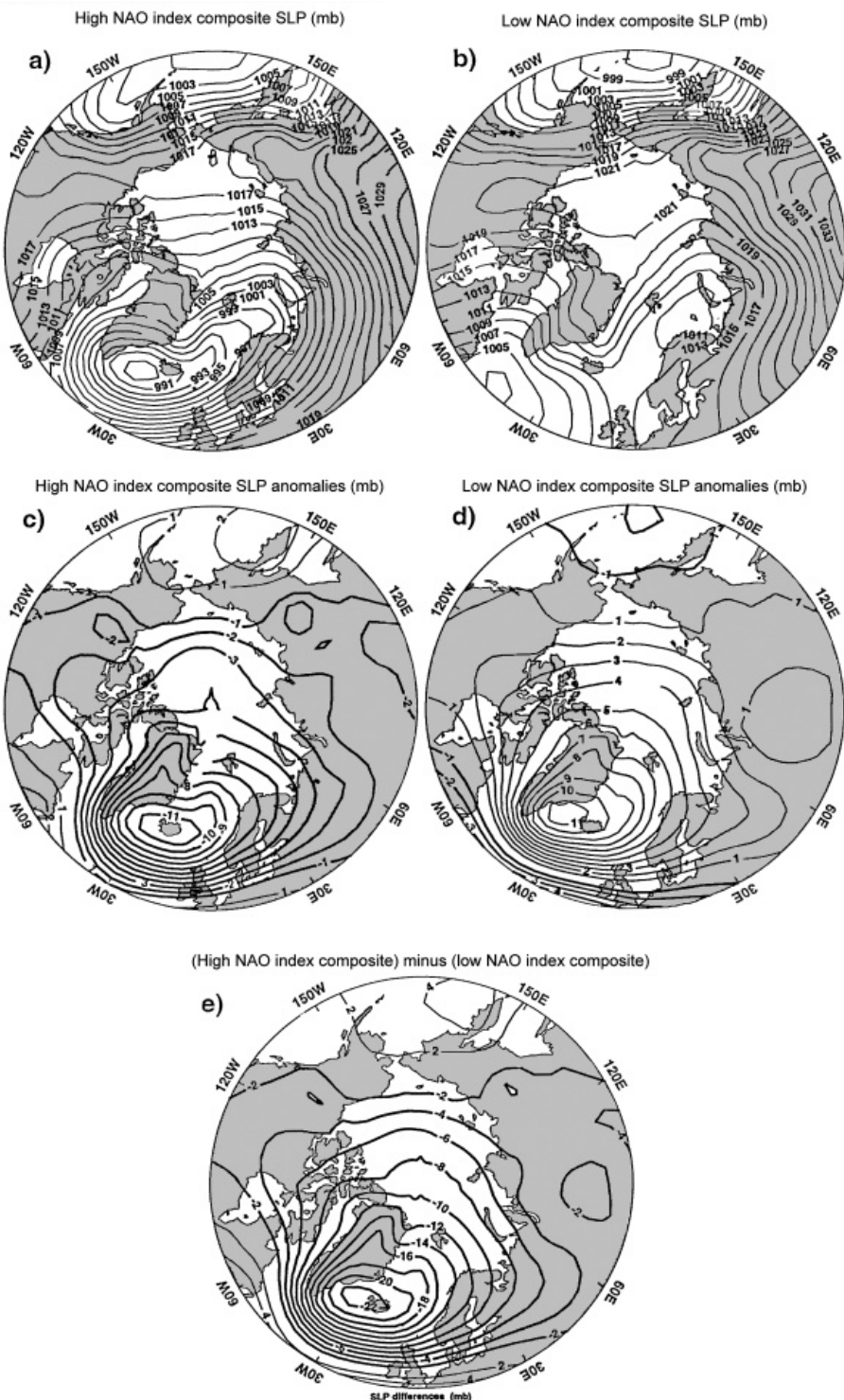


Figure 4.18. Distributions of (a), (b) winter sea level pressure and (c), (d) sea level pressure anomalies for composites of winter months representing high index and low index states of the NAO, (e) the change in sea level pressure from the high index composite to the low index composite (from Dickson et al., 2000, by permission of AMS).

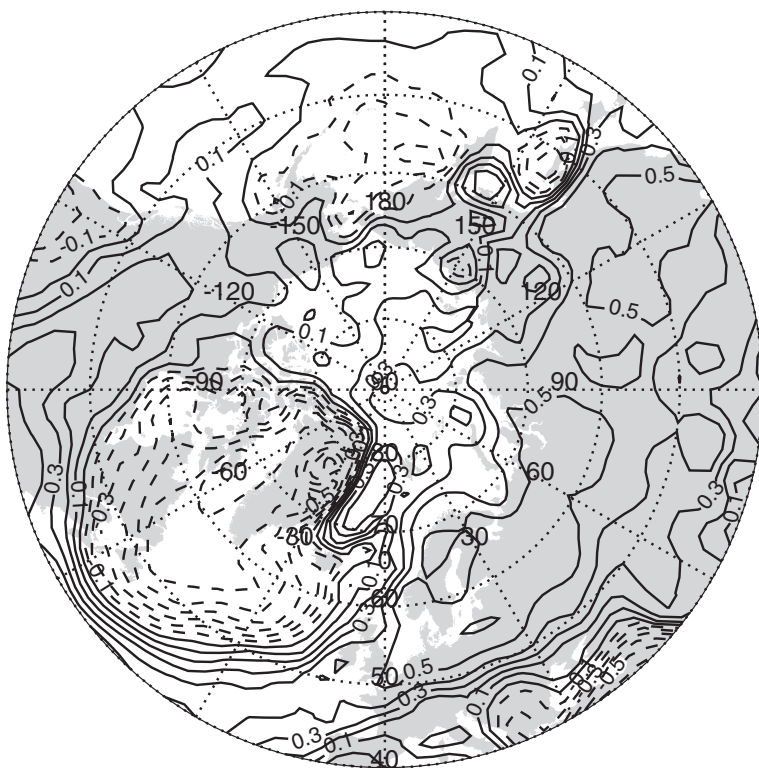


Figure 4.19. Spatial pattern of the linear correlation between the winter (November–February) averaged NAO index and surface air temperature, based on data from the NCEP/NCAR reanalysis for the 1960–2010 period (courtesy of A.P. Barrett, NSIDC, Boulder, CO).

that study is reproduced in Figure 4.20. There is an obvious poleward (equatorward) shift in cyclone activity between the positive (negative) NAO phases, broadly consistent with the different patterns of SLP associated with NAO extremes. For the region corresponding to the climatological center of the Icelandic Low, cyclone events are more than twice as common under positive NAO extremes as compared to negative extremes. Systems found in this region during the positive phase are also significantly deeper than their low NAO counterparts.

There is little evidence of any preferred time scale of variability in the NAO. The studies of Hurrell and van Loon (1997) and E. Cook, R. D'Arrigo, and K. Briffa (1998) document concentrations of spectral power in the NAO at 2.1, 8, and 24 years, but as noted by Hurrell et al. (2003) there are no significant peaks. Furthermore, large changes can occur from one winter to the next, and there is considerable variability within a given winter season. Although this behavior is consistent with the notion that much of the variability in the NAO is from processes internal to the atmosphere (Hurrell et al., 2003), one can expect surface influences. One such forcing that can operate on seasonal and shorter time scales is the distribution of sea ice. Some modeling studies (e.g., Alexander et al., 2004; Deser et al., 2004)

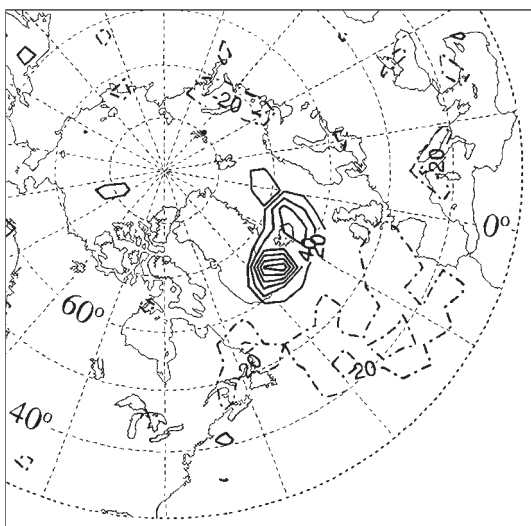


Figure 4.20. Positive minus negative NAO difference field of cyclone events for the cold season based on index extremes over the 1966–1993 period. The contour interval is 20. Positive differences are shown by solid contours with negative differences shown by dash-dot contours (from Serreze et al., 1997, by permission of AMS).

suggest that when the sea ice margin in the Atlantic sector retreats, it invokes a local change in heating, which alters the North Atlantic storm track. This appears to involve at least a weak response of the NAO. The observational study of J. Francis et al. (2009) lends some support, finding that summers with low sea ice extent (as assessed for the Arctic as a whole) tend to be followed by a neutral or negative NAO phase in autumn and winter. They argue that having large areas of open water at summer's end leads to strong warming of the lower atmosphere in autumn and winter (part of the process of observed Arctic amplification of recent SAT changes, see Figure 1.5), a reduction of static stability (the Arctic temperature inversion becomes weaker), increased cloudiness, and – because of the outside Arctic warming relative to lower latitudes – a reduction on the poleward gradient in atmospheric thickness that weakens the polar jet stream. J. Overland and M-Y. Wang (2010) come to similar conclusions. In a follow-on observational study, Francis and Vavrus (2012) argue that the Arctic amplification linked to ice loss contributes to slower easterly progression of Rossby waves in the upper level flow, influencing middle-latitude weather patterns.

Although low-frequency variability does not stand out as significant in a spectral analysis, a number of studies (e.g., Portis et al., 2001) highlight multidecadal epochs of the NAO. Looking back to the station-based index plotted as part of Figure 4.17, there was an epoch from about 1870 through about 1900 when the NAO was mostly negative, followed by mostly positive values from 1900 to 1950. This was followed by a negative period from 1960 through 1980, and then a positive epoch from the 1980s through the late 1990s. As realized in a number of studies conducted during the early 1990s and early 2000s, notably Hurrell (1995, 1996), this multidecadal trend from the negative to the positive phase on the NAO in large part accounted for the pattern of linear trends in winter SAT observed between the two periods, which, following from Figure 4.19, consisted of warming over northern

Eurasia and cooling over the northeastern North American and the northern North Atlantic. A prominent point of discussion at the time was the mismatch between this pattern of temperature trends and projections from climate model simulations with rising levels of atmospheric greenhouse gases, which mostly depict the strongest warming over the Arctic Ocean in autumn and winter (the pattern of Arctic amplification that is now clearly emerging in the observations). Since about the beginning of the twenty-first century, the NAO has varied between its positive and negative states; recent events of note include strongly negative states during the winters of 2009/2010 and 2010/2011 and a strongly positive state during the winter of 2011/2012. The latter followed the second lowest September sea ice extent in the satellite record.

There is evidence that low-frequency NAO variability involves large-scale ocean interactions. As reviewed by M. Hoerling, J. Hurrell, and T. Xu (2001), whereas the observed spatial pattern and amplitude of the NAO is typically well-simulated in AGCMs with fixed climatological annual cycles of solar radiation, trace gas compositions, and SST, such simulations do not reproduce interdecadal changes comparable in magnitude to those that are observed. This suggests a role of slowly varying SSTs. M. Rodewell, D. Rodewell, and C. Folland (1999) find that much of the multidecadal variability of the winter NAO over the past fifty years (up to the time of that study) can be simulated when the observed temporal evolution of North Atlantic SST distributions is included. They argue that the SST characteristics are communicated to the atmosphere through evaporation, precipitation, and atmospheric heating processes and that with knowledge of SSTs, it may be possible to predict European winter climate several years in advance.

Hoerling et al. (2001) counter that most evidence actually suggests that anomalous SST and upper-ocean heat content feedbacks to the atmosphere from the extra-tropics are rather small, implying that a strict focus on the North Atlantic is inappropriate. Their modeling study, which focused on the positive NAO trend from 1980s through the late 1990s, indicates a more important role of progressive warming of tropical SSTs, especially over the Indian and Pacific Oceans. Follow-on papers (Hoerling et al., 2004; Hurrell et al., 2004) strengthen this argument. These ocean changes alter the pattern and magnitude of tropical rainfall and atmospheric heating, which in turn forced a trend toward the positive phase of the NAO. C. Cassau and L. Terray (2001) also focus on the tropics but provide a somewhat different view – they find links between the positive phase of the NAO and the cold phase of ENSO (La Niña).

D. Dukhovskoy, M. Johnson, and A. Proshutinsky (2004) speculate on a role of internal Arctic processes involving heat and freshwater exchange between the Arctic Ocean and GIN seas. During the negative phase of the NAO, the atmospheric heat flux to the Arctic Ocean is small, and the freshwater flux to the Greenlan-Iceland-Norwegian seas is less than average. With a small heat flux, the atmosphere over the Arctic Ocean cools, leading to a more anticyclonic circulation and a stronger Beaufort Gyre, increasing the convergence of surface water and ice. More freshwater is retained in the Beaufort Gyre. Less freshwater outflow to the

Greenland-Iceland-Norwegian seas promotes deep oceanic convection in the central Greenland Sea in winter, associated with intense vertical heat fluxes to the atmosphere. This causes positive anomalies in surface air temperature and intensification of the Icelandic Low (a transition to the positive phase on the NAO). As a result of these processes, there is a growth of air temperature and sea level pressure gradients between the two basins. The gradients build to a point where they cannot be maintained and the basins then interact. An intensified horizontal heat flux to the Arctic Ocean weakens the atmospheric anticyclone and Beaufort Gyre. The accumulated freshwater in the Beaufort Gyre spills into the Greenland-Iceland-Norwegian seas, which become fresher, suppressing deep convection. With a fresher surface, sea ice is easier to form. Both processes reduce the vertical heat flux to the atmosphere (sea ice insulating the ocean from the atmosphere), acting to weaken the Icelandic Low (a transition back to the negative phase of the NAO). After several years, interaction between the basins fades. Gradients then rebuild and the cycle repeats itself.

4.7.2 The Arctic Oscillation (AO)

In 1998, a paper appeared in *Geophysical Research Letters* by D. Thompson, then a Ph.D. student at the University of Washington, Seattle, and his advisor, J. Wallace (Thompson and Wallace, 1998). Follow-on papers were published shortly thereafter (Thompson and Wallace, 2000; Thompson, Wallace, and Hergel, 2000, Wallace, 2000). Thompson and Wallace (1998) argued that NAO should be considered as a regional manifestation of a more basic mode of SLP variability, which has come to be known as the AO, or NAM. They defined the AO as the leading mode of SLP variability from an EOF analysis for the Northern Hemisphere winter (using data from 1900–1997). The major characteristics (Figure 4.21) are a primary center of action over the Arctic, focused in the area of the Icelandic Low, and opposing, weaker centers of action in the North Atlantic and North Pacific. The interpretation is that if pressures are low (high) over the Arctic, they are high (low) over the North Atlantic and North Pacific. Thompson and Wallace (1998) were not the first to perform a Northern Hemisphere analysis. As far as we are aware, the first arguments for more a fundamental mode of variability than the NAO come from the studies of E. Lorenz (1951), J. Kutzbach (1970) and Wallace and Guzler (1981).

However, as is obvious from Figure 4.21, the Arctic and Atlantic AO centers of action correspond closely to the NAO winter centers of action. Looking back at Figure 4.17, the time series of the AO (NAM) and NAO are also very similar. Not surprisingly, the spatial pattern of correlations between the winter AO and surface air temperature (Figure 4.22) is also quite similar to the spatial pattern based on the NAO index; notable differences include stronger positive correlations over northern Eurasia and a more strongly expressed region of negative correlations centered over southern Alaska.

Thompson and Wallace (1998) interpret the winter AO as the surface signature of modulations in the strength of circumpolar stratospheric vortex. Recall from earlier discussion that the mean winter circulation in the stratosphere is primarily zonally

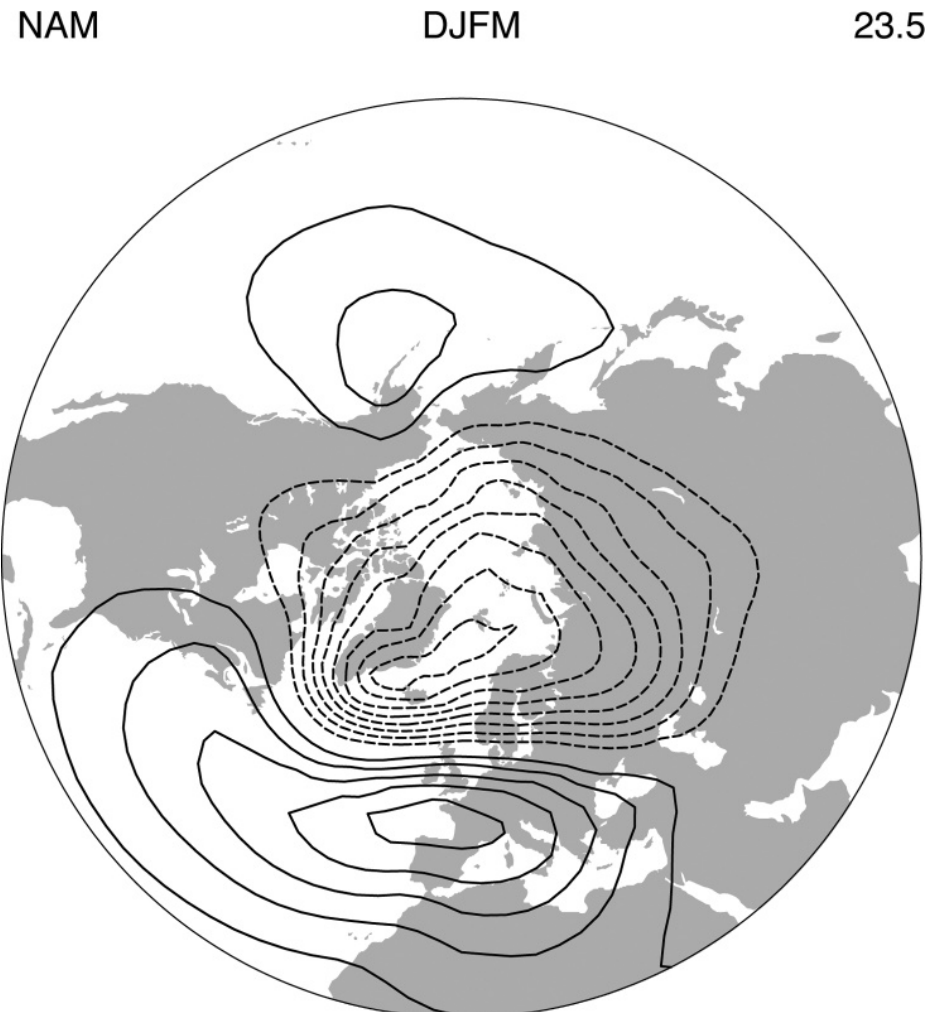


Figure 4.21. Normalized leading EOF of winter (December–March) sea level pressure anomalies over the Northern Hemisphere (20–90°N). The pattern (accounting for 23.5% of the variance in Northern Hemisphere sea level pressure) is displayed in term of amplitude (hPa) obtained by regressing the hemispheric sea level pressure anomalies on the leading principal component time series. The contour interval is 0.5 hPa and the zero contour has been excluded. The data cover the 1899–2001 period (from Hurrell et al., 2003, by permission of AGU).

symmetric (or annular), whereas that of the troposphere and the surface is characterized by a wavier pattern. The primary pattern of variability has the same basic features – in the stratosphere, it is primarily in the strength of the annular vortex, whereas for the troposphere and surface, it is the wavy pattern. The NAO framework focuses on the Atlantic sector, where the surface and tropospheric variability is strongly expressed. However, in the AO framework, the winter stratospheric variability and that for the troposphere and surface are not considered in terms of

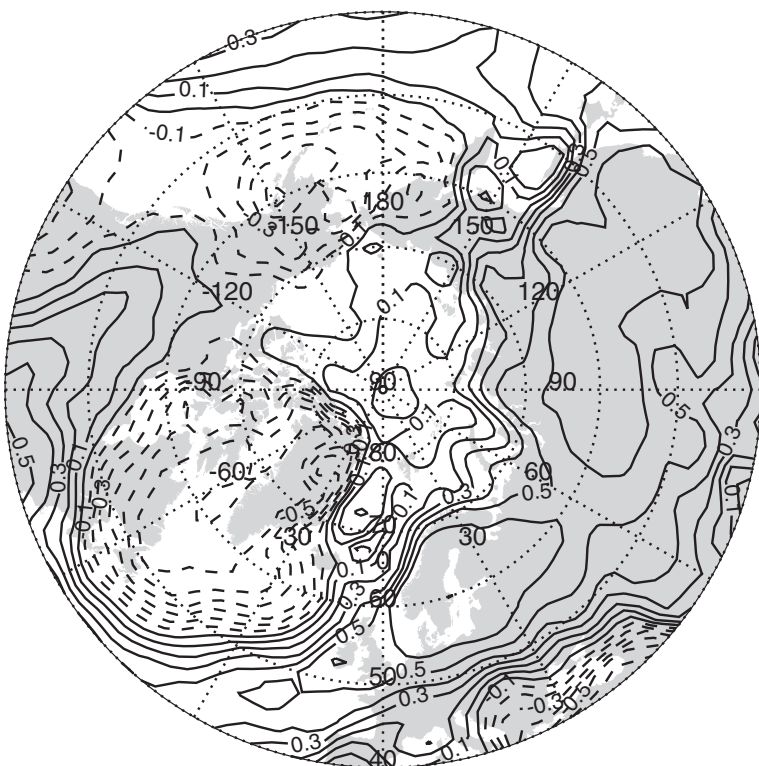


Figure 4.22. Spatial pattern of the linear correlation between the winter (November–February) averaged AO index and surface air temperature, based in data from the NCEP/NCAR reanalysis for the 1960–2010 period (courtesy of A.P. Barrett, NSIDC, Boulder, CO).

different modes, but as elements of a single, inherently annular modal structure that are physically linked through most of the depth of the atmosphere.

The winter AO resembles a similar mode in the Southern Hemisphere which is more symmetric from the stratosphere through to the surface. Put differently, its regional expressions are not as pronounced. The stronger asymmetry of the winter AO (seen especially in terms of the focus of the strong Arctic center of action to near the Icelandic Low) is viewed in terms of distortions on the inherently annular structure driven by the land sea distribution (the presence of a warm ocean extending to high northern latitudes) and orography. Were it not for these distorting influences, the AO would more closely resemble its more symmetric Southern Hemisphere counterpart. In turn, variations in the phase and strength of the winter AO, seen in terms of mass exchanges between the Arctic and mid-latitudes, are viewed in terms of controls from the stratosphere. Although the details of such controls are still not well understood, one appears to involve the sudden stratospheric warmings. Such warmings weaken or even reverse the stratospheric zonal winds. This in turn alters conditions for upward propagation of planetary waves, which ultimately may be seen in transitions from the positive to negative mode of the AO.

This emphasis on the winter stratosphere is also relevant to the interpretation of low-frequency variability. Low frequency variability in the NAO is thought of as being forced from the surface by slowly varying North Atlantic or tropical SSTs, the latter finding support from recent modeling studies. By contrast, in the AO framework, thinking turns to linkages with stratospheric ozone depletion or the buildup of greenhouse gases that are associated with stratospheric cooling. The basic idea is that such changes can “spin up” the polar stratospheric vortex, with the effects propagating down to the surface.

The concept of the AO as more fundamental than the NAO was not met with universal enthusiasm. Although many in the research community were quick to hail the AO as the new paradigm, others were skeptical. C. Deser (2000) concluded that the correlation between the Pacific and Azores centers of action is not significant and that the AO cannot therefore be viewed as reflecting such a teleconnection. M. Ambaum, B. Hoskins, and D. Stephenson (2001) find that even the correlation between the Pacific and Icelandic-Arctic centers of action is not significant. They argue that the AO is mainly a reflection of similar behavior in the Pacific and Atlantic basins. Other studies contributing to the debate include J. Fyfe (2003) and Ambaum and Hoskins (2002). Regardless, from a practical view, indices of the winter AO and NAO are very highly correlated and for many applications, one can use either paradigm.

However, a different picture emerges when attention is focused on seasonal changes in the structure of the pattern. Recall from discussion of the NAO that while the Icelandic Low and the Azores High exhibit seasonal variations in their strength, there are also seasonal shifts in the locations of these two centers of action. This is what drove Portis et al. (2001) to develop their seasonally mobile index of the NAO. In a similar vein, M. Ogi, K. Yamazaki, and Y. Tuchibana (2004), defined the AO separately for each calendar month through an empirical orthogonal function EOF analysis of geopotential height fields from 1,000 hPa to 200 hPa, poleward of 40°N, an approach argued to better capture seasonal changes in the structure of the mode. Based on their approach, the summer NAM has a smaller meridional scale than its winter counterpart, with the Arctic center of action lying over the central Arctic Ocean.

4.7.3 The Pacific Decadal Oscillation

Coupling between the atmosphere and the oceans is implicated in climate variations on scales of several years to decades. As just discussed, such coupling can help to explain low frequency variability in the NAO. The best-known coupled atmosphere-ocean phenomenon is ENSO, which results from interactions between the atmosphere and ocean in the tropical Pacific and operates on time scales of three to seven years. ENSO is associated with variability in the atmospheric circulation far from the tropical heating sources. ENSO can in turn be linked in various ways to “ENSO-like” patterns in the climate system, for which multi-decadal signals are prominent. Climate signals are best expressed in the extratropics, especially the northwest Pacific, including Alaska.

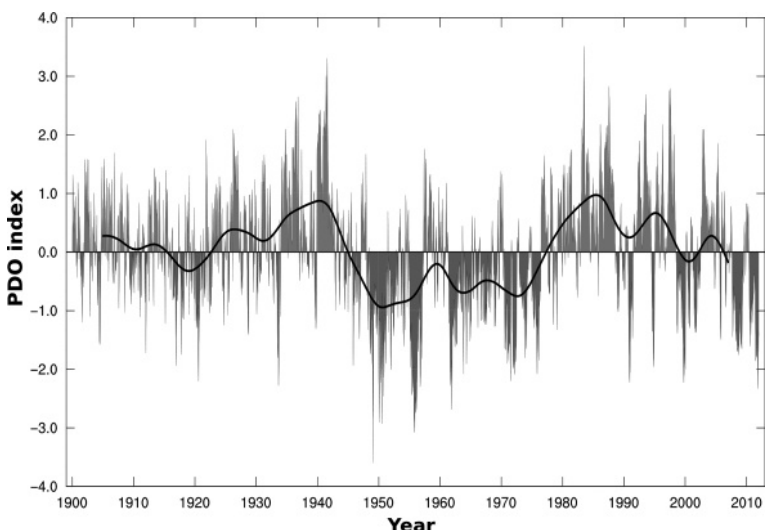


Figure 4.23. Monthly values of the Pacific Decadal Oscillation (PDO) index for the 1900–2011 period, the bold line shows the index values smoothed with a 121-month running average (by permission of Creative Commons Attribution-Share Alike 3.0 Unreported license (CC BY-SA 3.0), data from <http://jisao.washington.edu/pdo/PDO.latest>). (See plate section for color version.)

The most important of these ENSO-like patterns is the Pacific Decadal Oscillation (PDO). The term was coined by Steven Hare in 1996 while researching connections between Alaska salmon production cycles and Pacific climate (Mantua et al., 1997). The index of the PDO is defined as the leading principal component of North Pacific monthly SST variability poleward of 20°N. When SSTs are anomalously high along the North Pacific coast but anomalously low in the interior North Pacific, the PDO is said to be in its warm (positive) phase. In the warm PDO phase, SLPs are below average over the northern North Pacific – that is, the Aleutian Low is unusually deep. In the cold (negative) PDO phase, the anomaly patterns are broadly reversed, with positive SST anomalies in the interior North Pacific, negative SST anomalies along the North American coast, and a weaker Aleutian Low.

During the twentieth century, each PDO phase has typically lasted for twenty to thirty years. Cold PDO regimes prevailed from 1890–1924 and again from 1947–1976, while warm PDO regimes dominated from 1925–1946 and from 1977 through the mid-1990s (Figure 4.23). The PDO may now be entering a new negative phase. Much attention has been paid to the Pacific climate regime shift that transpired during the winter of 1976–1977, linked to the shift in the PDO from its cold to its warm phase, which had substantial impacts on marine ecosystems of the North Pacific. This appears to have been but one in a series of climate shifts linked to the PDO (Hare and Mantua, 2000). Air temperature anomalies over Alaska are known to be strongly tied to the phase of the PDO (Hartmann and Wendler, 2003). Compared to the negative PDO phase (1951–1975), mean annual and seasonal air temperatures during the positive phase period (1977–2001) examined in

their study were up to 3.1°C higher. The latter period also saw greater mean cloudiness, higher wind speeds, and higher precipitation totals, attended by lower SLP and geopotential heights. The lower SLP manifests a deeper Aleutian Low in winter and spring. Intensification of the Aleutian low increased the advection of relatively warm and moist air to Alaska during winter and spring. The regime shift has also strongly influenced surface air temperature trends in Alaska. When analyzing the total time period from 1951 to 2001, the temperature trends are positive. However, the twenty-five-year period trend analyses before 1976 (1951–1975) and thereafter (1977–2001) are both characterized by general cooling.

4.7.4 Arctic Dipole Anomaly

It is widely accepted that the extreme September minimum in Arctic sea ice extent observed in 2007 (a record minimum at the time as assessed over the satellite record) was driven in considerable part by a persistent summer pattern of atmospheric circulation that favored ice loss. Its key feature in the SLP field was an unusually high pressure over the northern Beaufort Sea (expressed as a strong Beaufort Sea High) paired with unusually low pressure over northern Siberia. The strong Beaufort Sea High is found just east of a pronounced ridge at the 500 hPa level (Figure 4.24). Resulting southerly winds between the pressure anomaly centers at the surface promoted transport of ice away from the coasts of Siberia and Alaska toward the North Pole, as well as strong melt in the East Siberian and Chukchi seas. The pattern also led to a strong surface pressure gradient across the Fram Strait (between Greenland and Svalbard) enhancing wind-driven transport of sea ice out of the Arctic Ocean and into the North Atlantic.

J. Wang and colleagues (2009) developed a framework for understanding this pattern through an EOF analysis of seasonal mean SLP for the region north of 70°N. They defined the first (leading) EOF mode as the AO (NAM), which for summer has a seasonal structure very similar to that shown by Ogi et al. (2004). The second mode, which they termed the Arctic Dipole Anomaly, has two centers of action of opposing sign, one over the northern Beaufort Sea and one over the Kara Sea. The positive phase of the Arctic Dipole Anomaly is characterized by a strong, northward-shifted Beaufort High and negative SLP anomalies centered over the Kara Sea. In their framework, the SLP anomaly pattern shown in Figure 4.24 linked to the extreme 2007 sea ice minimum (as well as other recent extreme minima in the record), is consistent with the combination of a positive summer mode of the Arctic Dipole Anomaly and a negative mode of the summer AO.

While subsequent studies questioned the statistical robustness of the Arctic Dipole Anomaly pattern, which as discussed was computed using data for a rather limited spatial domain, the term Arctic Dipole Anomaly (or more simply, Dipole Anomaly) has nevertheless stuck. In common usage, it refers to a summer circulation pattern in which SLP is anomalously high over the northern Beaufort Sea and unusually low over northeastern Siberia (positive phase) or vice versa (negative phase), with the understanding that the positive (negative) phase favors (disfavors)

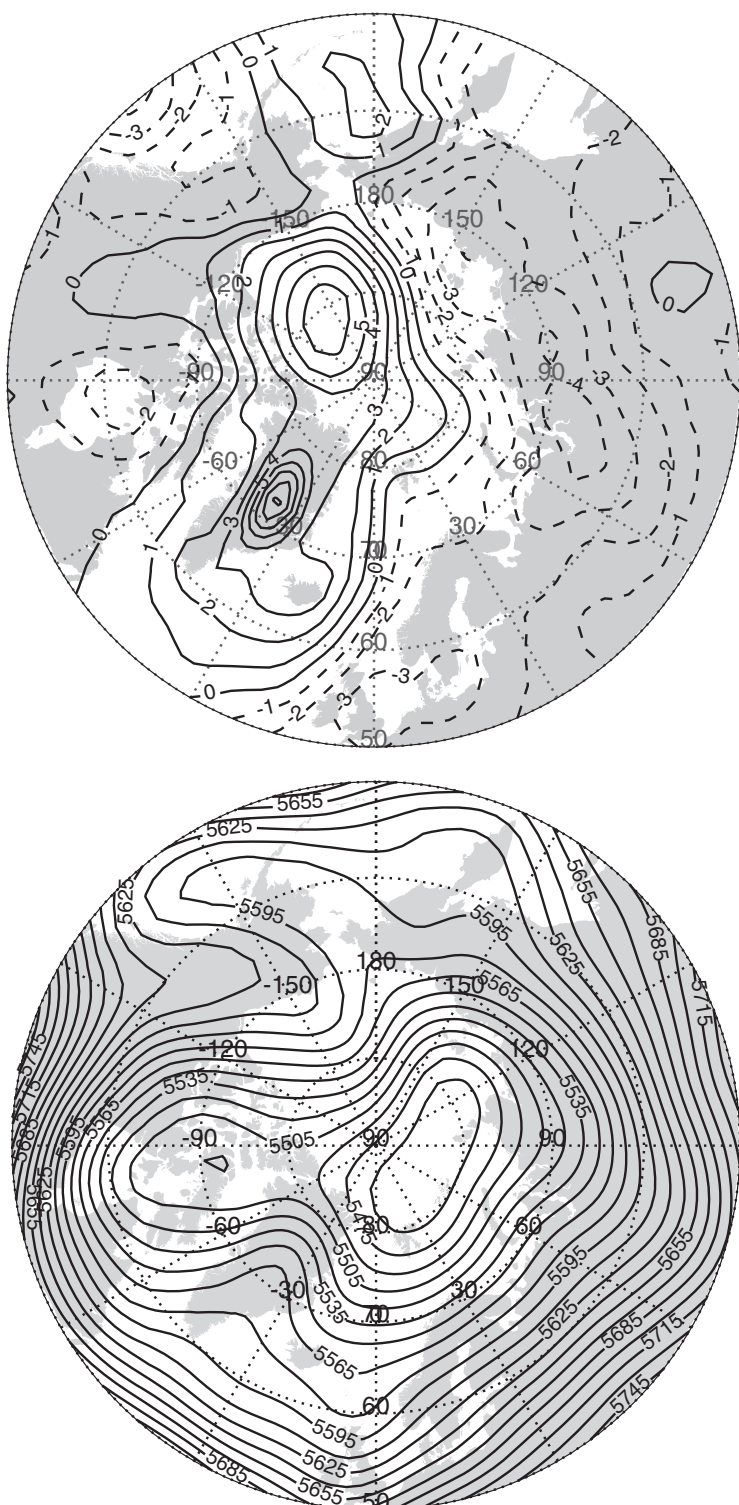


Figure 4.24. Spatial patterns of (a) sea level pressure anomalies and (b) 500-hPa heights for the summer (June–August) of 2007, based on data from the NCEP/NCAR reanalysis (courtesy of A.P. Barrett, NSIDC, Boulder, CO).

summer ice loss. The summer Arctic Dipole Anomaly defined in this way is clearly linked to the phase of the summer AO as identified by Ogi et al. (2004) which is in turn linked to the strength of the summer Arctic cyclone maximum over the central Arctic Ocean discussed by Serreze and Barrett (2008). Overland et al. (2012) show that the Arctic Dipole Anomaly has been a persistent feature of the summer atmospheric circulation over the 2007–2012 period, especially in June. Whether this pattern will continue to persist remains to be seen.

4.7.5 Pacific North American Pattern

The Pacific North American pattern, commonly referred to as the PNA, refers to the amplitude of the atmospheric longwave pattern (the “wavetrain”) extending from the North Pacific Ocean through North America. The positive phase of the PNA features above-average pressure heights in the vicinity of Hawaii, below-average heights located south of the Aleutian Islands, above average heights over the intermountain region of North America, and below average heights over the southeastern United States. When the anomaly pattern in pressure heights is the reverse, such that the amplitude of the wavetrain is smaller than normal, the PNA is in its negative phase. The PNA is one of the most important modes of variability affecting North America in winter, with the positive phase linked to above-average temperatures over western Canada, extending well into the Arctic and including Alaska, and below-average temperatures across the south-central and southeastern U.S.

The index of the PNA is typically based on an EOF analysis of the geopotential height field. The PNA is strongly influenced by the phase of ENSO. The positive phase tends to be associated with El-Nino while the negative phase tends to be associated with La-Nina. Although the PNA is best expressed in winter, it can be identified throughout the year. When evaluated on a monthly basis, such as is done by the NOAA Climate Prediction Center, the troughs and ridges in the wavetrain are seen to vary in intensity and location through the year. From Figure 4.25, it is evident that the main centers of action of the PNA pattern for the summer months are weaker than those in winter (the correlation between time series of the PNA index and pressure heights is lower), are shifted poleward, and are more closely spaced. During summer, a prominent center of action lies over the Arctic Ocean.

M. L’Heureux et al. (2008) viewed the unusual summer Arctic circulation of 2007 as an expression of an extreme positive phase of the summer PNA wavetrain. Note from Figures 4.24 and 4.25 the close relationship between the pronounced 500 hPa ridge extending into the Beaufort Sea, the strong Beaufort Sea High at the surface lying just east of the ridge axis, and the location of the summer center of action of the PNA located over the Arctic Ocean. In an attempt to find some common ground between different studies, Serreze and Barrett (2010) showed that a strong Beaufort High tends to be a feature of the positive phase of the summer PNA, the negative phase of the summer Northern Annular Mode, as well as the positive phases of the summer Arctic Dipole Anomaly and Pacific Decadal Oscillation. The

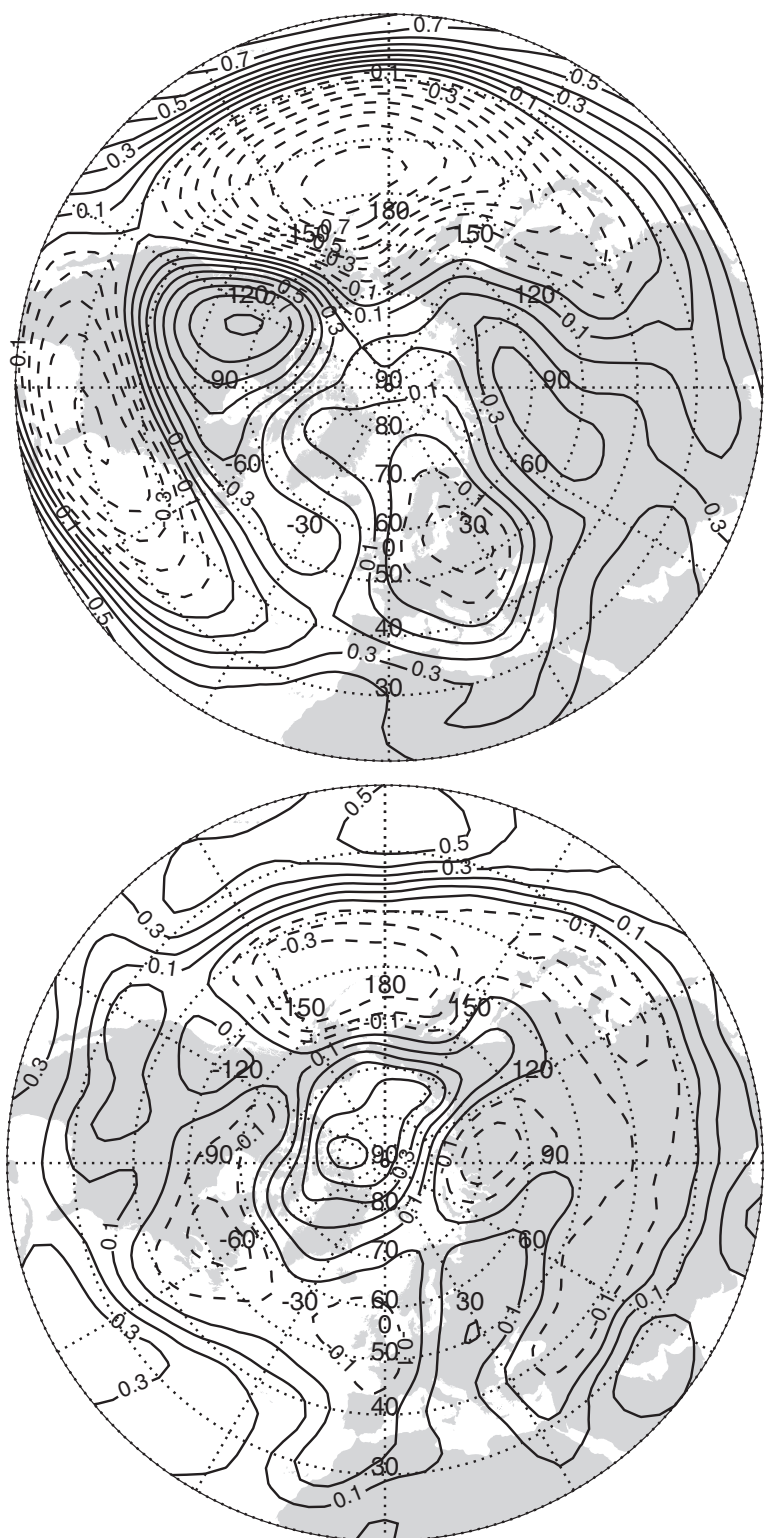


Figure 4.25. Spatial patterns of the correlation between the PNA index and 500-hPa heights for (a) winter, (b) summer, based on data from the NCEP/NCAR reanalysis for the 1960–2010 period (courtesy of A.P. Barrett, NSIDC, Boulder, CO).

unifying theme is that, to varying degrees, the high latitude 500 hPa ridge associated with the Beaufort Sea High represents a center of action in each pattern.

Focus Questions and Exercises

- 1) Imagine a world in which the island of Greenland was removed. Describe how patterns of cyclone activity in the northern North Atlantic would differ compared to the real-world situation.
- 2) Although one can establish a general spatial pattern of anomalies in surface air temperature in the Arctic corresponding to the positive (or negative) phase on the NAO (see Figure 4.19), if we compared the pattern of January temperature anomalies for two different years, but each corresponding to the same index value of the NAO, they might look quite different. Explain why this is so.
- 3) What changes in the seasonality and strength of the Arctic frontal zone might we expect to see through the twenty-first century?

5

Energy Exchanges at the Surface

Overview

As reviewed in Chapter 3, the mean annual cycle of energy storage in the Arctic atmosphere is determined by the interactions between the net radiation budget at the top of the atmosphere, horizontal energy transport convergence, and the vertical net surface flux. The vertical net surface flux was in turn shown to be the key driver of the annual cycle in the energy content of the underlying Arctic Ocean. In this chapter, we look at surface energy transfers in more detail. Even today, direct surface measurements of the various surface energy fluxes, especially in a spatially distributed sense, are rather sparse. However, a reasonably comprehensive picture can be assembled by using available surface observations along with satellite-derived products and model results.

Shortwave radiation exchanges at the surface are strongly influenced by the high albedo of snow and ice. Both shortwave and longwave radiation exchanges at the surface are greatly influenced by cloud cover; the former largely through cloud albedo, and the latter through impacts on the effective atmospheric emissivity and temperature. During winter, the surface net radiation budget is almost always directed away from the surface (upward). Over land, this upward net radiation flux is typically accompanied by a small downward sensible heat flux from the atmosphere to the surface, and a small upward conductive flux through the snow cover. Over the Arctic Ocean, the upward surface net radiation flux in winter is typically balanced by a small downward sensible heat flux and upward conductive fluxes through the snow cover, sea ice, and areas of open water. Away from areas like the Atlantic sector, where there

can be strong temperature advection, changes in the winter surface air temperature are closely tied to changes in the longwave radiation budget. Winter is characterized by strong temperature inversions, typically extending up to 1,000–1,200 m. The inversion layer is fundamentally maintained through an approximate radiative equilibrium associated with the different emissivities of the snow surface (nearly a blackbody) and the temperature maximum layer aloft (a selective emitter), with poleward energy transports balancing the radiation loss to space.

By April, the incoming solar flux is significant; although the surface net radiation across most of the Arctic turns positive, it remains small because of the high surface albedo. Between April and June, much of the positive net radiation is balanced by snow melt. During summer over the ocean, net radiation is primarily balanced by sea ice melt and replenishment of the ocean's sensible heat reservoir, both through conduction and absorption of solar radiation that penetrates into the ocean column. This is consistent with the observation that summer surface air temperatures over the sea ice cover remain near the freezing point. By comparison, over snow-free land surfaces, much of the downward net radiation is balanced by evaporation, sensible heating of the air, and heat conduction into the soil. As energy is not used in melt, higher surface air temperatures are observed. Temperature inversions are still frequent in summer, although they are shallower and weaker than their winter counterparts and are usually elevated from the surface.

For much of the year, the net cloud radiative forcing is positive in the Arctic – that is, clouds have a warming effect at the surface. The sign and magnitude of the cloud radiative forcing depends on the interplay between the solar flux above the clouds, cloud albedo, surface albedo, multiple reflections between the surface and cloud base, and the effect of clouds on increasing the downward longwave flux. A number of potentially important radiation feedbacks have been identified that directly involve the surface energy budget, the best known being the ice-albedo feedback.

5.1 The Energy Budget Framework

5.1.1 The Budget Equation

Recall from Chapter 3 that the net surface flux is

$$F_{\text{sfc}} = - (R_{\text{sfc}} + Q_H + Q_E) \quad (5.1)$$

where R_{sfc} is the net radiation at the surface and Q_H and Q_E are the turbulent sensible and latent (evaporative) heat fluxes. In accordance with the convention adopted in Chapter 3, the net surface flux is taken as positive upward into the atmospheric column (see Figure 3.5). However, R_{sfc} , Q_H and Q_E are taken as positive downward.

Expanding on Chapter 3, the net surface flux can be partitioned into three major terms, the magnitude and existence of which depend on the season and nature of the column underlying the atmosphere, which could variously represent ocean with or without at floating sea ice cover (and an overlying snow cover), bare soil, soil with vegetation on the top (which may in turn be covered by snow), an ice sheet or a glacier:

$$F_{\text{sfc}} = -(R_{\text{sfc}} + Q_H + Q_E) = -(M + C + B) \quad (5.2)$$

which can be rearranged as

$$(R_{\text{sfc}} + Q_H + Q_E) - (M + C + B) = 0 \quad (5.3)$$

M is melt, C is conduction of heat into or out of the underlying column, and B is the “bulk” heat gain (B), representing the absorbtion of solar radiation that penetrates into the column. As previously discussed, this is a very important mechanism for increasing the sensible heat content of the Arctic Ocean in spring and summer in open water areas. There is also a significant penetration and absorbtion of solar radiation within a snow pack and within sea ice and glacier ice. The bulk heating term is negligible within a bare soil column.

5.2 Further Understanding the Budget Terms

R_{sfc} is defined as the sum of the downward (sometimes termed “downwelling”) and upward (“upwelling”) shortwave (solar) and longwave radiation components at the surface, or

$$R_{\text{sfc}} = R_{\text{ss}}(1-\alpha) + R_{\text{ls}} - \epsilon\sigma T_s^4 \quad (5.4)$$

R_{ss} is the flux of incoming solar radiation at the surface and α is the surface albedo (the ratio between upward and downward solar radiation). Recall that solar radiation is defined as radiation with wavelengths of 0.15 to 4.0 micrometers (μm). $R_{\text{ss}}(1-\alpha)$ hence represents the net solar radiation at the surface. During polar darkness, and ignoring moonlight and starlight, the term is zero. Recall that longwave radiation represents wavelengths of about 4–300 μm . The incoming longwave flux is given by R_{ls} , while $\epsilon\sigma T_s^4$ is the outgoing longwave flux. The outgoing longwave flux is dependent on the (dimensionless) surface emissivity ϵ , the Stefan-Boltzman constant σ and T_s , the skin temperature in Kelvin (not to be confused with SAT, which is generally considered to be at about 1.5 m above the surface). Emissivity is defined as the ratio of radiant flux from a body to that of a perfect emitter (a blackbody) at the same kinetic temperature. A perfect emitter ($\epsilon = 1$) is also a perfect absorber of radiation. True blackbodies do not exist. However, most surfaces approximate blackbodies in the longwave spectrum ($\epsilon > 0.9$). Snow is an especially good emitter (and consequently absorber), with a longwave emissivity of typically 0.98 to 0.99. By comparison, the atmosphere is a selective or partial emitter, with an emissivity much less than 1. R_{ls} depends on atmospheric temperature, the water vapor content

of the atmosphere, other trace gases such as CO₂ and cloud cover. Whereas the last three influence the emissivity of the atmosphere (emissivity increases with an increase in all three), the temperature of the cloud base is also very important.

The net longwave budget (longwave in minus longwave out) is generally negative, but tends to become less negative (or sometimes even positive) when low, warm cloud cover (Arctic stratus) is present. Although Equation 3.1 (the top-of-atmosphere radiation budget) is analogous to Equation 5.4, in the latter equation we are dealing with the surface albedo (α) as opposed to the planetary albedo (A) and the upward longwave flux depends on the temperature and emissivity of the surface only (as opposed to the combined effects of the atmosphere and surface).

The sensible heat flux Q_H is directed upward (negative in our convention) when temperature decreases with height, and positive (downward) when temperature increases with height. The sensible heat flux is driven by both conduction and turbulent eddies. These turbulent eddies represent irregular fluctuations in the atmospheric flow near the surface in the boundary layer. Conduction is important in the first few millimeters above the surface, where large temperature gradients can exist and where turbulence is small (wind speed declines logarithmically toward the surface, and by definition drops to zero at the very surface). Above this very shallow near-surface layer, temperature gradients are much smaller. Conduction in the atmosphere is inefficient, so the vertical sensible heat transfer is mainly by turbulent eddies. The overall turbulent process can be thought of as a mixing of air molecules always working to reduce the vertical temperature gradient in an attempt to restore thermal equilibrium.

Similarly, when specific humidity decreases with height, Q_E is directed upward, again taken as negative in our convention. In the first few millimeters, the latent heat flux is mainly by diffusion. Above this shallow near-surface layer, vapor gradients are much smaller, and diffusion is inefficient, so the latent heat transfer is hence mainly by turbulent eddies. The latent heat flux works to destroy the humidity gradient. The latent heat flux is typically thought of as referring to phase changes from liquid to gas (evaporation) and gas to liquid (condensation), but may also include transfers from solid to gas (sublimation) and gas to solid (deposition or ablation). This would be the situation when it is very cold and no liquid water is present. Energetically sublimation and deposition involve the sum of the latent heat of vaporization ($2.5 \times 10^6 \text{ J kg}^{-1}$ at 0°C, note that the value depends on temperature) and the latent heat of fusion ($3.34 \times 10^5 \text{ J kg}^{-1}$).

As Q_H and Q_L are driven by turbulence, except very near the surface, they are commonly referred to as the turbulent heat fluxes.

The traditional approach to estimating Q_H and Q_L is through “profile” methods, based on vertical gradients of the horizontal wind, temperature, and specific humidity. The profile method contains various assumptions regarding the structure of the turbulent eddies. The preferred approach, now widely used because appropriate instruments are readily available, is termed the “eddy correlation method.” The magnitude and direction of the sensible heat flux can be stated in terms of the time average of the instantaneous covariance between anomalies of the vertical wind

and temperature (the eddy correlation). With temperatures decreasing with height, positive (upward) vertical wind anomalies transport positive temperature anomalies upward, while negative (downward) vertical wind anomalies transport negative temperature anomalies downward. The products are positive in both cases, yielding an upward sensible heat flux. If the temperature increases with height, upward (downward) wind anomalies transport negative (positive) temperature anomalies and the sensible heat flux is downward. The latent heat flux is determined from analogous relationships. A complete description of the profile and eddy correlation methods is provided by T. Oke (1987).

The melt term M represents a heat gain by the column underlying the atmosphere as it requires energy to transform water from its solid form to its liquid form that represents a higher latent heat state. Unless the surface is melting (i.e., a phase change is occurring), M is zero. It can never be negative. The melt term is considered separately from Q_E , as the latter deals with the energy associated with the change from the liquid (or solid) to the vapor phase (or vice versa of condensation or deposition is occurring).

The conductive heat flux C into or out of the column underlying the atmosphere can be expanded as $-K\partial T / \partial Z$, where K is the thermal conductivity and $\partial T / \partial Z$ is the vertical temperature gradient, with Z increasing upward. If temperature decreases upward, the flux is directed toward the surface and hence has a positive sign (the term is a heat loss from the underlying column and a heat gain by the overlying atmospheric column). The opposite is true when temperature increases upward. If the temperature gradient is zero, there can be no conductive flux. Over a snow-free tundra, for example, $-K(\partial T / \partial Z)$ refers to the conductive flux between the surface and the soil column. Expressions for the heat conduction through water, sea ice, snow, and glacier ice must use thermal conductivity coefficients appropriate to each material. Thermal conductivities of some natural materials are given in Table 5.1. Fresh snow is a rather poor conductor (hence a good insulator). By comparison, ice is a much better conductor. Note that the conductivities of ice and water depend on temperature and salinity.

Building again on Chapter 3, over the Arctic Ocean, the conduction term represents two processes. First, there can be a conduction of heat in open water areas. Second, there can be a conduction of heat through the sea ice and any overlying snow cover. Upward heat conduction through sea ice and any overlying snow cover implicitly includes the effects of sea ice growth. If sea ice is growing (bottom accretion of ice), there is a release of latent heat to the bottom of the ice. This appears as a heat gain by the ice, which helps to maintain an upward conductive flux (see later discussion and Chapter 7).

Regarding the bulk heating term B , recall that solar radiation can penetrate to a considerable depth through liquid water, sea ice, and snow. Although some (or in the case of a snowpack, most) of this penetrating radiation will be scattered back out of or out of the subsurface column, that which is absorbed represents a heat gain by the column underlying the atmosphere. This is an important part of seasonal heat gain in the upper part of the Arctic Ocean (Frey et al., 2011).

Table 5.1. Thermal conductivity K of selected natural materials

Material	Remarks	Thermal Conductivity ($\text{Wm}^{-1}\text{k}^{-1}$)
Sandy Soil, 40% pore space	Dry	0.03
	Saturated	2.20
Peat Soil, 80% pore space	Dry	0.06
	Saturated	0.50
Snow	Fresh	0.06
	Old	0.42
Ice*	0°C, pure	2.24
Water*	4°C, still	0.57

*Properties depend on temperature and salinity.

Source: Compiled by Oke (1987).

5.3 The Downward Solar Radiation Flux

5.3.1 The Clear-Sky Flux

The total downward flux of solar radiation R_{SS} represents a combination of direct beam and diffuse beam components which together are often termed global radiation. Diffuse radiation is largely isotropic (i.e., the flux is roughly the same no matter what direction it is coming from), although the intensity is higher under the portion of the celestial dome nearest the sun. The fundamental control on the global radiation flux reaching the surface is the TOA (or extraterrestrial) flux. The TOA flux is zonally symmetric. At the North Pole, the TOA flux is zero from the autumnal to spring equinoxes. By contrast, although the solar zenith angle (the angle between zenith and the sun) at the Pole at local noon on the summer solstice is still a large 66.5° , the attendant twenty-four-hour daylight yields a daily mean TOA flux of 522 W m^{-2} , compared to a value of only 383 W m^{-2} at the equator. Because of the combined effects of day length and solar zenith angle, the monthly mean TOA flux for northern high latitudes actually increases with latitude during May through August, decreasing with latitude in other months.

Because there is an intervening atmosphere, the solar flux at the surface is smaller than the TOA flux. In the absence of cloud cover, the solar radiation received at the surface depends on latitudinal variations in the solar zenith angle and elevation (which determine atmospheric path length), and associated path-length dependencies of non-cloud atmospheric scattering and absorption. Solar radiation is attenuated primarily through absorption by water vapor in several bands between 0.9 and $2.1 \mu\text{m}$, absorption by ozone in three bands ($0.20\text{--}0.31$, $0.31\text{--}0.35$ and $0.45\text{--}0.85 \mu\text{m}$) and absorption and scattering by aerosols. Ozone absorption is nearly complete at wavelengths shorter than $0.285 \mu\text{m}$ (in the ultraviolet region). As outlined in Chapter 4, most ozone absorption occurs in the stratosphere. The surface albedo also has a minor effect on the clear-sky solar radiation reaching the surface by

promoting multiple scattering between the surface and atmosphere. The clear sky flux can be estimated with the aid of radiative transfer models (Schweiger and Key, 1992). As noted in Chapter 2, the term “Arctic haze” has come into widespread use to describe the frequent occurrence of aerosol layers that are especially noticeable in late winter and spring, representing soot, dust, and sulfate aerosols emitted by industrial complexes which are then transported into the Arctic. The effect of aerosols on incoming solar radiation involves both scattering and absorption, depending on their properties.

The clear-sky transmittance over the Arctic, taken as the ratio between the incoming clear-sky solar flux at the surface and the TOA flux, typically ranges from 0.70 to 0.90. The clear-sky transmittance decreases as latitude increases because the atmospheric path length increases (the sun strikes the earth at a more grazing angle – the longer resulting atmospheric path length means more scatterers and absorbers). As path length decreases with elevation (the higher the elevation, the lower the density of atmospheric scatterers and absorbers), the clear-sky flux will be greater over surfaces such as the Greenland Ice Sheet. Measurements atop the Greenland Ice Sheet by T. Konzelmann and A. Ohmura (1995) point to a clear-sky transmittance of about 0.80. Although to a first order, the clear-sky atmosphere is hence relatively transparent with respect to solar radiation, non-cloud scattering and absorption is by no means insignificant in the Arctic.

5.3.2 Cloud Cover

A very important factor influencing global radiation is cloud cover. The Arctic is cloudy, especially during summer when low-level stratus is prevalent. Mean fields of cloud cover were presented back in Figure 2.27. By far, the dominant effect of clouds is to reduce the shortwave flux received at the surface, largely owing to their high albedo (60–75 percent for Arctic stratus). Cloud absorption is generally only a few percent (Herman and Curry, 1984). However, attenuation of the downward flux by clouds is partially offset for high albedo surfaces because of multiple reflections from the surface to the clouds and back to the surface (Wendler, Easton, and Ohtake, 1981; Shine 1984). The proportion of the downwelling shortwave flux resulting from multiple reflections can be significant (Loewe, 1963). In summer over sea ice and glaciers, one frequently encounters “flat light” or “whiteout” conditions, associated with a high surface albedo and low cloud or fog. These conditions represent a hazard to aviation, and, as the first author can attest, complicate navigation when traveling via snowmachine. In turn, the effect of radiative transmission through clouds is to change the spectral distribution of transmitted solar radiation. Although cloud absorption is generally small in terms of the total solar energy involved, clouds preferentially absorb in the near infrared. Because the surface albedo is wavelength-dependent, this leads to an increase in surface albedo under overcast compared with clear-sky conditions. We will return to this issue later.

As a young graduate student fascinated by clouds, the author made several hundred measurements of associations between the downward solar flux and cloud

Table 5.2. Relative transmission of cloud types for solar zenith angles (SZA) of 78° and 60° based on data from June through early August collected at St. Patrick Bay ice cap (82°N, 64°W)

Cloud Type	a) SZA=78°	b) SZA=60°	c) b-a
Cirrus/Cirrostratus	0.84	0.89	0.05
Altocumulus	0.58	0.78	0.20
Stratus	0.50	0.54	0.04
Fog	0.46	0.67	0.21
Altostratus	0.46	0.65	0.19
Stratocumulus	0.35	0.66	0.31
Snow	0.33	0.59	0.26
Average	0.50	0.68	0.18
(All cloud types)			

Note: Values represent the ratio between hourly totals of the surface shortwave flux for cloud cover of the given type >70% and all observations with cloud cover <30%.

Source: From Serreze and Bradley (1987).

conditions on and around a small ice cap on the Hazen Plateau of northern Ellesmere Island (N.W.T., Canada, approximately 82°N, 64°W). The data were collected during the summers of 1982 and 1983. Table 5.2 shows ratios of the solar radiation received at the surface during cloudy skies (greater than 70 percent cloud fraction) and nearly clear skies (less than 30 percent cloud fraction) for different cloud types and two solar zenith angles.

As expected, relative transmission is greatest for the thinner, higher cloud types (cirrus/cirrostratus) and least for the lower, thicker clouds and for conditions of snowfall. Note also the dependence on the solar zenith angle, pointing to the higher cloud albedos at large zenith angles. Polar clouds tend to have a higher relative transmission than clouds in middle latitudes. This is attributed to polar clouds being thinner and having lower water content than clouds in middle latitudes owing to more limited convection and lower specific humidities.

5.3.3 Distribution of Global Radiation

Satellite retrievals offer systematic assessments of global radiation and other surface radiative fluxes with complete Arctic coverage. Here we make use of two data sets, APP-x, based on AVHRR data, and ISCCP-D, which is based on a number of different satellite platforms. As discussed in Chapter 2, satellite-derived products such as APP-x and ISCCD-D suffer from a number of shortcomings, but the fields are certainly of high enough quality to illustrate basic spatial and temporal patterns in the Arctic.

Maps of the mean-monthly global radiation flux for March through October based on ISCCP-D are provided in Figure 5.1. March, September, and October are characterized by a primarily zonal patterns (i.e., the isolines are roughly parallel to latitude

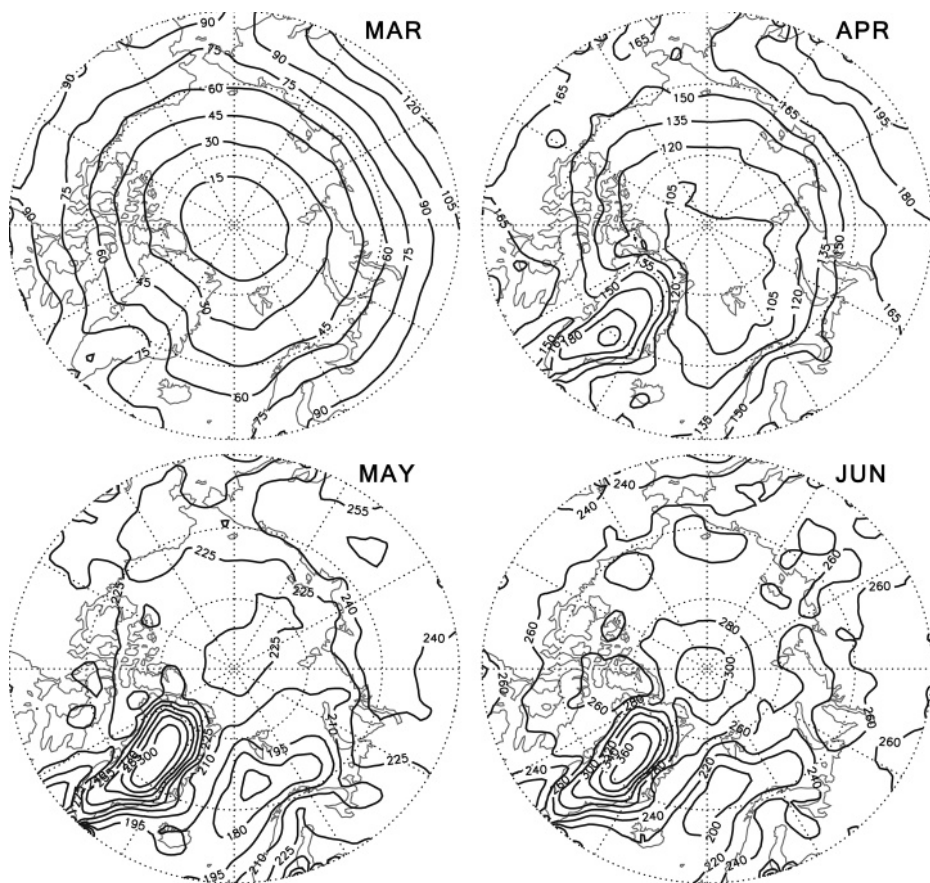


Figure 5.1. Mean monthly downwelling solar radiation at the surface (W m^{-2}) for March through October, based on ISCCP-D satellite data (courtesy of J. Key, NOAA, Madison, WI).

circles). This illustrates the dominant effects of the strong latitudinal decrease in the clear-sky downward solar radiation for these months. April through August are dominated by a strong asymmetric pattern. Greenland shows a pronounced peak over its central portions from April through August. This manifests the high elevation – the atmospheric path length is smaller and the central portions of the ice sheet are often relatively cloud free. Fluxes decrease sharply toward the Atlantic side of the Arctic, largely because of increasing cloud fraction (Figure 2.27) as well as greater cloud optical thickness.

There is also some tendency in summer for mean monthly fluxes to increase with latitude; most apparent in June, the month of maximum radiation. For this month, the clear-sky downward solar flux at the surface exhibits a marked increase of about 20 W m^{-2} , from 65°N to 90°N . The high values over the central Arctic Ocean also manifest the effects of the high albedo of the sea ice surface in promoting multiple scattering between the surface and clouds. For June, ISCCP-D fluxes over the high-

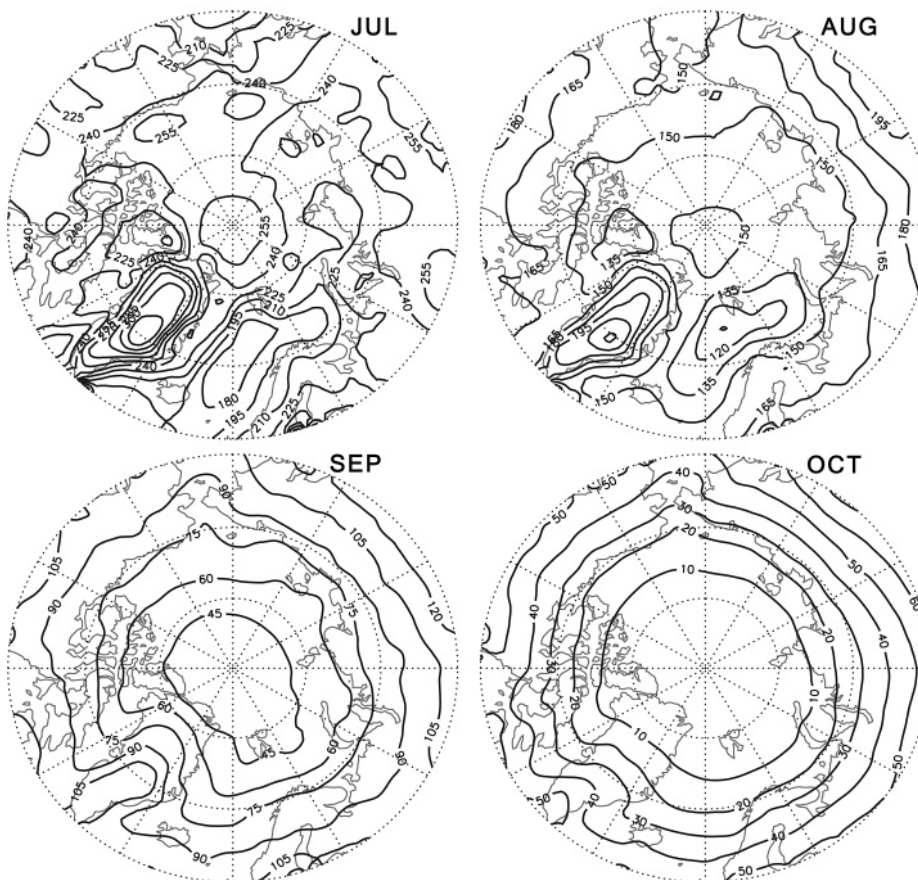


Figure 5.1. (Cont.)

elevation Greenland Ice Sheet peak at more than 360 W m^{-2} , and values in excess of 300 W m^{-2} are found near the Pole. June fluxes of $200\text{--}220 \text{ W m}^{-2}$ characterize the Atlantic side in the Norwegian and Barents seas, where cloud cover is both thick and extensive.

5.4 Surface Albedo

5.4.1 Definition

The “true” surface albedo refers to the ratio of solar radiation reflected by a surface to the incident direct beam illumination. This is termed the “directional-hemispheric reflectance” because the downwelling term is the direct beam irradiance at a specified angle and the reflected flux is integrated over the upward hemisphere. This differs from the albedo measured near the earth’s surface (examined here) where the downward flux contains a significant diffuse component (especially under cloud cover). The albedo measured near the earth’s surface is termed the bihemispherical

reflectance factor (Nolin and Liang, 2000). Albedo differs from spectral reflectance, which is the reflectance at a single wavelength or in a narrow spectral band.

5.4.2 Typical Surface Albedos of Major Surface Types

Typical albedos for major surface types in the Arctic are summarized in Table 5.3. There is a wide range of values even within the general categories. In part, the range is explained by small-scale topography as it influences the geometry of insolation and heterogeneities in the physical properties of the surface being considered. For example, the albedo of tundra or boreal forest can differ strongly over small space scales because of variations in species distribution, leaf area, soil characteristics, and soil moisture. Most surfaces are forward scattering and scatter differently over different portions of the solar spectrum. Hence the range also manifests variations in the spectral nature of the solar flux and the relative magnitude of direct versus diffuse components. Snow cover, both on land and sea ice, dominates the Arctic for much of the year and merits special attention. S. Warren (1982), Barry (1996), and A. Nolin and S. Liang (2000) provide comprehensive reviews. G. Maykut (1986) discusses the spectral reflectance and albedo characteristics of sea ice.

5.4.3 The Albedo of Snow

As outlined by Nolin and Liang (2000), snow can be considered as a layered particulate medium composed of ice spheres in air. Scattering by the spheres is primarily through refraction. Using the refractive indices of ice and an optically equivalent ice sphere radius, Mie theory (appropriate when the effective particle radius is much larger than the wavelength of the interacting radiation) can be used to calculate single-particle scattering and absorption (i.e., the scattering and absorption of a single snow grain). In turn, the single-particle scattering properties can be transformed into multiple scattering properties using radiative transfer approaches such as the delta-Eddington approximation that characterizes the strong forward scattering of snow (Mie scattering) in the solar wavelengths (Wiscombe and Warren, 1980). Although

Table 5.3. Representative albedos for Arctic surfaces
compiled from numerous sources

Fresh snow	0.70–0.90
Melting Snow	0.50–0.60
Water	0.06–0.10*
Dry Tundra	0.23–0.26
Wet Tundra	0.10–0.20
Multiyear Sea Ice	0.55–0.75
Thick First-Year Sea Ice	0.30–0.60
Meltponds on sea ice	0.15–0.40

* Varies widely with solar zenith angle.

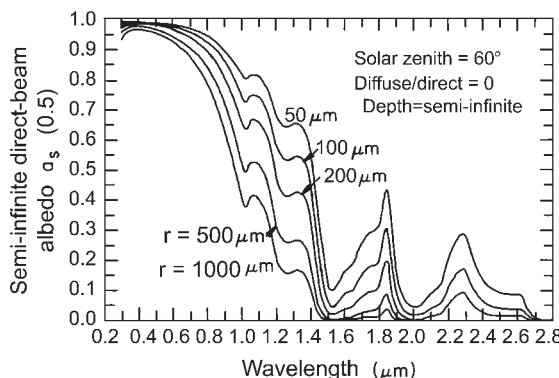


Figure 5.2. Direct beam spectral reflectance for a semi-infinite snowpack as a function of wavelength for grain radii from 50 to 1,000 μm and for a solar zenith angle of 60° (from Wiscombe and Warren, 1980, by permission of AMS).

snow grains are usually not spherical, considering the grains as optically equivalent spheres can approximate their optical properties. Scattering and absorption is a function of the snow optical depth. Optical depth, which is wavelength-dependent, is in turn affected by physical snowpack depth, snow density and grain size. Typical snow water equivalent depths for an optically thick snowpack at a wavelength of 0.46 μm are 20 mm for a particle radius of 50 μm and 200 mm for a particle radius of 1,000 μm . Smaller ice grains increase the number of scattering events. Hence, the smaller the grains, the thinner the snowpack can be and still appear optically thick.

An aggregation of ice particles will scatter nearly all energy in visible wavelengths. In the visible spectrum, ice particles scatter very strongly in the forward directions. If absorbing particulates (e.g., dust and soot) are mixed with the snow, scattering decreases and becomes more isotropic. In the near infrared region (0.7–4.0 μm), ice is still forward scattering but the property controlling the magnitude of scattering is the particle size. As snow ages, snow grains increase in size, which increases the probability of a photon being absorbed and reduces the effective volume scattering. The modeled direct-beam spectral reflectance of a snowpack of semi-infinite depth for different grain radii for a solar zenith angle of 60° is provided in Figure 5.2.

The liquid water content of snow rarely exceeds 5 percent. As the refractive indices of ice and liquid water are nearly identical, liquid water has little direct effect on the scattering. However, there is an indirect effect as water enables the growth of clusters of snow grains, which respond optically as individual grains. As a significant portion of the solar spectrum lies in the near infrared, changes in snow grain size significantly affect the albedo.

Building on the previous discussion, the albedo of a snow cover tends to increase with an increasing solar zenith angle. This is understood from the forward scattering of snow particles. For a large zenith angle, there is a high likelihood that a photon will be scattered upward and out of the snowpack. For a small solar zenith angle, there will be more interactions between a photon and snow grains, and a greater likelihood of absorption.

As mentioned previously, clouds preferentially absorb the longer solar wavelengths and cause more of the radiation to be diffuse. This shift in the spectral

characteristics of the incident flux is augmented by multiple scattering between the surface and cloud base (Wiscombe and Warren, 1980). These processes increase the proportion of visible band radiation for which scattering is greatest, hence increasing the albedo. Multiple scattering between a stratiform overcast sky and a snow surface can cause a 7–20 percent increase in snow albedo compared to clear skies (Petzold, 1977; Choudhury and Chang, 1981). The effect of increasing the diffuse component is to change the effective solar zenith angle (Warren, 1982). The effective solar zenith angle for overcast conditions is about 50°. Hence, if the true solar zenith angle is greater than 50°, the effect of clouds is to decrease the effective solar zenith angle and reduce the albedo. By contrast, if the true solar zenith angle is less than 50°, the effect of clouds is to increase the effective solar zenith angle and increase the albedo. According to Warren (1982) the effect of the spectral shift in the incident flux (enrichment of the visible-band portion) is normally greater than the effect of the changed zenith angle, such that cloud cover increases the albedo. The snow albedo can also be influenced by the surface morphology. J. Carroll and B. Fitch (1981) found a reduction in albedo of 4 percent during periods when the solar zenith angle is normal to sastrugi in the surface snow cover (resulting in shadowing) compared to periods when it is parallel to sastrugi.

5.4.4 A Typical Seasonal Cycle over Sea Ice

As part of the SHEBA experiment in 1997–1998 in the Beaufort Sea, detailed measurements were made of the surface albedo. The seasonal cycle shown in Figure 5.3 can be taken as very typical of the sequence of events over the perennially

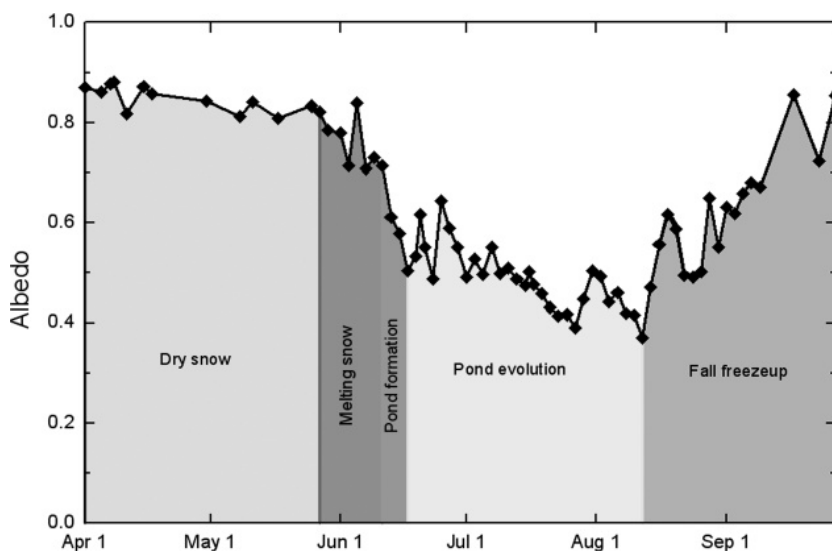


Figure 5.3. Seasonal cycle of surface albedo based on data collected during the SHEBA experiment (courtesy of Donald Perovich, USA CRREL). (See plate section for color version.)



Figure 5.4. Summer melt ponds on the sea ice surface (courtesy of Donald Perovich, USA CRREL). (See plate section for color version.)

ice-covered parts of the Arctic Ocean. During the pre-melt (dry snow period), which at the SHEBA site lasted until late May, the surface albedo decreased slightly, but remained above 0.80. The albedo then dropped quickly during the initial period of snowmelt and the initial formation of melt ponds on the sea ice surface. Relatively dark melt ponds (Figure 5.4) further evolved from about the middle of June through the first week of August. Although the albedo showed a further overall drop during this period, to minimum values of 0.35–0.40, there were several periods in which albedo temporarily increased, reflecting, in part, episodes of snowfall. Albedo then increased again as melt ponds froze and new snowfall events whitened the surface.

5.4.5 Scale Issues

Surface albedo is a very scale-dependent variable. The numbers in Table 5.3 and the seasonal cycle shown in Figure 5.3 refer to albedos that would be measured with upward and downward facing pyranometers (instruments used to measure solar radiation) from typically 1–10 m above the surface. The higher above the surface the reflected component is measured, the greater is the areal integration of albedo. Hence, some distinction should be made between local albedos and regional albedos. The regional surface albedo α_r can be expressed as:

$$\alpha_r = \sum \alpha_i A_i / \sum A_i \quad (5.5)$$

where α_i is the albedo of the different surfaces (*i*) over a region and A_i is the area covered by each surface. Developing appropriate parameterizations of regional

albedo over heterogeneous surfaces such as snow-covered vegetation or sea ice for use in climate models is an area of active research (see Barry, 1996). For example, the SHEBA program combined local measurements of albedo (e.g., Figure 5.3) with aircraft surveys to determine the areal coverage of different surface types.

5.4.6 Distribution of Surface Albedo

Although albedo is a frequently measured variable, surface or aircraft observations are insufficient to allow the construction of maps to assess the basic spatio-temporal patterns across the Arctic. However, satellite-derived surface albedo is a standard variable of ISCCP-D and APP-x. Monthly fields from APP-x are displayed for April through September (Figure 5.5).

Over land areas, regional albedos for April typically range from 0.40 to 0.80. Those over the Arctic Ocean are from 0.70–0.80. The high albedos over most of the Arctic are of course attributed to snow cover. Over the ice-covered ocean, Figure 5.5 integrates high-albedo snow surfaces along with lower albedo features such as open or recently refrozen leads in the ice cover, or areas where winds may have blown the sea ice clear of snow. Similarly, over land, the high albedo of the snow cover will be integrated with effects such as vegetation canopies, or areas where the snow cover is thin enough that darker underlying surfaces (e.g., tundra) “show through.” Furthermore, even in cold conditions, snow will age, acting to reduce the albedo. The sharp decline in albedo toward the North Atlantic relates to the decline in ice concentration in the marginal ice zone.

The difference between the April pattern and the May pattern illustrates the effects of surface melt. Albedos over land areas begin to drop from their April values, most apparent over the southern Arctic lands. Albedos remain high over the Arctic Ocean where it is colder and the snow has not begun to melt. There is a further reduction in albedo between May and June. By July, the snow cover is completely removed from the land surface and some of it has melted from the sea ice cover, forming melt ponds (Figure 5.4). However, albedos near the pole are still around 0.50. Albedos still remain high over central Greenland. Albedos are at a minimum during August and start to increase again in September because of the deposition of fresh snow cover and initial freeze-up of the sea ice surface.

5.5 Longwave Radiation Fluxes

5.5.1 Radiative Processes

During the polar night, the radiation budget is almost entirely determined by long-wave fluxes (starlight and moonlight provide a negligible shortwave flux). Referring back to Equation 5.4, infrared radiation is emitted by the surface as a function of its temperature and emissivity, scaled by the Stefan-Boltzman constant. Part of the emitted energy from the surface escapes to space through the atmospheric windows,

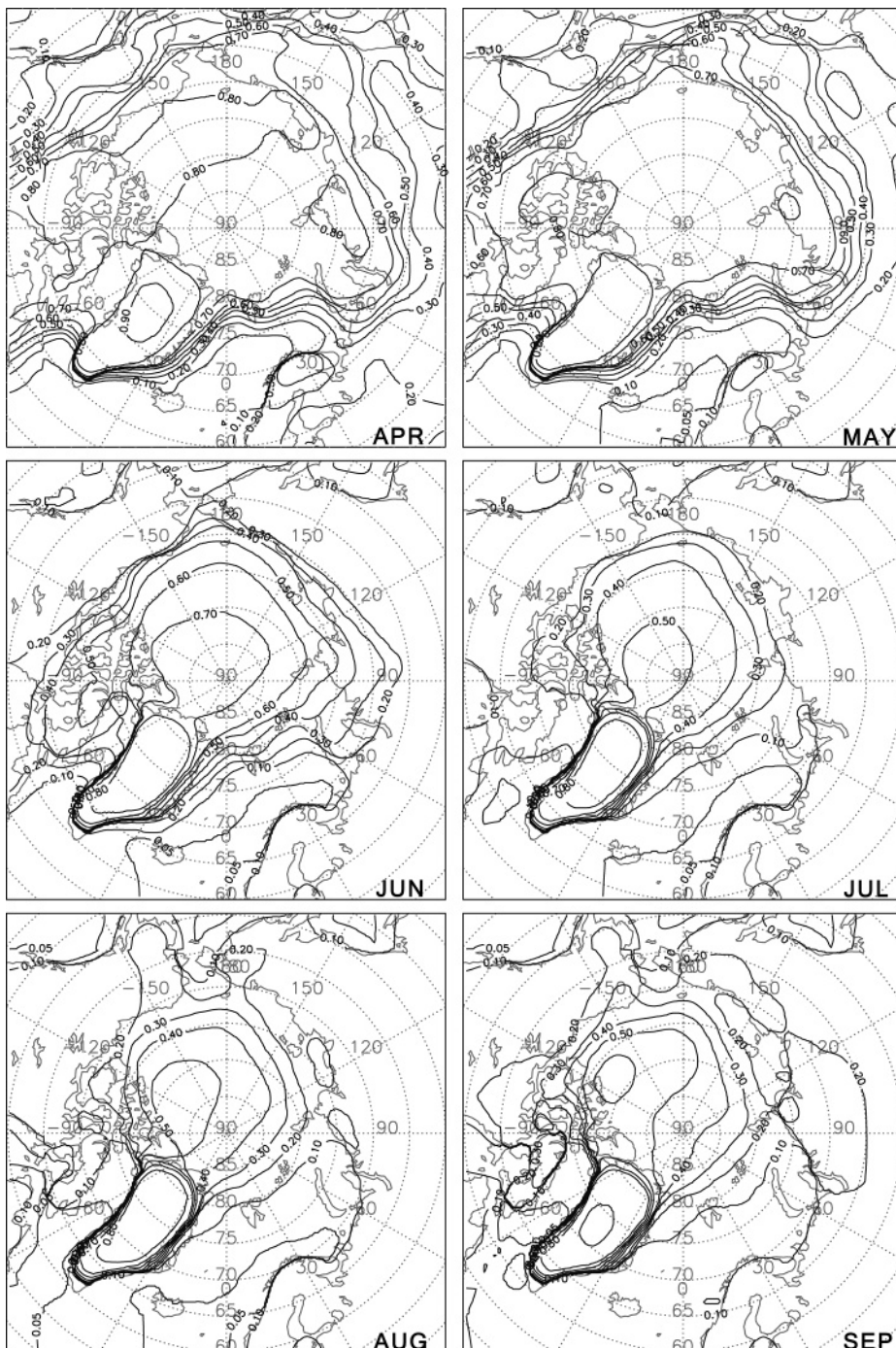


Figure 5.5. Mean monthly surface albedo for April through September based on APP-x satellite data (courtesy of J. Key, NOAA/NESDIS, Madison, WI).

primarily in the 8–12 μm region. The remainder is absorbed in the lower atmosphere and is re-emitted both upward and downward. The processes controlling the downward flux to the surface are rather involved, and merit further discussion.

Variations in the downward transfer of infrared radiation under clear skies depend primarily on the profiles of atmospheric temperature, water vapor, and (in winter) the presence of suspended ice crystals in the atmosphere, known as “diamond dust” (Curry, 1983; Curry et al., 1990) (although, arguably, diamond dust can be considered to be cloud cover). Water vapor and diamond dust increase the emissivity. Gasses such as carbon dioxide and methane tend to be well mixed in the atmosphere, but of course also influence emissivity. Most of the radiation to the surface emanates from the lowest layers of the troposphere, typically the lowest 100 m or so. In the winter, the moisture content of the Arctic atmosphere is low. In summer, however, the near-surface specific humidity is about a factor of five higher and hence has a stronger impact.

Cloud cover tends to increase the downward longwave flux. Clouds are more emissive than the clear-sky atmosphere. Clouds act to “close” the atmospheric windows that allow emission from the surface to space. They absorb upwelling radiation, and then radiate both upward and downward. The effective emissivity of clouds depends on the cloud optical thickness and height of the cloud base. Low stratus is an especially effective absorber and radiator. In turn, especially during winter when the atmosphere is particularly stable and strong surface-based inversions are present, the cloud base temperature often exceeds the surface temperature. Measurements during the Coordinated Eastern Arctic Experiment for autumn and winter indicate an increase in downwelling longwave radiation under cloudy skies of about 90 W m^{-2} . The cloud effect may be difficult to isolate, however, as cloudy conditions are often attended by horizontal heat advection raising atmospheric and surface temperatures.

5.5.2 Distribution of Downward and Net Longwave Fluxes

Again there are insufficient direct measurements of the downward longwave flux to compile maps for the Arctic. Although a number of empirical formulae have been derived that employ the surface air temperature, we rely on the ISCCP-D fields. Figure 5.6 and Figure 5.7 provide mean fields for the four mid-season months of the downward longwave and net longwave fluxes, respectively.

The spatial pattern of the mean downward longwave flux largely follows the distribution of cloud cover and SAT (see Chapter 2). During January, the highest values are in the Atlantic sector where cloud cover is extensive and optically thick and where air temperatures and specific humidity are highest. Note that, for all months, the relatively low values over central Greenland, which is above much of the cloud cover and where air temperatures and water vapor content are low. Comparisons between the January, April, and July maps reveal the effects of the seasonal increase in air temperature and humidity. For all months, however, the largest fluxes are over the Atlantic sector.

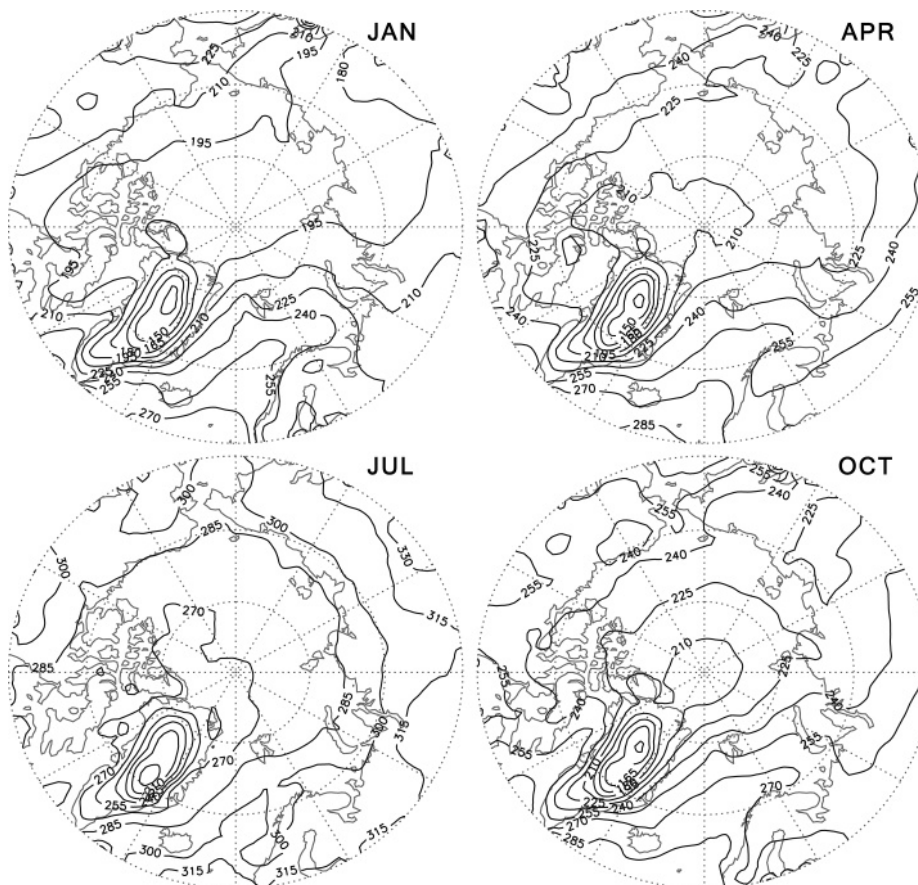


Figure 5.6. Mean monthly downwelling longwave radiation at the surface (W m^{-2}) for the four mid-season months based on ISCCP-D data (courtesy of J. Key, NOAA, Madison, WI).

The net longwave flux is negative in all months. Typical values over the Arctic Ocean are -20 to -40 W m^{-2} . Larger deficits are found over Greenland and land areas, for the latter especially during summer. This implies that over land, summer surface temperatures are fairly high while the lower troposphere remains fairly cool and dry. The large deficits over Greenland in all months point to the high elevation of the ice sheet. The smaller July deficits over sea ice of about -40 W m^{-2} (relative to land areas) are understood in that the melting sea fixes the skin temperature, limiting the magnitude of the upward longwave flux.

5.6 Distribution of Net Radiation

The net allwave radiation (or more simply net radiation) is the sum of the shortwave and longwave fluxes (Equation 5.4). Fields of net radiation based on ISCCP-D for

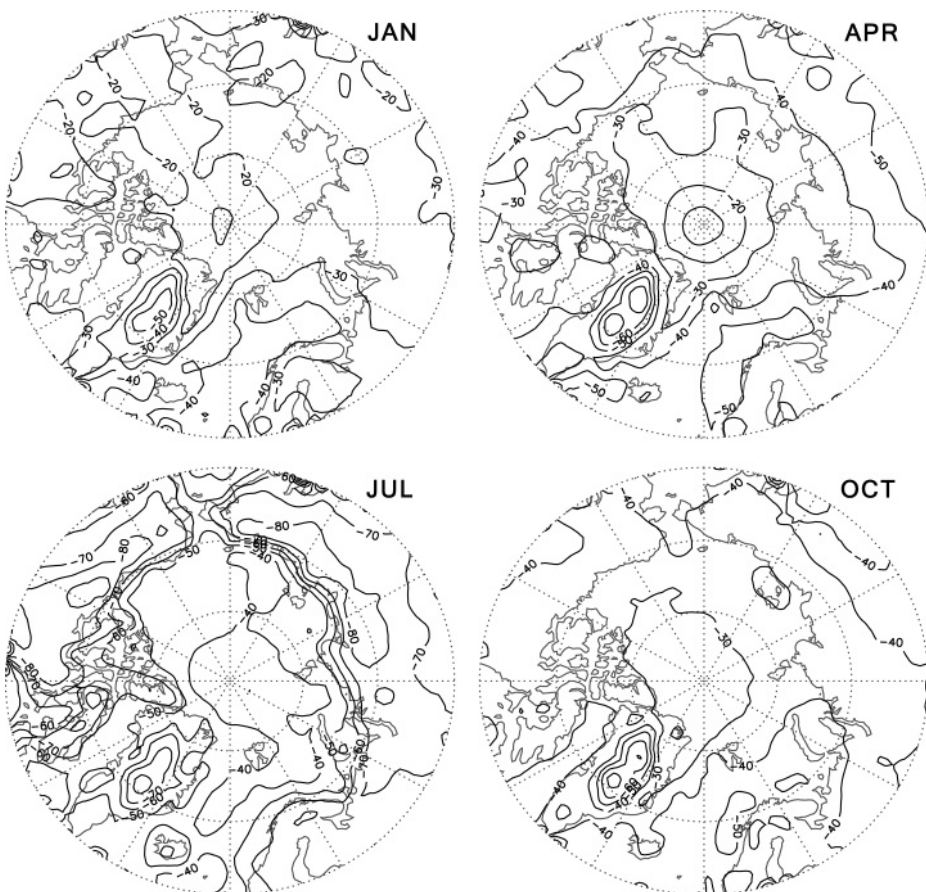


Figure 5.7. Mean monthly net longwave radiation at the surface (W m^{-2}) for the four mid-season months based on ISCCP-D data (courtesy of J. Key, NOAA, Madison, WI).

the four mid-season months are provided in Figure 5.8. Values across the Arctic are negative from October through March. During polar darkness, the fields are of course essentially identical to those for the net longwave flux. For April, the ISCCP-D fields indicate that net radiation is slightly positive over the Arctic Ocean. The downwelling solar flux is significant for this month, with central Arctic values ranging from 100–130 W m^{-2} (Figure 5.1). However, the high albedo of the surface means that most of this solar energy is lost back to space. June values of net radiation (not shown) over the central Arctic Ocean are about 80–95 W m^{-2} , compared to about 85–100 W m^{-2} in July. This asymmetry with respect to solar declination is largely attributed to albedo. Whereas solar radiation peaks in June, this is offset by the lower albedo in July. Over land areas, the flux peaks in June. July fluxes over land areas typically range from 115 to 140 W m^{-2} .

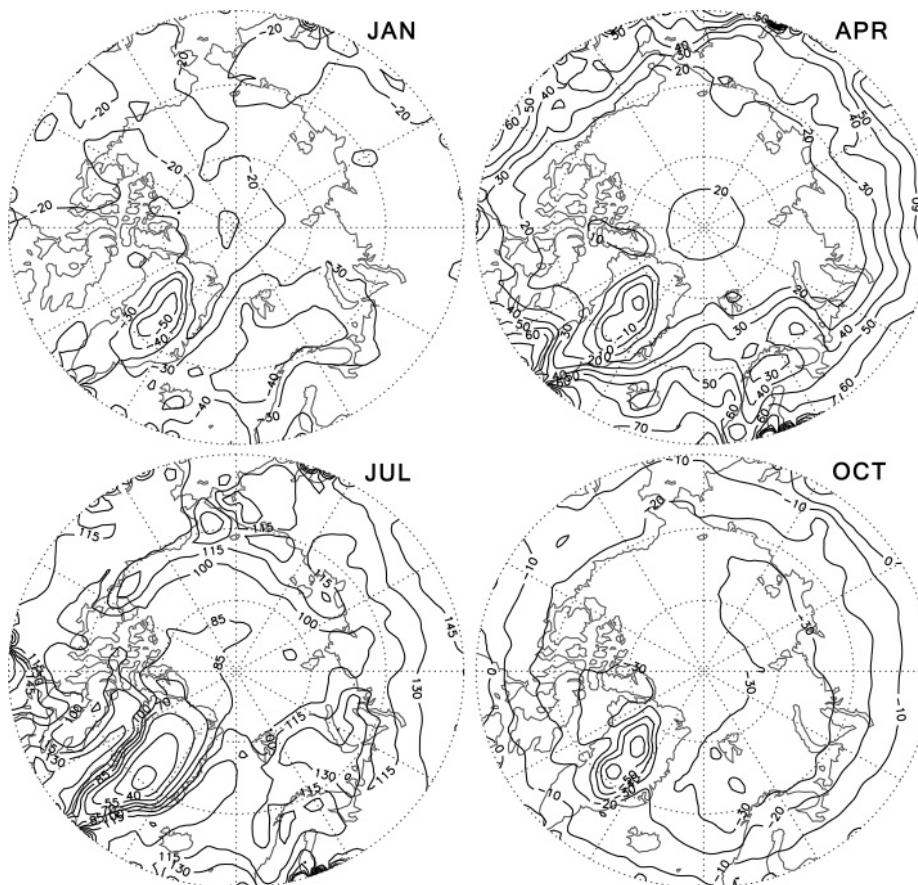


Figure 5.8. Mean monthly net allwave radiation at the surface (Wm^{-2}) for the four mid-season months based on ISCCP-D data (courtesy of J. Key, NOAA, Madison, WI).

5.7 Cloud Radiative Forcing

5.7.1 Definition and Characteristics

Cloud radiative forcing represents the change in the net radiation budget because of clouds. It can be broken into longwave and shortwave (solar) forcing components, the sum of the two being the net cloud radiative forcing. V. Ramanathan et al. (1989) formalized the forcing components as:

$$\text{Longwave Forcing} = \text{LW}_{\text{all}} - \text{LW}_{\text{clear}} \quad (5.6)$$

$$\text{Shortwave Forcing} = \text{SW}_{\text{all}} - \text{SW}_{\text{clear}} \quad (5.7)$$

where LW_{all} and SW_{all} are the net longwave and net solar fluxes under “all sky” conditions (combining data for all conditions, whether clear or cloudy conditions), and LW_{clear} and SW_{clear} represent the fluxes for clear-sky conditions. Cloud forcing

is positive for warming and negative for cooling. Calculations are typically based on monthly means of radiation fluxes. The two components of cloud radiative forcing compete with each other. Although cloud cover will reduce the downward solar flux to the surface because of cloud albedo (and to a much lesser extent cloud absorption), clouds tend to increase the longwave flux to surface. The issue at hand is which effect wins.

From a study of ten years of surface data from the NOAA Barrow Alaska Observatory and the nearby Atmospheric Radiation Measurement North Slope of Alaska site Barrow, X. Dong et al. (2010) found that the net cloud radiative forcing is at its most positive (clouds warm the surface) for all months except June, July, and August, when the net forcing is negative. The longwave component of the forcing is positive in all months with a winter minimum and an August peak of about 60 W m^{-2} . The shortwave forcing is zero in winter (when there is no solar flux) and peaks in August at about -90 W m^{-2} . The net cloud radiation forcing is at its most positive in October at about 45 W m^{-2} and most negative in July at about -40 W m^{-2} . The annual average net cloud radiative forcing was found to be $+3.5 \text{ W m}^{-2}$. By comparison, surface observations from the one year SHEBA experiment in the ice-covered Beaufort Sea (Intrieri, Fairall, and Shupe, 2002) show that the net cloud radiative forcing is positive except for a brief period in summer, with a much larger annual average of $+27 \text{ W m}^{-2}$.

The warming effect of clouds at the surface of the Arctic for most of the year (and for the annual average) contrasts with lower latitudes, where clouds have an overall net cooling effect. The key differences are that in the Arctic: (1) solar radiation is small or zero for much of the year, meaning that the (always) positive longwave forcing effect dominates; and (2) the surface albedo tends to be high. If the surface albedo is high, the net shortwave flux at the surface is already fairly small, such that a further reduction because of cloud albedo (compared to a low albedo surface) will be of lesser importance than the increase in the longwave flux. The longer period in summer that the net cloud radiative forcing is negative over Barrow compared to the ice-covered Arctic Ocean is consistent with the much lower summer albedo over land; with the lower albedo, the cloud shortwave effect is bigger. Not surprisingly, Dong et al. (2010) find that the longwave component of the forcing at Barrow is positively correlated with cloud fraction, cloud liquid water path and cloud radiative temperature. The shortwave forcing is negatively correlated with cloud fraction, cloud liquid water content and cloud radiative temperature (as they increase, the shortwave forcing becomes more negative), and is positively correlated with surface albedo.

Cloud radiative forcing can also be assessed at the top of the atmosphere (TOA). J. Curry and E. Ebert (1992) examined the seasonal cycle in cloud radiative forcing at both the surface and TOA for latitude 80°N using a single-column coupled model (Figure 5.9). Their results indicate that the total TOA cloud forcing is close to zero during winter and strongly negative in midsummer. This is primarily attributed to the high albedo of clouds. At the surface, values are positive except for two weeks in mid-summer. The competing effects of the shortwave and longwave forcing are most pronounced at the surface.

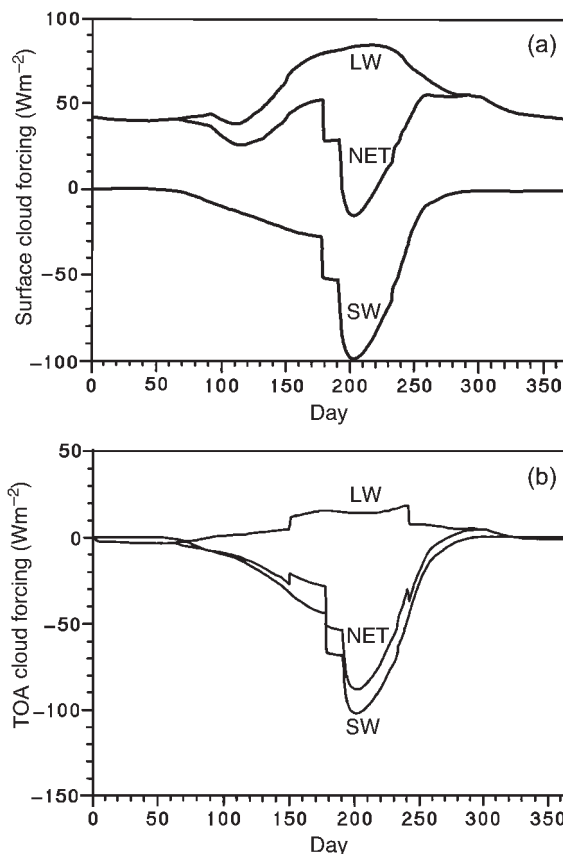


Figure 5.9. Modeled annual cycle of (a) the surface (b) TOA cloud radiative forcing (shortwave, longwave and net) at 80°N (from Curry and Ebert, 1992, by permission of AMS).

5.7.2 Fields of the Net Cloud Radiative Forcing at the Surface

Fields for the four mid-season months from ISCCP-D appear in Figure 5.10. The ISCCP-D data indicate that the cloud radiative forcing is positive for all of the Arctic from October through March. It turns negative over the Atlantic side of the Arctic in April. Except near the pole, it is negative everywhere from June through August. It is hence negative for a much longer time over the Arctic Ocean than suggested from observations and may represent shortcomings in the satellite-derived fields.

5.8 Radiation Fluxes from Surface Observations: Examples From Sheba

P. Persson et al. (2002) provide a complete description of the surface energy budget at the SHEBA site in the Beaufort Sea. This is one of many articles outlining SHEBA research results in the October 15, 2002 issue of the *Journal of Geophysical Research* (Vol. 107, C10). Figure 5.11 shows the mean annual cycles in net

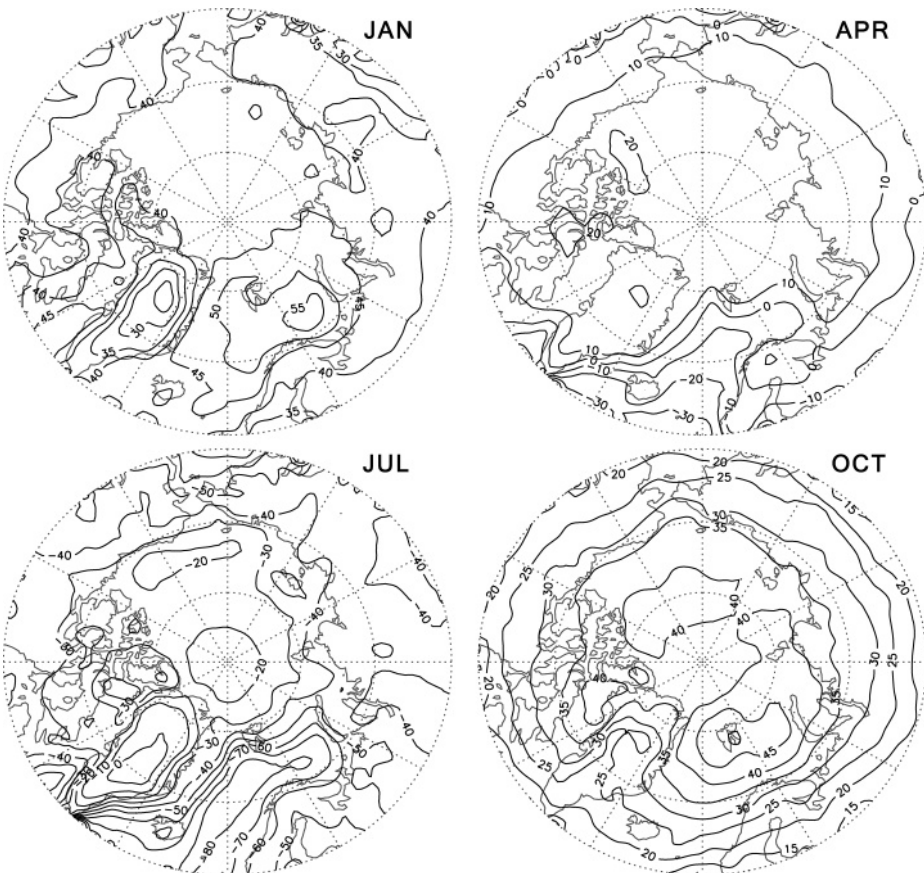


Figure 5.10. Mean monthly total cloud radiative forcing at the surface (W m^{-2}) for the four mid-season months based on ISCCP-D data (courtesy of J. Key, NOAA, Madison, WI).

radiation, albedo, incoming shortwave radiation, and incoming longwave radiation. The SHEBA results are given along with estimates from several other studies. The reader is referred to Persson et al. (2002) for details.

The annual cycle of net radiation at the SHEBA site shows a peak of about 80 W m^{-2} in July, and a minimum of about -15 W m^{-2} in January, the latter of course driven by the longwave deficit. Note how the July maximum in net radiation coincides with the July minimum in surface albedo (of about 0.56), rather than the June maximum in the downward shortwave radiation (of about 280 W m^{-2}). This is in agreement with the satellite-based results presented earlier. It is estimated that for ice of 1–2 m thick (as in the SHEBA region), during July and August, from $1\text{--}7 \text{ W m}^{-2}$ of solar radiation penetrates the ice into the ocean. The incoming longwave flux varies between 150 W m^{-2} in December to about 300 W m^{-2} during July and August. As discussed, this reflects the seasonality in lower-tropospheric air temperature, water vapor content, and cloud cover. Although the general shapes of the annual cycles at the SHEBA site are similar to those from previous estimates, there

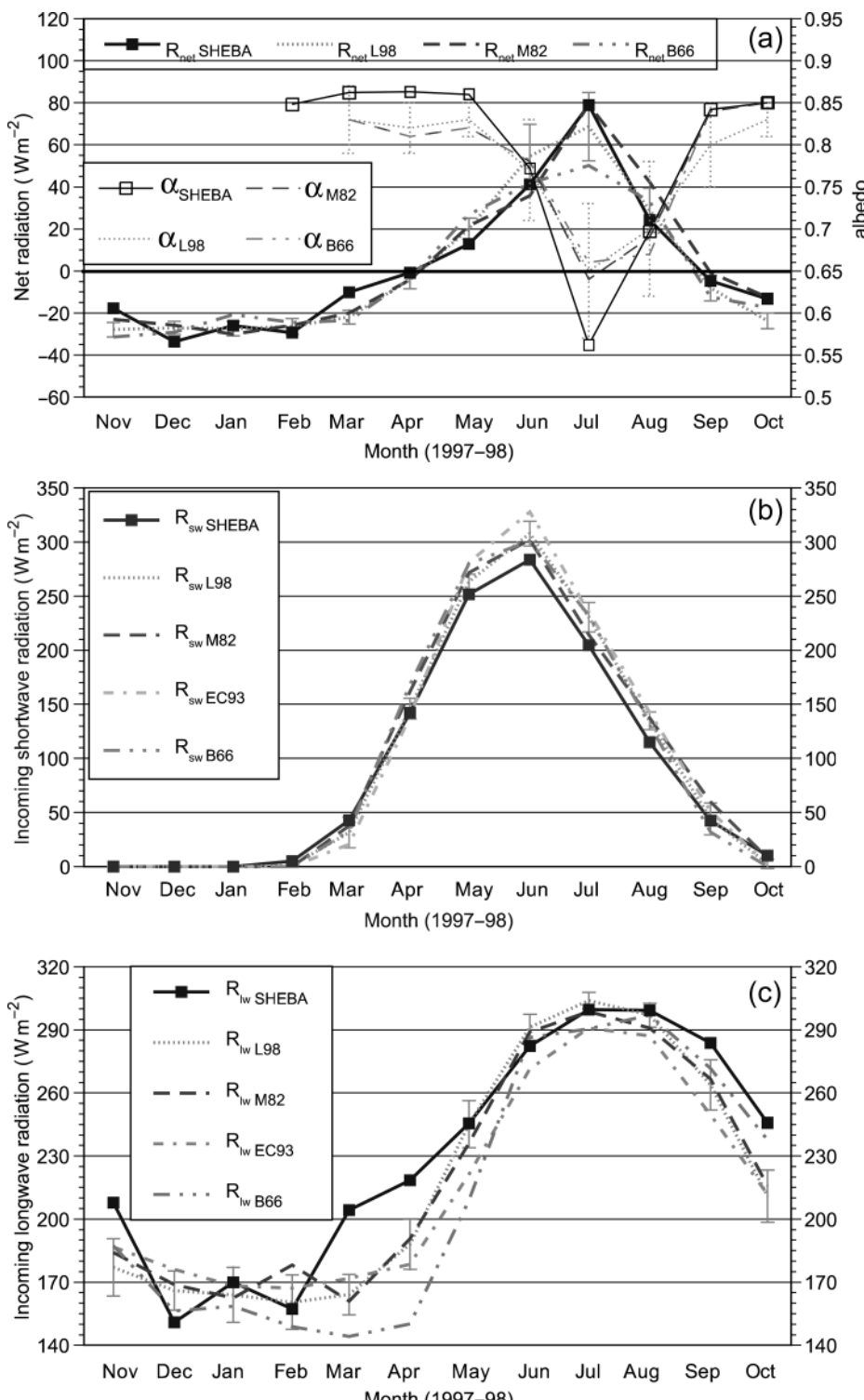


Figure 5.11. Monthly radiation balance components (W m^{-2}) for the central Arctic Ocean. Shown are (a) net radiation (heavy lines) and albedo (thin lines); (b) incoming shortwave radiation; and (c) incoming longwave radiation. In each panel, results from the SHEBA experiment are shown along with those from other studies (adapted from Persson et al., 2002, by permission of AGU).

are some notable departures. There are a number of reasons for this, including differences in ice and atmospheric conditions as well as measurement techniques. The average fluxes in Figure 5.11 mask considerable day-to-day variability associated with synoptic weather systems.

5.9 Partitioning of Net Radiation

5.9.1 Characteristics over Sea Ice

Figure 5.12, also from Persson et al. (2002), illustrates annual cycles of the turbulent energy fluxes and conduction at the SHEBA site in comparison with other estimates. The SHEBA results are representative of reasonably thick ice. They show the sensible heat flux as directed toward the surface in winter and variously toward or away from the surface in the other months. The salient point, however, is that the fluxes are small, peaking in February at about 8 W m^{-2} . The latent heat flux is also quite small, ranging from essentially zero in the winter months to about -7 W m^{-2} upward (i.e., evaporation and sublimation is occurring) in June. Again, there are some considerable differences with respect to other estimates. As with the radiative fluxes, the turbulent terms show large day-to-day variability. Typically, observed peaks correspond to synoptic events associated with increased wind speed.

During winter, the sea ice and its overlying snow cover separate the cold atmosphere from the relatively warm Arctic Ocean at its freezing point (-1.8°C for typical ocean salinities). Hence there is a temperature gradient in the snow and ice cover and an upward heat flux to the surface, which in our framework is negative, consistent with what is seen in Figure 5.12. This conductive flux includes the effects of latent heat release at the ice-ocean interface associated with ice growth. The amount of ice growth (or ablation) at the bottom of the ice is represented by the sum of the ocean heat flux, F_w , and the conductive heat flux through the snow and ice, $K_i \partial T_i / \partial z$:

$$F_w + K_i \partial T_i / \partial z < 0 \text{ (growth)} \quad (5.8)$$

$$F_w + K_i \partial T_i / \partial z > 0 \text{ (ablation)} \quad (5.9)$$

F_w has a mean annual value of about 2 W m^{-2} that is determined almost entirely by shortwave input through leads and areas of thin ice. Compared to previous studies, the winter conductive flux at the SHEBA site is rather small, peaking at about -5 W m^{-2} . Annually, the conductive heat flux to the surface of multiyear ice estimated from different studies ranges from $2\text{--}8 \text{ W m}^{-2}$, with the SHEBA year falling in the low end. According to Maykut (1986), the annual upward conductive flux is up to 40 W m^{-2} in the marginal ice zone of the northern North Atlantic Ocean. During summer, as air temperatures increase, the conductive flux becomes small or nonexistent. For July, the SHEBA turbulent fluxes and conduction taken together are quite small, meaning that the bulk of the net radiation surplus is going into melt.

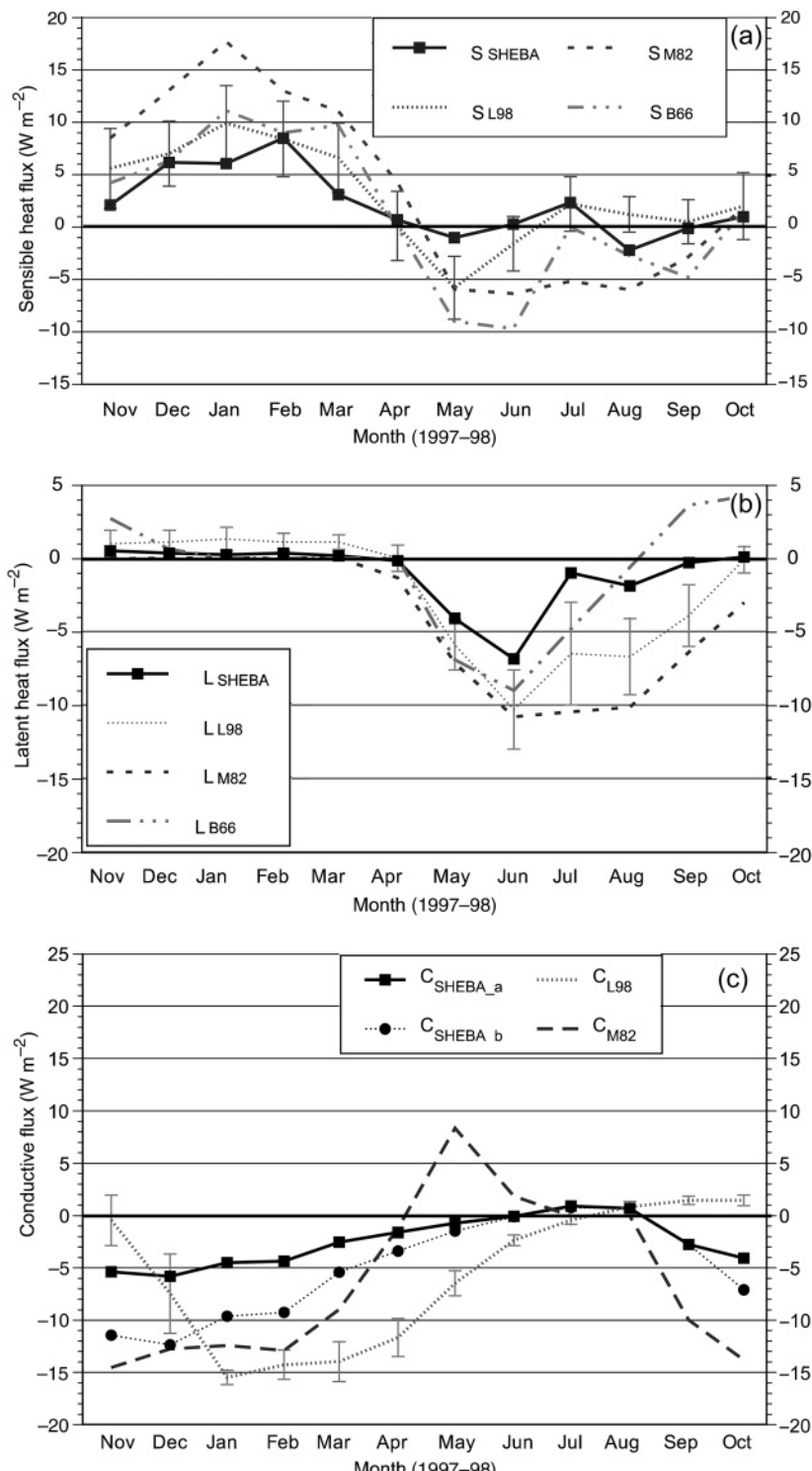


Figure 5.12. Monthly non-radiative energy balance components (W m^{-2}) for the Central Arctic Ocean. Shown are (a) sensible heat flux; (b) latent heat flux; and (c) conductive heat flux. In each panel, results from the SHEBA experiment are shown along with those from other studies (adapted from Persson et al., 2002, by permission of AGU).

Although the turbulent fluxes are quite small for the SHEBA region, over areas of thin ice and open water they can be large. In such areas, strong temperature gradients are formed in the boundary layer, and upward winter sensible heat fluxes may reach 600 W m^{-2} . Measurements over and near freezing leads and polynyas (Badgley, 1966; Smith et al., 1983; Makshtas, 1984;) suggest that heat is transferred only 10–15 m above the surface (Andreas et al., 1979) and is relayed back to the ice downwind by condensation, ice crystal precipitation, the sensible heat flux and longwave radiation from cloud formation downwind of the lead. However, condensate plumes emanating from wide (greater than 10 km) open water areas (leads) that extend to 4 km in the atmosphere and persist for up to 200 km downwind have been identified using backscatter measurements from an airborne downward pointing lidar (Schnell et al., 1989; Andreas et al., 1990). Such deep convection events appear to require a combination of a large air-sea temperature contrast (providing a large sensible heat flux), low wind speeds, and a weak Arctic temperature inversion. This combination, however, is rare in Arctic conditions (Serreze et al., 1992a). Shallow convection (less than 1 km) above narrow leads is believed to result in locally high concentrations of ice crystals near the surface, substantially augmenting the downwelling radiation flux (Curry et al., 1990).

5.9.2 Characteristics over Tundra

The fundamental difference between the Arctic Ocean and tundra is how net radiation is apportioned in the energy used to melt snow and ice (Ohmura, 1984). Once the snow is melted from the tundra, energy can be apportioned in sensible heating and to evaporate water. The snowmelt process over tundra tends to be completed over a rather short time interval, typically a few weeks (Weller and Holmgren, 1974). The consumption of heat through melt on the ice-covered ocean is much larger than on the tundra. Consequently, and for summer conditions, sensible heat is typically (but not always as seen in the SHEBA data) transferred from the atmosphere to the surface of the ocean, while it is carried from the surface to the atmosphere in the tundra. Evaporation is, on average, the most significant summer heat sink on tundra and is considerably larger than for the ice-covered ocean.

As shown by Ohmura (1984), a similar contrast exists between tundra and glaciers. It is often noted that during summer melt, glaciers exert a cooling effect on the surface air temperature in comparison with ice-free tundra surfaces at similar elevations (e.g., Müller and Roskin-Sharlin, 1967; Ohmura, 1984; Bradley and Serreze, 1987), primarily associated with the consumption of energy through ice melt. However, the higher parts of the Greenland Ice Sheet do not usually experience melt under present climate conditions. Here, sublimation can be an important process (Box and Steffen, 2001). These sublimation processes are examined in Chapter 8.

We can make some comparisons between the Arctic Ocean and the land surface by comparing the SHEBA results with Alaskan data collected through the NSF LAII program. A. Lynch et al., (1999b) synthesized results from two sets of measurements for the snow-free period (June, July, and August) of 1995. The first set represents

Table 5.4. Mean monthly energy balance at Alaskan coastal and upland sites (the latter in parentheses) for June, July, and August as measured by various investigators

	June			
	R_{sfc}	Q_H	Q_E	F_{sfc}
Chapin and Eugster	NA(58.4)	NA(-31.2)	NA(-26.3)	NA(-13.8)
Kane and Hinzman	128.1(120.8)	-39.6(-21.3)	-61.0(-80.2)	-27.5(-19.3)
Oechel and Vourlitis	124.9(114.3)	-43.0(-47.8)	-39.6(-38.9)	-40.5(-23.0)
England and Kim	NA(126.4)	NA(NA)	NA(NA)	NA(-8.8)
	July			
	R_{sfc}	Q_H	Q_E	F_{sfc}
Chapin and Eugster	120.7(NA)	-46.7(NA)	-33.2(NA)	-40.8(NA)
Kane and Hinzman	122.6(110.5)	-57.2(-37.5)	-38.1(-53.3)	-27.3(-19.7)
Oechel and Vourlitis	107.1(103.0)	-51.9(-38.9)	-50.2(-57.0)	-26.7(-15.7)
England and Kim	NA(105.8)	NA(NA)	NA(NA)	NA(-7.1)
	August			
	R_{sfc}	Q_H	Q_E	F_{sfc}
Chapin and Eugster	NA(NA)	NA(NA)	NA(NA)	NA(NA)
Kane and Hinzman	75.7(73.0)	-14.7(-26.0)	-48.6(-37.7)	-12.4(-9.2)
Oechel and Vourlitis	68.2(70.0)	-33.3(-27.8)	-22.6(-41.5)	-10.1(-10.6)
England and Kim	NA(94.2)	NA(NA)	NA(NA)	NA(-3.4)

Note: All values are in W m^{-2} . NA indicates that data are not available.

Source: From Lynch et al. (1999b).

data collected by four research groups over an area near Prudhoe Bay, AK, called the Betty Pingo site. The coastal site is located in a wetlands complex. Although there is fairly little topographic relief, the area has varied surface characteristics. The vegetation is dominated by sedges with an average height of 10–15 cm. In drier areas, the sedges are intermixed with lichen, moss, dwarf willow and birch, and a variety of flowering herbaceous species. The second set of measurements is from Sagwon Bluffs, an upland site approximately 100 km south of Betty Pingo with an elevation of 300 m in a transitional zone between the coastal plain and foothills of the Brooks Range. The vegetation is characteristic of tussock tundra. Mean fluxes for June, July, and August for 1995 from the different investigators are provided in Table 5.4. Recall that the net surface flux is the sum of the net radiation and the sensible and latent heat fluxes. In the case of the data summarized in Table 5.4, the net surface flux is represented by a conductive heat flux into the soil column.

There is considerable scatter between values at each location in the lowland and upland sites. Note for example the much lower June value of R_{net} at Sagwon Bluffs from Chapin and Eugster compared to the other estimates for this area. Although owing in part to differences in methodology, the frequency of measurement as well

as instrument problems, it primarily reflects local variability in site properties and cloud conditions. Nevertheless, at both sites there is a general decline in net radiation from June through August. Net radiation in June at the coastal and upland sites is fairly similar. Like net radiation, the sensible heat flux generally declines through the growing season, with no consistent difference between the upland and lowland sites in any month. By contrast, the latent heat flux increases from June to July, then decreases in August. This is associated with the seasonal pattern of leaf area development. In turn, the latent heat flux is higher in the upland than coastal sites during July and August, manifesting site differences in leaf area and air temperature.

Building on Ohmura's (1984) observations, a conclusion that can be drawn from a comparison between Table 5.4 and the SHEBA results is the much larger fraction of the net radiation over tundra represented by the sensible and latent heat fluxes. Furthermore, over the tundra, there is a summer conductive heat flux into the ground, warming the soil; whereas over the sea ice, nearly all of the net radiation goes into melt. The higher and upward-directed sensible heat fluxes over the tundra are in turn consistent with higher surface air temperatures.

5.9.3 Contrasts across the Arctic Treeline

As another component of the LAII program, surface energy fluxes for spring and summer were collected at two sites near Council on the Seward Peninsula of Alaska. The sites represent tundra and adjacent white spruce forest. Measurements were made from tower-mounted instruments. At the boreal forest site, they were measured at the top of the canopy. The contrasts in surface energy budgets are considered to be representative of those expected along the boreal forest – tundra transition. Part of the interest in collecting these data was to reexamine the idea that heating contrasts along the transition zone may help to “anchor” the location of the summer Arctic frontal zone (see Chapter 4).

J. Beringer et al. (2001) examined daily averages and the mean diurnal cycle of energy balance components during the spring transition (May) and summer (June–August) based on data for the years 1999 and 2000. During summer, the mean albedo of the forest canopy of 0.095 was lower than that of the tundra because of its darker color and more complex canopy structure. The forest site absorbed 11 percent more net radiation on a daily basis (11 W m^{-2}). In turn, the greater leaf area in the forest yielded less radiation at the ground surface and hence a smaller ground heat flux than at the tundra. Bowen ratios (Q_h/Q_e) between the two sites showed no consistent differences.

As a result, on average, the summer sensible flux over the forest averaged 60 W m^{-2} higher than over the tundra two hours either side of solar noon (second panel). This is a large difference. Pielke and Vidale (1996) argue that a maintained heating contrast of 50 W m^{-2} would be sufficient to manifest itself as a synoptic front. However, the observed contrast only occurs for a few hours per day. When average daily results are considered, the contrast in the sensible heat flux is only about 5 W m^{-2} , similar to daily mean contrasts of about 12 W m^{-2} observed over

the northern Canadian treeline (Lafleur and Rouse, 1995). Gradual forest-tundra transitions, which are common, are likely to show weaker heating gradients than between the distinct stands of tundra and boreal forest examined in the Beringer et al. (2001) study.

The heating contrast is much sharper in spring because of masking of snow by the forest canopy. This resulted in a much higher albedo over the tundra (0.68) compared to the forest (0.16) and 142 W m⁻² more sensible heating on a daily basis. However, this transition period lasts only two to three weeks when solar radiation is strong and the surface is still snow covered. But it is only in summer that the Arctic frontal zone can be clearly distinguished from mid-latitude frontal activity. Atmospheric soundings made over the two sites show that in both spring and summer, heating differences are also confined to a shallow layer. These findings lend further credence to the idea that the summer Arctic frontal zone is primarily driven by large-scale land-ocean heating contrasts and topography (see Chapter 4).

5.10 Skin Temperature, Surface Air Temperature, and Vertical Structure

5.10.1 The Radiative Boundary Layer

A number of winter studies (e.g., Overland and Guest, 1991; Overland et al., 1997; Overland et al., 2000) have examined linkages between the skin temperature (the temperature at the very surface), the overlying surface air temperature (SAT, the temperature at about 2 m height), the vertical temperature structure of the lower troposphere and the surface energy budget over the central Arctic sea ice cover. In summary, the skin and air temperature, along with the vertical temperature structure, can be considered as primarily driven by the longwave radiation exchanges. As we saw earlier, the mean surface net radiation deficit of typically 20–40 W m⁻² in winter is maintained by small energy transfers to the surface of sensible heat and a small upward conduction of heat through the sea ice and snow cover. The skin temperature, and thus the upward longwave radiation flux, change primarily in response to changes in downward longwave radiation and attendant adjustments in the small non-radiative terms. As the skin temperature adjusts to the downward longwave flux, the overlying SAT comes toward equilibrium with the surface through adjustments in the sensible heat flux. In general, the snow surface temperatures do not depart from the surface air temperature by more than a few degrees, except in very calm conditions. The same general statements can be made with respect to much of the Arctic land surface in winter.

The Arctic in winter is hence considered to have a radiative boundary layer (RBL) – that is, the surface energy balance changes when the downward longwave radiation flux changes, such as would attend alterations in cloud cover. This is not always the case as during storms with strong temperature advection. Clearly, toward the Atlantic side of the Arctic, the effects of temperature advection become

pronounced. As we have also seen, very large turbulent fluxes can be found over leads. However, as a general statement, the winter SAT regime is strongly coupled to the skin temperature and the longwave fluxes.

The situation is quite different in summer and the concept of the RBL falls apart. The surface energy budget is fundamentally driven by the shortwave, rather than the longwave fluxes (although the latter are certainly important, as with regard to the net cloud radiative forcing). As we have seen, over a snow-free tundra surface in summer, vertical sensible and latent heat fluxes can be large, strongly driving the surface and air temperature. Over the sea ice, the surface energy budget is strongly impacted by the melting surface, fixing surface temperature to the freezing point (hence fixing the upwelling longwave flux) and greatly limiting variations in near surface temperature.

5.10.2 Low Level Temperature Inversions

A prominent feature of the Arctic environment is the frequent occurrence of low-level temperature inversions (i.e., temperature increases with height). This was first demonstrated by C. Brooks (1931) from kite ascents over Siberia. More detailed studies from kite and captive balloon ascents made by Sverdrup (1933) during the *Maud* expedition provided some of the first detailed information on inversion structure. H. Wexler (1936) was the first to address physical controls behind the formation of Arctic inversions. Other early studies of inversion characteristics include E. Vowinkel and S. Orvig (1967, 1970), based on soundings from the Russian NP data stations over the central Arctic Ocean (NP-4, NP-6, and NP-7) and Arctic coastal sites. More recent efforts include J. Kahl (1990), Overland and Guest (1991), and Serreze et al. (1992b).

The usual situation in the Arctic during winter is a surface-based inversion (typical for land) or an inversion above a shallow (30–80 m) mixed layer (typical for the ice covered ocean), a broad region of warm air with a temperature maximum of around 1,000–1,200 m, and a negative lapse rate aloft. During winter, inversions are evident in nearly all sounding profiles. The temperature difference between the inversion base and top averages 10–12 K. The frequency of inversions over land areas decreases through spring and summer, but they are still found in about 50 percent of soundings for June and July. Over the central Arctic Ocean, inversions are still present in the great majority of summer soundings. However, summer inversions are weaker than their winter counterparts, are thinner and tend to be elevated above the surface. Over the ocean, the inversion base is about 200–400 m above the surface during May–August, with the top located between 750–1,000 m. The SHEBA observations showed an inversion persisting in summer at about 400 m altitude with an intensity of about 5 K (Uttal et al., 2002). Over land, the depth of the summer mixed layer is greater.

Typical vertical temperature structures for winter are provided in Figure 5.13 based on averaged radiosonde data from six island stations around the perimeter of the Arctic Ocean (Overland et al., 1997). Also illustrated (Figure 5.14) is the

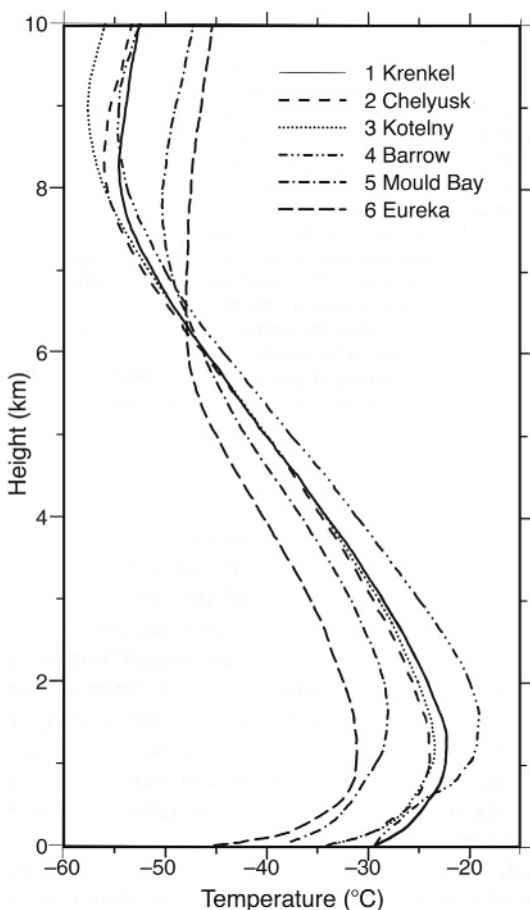


Figure 5.13. Mean temperature profiles for February 1987 from six stations located around the periphery of the Arctic Ocean: (1) Krenkel (81°N , 58°E); (2) Chelyuskin (78°N , 104°E); (3) Kotelny (76°N , 138°E); (4) Barrow (71°N , 86°W); (5) Mould Bay (76°N , 119°W); and (6) Eureka (80°N , 86°W) (from Overland et al., 1997, by permission of AMS).

typical annual cycle of inversion characteristics based on more than 6,000 radiosonde ascents for station Zhigansk in Siberia (68.8°N , 123.4°E) and more than 2,000 ascents over the central Arctic Ocean from the NP program (Serreze et al., 1992b). The latter figure shows the predominance of strong surface or near surface based inversions in winter and the weaker elevated inversions in summer. The shallow mixed layer typically present in winter over the Arctic Ocean is masked because of the limited resolution of the radiosonde data very near the surface. This mixed layer is related to the conductive heat flux through the snow and ice. Note that these are mean conditions – the inversion depth and intensity vary regionally and exhibit considerable variability on daily to weekly time scales.

The Arctic inversion has a number of important climate effects. An inversion represents strong vertical stability, limiting the depth of vertical mixing of sensible heat and moisture. As noted previously, condensate plumes emanating from wide open water areas, that extend to 4 km in the atmosphere and persist for up to 200 km downwind, have been identified during winter. The frequency at which such events can occur is determined in part by the strength of the inversion layer. Elevated concentrations of pollution gases and aerosols have been observed to coincide with

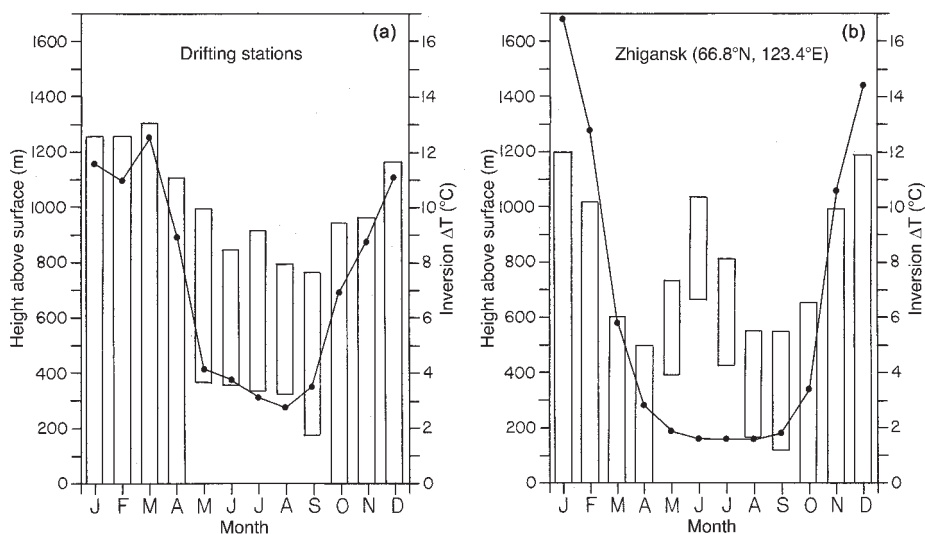


Figure 5.14. Monthly median inversion top (top of bars), base (bottom of bars) and temperature difference (solid lines) from (a) drifting station data from the central Arctic Ocean; and (b) station Zhigansk over the Siberian tundra (from Serreze et al., 1992b, by permission of AMS).

the top of the inversion layer (Bridgman et al. 1989). Photochemical destruction of boundary-layer ozone at Arctic sunrise (Barrie et al., 1988; Oltmans et al., 1989) appears to involve a process in which ozone-depleted air within the inversion layer is occasionally replaced by above-inversion, ozone-rich air, via mixing processes.

Wexler (1936) was the first to propose maintenance of the winter Arctic temperature inversion in terms of approximate longwave radiative equilibrium. He considered an ideal sounding consisting of a surface inversion of infinitesimal thickness below an isothermal layer extending up to a nearly adiabatic temperature layer. Wexler hypothesized that the nearly blackbody emission of the snow surface was in radiative equilibrium with the partial emission of the isothermal layer. Put differently, because the atmosphere has a lower emissivity than the surface, radiative equilibrium requires that the surface be radiating at a lower physical temperature than the air in the isothermal layer. A shortcoming of this idea is that the system is not closed – the isothermal layer radiates longwave energy upward into space. Hence, its temperature will drop and the inversion will weaken. Also, over the Arctic Ocean in winter, the longwave radiation emitted from the surface is primarily balanced by both the downward longwave radiation and a conductive heat flux through the ice. His concept was important, however, in stating that the surface and temperature maximum layer are strongly coupled through radiative processes.

Overland and Guest (1991) examined the problem of the winter temperature inversion over the Arctic Ocean using a one dimensional atmospheric radiation model. A steady thermodynamic model for the skin temperature was employed balancing the surface longwave radiation deficit with a conductive heat flux through

the sea ice and overlying snow cover. No lateral heat advection by the atmospheric circulation was permitted. The model was calibrated against observed clear-sky temperature profiles. The modeled downward longwave radiation to the surface was less than observed. It was concluded that the “missing” downward radiation could be accounted for by including the emissivity effects of “diamond dust” in the lower troposphere (Curry, 1983; Curry et al., 1990). A correction for an ice crystal layer with an emissivity of 0.21 provided the necessary downward longwave flux to match observations.

After calibration, the model was initialized with a linear temperature profile and allowed to evolve over ninety days. Initially, a realistic temperature inversion was observed to develop. However, the temperature maximum layer radiated strongly into space, and cooled rapidly. With less downwelling longwave radiation directed downward to the surface, the surface temperature declined, less slowly than the temperature maximum layer because of compensation by the conductive flux through the sea ice and snow cover. In accord with the dependency of longwave emission on the fourth power of temperature, as the temperature of the profile declined over time, the cooling rate declined. The end result was an essentially isothermal profile. Adding an extra sensible heat flux from leads could not make up for the radiative loss to space.

Overland and Guest (1991) then repeated the experiment by including a steady lateral heat advection from lower latitudes using values estimated by Nakamura and Oort (1988). Eureka! With the inclusion of advection to offset radiative loss to space, the model temperature profile evolved to develop a steady inversion. In summary, these results point out that while the winter inversion structure can be considered to a crude first order in the context of a radiative equilibrium (coupling the skin temperature to the atmospheric temperature maximum) an inversion cannot be maintained in the absence of lateral advection. These results also point to the significance of “diamond dust” in maintaining the downward longwave flux. Note that other factors, such as subsidence under anticyclonic condition, could affect the inversion structure.

Cloud cover has strong influences on inversion structure. As discussed, clouds increase the downward flux. Serreze et al. (1992b) compared winter mean temperature profiles over the Arctic Ocean (using radiosonde data from the NP program) for relatively clear (less than 50 percent cloud cover) and relatively cloudy conditions (greater than 50 percent cloud cover). For relatively cloudy conditions, the mean temperature difference between the inversion base and top was 9.2 K, compared with 13.2 K for clear skies. Temperatures were higher in the cloudy cases throughout the atmospheric profile from the inversion base to inversion top, but with the temperature difference largest near the surface. The SAT (based on the lowest temperature level in the soundings) under cloudy skies was 245K, compared to 238K for clear skies.

In explanation, some of the upward longwave radiation from the surface and from the atmospheric layers below the cloud base that would escape to space is absorbed by the cloud and reradiated downward. If we assume that there is no difference

in advection between the mean clear and cloudy cases, then the reduction in the longwave radiative cooling rate will result in a warmer atmospheric profile. As the difference in the effective emissivity between the surface and temperature maximum layer is reduced, radiative equilibrium requires that the difference in surface temperature and that of the temperature maximum is less than for clear skies with the shape of the profile adjusting accordingly.

The surface net radiation budget turns positive in spring in response to solar input, helping to break down the inversion structure. The seasonal increase in cloud cover assists in this process. Once the snow over the tundra melts, the strength and frequency of inversions decline as the upward turbulent sensible heat flux becomes stronger. Over Arctic lands during summer, convection with consequent release of latent heat is not unusual. Over sea ice, summer melting of the surface means that the upward longwave radiation flux cannot vary. One result of this is that the surface cannot adjust to achieve quasi radiative equilibrium. However, the fixed surface temperature ($\sim 0^{\circ}\text{C}$), is often associated with shallow surface-based inversions (Busch et al., 1982).

As discussed in Chapters 1 and 2, the strong downward trend in end-of-summer sea ice extent has led to an increase in seasonal heat uptake in the ocean mixed layer. This fosters large upward radiative and turbulent energy fluxes in autumn and to a lesser extent winter, which is recognized as a major driver of observed strong rises in air temperature, largest at the surface and larger than for the Northern Hemisphere as a whole (termed Arctic amplification). This leads to a reduction in autumn and winter inversion strength over the Arctic Ocean.

5.11 Radiation-Climate Feedbacks

5.11.1 The Concept of Feedbacks

The basic idea behind a feedback is that an initial perturbation to the climate system can be either amplified (a positive feedback) or dampened (negative feedback) through interactions with other climate variables. W. Kellogg (1973) developed a simple conceptual framework to understand feedbacks, which still finds wide use. M. Schlesinger (1985) provides a formalized description for use in surface energy balance models. As outlined in the review by Curry et al. (1996), there are a number of radiation-climate feedbacks identified as potentially important in the Arctic: (1) ice-albedo feedbacks; (2) cloud-radiation feedbacks; (3) water vapor feedbacks; (4) cloud-temperature feedbacks; and (5) cloud phase and precipitation feedbacks. The first three are very much tied into the surface energy budget and are briefly reviewed.

5.11.2 The Ice-Albedo Feedback

This is probably the best known of climate feedbacks. If the climate warms, the extent of snow and ice cover will decrease. The earth's surface albedo decreases,

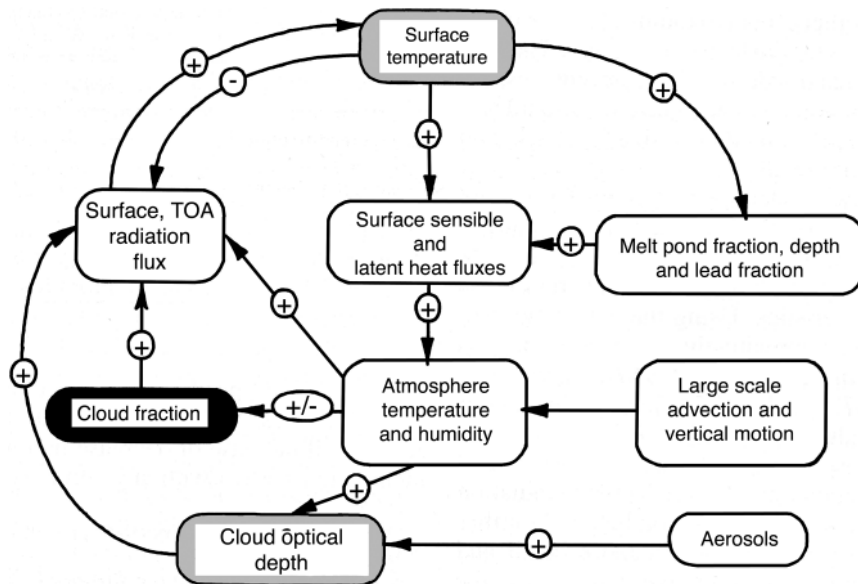


Figure 5.15. Schematic of the ice-albedo feedback mechanism using the framework of Kellogg (1973). The direction of the arrow indicates the direction in the interaction. A “+” indicates a positive interaction (an increase in the first quantity leads to an increase in the second). A “-” indicates a negative interaction (an increase in the first quantity leads to a decrease in the second quantity). A “+/-” indicates that the sign of the interaction is uncertain or that the sign changes over the annual cycle (from Curry et al., 1996, by permission of AMS).

meaning greater absorption of solar radiation at the surface. The climate hence warms more, melting more snow and ice, and so on. The mechanism can work in reverse, whereby cooling allows more snow and ice to remain on the surface, increasing the earth’s albedo, causing further cooling. The feedback is positive in that through the chain of events, the initial perturbation (warming or cooling) is reinforced. The ice-albedo feedback is an important process in simulations of global warming in response to increased concentrations of greenhouse gases (see Chapter 9) and to simulations of global cooling during Ice Age maxima (see Chapter 10).

Although most attention has been paid to the feedback process associated with changes in the areal extent of snow cover and sea ice, there are also feedbacks associated with processes within the snow and ice zones. This is illustrated conceptually for the case of the sea ice cover (Figure 5.15). The outer loop represents the feedback associated with areal extent whereby an initial perturbation (e.g., increased or decreased ice extent) instigates a chain of events amplifying the perturbation (this loop also holds with respect to areal changes in terrestrial snow cover). The interior part of the figure illustrates processes occurring within the multiyear ice pack. Warming leads to more melt ponds, and more melt ponds will reduce the albedo. Similarly, warming results in less snow cover, which reduces surface albedo. This also means thinner ice, reducing the albedo. Albedo is also reduced with higher temperatures because of an increase in lead fraction.

However, there are competing interactions. Although warming leads to more melt ponds, reducing albedo, less snow cover means fewer melt ponds, which increases albedo. The sign of other interactions is poorly understood or changes seasonally. Sorting out the sign and relative magnitude of the different linkages represents a major challenge to the modeling community. The study by J. Curry, J. Schramm, and E Ebert (1995), using a one-dimensional sea ice model, suggests that the magnitude of the positive ice-albedo feedback mechanism is increased by the inclusion of melt ponds and diminished by the inclusion of ice thickness distribution and ridging (see Chapter 7 for a discussion of sea ice characteristics).

5.11.3 Cloud-Radiation Feedback

Numerous modeling studies suggest that changes in cloud fraction that would accompany global warming will modify the surface temperature. However, the sign of the feedback between different models ranges from negative (clouds cause cooling) to strongly positive (clouds cause warming). The issue is complicated in that there are feedbacks not only related to cloud fraction, but to cloud height, optical depth, and cloud microphysical properties. In turn, because of its unique thermodynamic and radiative environment, conclusions drawn from global studies may be inappropriate in the Arctic.

The cloud-radiation feedback mechanism in the Arctic is illustrated conceptually in Figure 5.16. A perturbation in the surface radiation balance may arise from increased greenhouse gas concentrations and/or increasing aerosol amounts. A perturbation in the surface radiation balance of the snow/ice changes the snow/ice characteristics (e.g., ice thickness and areal distribution, surface temperature, and surface albedo). These changes, especially in the surface temperature and fraction of open water, modify fluxes of radiation and surface sensible and latent heat, modifying the atmospheric temperature, humidity and dynamics. This will in turn modify cloud properties (e.g., cloud fraction and optical depth), which will in turn modify the radiative fluxes. Resolving the interactions requires an understanding of changes in cloud fraction coverage and vertical distribution as the vertical temperature and humidity profile changes and adjustments in cloud water content, phase, and particle size as atmospheric temperature and composition change.

As outlined earlier, for most of the year, the observed net cloud radiative forcing at the surface is positive in the Arctic (clouds cause warming). However, with respect to feedback processes, a major uncertainty is how cloud characteristics (e.g., optical depth, microphysical properties) will be altered in a changing climate. Because of the impact of clouds on the surface radiation flux, cloud-radiative feedback processes in the Arctic are very much intertwined with the ice-albedo feedback. At present, the sign of the cloud radiation feedback is still uncertain, but appears to be positive.

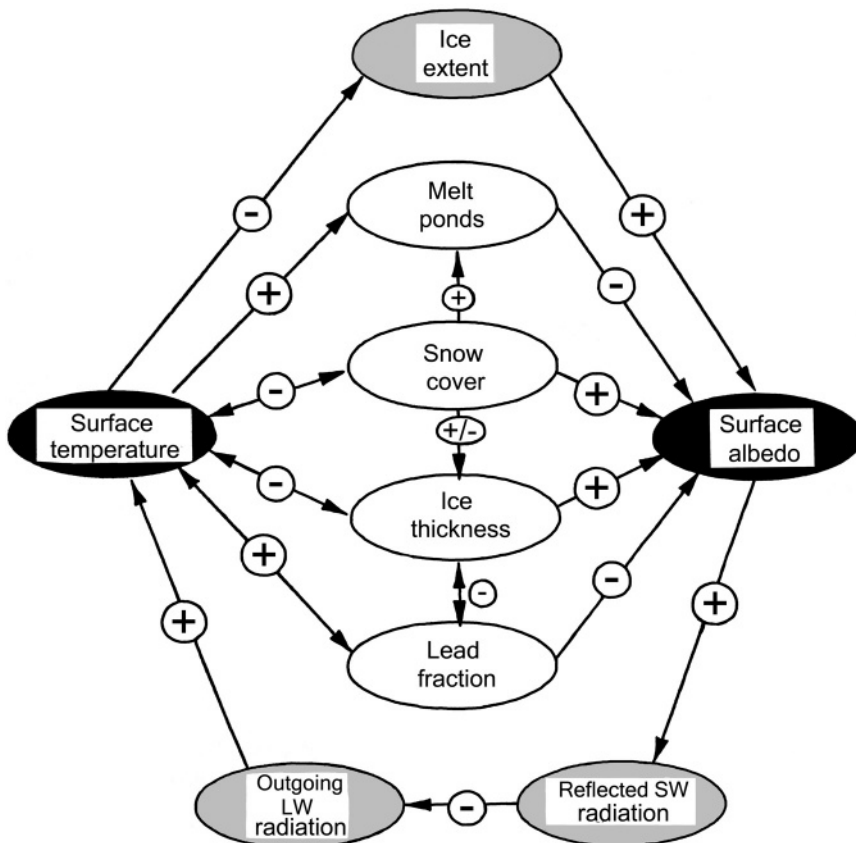


Figure 5.16. Same as in Figure 5.15, except for the cloud-radiation feedback mechanism (from Curry et al., 1996, by permission of AMS).

5.11.4 Water Vapor Feedback

Water vapor feedback is fairly straightforward in principle. The amount of water vapor that the atmosphere can carry increases with increasing temperature. Assuming there is water available to evaporate, an initial warming will result in an increase in humidity. However, as water vapor is a greenhouse gas, the increase in humidity leads to further warming. Like albedo feedback, the strength of the water vapor feedback is a key determiner of the planet's climate sensitivity – that is, the change in global average surface air temperature in response to a climate forcing of a given magnitude. As discussed, the Arctic is now experiencing an outsized warming compared with the Northern Hemisphere as a whole. Both radiosonde data and output from atmospheric reanalyses point to positive trends in column-integrated water vapor over the Arctic over the past several decades, largest in summer and early autumn, and most pronounced in the northern North Atlantic, including the Greenland, Norwegian and Barents seas, the Canadian Arctic Archipelago and (on

the Pacific side) the Beaufort and Chukchi seas. This pattern is linked to positive anomalies in air and sea surface temperature and negative anomalies in end-of-summer sea ice extent (Serreze, Barrett, and Stroeve, 2012). However, the extent to which the increased Arctic water vapor is acting as a feedback remains to be determined.

5.11.5 Integration of Feedbacks

Although there is a great deal of uncertainty, the best estimate is that, apart from the aerosol-dehydration feedback proposed by J-P. Blanchet and E. Girard (1995), all of the individual climate feedbacks in the Arctic are positive. This, of course, ignores the obvious negative feedback associated with the Stefan-Boltzman relationship (that as surface temperature rises, radiative cooling increases to the fourth power of the temperature). One must also be aware that in the real world, positive feedback mechanisms may promote negative (compensating) feedbacks. For example, if the ice-albedo and cloud feedbacks were to promote large warming in the Arctic, there ought to be a corresponding change in poleward heat transports by the atmospheric circulation. Other possibilities include unforeseen negative cloud feedbacks or negative feedbacks between the sea ice and ocean (Curry et al., 1996). In many ways, our understanding of climate feedbacks in the Arctic is still in its infancy.

Focus Questions and Exercises

- 1) It has been argued that cloud cover is the single most important driver of spatial and temporal variations in the Arctic surface radiation budget. Do you agree or disagree and why?
- 2) Imagine that you have been measuring all components of the surface energy balance (radiative and non-radiative terms) in units of watts per square meter over an area of sea ice close to the North Pole during early April. The air temperature is -25°C . Suddenly, right where you are measuring these energy balance terms, a large lead opens up in the ice cover. Describe how the components of the energy balance will change. Consider the situation 15 minutes, 6 hours, 24 hours, and 48 hours after the lead first opens (hint – if it's really cold, the lead will freeze over fairly quickly). It might help as part of your description to make a table of reasonable values of the energy fluxes at the three times.
- 3) The amount (thickness) of first-year ice that grows at two different locations on the Arctic Ocean over the period of October through March can be quite different, even if the average air temperature at the two locations is very similar. How can this be?

6

Precipitation, Net Precipitation, and River Discharge

Overview

One of the keys to understanding the Arctic climate system is the determination of freshwater transfers. As introduced in Chapter 2, the Arctic Ocean is characterized by a fairly fresh surface layer, primarily maintained by river discharge, the import of low salinity seawater through the Bering Strait, and net precipitation over the Ocean itself. This fresh surface layer allows sea ice to readily form. In turn, the major exports of freshwater are the ice and water fluxes to the North Atlantic through the Fram Strait and through the Canadian Arctic Archipelago. Following the water through the atmospheric, terrestrial, and oceanic branches of the Arctic hydrologic cycle, and assessing links between these fluxes, freshwater storages, and the global climate system is a vibrant area of research. But the problem cannot be tackled all at once. Here, the focus is on a large, yet digestible piece – precipitation, net precipitation, and river discharge to the Arctic Ocean. Aspects of the ocean branch will be examined as part of Chapter 7.

Precipitation is a difficult quantity to accurately measure in the Arctic. Evapotranspiration is even more difficult to obtain. Although annual average precipitation totals over the Arctic range widely, there is also strong seasonality. Precipitation over the Atlantic sector exhibits a general maximum during the winter half of the year, whereas elsewhere a warm season maximum is the rule. Annual net precipitation (precipitation less evapotranspiration, which can be assessed from atmospheric reanalysis data) is typically 150–300 mm over land, 150–200 mm over the central Arctic Ocean and more than 1,000 mm near the Icelandic Low.

Although precipitation over much of the land area peaks in summer, evapotranspiration rates are fairly high, such that summer net precipitation is small or even negative in these areas. Over land regions, a considerable fraction of summer precipitation results from regional recycling of water vapor, pointing to the strong effect of the land surface. From autumn through spring, most of the precipitation is stored as snow. Consequently, river discharge to the Arctic Ocean exhibits a pronounced early summer peak as the snow melts. For much of the Arctic, river discharge is strongly impacted by the presence of permafrost which limits infiltration. The bulk of the river discharge to the Arctic Ocean is contributed by four major river systems: the Ob, the Yenisey, the Lena, and the Mackenzie. Discharge from Arctic draining rivers in Eurasia has exhibited a positive trend over the period of record, consistent with increased net precipitation as assessed from atmospheric reanalysis data.

6.1 Precipitation

6.1.1 Difficulties in Measurement

There is still uncertainty regarding even mean precipitation totals in the Arctic. The basic problems were articulated in Chapter 2. To reiterate the major issues: (1) there is significant gauge undercatch of solid precipitation for which there are only imperfect adjustment procedures, the problem is compounded by the variety of gauge types and reporting practices used by different countries and by a switch to automated stations for some locations in Canada; (2) while the station network has always been sparse, it has further declined since about 1990; and (3) precipitation estimates based on satellite data retrievals or from atmospheric reanalyses can have large biases. Figure 6.1 highlights the large size of bias adjustments applied to gauge data, using (as an example) data from the NP drifting stations. Note in particular, that the application of corrections for wind loss and the neglect of trace events acts to shift the annual peak in precipitation from July to September! To highlight the network problems, Figure 6.2 shows the distribution of land stations north of 40°N with at least ten years of data over the 1960–1989 period. Note the sparse network over northern Canada and Siberia. There is a network of observations over central Greenland, but these are from automated stations for which data quality is open to question. The situation is even worse over the central Arctic Ocean, where the NP stations provided spotty coverage from 1950 through 1991, and, with renewal of the program, from 2003 onward.

6.1.2 Fields of Estimated Monthly Precipitation

Annual mean precipitation is shown in Figure 2.28. Maps for the four mid-season months based on the same data sources appear in Figure 6.3. A number of different

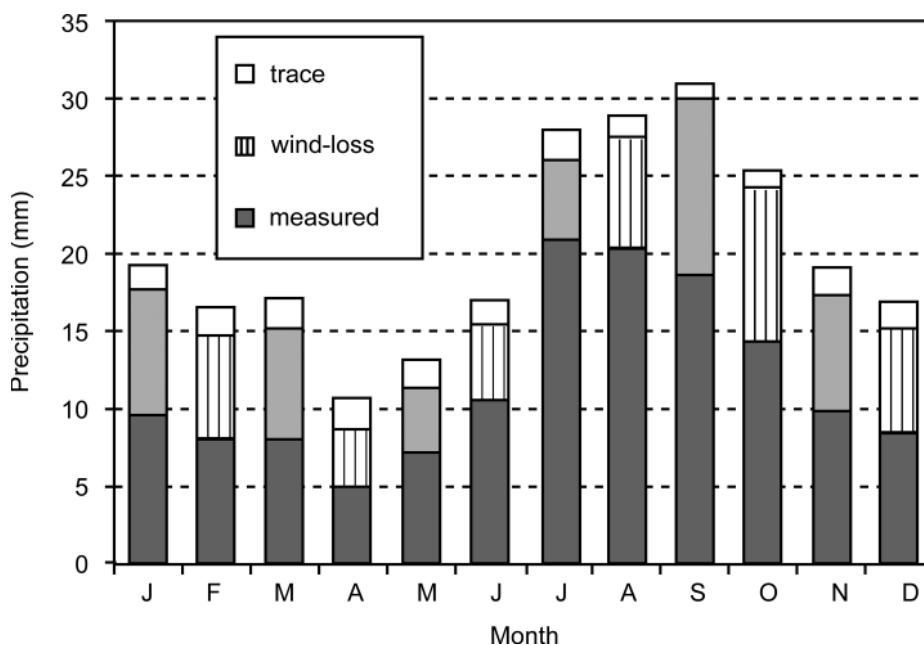


Figure 6.1. Monthly precipitation for the central Arctic Ocean based on data from the Russian North Pole manned camps with daily bias adjustments. Raw precipitation totals are shown along with the adjustments for winds and neglect of trace amounts. Adjusted precipitation is represented by the total length of the bars (from Yang, 1999, by permission of AGU).

monthly station data sets (e.g., Groisman et al., 1991; Mekis and Hogg, 1999; Yang, 1999) were employed for land areas and for the Arctic Ocean. These records, which are of highly variable length, were gridded and then adjusted for gauge undercatch using the same coefficients employed by Legates and Willmott (1990). The fields were then blended with precipitation forecasts from the NCEP/NCAR reanalysis for which systematic biases were removed using statistical distributions from the bias-adjusted gridded stations records. The techniques represent an outgrowth of those described by Serreze et al. (2003b). Over open (ice-free) ocean, use was made of updated and improved satellite-derived records from the Global Precipitation Climatology Project (Huffman et al., 1997). Precipitation values over central Greenland rely on interpolation from coastal sites and should be viewed with due caution – results for this region based on snow accumulation and modeling will be examined separately.

For a large part of the Arctic, winter is quite dry. January precipitation totals over much of eastern Eurasia, northern Alaska, northern Canada and the central Arctic Ocean are between 10 and 20 mm. These are regions far removed from Atlantic and Pacific moisture sources and for which winter cyclone activity is infrequent. Winter month precipitation totals are much higher in the Atlantic sector of the Arctic. This arises from frequent cyclone activity along the North Atlantic cyclone track, especially in the vicinity of the Icelandic Low, and associated moisture flux

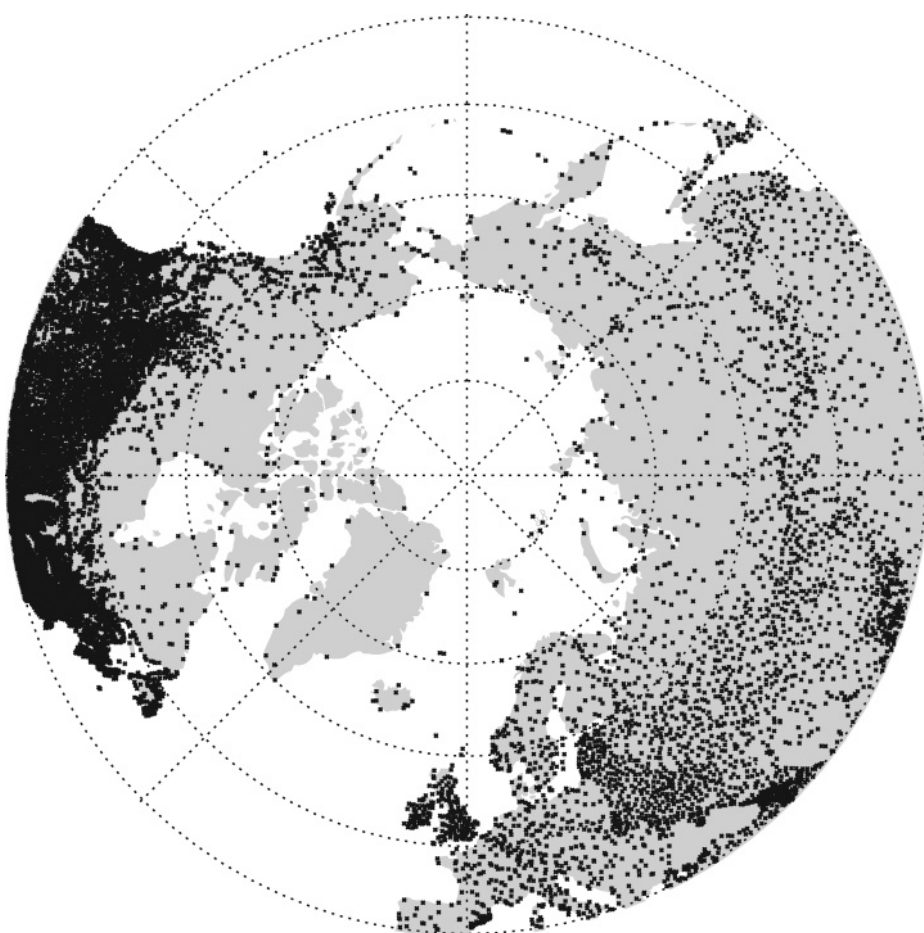


Figure 6.2. Distribution of precipitation measuring stations north of 40°N with at least ten years of record for the 1960–1989 period, based on blending various data sets (by the authors).

convergence. Along the coasts of Scandinavian and eastern Greenland, precipitation is enhanced by orographic uplift of moist airmasses. The decrease in precipitation poleward toward the Kara Sea manifests the poleward decay of the primary North Atlantic cyclone track. The other area of high precipitation is along the Pacific side, which is associated with the northern end of the East Asian storm track, and orographic uplift.

By April, the primary cyclone tracks have weakened, and there is a decline in precipitation in the Atlantic sector and on the Pacific side of the Arctic as compared with January. Precipitation over northern Canada, Alaska, eastern Eurasia, and the central Arctic Ocean is still quite low. As seen in the July field, the precipitation pattern for summer is quite different. Although the primary storm tracks are weakest at this time, the highest Arctic totals are still generally found in the Atlantic and Pacific sectors. However, precipitation is at its annual maximum over most

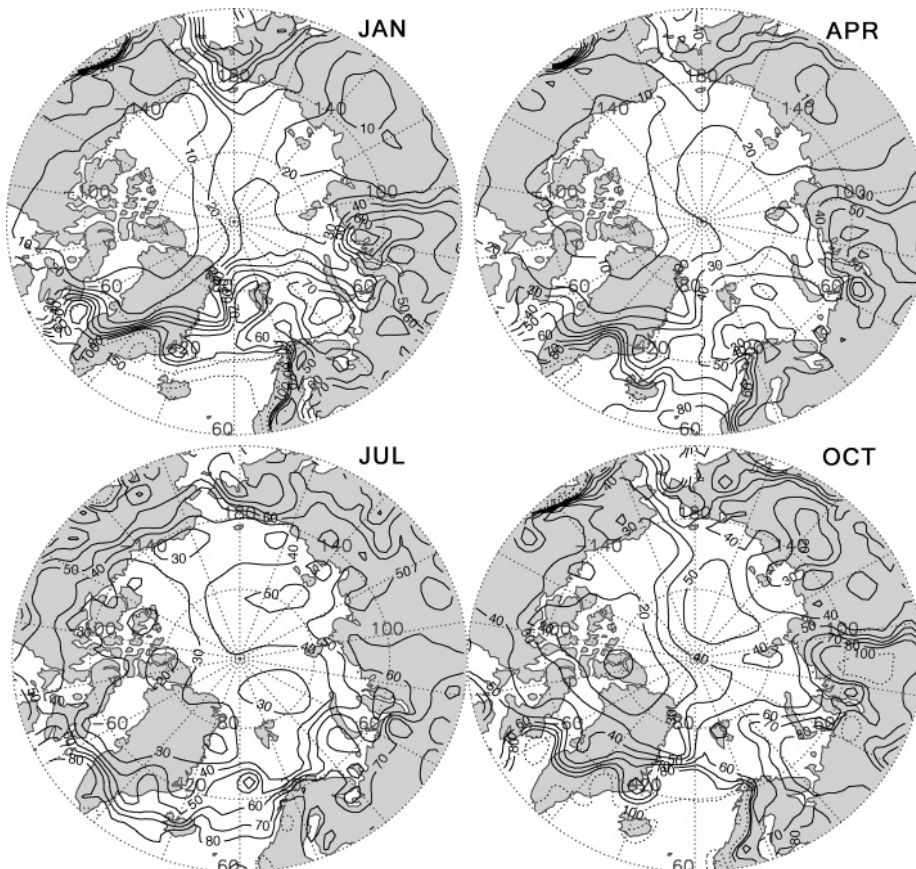


Figure 6.3. Mean precipitation north of 60°N for the four mid-season months, based on data from land stations and the Arctic Ocean with bias adjustments, the NCEP/NCAR reanalysis and satellite retrievals (over open ocean). The fields are based primarily on data for 1960–1989. Contours are at every 10 mm up to 80 mm and at every 50 mm (dashed) for amounts of 100 mm and higher (by the authors).

land areas. The onset of the summer pattern features a strong transition between May and June. Several processes are responsible for the terrestrial summer maximum. Cyclone activity over land areas is more frequent in summer than in winter (see Chapter 4). Also, following melt of the snow cover, strong surface heating of the land surface and plant photosynthesis promotes evapotranspiration. Convective precipitation becomes fairly common, at least in the Low Arctic. Summer convective precipitation over land is not unknown even at quite high latitudes. The first author observed convective precipitation during the summer of 1982 over the Hazen Plateau of northern Ellesmere Island (82°N). His fascination turned to dismay when it was discovered that the short aluminum tower on which the meteorological instruments were mounted acted as a lightning rod!

A regional contributor to the summer precipitation maximum over land areas and the central Arctic Ocean is the summer Arctic frontal zone (Serreze et al., 2001).

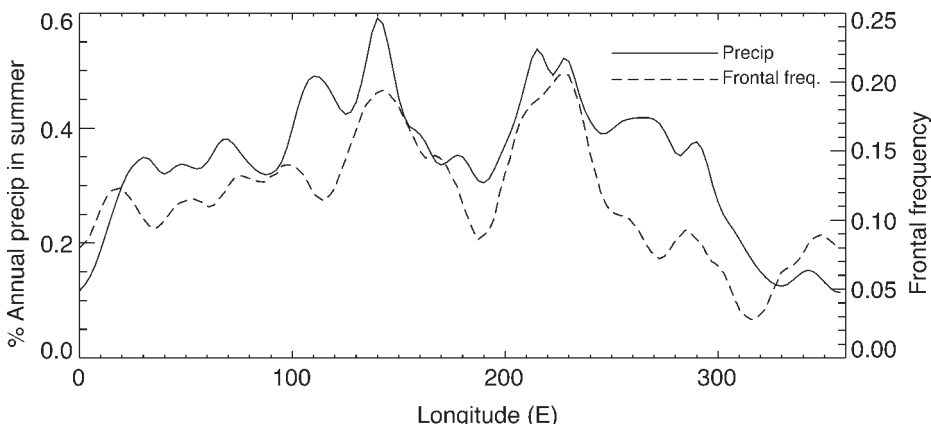


Figure 6.4. Longitudinal distribution of summer frontal frequency (fronts per day) and the fraction of annual precipitation falling in summer, averaged from 62.5 to 67.5°N. The precipitation data include bias adjustments (from Serreze et al., 2001, by permission of AMS).

As outlined in Chapter 4, summer sees development of a band of high frontal frequencies along Eurasia from about 60–70°N, best expressed over the eastern half of the continent. A similar band is found over Alaska. Although most strongly developed in summer, the Alaskan feature is present year-round. The high frequency of summer frontal activity is linked to heating contrasts between the Arctic Ocean and snow-free land, with the coastal baroclinicity sharpened by coastal orography. Cyclogenesis is common in preferred areas over eastern Eurasia, Alaska, and Canada where the frontal zone is best expressed.

The hydrologic impact of the frontal zone is evident when plotting the longitudinal distribution of summer frontal frequencies (fronts per day) and the fraction of annual precipitation that falls in summer, averaged from 62.5°N to 67.5°N (Figure 6.4). At 140°E, where the Eurasian frontal zone is well expressed, nearly 60 percent of annual precipitation falls during summer. Where the Alaskan frontal zone is well-expressed, more than 50 percent of annual precipitation falls during summer. The late summer and early autumn precipitation maximum over the Arctic Ocean occurs as cyclones from the weakened, but still present North Atlantic cyclone track and systems generated over Eurasia (many along the frontal zone) migrate into the region. From Yang's (1999) analysis of the North Pole records (Figure 6.1), mean precipitation over the central Arctic Ocean peaks in September at about 30 mm, roughly three times the total for April, the driest month.

The October field in Figure 6.3 illustrates the transition back toward the winter pattern. For land areas except west-central Eurasia, precipitation has declined from its summer maximum. This is also true for most of the Arctic Ocean (again, see Figure 6.1). However, precipitation picks up sharply in the Atlantic and Pacific sectors as the primary storm tracks gain strength.

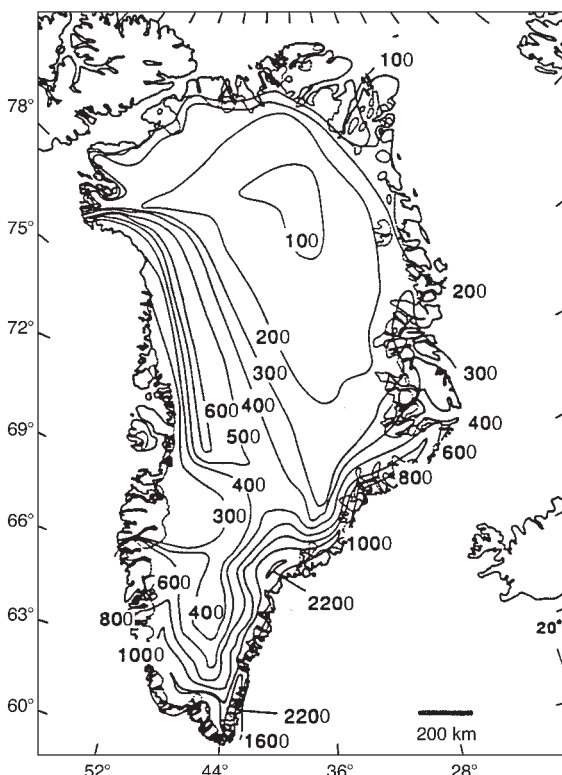


Figure 6.5. Annual accumulation over the Greenland Ice Sheet in mm water equivalent. The contour intervals are 200 mm, but 100 mm if smaller than 400 mm and 600 mm if larger than 1000 mm (from Chen et al., 1997, by permission of AMS).

6.1.3 Precipitation over Greenland

Direct observations of precipitation over Greenland are particularly scanty. Stations with long records are limited to the coasts. As noted earlier, over the past couple of decades, data over the ice sheet have been acquired from automatic weather stations. But quite a few measurements have been made of annual snow accumulation over the ice sheet. G. Bender (1984) provides a synthesis of observed annual accumulation (snow water equivalent) over the ice sheet, modified along the coast with a simple model of orographic precipitation. The resulting map, further modified by Bromwich, Keen, and Bolzan (1993) is provided as Figure 6.5. This is a much better analysis than can be provided from interpolating sparse station data and other coarse resolution records. The main features of the map are very low accumulation (100 mm) over the northern portions of the island with the highest values along the southeast coast linked to orographic precipitation. Peak values along the southeast coast exceed 2,000 mm. These local features are not captured in Figure 2.28. Fairly high accumulations values are also found along the western coast related to orographic uplift and cyclone activity in the Davis Strait.

A somewhat more recent effort to assess Greenland precipitation comes from the study of Bromwich et al. (2001). It is based on enhancements to the dynamic model of Chen et al. (1997). The model is based on the omega equation (which

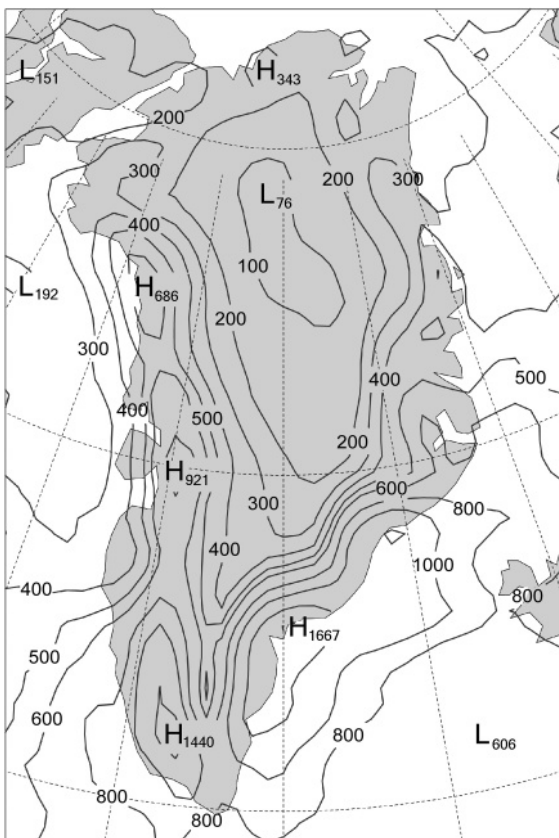


Figure 6.6. Modeled annual precipitation averaged for 1985 through 1999 (mm). The contour interval is 200 mm, but 100 mm if smaller than 400 mm, and 300 mm if larger than 1,000 mm (from Bromwich et al., 2001, by permission of AGU).

describes vertical motion which is important with respect to both synoptic-scale and orographic precipitation). It was driven by ECMWF data. Figure 6.6 shows the field of modeled annual precipitation for Greenland and the surrounding region averaged for the years 1985 through 1999. The modeled precipitation captures the general features seen in Figure 6.5. In particular, it reproduces the low amounts over the central ice sheet and the high values along the southeast coast. Aspects of accumulation over Greenland will be further examined in Chapter 8.

6.1.4 Precipitation Frequency and Phase

“Present weather” codes that represent part of the synoptic reports in the ICOADS data base were used by Serreze, Maslanik, and Key (1997) to examine the characteristics of precipitation frequency and phase (solid, liquid, mixed) over the Arctic Ocean. Figure 6.7 gives a feel for the contrasts between January and July precipitation frequency and phase. These maps bin ICOADS reports from 1950–1999 into a very coarse grid cell array. Over the central Arctic Ocean, the ICOADS records are primarily from the NP stations. Precipitation frequency represents the percent of all ICOADS observations for which any precipitation was observed. Similarly, the

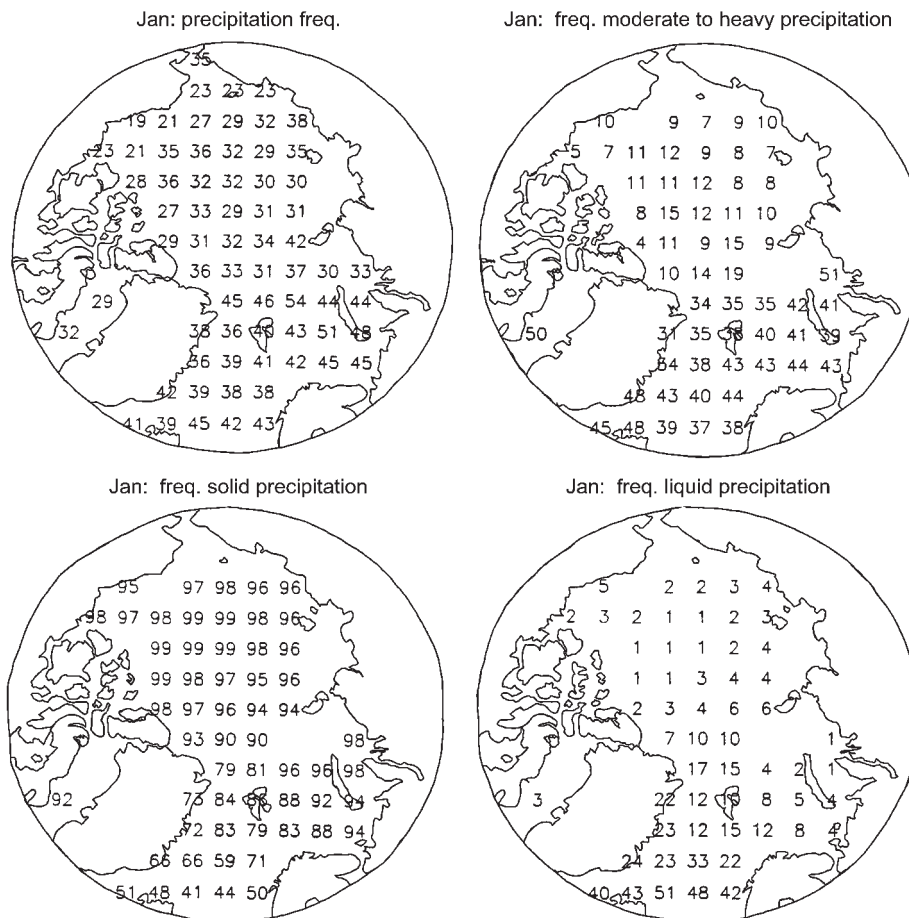


Figure 6.7. Precipitation frequency, the frequency of moderate to heavy precipitation, solid precipitation frequency and liquid precipitation frequency, based on present weather reports in ICOADS records over the 1950–1995 period. Maps are provided for January and July. See text for details (from Serreze et al., 1997, by permission of NSIDC, Boulder, CO).

frequency of moderate to heavy precipitation is the percent of all ICOADS observations when moderate to heavy precipitation was observed. The maps for phase are based on the percent of all ICOADS observations of precipitation for which the precipitation was in solid or liquid form (because of mixed precipitation, the two may not sum to 100 percent). Note that the ICOADS records do not provide precipitation amounts – only occurrence, relative intensity and phase.

As expected from precipitation totals (Figure 6.3) January precipitation frequency is higher over the Atlantic sector as compared to the central Arctic, that is, there are more events. There is an opposing pattern in July. Nevertheless, it shows that while total winter precipitation in the central Arctic is quite light, the actual occurrence of precipitation is still common. In many cases these would be recorded

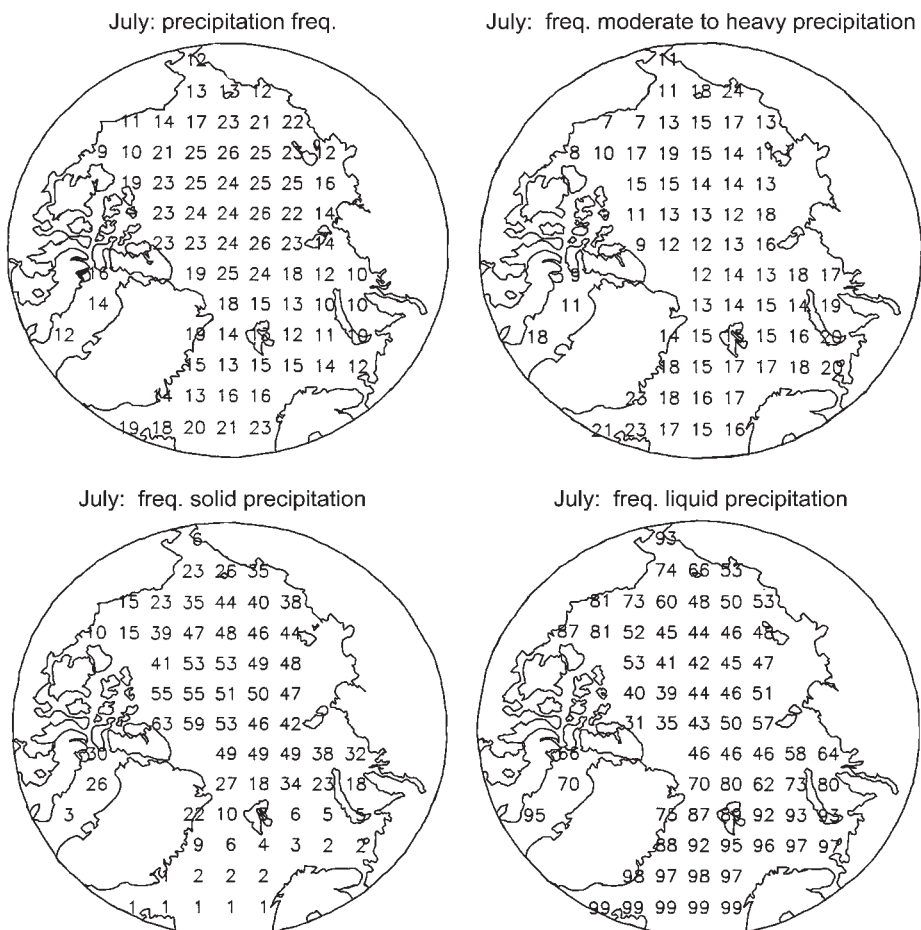


Figure 6.7. (Cont.)

as trace events – the precipitation totals shown in Figure 6.1 include a correction for such events. For January, the contrast between the Atlantic sector and central Arctic Ocean also holds with respect to the frequencies of moderate to heavy precipitation. In July, moderate to heavy precipitation is more evenly distributed across the Arctic Ocean. The annual cycle in precipitation frequency (not shown) only roughly follows that of total precipitation over the central Arctic Ocean.

Over the central Arctic Ocean, nearly all January precipitation is in solid form. On rare occasions, the incursion of a very warm air mass can foster liquid precipitation in parts of this region. The January frequency of solid (liquid) precipitation is sharply lower (higher) over the northern North Atlantic where temperatures are highest. Even in July, about half of the precipitation near the pole falls in solid form. These snow events help to maintain a high surface albedo in this area. Solid precipitation over the Atlantic sector in July is very rare.

6.2 Evapo-Transpiration and Net Precipitation

6.2.1 Evapo-Transpiration

Evapo-transpiration (ET; the combination of evaporation from the surface and transpiration from plants) is equivalent to the latent heat flux examined in Chapter 5, but in different units; namely, water depth over a selected time period. Assuming liquid to vapor energy transformations (or vice versa), the relationship is as follows:

$$ET = (L/\rho L_v) t \quad (6.1)$$

where L is the latent heat flux, L_v is the latent heat of evaporation (see Chapter 5) and ρ is the density of water (which also varies slightly with respect to temperature) and t is time. If the desired value of ET is mm per day, and one assumes a water density of 10^3 kg m^{-3} and the latent heat of evaporation at 0°C , one can simply multiply the average latent heat flux by a conversion factor of 0.03456. For example, we saw that in July at the SHEBA site (Figure 5.12), there was an average latent heat flux of about 7 W m^{-2} (directed upward). From Equation 6.1, this yields a daily evaporation rate of 0.24 mm per day, or 7.5 mm per month. This is a rather small value. Taking from Table 5.4 a mid-range value for the latent heat of 50 W m^{-2} for summer months over the Alaskan tundra (based on field measurements), yields a monthly ET nearly an order of magnitude higher. In a cold environment where surface is completely frozen, one would replace L_v in Equation 6.1 with the latent heat of sublimation.

Direct estimates of the latent heat flux (and hence of ET) in the Arctic are particularly sparse. Along with direct measurements (generally based on the profile and eddy correlation methods reviewed in Chapter 5), estimates have been compiled from more simple energy budget considerations (e.g., Zubenok 1976; Lydolph 1977; Fisheries and Environment Canada 1978), as a residual (e.g., Kane et al., 1992; Serreze et al., 2003a) and from Land Surface Models (LSMs) (Slater et al., 2001). Residual estimates of ET can be made at the watershed scale via the water balance equation at the surface: $ET = P - R$ (where for a long-term annual average the storage terms in snow cover and the soil can be neglected) or via the atmospheric moisture balance (the “aerological method”), discussed later. Briefly, and as described more completely in Chapter 9, LSMs address interactions between the land surface, atmosphere, and underlying surface. Time series of basic variables (generally downward shortwave and longwave radiation, precipitation, near-surface winds, humidity, and air temperature) represent model forcings. The model ingests these forcings and generates numerous outputs, one of which is ET. These forcing can variously be direct observations or outputs from an atmospheric model (often atmospheric reanalyses) to which the LSM is coupled. The estimated ET is only as good as the physics of the LSM and of the driving fields.

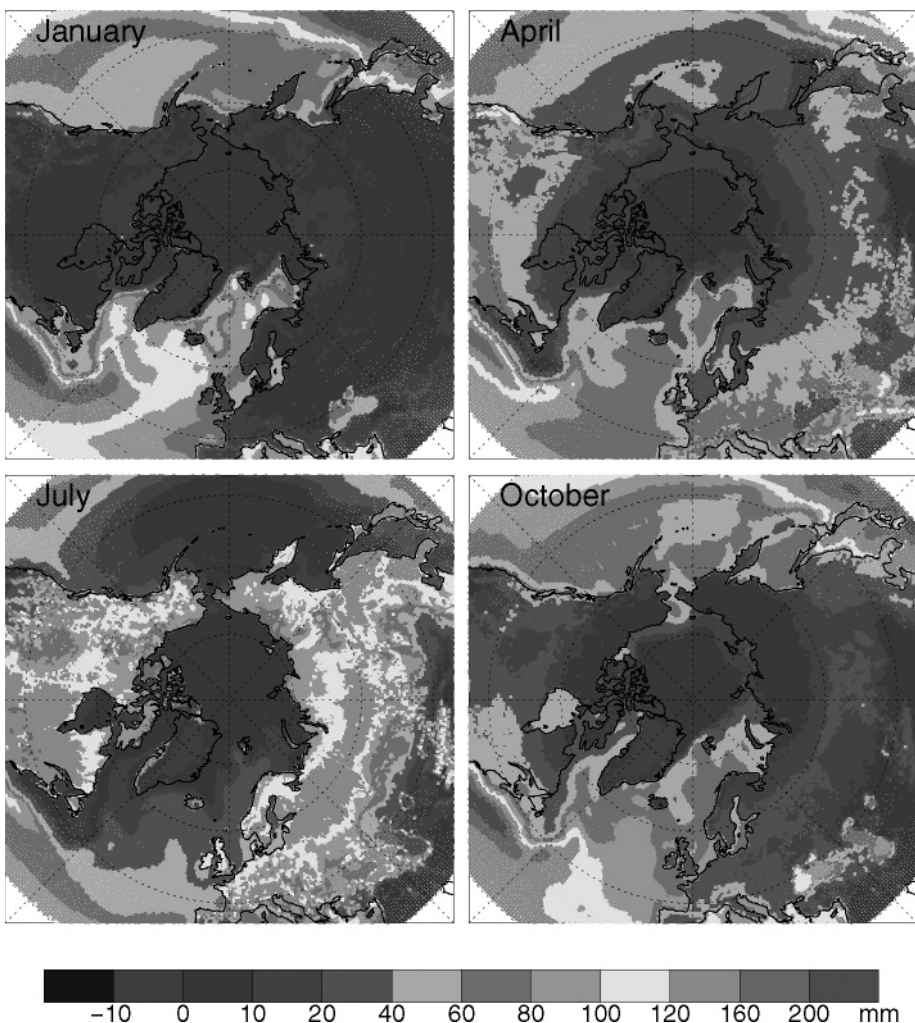


Figure 6.8. Evapotranspiration (mm, taken as positive upwards) for the four mid-season months based on MERRA data over the 1979–2009 period (courtesy D. Slater, NSIDC). (See plate section for color version.)

6.2.2 ET from a Reanalysis System

Figure 6.8 provide mean fields of ET for the four mid-season months over the 1979–2009 period, based on the MERRA (Modern Era Retrospective Analysis for Research and Applications) reanalysis. MERRA, produced by NASA, was designed with a focus on representing the hydrologic cycle and includes a state-of-the-art LSM. Of note in January is the low ET over Arctic land areas and the ice covered Arctic Ocean. Indeed, according to MERRA, for large areas over land, January ET is slightly negative, implying deposition (vapor to solid phase). Whereas deposition can certainly occur in winter (as can riming), observations point to a more important role of sublimation (solid to gas), especially during blowing snow events

(Kane et al., 1991; Hinzman et al., 1996). The small negative values in MERRA likely reflect shortcomings in MERRA's depiction of ET in very cold conditions with a stable boundary layer. Consistent with the presence of open water underlying a fairly cold and dry atmosphere, January ET over the Norwegian Sea locally exceeds 100 mm. However, these values pale in comparison to monthly means of more than 200 mm further south along the coast of North America where sea surface temperatures are fairly high and there are strong winds linked to the North Atlantic cyclone track. Similarly high January ET totals are found over the North Pacific. Compared to winter, ET totals over land areas are higher in spring, but remain very low over the ice-covered Arctic Ocean.

ET peaks over land areas in summer. A broad band of values from 120–160 mm extends across over the Eurasian subarctic, with values of 60–80 mm extending up to the Arctic coast. ET over the melting sea ice surface remains low; the skin temperature cannot depart from the freezing point, and the saturation vapor pressure for a melting (pure water) surface is only 6.1 hPa, limiting the magnitude of vertical vapor gradients. ET over the Norwegian Sea is lower than in winter, manifesting smaller vertical gradients in humidity and weaker winds. The field for October captures the transition back to the winter pattern.

6.2.3 Net Precipitation from the “Aerological Method”

In hydrologic analyses, net precipitation, or P-ET, is itself is a valuable term, and can be obtained in the absence of direct surface measurements of the two variables. Consider the moisture budget of an atmospheric column, extending from the surface to a height above which moisture content is negligible (e.g., 300 hPa). The budget can be expressed as

$$\partial W/\partial t = ET - P - \nabla \cdot Q \quad (6.2)$$

where the moisture content of the atmosphere, W , is expressed as precipitable water (the equivalent water depth of the vapor in the column). Time is given by t , ET is the surface evapo-transpiration rate, Q is the vertically integrated water vapor flux (a vector) from the surface to the top of the column and $\nabla \cdot Q$ is its divergence, and P is the precipitation rate. The equation hence summarizes the processes contributing to a time change in the column precipitable water ($\partial W/\partial t$). If there is ET from the surface into the column, precipitable water increases unless there is a corresponding moisture outflow. If there is precipitation, precipitable water decreases. It follows that if there is a horizontal divergence, precipitable water decreases, while it increases if there is convergence.

Rearrangement yields an expression for P-ET:

$$P - ET = -\nabla \cdot Q - \partial W/\partial t \quad (6.3)$$

For long-term annual means (and assuming a stationary climate), the last term of Equation 6.3 (the time change) is zero and may hence be dropped. The aerological approach neglects the atmospheric flux of water in the liquid and solid phases in

clouds. The liquid and solid flux is generally significant only in localized regions and for short time periods, such as over warm ocean currents and in cumulus clouds in the tropics.

The convenient aspect of Equation 6.3 is that the terms on the right can be calculated from vertical profiles of specific humidity and winds based on atmospheric reanalyses. This circumvents some of the problems with the direct observations of P and ET as well as biases in these surface variables typically present in reanalysis outputs (see Chapter 9 for more information). Having gridded fields of humidity and winds means that one can obtain gridded fields of P-ET (e.g., Cullather et al., 2000; Rogers et al., 2001). Before the advent of atmospheric reanalyses, most studies of P-ET using the aerological approach focused on large areal averages (e.g., the region north of 70°N), based on interpolating radiosonde data to the domain boundaries and averaging precipitable water over the domain (e.g., Walsh et al., 1994; Serreze et al., 1995a).

The atmospheric and surface branches of the hydrologic cycle can be linked by developing a similar expression for the surface:

$$P - ET = \nabla \cdot F + \partial S / \partial t \quad (6.4)$$

where S is the water content of the column underlying the atmosphere and \mathbf{F} represents lateral transports of water. The latter can be a complicated term because it includes both surface runoff and subsurface flows in terrestrial regions and the advection of ice and water in the oceans. Strictly speaking, P-ET is the same in Equations 6.3 and 6.4 only if one assumes that the surface is an atmospheric column's only "source" of ET and its only "sink" of P (Walsh et al., 1994).

While the aerological approach is attractive, it has its drawbacks. Humidity fields from reanalyses may contain errors related to shortcomings in data assimilation methods (both for radiosondes and satellite retrievals). For example, it appears that all modern reanalysis systems – including MERRA, the NCEP Climate Forecast System Reanalysis (CFSR), and ECMWF ERA-Interim – have a positive cold-season humidity and temperature biases below the 850 hPa level (Serreze et al., 2012). The vapor flux convergence is also sensitive to errors in the wind fields, which reflect the available density of assimilation data and temporal changes in the reporting network, and quality of the atmospheric model. In general, P-ET computed from the aerological method and from the reanalysis forecasts of P and ET do not balance (i.e., water is not conserved in reanalyses).

Despite such shortcomings, the aerological approach applied to atmospheric reanalysis seems to work fairly well. This is supported from the study of Cullather et al. (2000), who compared the annual meridional flux of moisture across 70°N from the NCEP/NCAR and ERA-15 reanalyses against values computed via interpolation of radiosonde data. Annual-average fluxes from both models are significantly higher than the radiosonde estimates during summer, with better correspondence during winter. Closer examination points to the radiosonde network being insufficiently dense to capture the major moisture transport "pathways" into the Arctic (Zhu and Newell, 1998). Put differently, the reanalyses seem to provide more realistic depictions of the flux. Aerological P-ET averaged for the region north

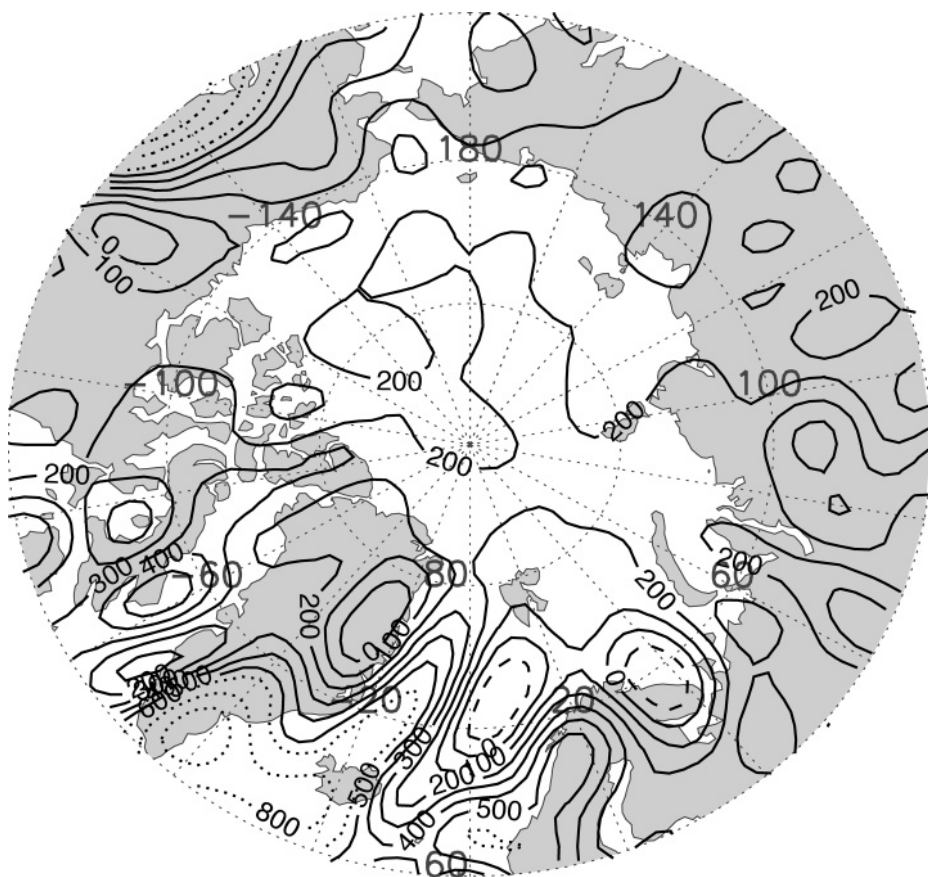


Figure 6.9. Aerological estimates of mean annual precipitation minus evapotranspiration (P-ET) based on NCEP/NCAR data for the 1970–1999 period. Contours are at every 100 mm up to 500 m (negative values dashed) and at every 200 mm for amounts of 600 mm and higher (by the authors).

of 70°N from the two models is very similar, with a value of 188 \pm 6 mm per year, compared with the radiosonde-derived estimate of 163 mm per year.

The mean annual field of P-ET based on the NCEP/NCAR reanalysis over the 1970–1999 period is provided in Figure 6.9. Fields for the mid-season months appear in Figure 6.10. The fields shown here are similar to those from other reanalyses. Annual P-ET over the central Arctic Ocean is 200–300 mm, broadly similar to annual precipitation. The implication is that annual ET is small in this region, which is borne out clearly from the SHEBA results discussed earlier and from the MERRA ET fields (Figure 6.8). A further implication is that estimates of precipitation over the central Arctic Ocean can be obtained from the P-ET field in the absence of surface observations. The annual excess of P over ET is greatest off the Greenland coast and around Iceland as well southern Alaska where precipitation is high. Note the area of negative P-ET south of Svalbard. Like the annual cycle in precipitation, P-ET has a summer maximum and cold season minimum over the Arctic Ocean while the areas off eastern Greenland and along southern Alaska have a cold season

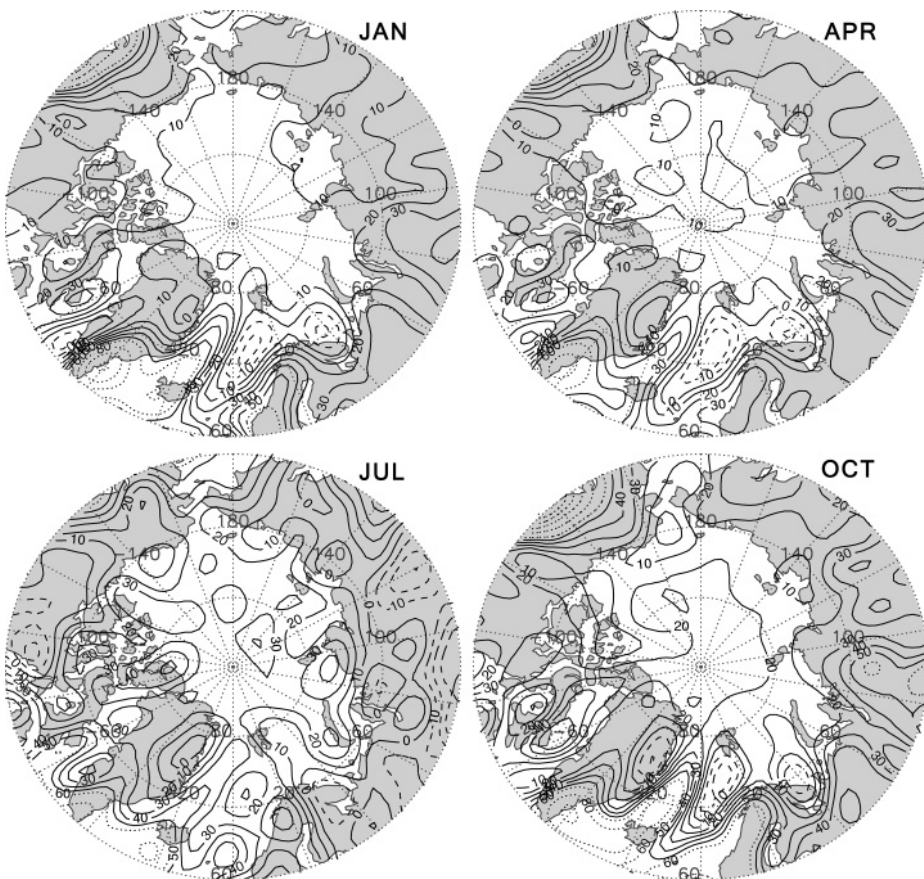


Figure 6.10. Aerological estimates of mean precipitation minus evaporation ($P-E$) for the four mid-season months based on NCEP/NCAR data for the 1970–1999 period. Contours are at every 10 mm for amounts up to 50 mm (negative values dashed) and at every 20 mm for amounts of 60 mm and higher (by the authors).

maximum and summer minimum. By comparison, $P-ET$ over much of the land area is at a minimum in summer, in rough antiphase with precipitation. Over Eurasia, $P-ET$ in June and July is negative over large areas. This manifests fairly high summer ET rates, as seen in the MERRA ET fields. We will return to this issue shortly. The region of negative $P-ET$ south of Svalbard is not present in the summer months. The feature appears to be associated with strong evaporation in the cold months associated with the contrast between open water and the cold, dry overlying atmosphere (see Figure 6.8). The impact of strong convective heating in this area on the heat budget of the polar cap was examined in Chapter 3.

6.3 Hydrologic Impacts of the NAO and AO

Recall from Chapter 4 that the North Atlantic Oscillation, or NAO, is an atmospheric teleconnection characterized by covariation in the strength of the Icelandic Low and

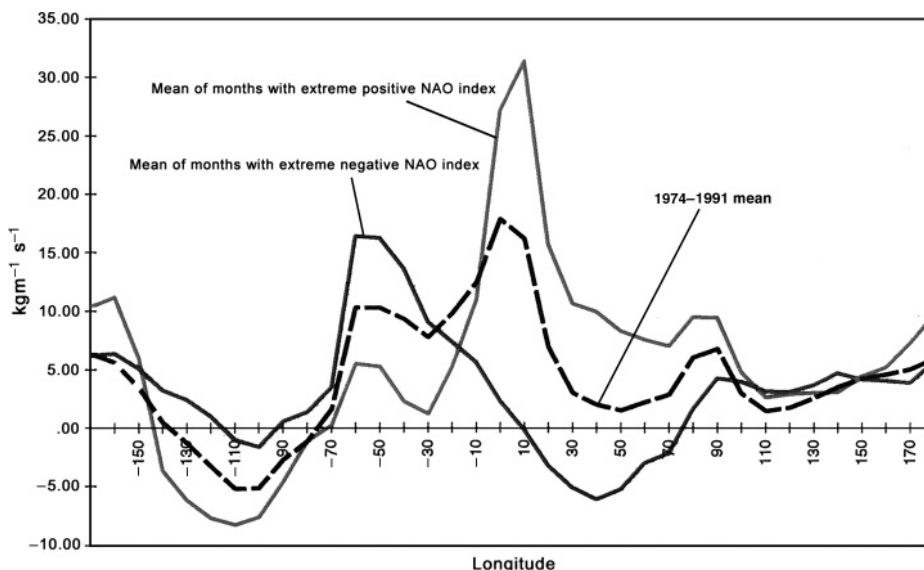


Figure 6.11. Vertically integrated meridional moisture flux crossing 70°N in winter expressed as a function of longitude for composites of winter (DJF) months representing positive-index and negative-index NAO extremes. The 1974–1991 winter mean is also shown (from Dickson et al., 2000, by permission of AMS).

the Azores high, the two major atmospheric centers of action in the North Atlantic. As discussed there, and apparent in Figure 4.19, the phase of the NAO, particularly in winter, is associated with anomalies in surface air temperature encompassing large parts of the Arctic, similar in structure to those associated with the phase of the Arctic Oscillation, or AO (Figure 4.22). It should come as no surprise that the NAO/AO also has pronounced hydrologic impacts (in Chapter 7 we examine impacts on the sea ice cover).

As part of their summary of high-latitude NAO impacts, Dickson et al. (2000) compared patterns of the vertically integrated moisture flux across 70°N for winters associated with NAO extremes. The data set spanned the years 1974–1991. Their analysis (Figure 6.11) shows that the poleward meridional moisture flux for longitudes along the Nordic seas is much higher under the positive NAO phase when the Icelandic Low is strong. The positive NAO is also associated with a stronger southerly moisture flux between about $70\text{--}140^{\circ}\text{W}$ over Canada. In turn, there are strong NAO precipitation signals in the Atlantic gateway to the Arctic. Dickson et al. (2000) compiled composite differences of Northern Hemisphere precipitation with respect to NAO extremes using a blended land/ocean data set for 1979–1995. The largest precipitation increases (up to 150 mm per winter) during positive NAO conditions are found in the Norwegian-Greenland seas and Scandinavia.

Rogers et al. (2001) performed a comprehensive assessment of relationships between the NAO and AO with P-ET as averaged over the north polar cap (the region north of 70°N). P-ET was calculated from the aerological method using data from the NCEP/NCAR reanalysis. For winter, spring, summer, and autumn,

basin-averaged P-ET correlates with the NAO (AO) index at 0.49(0.56), 0.42(0.57), 0.29(0.56), and 0.49(0.36), respectively. The strongest relationship is for annual P-ET, which correlates with the NAO (AO) at 0.69(0.49). In accord with the analyses just described, the strongest P-ET signals associated with the NAO are found in the Atlantic sector and extending north into the Arctic Ocean during winter (see also Hurrell et al., 2003).

Recall also from Chapter 4 that the structure of the AO depends on how the AO is calculated. When the AO is calculated separately for each calendar month, as done by Ogi et al. (2004), the summer pattern has a distinct center of action lying over the central Arctic Ocean; the positive mode is associated with low sea level pressure over the central Arctic Ocean, linked in turn to a high frequency of cyclone activity. It hence follows that the summer AO mode is associated with positive precipitation anomalies over the central Arctic Ocean.

6.4 Annual Cycles for the Major Terrestrial Drainages

6.4.1 P, P-ET and ET

Figure 6.12 shows mean annual cycles (1960–1989) of estimated P, P-ET, and ET for the four major drainage basins of the Arctic (the Ob, the Yenisey, the Lena, and the Mackenzie). The monthly values of P and P-ET are simple averages of the data at all grid points located within each basin. ET is computed as a residual from the basin-mean values of P and P-ET.

Following earlier results, in all four basins, precipitation is at a minimum in February and March and is at a maximum during July. P-ET tends to peak during autumn. These autumn maxima arise from the combined effects of a stronger vapor flux convergence and a strong seasonal decrease in precipitable water (i.e., a decrease in water vapor storage). The general inverse relationship between the annual cycles in P and P-ET is best expressed in the Ob (the westernmost basin). Here, mean P-ET for June and July is about -10 mm. Mean July P-ET is close to zero for the Mackenzie. Walsh et al. (1994) obtained qualitatively similar results for the Mackenzie using fluxes calculated from interpolated radiosondes data. The July maxima in ET estimated as the residual lie between 60–75 mm, highest for the Ob. The Ob also has the highest winter ET rates.

6.4.2 Precipitation Recycling

The amount of precipitation falling over a region can be divided into: (1) precipitation associated with water vapor transported into the region (adverted precipitation); and (2) precipitation associated with water that evaporates from the surface of the region and falls within the same region (locally derived precipitation). The precipitation recycling ratio is defined as P_m/P , where P_m is the precipitation of local origin and P is the total precipitation. The recycling ratio can be thought of as providing

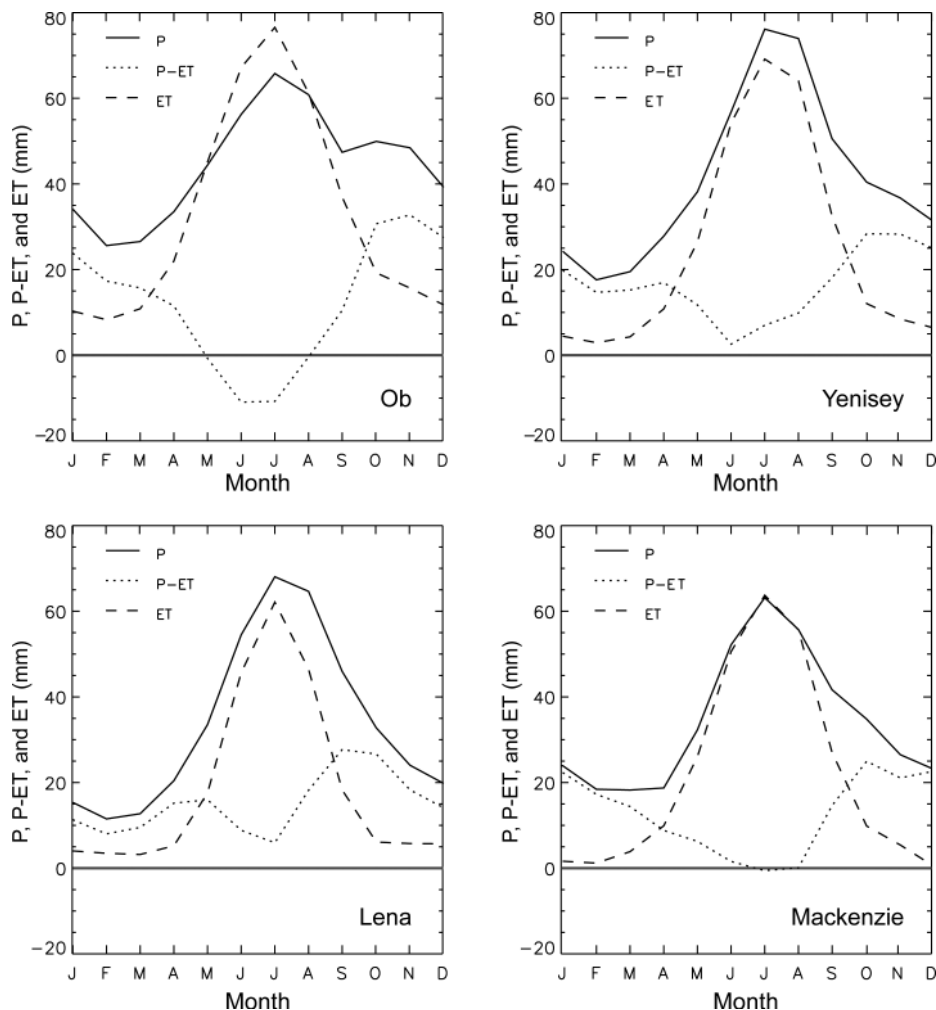


Figure 6.12. Mean monthly precipitation (P), precipitation minus evapotranspiration (P-ET), and evapotranspiration (ET) for the four major Arctic-draining watersheds, based on data from 1960 through 1989 (mm). ET is calculated as a residual from P and P-ET (adapted from Serreze et al., 2003a, by permission of AGU).

a sense of the importance of land-surface processes on the hydrologic budget. The topic has a long history, starting with Mikhail Budyko and associates in the Soviet Union in the 1950s. Notable studies include K. Brubaker, D. Entekhabi, and P. Eagleson (1993), E. Eltahir and R. Bras (1996), and Trenberth (1998). Estimates of the recycling ratio are contingent on the size of the region considered. The ratio is smaller for areas of limited extent and increases for larger regions. Obviously, all precipitation is recycled at the global scale.

Serreze et al. (2003a) examined monthly precipitation recycling for four areas with identical area and shape. The four regions are bounded by 50°N and 70°N latitude and each span 25°E longitude bands from 60–85°E (west-central Eurasia),

85–110°E (central Eurasia), 110–135°E (east central Eurasia) and 110–135°W (western North America). The area of each region is 3.08×10^6 km². These regions were chosen to roughly represent the four major Arctic watersheds. Equal areas were chosen (rather than areas defined by the true basin boundaries) to allow for direct comparisons. The western North American domain (Mackenzie) does include some ocean areas as well as coastal regions where precipitation is very high. Results are based on the 1960–1999 period for the Eurasian domains and 1960–1989 for the western North American domain.

A number of different formulations of the recycling ratio can be found in the literature. Following the recommendation of Trenberth (1998), Serreze et al. (2003a) employed the formulation of Brubaker et al. (1993). This is given as:

$$\frac{P_m}{P} = \frac{1}{1 + \frac{2 * F^+}{ET * A}} \quad (6.5)$$

where A is the area of the region and F+ is the advective moisture term. The advective moisture term is calculated as the line integral of the component of the vertically integrated moisture flux directed into the region. It should not be confused with the vapor flux convergence, which is the difference between F+ and the component of the moisture flux directed out of the domain (F-). Calculation of F+ uses the monthly mean vertically integrated moisture fluxes at the 2.5 × 2.5 degree grid available from the NCEP/NCAR reanalysis. ET is averaged over the region and is based on the difference between P and P-ET as obtained from the aerological approach. The formulation assumes equilibrium conditions and a well-mixed atmosphere. This means no changes in atmospheric moisture content, and, that the ratio of advected to locally derived precipitation is equal to the ratio of average advected to evaporated moisture in the air. Inspection of Equation 6.5 shows that a large precipitation recycling ratio will result when the moisture advection term F+ is small in comparison with ET.

For the Eurasian domains (Figure 6.13), the ratio is largest during July. This is primarily attributed to the peak in ET as the term F+ still tends to be fairly large in summer. By contrast, the peak for the western North American (Mackenzie) domain is one month earlier in June. Peak values range from 0.22 (Central and Eastern Eurasia, or Lena) to 0.28 (central Eurasia, or Yenisey). This points to a significant effect of the land surface on the summer hydrologic regime. Winter values range from 0.0 to 0.11, largest for western North America.

6.5 River Discharge and Runoff

6.5.1 River Discharge Data

River discharge is measured as water volume per unit time. The unit time is often implied (e.g., we might say that we have a certain mean discharge for June). Runoff

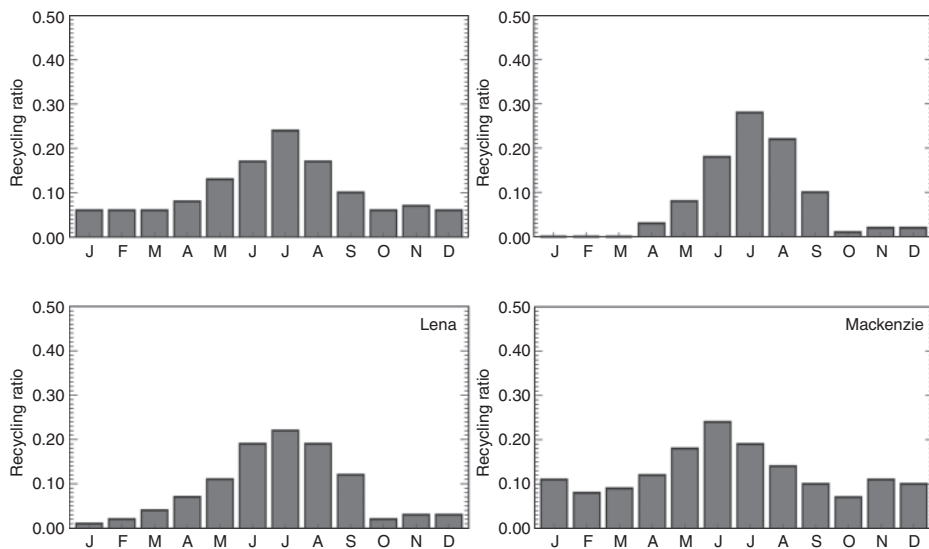


Figure 6.13. Mean monthly precipitation recycling ratio (P_m/P) for four domains chosen to approximate represent the Ob, the Yenisey, the Lena, and the Mackenzie basins (from Serreze et al., 2003a, by permission of AGU).

is simply discharge divided by the area of the contributing watershed, and hence has units of depth per unit time. In water balance studies it is common to make use of runoff as it has the same units typically used for precipitation and evapotranspiration.

The most comprehensive network of discharge gauging stations in the terrestrial Arctic drainage is represented by R-ArcticNET, which was compiled from original national sources by investigators at the University of New Hampshire, Durham. Version 4.0 of R-ArcticNET holds data from more than 3,700 sites. Figure 6.14 gives the location of the subset of gauges for basins of at least 10^4 km^2 . Also shown is a digital river network at 30 min \times 30 min (longitude \times latitude) (known as STN-30p) developed by C. Vorosmarty et al. (2000) for the pan-Arctic drainage. The lines over the Arctic Ocean roughly indicate the sea basins into which the different river systems empty. The river network does not include the Greenland Ice Sheet, but does include the ice-free portions of Greenland. Within the confines of the terrestrial Arctic drainage at this resolution there are 1,967 individual drainage systems discharging to the ocean, encompassing a land area of $22.4 \times 10^6 \text{ km}^2$. As summarized by R. Lammers et al. (2001), typical errors for measured discharge are within the range of $-/+ 2$ to 5 percent for non-ice conditions in river cross sections without floodplains and $+/- 5$ to 12 percent for rivers with floodplains. Maximum errors are in mountain rivers and can be as high as 25 percent. When temperatures are low, the discharge estimates are more uncertain owing to anchor ice, frazil ice, and backwater conditions, as well as floodplain icings (aufeis, see Chapter 2, also see Barry and Gan, 2011, chapter 6).

More than 70 percent of the total Arctic drainage area has been monitored by at least one gauge since 1936 (Figure 6.15). However, in the North American part of

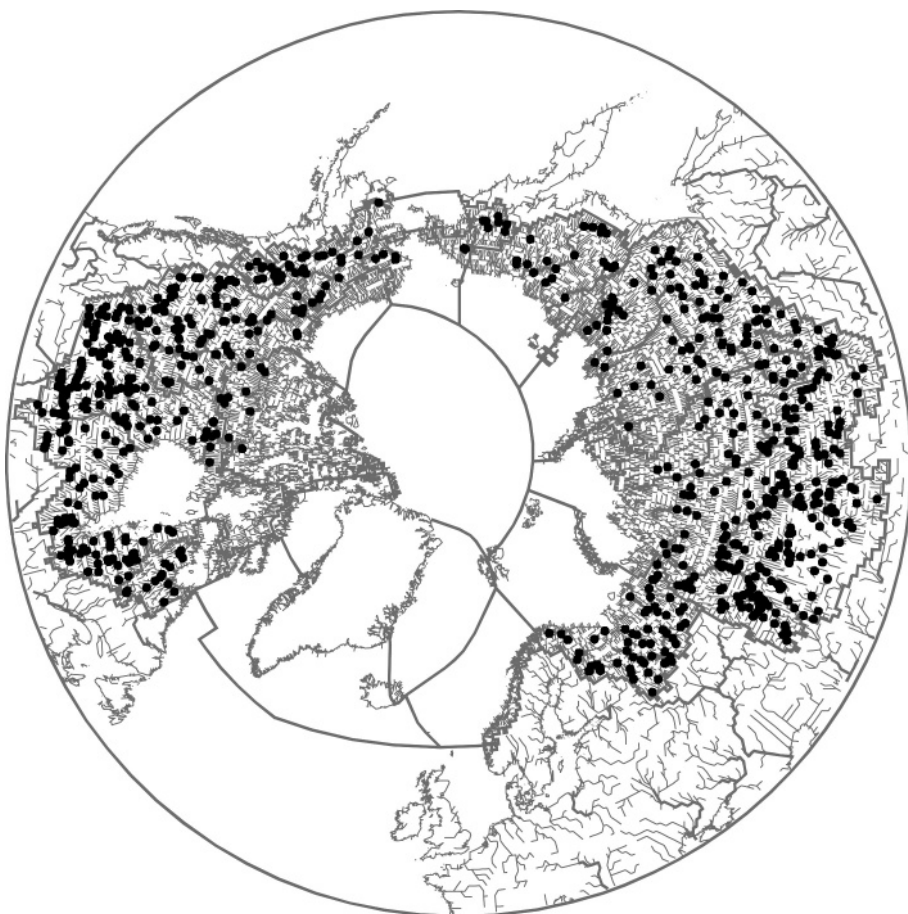


Figure 6.14. River system for the Arctic terrestrial drainage based on the STN-30 digital network and location of discharge gauging stations for basins with areas greater than 10,000 km² (from Lammers et al., 2001, by permission of AGU).

the drainage, the total gauged area did not surpass 50 percent until 1964. Since 1985, there has been a large decrease in the number of gauges over Eurasia. Fortunately, this has not significantly reduced the total monitored area as the gauges no longer in operation are usually not the most downstream gauges.

6.5.2 The Major River Systems

Most of the river discharge to the Arctic Ocean is delivered through a small number of large rivers. Following from the previous discussion, only twelve hydrological gauges are sufficient to capture 91 percent of the total monitored area and 85 percent of the total monitored discharge (Shiklomanov et al., 2000, Lammers et al., 2001). The four largest drainage basins (the Ob, the Yenisey, the Lena, and the Mackenzie; see Figure 2.8) contribute about 68 percent of the total gauged volume

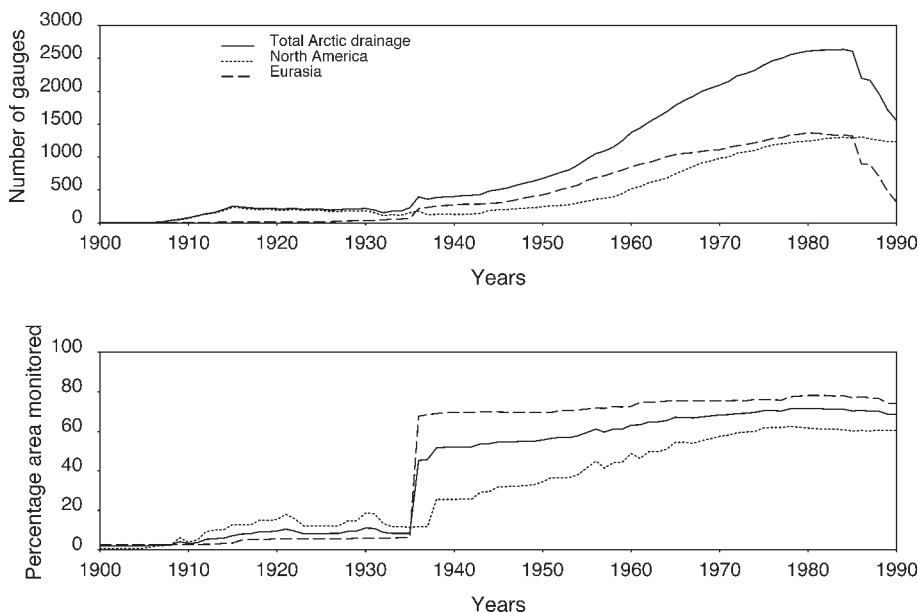


Figure 6.15. Number of gauges in the R-ArcticNET database through time and the percentage of the drainage area monitored. Data are shown for North America, Eurasia, and the Arctic drainage as a whole. Only gauges monitoring an area greater than 10,000 km² are used for the percentage of area monitored (adapted from Lammers et al., 2001, by permission of AGU).

discharge to the Arctic Ocean on an annual basis. The Lena, the Ob, and the Yenisei alone contribute on average 57 percent of the total discharge.

6.5.3 Surface of Mean Annual Runoff

Recall that runoff is discharge divided by the catchment area. It has units of water depth. Gauge data can be used to construct surfaces of runoff. Figure 6.16 is the mean annual runoff surface over the January 1960 to December 1989 period for the monitored part of the Arctic drainage. Following N. Arnell (1995), calculations of runoff were made for all “interstation areas.” These were obtained by subtracting all upstream discharge values from the discharge value at the next downstream gauge. Runoff was then calculated by dividing the interstation discharge by the interstation drainage area. The monthly interstation runoff values for each gauge were then distributed to the interstation regions to provide a gridded field.

The spatial resolution of the runoff surfaces that can be obtained depends on the density of the gauge network, which varies greatly. For large interstation areas, inconsistencies can be introduced because of the long transit time of water moving downstream in the river system. Flow diversions and impoundments (dams and irrigation channels) can significantly alter the natural drainage. Known problem areas include the Nelson/Churchill rivers in western Canada, the La Grande hydroelectric

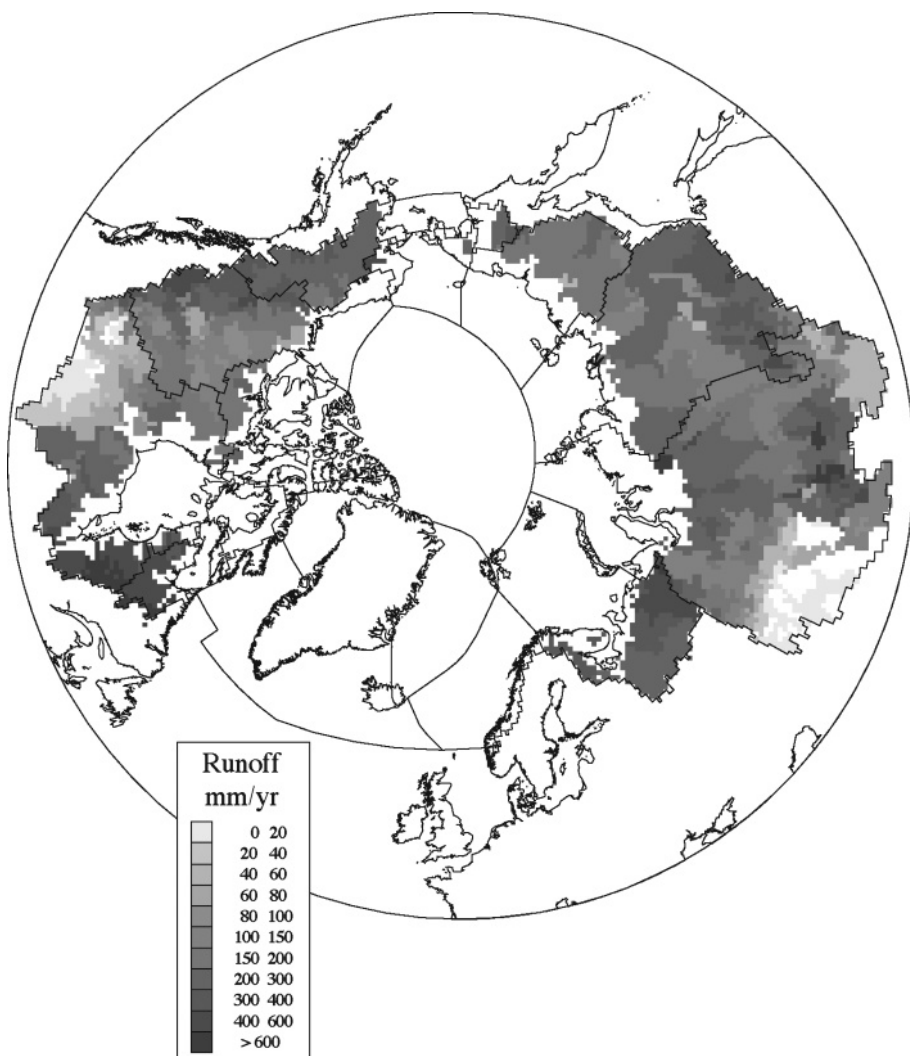


Figure 6.16. Mean annual runoff surface for the Arctic Drainage over the January 1960–December 1989 period. White areas within the southern Ob basin represent internal drainage basins. Large areas along the Arctic Ocean coast and the Canadian Arctic Archipelago (shown as white) are ungauged (from Lammers et al., 2001, by permission of AGU). (See plate section for color version.)

complex east of James Bay, the southern Ob, the main stem of the Yenisey River, and the lower Lena. B. Ye, D. Yang, and D. Kane (2003) provide a comprehensive assessment of problems in the Lena. However, at least for annual discharge, anthropogenic effects are considered to be as yet fairly minor for the Arctic drainage as a whole as compared to other parts of the world (Lammers et al., 2001). Some strong impacts have been documented with respect to winter discharge.

Annual runoff is highest over the mountainous regions of central and Eastern Siberia and along the Rocky Mountains in western Canada, the European part of

Russia and the eastern Hudson Bay drainage in Quebec. Areas of low runoff include the southwestern Ob Basin and the south-central part of the drainage in Canada. The mean annual runoff as averaged across the Arctic drainage is calculated at 212 mm yr^{-1} . There should be a correspondence between mean annual runoff and mean annual P-ET as computed from atmospheric reanalyses. Annual P-ET fields interpolated to the Arctic drainage do capture the general features of observed runoff. There is also considerable disagreement, however, related to the different resolutions of the data sets and to errors in the reanalysis fields.

The ungauged areas of the Arctic drainage can be assessed by comparing Figure 6.16 and Figure 6.14. The ungauged areas include much of coastal Eurasia, the Arctic islands, northern Alaska, and the Canadian Arctic Archipelago. It remains a challenge to estimate runoff from these ungauged areas and assess their contribution to the freshwater budget of the Arctic Ocean.

6.5.4 Annual Runoff for the Major Drainage Basins

Table 6.1 provides basin-averaged values for the four major river systems of precipitation (P), P-ET, ET, and runoff (RU) along with estimates of the runoff ratio (RU/P) and the fraction of precipitation lost through ET (ET/P). These are calculated over the water year. The water year is often more convenient and physically meaningful for hydrologic applications than the standard calendar year. Here, the water year is defined as October (when snowfall starts to accumulate) through September (the end of the summer). Precipitation is based on the analysis of Serreze et al. (2003a). Runoff is based on updated records in R-ArcticNET. In contrast to previous results, ET is estimated as the difference between P and RU. The means for the Eurasian basins are based on the water years 1960/1961 through 1997/1998 (thirty-nine years). For the Mackenzie, the shorter time series of precipitation and of discharge (at Red River station) results in only seventeen years with shared records.

L. Bowling, D. Lettenmaier, and B. Matheussen (2000) summarize various estimates of RU/P for the major Arctic-flowing rivers. RU/P can be thought of as the efficiency in which precipitation is converted to runoff. Values for the Ob range from 0.25 to 0.33. These are considerably lower than estimates for the Yenisey

Table 6.1. Components of the water budget averaged for water years (October through September) for the four major drainage basins

	P (mm)	ET (mm)	RU (mm)	RU/P	ET/P	Basin Area (10^6 km^2)
Ob	533	396	138	0.26	0.74	3.02
Yenisey	495	256	239	0.48	0.52	2.58
Lena	403	182	221	0.55	0.45	2.44
Mackenzie	411	241	171	0.41	0.59	1.69

Note: Basin areas are also provided.

Source: From Serreze et al. (2003a).

Table 6.2. Mean SAT (January and July), number of snow-free days, percent of wetlands and percent permafrost cover for the four major drainage basins

	January (°C)	July (°C)	Snow-Free Days	Wetlands Cover (%)	% Area Underlain by Permafrost
Ob	-18.7	18.1	186	6.6	4–10
Yenisey	-26.5	15.2	163	3.7	36–55
Lena	-35.0	14.7	144	0.8	78–93
Mackenzie	-25.0	13.8	167	6.5	32–58

Source: From Serreze et al. (2003a).

(0.47 to 0.54) and the Lena (0.46 to 0.61). Existing estimates for the Mackenzie are intermediate (0.30 to 0.46). The ranges for each watershed reflect the use of different precipitation data sets. The runoff ratios in Table 6.1 are in accord with previous estimates. The basins can be similarly contrasted in terms of ET/P. Water-year precipitation in the Ob is comparable to that for the Yenisey but is about 20 percent higher than for the Lena and Mackenzie. However, a greater fraction of the precipitation is lost through ET in the Ob.

The contrast between the Ob and the other basins in terms of RU/P and ET/P is understood from differences in climatological surface air temperature, land cover, and permafrost extent. Table 6.2 lists basin averages of mean January and July surface air temperature, the annual mean number of snow-free days and the percent of the surface represented by wetlands, and the percent of the basin areas covered by permafrost. The range in permafrost coverage reflects a range of assumptions used in the calculations (see Serreze et al., 2003a). There is a progression from moderately low January temperatures in the Ob (-18.7°C) to very cold conditions in the Lena (-35.0°C). Low mean temperatures also characterize the Mackenzie basin. The temperature distribution is in accord with the higher winter ET rates in the Ob. July temperatures are also highest in the Ob, consistent with the higher summer ET in this area. As would be expected, the number of snow-free days is also much greater in the Ob, pointing to earlier and more prolonged warming of the soil. This will also contribute to higher ET rates. Furthermore, in comparison to the other Eurasian basins, a larger part of the Ob is characterized as wetlands. ET over these areas is not limited by available moisture. More than 6 percent of the Mackenzie is also characterized as wetlands. The net effect of higher ET in the Ob is to reduce RU/P and increase ET/P relative to the other basins.

The differences in runoff ratios are also related to permafrost. Figure 2.15 shows the distribution of continuous, discontinuous and sporadic permafrost across the Northern Hemisphere. Permafrost acts as an impermeable barrier, such that precipitation can be rapidly channeled into streams and rivers rather than recharging soil moisture and groundwater. It will also restrict plant growth through the growing season and limit root depth, reducing water losses through ET. The effect of both is to increase RU/P. From Table 6.1, the largest contrast in RU/P is between the Ob and

Lena. Only 4–10 percent of the Ob basin is underlain by permafrost (contributing to low RU/P), in contrast to 78–93 percent of the Lena, which is mostly represented by continuous permafrost (contributing to high RU/P). The extent of permafrost in the Yenisey and Mackenzie is between that for the Ob and Lena. In turn, these two basins have intermediate runoff ratios.

6.5.5 Mean Hydrographs

Long-term annual mean runoff ought to approximately balance P-ET, but this is not true of means for seasonal and shorter time scales. The most obvious reason is that for much of the year, the net precipitation is stored in the snowpack. There are also subsurface storages. The typical annual cycle is as follows: In the cold months, runoff is small, and can even cease for small rivers. Runoff begins to climb in April or May when the snowpack begins to melt. It then increases sharply, generally with a June peak. This is the same general pattern we would see for any region in the Northern Hemisphere (e.g., the Colorado Rocky Mountains) where there is significant seasonal snowpack storage. As assessed over the Arctic drainage as a whole, approximately 60 percent of the discharge occurs from April to July (Lammers et al., 2001). However, the shapes of the mean hydrographs (plots of runoff or discharge versus time) vary between different basins in response to temperature as it influences snowmelt and ET, the mean water equivalent of the snowpack, the seasonality of precipitation, permafrost conditions, soil moisture and groundwater recharge, runoff storage in wetlands and other factors.

Differences in the mean water-year hydrographs for the Ob, the Yenisei, the Lena, and the Mackenzie (Figure 6.17) capture some of these processes. Although runoff peaks in June for all basins, the peaks are much sharper in the Yenisey and Lena as compared with the Ob. In part, this manifests lower mean temperatures in the Yenisey and Lena from autumn through spring, meaning a longer period of snow accumulation and delayed spring melt. Once it becomes warm enough in June, the rapid melt of the snowpack gives rise to sharp runoff peaks. Especially for the Lena, the large extent of continuous permafrost fosters rapid movement of meltwater to streams, further contributing to the sharp June runoff peak. Over the 1970–1999 period, 35 percent of total discharge at the mouth of the Lena occurs in June and a further 20 percent in July (Yang et al., 2002). By contrast, especially for the Ob, a large proportion of precipitation is lost through ET, especially in summer, and is not available for runoff. Other effects not considered here include snowmelt storage in lakes and wetlands and aufeis (see Chapter 2) that can subdue peak discharge. Storage in lakes and wetlands can be pronounced for North American rivers such as the Mackenzie. River and lake ice is a further storage component.

6.5.6 Variability

Precipitation, evaporation, and river discharge are all highly variable on monthly and shorter time scales. Figure 6.18 provides one example. This figure shows for

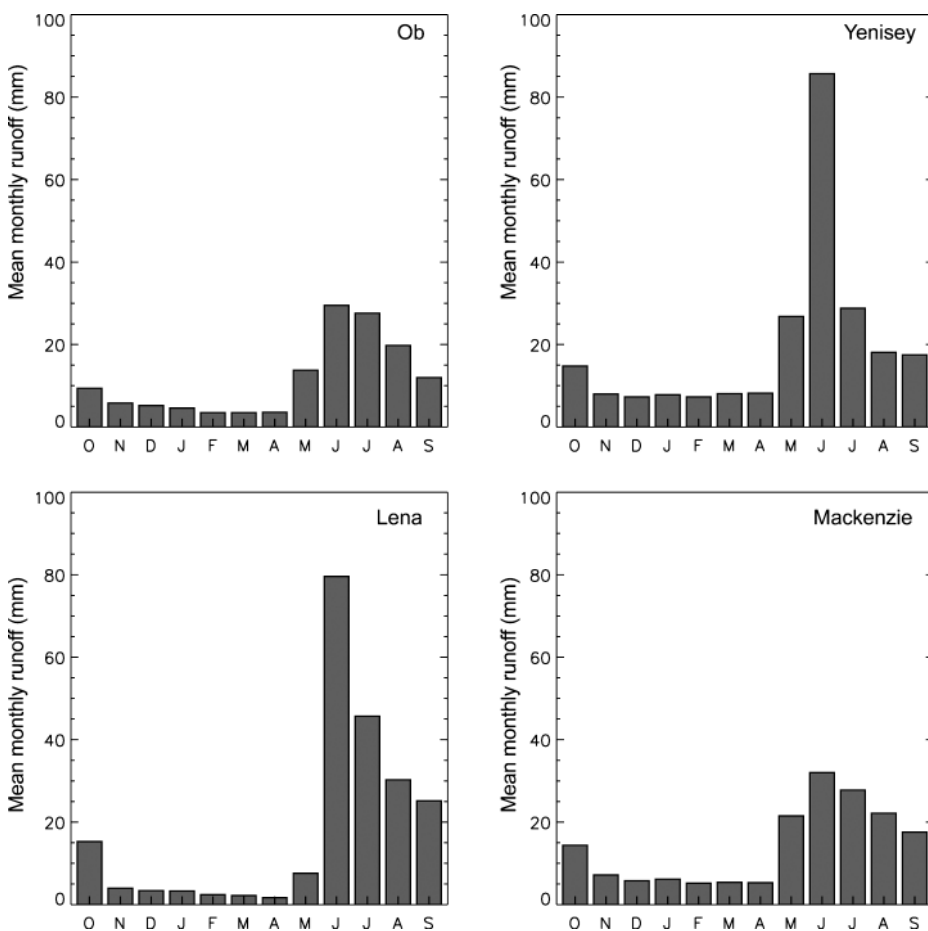


Figure 6.17. Mean hydrographs for the four major Arctic-draining rivers (at the gauge sites closest to the river mouths) expressed in terms of runoff (mm) (adapted from Serreze et al., 2003a, by permission of AGU).

two years (1980 and 1981) daily time series of precipitation for the Lena basin, based on averaging data for all monitoring stations within the basin. Also given is the mean annual cycle, based on monthly means for the 1960–1992 period. It is clear that the mean annual cycle, even on the large scale of the Lena, is superposed on highly variable precipitation on a day to day basis. As would be expected, the largest daily precipitation events tend to be associated with well-defined cyclonic systems (Serreze and Etringer, 2003).

Another example is provided by monthly discharge at the mouth of the Lena River over the 1936–1995 period (Figure 6.19). One of the key features is the large year-to-year variability from May through October. This relates to variations in the water equivalent of the snowpack, temperature as it influences snow melt, and the relative frequency of widespread and intense precipitation events (such as those just discussed). The variability is especially pronounced in May, pointing to variations

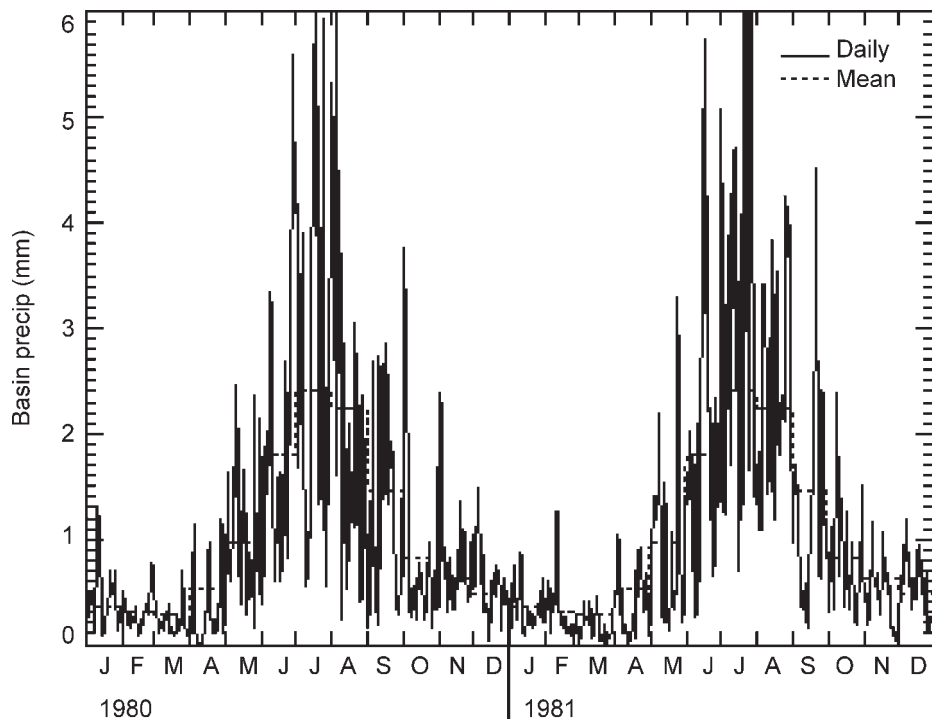


Figure 6.18. Daily average precipitation over the Lena for 1980 and 1981 (solid line) along with the mean annual cycle (dotted line) over the 1960–1991 period (from Serreze and Etringer, 2003, by permission of John Wiley and Sons).

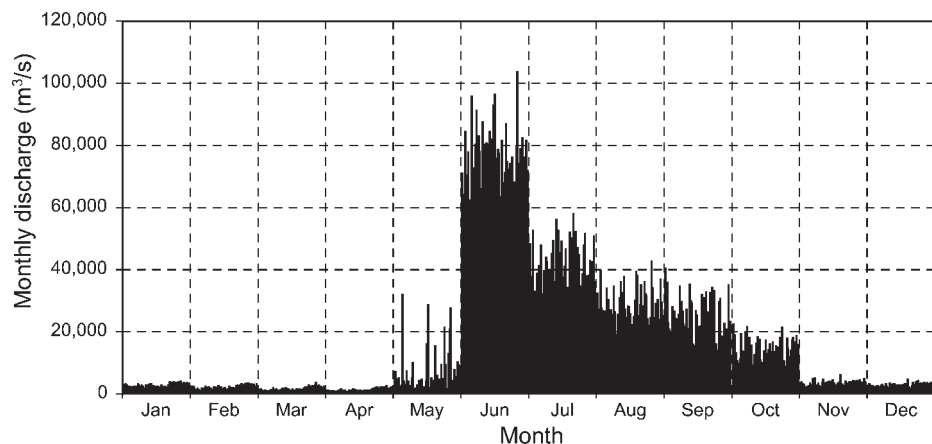


Figure 6.19. Monthly discharge ($\text{m}^3 \text{s}^{-1}$) at the mouth of the Lena over the 1936–1999 period. For each month, the plot shows the discharge for all years (from Yang et al., 2002, by permission of AGU).

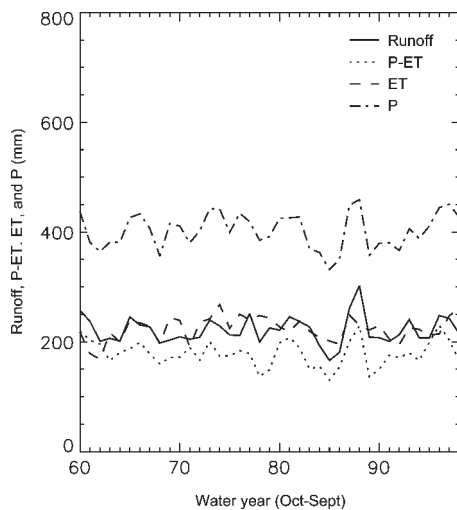


Figure 6.20. Water-year time series of runoff, precipitation (P), precipitation minus evapotranspiration (P-ET), and ET for the Lena. ET is calculated as a residual from P and P-ET. P is adjusted for estimated gauge undercatch and P-ET is from aerological estimates using NCEP/NCAR reanalysis data (adapted from Serreze et al., 2003a, by permission of AGU).

in the timing of snow melt. Early melt leads to greater discharge in May. Other factors being equal, less of the snowpack is left during June, reducing runoff in this month. A late snow melt typically means less runoff in May, and more in June. For smaller watersheds, variability in discharge will be more pronounced – for example, a single summer precipitation event over a small watershed in the Lena can result in a pronounced hydrograph peak, which may be reflected only weakly at the mouth of the Lena some time later. Another factor that can lead variations in runoff is ice jams, which block the flow of river. When the jam breaks, there is a rapid discharge of water. Ice jams can sometimes cause catastrophic flooding of downstream communities.

A final example is provided by water-year time series of runoff, P-ET, ET, and P for the Lena (Figure 6.20). P-ET is based on aerological estimates from the NCEP/NCAR reanalysis. The precipitation data contain adjustments for estimated gauge undercatch. ET is again estimated as a residual. Runoff is based in records in R-ArcticNET. The time series of annual P and P-ET are highly correlated, as they are in the other major river basins. In the Ob, the Yenisey, and the Mackenzie, the correlation between water year runoff and precipitation is quite weak, as is the correlation (shared variance) between runoff and P-ET. But this is not true for the Lena. Over the 1960–1999 period, the squared correlation between water year runoff and P-ET and between runoff and precipitation is 0.52 and 0.61, respectively.

These interbasin differences may point to effects such as diversions and impoundments, but these are not considered to be major at the present time, at least for water year means. The primary reason for these differences lies with the extensive permafrost in the Lena. Most of the Lena is underlain by continuous permafrost. As discussed, the impermeable permafrost layer promotes rapid movement of precipitation into river networks and will dampen interannual variations in groundwater recharge. The low correlations for the Ob, the Yenisey, and the Mackenzie, where there is less permafrost, point to recharge effects.

6.5.7 Trends in Discharge

Annual discharge from Eurasian rivers draining into the Arctic Ocean is increasing. This was first documented by Peterson et al. (2002), who found that the annual discharge aggregated for the six largest Eurasian rivers draining into the Arctic Ocean increased by about 7 percent over the 1936–1999 period. Aggregate discharge was computed to be 128 km³ greater than it was when routine measurements began. To put this change into perspective, the annual mean discharge from the Yenisey River is about 630 km³ yr⁻¹. Pointing to controls by atmospheric circulation patterns, they showed that annual Eurasian discharge was correlated with the index of the NAO. Yang et al. (2002) examined changes in discharge at the mouth of the Lena Basin for the 1935–1999 period. They noted significant increases (35–90 percent) in discharge during the cold season, decreases in river ice thickness and a hydrologic shift toward more discharge in May, and lower daily maximum discharge in June. Hydrologic changes in summer were less apparent. Serreze et al. (2003a) noted similar, albeit larger winter discharge increases in the Yenisey as well as shifts in peak discharge to earlier in the season.

J. McClelland et al. (2004) argued that while both the annual trend in discharge and the shift in peak discharge to earlier in the season represent true climate signals, the winter increases in discharge are largely a result of dam operations, with this effect most pronounced in the Yenisey. They interpreted the upward trend in annual discharge as primarily a result of increasing precipitation, with changes in permafrost conditions (melting ground ice, effects of altered active layer depth on near-surface groundwater flow) as well as increases in forest fire frequency possibly playing contributing roles. Regarding the latter, fire scar chronologies in some forests of central Siberia and the Russian Far East point to substantial increases in fire frequency (Arbatskaya and Vaganov, 1997; Cushman and Wallin, 2002). With loss or damage of vegetation, evapotranspiration decreases, so more of the precipitation becomes runoff. In a subsequent paper focusing on the 1964–2000 period, McClelland et al. (2006) highlighted that while discharge from Arctic-draining rivers in Eurasia was increasing, discharge from rivers in North America had exhibited a small decrease (Dery and Wood, 2005). Interest in the changing hydrology of northern high latitudes continued with the observation of a record-high aggregate annual discharge from the six largest Arctic-draining Eurasian rivers in 2007 (Rawlins et al., 2009).

Based on evaluation of atmospheric reanalysis data, Zhang et al. (2012) found that the increasing discharge of Eurasian rivers can be explained as a consequence on increasing atmospheric vapor flux convergence. The record discharge observed in 2007 fits this picture; this event was a reflection of strong positive anomalies in late winter snow water equivalent across much of northern Eurasia and positive net precipitation anomalies through summer. Results from most global climate models point to increases in atmospheric vapor flux convergence and net precipitation (hence river runoff) over northern high latitudes through the twenty-first century. This is related to the larger vapor-holding capacity of a warmer atmosphere. Whether we

are seeing this climate change signal is still unclear. Unresolved issues include the strong asymmetry between discharge from Eurasia (increasing) and North America (decreasing) and the relative importance of factors, such as changing forest fire frequency. Most recent research has dismissed thawing ground ice as a significant contributor to changing discharge. Reiterating statements in Chapter 2, assessing changes in Arctic precipitation that ought to be related to altered discharge is made very difficult because of the sparse observational network and other measurement problems.

Focus Questions and Exercises

- 1) Precipitation over Arctic land areas tends to have a summer maximum and winter minimum. We see the same seasonality in precipitation over the ice-covered central Arctic Ocean. By comparison, precipitation over the northern North Atlantic tends to have a cold-season maximum and summer minimum. Explain these differences in the seasonality of precipitation.
- 2) Draw a monthly hydrographs for the Lena River at the point where it empties into the Arctic Ocean. Label the axes. Draw a second hydrograph for the Lena that you might expect to see in the year 2050. Explain the differences between the two hydrographs.
- 3) Explain why the rate of evaporation over a melting sea ice cover in July will be much lower than over an open lead in the sea ice cover in January.

Arctic Ocean–Sea Ice–Climate Interactions

Overview

The mean seasonal variation of sea ice extent was reviewed in Chapter 2 along with some basic aspects of sea ice circulation, morphology, and the factors contributing to sea ice growth. As introduced there, the existence of the ice cover is not simply a function of low winter temperatures; its formation and persistence is fostered by the existence of a relatively fresh surface layer, maintained by river runoff, the import of low-salinity water through the Bering Strait, net precipitation over the Arctic Ocean, and the distillation process associated with ice formation itself. Seasonally, summer melt of the fairly fresh ice is also important. The characteristics of river runoff were examined in Chapter 6. In Chapter 3, we discussed the role that sea ice plays in the Arctic’s atmospheric energy budget, with sea ice melt maintaining a downward net surface flux (from the atmosphere to the ocean) in summer, and sea ice growth adding heat to the atmosphere in winter. Chapter 5 shed further light on this issue through a review of surface energy exchanges. In Chapter 4, we documented sea ice impacts on regional aspects of the atmospheric circulation through enhanced baroclinicity along the ice margins, and how the atmospheric circulation may now be responding to observed reductions in ice extent. The present chapter extends our understanding of sea ice and its interactions with the atmosphere and ocean.

The growth of sea ice up to about 1 m in thickness can be approximated in terms of freezing degree days. This is because the temperature gradient in thin ice is essentially linear. By contrast, the growth of thicker ice, primarily multiyear ice, which has historically attained

equilibrium thicknesses of 3.5–4.5 m while surviving ten years or more, is complicated by thermal history, seen as nonlinear vertical temperature gradients. Ice melts at both its top and bottom surfaces, with the process again less straightforward for thick ice. For example, in October when thin ice is growing quickly in leads, thick ice may still be decreasing in thickness owing to bottom melt, the reason being that the autumn cooling has not yet affected the lowest part of the ice. Over the past several decades, the Arctic has lost much of its thickest and oldest multiyear ice.

The Arctic sea ice cover can be separated into different zones – the Perennial Ice Zone, the Seasonal Ice Zone, the Marginal Ice Zone, the Fast Ice Zone, and the Shear Zone. Apart from areas of fast ice locked to the shoreline, the ice cover is in a state of near constant motion. The large-scale annual mean drift pattern is characterized by the clockwise Beaufort Gyre, centered in the Canada Basin, and a mean drift of ice from the Siberian coast, across the pole and through the Fram Strait, known as the Transpolar Drift Stream. This pattern is maintained by roughly equal contributions from winds and ocean currents. On shorter (monthly to daily) time scales, variations in ice motion are primarily wind-driven. Ice deformation, characterized by shear and divergence that results from winds and ocean currents that exert forces on the ice, is associated with the formation of leads, polynyas, pressure ridges and underlying keels. For example, the mean Beaufort Gyre circulation tends to push ice up against the coasts of the Canadian Arctic Archipelago and Greenland. As a result of ridging, the thickest ice in the Arctic tends to be found in this region. Ice is thinner along the Siberian shelf seas, where the prevailing winds and current transport newly formed ice offshore. Thinner ice then forms along the coast in open water areas. Anomalies in ice extent, concentration, and thickness represent responses to winds, ocean currents, and both atmospheric and oceanic thermodynamic forcing, superposed on downward linear trends in all months, smallest in winter and largest in September. Figure 7.1 provides a schematic of sea ice types, processes, and morphology that are addressed throughout this chapter.

In winter, the North Atlantic, especially the Greenland Sea, is an area of deepwater production, which is important for driving the ocean's thermohaline circulation. A key observation bearing on why deepwater production occurs in the North Atlantic but not in the North Pacific is that surface salinities are higher in the North Atlantic. Although the processes are still not completely understood, atmospheric transfers of freshwater from the Atlantic to the Pacific basin continually sharpen the salinity difference, and ocean transfers work to destroy the salinity difference. The Arctic Ocean serves as a “back door” by which relatively fresh water is transported through the Bering Strait and into the North Atlantic via the Fram Strait and the Canadian Arctic Archipelago. But the Fram Strait ice and ocean flux is sensitive to the regional atmospheric circulation and to

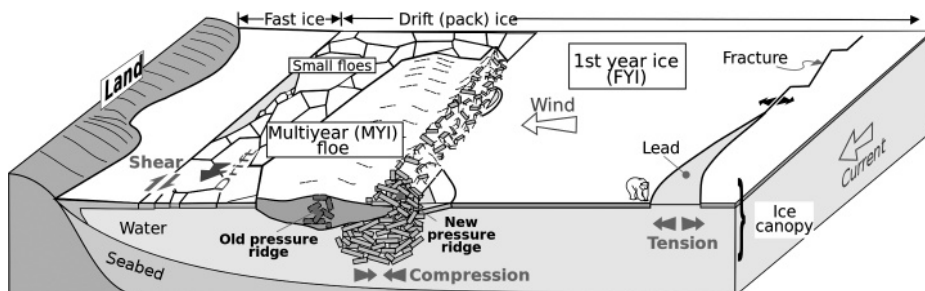


Figure 7.1. Schematic of basic sea ice types, morphology, and processes (Wikimedia Commons, author Lusilier, licensed under the Creative Commons Attribution-Share Alike 3.0 unreported license). (See plate section for color version.)

river input into the Arctic Ocean. There is evidence that a change in the freshwater output via the Fram Strait could reduce salinities in the North Atlantic and alter deepwater production; this seems to have occurred in the late 1960s and 1970s during the so-called Great Salinity Anomaly. The sensitivity of deepwater production to such processes, however, remains in debate. As reviewed in Chapter 10, the last glacial cycle was characterized by periods when North Atlantic deepwater production either ceased or was greatly reduced, albeit from very different processes.

7.1 Sea Ice Formation, Growth, and Melt

7.1.1 The Existence of the Sea Ice Cover

To build on concepts introduced in Chapter 2, it is useful to draw from the review of Maykut (1985) and compare the processes of ice formation in a freshwater body with those that occur in the Arctic Ocean. A water molecule has one oxygen and two hydrogen atoms, strongly joined by covalent bonds. Water molecules are in turn attracted to each other by weaker hydrogen bonds that exist between the positively charged hydrogen atoms and the negatively charged oxygen atoms of neighboring water molecules. Figure 7.2 gives the temperature versus density relationship for fresh water. For most substances, decreased temperature results in higher density. But fresh water is an unusual substance. Down to a certain temperature, cooling results in increased density. Below this temperature of density maximum (T_m) of 3.98°C , further cooling results in lower density. The solid form of water is in turn roughly 10 percent less dense than liquid water at the freezing point, which is another way of saying that ice floats. The reason this occurs is that as the water cools below the temperature of maximum density, the disorganized hydrogen bonds adjust to hold the negatively charged oxygen atoms apart, producing an organized crystal lattice (ice), which – for a given mass – occupies a larger volume than liquid water.

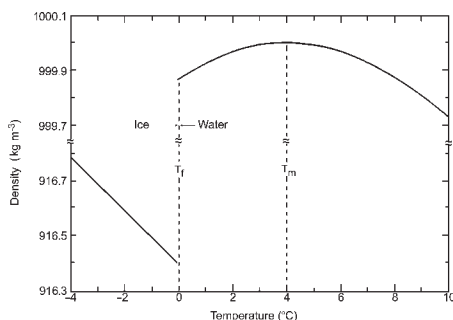


Figure 7.2. Temperature versus density plot for fresh water and ice at standard atmospheric pressure (from Maykut, 1985, by permission of Applied Physics Laboratory, University of Washington, Seattle, WA).

Imagine that winter is approaching, and that the temperature in a fresh water column (e.g., in a lake) is initially higher than the maximum density temperature T_m . The water column is cooling from the top, which sets up a vertical temperature gradient in the water. However, as density increases as temperature decreases, the cooling destabilizes the column. This generates vertical convection, mixing the cooler surface water downward and the warmer water at depth upward. This process continues until the entire water column reaches the temperature of maximum density. From this point on, any further surface cooling is associated with a decrease in density. This allows the water column to become stably stratified, meaning that the lower density water is at the top. Once the column is stably stratified, conduction, rather than convection, dominates the heat transport. As compared to convection, conduction is a comparatively inefficient mechanism for heat transport. Because it is difficult to bring up warm water from lower depths, surface cooling can proceed quickly until the freezing point (T_f) is reached. Further cooling results in a slight supercooling and ice formation proceeds. Because of the stable stratification, ice can readily form at the surface, even though the bulk of the water column is significantly above the freezing point.

If salt is added, the situation changes radically. With salinities below 24.7 psu, the temperature of maximum density is higher than the water's freezing point. At salinities above this value, the temperature of maximum density equals the freezing point (Figure 7.3). Furthermore, the presence of salt in solution depresses the freezing point of water. For water with a typical ocean salinity of about 35 psu, the freezing point is -1.8°C . Imagine that it is autumn in the Arctic Ocean. As in the case of a freshwater body, cooling of the water surface initially results in a density increase and vertical mixing. The plot in Figure 7.2 could lead one to believe that the entire water column would have to be cooled to the salinity adjusted freezing point before ice could form. Because much of the Arctic Ocean is 2–3 km deep, ice formation would seem to be rather difficult. The reason it can readily form is that there is strong, preexisting stability in the upper ocean, which limits the depth of water that needs to be cooled.

The basis of this salinity structure was examined in Chapter 2. To reiterate, the low-salinity surface layer (Figure 2.7) is maintained by discharge from the rivers draining into the Arctic Ocean, the inflow of comparatively low-salinity waters through the Bering Strait, and positive net precipitation over the Arctic Ocean. Seasonally, summer melt of the ice is important (see following discussion). Beneath

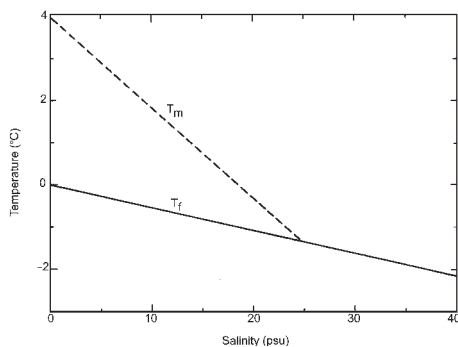


Figure 7.3. The effect of salinity on the temperature of maximum density (dashed curve) and the freezing point temperature (solid curve) (from Maykut, 1985, by permission of Applied Physics Laboratory, University of Washington, Seattle, WA).

the surface layer is the Atlantic layer. The Atlantic layer is comparatively warm, with temperatures above 0°C. It represents a potential source of ocean heat to the surface, which would inhibit ice formation. But at the low temperatures on the Arctic Ocean, the vertical density structure is determined by salinity, rather than temperature. The halocline between the surface and warm Atlantic water hence acts as a strong density gradient (pycnocline) that suppresses vertical mixing.

In the Arctic Ocean, the depth to which the water must be cooled before freezing can commence (Z_c) is typically 10–40 m, although values in excess of 70 m have been observed. Where Z_c is 50 m, there can be a delay of up to two months in the date of initial ice formation compared to where Z_c is 10 m. The surface mixed layer varies seasonally. As new ice forms in autumn, brine is rejected from the ice, which mixes downward, increasing the density of the surface layer and weakening the pycnocline. In summer, ice melt freshens the surface layer. This enhances the density stratification in the uppermost 30–50 m, strengthening the pycnocline, further decoupling heat exchange with Atlantic water (Carmack, 1990).

7.1.2 Primary Sea Ice Types

Sea ice is a complex material, comprising a solid component of ice crystals, a liquid component of brine solution in pockets, and a gaseous component of air pockets. Although there are many different types of sea ice (World Meteorological Organization, 1989), some of which will be introduced in the next section, there are several basic categories. First-year ice (FYI), which historically has comprised about 40 percent of the Arctic sea ice cover (Rothrock and Thomas, 1990; Romanov, 1991), represents the ice growth of a single season. In the broadest definition, new, or young ice, falls into the FYI category. The growth and melt of first-year ice in the marginal seas is primarily responsible for the large seasonal variations in total ice extent shown in Figure 2.4. Away from coastal regions, about 60 percent of the ice cover has historically been represented by second-year ice which has survived one summer melt season and ice that has survived more than one melt season. For operational applications and remote-sensing mapping, all ice that has survived at least one melt season is classified as multiyear ice (MYI). MYI may typically attain a thickness of 3.5–4.5 m thick, whereas FYI typically gets up to about 2 m, limiting

the amount of ice that can form in one winter season. Historically, some MYI floes have been observed to be ten years or more in age. As sea ice forms, salt in the form of brine is rejected. Typical mean salinities for FYI thicker than 1 m range from 2 to 6 ppt. Owing to gravity-induced brine drainage, the salinity of MYI is considerably lower than that of FYI (Weeks and Ackley, 1986), with salinity varying with depth, being lowest in the top part of the floe. Old MYI is essentially fresh water. The small amount of remaining salt is trapped in brine pockets.

Ice age can be tracked via remote sensing techniques. Figure 7.4 shows the spatial pattern of ice age for September 2012 and 2007 (2007 having the second lowest extent in the satellite record) along with the time history of September ice age classes for the Arctic as a whole back to 1983. The time history shows an overall transition toward both less ice and less coverage by the older ice age classes; especially notable is the decline in the coverage of MYI that is four years or older.

7.1.3 Sea Ice Growth and Melt

Reviews of sea ice growth and melt processes are given by Maykut (1985, 1986), W. Weeks and S. Ackley (1986), C. Parkinson et al. (1987), Barry et al. (1993), P. Wadhams (2000), and Barry and Gan (2011). Initial ice formation occurs at the surface as small platelets and needles termed frazil ice. Frazil crystals are generally less than 3–4 mm in size. Continued cooling forms a slurry of unconsolidated frazil crystals, termed grease ice. Under calm conditions, frazil crystals freeze together forming a solid, continuous ice cover of 1–10 cm thickness. However, in the more typical situation, a solid ice cover is inhibited by wind-induced turbulence in the water. Winds and waves advect frazil ice downwind where accumulations of up to 1 m thick can form in front of obstacles (e.g., existing ice floes).

Once the fraction of ice-covered area exceeds 30–40 percent, there is sufficient bonding between individual ice crystals to drastically reduce their mobility, initiating the transition to a solid ice cover. In the ocean, this is usually seen in the transition to pancake ice, rounded masses of semi-consolidated slush of 0.3 to 3.0 m in diameter formed by wind and wave action. Initially, the ice remains near the salinity-adjusted water freezing point, with large turbulent heat and longwave radiation losses from the surface resulting in rapid ice formation. As the ice thickens, the ice surface temperature declines. Additional growth then occurs mainly by bottom accretion. As outlined in Chapter 3, the latent heat release from ice growth represents a significant source of heat to the Arctic atmosphere during winter.

Field investigations have shown that the growth rate of young sea ice (less than 100 cm) is closely related to the cumulative number of freezing degree days. A number of empirical formulae have been developed to express this relationship (see Maykut, 1986), for example:

$$H = 1.33\theta^{0.58} \text{ (Lebedev, 1938)} \quad (7.1)$$

$$H^2 + 5.1H = 6.7\theta \text{ (Anderson, 1961)} \quad (7.2)$$

$$H^2 + 50H = 8\theta_1 \text{ (Zubov, 1945)} \quad (7.3)$$

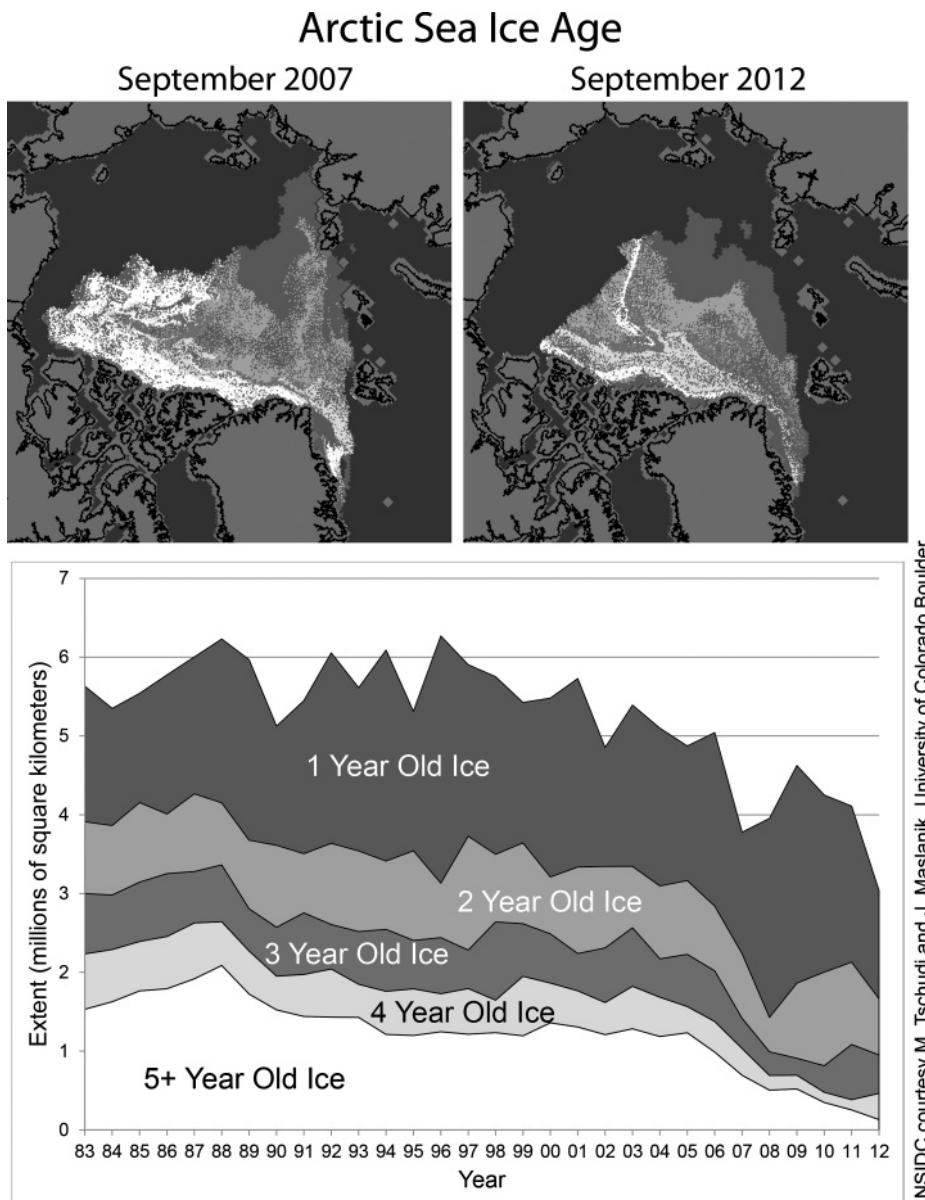


Figure 7.4. Ice age based on a tracking algorithm applied to satellite data. The top panel shows the spatial pattern of ice age classes for September 2012 and September 2007; the bottom panel shows the time history of September age classes for the Arctic Ocean as a whole back to 1983 (from NSIDC, courtesy of J. Maslanik and M. Tschudi, University of Colorado Boulder). (See plate section for color version.)

where H is ice thickness and θ is freezing degree days ($^{\circ}\text{C}$ per day). While formulae given by these investigators were developed for ice in different locations, with differing climate and snowfall conditions, the results over an ice thickness range of 0–100 cm are rather similar.

The strong relationship between the growth rate and freezing degree days for young (thin) ice is explained in that the temperature gradient in the ice is essentially linear. In the simplest case, it can be assumed that the temperature gradient in the ice is the difference between the temperature at the ocean–ice interface (at the salinity-adjusted freezing point) and the ice surface temperature, divided by the ice thickness. As outlined in Chapter 5, the rate of growth (or ablation) at the bottom of the ice is represented by the sum of the ocean heat flux (F_w) and the conductive heat flux through the ice ($K_i \partial T / \partial z$). When their sum is negative, growth (accretion) occurs. When their sum is positive, ablation occurs. With the assumption of a linear temperature gradient, the thickness responds immediately to changes in the thermal forcing at the surface.

The rate of growth of young ice is very sensitive to H . As H increases, the temperature gradient in the ice decreases, slowing the growth rate. This is a fine example of a negative feedback – although one needs to conduct heat through the ice to the surface to form ice, the very formation of the ice acts to inhibit its further production. Turning back to Chapter 3, it should come as no surprise that the heat release to the atmosphere in winter associated with ice production is primarily in the marginal ice zones, where most new ice is formed. The growth rate decreases by almost an order of magnitude between $H = 10$ cm and $H = 100$ cm. Clearly, the growth rate depends on the magnitude of F_w . If the ocean heat flux becomes larger, ice growth decreases. Snow cover is also important. If one includes a layer of snow and specifies that the conductive flux through the snow is equal to that in the ice, the growth rate decreases. This is because with the snow, the ice is effectively thicker. In reality, conduction through snow tends to be much less efficient than through ice (Table 5.1), leading to still slower growth rates.

As ice becomes thicker than about 100 cm, the relationship between the growth rate and freezing degree days (or air temperature) weakens. To describe the growth of MYI or thicker FYI, one must abandon the idea of a linear temperature gradient in the ice. As discussed by Maykut (1986), the growth of thicker ice depends more on its thermal history than on the surface heat balance at one moment in time. Observations have shown that in early summer, accretion may occur at the bottom of the ice while melt is occurring at the top, the reason being that the summer warming has not penetrated to the lowest part of the ice. Conversely, in October, when ice is growing quickly in leads, thick ice is generally decreasing in thickness owing to bottom ablation, the reason being that the autumn cooling has not yet affected the lowest part of the ice.

The formation of a typical thick (3.5–4.5 m) MYI floe can be conceptually viewed in terms of a process leading to quasi-equilibrium condition. Consider an FYI floe that has survived the summer melt season. By definition, it is now multiyear ice. During the second winter, there will be ice growth at the bottom of the MYI floe. The thickness that is added to its bottom, however, is less than what will be added to nearby FYI. This is because the MYI floe is thicker than the FYI, meaning that the bottom growth starts later in autumn, and, once started, proceeds at a slower rate. Still, it ends up thicker than it was at the end of the first winter. In

subsequent years, the amount of ice that is melted on top in summer stays about the same, while, because of the increasing thickness, less and less ice forms on the bottom each winter. Assuming a steady climate, a rough equilibrium is ultimately achieved, with the winter addition of thickness (primarily at the bottom) equaling the thinning during summer (primarily from the top). How thick the ice gets basically depends on the air temperature and the vertical oceanic heat flux. A further critical factor is the amount of ice deformation induced by winds and ocean currents. This is discussed in Section 7.3.3. Whereas the typical thickness is in the range of 3.5–4.5 meters; in sheltered fiord sites in the Arctic where the oceanic heat flux is very small, it can be much thicker. However, as is clear from previous discussion and from Figure 7.4, the idea of an equilibrium thickness no longer appears to be valid; the Arctic sea ice cover is losing its older MYI, and the MYI that is present seems to be thinning. Some of the first observational evidence for thinning came from analysis of submarine sonar records. Comparisons between sea ice draft data acquired during submarine cruises between 1993 and 1997 with earlier records (1958–1976), indicate that the mean ice draft at the end of the summer melt period between the two periods had decreased by 1.3 m in most of the deep water regions of the Arctic Ocean (Rothrock, Yu, and Maykut 1999). Ice draft is the part of the ice below the water surface.

Maykut and Untersteiner (1971) developed the first general thermodynamic ice model. Their model accounts for nonlinear temperature gradients attributed to lagged responses to seasonal forcing, penetration of shortwave radiation into the ice, and the presence of snow cover. It also incorporates a treatment of brine pockets trapped in the ice. Cooling of the ice causes brine to freeze, releasing latent heat and slowing the cooling rate. Increasing temperatures cause melting of ice surrounding brine pockets, slowing the rate of warming. Put differently, brine pockets act as thermal buffers to retard temperature changes in either direction (Maykut, 1986). Today, nearly all coupled global climate models include a dynamic-thermodynamic sea ice model, meaning that along with thermodynamic growth and melt, the ice moves and deforms in response to winds and ocean currents. The following sections address ice motion and deformation (convergence, ridging, shearing, and divergence); modeling the sea ice cover will be explored in Chapter 9.

7.2 Mean Circulation, Ice Zones, Concentration and Thickness

7.2.1 Mean Annual Circulation

Since 1979, the IABP has maintained a network of drifting buoys in the Arctic Ocean. Ice drift records are also available from the NP program. Additional data have been collected by manned U.S. drifting camps (e.g., T-3). Figure 7.5 shows the mean annual pattern based on these data. Recall that ice drift (and age) can also be tracked by applying algorithms to satellite imagery.

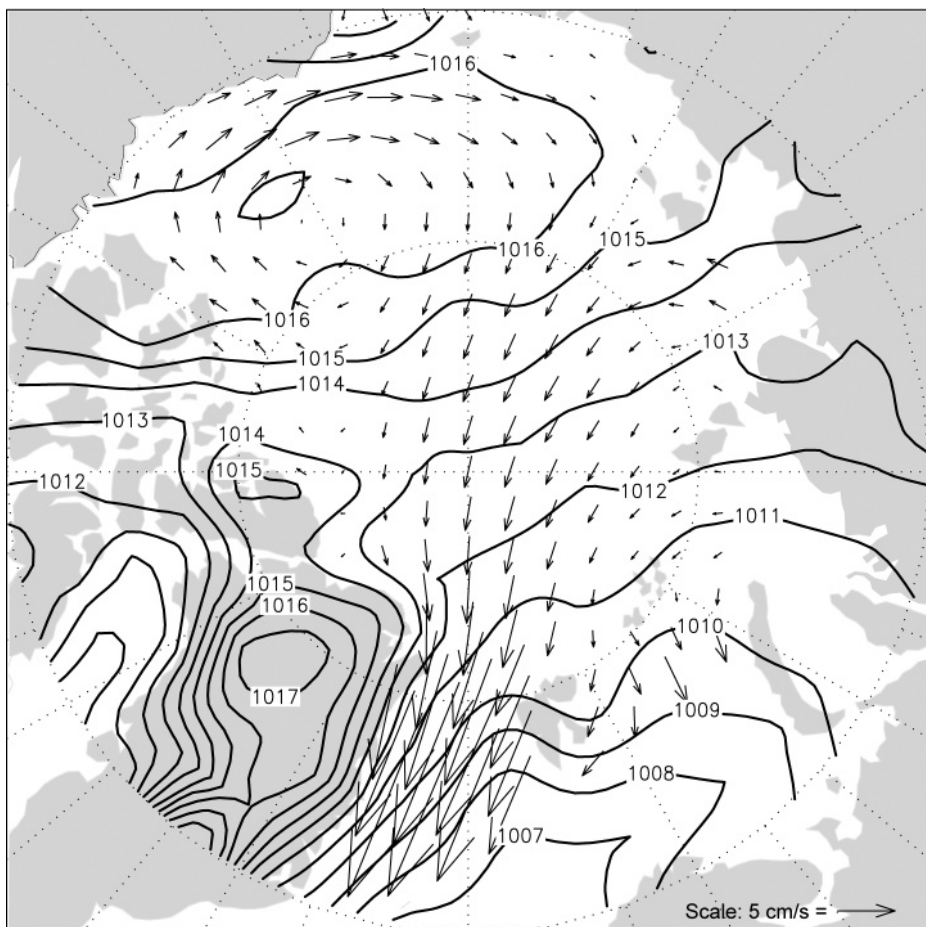


Figure 7.5. Mean annual sea ice drift in the Arctic, based on data from the IABP, the North Pole program and other sources with overlay of sea level pressure from NCEP/NCAR (ice drift field courtesy of I. Rigor, Polar Science Center, University of Washington, Seattle, WA, sea level pressure field by the authors).

The mean annual drift of the pack ice consists of two primary features: the Beaufort Gyre, the clockwise (anticyclonic) motion of ice in the Canada Basin; and the Transpolar Drift Stream (TPDS), characterizing the motion of ice away from the Siberian coast, across the pole, and through the Fram Strait. This mean pattern reflects roughly equal contributions by winds and surface currents. Hence, the mean ice drift pattern roughly resembles the distribution of mean sea level pressure. The overlay of annual sea level pressure in Figure 7.5 is for 1979–1999, the period on which most of the drift data are based.

With a mean drift speed of 1–3 cm s⁻¹, typically, five to ten years are required for ice to make one circuit around the Beaufort Gyre (Thorndike, 1986). Ice can circulate around the gyre for many years. It can take up to three years for a parcel of ice to move along the TPDS (Thorndike, 1986). Ice velocities in the

TPDS progressively increase toward the Fram Strait, where mean drift speeds are 5–10 cm s⁻¹. Even larger ice velocities are observed in the Greenland Sea. Approximately 20 percent of the total ice area of the Arctic Basin annually exits through the Fram Strait (Thorndike, 1986), of which 80 percent consists of MYI (Gow and Tucker, 1987).

7.2.2 Sea Ice Zones

The sea ice cover can be divided into different ice zones. Again following Maykut (1985), the perennial ice zone (PIZ) is where ice is present throughout the year. The PIZ can be broadly considered as the area north of the mean September ice extent shown in Figure 2.4 (the PIZ has, however, shrunk over the past several decades). During winter, the PIZ typically consists of 10–15 percent FYI formed in leads, and the remainder is MYI. In summer, much of the FYI melts. The Arctic's perennial ice zone contains about two thirds of all the MYI in the world's oceans. The seasonal ice zone (SIZ) is where ice is present only on a seasonal basis. It can be considered as the area between the seasonal maximum and minimum ice extent (Figure 2.4). Undeformed ice in the SIZ is typically less than 2 m in thickness – the limit of annual thermodynamic ice growth – but large amounts of ridged ice are also present (ice deformation will be addressed in detail in Section 7.3).

The fast ice zone refers to areas where ice is anchored to the bottom of the shoreline, usually to 2 m depth, but up to 18 m in the southern Beaufort Sea by grounded pressure ridges (Kovaks and Mellor, 1974; Mahoney et al., 2007). Fast ice forms early in the winter in shallow water where the water column can cool rapidly to the freezing point. Fast ice development is most extensive in areas where the shelf slope is gentle, such as the Mackenzie delta and Laptev Sea. Fast ice is typically undeformed over large areas but can contain pressure ridges and keels. Near the shore, it is typically highly deformed and is very difficult to navigate (Figure 7.6). Ice that fills bays and channels in regions like the Canadian Arctic Archipelago is also considered to be fast ice. Fast ice in the Canadian Arctic Archipelago has historically been quite thick (greater than 5 m). Fast ice breakup can be estimated from cumulative thawing-degree days. Studies based on this approach have been carried out in Baffin Bay (Jacobs, Barry, and Weaver, 1975) and for the Beaufort Sea coast (Barry, Mortiz, and Rogers, 1979).

The shear zone is a region of highly deformed ice along the coasts of Alaska, the Canadian Arctic Archipelago and northern Greenland. The shear zone can be considered as a boundary between the fast ice and the central (perennial) pack ice, which is in near constant motion. The shear zone is readily observed in satellite imagery. The MODIS image in Figure 7.7 for July 21, 2001 shows a section of the shear zone along the coast of the Canadian Arctic Archipelago. North is approximately to the right. Borden Island is at the top of the figure and Axel Heiburg Island is at the bottom. The shear zone runs from the top middle to bottom right. Fast ice is to the left of the zone while the moving pack ice is to the right. The pack ice has a mean component of motion toward the top of the image associated with the



Figure 7.6. Highly deformed sea ice near Barrow, Alaska, during the spring of 2008 (photograph by M.C. Serreze). (See plate section for color version.)

Beaufort Gyre circulation. When there is strong shear, there is also a component of motion into the shore. This results in convergence and the formation of thick, ridged ice (seen as the light colored streaks). There is also locally strong divergence, producing leads. The very obvious lead north of (to the right of) Borden Island is roughly 1–2 km wide. On the basis of submarine sonar data, Wadhams (1980) suggests that the shear zone extends about 400 km off the coast of Ellesmere Island, where ice motion is normal to the coast, and about 160 km off Alaska, where the motion is more parallel to the coast.

Recall from Chapter 2 that the marginal ice zone (MIZ) represents the boundary between the sea ice and open water. The boundary is generally (but not always) gradual, perhaps 100–200 km in width. Figure 2.6 shows an example of conditions along the MIZ. Penetration of surface waves into the ice pack breaks ice into small floes with an average size increasing rapidly with distance from the ice edge. During winter, the MIZ is associated with strong horizontal temperature gradients. Enhanced baroclinicity along the MIZ may influence cyclone development. Horizontal variations in the density structure along the MIZ can also produce mesoscale phenomena in the ocean, such as eddies, jets and upwelling. Biologic activity is high along the MIZ.

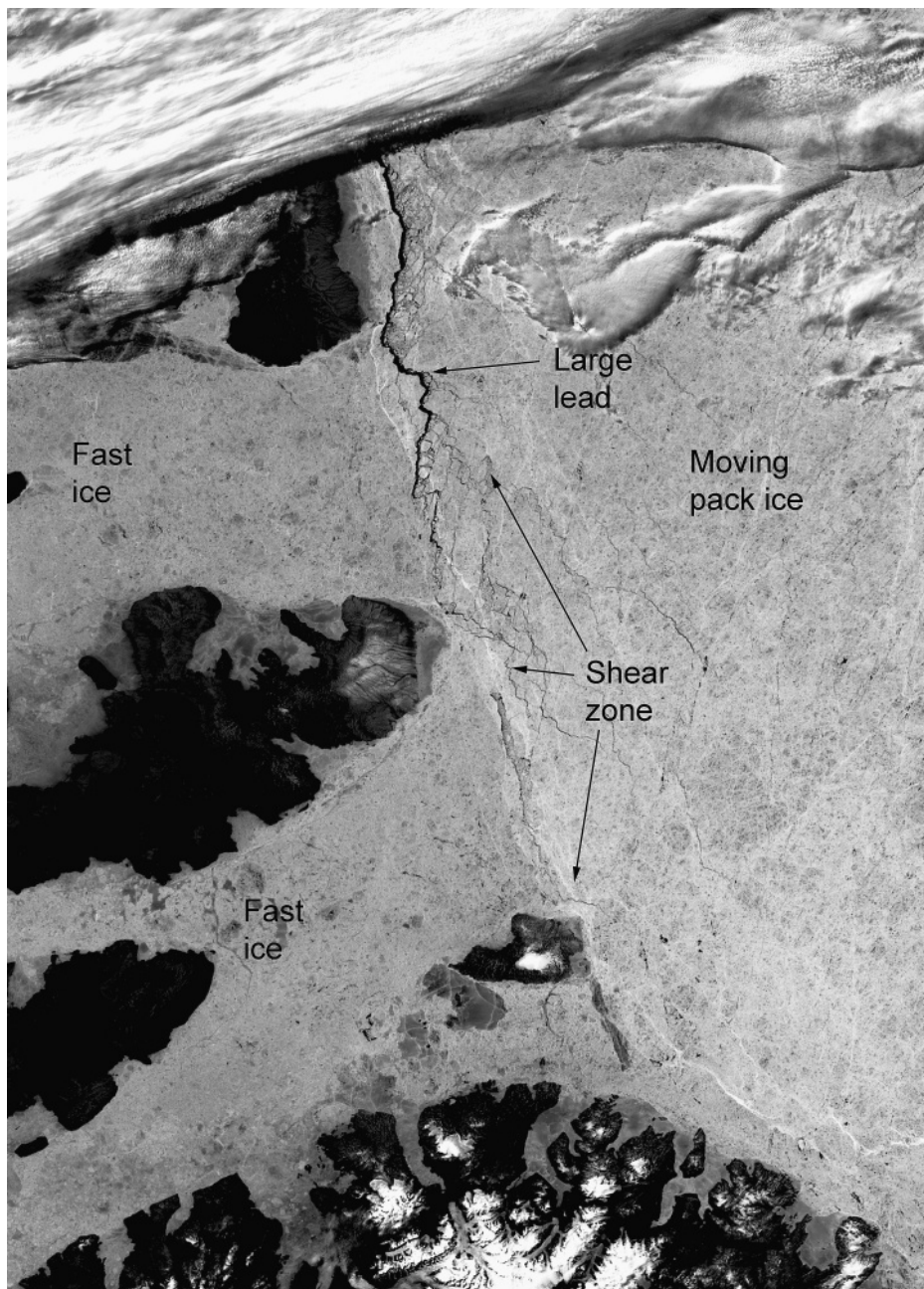


Figure 7.7. MODIS satellite image showing the shear zone along the coast of the Canadian Arctic Archipelago. North is roughly to the right. Axel Heiburg Island is at the bottom. The image covers an area of approximately 526 km by 376 km, with a resolution of 250 m (courtesy of T. Haran, NSIDC, Boulder, CO).

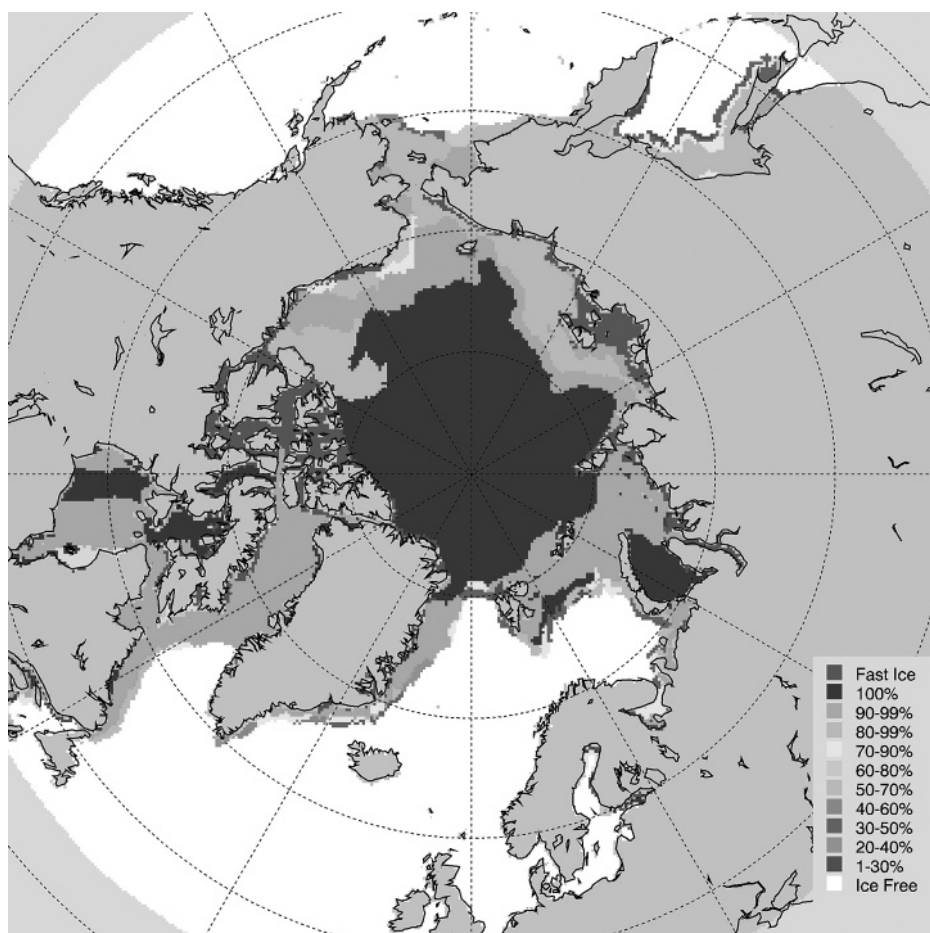


Figure 7.8. Ice concentration for the Arctic and peripheral seas (see color bar) for the January 5–11, 1994 period, based on the analysis of the National Ice Center (courtesy of K. Knowles, NSIDC, Boulder, CO). (See plate section for color version.)

7.2.3 Ice Concentration

Ice concentration was also introduced in Chapter 2. Recall that concentrations (the part of a given area covered by ice) in the interior pack (the PIZ) typically exceed 97 percent during winter but decreases during summer to 85–95 percent, with large variability and lower concentrations in the MIZ. Figure 7.8 shows a typical pattern of ice concentration for winter based on charts from the National Ice Center (NIC). This represents conditions for the seven-day period of January 5–11, 1994. The NIC charts are based on a combination of various forms of satellite imagery along with ship and aircraft reports. Note the high ice concentrations over the interior pack ice and the generally decreasing concentrations to the south. Fast ice is found along the shores of Siberia, Alaska, and in the straits of the Canadian Arctic Archipelago.

Building on previous discussions, leads (fractures) in the sea ice cover are typically on the order of 10–1000 m wide, but can exceed 10 km near coasts and in the shear zone. The orientations of major fractures are broadly correlated with large-scale wind fields, and they have similar synoptic space and time scales (Miles and Barry, 1989). Polynyas (irregularly shaped openings) may be found throughout the pack ice (see Figure 2.6) but recur along coasts with offshore winds and are common in the shear zone. One of the most prominent recurrent polynyas is the North Water of northern Baffin Bay-Smith Sound, forced partly by strong northerly winds advecting ice southward (Mysak and Huang, 1992) and partly by upwelling (Steffen, 1985). As reviewed in Chapter 5, leads and polynyas comprise only 1–2 percent of the total winter ice area, but the heat flux they provide to the atmosphere is 1–2 orders of magnitude larger than that from surrounding thicker ice (Maykut, 1978, 1986).

7.2.4 Ice Thickness

Information on the spatial-temporal distribution of ice thickness is provided by under-ice submarine transects and moored under-ice buoys, which measure ice draft with upward-looking sonar, as well as satellite altimetry, such as from the ICESat and CryoSat-2. Draft is the part of the ice (roughly 90 percent) that projects below the water surface. Mean ice thickness is typically considered from the thickness of ice that is present averaged along with open water (zero ice thickness). Figure 7.9 provides an estimate of the mean winter ice thickness based on submarine sonar data. Immediately obvious is that the thickest ice is along the northern coasts of Canada and Greenland, where it ranges from 6–8 m. As discussed, this is a result of the mean Beaufort Gyre ice circulation having a component of on-shore motion, resulting in ridging. Thinner ice in the Eurasian shelf seas arises from the continual transport of ice away from this region toward the Fram Strait, forming open water areas where new, thin ice can grow in autumn and winter. It hence follows that the Eurasian shelf seas are the primary areas of new ice production in the Arctic. This region is sometimes referred to as the “ice factory” of the Arctic Ocean.

Given that mean thickness is somewhat of a statistical abstraction, it is better to characterize the thickness in terms of a probability density function (PDF). The PDF for spring, based on submarine sonar data in the 1970s and 1980s, primarily in the PIZ, is characterized by peak probabilities at around 3 m, and a long tail with increasingly lower probabilities of thicknesses of 6 m or more, much greater than the 3.5–4.5 m representing the typical maximum thickness of undeformed MYI. This thick ice represents ice that has been deformed by rafting and ridging, which will be addressed in more detail in Section 7.3. As another way of looking at thickness probabilities, R. Bourke and A. McLaren (1992) found that pressure ridges with keels 9 m deep tend to recur once every 50–200 m of submarine track.

Spatial fields of estimated ice thickness and PDFs for the ice cover as a whole from ICESat appear in Figure 7.10 for three periods: February–March of 2006, March–April of 2007, and February–March of 2008. The PDFs are separated into

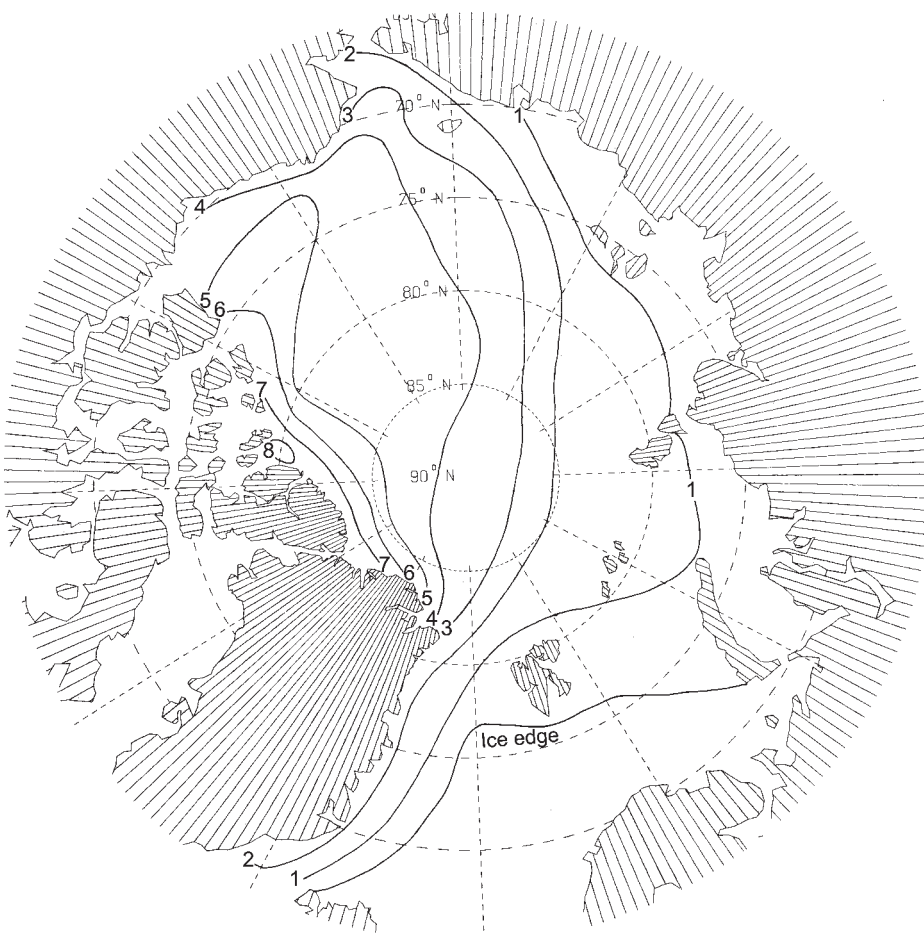
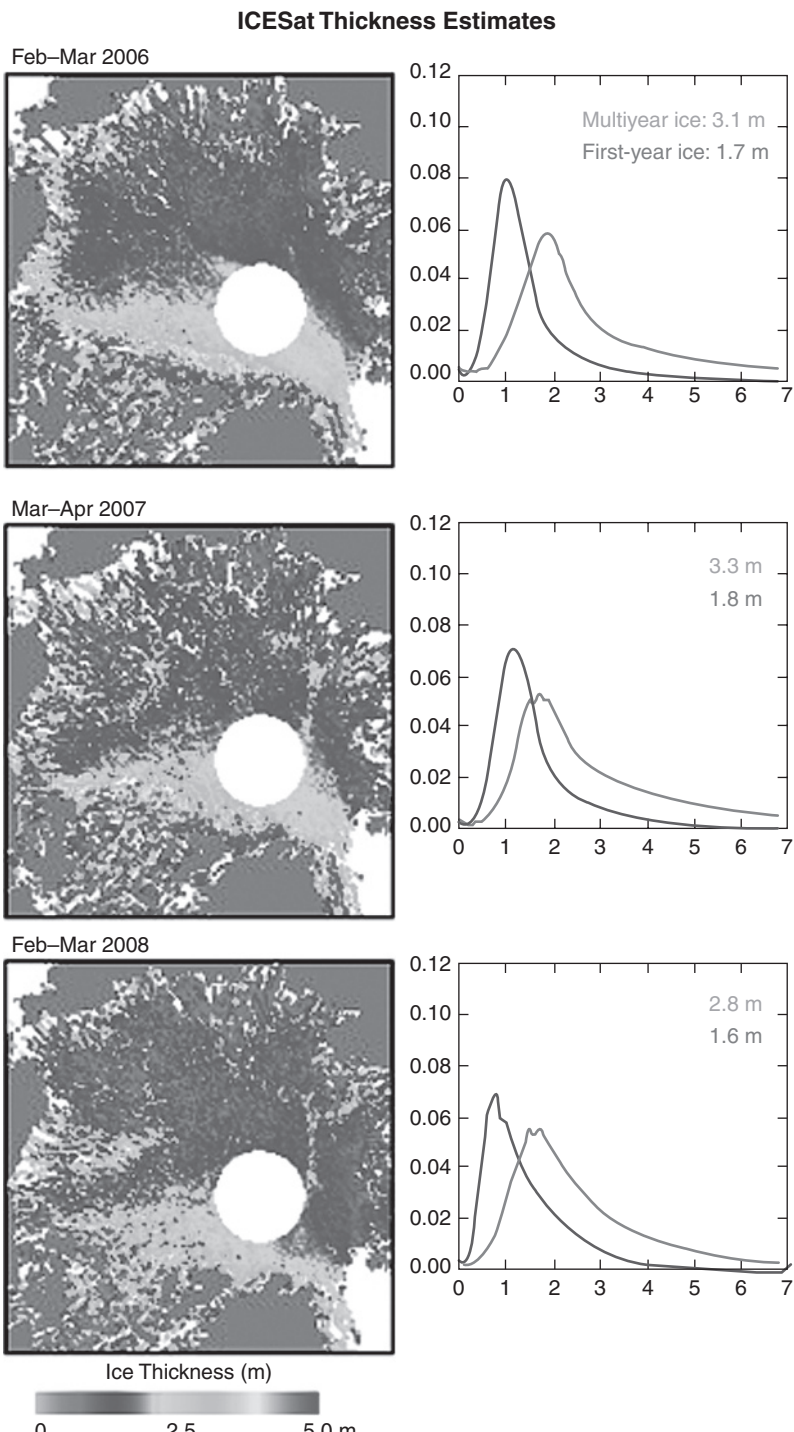


Figure 7.9. Estimated distribution of mean winter sea ice thickness (meters) in the Arctic (from Bourke and Garrett, 1987, by permission of Elsevier).

those of FYI and MYI. Although the fields for each year show the expected pattern of thinner ice along the Eurasian side of the Arctic Ocean and thicker ice along the northern shore of the Canadian Arctic Archipelago and northern Greenland, there is considerable variability from year to year. Depending on the year, the peak probability of MYI thickness is from 3.1 m to 2.8 m, while that for FYI ranges from 1.7 m to 1.6 m. The notable feature of all of the PDFs is the long tail of lower probabilities of thick ice classes resulting from deformation. Based on multiple lines of evidence, ranging from comparisons between sea ice draft data collected during submarine cruises between 1993 and 1997 with earlier records (1958–1976) (Rothrock et al., 1999), analysis of satellite-tracked ice age (Figure 7.4), studies of the complete ICESat record going back to 2003, and modeling (e.g., Rothrock, Zhang, and Yu, 2003), ice thicknesses for the years shown in Figure 7.10 are generally lower than for previous decades.



National Snow and Ice Data Center courtesy Ronald Kwok, NASA Jet propulsion Laboratory

Figure 7.10. Spatial fields of estimated sea ice thickness and probability density functions (PDFs) (probability given on the y-axis) based on ICESat retrievals for February–March 2006, March–April 2007, and February–March 2008. PDFs are given from both multiyear ice and first-year ice. The white circle indicates the region north of satellite coverage (from NSIDC, courtesy of R. Kwok, NASA, JPL). (See plate section for color version.)

7.3 Circulation Variability and Deformation

7.3.1 The Momentum Balance

Detailed reviews of sea ice dynamics and kinematics are given by A. Thorndike (1986) and W. Hibler (1986). The motion of sea ice can be described by a momentum balance:

$$m\partial\mathbf{u}/\partial t = m\mathbf{f}\mathbf{k} \times \mathbf{u} + \mathbf{T}_a + \mathbf{T}_w + \mathbf{F} - mg\nabla H \quad (7.4)$$

The term on the left side is the time change in momentum (i.e., acceleration), where m is the ice mass per unit area and \mathbf{u} is the ice velocity. The first term on the right side is the stress attributed to the Coriolis force, where f is the Coriolis parameter and \mathbf{k} is a unit vector normal to the surface. \mathbf{T}_a and \mathbf{T}_w are air and water stresses, and \mathbf{F} is the internal ice stress, which describes floe-to-floe (ice) interaction. The final term, $mg\nabla H$ describes ocean tilt, where H is the height of the sea surface and g is gravitational acceleration (because of regional density variations in the ocean and other factors, the height of the ocean surface is not the same everywhere, meaning that there are slopes, and this has to be accounted for in the momentum balance). The relative magnitudes of the momentum balance terms vary seasonally and spatially. The dominant terms, however, are the air and water stresses, the Coriolis force, and ice interaction (Hibler, 1986). Whereas ice interaction can be large in winter and near coasts, the term is often small in summer and away from coasts. In these situations, it is appropriate to consider the pack ice to be in a state of “free drift” (McPhee, 1980).

F. Nansen (1902) was the first to observe that on a day-to-day basis, the pack ice generally moves at about 2 percent of the surface wind speed and 30° to the right of the wind velocity vector. N. Zubov (1945) made similar observations. Using data from the Arctic Ice Dynamics Joint Experiment and the IABP, Thorndike and R. Colony (1982) developed a linear regression model to show that away from coasts, typically 70 percent of the variance in ice motion at daily to monthly time scales is explained by the local surface geostrophic wind. On average, the ice moves 8° to the right of the geostrophic wind direction and at 0.008 of its speed. However, strong seasonality occurs in the mean drift angle, ranging from 5° in winter to 18° in summer, in response to the ice compactness. In turn, the wintertime scaling factor is approximately 0.007, increasing in summer to about 0.011. Using a longer data record, Serreze, Barry, and McLaren (1989) obtained similar results.

Seasonal variations in the characteristics of ice drift are in part attributable to changes in the magnitude of the internal ice stress term. While the inclusion of internal stresses does not generally destroy the linear relationship between ice velocity (U) and the geostrophic wind (G), it is manifested by a change in the ratio $|U|/|G|$ and the turning angle (Moritz, 1988). Typically, both are reduced. The stability of the atmosphere also has an impact (Thorndike and Colony, 1982). Given the same geostrophic wind, increased low-level stability in winter acts to reduce the surface

wind stress and to increase the turning angle between the geostrophic wind and the wind stress vector (Albright, 1980). On annual and longer time scales, variations in ice motion are approximately 50 percent wind driven and 50 percent current driven. Because winds are highly variable, their forcing tends to cancel out on longer time scales, so that relatively steady current effects play a stronger role.

7.3.2 Variability in the Large-Scale Motion Field

The mean annual characteristics of ice motion across the Arctic have already been covered. Here, we show some examples of seasonal and interannual variability. That mean patterns of sea ice drift exhibit pronounced seasonality is broadly understood from the seasonality in the mean sea level pressure field. During winter, there is a low pressure trough in the Atlantic sector of the Arctic with higher pressures over the central Arctic Ocean. This is seen as a strong Beaufort Gyre, a Transpolar Drift Stream, and a pronounced ice flux through the Fram Strait (Figure 7.11). The winter pattern is quite similar to that for the annual average (Figure 7.5). In summer, the pressure trough over the Atlantic sector is essentially gone and a weak ridge develops over the Barents and Kara seas. Weak low pressure is found centered near the pole, and anticyclonic conditions prevail in the Beaufort Sea. In turn, the Beaufort Gyre retreats south into the Beaufort Sea. Ice motion is more cyclonic over the Eurasian side of the Arctic, and the Fram Strait outflow is weaker (Figure 7.12). It is nevertheless evident from the mean annual, winter and summer plots that the relationships between mean drifts and mean pressure fields are only general.

As illustrated in the examples provided in Figure 7.13 and Figure 7.14, mean drift patterns differ considerably from month to month. These two figures, showing mean drifts for January 1989 and 1991 with corresponding sea level pressure overlays, employ the displacement of ice features observed in SSM/I passive microwave imagery (Agnew, Le, and Hirose, 1997; Emery, Fowler, and Maslanik, 1997). The advantage of these satellite records is that gridded fields of ice motion can be obtained at 25 km spatial resolution and daily temporal resolution. These are the same data used to track ice age. Whereas daily fields can be calculated from the IABP data, the low density of stations for any one day means that finer-scale features are missing. The SSM/I data also provide fuller spatial coverage, providing ice drift information in areas such as Baffin Bay. A disadvantage of passive-microwave ice motion products is that the accuracy of the retrievals degrades during summer because of melt effects.

Neither of the two Januaries show evidence of the mean Beaufort Gyre circulation. In January 1989, there is generally cyclonic drift over most of the central Arctic Ocean around a broad pressure trough. By contrast, for January 1991, the dominant feature is a motion of ice from the Eurasian coast, across the Arctic and toward Alaska. In Baffin Bay, there is no obvious relationship between the ice drift and the inferred wind field, pointing to a strong role of ocean currents.

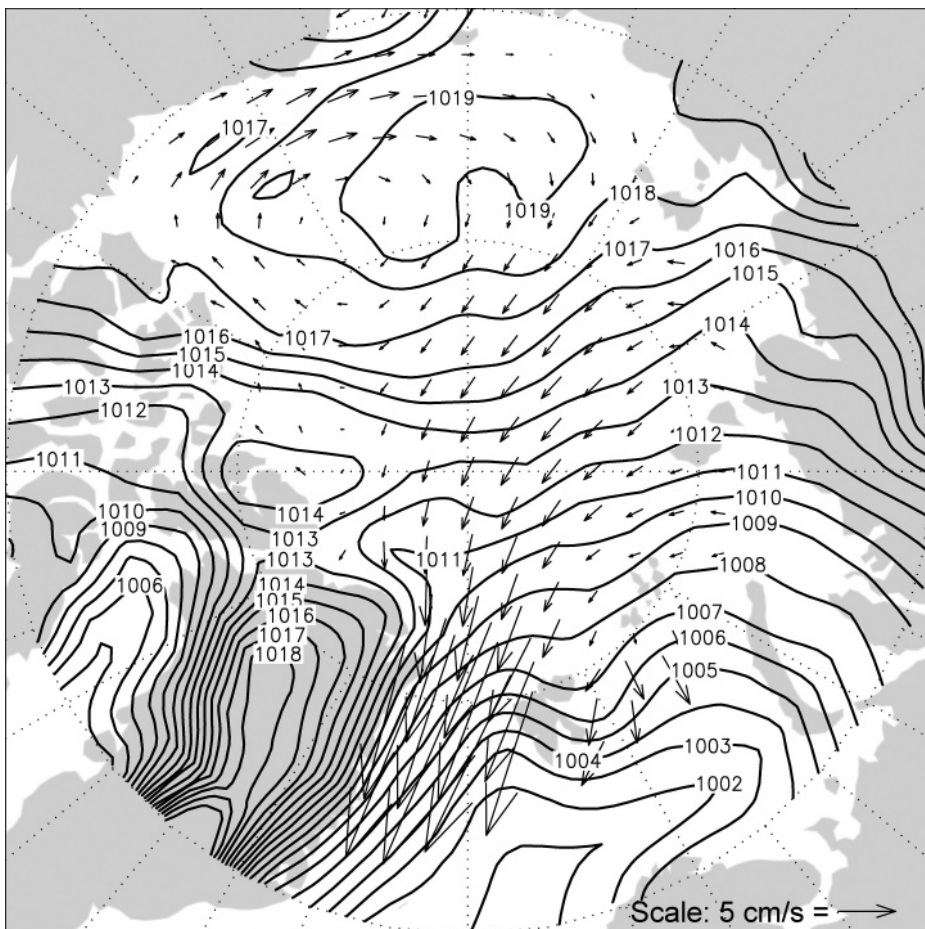


Figure 7.11. Mean pattern of sea ice drift in the Arctic for winter, based on data from the IABP, the North Pole program, and other sources with overlay of sea level pressure from NCEP/NCAR (ice drift field courtesy of I. Rigor, Polar Science Center, University of Washington, Seattle, WA, sea level pressure field by the authors).

7.3.3 Sea Ice Deformation

Ice thickness and concentration are strongly determined by differential ice velocity. Consider two neighboring plates (floes) of ice. If the velocity difference between the neighboring plates is such that they tend to move apart (diverge), a lead is created. During winter, new ice may form in the lead. If the motion changes, such as by a change in the winds so that the neighboring plates move toward each other (converge), the lead closes. Any new ice that was formed in the lead must rearrange itself to occupy a smaller area. The typical processes for this are rafting, where one plate of ice rides atop the other, and ridging, where the ice is crushed into pieces that pile into ridges rising up to several meters above and sometimes many meters below the surrounding ice (keels) (Figure 7.1). Deformed ice is hence thicker than undeformed ice and it is the thick, deformed ice that accounts for the long tail in ice

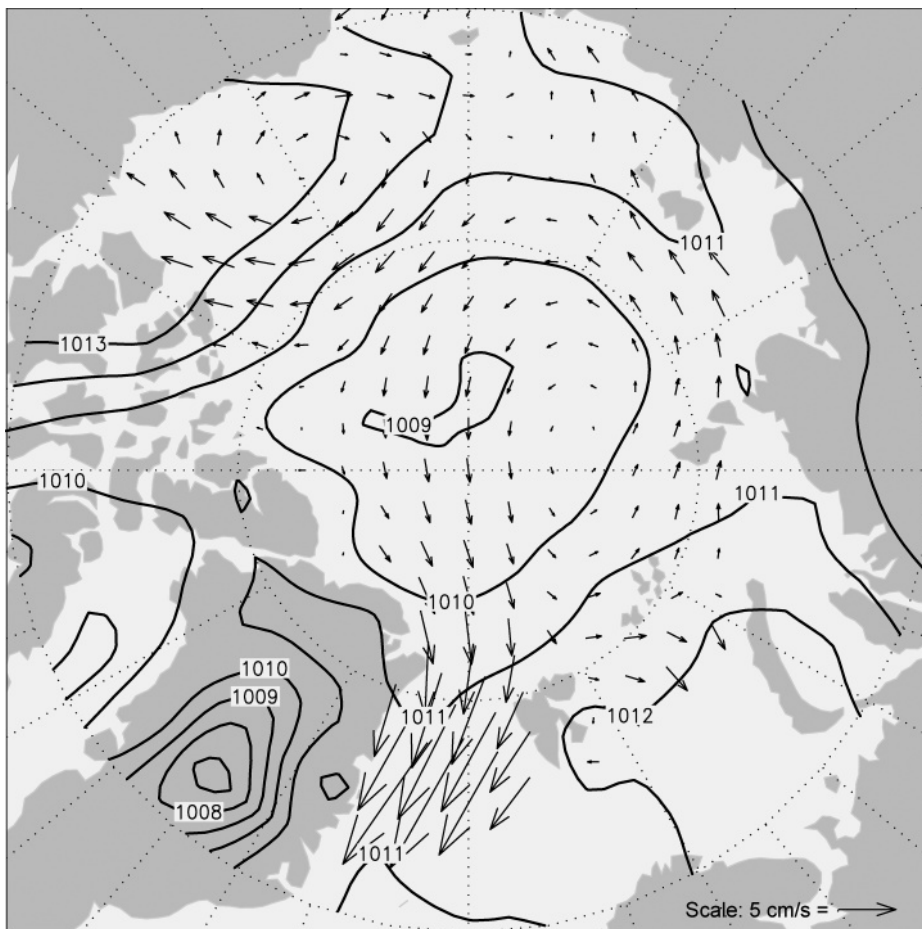


Figure 7.12. Mean pattern of sea ice drift in the Arctic for summer, based primarily on data from the IABP, the North Pole program and other sources with overlay of sea level pressure from NCEP/NCAR (ice drift field courtesy of I. Rigor, Polar Science Center, University of Washington, Seattle, WA, sea level pressure field by the authors).

thickness PDFs such as shown in Figure 7.10. Thick deformed FYI is in turn more likely to survive a summer melt season to become MYI than is undeformed FYI. The large ice thicknesses north of the Canadian Arctic Archipelago are associated with ridging and rafting. The basic idea is that the sea ice accommodates divergence by increasing the area of open water rather than thinning. It accommodates convergent motion by reducing the area of open water and by rafting and ridging (Thorndike, 1986).

A standard data product from the IABP is ice velocity derivatives, from which divergence and shear (which together represent total deformation) can be calculated along with vorticity (the rotational part of the flow). Similar products can be made from satellite-derived ice motion fields. Care must be exercised in interpreting such data because the true ice motion field is granular, with velocity discontinuities

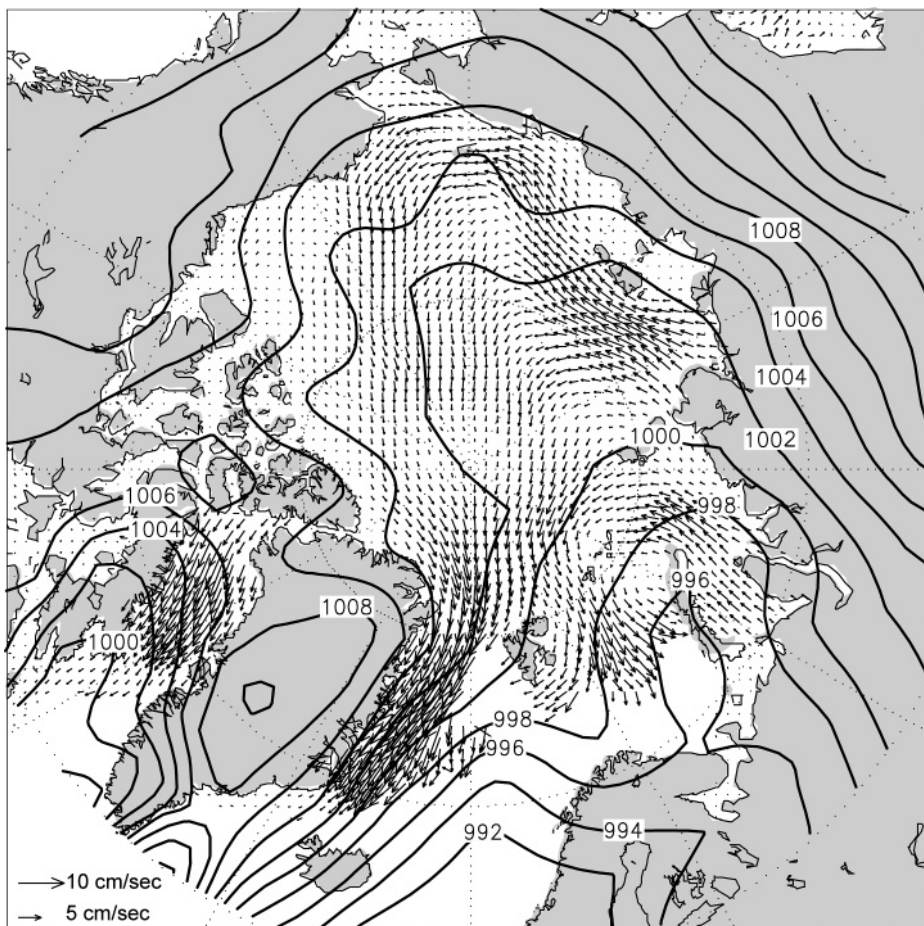


Figure 7.13. Mean pattern of sea ice drift in the Arctic for January 1989, based on SSM/I retrievals with overlay of sea level pressure from NCEP/NCAR (ice drift field courtesy of C. Fowler, University of Colorado, Boulder, CO, sea level pressure field by the authors).

along the floe boundaries or larger ice aggregations. Put differently, the field is inherently non-differentiable. If we calculate from IABP or SSM/I velocity fields that an area of the pack ice is converging, this is interpreted as an aggregate closing of the pack ice over some length scale much larger (tens to hundreds of km) than the typical distance between floes. If the ice concentration is less than 100 percent, the aggregate closing is seen as a regional increase in ice concentration. If the concentration is 100 percent, the aggregate closing implies the development of ridges and keels, increasing the ice thickness. Locally, however, the motion could be non-divergent. Divergent flow calculated over some length scale is interpreted similarly. The aggregate opening is seen as a decrease in the regional ice concentration, even though the motion could be locally nondivergent or convergent. Similarly, in an area of large-scale shear only, there can be local opening, closing, and the development

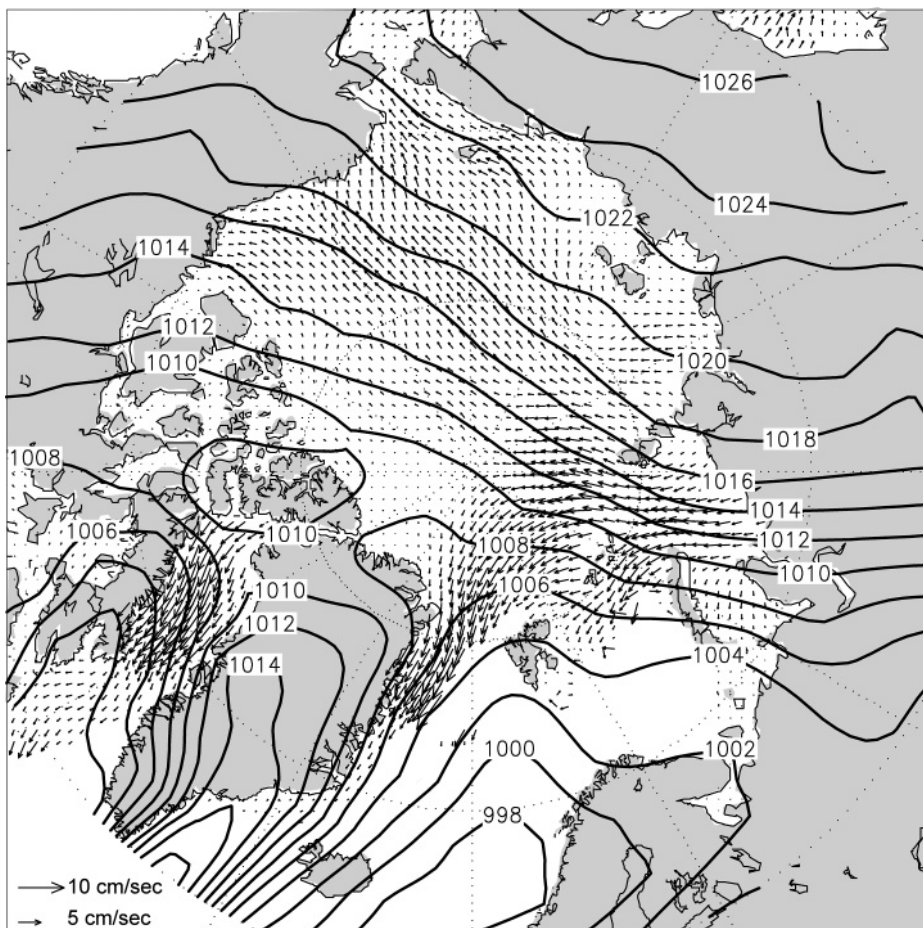


Figure 7.14. Mean pattern of sea ice drift in the Arctic for January 1991, based on SSM/I retrievals with overlay of mean sea level pressure from NCEP/NCAR (ice drift field courtesy of C. Fowler, University of Colorado, Boulder, CO, sea level pressure field by the authors).

of ridges and keels. By the same token, the large-scale vorticity field masks local deviations from the general rotational flow. Note also that estimates of ice deformation are prone to error as they are sensitive to small errors in the velocity field.

Using results from Thorndike and Colony's (1982) linear regression model, one can obtain estimates of the large-scale divergence and convergence from the geostrophic wind at sea level and the turning angle of the ice velocity with respect to the geostrophic wind. Because the turning angle is to the right of the geostrophic wind, cyclonic ice motion is associated with divergence, and anticyclonic motion is associated with convergence. As discussed, the turning angle is larger in summer, when the ice motion approaches "free drift," and smaller in winter, when internal ice forces are strong. Serreze et al. (1989) applied the Thorndike and Colony approach to estimate ice divergence in the Canada Basin during summer. They found that because

of frequent episodes of cyclonic ice motion, forced by the frequent migration of atmospheric lows into the region, the calculated divergence in the interior ice pack can be large. For example, during the thirty-day period of August 13 to September 11, 1980, when the ice motion was strongly cyclonic, aggregate divergence rates of up to 0.75 percent per day were calculated. Over the thirty-day period, this amounts to a total opening of more than 20 percent. Estimates based in the IPAB data were somewhat lower (0.50 percent per day). This is counter to the situation for most of the year, when ice motion in this area tends to be anticyclonic (the Beaufort Gyre) and hence slightly convergent.

As part of the SHEBA field study, H. Stern and Moritz (2002) evaluated time series of ice divergence at several different scales centered over the main SHEBA camp (Figure 7.15). They based these estimates on the Radarsat (synthetic aperture radar, or SAR) Geophysical Processor System, using same basic feature-tracking approach just described with respect to SSM/I. However, the ice motion fields from Radarsat are at a much finer (5 km) spatial resolution. Although the basic time series structure as well as the magnitudes of divergence are similar at the different scales, (all fairly large, ranging from 50x50 km to 200x200 km), there are differences. Divergences/convergences exceeding 1 percent per day are not uncommon. The extremes are around 4–5 percent per day.

Stern and Moritz (2002) discuss the annual cycle with reference to Figure 7.15. In autumn and early winter, as the pack ice is growing and becoming stronger, the divergence is mostly positive (new leads form and new ice grows). There is a cumulative divergence of about 25 percent between November 1 and December 25. January contains large divergence and convergence events. Winds are moderate through the month, varying from northerly to easterly. The ice drifts generally westward and leads form with a generally northwest-southeast orientation. At the end of January, wind speeds pick up quickly, and the direction changes to slightly south of easterly. This causes large convergences. Leads that were formed earlier in the month close and ridging occurs. From February through July, divergent and convergent events are small, but the ice undergoes a gradual convergence of about 15 percent as the SHEBA station drifts within the Beaufort Gyre. The large divergence at the end of July is associated with a storm. After this time, the nature of the deformation becomes more random, consistent with low summer ice strength associated with “free-drift.” After about September 11, the ice enters a period when, in response to seasonal cooling, it begins to gain strength and eventually redevelops the more winter-like property of “plates and cracks.” The ice pack became well consolidated by October 4.

7.4 Drivers of Large-Scale and Regional Sea Ice Variability

7.4.1 Overview

As already pointed out, there are downward linear trends in Arctic sea extent over the period of satellite observations for all months, smallest in the winter months and

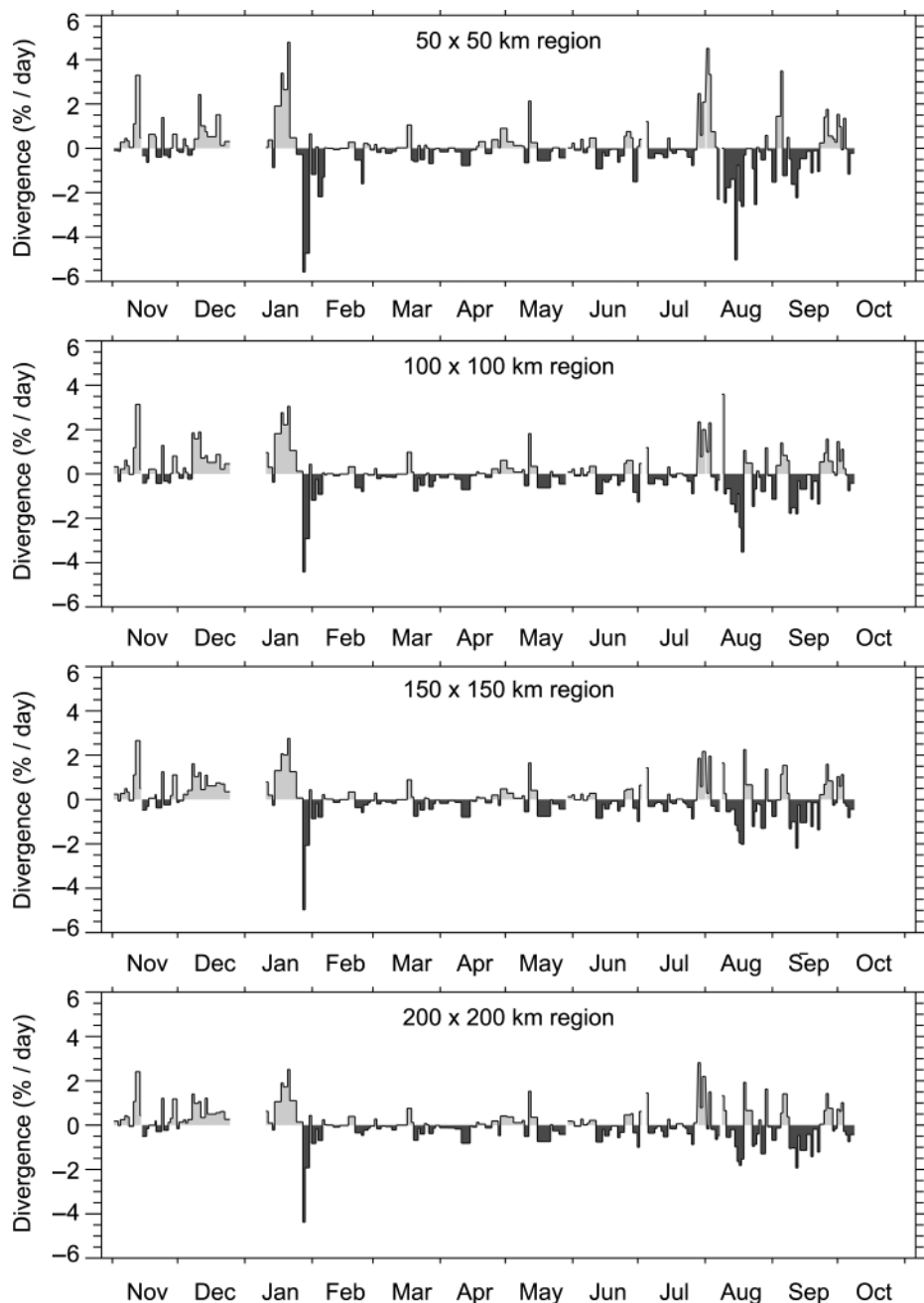


Figure 7.15. Time series of sea ice divergence (in percent per day) in the vicinity of the SHEBA station calculated at four different spatial scales (average sizes) centered on the station, based on the RADARSAT RGPS (from Stern and Moritz, 2002, by permission of AGU).

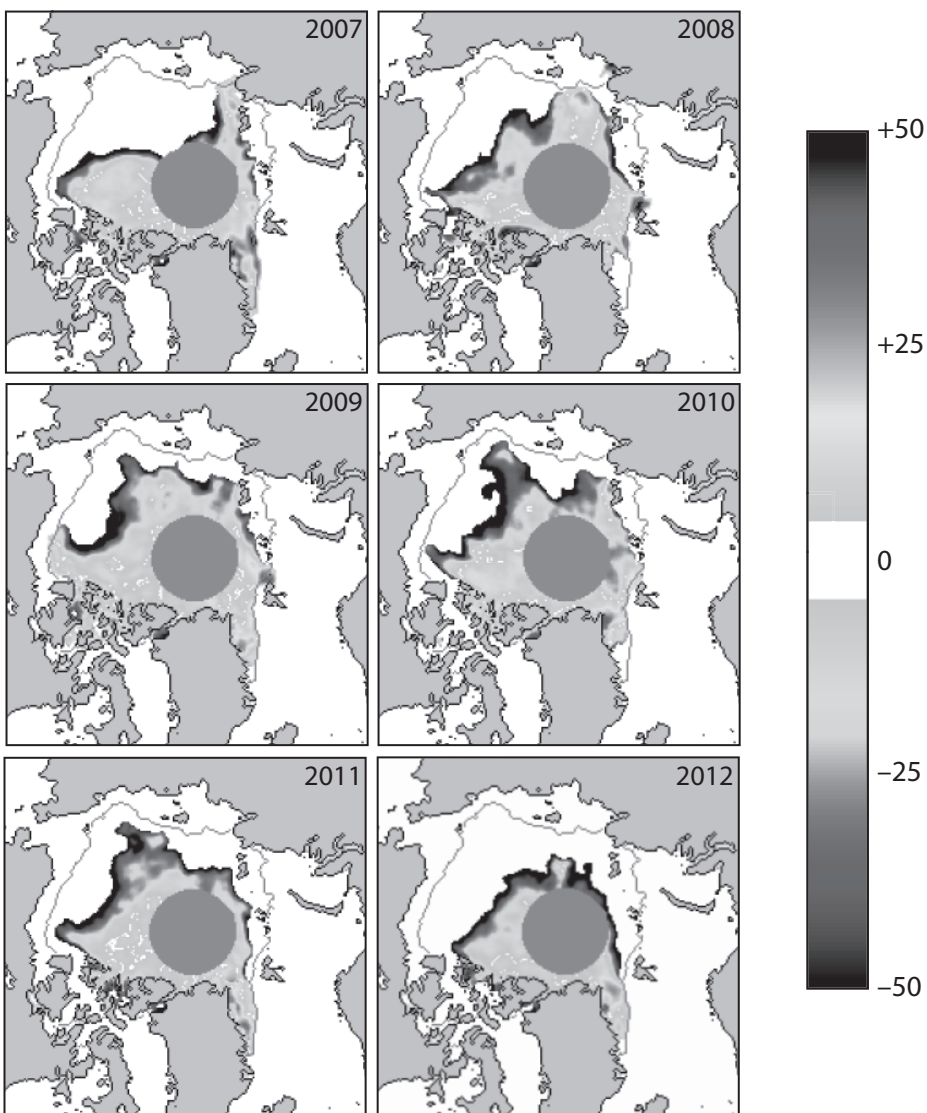


Figure 7.16. Mean September ice extent (all colored regions) and anomalies in ice concentration (in %, see color bar) for the years 2007 through 2012, based on satellite passive microwave data. The median September ice extent is shown by the gray line. Concentration anomalies and median extent are both referenced to the 1979–2000 period, which includes data from SMRR. This accounts for the larger “polar hole” of no data coverage compared to the SSM/I SSMIS period 1987–present (courtesy of W. Meier, NSIDC, Boulder, CO). (See plate section for color version.)

largest for September, the end of the melt season. This has been attended by general thinning of the ice cover. However, a closer look at the record reveals that the September trend in total Arctic sea ice extent (Figure 1.6), as well as trends in other months, is superposed on large variability from year to year; and this strong year-to-year variability in total extent is accompanied by especially pronounced variations

in regional extent (and concentration). This is evident in Figure 7.16, which shows September ice extent and concentration for the years 2007–2012; these six years have the lowest extent in the satellite record based on data through 2012. Although they share the general pattern of extensive open water along the shores of Siberia and Alaska, each year has unique features. Arctic wide and regional sea ice variability are strongly tied to variations in atmospheric circulation patterns. In some cases, it appears that the ice cover has multiyear and even decadal “memory” of forcing by anomalous atmospheric circulation patterns. There is also growing evidence that the general climate warming viewed as driving the basic downward trend in ice extent has altered the response of the ice cover to natural climate variability. Changes in ocean heat transport, including both the import of warmer Pacific waters through the Bering Strait and the import of warmer Atlantic waters to the Arctic, have played potentially important but still unclear roles in sea ice variability and trends. The following sections illustrate some of these points.

7.4.2 Case Study for 1990

At the time, September 1990 had the lowest September sea ice extent in the satellite record. It was examined by Serreze et al. (2003b) as a case study. The low extent was mostly attributed to extensive open water in the Chukchi, East Siberian and Laptev seas. The onset of the anomaly was observed in spring. Over the May–June period, positive near surface temperature anomalies encompassed all of the Arctic Ocean, but largest along the Siberian coast. The sea level pressure field for May was characterized by a mean low of 996 hPa centered at about 80°N, 100°E (Figure 7.17). This corresponds to a local anomaly of about 20 hPa. This significant atmospheric event was associated with strong southerly winds along the Siberian coast. The location of the mean low is furthermore consistent with the temperature anomalies (especially strong positive anomalies were found east of the low) and the observation of early coastal melt. The strong winds also explain the development during this month of areas of open water and low concentration ice in the Laptev and East Siberian Seas. This resulted in an early reduction of the surface albedo, further enhancing the melt process through the albedo feedback effect (see Chapter 5). Increased cloud cover in June may have also played a role (the radiative cloud forcing is positive in this month). Even though the ice extent anomaly was already large by July, it grew rapidly during August. This resulted from the development of a strong anticyclone centered north of Alaska, associated with strong easterly winds in Chukchi and East Siberian seas. As the ice motion tends to be to the right of the geostrophic wind, the result was a poleward motion of ice away from the coast.

7.4.3 The SHEBA Anomaly

We next examine a pronounced regional anomaly that developed in summer 1998, examined as a case study by Maslanik, Serreze, and Agnew (1999). It is sometimes referred to as the “SHEBA anomaly” as it occurred during the SHEBA field year,

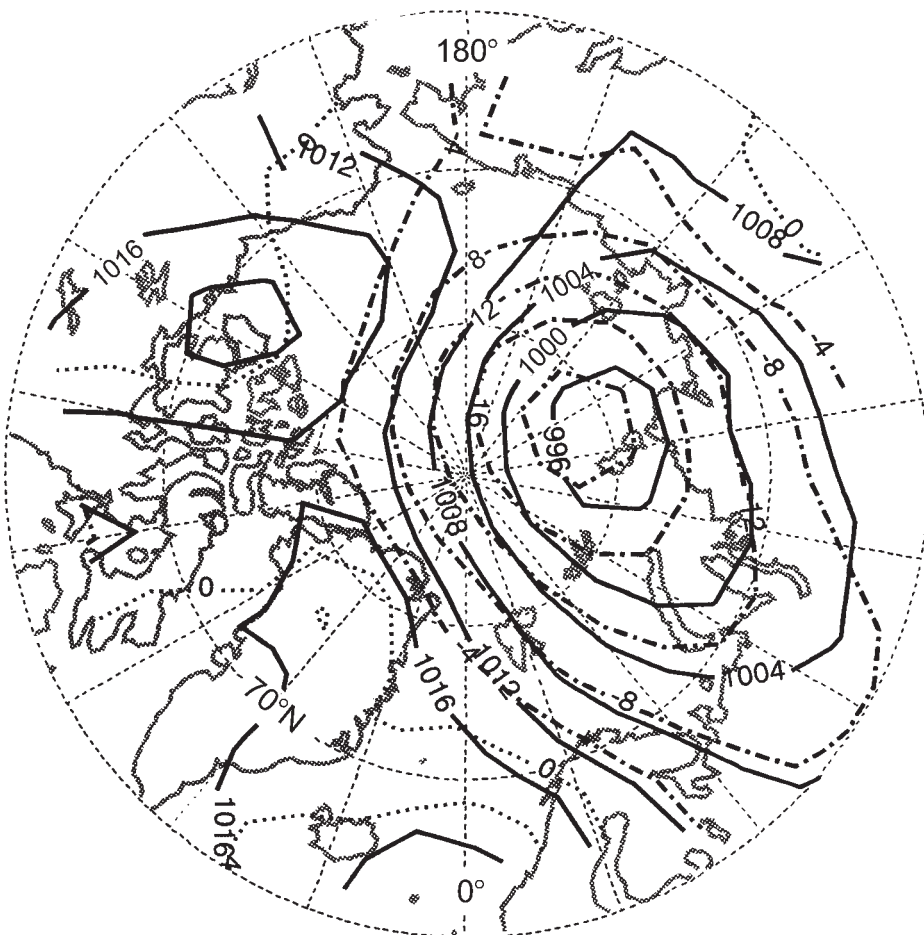


Figure 7.17. Mean sea level pressure and anomalies (hPa) for May 1990 from NCEP/NCAR (from Serreze et al., 1995, by permission of AGU).

and was characterized by extensive open water in the Beaufort and Chukchi seas. Open water formed earlier in this region than in prior years, and September ice extent was 25 percent less than the previous minimum over the 1953–1997 period. The times series of Beaufort Sea ice extent at the end of September clearly shows the year of 1998 standing out as an extreme (Figure 7.18). Note that ice extent was also quite low in the preceding summer of 1997. Over the period of record examined by Maslanik et al. (1999), 1997 and 1998 were the only two successive years when summer ice extent in the Beaufort Sea was at least one standard deviation below the mean.

In a previous paper, Rogers (1978) diagnosed variability in ice conditions in the Beaufort Sea from composite differences in summer-averaged sea level pressure fields between heavy and light ice years. Light ice years are associated with positive pressure differences over the northern Canadian Arctic Archipelago and north-central Siberia, and negative differences over the East Siberian Sea. This strengthens

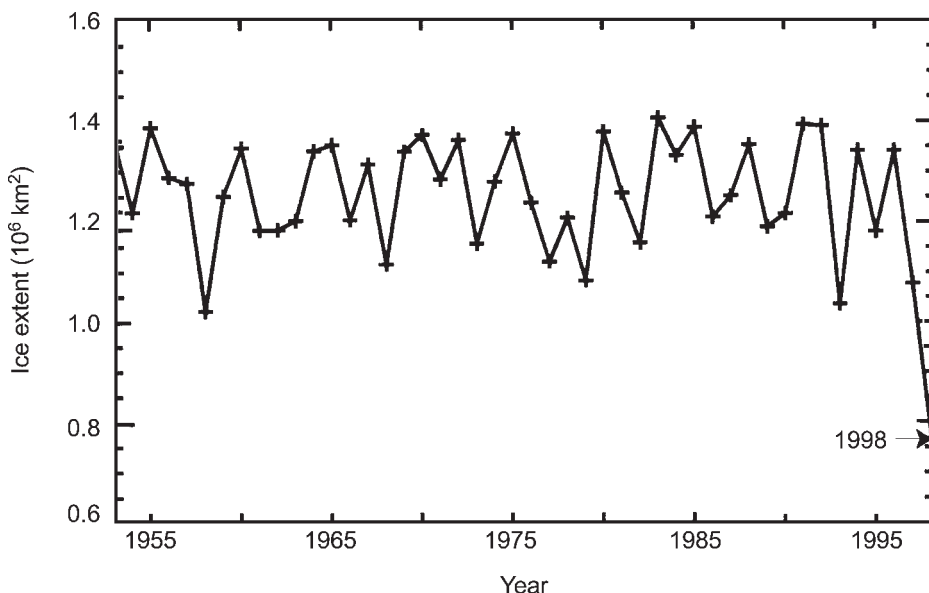


Figure 7.18. Sea ice extent at the end of September for the Beaufort Sea region over the 1953–1998 period (from Maslanik et al., 1999, by permission of AGU).

the mean easterly and southerly winds over the Beaufort Sea and favors positive temperature anomalies, promoting melt and the transport of ice to the west and north. The sea level pressure and temperature anomalies for the summer of 1997 exemplify the pattern outlined by Rogers (1978) for light ice years. The situation in summer 1998 was somewhat different. Stronger regional pressure gradients favored stronger ice motion to the west and north. There were also more positive temperature anomalies over the southern Beaufort Sea as compared to 1997 and other light ice years. In response to the general westward ice drift, ice concentration and extent were well above normal in the East Siberian Sea.

The region of open water that developed in the previous summer of 1997 was replaced the following autumn and winter by primarily thin, first-year ice. First-year ice, being relatively thin, will tend to melt out preferentially the next summer. M. McPhee et al. (1998) predicted that because of this preconditioning, a negative ice anomaly would develop in summer 1998. Although his prediction turned out to be correct, the atmospheric conditions favoring ice reductions were even better expressed in 1998 than 1997. The larger size of the 1998 anomaly hence appears consistent with the dual effects of preconditioning and summer atmospheric forcing. As pointed out by Maslanik et al. (1999), the extreme size of the 1998 anomaly also requires consideration of other aspects of preconditioning. The November 1997–April 1998 circulation at sea level points to a decrease in northerly winds over the Canada Basin, reducing the transport of older, thicker ice into the Beaufort Sea that would normally be supplied by the Beaufort Gyre circulation. This allowed the large expanse of thin first-year ice to remain in the Beaufort Sea, contributing to the large ice loss in the summer of 1998.

7.4.4 Influences of the NAO and AO

Several studies documented an upward trend in either ice volume or ice area fluxes through the Fram Strait and into the North Atlantic from the late 1970s through much of the 1990s (e.g., Kwok and Rothrock, 1999) coincident with the period discussed in Chapter 4 when the North Atlantic Oscillation, or NAO, exhibited a shift from a generally negative to a generally positive phase. In explanation, the shift in the NAO phase was linked to strengthening of the sea level pressure gradient across the Fram Strait (meaning a more north to south wind flow through the strait). Sea ice extent east of Greenland nevertheless tends to be below average under the positive NAO state (e.g., Deser et al., 2000; Dickson et al., 2000). As offered by Dickson et al. (2000), part of the explanation is that the positive NAO phase favors a stronger poleward flux of relatively warm ocean waters that inhibits ice formation. The relationship between the NAO index and the Fram Strait outflow is furthermore inconsistent. Even with a negative NAO index, it is possible to achieve a strong pressure gradient over the Fram Strait and a large ice outflow. This appears to have been the case during the period of the Great Salinity Anomaly, which will be examined shortly. The observed relationship between ice extent east of Greenland and the NAO assessed by Dickson et al. (2000) is summarized in Figure 7.19. The figure plots the median ice border at the end of April for the 1963–1969 (low index) and 1989–1995 (high index) periods.

The downward trend in September sea ice extent over the satellite record is dominated by reductions along the Siberian and Alaskan coasts. There is evidence of links between the onset of this pattern and the past behavior of the Arctic Oscillation, or AO (recall from Chapter 4 that the AO, also known as the Northern Annular Mode, is closely related to the NAO). We review the issue with the aid of Figure 7.20, adapted from the study of Rigor, Wallace, and Colony (2002). The top panel shows observed linear trends in summer sea ice concentration and winter sea ice motion based on the 1979–1998 period. The bottom panel shows the components of summer sea ice concentration and winter sea ice motion regressed on the winter AO index. The observed trends in winter sea ice motion indicate a change to a more cyclonic pattern. Care should be exercised in the interpretation. Although the actual winter ice motion remained generally anticyclonic, the trend over the study period was toward more cyclonic conditions. The main point is that the patterns in the two panels are very similar – most of the change in summer sea ice concentration and winter ice motion relates to the trend in the winter AO. It appears that changes in the winter wind field associated with the general trend in the winter AO toward its positive phase led to changes in the sea ice motion tending to both advect ice away from the Siberian and Alaskan coasts and (because of the cyclonic tendency) promote more ice divergence (or less convergence). This led to an anomalous coverage of thin ice. With thinner ice in spring, the stage was set for large summer ice losses that started to be observed in the 1990s.

The subsequent analysis of Rigor and Wallace (2004) provides a different perspective on the role of the AO. Using a simple sea ice model, they found that

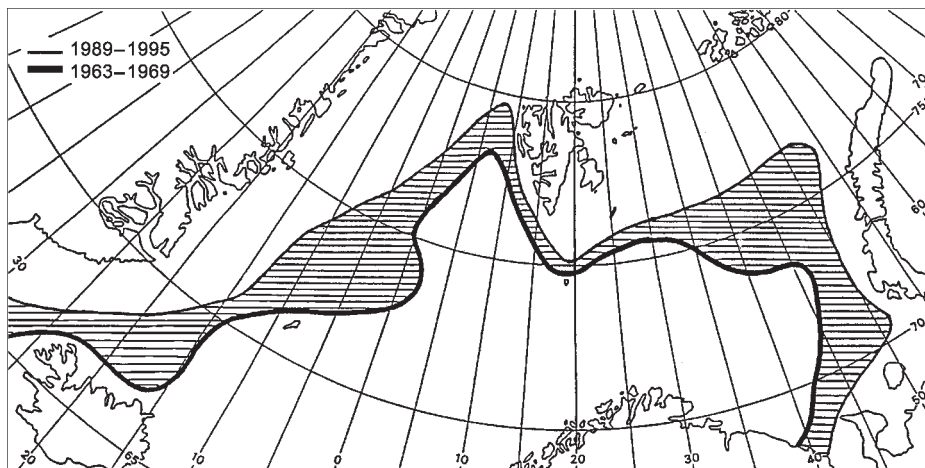


Figure 7.19. The median ice border at the end of April for the 1963–1969 and 1989–1995 periods, corresponding, respectively, to minimum and maximum phases of the NAO index. The more northerly position of the ice edge for the 1989–1995 period corresponds to a reduction in ice extent of about 587,000 km² from the 1963–1969 period (from Dickson et al., 2000, by permission of AMS).

circulation patterns associated with positive AO conditions, particularly dominant over the 1989–1995 period, decreased the areal extent of old thick ice, mostly via transport through the Fram Strait. The Arctic was then left with an anomalous coverage of younger and thinner ice. During the summers of 2002 and 2003, this younger, thinner ice circulated back into Alaskan coastal waters via the Beaufort Gyre circulation, where extensive ice melt occurred. These recent minima in ice extent are therefore viewed as a delayed response to the 1989–1995 high AO index phase.

It has also been shown that September Arctic ice extent following summers with a positive phase of the summer AO tends to be greater than following summers with a negative phase of the summer AO (Ogi and Wallace, 2007). As outlined in Chapter 4, Ogi et al. (2004), defined the AO separately for each calendar month, an approach argued to better capture seasonal changes in the structure of the mode. Based on their approach, the summer AO has a smaller meridional scale than its winter counterpart, with the Arctic center of action lying over the central Arctic Ocean. When the summer AO is positive, the prevailing atmospheric circulation has a cyclonic anomaly – in general, the positive AO phase is linked to a high frequency cyclone activity. Because of the more cyclonic wind pattern, the sea ice motion tends to be cyclonic and hence divergent, spreading the ice over a larger area. In turn, the stormy pattern tends to bring fairly cool conditions and even snowfall events, inhibiting summer melt. The negative phase of the summer AO is associated with an anticyclonic circulation pattern, which favors ice convergence and relatively warm conditions, in turn favoring melt.

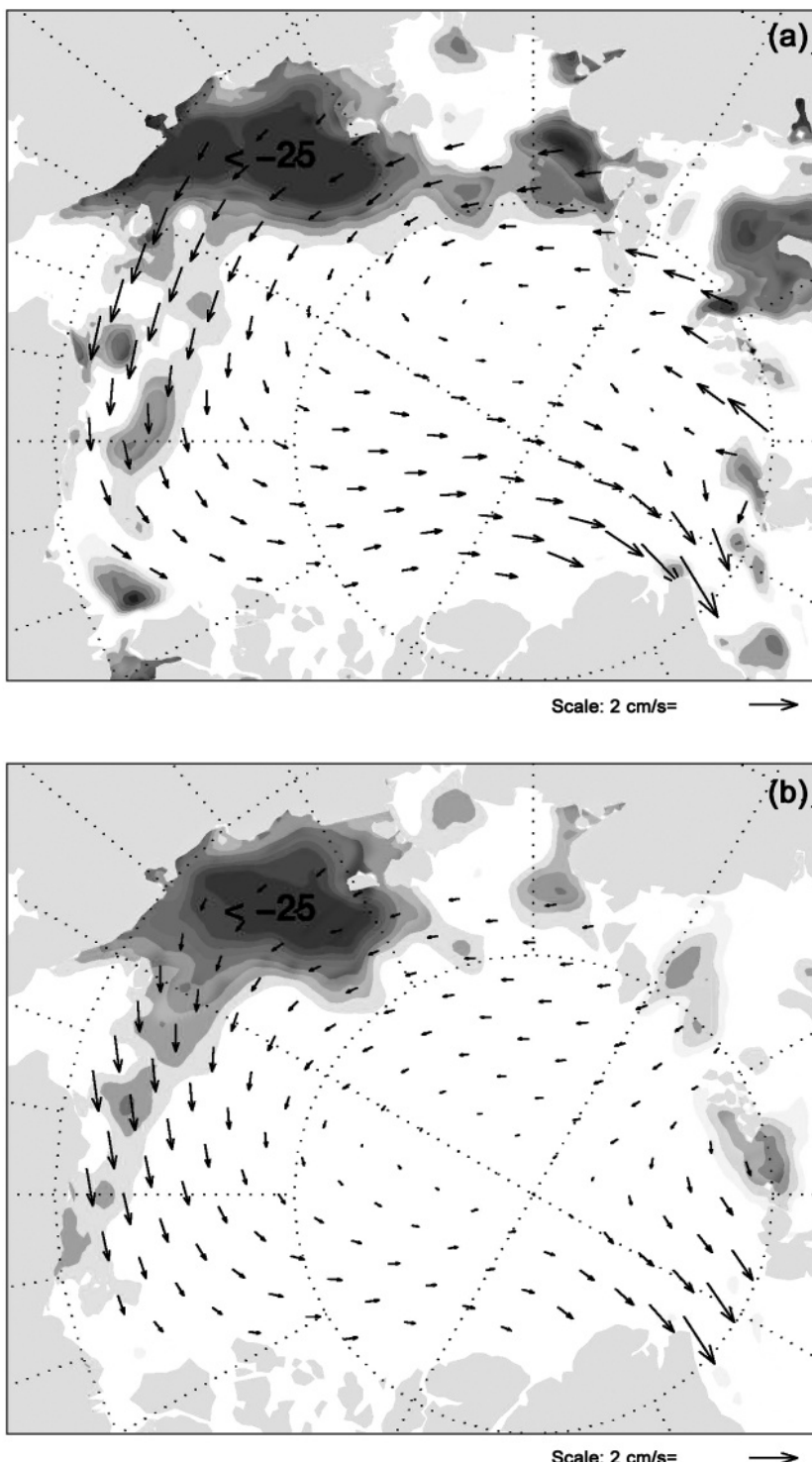


Figure 7.20. Large-scale trends in observed winter sea ice motion and summer sea ice concentration (a) and regressions on the prior winter AO index (b). Results are based on the 1979–1998 period. Shading is proportional to the magnitude of the ice concentration trends (adapted from Rigor et al., 2002, by permission of AMS).

7.4.5 The Arctic Dipole Anomaly

Again looking back to Chapter 4, recall that the Arctic Dipole Anomaly has been defined as an atmospheric circulation pattern which in its positive mode features above average sea level pressure centered north of the Beaufort Sea (essentially a strong Beaufort Sea high) and below average pressure centered over the Kara Sea. Resulting southerly winds between the pressure anomaly centers at the surface favor transport of ice away from the coasts of Siberia and Alaska toward the North Pole, as well as strong melt in the East Siberian and Chukchi seas. The pattern also favors a strong sea level pressure gradient across the Fram Strait (between Greenland and Svalbard) that enhances the wind-driven transport of sea ice out of the Arctic Ocean and into the North Atlantic. The negative phase has a broadly opposing pressure anomaly pattern. The positive pattern was very well-developed throughout the summer of 2007 and was a key factor in this year having the second lowest September sea ice in the satellite record (based on data through 2013). It is widely viewed that because of the general thinning of the ice cover over the past few decades, making large areas more vulnerable to melting out in summer, the effects of the dipole anomaly circulation pattern on promoting ice loss in the summer of 2007 was much greater than would have been the case twenty years ago, when the ice was thicker and more resilient.

7.4.6 Ocean Heat Transport

Recall from Chapter 2 that, under the Arctic halocline, there is a warm, salty layer arising from the inflow of Atlantic waters. Although the strong stability associated with the cold Arctic halocline inhibits mixing of this warm water upward to affect the ice cover, there is growing evidence that some of this heat may indeed be having an effect. Evidence first arose from a series of oceanographic studies in the late 1990s, which indicated that in comparison with earlier climatologies, the Arctic Ocean in the 1990s was characterized by a more widespread influence and warming of Atlantic-derived waters. The Atlantic-derived sub-layer warmed 1–2°C compared with Russian climatologies of the 1940s–1970s and the level of the subsurface temperature maximum extended (shoaled) upward (to about 200 m from some observations). The Atlantic water influence also spread west. Evidence also arose of a weakening of the cold halocline in the Eurasian Basin (Steele and Boyd, 1998), largely attributed to eastward diversion of Russian river inflow in response to changes in the atmospheric circulation. The Atlantic layer changes were ascribed to increases in the Atlantic inflow through the Fram Strait and the Barents Sea region, and some warming of this inflow. The changing inflow appeared to have links with altered surface winds as the winter NAO/AO shifted toward a predominantly positive phase (Dickson et al., 2000). Modeling studies (Maslowski et al., 2000) suggested that the Atlantic layer changes promoted a stronger upward ocean heat flux, contributing to the sea ice losses. Whether weakening of the cold halocline played an additional role is not clear. Work by W. Maslowski, W. Marble, and W. Walewski (2001) also pointed to an influence of a warmer inflow of Pacific waters through the Bering Strait.

As of the writing of this textbook, warming of Atlantic-layer (150–900 m) waters in the Arctic has continued (Polyakov et al., 2005, Polyakov et al., 2010). The warming process has been uneven; a temperature increase of about 1°C in the mid1990s was followed by cooling, then another warming event peaking in 2007, resulting in higher temperatures than observed in the 1990s. The most extreme warming occurred in the Eurasian and Makarov Basins, associated with weakening of the upper ocean stratification in the Eurasian Basin. Based on these observations and modeling, I. Polyakov et al. (2010) argue that there has been a substantial additional ocean heat flux to the bottom of the sea ice cover resulting in thinning on the order of 30 cm, comparable to that attributed to atmospheric warming. They view this ocean-induced thinning as making the ice more vulnerable to disruption by extreme atmospheric events, such as observed in the summer of 2007. The subsequent study of Spielhagen et al. (2011), based on paleoclimate evidence, concludes that the early-twenty-first century temperatures of Atlantic water entering the Arctic are unprecedented over the past 2,000 years. In recent winters, ice free conditions in the Barents Sea and the vicinity of Svalbard, in the vicinity where the Atlantic inflow subducts under the Arctic halocline, have extended further north as compared to past decades. This may well manifest the enhanced oceanic heat transport inhibiting winter ice growth (Alexeev et al., 2013). This increased transport, in turn, can be linked to the warm phase of the Atlantic Multi-decadal Oscillation (AMO). The AMO describes a multidecadal oscillation in North Atlantic sea surface temperatures, with the largest changes in the higher latitudes of the Atlantic. The AMO can be linked to the strength of the component of the thermohaline circulation that transports warm surface waters poleward in the North Atlantic. The changing behavior of the AMO has also been invoked more generally to explain the pattern of Arctic warming from about 1920 to 1940, cooling up to about 1970, and renewed warming thereafter (Chylek et al., 2009).

Other studies point to a role of warmer Pacific Surface Water entering the Arctic Ocean via the Bering Strait. K. Shimada et al. (2006) find a link between increases in Pacific Surface Water temperature in the Arctic Ocean beginning in the late 1990s, concurrent with the onset of sharp sea ice reductions in the Chukchi and Beaufort seas. They argue that delayed winter ice formation allows for more efficient coupling between the ocean and wind forcing. This redirects PSW from the shelf slope along Alaska into the Arctic Ocean, where it is more efficient in retarding winter ice growth. An imbalance between winter ice growth and summer melt results, accelerating ice loss over a large area.

7.5 The Fram Strait Outflow, the Thermohaline Circulation and the Arctic Back Door

7.5.1 The Fram Strait Outflow

As the primary region for the export of sea ice and low-salinity water out of the Arctic and hence a key player in the freshwater budget of the Arctic Ocean (see

Chapter 2), the Fram Strait outflow merits special attention. A number of efforts have been made to estimate the ice area or volume flux through the Fram Strait based on mass balance requirements, measurements of ice drift, and thickness through the strait, models or a combination of models and observations. The total ice flux is comprised of a wind-driven and a current-driven component. Determining the volume flux requires accounting for the ice velocity through the strait, the ice concentration and ice thickness.

Some early estimates based on direct measurements include Wadhams (1983) and Vinje and O. Finnekasa (1986). Vinje and Finnekasa (1986) also used an indirect method to estimate the flux. A regression equation was developed between available time series of the observed monthly averaged drift speed profile across the strait and the monthly difference in sea level pressure between the Fram Strait (81°N , 15°W) and the central area of the Norwegian Sea (73°N , 5°E). The slope of the regression equation represents the fraction of the ice velocity attributed to time-varying winds, and the y-intercept represents the constant effect of the ocean current. The regression equation was used to compile volume flux time series by incorporating climatological monthly values of the ice thickness and concentration. The advantage of this approach is that, because long time series of sea level pressure are available, long time series of the estimated flux can be obtained.

Time series of estimated ice concentration and velocity are available from satellite data since the late 1970s. Moored upward-looking sonar (ULS) sites in and around the strait have provided estimates of ice thickness since about 1990. R. Kwok and D. Rothrock (1999) took advantage of satellite and ULS data to obtain the cold-season (October–May) area flux over the 1978–1996 period. Ice velocities across the strait were obtained from an ice tracking procedure using sequential images from SMMR and SSM/I. The derived velocities were used in conjunction with SMMR and SSM/I ice concentration data to obtain area flux time series. They obtained monthly volume fluxes by adjusting the velocities based on profiles of mean monthly ice thickness from ULS. However, their technique was not applied to summer months because of biasing of the passive microwave data by melt effects.

Vinje (2001) used a regression-based approach along with the best available estimates of ice velocity and ice thickness from SAR, buoy drifts and ULS to provide an ice volume record extending from 1950 to 2000. The mean annual flux is about 2900 km^3 . Using nine years of ULS data, Kwok, G. Cunningham, and S. Pang (2004) report a somewhat lower value of $2,200 \text{ km}^3$ per year. Vinje estimated that 60 percent of the total annual ice volume flux is wind driven, and about 40 percent is attributed to the background ocean current. The mean cross-strait ice thickness is 2.56 m. A striking feature of the outflow based on this study is its pronounced annual cycle (Figure 7.21). The largest volume fluxes are found in autumn and winter, when there are strong northerly winds in the strait. The flux is smallest in summer when the northerly winds slacken and are replaced by weak southerlies in July and August. A comparison between the two lines in Figure 7.21 illustrates the effects of adjusting for the mean annual cycle of ice thickness. The adjustment accounts for the thicker ice observed from March through July and the thinner ice for the rest of the year. A conspicuous feature of Vinje's (2001) reconstructed monthly time series

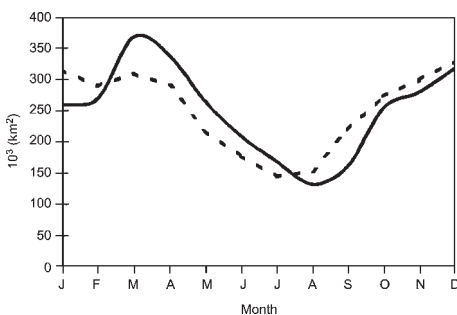


Figure 7.21. Mean annual cycle of the ice volume flux through the Fram Strait. The dotted line shows the 1950–2000 parameterized mean monthly flux. The solid line shows the volume flux adjusted for the mean ice thickness observed from 1990–1996 using upward-looking sonar (from Vinje, 2001, by permission of AMS).

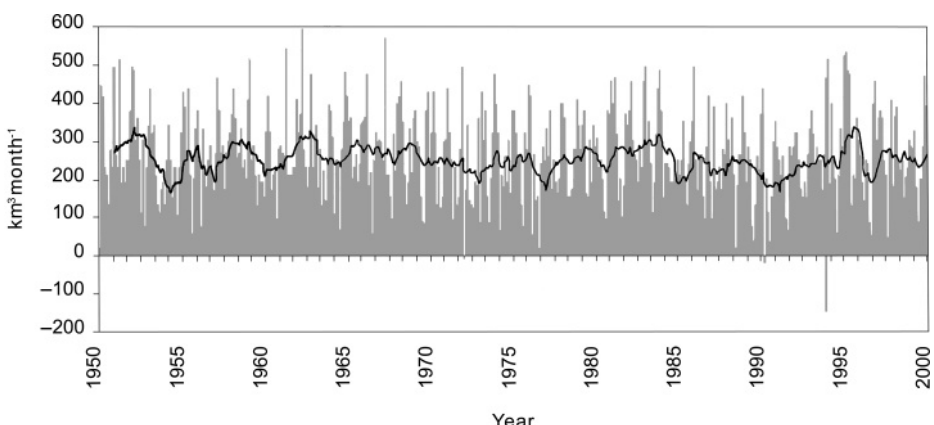


Figure 7.22. Time series of the parameterized monthly ice volume flux through the Fram Strait (grey columns) and the twelve-month running mean (black line) (from Vinje, 2001, by permission of AMS).

(Figure 7.22) is the large variability. Although there are no obvious long-term trends in Figure 7.22, other investigators have noted a trend in either the volume or area fluxes from the late 1970s through much of the 1990s (e.g., Kwok and Rothrock, 1999), which can be related to the shift in the NAO/AO that has been discussed previously. Kwok et al. (2004) cite a squared correlation between the winter Fram Strait ice area outflow and the NAO index of 0.62.

7.5.2 The THC – Basic Considerations

Ocean transports act along with atmosphere transports to convey heat from low to high latitudes (Chapter 3). Much of the oceanic heat transport is associated with the global thermohaline circulation (THC). The THC, also referred to as the Great Ocean Conveyer (and similar names), is the ocean circulation driven by horizontal and vertical gradients in ocean salinity and temperature (hence density gradients). In the northern North Atlantic, there is an intense winter heat loss from the ocean to the atmosphere. Cooling of the water causes its density to increase. This cool water sinks, causing deep water (North Atlantic Deep Water, or NADW) to be formed

in the Greenland-Iceland-Norwegian (GIN) seas. In a thermally direct circulation, these sinking regions are fed by warm, saline waters brought in by the THC from lower latitudes, with the cold NADW then returning to the south at deep ocean depths. The Atlantic Meridional Overturning Circulation (AMOC) (Srokosz et al., 2012) can be broadly thought of as the Atlantic part of the THC. Variations in the strength of the AMOC are in turn related to the AMO (Knight et al., 2005).

Unlike the Atlantic, no deep sinking of waters is observed in the high latitudes of the North Pacific. The difference between the Atlantic and Pacific can be readily observed in regional climate. The moderating effect of oceanic heat loss in the high latitudes of the North Atlantic (which is heat gained by the atmosphere) leads to high surface air temperatures over northern Europe and northwestern North America. Northern Europe is much warmer than comparable latitudes in the Pacific. If the present state of the THC were to change, this could have pronounced effects on climate (Manabe and Stouffer, 1999; Weaver et al., 1999; Clark et al., 2002). A considerable body of evidence points to links between the THC and Arctic freshwater fluxes through the Fram Strait.

7.5.3 The Arctic “Back Door”

The nature of the THC is an area of intense study. No complete explanation can be offered as to why deepwater forms in the North Atlantic and not in the North Pacific and how the Arctic maintains or modulates this state. The issue is a complex one and only the major points are outlined here. A. Weaver et al. (1999) and A. Stigebrandt (2000) provide further reading.

One observation bearing on the problem is the more stable stratification in the North Pacific as compared to the North Atlantic. In the North Pacific, surface water salinities are on average 32.8 psu with deep waters at 34.6 to 34.7 psu. By contrast, in the North Atlantic, surface waters are 34.9 psu, with deep waters between 34.9 and 35.0 psu. Even if North Pacific waters are cooled to their freezing point, they are so fresh that they can sink to only a few hundred meters, whereas those in the North Atlantic can sink to great depths.

Regarding how the stratification difference between the two basins is maintained, B. Warren (1983) highlights that there is nearly twice the evaporation over the North Atlantic as over the North Pacific (1030 mm yr^{-1} versus 550 mm yr^{-1}). The higher evaporation in the North Atlantic is associated with higher SSTs, in part owing to the greater northward advection of warm, subtropical waters by the Gulf Stream. It has also been proposed that because of the narrower width of the Atlantic as compared to the Pacific, a greater fraction of its area is prone to incursions of cold, dry continental air that favor evaporation and heat loss at the sea surface. There is also a net transport of water vapor from the Atlantic to the Pacific. The idea is that the low-elevation Isthmus of Panama allows a transport of moisture from the Atlantic to the Pacific via the trade winds, whereas the high-elevation Rocky Mountains inhibit transport from the Pacific to the Atlantic by the westerly flow. For a steady state, imbalances in net precipitation between different ocean basins brought about

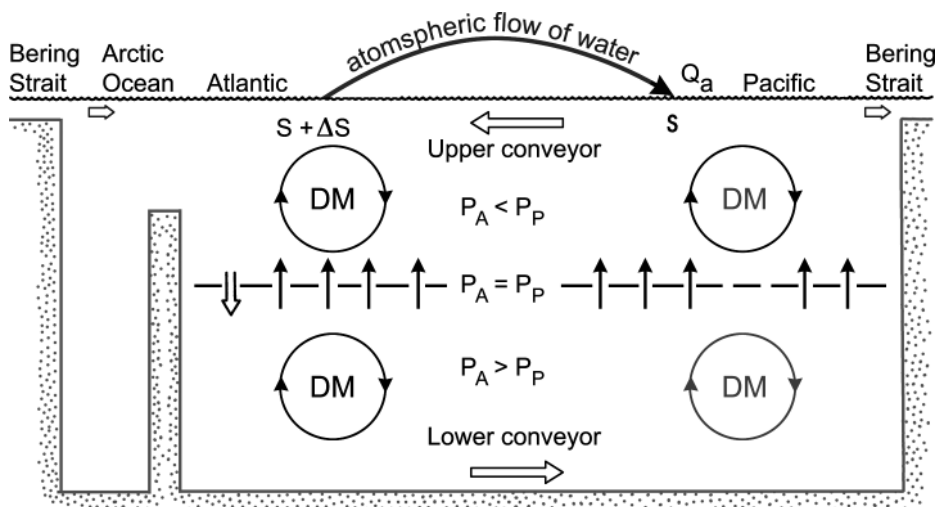


Figure 7.23. Conceptual model of the present-day atmospheric and oceanic transports and its consequences. DM is diapycnal mixing, P_A (P_P) is pressure in the Atlantic (Pacific) and S is salinity (from Stigebrandt, 2000, by permission of Springer-Verlag).

by evaporation and atmospheric transport have to be compensated by transports in the ocean.

Figure 7.23 provides a conceptual view of the problem. The net atmospheric transport of water from the Atlantic to the Pacific (denoted by the curved arrow at the top) means higher salinities in the Atlantic, promoting deepwater production. Spatial salinity variations in the upper ocean correspond to density variations, and hence corresponding variations in sea level (the “steric effect”). Assuming a level of no motion at 1,200 m depth, the sea level in the fresher North Pacific stands about 0.65 m higher than in the North Atlantic. This leads to a flow of low-salinity water from the North Pacific through the Bering Strait, through the Arctic Ocean, and then into the North Atlantic through the Fram Strait. As articulated by M. Steele, D. Thomas, and Rothrock (1996), this “back door” through the Arctic Ocean (the upper conveyor of Figure 7.23) works to reduce the salinity difference between the basins. To close the loop, there must also be a lower ocean conveyor with a net salt transport from the Atlantic to the Pacific. To summarize, the atmospheric freshwater transports are continually working to strengthen the salinity difference between the Atlantic and Pacific, while the ocean circulations are working to destroy the differences. The Arctic “back door” is a key element of the oceanic freshwater exchange.

In the limit of an infinitely fast transfer rate of freshwater through the Arctic Ocean into the Atlantic, the salinity imbalance between the Pacific and Atlantic would be removed and convection in the North Atlantic might cease (Steele et al., 1996). However, as pointed out by Steele et al., this scenario is unnecessarily extreme. The deepwater formation regimes of the northern North Atlantic appear to be “delicately poised” with respect to their ability to sustain convection (Aagaard

and Carmack, 1989). Density is largely a function of salinity at low temperatures. Consequently, only a moderate freshening, such as from a change in the Fram Strait outflow, could cause freshwater capping, leading to a reduction or cessation of deepwater formation, an idea first proposed by P. Weyl (1968). Because of the differential compressibility of seawater, with cold water being more compressible (the thermobaric effect) it is likely that within some critical range, small amount of salinity stratification actually serves to promote convection (Aagaard and Carmack, 1989). However, too much freshwater caps the convection.

The study of M. Holland et al. (2001), based on a global coupled ice-ocean-atmosphere model, suggests that realistic variations in the Fram Strait ice export can lead to decadal-scale variability in the THC. The basis of this interaction is that reduced ice export leads to less ice melting in the North Atlantic. This destabilizes the ocean column, causing more deepwater formation. This results in a strengthening of the THC (that is, stronger ocean heat transport), which then reduces ice growth in the GIN seas. This warms and freshens the surface, reducing the original anomalous high ocean density, acting as a negative feedback on the system. The sensitivity of the THC to freshwater export to the North Atlantic finds further support from simulations of coupled ice-ocean models (e.g., Häkkinen, 1993, 1999).

An interesting facet of the THC debate is that the Arctic “back door” can be influenced by changes within the Arctic itself. The Fram Strait outflow is sensitive to the regional atmospheric circulation. Freshwater inputs to the Arctic Ocean from river runoff are larger than the Bering Strait inflow. Changes in the atmospheric circulation and river discharge, as well as in net precipitation over the Arctic Ocean itself, will also ultimately be seen in the Fram Strait outflow. The Holland et al. (2001) study also indicates that variability in the THC affects the atmospheric state, altering air temperature, precipitation and runoff.

7.5.4 The Great Salinity Anomaly

As also noted by Holland et al. (2001), model simulations of the variability and sensitivity of the THC appear to depend strongly on model design and complexity. Whether the THC is as sensitive to disruption as some models have indicated is still in debate. However, there is observational evidence, the best example being the “Great Salinity Anomaly” (GSA) of 1968–1982. During the late 1960s and early 1970s, the upper 100 m of the waters in the GIN seas underwent reductions in salinity from 0.1 to 0.5 psu, with water temperature anomalies of -1 to -2 K. This was associated with positive anomalies in sea ice extent in the Greenland Sea, peaking during 1968–1969 and propagating with the salinity anomalies into the Labrador Sea in 1971–1972. The salinity anomaly circulated around the Atlantic sub-Arctic gyre, returning to the Greenland Sea in 1981–1982 (Dickson et al., 1988).

Observational studies (Walsh and Chapman, 1990; Wohlleben and Weaver, 1995) as well as model evidence (Häkkinen, 1993) suggest that strong northerly winds caused an increase in the sea ice transport through the Fram Strait and into the Greenland Sea. The large freshwater flux anomaly associated with this transport

was likely enhanced by the relatively large transport of particularly thick ice from north of Greenland. Dickson and colleagues (1988) estimate the excess freshwater associated with this event to be about 2,300 km³, similar to the mean annual Fram Strait ice flux. Häkkinen's (1993) study also suggests an increased oceanic transport of fresh anomalies in the East Siberian Sea, moving across the Arctic and entering the Greenland Sea about four years later. The GSA caused cessation of convection as recorded at weather station "Bravo" (56°N, 51°W) (Lazier, 1980). Other lines of evidence indicate that it was associated with a 30 percent reduction in the strength of the Gulf Stream system (Greatbatch et al., 1991; Ezer, Mellor, and Greatbach, 1995).

The GSA nevertheless remains somewhat of a puzzle. Vinje's (2001) monthly time series (Figure 7.22) shows no obvious indication of a large change in the Fram Strait flux during the late 1960s. But there were no direct observations of the volume flux during this time. Additional GSA-like events have been documented by Belkin et al. (1998). They suggest that some of these events have a local source owing to enhanced ice formation in the Labrador Sea/Baffin Bay areas; whereas others, such as the GSA of the late 1960s to early 1970s, are remotely forced by enhanced freshwater export via either the Fram Strait or through the Canadian Arctic Archipelago. As reviewed in Chapter 10, there is convincing evidence of periods with a much weaker or altered AMOC during the last glacial cycle, the causes of which are still incompletely understood.

Focus Questions and Exercises

- 1) Imagine that a dam was placed across the Bering Strait so that there was no inflow of ocean waters from the North Pacific. Describe the potential consequences of this change on the salinity contrast between the northern North Atlantic and northern North Pacific.
- 2) Imagine a world in which there were no large rivers draining into the Arctic Ocean. What changes might you expect in the Arctic sea ice regime? On the salinity of the northern North Atlantic?
- 3) As the Arctic sea ice cover thins, episodes of sea ice divergence and convergence will tend to become stronger, meaning more leads and more ridging. Do you agree or disagree? Why?

Climate Regimes of the Arctic

Overview

The Arctic is home to a wide variety of climate conditions. This spectrum reflects, among other things, regional characteristics of the atmospheric circulation, elevation, distance from moisture sources (continentality), and properties of the surface. The present chapter both summarizes and builds on what we have already learned through a focus on some of these different climatic regimes. Up to now, relatively little attention has been paid to the Greenland Ice Sheet. This region is hence given special emphasis.

The Greenland Ice Sheet represents an extensive high elevation surface for which the albedo remains high throughout the year. Although these features distinguish its climate from other regions of the Arctic, ice sheet climates are nevertheless quite varied. The interior is very cold and dry, with summer temperatures well below freezing. Annual precipitation over the central part of the ice sheet, isolated from moisture sources, is around 100–200 mm. By comparison, the southeast coast is relatively warm and very moist. This region is strongly influenced by the North Atlantic cyclone track. Locally, in favored areas of orographic uplift, precipitation may exceed 2,000 mm. Some particularly interesting aspects of the ice sheet are its pronounced katabatic wind regime, related to radiational cooling, the significant role of sublimation on the moisture budget, and Greenland tip jets, which arise from interactions between coastal topography and the synoptic-scale wind flow. In 2012, almost all of the ice sheet briefly experienced summer melt, and summer melt extent has shown a general increase over the past several decades. The annual

mass balance of the ice sheet is now clearly negative, contributing to sea level rise.

Polar desert, the most extreme form of tundra, is widespread in the Canadian Arctic Archipelago, the unglaciated parts of northern Greenland, and the islands of the Siberian Arctic. Mean annual temperatures are well below freezing and only exceed the freezing point for one or two summer months. Annual precipitation is low, typically with a summer or early autumn maximum. Topoclimates and microclimates are often strongly developed, which can be associated with extremely low minimum winter temperatures. By comparison, local topography in some regions can give rise to foehn conditions and spells of unexpectedly high summer temperatures.

Maritime conditions are well expressed in the Atlantic sector. These regions are characterized by extensive cloudiness year round, high humidity and a fairly small annual temperature range. Precipitation in many maritime areas is quite high. In accord with seasonality in the strength of the North Atlantic storm track, there is a general cold season maximum. Maritime conditions also characterize much of the Bering Sea region. Areas along the Beaufort and Chukchi sea coasts are sometimes considered maritime, but conditions are really closer to those for polar desert.

Over the central Arctic Ocean, mean winter air temperatures are typically -30°C to -33°C , contrasting with July, when – because of the melting ice surface – mean air temperature tend to hover around the freezing point. Precipitation is generally low, with a late-summer to early-autumn maximum, corresponding to maximum cyclone activity. August cloud cover is near 90 percent.

8.1 The Greenland Ice Sheet

8.1.1 General Features

The Greenland Ice Sheet (Figure 8.1) is by far the largest terrestrial ice mass in the Arctic and is the second largest in the world (following the Antarctic Ice Sheet). The ice sheet covers an area of $1.71 \times 10^6 \text{ km}^2$. Other glaciers and ice caps on Greenland cover a further $0.49 \times 10^6 \text{ km}^2$ (Table 2.1). The ice sheet reaches a maximum elevation of just more than 3,200 m at Summit (72.6°N , 37.5°W). A secondary elevation maximum on the southern part of the ice sheet rises to about 2,800 m. The surface slope over most of the Greenland Ice Sheet is barely 1 degree, but is much greater at the margins. The margins of the ice sheet are also characterized by numerous fiords and associated ice streams and valley glaciers that drain the ice sheet. Greenland is the source of most of the icebergs found in the North Atlantic. The maximum thickness of the ice

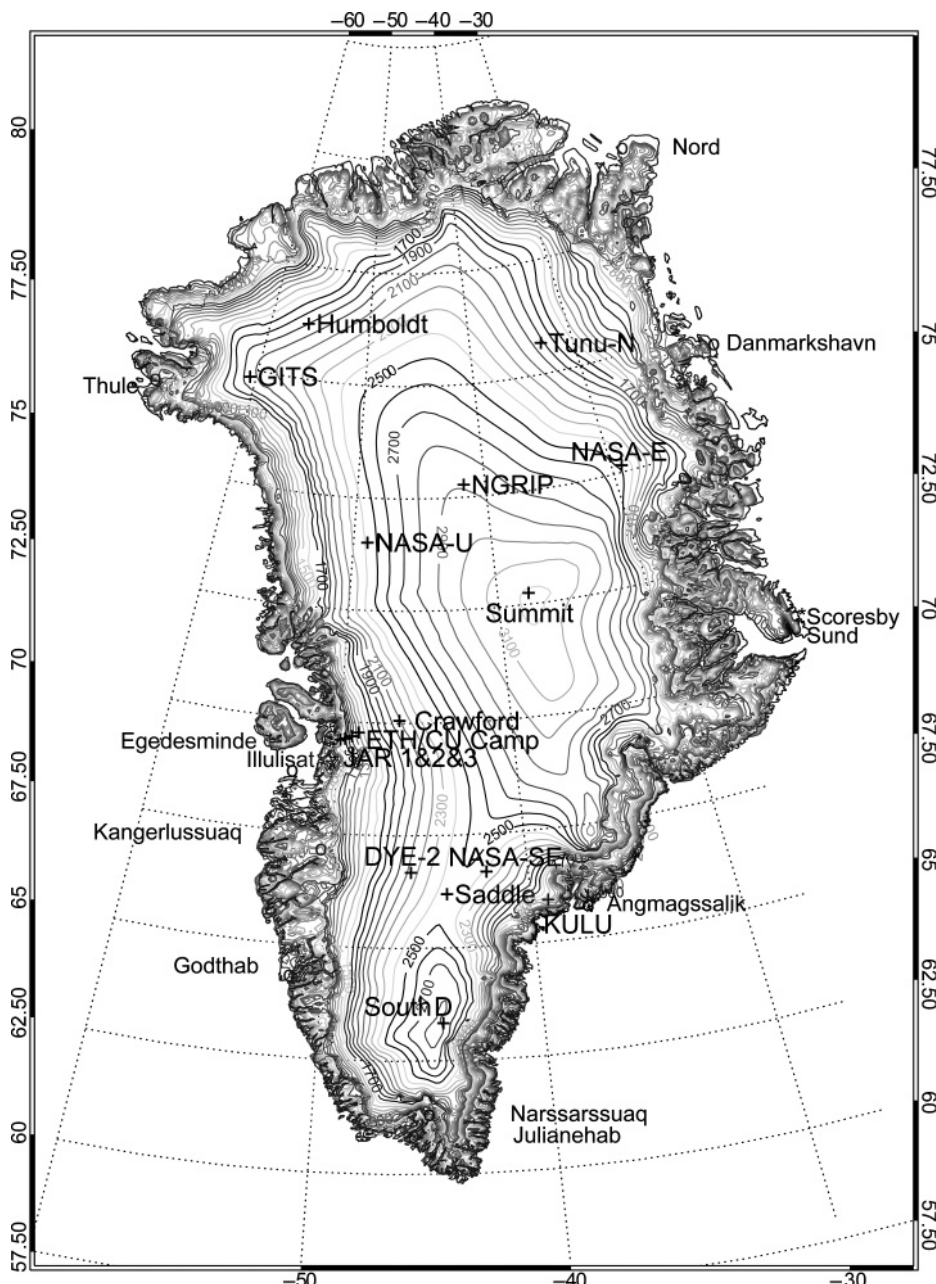


Figure 8.1. The location of GC-Net automatic weather stations in Greenland (marked +) and coastal settlements (from Steffen and Box, 2001, by permission of AGU).

sheet has been estimated at 3,367 m. The estimated ice volume is 2.93×10^6 km³ (Bamber et al., 2001). With adjustment for isostatic rebound, the water locked up in the Greenland Ice Sheet corresponds to an approximate global sea level equivalent of 7.2 m. By comparison, the much larger Antarctic Ice

Sheet, which covers about 12.3×10^6 km² with a volume of 26.5×10^6 km³, contains an adjusted 58 meters of sea level equivalent (Huybrechts et al., 2001; BEDMAP 2). Nevertheless, we are obviously dealing with a large amount of ice. J. Zwally and M. Giovinetto (2001) estimated that 88 percent of the coterminous Greenland Ice Sheet lies in the accumulation zone (where annual mass gains exceed mass losses), with the other 12 percent lying in the ablation zone (where annual mass losses exceed mass gains). The changing mass balance of the ice sheet will be addressed shortly.

Climate data for Greenland are available from several field programs. Beginning in 1987, an automatic weather station (AWS) network was established in Greenland by C.R. Stearns. Data from these stations provide a valuable addition to the few previous expedition measurements discussed by P. Putnins (1969) and Barry and G. Kiladis (1982). Since 1995, extensive climatic data have been collected by AWSs through NASA's Program for Arctic Regional Climate Assessment (PARCA) (Steffen et al., 1996; Thomas, 2001). The Greenland Climate Network (GC-Net) established under PARCA provides climate data from eighteen AWSs. The sites are distributed to sample from different climatic zones (Figure 8.1) and range in altitude from 568 m (JAR-2) to 3,208 m (Summit).

8.1.2 Surface Air Temperature

The high elevation, large extent, and high albedo of the ice sheet are significant factors for local and regional surface air temperatures although latitude and distance inland are also involved. K. Steffen and J. Box (2001) provide a useful summary. For both the eastern and western slopes of the ice sheet, surface air temperatures decrease by about 0.8°C per degree of latitude. As for general elevation effects, from normalizing all AWS station data to 70°N, annual mean surface air temperatures decrease at a rate 0.71°C per 100 m. The slope gradient in temperature shows large seasonality, however. Based on differences between selected stations, the decline ranges from 0.9–1.0°C per 100 m in November to as low as 0.4°C per 100 m in June. Regarding free-air lapse rates (as measured by radiosondes), the ice sheet is characterized by pronounced low-level inversions (see Chapter 5), which are most strongly expressed during the winter season.

Figure 8.2 gives the mean annual cycles of temperature for sixteen of the PARCA sites. February is the coldest month at every site, while July is the warmest. The annual mean temperature is only –30°C at NGRIP (75.1°N, 42.3°W, 2950 m), ranging from –14°C in July to –46°C in February. The only station with a mean July temperature exceeding the freezing point is JAR-1 (+0.2°C), located on the west slope (69.5°N, 49.7°W, 962 m). At Summit, summer daily high temperatures are near –8°C and winter minima are around –53°C. There is strong daily variability in winter, which is associated with synoptic activity and katabatic winds. Steffen and Box (2001) find that the annual mean temperature range is between 23.5°C to 30.3°C for the western slope.

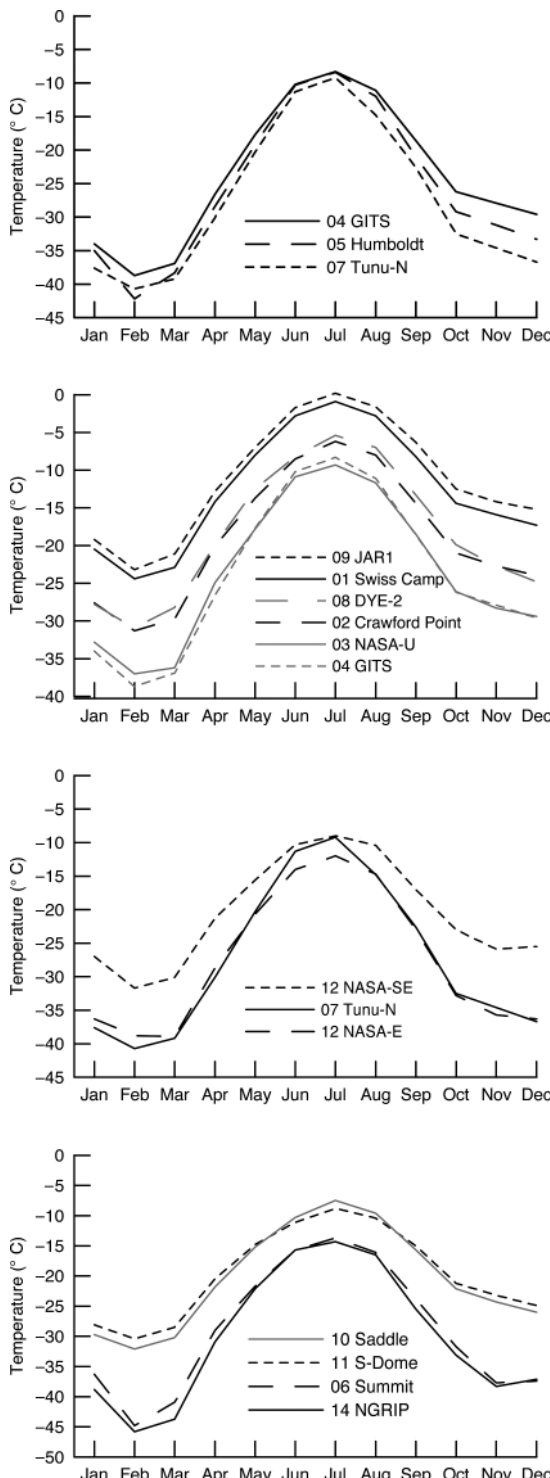


Figure 8.2. Monthly mean air temperatures for different sites in Greenland (see Figure 8.1 for locations) (from Steffen and Box, 2001, by permission of AGU).

8.1.3 Radiation Regime

Some aspects of the Greenland's radiation were already examined in Chapter 5. To summarize and expand, during winter, net allwave radiation is strongly negative. This is a function of the high elevation of the ice sheet and the relative lack of cloud cover compared to other areas of the Arctic, which helps to keep the downward longwave radiation flux low. Solar radiation is of course essentially absent in winter. It follows that compared to other Arctic regions, the summer downward solar radiation flux over the ice sheet is quite high (Figure 5.1), again owing to more limited cloud cover and (from the high elevation) less attenuation of the incident flux by aerosols and water vapor. But even in July, net allwave radiation over the higher elevation parts of the ice sheet is less than about 40 W m^{-2} (Figure 5.8). In part, this manifests to the fairly small flux of downward longwave radiation. There is hence strong compensation between the two incoming radiation terms. However, the much larger contributor to the low net allwave radiation in summer is the high albedo – most of the incident solar flux is lost to space. From Figure 5.5 it is seen that even in July, the mean surface albedo over most of the ice sheet is around 0.80 although much lower values can be found in the warmer parts subject to summer melt.

The role of albedo is highlighted in radiation measurements collected by Konzelmann and Ohmura (1995) in 1990 and 1991 at the Swiss Camp (69.6°N , 49.3°W , 1149 m). Swiss Camp is located in West Greenland, near the mean equilibrium line. These data show that the decrease in incoming solar radiation through the summer melt season associated with increased cloud cover (principally observed in August as a result of stratus) is essentially offset by the tendency for clouds to increase the downwelling longwave radiation. Because of the melting surface, the outgoing longwave radiation flux is steady. Hence, variations in the net surface (all-wave) radiation are determined largely by variations in albedo. Albedo decreased from 0.86 in May to 0.72 in July. Overall, a positive net radiation balance can be expected from late May to mid-August. But even in July, net radiation averaged for the two years was only 37 W m^{-2} . This is consistent with the satellite-derived estimates given in Figure 5.8.

8.1.4 Wind Regime and Tip Jets

A prominent feature of the Greenland climate is its katabatic wind regime. In the right conditions, such drainage winds can reach gale force. In its most generic sense, a katabatic wind (from the Greek word *katabikos* – to go down) refers to any downslope wind flowing from high elevation mountains, plateaus, or hills down to valleys or plains. But more commonly, the term is reserved for winds that, despite the effects of adiabatic compression during descent, are colder than the air displaced at the bottom of the incline. A wind that is warmer than the air being displaced at the bottom of an incline is commonly referred to as a foehn, although there are many local names (e.g., Chinooks in the lee of the Rocky Mountains and the Santa Ana in the lee western side of the San Bernadino Mountains, California).

Dynamically, katabatic winds in Greenland are the same as those found in Antarctica. They relate to flows that are forced by radiational cooling of the lower atmosphere adjacent to the sloping terrain on the ice sheet. Cooling of the low-level environment means that the density of the air very near the surface is greater than that situated some horizontal distance away from the sloping terrain. This establishes a horizontal pressure gradient force. However, high density air moving horizontally then encounters the lower density adjacent air. The result is a force with a component directed down the slope (Parish and Cassano, 2003). However, one must also consider the effects of the Coriolis force and frictional drag. For horizontal scales of motion of several kilometers and time scales of a few minutes, the Coriolis force can be ignored. For motions of hundreds of kilometers or time scales of hours, as is generally the case for Greenland, the Coriolis force is important, and will deflect the wind to the right of the motion. Friction acts to slow the winds. Because of the Coriolis force, Greenland's katabatic winds, when not greatly influenced by local topography (as would be the case in the upper regions of the ice sheet), tend to flow with a pronounced component across the fall line. However, winds near the coast are channeled by valleys and fiords. Intense katabatic winds are favored by particular synoptic conditions that enhance the large-scale pressure gradient. As discussed in Chapter 4, katabatic winds along the coast are also known to assist in the development of mesoscale polar lows.

Measurements at Swiss Camp during 1990–1999 yield a maximum monthly mean wind speed of 9–11 m s⁻¹ during November–January with a minimum of 5 m s⁻¹ in July. The prevailing direction is from 120–130°, reflecting a katabatic regime (Steffen and Box, 2001). Winds show strong directional consistency over most of the ice sheet. G. Heinemann and T. Klein (2002) undertook a limited-area model analysis of all of Greenland for January 1990. Their results show a clear signal of katabatic winds in the mean wind field. The strongest katabatic winds are observed in western Greenland north of 70°N and in eastern Greenland north of 75°N. Katabatic storms are well known along the southeastern coast of Greenland and in the east coast valleys near Angmassalik. By disrupting the surface-based temperature inversion, katabatic wind events can cause rapid changes in surface air temperature.

A special type of winds associated with the topography of Greenland is tip jets, which are seen as short lived, shallow, and narrow high wind speed events that extend from the southern tip of Greenland (Cape Farewell) to a few hundred kilometers away from the coast. They occur multiple times each winter. The vicinity of Cape Farewell is recognized as the windiest place on the ocean's surface (Sampe and Xie, 2007). There are two basic types: (1) westerly (sometimes known as forward) tip jets, so named because the winds have a westerly (from the west) component with the jet extending eastward from the tip of Greenland (Figure 8.3); and (2) northeasterly (sometimes known as reverse) tip jets, when winds are from the northeast and the jet extends southwestward from the southern tip of Greenland (Moore, 2003; Vage et al., 2009). At times, wind speeds in the core of the jets can reach 50 m s⁻¹. Both types of tip jets represent interaction between the steep

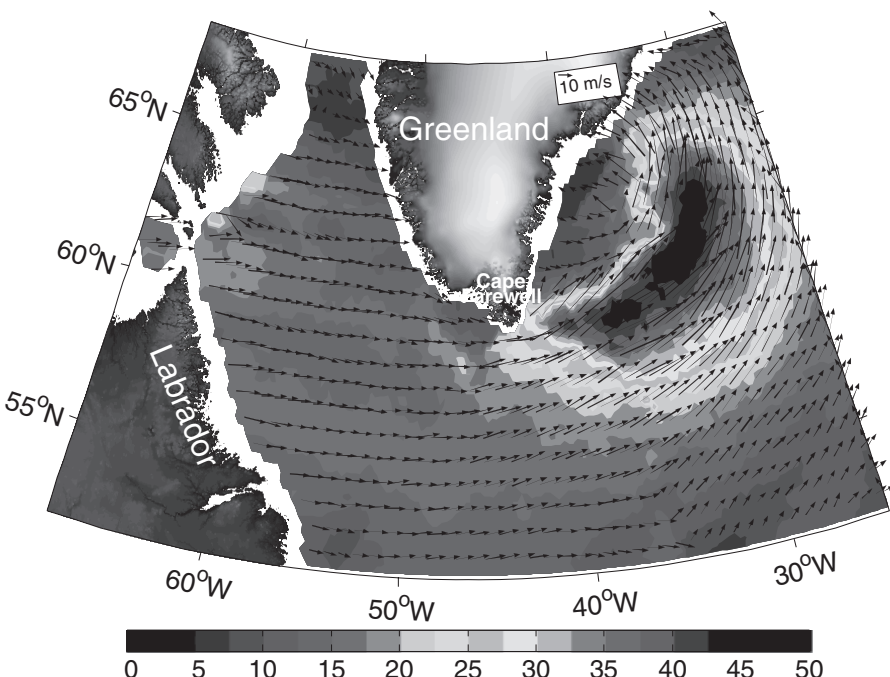


Figure 8.3. Winds speeds in m s^{-1} (see color bar) and wind direction (vectors) for a forward Greenland tip jet event that occurred on December 5, 2002, based on data from the NOAA QuikSCAT satellite (courtesy of Kjetil Våge, Woods Hole Oceanographic Institute, Woods Hole, MA). (See plate section for color version.)

topography of the coast and the synoptic scale wind flow. The frequency of westerly tip jets is higher when NAO is in its positive phase and lower when the NAO is in its negative phase. The frequency of northeasterly tip jets shows the opposite relationship with the NAO (Moore 2003).

Westerly Greenland tip jets tend to occur when a deep synoptic-scale cyclone, moving along the North Atlantic cyclone track, is located off the southeast coast of Greenland. The strong tip jet winds result in intense air-sea interaction, which appears to be able to initiate deep ocean convection in the Irminger Sea (Pickart et al., 2003). J. Doyle and M. Shapiro (1999) argued for two mechanisms to explain the westerly tip jet: (1) conservation of the Bernoulli function, which is the sum of enthalpy, kinetic energy, and potential energy per unit mass; and (2) flow around the barrier of southern Greenland. Which process operates is determined by the combination of wind speed (U) normal to the barrier, atmospheric stability expressed in terms of the Brunt-Vaisala frequency (N), and the height of the barrier (H), as expressed in the Froude number:

$$F = U/NH \quad (8.1)$$

If the Froude number (F) is greater than 1, air can surmount the barrier of southern Greenland. Through conservation of the Bernoulli function, air will accelerate

down the lee side, converting potential into kinetic energy, giving rise to a tip jet. If the Froude number is less than 1, air will flow around the barrier. It appears that for westerly tip jets, flow around the barrier is most important (Vage et al., 2009). With the low located off the southeast coast of Greenland, air on the west side of Greenland is dammed, leading to locally high pressure along the west coast. The air moves southward along the west coast. When air gets to the tip of Greenland, the barrier is removed, and the piled-up (dammed) air accelerates down the pressure gradient. It then adjusts to the mean pressure field, which is why the winds are westerly.

Northeasterly tip jets tend to occur when a cyclone center is located south of Cape Farewell (the southern tip of Greenland). In this case, the wind flow at low levels is directed into the east coast of Greenland. This damming creates a barrier wind. However, the barrier flow is cross isobaric, so the wind accelerates as it travels southwest, with the barrier to the right of the flow. As the strong barrier wind approaches Cape Farewell and the topography decreases in elevation, the pressure gradient force away from the barrier decreases and eventually disappears as the wind passes the end of the island. The wind speed remains high, meaning a large Coriolis force that turns the flow anticyclonically (Outten, Renfrew, and Petersen, 2009). The anticyclonic flow has an outward centrifugal force pulling in the same direction as the synoptic-scale pressure gradient force, leading to further acceleration of the wind. More recent work (Moore, 2012; Moore and Pickert, 2012) shows that tip jets and barrier flow occur also in other regions along the Greenland coast with steep topography, parts of the northern Bering Sea, and probably also in Norway, Iceland, and Svalbard.

8.1.5 Precipitation, Accumulation and Sublimation

Some aspects of precipitation and accumulation over the ice sheet were outlined in Chapter 6. Accumulation basically represents the net effects of direct precipitation, its redistribution on the surface via wind scour and drifting, and mass losses attributed to melt and evapo-sublimation. Accumulation is typically assessed via snow pits or ice cores. Based on coastal station observations of precipitation, adjusted for wind speed, and accumulation data from recent ice cores, the annual precipitation averaged over the ice sheet is estimated to be 340 mm (Ohmura et al., 1999). On average, only 40 percent of the total precipitation at the coastal stations is in solid form. However, at Danmarkshavn, this figure rises to 83 percent. There are zones of maximum precipitation exceeding 2,000 mm in the southeast coastal area and 600 mm in the northwest. Amounts in the north-central area are around 100 mm. The southeastern maximum is strongly influenced by orographic uplift of southeasterly flow associated with traveling cyclones. The northwestern maximum is related to flow off northern Baffin Bay and uplift. A trend surface analysis of accumulation data (van der Veen, Bromwich, and Castho, 2001) indicates that 80 percent of the spatial variance in average accumulation is a result of the large-scale atmospheric circulation and its interaction with the ice sheet topography. From regression

analyses, they suggest that the penetration distance for precipitation from cyclones located off the coasts is about 200 km. The low precipitation over the high central parts of the ice sheet is consistent with this basic view.

The analysis of Ohmura et al. (1999) is in general accord with the model generated precipitation map given in Figure 6.6. Although maps of accumulation and precipitation are not directly comparable, Ohmura's (1999) map is broadly similar to the accumulation map given in Figure 6.5 that shows local peaks greater than 2,000 mm. But Figure 6.5 shows differences with the estimate of accumulation discussed by R. Bales et al. (2001). Details of precipitation and accumulation over Greenland hence still seem to be somewhat uncertain.

Sublimation was briefly introduced in Chapter 5. It refers to the exchange of water vapor between ice and the overlying atmosphere during sub-freezing conditions (typical of Greenland) in which water molecules are transferred directly from the solid to gas phase, or vice-versa. This contrasts to evaporation, which deals with transfers between the liquid and gas phases. The combination of the two is termed evapo-sublimation.

In the ablation area of the ice sheet, Ohmura et al. (1999) estimate annual evapo-sublimation at between 60–70 mm. Over the higher parts of the ice sheet it is probably 20–30 mm during the three summer months. Box and Steffen (2001) estimated the sublimation term separately over the ice sheet based on application of two methods to GC-Net data. One is from single-level “bulk” estimates of the type commonly used in global climate models, whereas the second uses measurements of wind and humidity at two levels. Details are provided in that paper.

Sublimation over the ice sheet is highly variable in both space and time. Maximum sublimation rates from the surface to the atmosphere tend to occur when temperatures are relatively high and winds are strong. Vertical temperature differences allow for gradients in specific humidity, which in turn drive sublimation. Large vertical temperature differences do not occur under strong winds without a heat source to the surface. Hence, large sublimation rates can occur when melt episodes reduce the surface albedo, promoting increased absorption of solar radiation. Under clear skies, sublimation rates are largest toward the middle of the day when solar heating is strongest. Deposition can occur under favorable synoptic conditions with a reversed humidity gradient. Deposition can also occur at nighttime owing to radiative cooling. Sublimation between even nearby sites may differ greatly.

The annual map from Steffen and Box (2001) from the two-level method shown in Figure 8.4 represents a trend-surface fit to calculated sublimation in terms of elevation and longitude. Even though results from the single and two-level approaches differ in the magnitude of sublimation rates, the spatial patterns are very similar. They both show sublimation as upward (surface to atmosphere, positive values in the convention of the figure) over most of the ice sheet, and greatest in the warmer lower elevations during the summer season. The highest elevations show a small vapor transfer from the atmosphere to the surface (deposition, negative values in the convention of the figure). Overall, they estimate that mass losses by sublimation account for at least 12 percent and possibly up to 23 percent of annual precipitation,

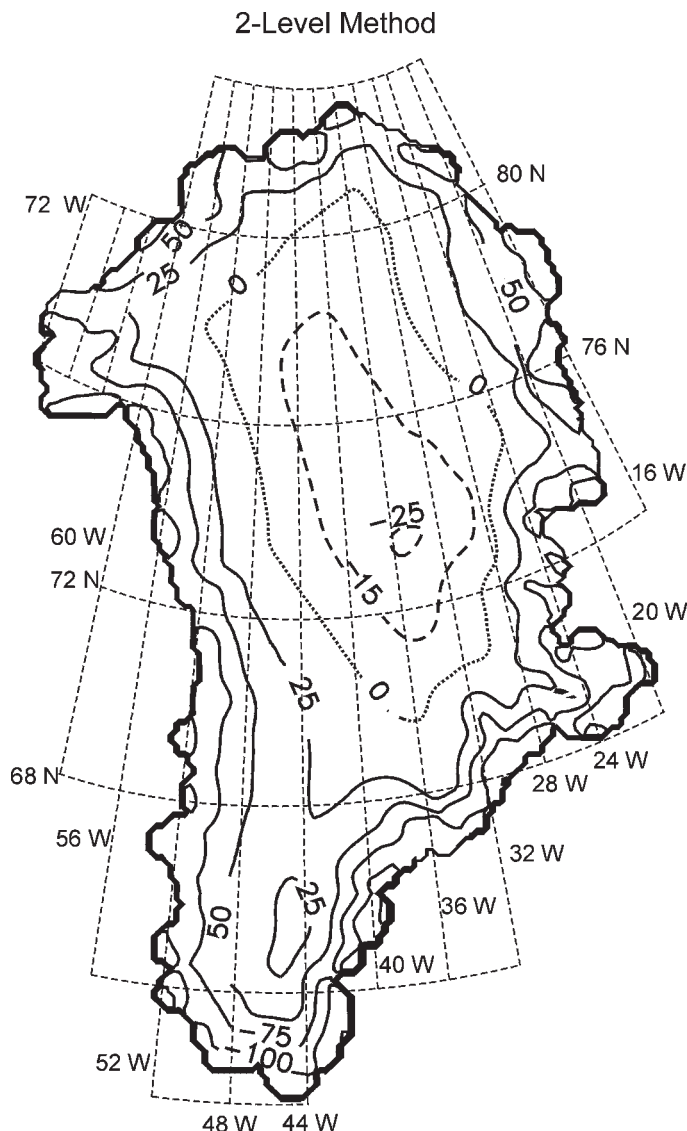


Figure 8.4. Map of estimated mean annual sublimation (millimeters) for the Greenland Ice Sheet. Positive values mean transfer from the surface to the atmosphere (from Box and Steffen, 2001, by permission of AGU).

depending on which method of calculation is used. Either way, sublimation emerges as a fairly important term for the Greenland Ice Sheet mass budget.

8.1.6 Surface Melt Regime

Large parts of the ice sheet experience summer melt. The presence of surface melt can be assessed using satellite passive microwave brightness temperatures (Abdalati and Steffen, 1995). Figure 8.5 illustrates the portion of the ice sheet that underwent

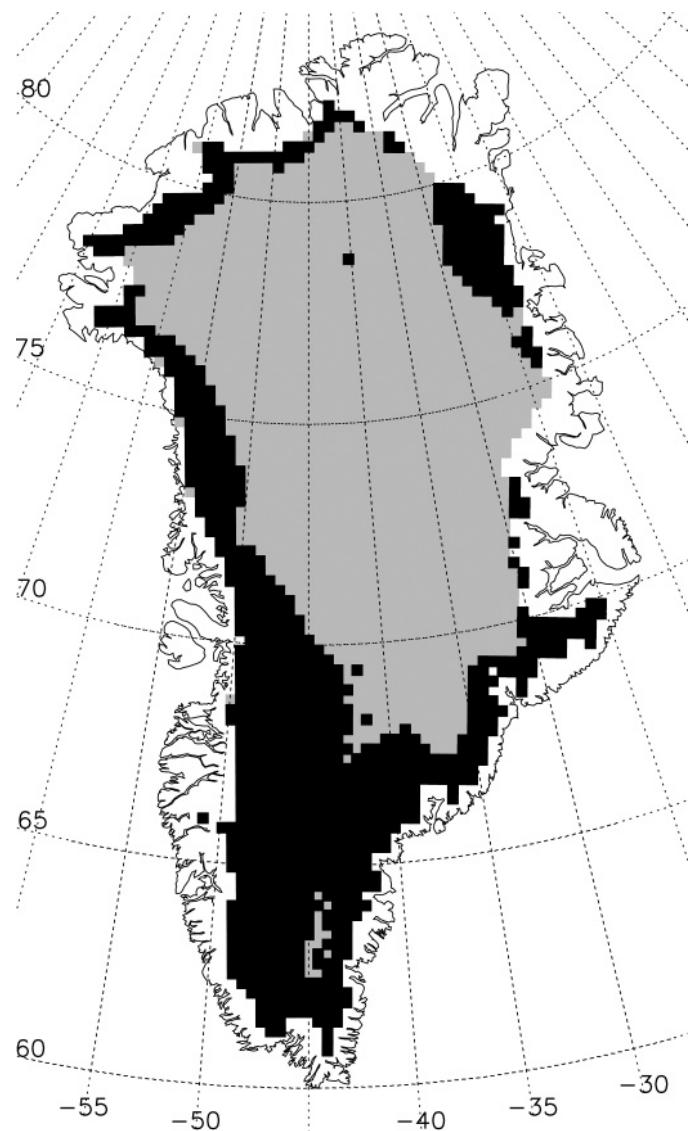


Figure 8.5. Surface melt extent (black areas) for the summer of 1999 based on satellite passive microwave retrievals (adapted from Abdalati and Steffen, 2001, by permission of AGU).

surface melt during the summer of 1999 (from Abdalati and Steffen, 2001), which, based on data through the end of the twentieth century, could be considered a fairly representative year. The melt area shows a general association with latitude and elevation – melt occurs in the southern and coastal regions of the ice sheet but not in the highest and hence coldest parts. For the ice sheet considered as a whole, the area undergoing surface melt correlates strongly with surface air temperature anomalies. As introduced in Chapter 2, there has been a general increase in surface melt area since the advent of passive microwave records in 1979 (Abdalati and Steffen, 2001;

Mote, 2007; Tedesco et al., 2010). The summer of 2007 saw extensive melt, 60 percent greater than the previous high recorded in 1998, which was then surpassed by another remarkable melt event in 2012. Satellite data show that during July 2012, more than 98 percent of the ice sheet experienced at least a brief period of surface melt. Evaluation of ice core data indicate that the last time such extensive melt occurred was in 1889 and the next previous event was approximately seven centuries earlier (Nghiem et al., 2012). Extensive melt events can be related to anomalous atmospheric circulation patterns; the 2012 event was linked with a very strong ridge in the mid-tropospheric flow. Where melt is observed in higher regions, it may only be occurring in a near surface layer. At lower elevations, meltwater that is formed will percolate to lower depths and re-freeze. It is only near the coast that actual runoff is observed, either directly from the surface or from the base of glaciers draining the ice sheet. The surface melt in 2012 caused extensive local flooding, notably in the town of Kangerlussuaq, which hosts one of the island's busiest commercial airports.

8.1.7 Mass Balance

The changing mass balance of the Greenland and Antarctic Ice Sheets has been a subject of increasing interest as well as concern. As of the writing of this textbook, since 1998, there have been at least twenty-nine individual mass balance estimates (Shepherd et al., 2012). Satellite remote sensing resources to estimate mass balance include gravimetric measurements from NASA's GRACE and ICESat missions and Interferometric Synthetic Aperture Radar. Satellite information has been complemented by data from NASA's Operation IceBridge series of aircraft overflights, regional models, such as RACMO2 (Regional Atmospheric Model Version 2) and surface observations. Although estimates have ranged widely depending on the time period examined and the techniques employed, it is clear that the mass balance of both ice sheets is negative, contributing to the current estimated sea level rise of 3.1 mm per year, that the mass losses for Greenland are larger than for the Antarctic Ice Sheet, and that the mass loss from Greenland in particular has accelerated over the past decade. Authors of many past studies recently collaborated on a major effort to provide a reconciled estimate of mass balance. Figure 8.6 shows the cumulative annual mass balance (Gigatonnes and equivalent sea level rise) for the Greenland and Antarctic ice sheets and for the ice sheets combined. The accelerating mass loss from Greenland stands out.

Ice sheet mass balance represents the difference between accumulation (precipitation) and mass losses, the latter primarily representing runoff, evapo-sublimation and iceberg discharge (calving). As assessed for the 2000–2008 period, M. van den Broeke et al. (2009) estimate that the mass loss from Greenland is roughly split between surface processes (precipitation and runoff, the latter associated with seasonal melt just discussed) and ice sheet dynamics. Attention has focused on the observation that some of the major glaciers that drain the Greenland Ice Sheet, including the Jakobshavn, Kangerdlugssuaq, and Petermann glaciers, are exhibiting

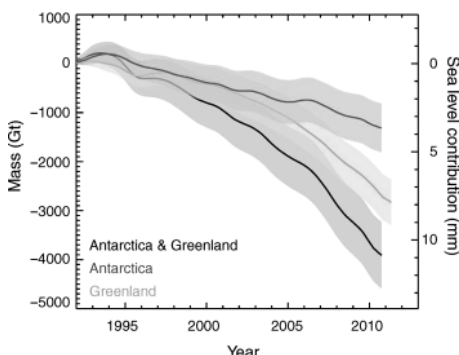


Figure 8.6. Cumulative annual mass balance (Gt) and sea level contribution (mm) over the 1992–2011 period for Greenland, Antarctica, and Greenland and Antarctica combined (adapted from Shepherd et al., 2012, by permission of AAAS). (See plate section for color version.)

accelerated flow, increasing iceberg calving rates. Jakobshavn Glacier, which drains 6.5 percent of the ice sheet and produces around 10 percent of all Greenland icebergs, has been the focus of considerable research. One explanation for the acceleration, termed the “Zwally effect” (named after Jay Zwally), is that (1) there has been an increase in seasonal surface melt and runoff; (2) the extra meltwater reaches the glacier base via moulins and crevasses; and (3) the flow is large enough and is added quickly enough to reduced friction at ice/bedrock interface, meaning more basal sliding of the ice (Zwally et al., 2002). Although the Zwally effect has been observed at Swiss Camp, it is seasonal in nature, and it not viewed as the primary contributor. Attention has shifted to thinning of the calving tongues of the outlet glaciers, which reduces backpressure (Thomas, 2004). This thinning can arise from both surface melt and melt at the base of the calving tongues by ocean heat. If there is thinning, the glacier becomes more buoyant, exerting less backpressure on the upstream ice. Thinning also reduces backpressure through reduced friction on the fiord walls. The reduced resistive force at the calving front is then propagated up the glacier via longitudinal extension. This results in both a retreat of the floating tongue and a more rapid flow of the glacier.

8.2 Polar Desert

8.2.1 Basic Characteristics

Recall from Chapter 2 that the term tundra applies to a wide range of Arctic vegetation, although its basic meaning is treeless. Tundra accounts for about 20 percent of the land surface within the Arctic Circle. At the southern end of tundra, we encounter the forest-tundra ecotone, some 50–100 km wide, which in turn transitions to boreal forest. The range of climatic conditions in tundra areas is large (Barry et al., 1981), not only between major tundra types (Chapter 2), but over short distances within a tundra type. The latter issue is highlighted in energy balance studies from the LAII program (Table 5.4) Polar desert is the most extreme of tundra types. Polar desert is particularly fascinating, and warrants more discussion.

Polar desert is widespread in the Canadian Arctic Archipelago, northern Greenland, and the islands of the Siberian Arctic (Korotkevich, 1972). In the New

Siberian Islands, about half the surface is occupied by ice caps and the rest by polar desert (Golubchikov, 1996). Figure 2.14 shows its extent based on vegetation criteria. Conventional climate data are inadequate for mapping its distribution attributed to the general lack of evaporation data and the inappropriateness of standard climatic classification criteria for the Arctic (Bovis and Barry, 1974).

In the polar deserts, mean annual temperatures are quite low and only exceed the freezing point in one or two summer months. Mean winter month temperatures are typically -30 to -35°C , while means of the warmest month, July, are typically 1 to 5°C . The fairly low summer maxima, while partly a function of latitude, are also attributed to persistent multiyear sea ice along the northern coasts of Greenland and the Canadian Arctic Archipelago, and around many of the Siberian islands. Areas in the continental interior of the Arctic and subarctic can have similar (or even lower) winter air temperatures than polar desert, but July mean temperatures are considerably higher, yielding a pronounced annual temperature range.

Polar desert climates have been described for Peary Land, north Greenland (Putnins, 1969), Ellesmere Island (Lotz and Sagar, 1963; Barry and Jackson, 1969; Alt et al., 2000), Devon Island (Courtin and Labine, 1977), the northern Taymyr Peninsula and the Siberian Arctic Islands (Korotkevich, 1972). The areas in Peary Land and the Canadian Arctic Archipelago are characterized by high continentality with monthly mean temperatures in the winter months of -30°C or below and July values of $4\text{--}5^{\circ}\text{C}$. In Severnaya Zemlya, mean annual air temperatures are -13 to -16°C . Means for winter months of -28 to -33°C compare to those of around 1°C during summer months. Even in July, frost is recorded on eighteen days. Climatic differences between coastal weather stations and inland sites like Lake Hazen and Tanquary Fiord on Ellesmere Island have been pointed out by Jackson (1959b) and Barry and Jackson (1969). Based on six years of data, B. Alt et al. (2000) show that mean July temperatures average 3°C higher in the interior of the Fosheim Peninsula at Hot Weather Creek than at Eureka on the coast. In winter, inland temperatures are $1.5\text{--}3.5^{\circ}\text{C}$ lower than at the coast.

Especially striking are variations in the frequency of extreme minimum temperatures. On Ellesmere Island, the frequency of minima below -45°C during February 1950–1960 was 21 percent at Eureka but less than 2 percent at Alert (Hagglund and Thompson, 1964). These are both coastal sites. By comparison, Lake Hazen, an inland site, recorded minima of -45°C or below on all but three days in December 1957 (Jackson, 1959a). In some inland areas, summer conditions are surprisingly mild. Remarkably for the latitude, there are sixty-five frost-free days at Tanquary Fiord (81.4°N , 71.9°W) and seventy at Brónlunds Fiord on Greenland (82°N , 30.5°W). One could conceivably grow lettuce! Over the 1989–1993 period, the melt season (days with mean temperatures above freezing) at Eureka ranged from seventy-two to ninety-five days. At Hot Weather Creek, the corresponding values are seventy-four to ninety-six days (Alt et al., 2000).

As the preceding results imply, topoclimates and microclimates are strongly developed in many polar desert areas. It is not uncommon for the local topography to give rise to foehn conditions and resulting spells of high summer temperatures. Air temperatures of 18°C have been recorded under these conditions on the eastern

lowlands of the New Siberian Islands (L.S. Berg, cited by Golubchikov, 1996) and in Tanquary Fiord, Ellesmere Island (Barry and Jackson, 1969). Extremes of around 28°C reported from the interior of Wrangel Island (Golubchikov, 1996) may arise from occasional warm air incursions from the Siberian lowlands combined with foehn subsidence.

Precipitation in polar desert areas is low and occurs mainly as snow. On Ellesmere Island, mean daily precipitation on summer days with measurable amounts is between 0.8 and 1.5 mm with maximum falls typically around 4–8 mm at Eureka (Alt et al., 2000). On rare occasions, summer precipitation can be associated with convective storms. Annual precipitation is typically 100–300 mm. Winter snow depths are generally around 200–400 mm but highly variable. Exposed parts of the surface may be blown free of snow for most of the winter. In other areas, drifting may result in a fairly deep snowpack. Where drifting is especially pronounced and in sheltered areas, snow can linger through the summer.

8.2.2 An Example – Resolute Bay, NWT

Resolute Bay (Cornwallis Island, Canadian Arctic Archipelago) is typical of a polar desert location. Figure 8.7 summarizes this site's mean annual cycles of surface air temperature, precipitation, cloud cover, and downward solar radiation. Mean temperature ranges from a low of about –33°C in February to 4°C in July. Precipitation exhibits a pronounced August maximum of about 33 mm, compared to winter-month precipitation totals of less than 5 mm. Note that these are raw station precipitation totals with no adjustments for wind-induced gauge undercatch and trace amounts. This contrasts with the spatial fields of precipitation in Figure 6.3, which contain bias adjustments and are also heavily smoothed through the interpolation procedures. Even assuming that bias adjustments would double estimated winter precipitation, the winter aridity at this site is clear.

Winter-month cloud cover (the average percent of the celestial dome covered by cloud) is only about 40 percent, fostering longwave losses to space which contribute to low temperatures. Cloudiness increases through spring and summer to a maximum of more than 80 percent in August and September. The annual cycle is only in rough accord with that of precipitation. Note the sharp rise in cloud cover between April and May when low-level Arctic stratus begins to dominate. The daily average solar radiation in June is about 280 W m^{-2} .

8.3 Maritime Arctic

8.3.1 Characteristics

The major characteristics of the maritime Arctic are extensive cloudiness, high humidity and a small range in annual temperature. Such climatic conditions are best developed in the Atlantic sector of the Arctic, such as Svalbard (Figure 8.8) and Iceland. On Jan Mayen, Svalbard, the mean temperature is near –7°C in February

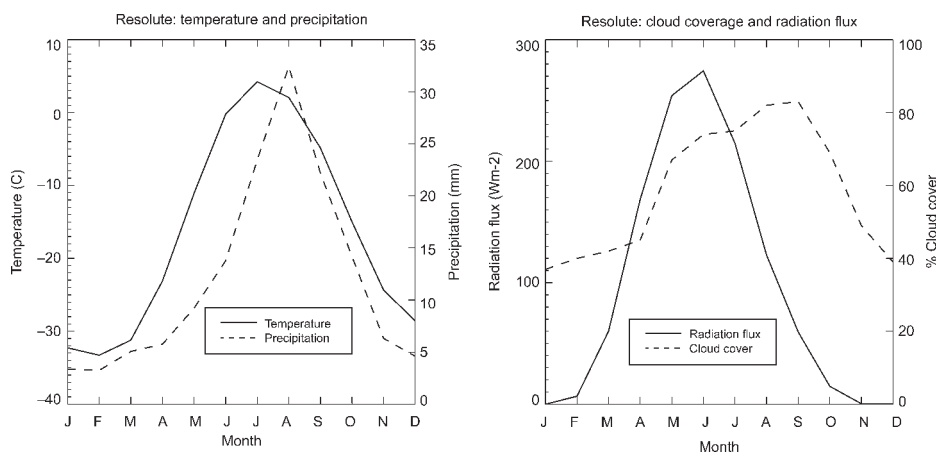


Figure 8.7. Mean annual cycles of surface air temperature, precipitation, cloud cover, and downward shortwave radiation for Resolute Bay, NWT, based several data sources (courtesy of M. Lavrakas, NSIDC, Boulder, CO).



Figure 8.8. Maritime Arctic environment in summer, Kings Bay, Svalbard (courtesy of M.C. Serreze, NSIDC, Boulder, CO). (See plate section for color version.)

and 7°C in August. There is fairly ample precipitation in all months with an autumn maximum. Nome in western Alaska is another example of a maritime site, but in this case reflecting Pacific influences. It has a similar precipitation regime but higher totals. Here the mean monthly relative humidity is between 76 and 82 percent. The

distribution and characteristics of the polar marine climate have recently been described in more detail by Ballinger et al. (2013).

Some investigators cite areas such as the Bering Strait and the coasts of the Beaufort and Chukchi Seas as having maritime climates although winter temperatures are much lower. Climatic conditions for Barrow, Alaska, have been discussed extensively (e.g., Moritz, 1979; Dingman et al., 1980; Shulski and Wendler, 2007). During the snow-free season along such coastal areas, there is often a rapid increase of temperatures inland. This is seen clearly in the July mean field of surface air temperature (Figure 2.24). Recall from Chapter 4 that this coastal temperature gradient extends through a considerable depth of the lower troposphere and defines the summer Arctic frontal zones.

8.3.2 Examples – Svalbard and Barrow

Following from this discussion, a good example of a maritime Arctic climate is Isfjord Radio (Svalbard) (Figure 8.9). Note first the sharply higher winter air temperatures as compared to Resolute Bay, the polar desert site (Figure 8.7). The maximum summer temperature, however, is similar at about 5°C. The sites also differ strongly in terms of precipitation. Compared to the summer maximum at Resolute Bay, Isfjord exhibits a distinct autumn/winter precipitation maximum and late spring/early summer minimum. There is also a more even seasonal distribution of cloud cover, ranging from about 60 percent in winter to 80 percent in August and September. This manifests the Atlantic cyclone influences.

The precipitation regime is broadly similar to that of Iceland, well to the south. During autumn/winter, the North Atlantic storm track is strong. Coupled with the availability of abundant oceanic moisture sources and relatively high evaporation rates, precipitation is high. Serreze and Etringer (2003) estimate that in the vicinity of Iceland, about half of the mean January precipitation is contributed by the large-scale vapor flux convergence and half by surface evaporation.

Figure 6.9 indicates that January mean P-ET in the Svalbard area, representative of winter months, is quite small (0–10 mm). As the change in atmospheric water vapor storage is also small at this time, P-ET is essentially the vapor flux convergence (see Chapter 6 for discussion of the aerological moisture budget). Because the winter vapor flux convergence is so small in the vicinity of Svalbard, this indicates that – compared to the Iceland region – correspondingly more of the winter precipitation is derived from surface evaporation.

Extensive cloud cover, open water, latent heat release, and poleward heat fluxes associated with frequent cyclone activity combine to keep winter surface temperatures remarkably high given the latitude (roughly 80°N). The North Atlantic storm track is weaker in summer. Because of the weaker temperature contrasts between the ocean and lower atmosphere, surface evaporation declines. Precipitation-generating mechanisms are therefore weaker than in winter. However, cloud cover is still extensive, which moderates the surface air temperature. The June peak value in average downward solar radiation (about 200 W m^{-2}) is much lower than that for Resolute

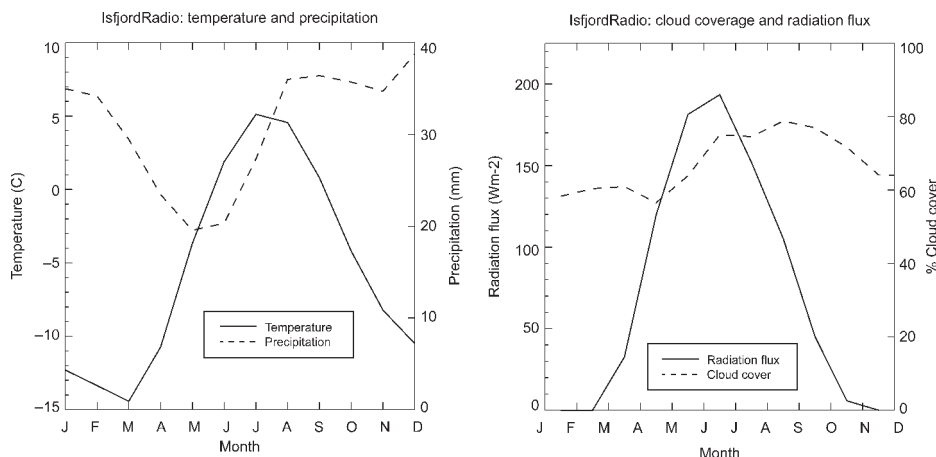


Figure 8.9. Mean annual cycles of surface air temperature, precipitation, cloud cover, and downward shortwave radiation for Isfjord Radio (Svalbard), based on several data sources (courtesy of M. Lavrakas, NSIDC, Boulder, CO).

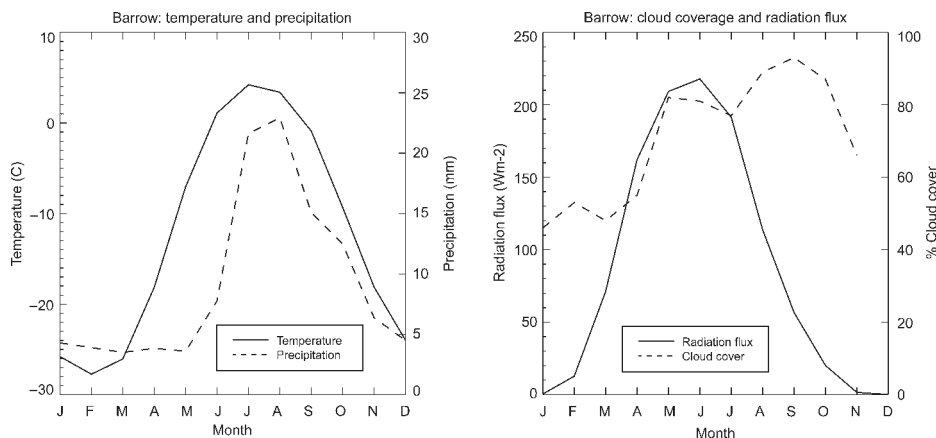


Figure 8.10. Mean annual cycles of surface air temperature, precipitation, cloud cover, and downward shortwave radiation for Barrow, AK, based on several data sources (courtesy of M. Lavrakas, NSIDC, Boulder, CO).

(about 280 W m^{-2}). This is not really a result of latitude but rather cloud cover. Although the June cloud fraction is about the same at both locations (70–75 percent), clouds over Isfjord Radio tend to be optically thicker.

Barrow is also considered by some investigators to fall in the category of an Arctic maritime climate (Figure 8.10), but conditions are quite different from those in the Atlantic sector and are really closer to those for polar desert. R. Pryzbylak (2003) properly considers this site to be transitional. Winter temperatures are somewhat higher than those for the Resolute Bay polar desert site. This results in a smaller annual temperature range (32°C) than for Resolute Bay, but still much

greater than at Isfjord Radio (22°C). Like Resolute, conditions are quite dry, with less than 5 mm of precipitation (discounting gauge biases) from December through May, and an August maximum of about 23 mm. Compared to Resolute, there is slightly more winter cloud cover.

8.4 Central Arctic Ocean

Data from the NP program, the IABP, and the SHEBA project provide a reasonably comprehensive picture of the climate of the central Arctic Ocean. Figure 2.24 provides information on mean surface air temperatures for the central Arctic Ocean from IABP records. Aspects of surface energy exchanges based on SHEBA data are summarized in Chapter 5. Characteristics of snow cover over the Arctic Ocean from the NP records are discussed in Chapter 2.

Figure 8.11 gives mean annual cycles of climate elements for the central Arctic Ocean by aggregating all of the available NP observations. The NP data were collected over thick ice floes. Mean temperature ranges from about -33°C in January (similar to Resolute) to 0°C in July. The proximity of the July mean temperature to the freezing point reflects the effects of the melting ice surface. Precipitation peaks in late summer and early autumn, corresponding broadly to the seasonal maximum in cyclone activity in this region. This represents a combination of systems migrating into the Arctic Ocean from the weakened (but still present) North Atlantic cyclone track and those generated over Eurasia, many in association with the summer Arctic frontal zone (Chapter 4). As evaporation rates are low, precipitation and P-ET are quite similar, with the precipitation hence primarily driven by the large-scale vapor flux convergence. As seen in Figure 6.7, even in July, roughly half of the precipitation that falls is in solid form.

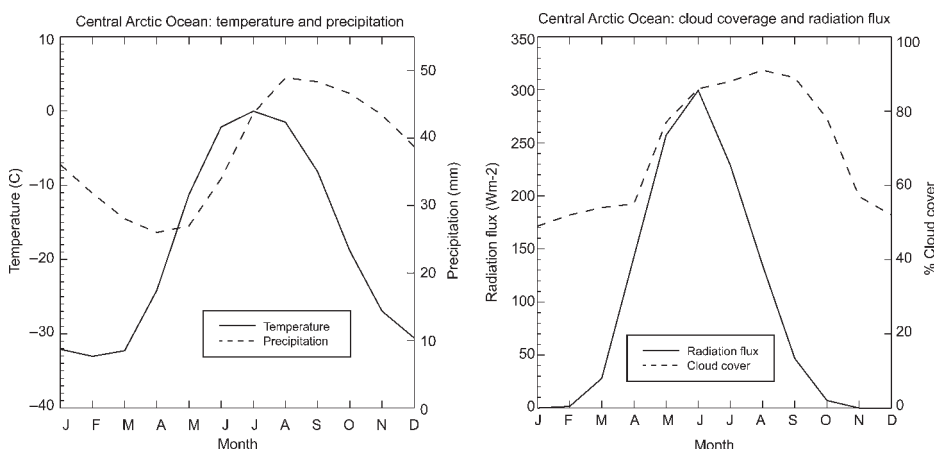


Figure 8.11. Mean annual cycles of surface air temperature, precipitation, cloud cover, and downward shortwave radiation for the central Arctic Ocean, based on data from the Russian North Pole program (courtesy of M. Lavrakas, NSIDC, Boulder, CO).

8.5 Mountains and Uplands

Mountains and uplands in the Arctic exert both local and regional modifications on climate. Mountains and plateaus, many containing glaciers and ice caps, are found in the eastern section of the Canadian Arctic Archipelago (Baffin, Devon, Ellesmere, and Axel Heiberg islands), coastal east and west Greenland, Scandinavia, the western Eurasian Arctic islands (Svalbard, Novaya Zemlya), and on the mainland in Alaska, the Urals of Russia, and northeastern Siberia (Chapter 2). The Ural Mountains (up to 1885 m) run north-south and form the conventional boundary between European and Asian Russia. They have a number of small glaciers, mostly in cirques. The Brooks Range forms the true Arctic mountains of Alaska. Orientated nearly east-west, they rise to 1,500–3,000 m and have small glaciers like the McCall.

The literature on upland and mountain climates in the Arctic is fairly extensive. Major field programs have been conducted on the Barnes and Penney ice caps on Baffin Island (Orvig, 1954), Franz-Josef Land (Krenke, 1961), Meighen Island (Alt, 1975), Devon Island (Holmgren, 1971) Axel Heiburg Island (Müller and Roskin-Sharlin, 1967), and other regions. These have provided detailed information on surface energy budgets and meteorological conditions. Upland, mountain, and ice cap climates are quite diverse, but can be broadly characterized in terms of the combined effects of elevation, the high albedo of snow and ice surfaces and the influence of summer melt on depressing surface air temperatures.

The last effect is a good example of local climate modification. For example, Bradley and Serreze (1987) examined the cooling effect of a small (roughly 5 km²) ice cap on northeast Ellesmere Island based on data collected during the summer of 1982. Meteorological stations were maintained over the middle of the ice cap and on a tundra surface (polar desert) several kilometers away at very nearly the same elevation. At 150 cm above the surface, they measured a cooling effect of the ice cap (with respect to the tundra site) ranging from 0.5 to 1.4°C. The cooling effect was larger very near the surface (15 cm), ranging from 1.5 to 2.5°C. Surface melt over the ice cap associated with the cooling effect was teamed with a persistent near surface temperature inversion, such that the sensible heat flux was directed downward while it was upward over the tundra location. During snow-free conditions, the albedo at the tundra site of about 0.10 compared with ice cap values from 0.4 to 0.7.

Regarding regional influences, while katabatic winds associated with Arctic ice caps are not nearly as well expressed as over Greenland, they can certainly be present, such as on and around the large Devon ice cap. By contrast, the Brooks Range is known to play an important role in the regional circulation in winter when it gives rise to a westerly “barrier wind” as a result of the thermal wind component that results from the cold air trapped at low levels north of the range (Barry, 2008, 135). Summer influences of the Brooks Range on the Arctic frontal zone were examined in Chapter 4.

Several recent studies (Golubchikov, 1996; Shahgedanova, 2002; Glazovsky, 2003) document the characteristics and variety of mountain and upland conditions in the Eurasian Arctic. The Urals extend some 3,000 km southward from the Arctic coast.

Table 8.1 Equilibrium line attitude (ELA), annual accumulation, and solid precipitation for various mountain and upland regions in Eurasia

	Mean ELA (m.)	Accumulation (mm water equivalent)	Solid Precipitation (mm water equivalent)
Franz Josef Ld.	260	300	300
Novaya Zemlya	480	610	610
Polar Urals	850	1,700	1,060
Sev. Zemlya	450	230	200
Byrranga Mts.	850	330	210

Source: From Glazovsky (2003).

The range is about 100 km wide in the Polar Urals (north of 64°N) and 300–400 km in the Middle and Southern Urals (59–51°N). In the Northern Urals (59–64°N) annual precipitation totals reach 700–800 mm on the western slopes, while amounts are some 100–150 mm less on the eastern slopes. Amounts decrease northward in the Polar Urals sector to 500–600 mm. In northeastern Siberia, valley glaciers occupy some 200 km² in the Suntar-Khayata Range (62°N, 142°E), which rises to 2,500–2,900 m. Annual precipitation, falling mostly in summer, is 500–700 mm on the western slopes at about 2,000 m. Further to the northeast, in the Chersky-Momsky Mountains (2,500–3,100 m), there are mainly cirque glaciers. Here the regional snow line (the average lower elevation limit of snow persisting throughout the year) is around 2,200–2,300 m. Precipitation increases from 400–500 mm in the northern ranges to 800–1,000 mm in the southern areas. Nevertheless, rock desert is widespread above about 700 m in the north and at 1,000 m at latitude 62°N. There are extreme climate contrasts between valley bottom and ridge top sites in this area. In winter, intense inversions are associated with frequent cases of surface air temperatures below –60°C.

In the Eurasian Arctic the equilibrium line altitude (ELA, the altitude on a glacier, ice cap or ice sheet for which annual mass gains equal annual mass losses) shows a general northward decrease from 600–1,000 m above sea level in the Polar Urals and Byrranga Mountains to 480 m in Novaya Zemlya, 450 m in Severnaya Zemlya, and 260 m to only 150 m on some of the islands of Franz Josef Land (Table 8.1). The mean precipitation listed in Table 8.1 masks strong regional variations. For example, differences in solid precipitation between the windward and leeward sides (with respect to the prevailing winds) are 240 mm on Franz Josef Land, and 600 mm on Novaya Zemlya.

8.6 Urban Modifications of Local Climate

8.6.1 Heat Islands

Urban heat islands (UHIs, which can be defined in terms of the surface air temperature in an urban area relative to that in surrounding undeveloped areas) are

commonly well developed in high latitudes during the polar night when anthropogenic heat supply is a major component of the energy balance. Most UHI studies have been carried out at middle and lower latitudes, but work has also been undertaken at Fairbanks, Alaska (Benson and Bowling, 1975; Bowling, 1986; Magee, Curtes, and Wendler, 1999) and at Barrow, Alaska (Hinkel et al., 2003). Barrow (71°N) is on the Arctic coast and has a mostly indigenous Inupiat population numbering about 4,600 people. Hourly air and soil temperature data were logged at fifty-four sites in a 150 km^2 area during 2001–2002. During December–March the average air temperature at the official Barrow station is -25.3°C , and the 2001–2002 winter was typical. The coldest sites are farthest from the landfast ice-covered ocean and the settlement area. The UHI effect averaged 2.2°C . It peaked at $5\text{--}6^{\circ}\text{C}$ in January–February when the air temperature was below about -30°C , presumably when there was maximum use of energy for domestic heating. There is a strong relationship between UHI intensity and wind speed; for winds less than 2 m s^{-1} the UHI effect averaged 3.2°C and fell to about 1°C for winds of $4\text{--}6\text{ m s}^{-1}$. Maximum UHI intensity was observed from late evening to early morning.

8.6.2 Ice Fog

Detailed studies of ice fog characteristics were carried out at Fairbanks, Alaska in the 1960s by Benson (1970). The most notable feature of its formation involves the injection of hot supersaturated exhaust air into a very cold (less than -35°C) saturated air mass. This forms $\sim 10\text{ }\mu\text{m}$ diameter ice crystals in contrast with the roughly $30\text{ }\mu\text{m}$ diameter crystals that form as “diamond dust” in suspension at about -40°C . Low temperatures at Fairbanks conducive to ice fog development are associated with radiational cooling over the extensive valley flats, forming a “cold air lake.” Strong inversions form with temperature gradients of $0.2\text{--}0.3^{\circ}\text{C m}^{-1}$ in the lowest 50 m. In the 1960s the main water source for the ice fogs was cooling water from power plants, which exceed the total from other fuel combustion sources by a factor of two. The ice fogs are shallow with an average thickness of 10 m and rarely exceed 30 m. There were 5–6 ice fog episodes in each of the two winters studied by Benson, but the colder winter had more ice fog days (forty days in 1961–1962, compared with twenty-five days in 1962–1963), and one episode lasted fifteen days. The area affected averages 60 km^2 , with extreme events covering up to 200 km^2 . Apart from the effects on visibility, anthropogenically produced ice fogs can have serious health effects owing to pollutants such as lead, chlorine, bromine, and sulfate that are adsorbed by the ice crystals.

Focus Questions and Exercises

- 1) What are the major difficulties in obtaining reliable estimates of the mass balance of the Greenland Ice Sheet?

- 2) Discuss how and why the seasonal cycles of incoming solar radiation, temperature cloud cover and precipitation for north-central Greenland would differ from the seasonal cycles of these climate elements for the maritime Arctic site Isfjord Radio (Figure 8.9).
- 3) Why are the lowest winter air temperatures recorded over the central Arctic Ocean typically higher than those recorded at Fairbanks, Alaska, which is at a much lower latitude?

Modeling the Arctic Climate System

Overview

Much of our current understanding of the Arctic climate system comes from numerical models. Numerical modeling experiments help us to understand interactions and feedbacks between variables and system components that can be difficult, if often impossible, to address from observations alone. A powerful tool in this regard is sensitivity experiments, whereby results from a control simulation, with “standard” model inputs or boundary conditions (e.g., atmospheric composition, sea ice extent) are compared to results from simulations in which inputs or boundary conditions are altered, thereby capturing the importance of the alteration on the modeled system. From previous chapters, the reader should already be familiar with some of the applications of numerical models. In Chapter 5, we discussed aspects of cloud radiative forcing based on output from radiative transfer models. Chapter 7 briefly examined the application of thermodynamic models to understand sea ice growth. Many studies of the atmospheric circulation discussed in Chapter 4 make use of output from atmospheric reanalysis systems, in which historical atmospheric and surface observations are assimilated within a weather prediction model to provide multidecadal gridded time series of atmospheric and surface variables (e.g., pressure heights, winds, and humidity at various pressure levels, precipitation, and evapotranspiration). Reanalyses are especially valuable in Arctic research as they provide information on variables which are only sparsely observed, such as precipitation and evapotranspiration.

Modeling continues to be one of the most rapidly evolving fields in climate science. As stated in the first edition of this textbook and reinforced here, any attempt to define the “state of the art” is destined to become becoming quickly dated. In recognition, we limit ourselves to an overview of the major directions of modeling the Arctic climate system and some of the key challenges. Basic features of model architecture are outlined, but discussion is minimized to help maintain flow.

9.1 General Model Types

Single Column Models (SCMs): As the name suggests, these have been developed to examine processes in a single column, such as that extending from the surface through some depth in the atmosphere, or from the surface to some depth of the soil. Examples are radiative transfer models and models of active layer thickness in permafrost regions. An attraction of SCMs is that detailed physics can be incorporated with relatively modest computer resources. Frequently, SCMs are applied to a two-dimensional grid of horizontally distributed points or cells (with no communication between grid cells). They are also commonly used to test parameterizations (semi-empirical representations of complex processes such as convection) for subsequent inclusion in global climate and numerical weather prediction models. SCMs can be forced from observations, synthetic data (artificial data with statistics that mimic reality) or output from another model.

Land Surface Models (LSMs): LSMs address interactions between the land surface, atmosphere, and underlying surface. In a typical “stand alone” application (i.e., in which the LSM is not directly coupled to another model), time series of basic variables (generally downward shortwave and longwave radiation, precipitation, near surface winds, humidity, and near surface air temperature) represent model forcings. The model ingests these forcings and generates output state variables and fluxes, including soil moisture, soil temperature, snow water equivalent, runoff, latent and sensible heat fluxes, and upward shortwave radiation. LSMs are run variously for a single column or over a two-dimensional grid (as with SCMs). An attraction of LSMs for Arctic studies is that the output variables, such as evapotranspiration and soil moisture, are often sparsely observed. LSMs are often coupled with river routing schemes so as to provide simulated discharge. LSMs of varying complexity also represent a component of coupled global climate models and numerical weather prediction models (and hence atmospheric reanalyses). LSMs are run at varying resolution. For “stand-alone” applications to a two-dimensional grid, a horizontal resolution of 50–100 km could be considered typical. LSM have become increasingly complex; some have evolved to simulate biogeochemical cycles (e.g., carbon and nitrogen cycles), land use, and vegetation dynamics.

Sea Ice and Coupled Ice/Ocean Models: Sea ice models have been widely used to examine the dynamic and thermodynamic interactions inherent to the sea ice system. The earliest sea ice models were thermodynamic only (ice motion was

not included). Dynamic/thermodynamic sea ice models represent the next level of complexity and are typically driven by wind, temperature, and ocean heat flux data through application of the momentum balance and thermodynamic equations described in Chapter 7. Model outputs include fields of ice motion, thickness, and concentration. Dynamic/thermodynamic sea ice models of varying complexity can in turn be coupled to ocean models. Modern models typically include ice thickness distributions – that is, the fraction of the ice cover in each of (typically) 5–10 ice thickness categories. An area of continuing development is data assimilation, such as of satellite-derived ice velocity and concentration.

Global Climate Models (GCMs): Global climate modeling is an especially active research area, with applications to understanding the earth's past, present, and potential future climate. GCMs (also known as General Circulation Models) are applied to a three-dimensional grid over the globe. There is a wide variety of model types. Atmosphere-only models (often referred to as AGCMs) include LSMs of varying complexity, and either prescribed SSTs or an upper-ocean mixed layer typically 50–100 m in depth. More robust GCMs are coupled atmosphere-ocean general circulation models (AOGCMs). They involve coupling AGCMs with ocean general circulation models, sea ice models, and LSMs. Some GCMs now simulate biogeochemical cycles (e.g., carbon and nitrogen cycles), land use, vegetation dynamics, and atmospheric chemistry. Such highly complex models are known as Earth System Models. Most GCMs utilize a spectral coordinate system. In such a framework, prognostic field variables (e.g., temperature and winds) are represented as sums of a finite set of spectral modes rather than at grid points. The advantage is that horizontal derivatives can be calculated exactly for the spectral modes represented in the model.

Whereas the growing complexity of GCMs from AGCMs to AOGCMs Earth System Models reflects the growth in computing power since the first-generation models were developed in the 1970s, major modeling centers, such as NCAR, have developed well-structured modeling systems enabling different levels of model complexity and coupling to be selected based on the sensitivity experiment of interest. For example, to better understand the role of changing ocean conditions on the evolution of the Arctic sea ice cover through the twenty-first century, one might compare a simulation from the modeling system in a fully coupled mode with a simulation in which there is no ocean coupling. Large modeling centers routinely conduct ensemble simulations in which a series of simulations are conducted using the same set of climate forcings (e.g., observed changes in atmospheric composition and other factors over the twentieth century along with projected changes over the twenty-first century) but starting from slightly different initial conditions. In starting with different initial conditions, at any given time, each simulation (ensemble member) may be in a different phase of the model's own internal climate variability. By then looking at the ensemble members as a group, one can assess both the forced component of change (e.g., the temperature change over the twentieth century averaging results from all ensemble members together) in comparison to natural variability (e.g., from the spread in simulated temperatures from the different ensemble members).

Regional Climate Models: As the name implies, such models are applied to regional domains. They are typically run at a horizontal resolution of 10–100 km and with high vertical resolution. They couple an atmospheric model to LSMs, sea ice, and (for some) ocean models. The atmospheric model is driven at the model boundaries by output (e.g., of temperature, wind, and humidity at a series of atmospheric levels) from numerical weather prediction models or GCMs.

Numerical Weather Prediction (NWP) Models: These are used for short- to medium-range weather forecasting for which accurate specification of the initial atmospheric state is of key importance. Global NWP models can be thought of as AGCMs (including an LSM with prescribed boundary conditions such as SSTs and sea ice concentration) that are constrained by data assimilation. One obtains “analyses,” which represent an optimal blend of the atmospheric model output and observations, and forecasts of variables such as precipitation and radiation fluxes. While analyses are generally thought of as “truth,” biases can be present because of problems in the atmospheric model, assimilation approaches, and the amount and quality of assimilation data. Strong biases can be present in the surface fields. In an operational setting, NWP models are undergoing continual improvement, the intent being to improve forecast skill. These changes, however, complicate retrospective analyses from archived fields. In recognition, atmospheric reanalyses have been performed with fixed versions of both the atmospheric model and the data assimilation system. This results in more temporally consistent outputs spanning multiple decades. Wide use has been made of output from atmospheric reanalyses in previous chapters.

Ecosystem Models: An ecosystem represents a system of organisms and the environment in which they interact. Ecosystem models are used to simulate functional and structural dynamics of terrestrial ecosystems. Functional dynamics of ecosystems includes the transfer of water, energy, carbon, and nitrogen between the atmosphere, soil, and vegetation. Structural dynamics of ecosystems includes changes that occur after disturbances (e.g., fire) or changes that occur in response to climate change (e.g., the migration of trees into tundra regions). Functional and structural changes of ecosystems can influence regional climate by affecting water and energy exchange with the atmosphere and may influence global climate by affecting the concentrations of radiatively active gases. Traditionally, LSMs represented a functionally and structurally static conceptualization of ecosystems (vegetation cover and type is specified and unchanged through the simulation), but have subsequently incorporated concepts from ecosystem models to better represent how interannual to century-scale variations in ecosystem structure and function influence climate. When vegetation can change, the term “dynamic vegetation model” is often used. Components of ecosystem models are part of Earth System Models.

9.2 Single Column Models

Chapter 5 has already provided a few examples of the applications of single column models. These include assessments of cloud radiative forcing over the sea ice cover

(Section 5.6), processes that maintain the low-level Arctic temperature inversion (Section 5.10.2), and the application of a radiative transfer model to a grid array to provide fields of surface radiation fluxes and surface albedo from AVHRR data (the APP-x products; see, for example Figure 5.5).

Another good example is provided by the study of Zhang et al. (2001), who examined relationships between atmospheric thickness (1,000 to 500 hPa), mean atmospheric temperature (surface to 10 km), and total atmospheric water vapor content (precipitable water, surface to 10 km) on the atmospheric downward longwave flux at the surface at two sites in Alaska (Barrow and McGrath) during the snowmelt period. Radiation fluxes in this model were computed using a one-dimensional atmospheric radiative transfer model for shortwave and longwave radiation combined with a surface energy balance equation. The radiative transfer model (Stamnes et al., 1988) has routines to include the effects of clouds, Arctic haze, carbon dioxide, water vapor, ozone and snow. Snow optical properties are based on assumed mean snow grain radii ($200 \mu\text{m}$) and density (350 kg m^{-3}). The model was driven by twice-daily atmospheric pressure, temperature, and water vapor concentrations from radiosonde observations for the years 1980 through 1991.

Figure 9.1 shows some of the results for Barrow. The most striking feature is the impact of precipitable water on the downward longwave radiation. Longwave radiation increases logarithmically with an increase in precipitable water. The impact on the downward longwave radiation is hence much greater at low precipitable water values. This compares to a linear relationship between the longwave flux and mean atmospheric temperature (and the 1,000- to 500-hPa thickness). The conclusion drawn from this modeling study is that the impacts of changes in precipitable water (especially at low values of precipitable water) are much greater than those of temperature. There are a number of empirical formulae to estimate the downward longwave flux. Figure 9.1a shows the longwave flux estimated from the formula of C. Parkinson and W. Washington (1979) based on the near-surface temperature. Compared to results from the radiative transfer model, the Parkinson and Washington formula underestimates the radiation flux when the near surface temperature is relatively high and overestimates the flux when the near-surface temperature is comparatively low.

We next turn to the study of C. Bitz et al. (1996). The focus of this effort was to model the natural variability of the Arctic climate system using a single-column energy balance model of the atmosphere, sea ice, and upper-ocean. Variability was induced by forcing the model with synthetic data, including realistic random perturbations of incoming solar radiation, the meridional transport of atmospheric energy into the column, cloudiness, and snowfall. Figure 9.2 provides a schematic. Conduction of heat through the ice is treated such that the number of ice layers remains fixed while total ice thickness varies (consequently the layer thicknesses vary). The sea ice is modeled as a slab with no leads, with the upper ocean treated as a slab mixed layer. When the ice surface is snow-free, solar radiation penetrates the sea ice, heating its interior and the ocean mixed layer. Surface albedo depends on sea ice thickness and snow thickness. The atmospheric model has eighteen layers and includes heating rates from different atmospheric gases and atmospheric

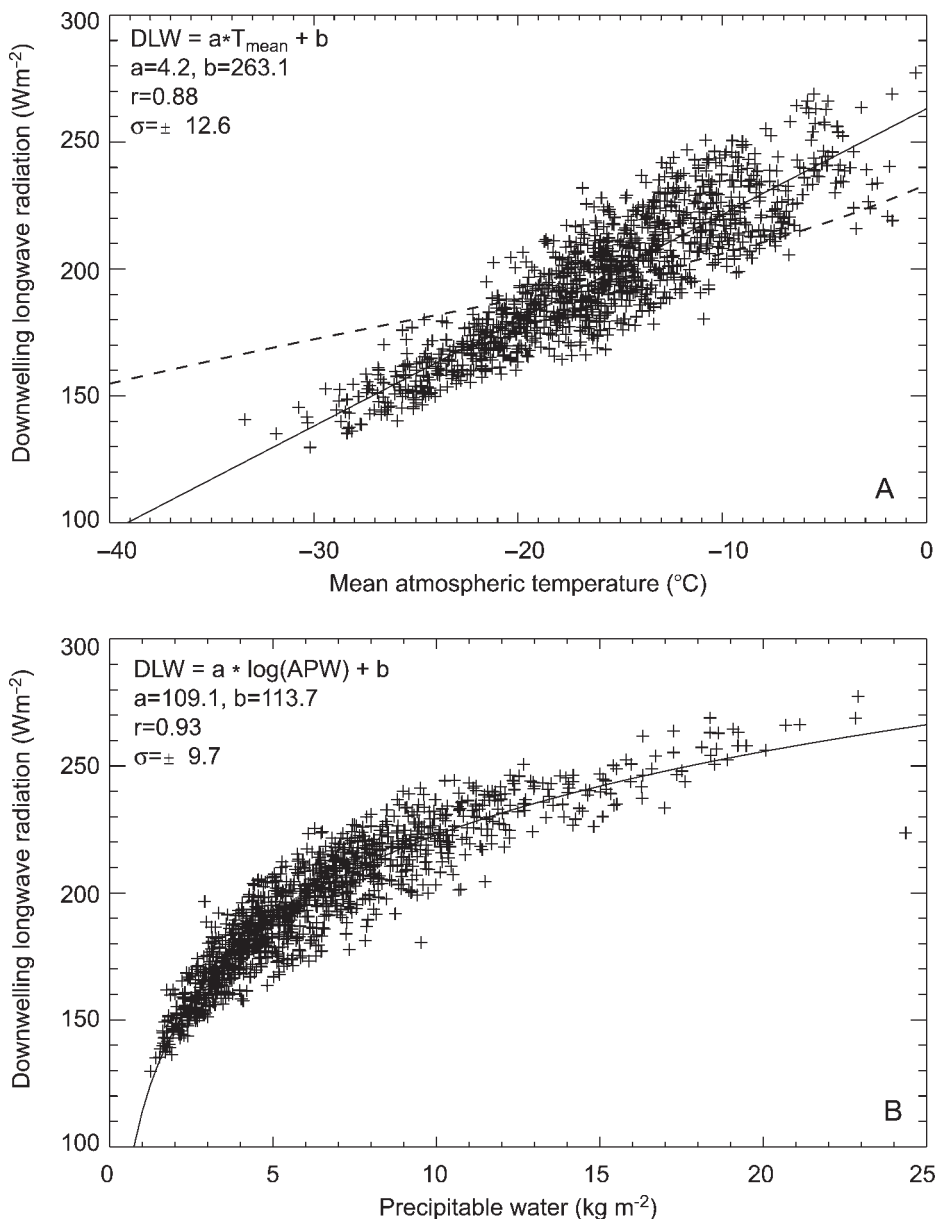


Figure 9.1. Variations of atmospheric downwelling longwave radiation at Barrow with respect to (a) mean atmospheric temperature (surface to 10 km) and (b) precipitable water (surface to 10 km) during the snowmelt period of 1980–1991. DLW is the downwelling longwave radiation, T_{mean} is the mean atmospheric temperature, and APW is the mean precipitable water. Regression equations are also shown, where a and b in the legend of each panel are the regression constants, r is the correlation coefficient, and σ is the deviation of downwelling longwave radiation from the regression line. The thin lines are the regression lines, and the dashed line is the estimated longwave flux from the Parkinson and Washington (1979) empirical formula, based on the near-surface temperature (using the same scale as for mean atmospheric temperature) (from Zhang et al., 2001, by permission of AMS).

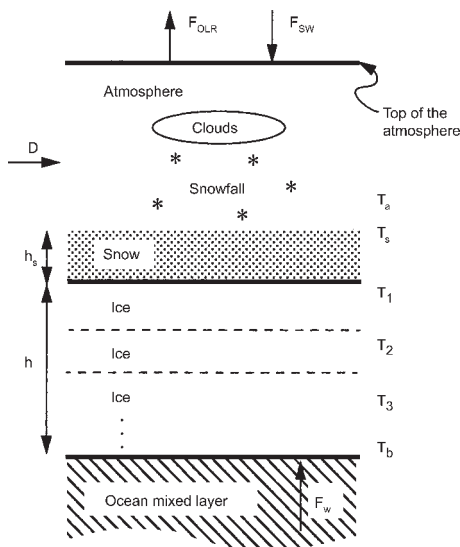


Figure 9.2. Schematic of the Bitz et al. (1996) single-column atmosphere-sea-ice-upper ocean climate model. F_{sw} and F_{olr} are incoming shortwave and outgoing longwave radiation, respectively. D is the atmospheric energy flux convergence, F_w is the ocean heat flux, T_a is the surface air temperature, T_s is the sea ice/snow temperature, T_1 is the temperature at the top of sea ice layer 1, T_b is the temperature of the ocean mixed layer and the bottom temperature of the sea ice, h is the thickness of sea ice, and h_s is the thickness of snow (from Bitz et al., 1996, by permission of AMS).

scattering of solar radiation. Clouds are modeled as a single layer. Along with horizontal energy transports, the model includes vertical convective transport of latent and sensible heat, and the radiative effects of ice crystal precipitation.

One of the interesting results from this study is that the volume of perennial sea ice is simulated to vary predominantly on decadal time scales. As assessed from sensitivity studies, variations in ice volume are most sensitive to perturbations in atmospheric forcing not in winter, the period of ice growth, but in late spring, at the onset of melt, pointing to the importance of ice-albedo feedbacks. The model calculations suggest that natural variability in the thermodynamic forcing on Arctic Ocean sea ice volume could (by variations in sea ice export from the Arctic Ocean) lead to freshening of the North Atlantic, comparable to that associated with the Great Salinity Anomaly (see Chapter 7).

The ISCCP-D and APP-x surface radiation flux fields outlined in Chapter 5 represent the application of a single-column model to a two dimensional grid. Another example of this general strategy is the study of C. Oelke et al. (2003). They simulated the active layer of permafrost over the Arctic terrestrial drainage at a 25×25 km resolution using a heat conduction model with phase change developed by L. Goodrich (1982). Soil is divided into layers with different thermal properties for frozen and thawed soils. Information on the spatial distribution of soil bulk density, and the relative compositions of clay, silt, and sand that influence thermal conductivity are taken from existing maps. Soil water content varies with each layer. Initial soil temperatures were chosen according to the permafrost classification of the grid cells based on the International Permafrost Association map (Figure 2.15).

The primary forcings for the model are daily near-surface air temperature (SAT) and snow thickness. SAT was based on fields from the NCEP/NCAR reanalysis, adjusted to address better the effects of topography. Snow thickness was obtained by adjusting SSM/I snow water equivalent retrievals by climatological snow densities

for different climatic zones (tundra, taiga, prairie, alpine, and maritime regions), based on the classification of Sturm et al. (1995) (see Chapter 2). SSM/I cannot detect areas of thin snow. Areas of thin snow were identified through comparisons between the SSM/I fields and NOAA weekly snow charts and given an assumed thickness of 3.0 cm.

Figure 9.3 summarizes results for two grid cells over the period of August 31, 1998 through December 31, 2000, which includes two complete freezing and thawing seasons. The first grid cell is at 51°N at 1664 m in southern Siberia, in a region of continuous permafrost with taiga snow. The middle panel depicts the time evolution of the vertical cross section through the soil. Shaded regions in the profiles show where the soil is thawed. Spring and summer thawing occurs from the top down. Autumn/winter freezing is also primarily from the top down. Consequently, from autumn into early winter, there exists a frozen surface layer with a thawed layer below. It takes until the middle of winter for the thawed layer at depth to completely refreeze. This late freeze-up reflects the insulating effects of overlying snow cover. The bottom panel shows the time evolution of the depth of thawed soil. The active layer represents the maximum depth that experiences seasonal thaw (i.e., the maximum value shown in the bottom panel). For the Siberian grid cell, a fairly deep active layer develops in each year, largest in 2,000 with a value of 177 cm. The second grid cell is located in Canada on Prince Patrick Island at 76°N. This is in a much colder climatic zone than for the Siberian example. While the ground is snow covered for a longer period, the snow cover (tundra snow) is thinner because of the scant precipitation. In turn, the active layer depth is shallower.

Some idea of the spatial characteristics of the simulated active layer over the Arctic terrestrial drainage is provided in Figure 9.4. The maximum thaw depth (active layer thickness) is given for 1999, along with the day of year at which the maximum thaw depth occurred. There is a general decrease with latitude in thaw depth but with minimum values around coastal Greenland and the Canadian Arctic Archipelago. Topographic effects are apparent. The area northwest of Hudson Bay is characterized by high bulk density bedrock areas with high thermal conductivity and hence deeper maximum thaw depths. In general, as latitude increases, the date at which the maximum depth occurs shifts to earlier in the year. This relates to the shorter period of warmth at higher latitudes.

9.3 Land Surface Models

Numerous LSMs of differing complexity and architecture are in existence. In general, they are being continually refined to enable the simulation of increasingly complex climate interactions and feedbacks. A given LSM may exist in a number of different versions designed for particular applications. A few examples of LSMs in wide use include:

VIC (Variable Infiltration Capacity Model): VIC was developed at the University of Washington Seattle and with the purpose of producing realistic runoff and

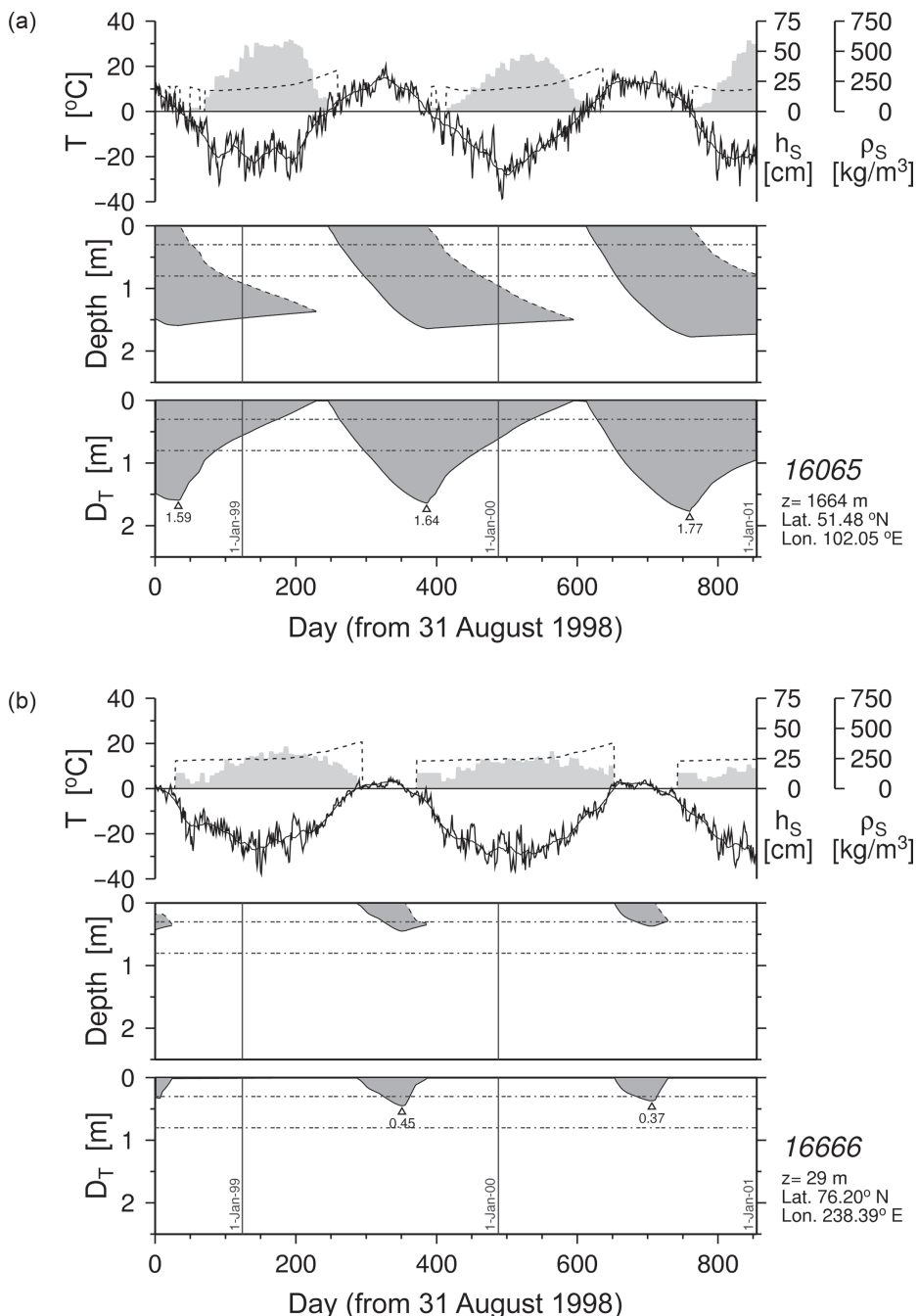


Figure 9.3. Time series (August 31, 1998 to December 31, 2000) from an active layer thickness model for model grid cells in (a) Siberia and (b) northern Canada. The top panels for each location show surface air temperature (including a thirty-one-day running mean), snow height h_s (shaded), and snow density ρ_s (thin dashed line). The middle panels show the depth of the thawed layer (shaded regions), the development of thawing planes (solid line), and freezing planes (dashed lines). The bottom panels show the total thaw depth (with maximum values labeled). Also plotted on the middle and bottom panels by horizontal dash-dotted lines are the boundaries of the major soil layers at 0.3 and 0.8 m depth. Grid cell elevations z , latitude and longitude are also given (from Oelke et al., 2003, by permission of AGU).

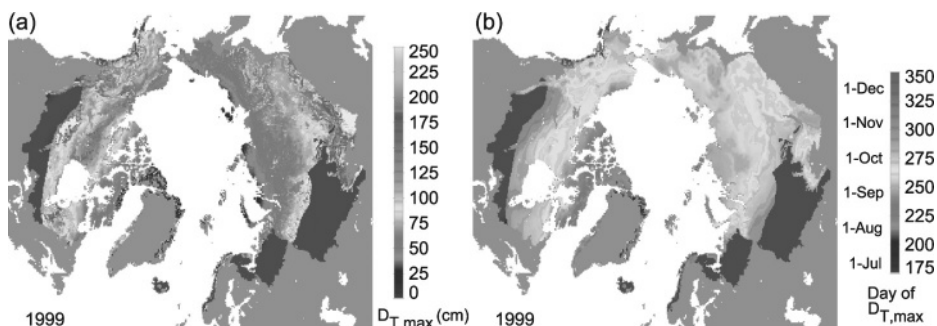


Figure 9.4. Modeled maximum depth of active layer (a) and the date of maximum thaw depth (b) for 1999 over the Arctic terrestrial drainage. Areas with no permafrost in the drainage and the Greenland Ice Sheet are indicated by dark grey shading (from Oelke et al., 2003, by permission of AGU). (See plate section for color version.)

streamflow via parameterizations of subgrid soil moisture variability, as well as spatial variability in precipitation forcings and land cover. VIC is a research model and has been applied to many watersheds across the globe. Originally developed in the early 1990s (Liang et al., 1994), VIC is under constant development to respond to new problems and applications. Considerable attention has been paid to improving the representation of important high latitude processes such as sublimation, snow redistribution, soil freezing, and the dynamics of lakes and wetlands.

NOAH: The NOAH land surface model is a community effort led by NCEP and involving collaboration between public and private institutions (Elk et al., 2003). Originally developed in 1993, NOAH has been used operationally in NCEP NWP models since 1996 and has undergone constant refinement. NOAH is an integral part of the Weather Research and Forecasting (WRF) mesoscale numerical weather prediction system designed for operational forecasting and atmospheric research.

CLM: The Community Land Model (CLM) was developed for use within the NCAR Community Climate System Model global climate model, which has subsequently evolved into the Community Earth System Model (CESM). CLM, a community effort, represents an evolution of land surface models beyond the treatment of surface energy fluxes and applications to hydrometeorology to include biogeochemical cycles (e.g., carbon and nitrogen cycles), land use, and vegetation dynamics. It is built on the philosophy that terrestrial ecosystems are key determinants of climate (Bonan, 2008). CLM4, the latest version as of this writing, features revised hydrology and snow parameterizations, organic soils, a 50 m deep ground column, and updated distribution of plant functional types (Oleson et al., 2010).

CHASM: CHASM (CHAmeleon Surface Model) was developed to explore the complexity of the surface energy balance (Desborough, 1999) and contains options that allow it to utilize a range of hydrologic parameterizations and surface energy balance configurations. In its simplest form it collapses to the simple “bucket” model of S. Manabe (1969), whereas in its most complex mode it has a tiled mosaic structure (e.g., Koster and Suarez, 1992). A tile is a homogeneous land surface type (e.g., boreal forest or tundra). Each grid cell can have numerous tiles, for which the energy balance is calculated separately.

Canadian Land Surface Scheme (CLASS): This model (Verseghy, 1991; Verseghy, McFarlane, and Lazar, 1993) was specifically designed with cold land processes in mind and was among the first to incorporate a separate snow layer. CLASS was the focus of extensive activity by the Canadian Mackenzie GEWEX study group, which has targeted more realistic treatments of soil, land cover, hydrologic routing, and sublimation.

ECMWF: This tiled land surface scheme, first described by P. Viterbo and A. Beljaars (1995), is designed for operational use within the ECMWF weather forecast model. It includes up to six land surface tiles (bare ground, low vegetation, high vegetation, intercepted water, shaded snow, and exposed snow). Recent advances include a new soil hydrology and snow scheme. Vegetation seasonality is described by the leaf area index (LAI) from climatological data.

Model intercomparison projects (MIPs) can provide valuable insight into the relative performance and behavior of different models. The Project for Intercomparison of Land Surface Parameterization Schemes (PILPS 2e), within the GEWEX Global Land-Surface/Atmosphere System Study (Bowling et al., 2003) was a MIP aimed at evaluating the performance of uncoupled (“stand alone”) LSMs in northern high latitudes. The project was motivated by the need to improve high-latitude land surface representations within NWP models and GCMs.

PILPS 2e compared simulations of land-surface processes from twenty-one models run for the Torne-Kalix (58,000 km²) catchment in northern Scandinavia (Figure 9.5). The location was selected because reasonably detailed and high quality surface observations for a twenty-year period (1979–1998) were available. Identical atmospheric forcing data from these surface observations (precipitation, air temperature, specific humidity, wind speed, downward shortwave, and longwave radiation) were provided to each modeling group. Land cover classifications, leaf area index, and soil characteristics were also provided.

Among the problems identified under PILPS activities especially critical to model performance in the Arctic are: (1) treatment of snowpack redistribution attributed to wind, and the accompanying issue of parameterization of sublimation; (2) snowfall interception by tree canopies and the fate of this intercepted snow in boreal forests; (3) the effects of lakes and wetlands on the timing of runoff, its availability for evaporation, and the regional energy balance; and (4) soil freezing and permafrost.

For example, J. Pomeroy, D. Gray, and P. Landine (1993) and Pomeroy and R. Essery (1999) demonstrated that incorporation of blowing snow physics is necessary to simulate adequately sublimation losses in prairie snow environments. Similar issues exist in Arctic environments. Other and arguably more first-order problems identified by Slater et al. (2001) as part of the precursor PILPS 2d effort include: (1) difficulties in adequately modeling the albedo and fractional coverage of snow, and associated effects on ablation; (2) the wide variety of model structures and resulting impacts on surface energy budget treatments; (3) the tendency for “colder” models to create a stability-induced cutoff of turbulent heat fluxes,

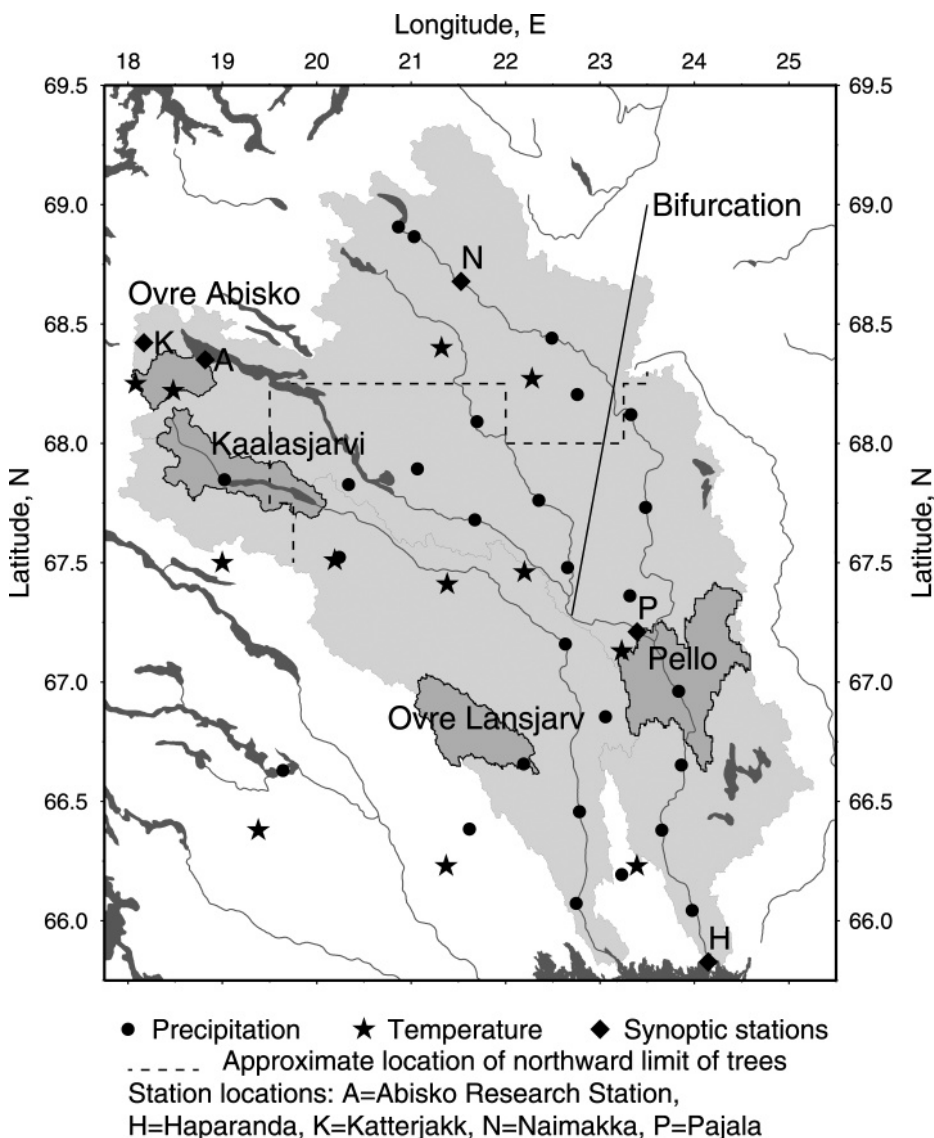


Figure 9.5. The Torne-Kalix river system modeled under the PILPS 2e project and location of observation stations (from Bowling et al., 2003, by permission of Elsevier).

yielding a larger sensitivity to downwelling longwave radiation when surface net radiation is negative.

Figures 9.6 and 9.7 summarize some results from the model intercomparison. Quite striking is the large scatter in predicted March snow water equivalent. Averaged modeled snow water equivalent over the basin ranges from 119 to 268 mm. Models with high latent heat flux and an average downward sensible heat flux (a heat source for the surface) tend to have the lowest snow accumulation. Not surprisingly given the scatter in snow water equivalent, mean annual runoff also differs substantially,

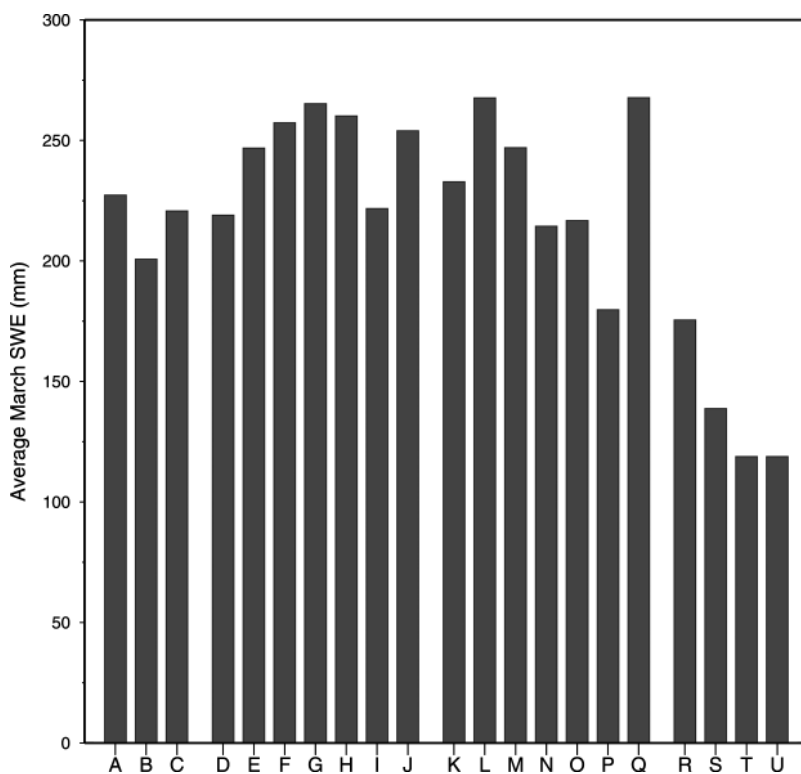


Figure 9.6. Basin averaged snow water equivalent (SWE) for March (approximately the month of the annual maximum) from the 21 PILPS 2e land surface models (listed as a–u) over the 1989–1998 period (from Bowling et al., 2003, by permission of Elsevier).

from 301 to 481 mm. For some models, subsurface runoff dominates, whereas for others, runoff is solely from the surface. Differences in modeled snow accumulation and surface-subsurface runoff partitioning contribute to large variations in the shapes of mean hydrographs.

In a more recent effort, A. Slater et al. (2007) compared the performance of five LSMs (CHASM, NOAH, CLM, VIC, and ECMWF) in their ability to simulate hydrologic processes across the Arctic terrestrial drainage. All of the models were forced by the same data derived from the ERA-40 atmospheric reanalysis for the 1980–2001 period. The primary conclusion is that no single model has the best or worst performance when compared to observations – performance depends on the variable, or variables, in question. As assessed for large Arctic-draining watersheds such as the Lena, there is up to a 30 percent difference between the five models in how annual precipitation is partitioned between runoff and evapotranspiration. Capturing the correct base flow of rivers was found to be a consistent problem, and model hydrographs have a tendency to peak too early in summer, indicating that snow melt occurs too early. The five models were found to have similar errors in snow water equivalent while differing widely in snow quantities such as snowfall, snow depth, and sublimation rates. Figure 9.8 shows the annual cycle of monthly

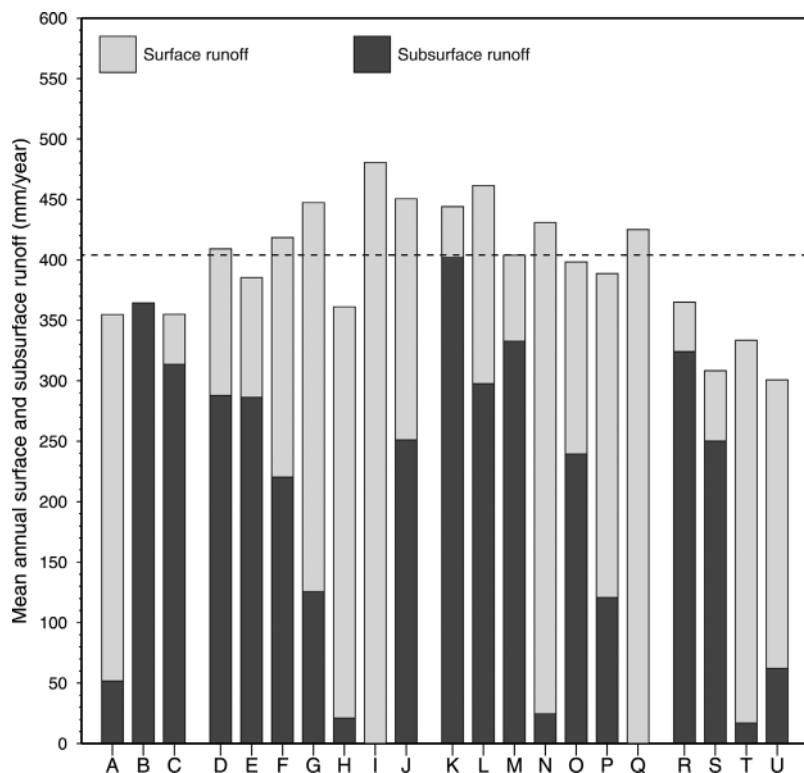


Figure 9.7. Total basin mean annual surface and subsurface runoff from the twenty-one PILPS 2e land surface models (listed as a-u) over the 1989–1998 period. The dashed horizontal line is the observed mean annual runoff at the mouths of the Torne and Kalix rivers combined (from Bowling et al., 2003, by permission of Elsevier).

mean evapotranspiration from each model for the four major Arctic-raining watersheds. Even though all of the models correctly capture the summer maximum and winter minimum in evapotranspiration, there are large differences for every month. As overall, VIC has the highest runoff values of the five models, it follows naturally that it has the lowest overall ET. However, because VIC has been calibrated to observed discharge, for long-term annual means, its evapotranspiration is arguably closer to the truth.

9.4 Sea Ice and Ice-Ocean Models

The first robust thermodynamic sea ice model was developed by Maykut and N. Untersteiner (1971). This one-dimensional model passes heat fluxes from the atmosphere and ocean into the ice and overlying snow cover by conduction. The temperature of the snow (or air-ice) interface is determined by the surface energy balance. The balance at the ice-ocean interface determines the melt/freeze state at the sea ice bottom. The first successful three-dimensional dynamic-thermodynamic

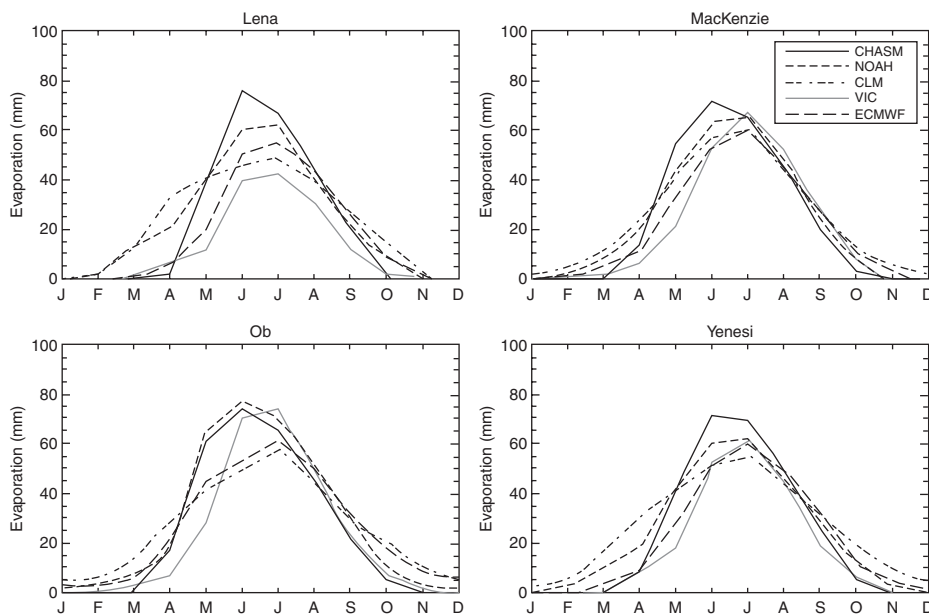


Figure 9.8. Monthly mean evapotranspiration (mm per month, positive upwards in this figure) for the four major Arctic-draining watersheds (the Lena, the Mackenzie, the Ob, and the Yenesi) from five land surface models driven by data from the ERA-40 atmospheric reanalysis for the 1980–2001 period (from Slater et al., 2007, by permission of AGU).

model (dynamic meaning that ice motion is simulated) is that of Parkinson and Washington (1979). Four vertical layers are represented within each grid cell: a mixed layer ocean, an ice layer, a snow layer, and an atmospheric boundary layer. At the ice-ocean interface, ocean currents provide water stress and a constant dynamic topography (recall that because of density variations, the ocean surface is not entirely flat). A constant ocean heat flux is also used. Atmospheric heat fluxes and surface stresses are applied at the air-ice interface. Ice dynamics is treated as free drift (see Chapter 7). The basic Parkinson and Washington (1979) thermodynamics approach is still widely used.

Hibler (1979) developed the first widely used dynamic-thermodynamic model which included the effects of internal ice stress (floe-to-floe interactions). The model, driven by observed winds and near surface air temperature, was able to reproduce observed patterns of ice drift and ice thickness. The model incorporates the equations of continuity for ice thickness and concentration. In early versions of the model, ice growth rates were prescribed. Hibler (1980) subsequently developed formulations whereby the growth rates are calculated from a heat budget; Hibler also included a variable ice thickness distribution model.

All dynamic-thermodynamic models of the Hibler variety contain a constitutive law, which relates the ice deformation to the forces applied. A variety of formulations have been examined. For example, the “cavitating fluid” approximation differs

from free drift by allowing nonzero ice pressure under converging conditions but, like free drift, offers no resistance to divergence or shear (Flato and Hibler, 1992). The Hibler (1979) model uses a viscous-plastic constitutive law, which relates the strength of the ice interaction to a thickness distribution. This basic formulation, which still finds wide use, allows the ice strength to be greater in regions of ice convergence and weaker in regions of divergence. Other formulations include the modified Coulombic law described by Hibler, P. Heil, and V. Lytle (1998) and Hibler and E. Schulson (2000).

Snow cover is not included explicitly in the Hibler (1979) model; the effects of snow cover are approximated by setting the ice surface albedo to that of snow when the surface temperature is below freezing and to that of snow-free ice when the surface is at the melting point. J. Walsh, Hibler, and B. Ross (1985) include treatments of “thick” ice and snow using seven thickness levels. In most sea ice models, heat calculated via the energy balance is used to melt all of the snow before it is used to melt ice at the upper surface.

The field of ice-ocean modeling has quickly grown. Such models couple a dynamic-thermodynamic ice model of the Hibler variety with ocean models of varying complexity. The first ice-ocean model was that of Hibler and F. Bryan (1987), which coupled the Hibler ice model to the Bryan-Cox multilevel ocean model (Bryan, 1969). Other early efforts include A. Semtner (1987), G. Fleming and Semtner (1991) and S. Riedlinger and R. Preller (1991).

The study of Zhang, Rothrock, and Steele (2000) is a good example of the application of an ice-ocean model. They examined the response of Arctic sea ice to forcing by the North Atlantic Oscillation (NAO; see Chapter 4). The model had a horizontal resolution of 40 km, with twenty-one ocean levels and twelve ice thickness categories. The model was forced by winds, SAT, specific humidity, and longwave and shortwave radiation fluxes.

Figure 9.9 shows simulated annual mean ice velocity and mean sea level pressure fields for the two periods (1979–1988 and 1989–1996), along with corresponding ice velocity anomaly fields. These two decades characterize the generally low and high index phases of the NAO, respectively (see Chapter 4). Readily seen are large differences in the shape and intensity of the Beaufort Gyre and Transpolar Drift Stream. Note the strongly cyclonic anomaly during the high NAO phase (1989–1996) and the implied increase in the Fram Strait outflow. Figure 9.10 gives simulated fields of mean annual ice thickness for the two periods and the difference field. Observations show a pattern of thicker ice off the Canadian Archipelago and north Greenland coast and thinner ice on the Siberian side of the Arctic (Figure 7.9). The model captures this basic pattern, but over both decades gives unrealistically large thicknesses along the Alaskan coast. However, useful information is provided by the difference fields – the model results suggest a general tendency for the ice under the persistently positive NAO phase of 1989–1996 to have been thinner in the eastern Arctic and thicker in the western Arctic. These findings support arguments by G. Holloway and T. Sou (2002) that at least part of the observed thinning of the perennial ice cover over the central Arctic Ocean in the 1990s as assessed from submarine

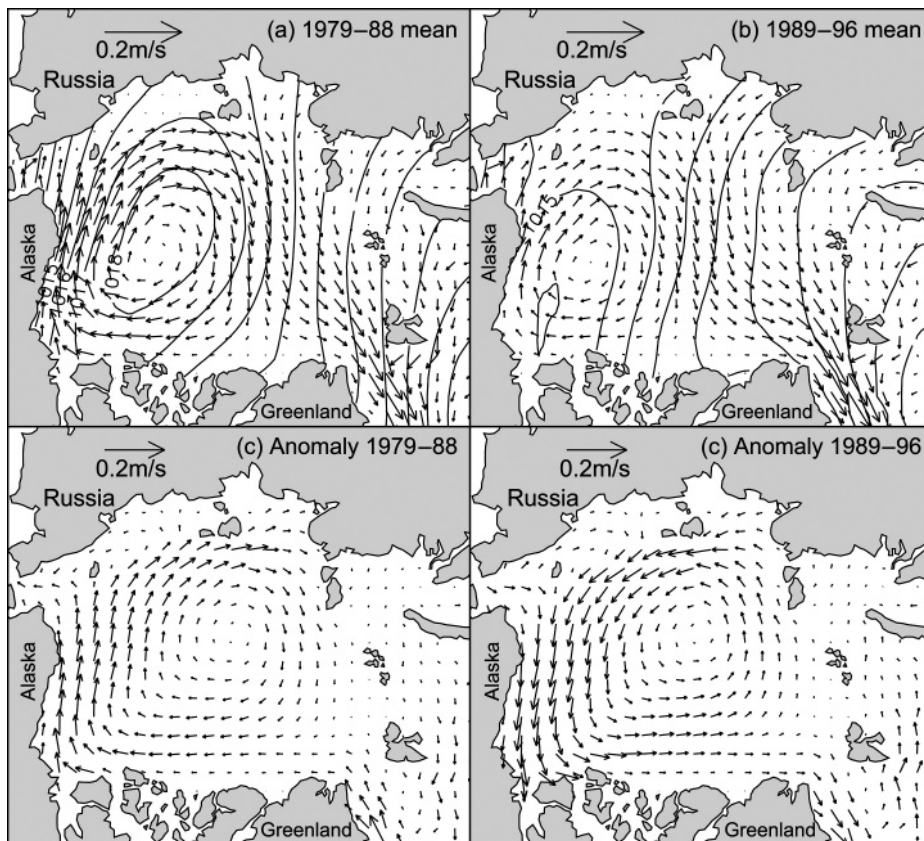


Figure 9.9. Simulated mean ice velocity and mean annual sea level pressure for (a) 1979–1988; (b) 1989–1996; anomaly fields of ice velocity based on the difference (c) between the 1979–1988 mean and the 1979–1996 mean, and (d) between the 1989–1996 mean and the 1979–1996 mean. Vectors are given at every sixteenth grid point with contours of sea level pressure given at every 1 hPa (from Zhang et al., 2000, by permission of AMS).

sonar records (Rothrock et al., 1999) represents a redistribution of thick ice to along the North American coast.

The Arctic Ocean Model Intercomparison Project (AOMIP) was initiated in 2001 (Steele et al., 2001) as an international effort to understand the behavior of different models under realistic forcing. A first five-year AOMIP research cycle was completed in March 2007. A second cycle focused on validation and improvement of Arctic Ocean models in a coordinated fashion, investigating variability of the Arctic Ocean and sea ice at seasonal to decadal time scales, and identifying mechanisms responsible for observed changes. Many different models and modeling groups have participated in AOMIP. As with any MIP, it is necessary to force and validate all models in as similar a manner as possible. AOMIP has collected and created a variety of standardized model forcing data sets including bathymetry, river runoff, precipitation, and winds. AOMIP has subsequently evolved into the Forum for Arctic Modeling and Observational Synthesis. Some key insights from

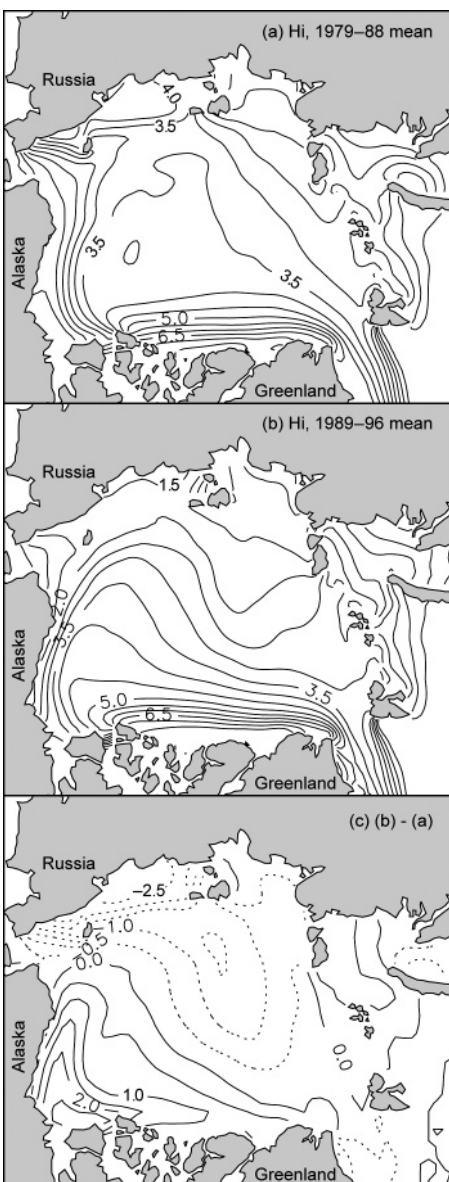


Figure 9.10. Simulated mean ice thickness fields for (a) 1979–1988, (b) 1989–1996, and (c) their difference field (b-a). The contour interval is 0.5 m (from Zhang et al., 2000, by permission of AMS).

AOMIP/FAMOS activity are that (1) wintertime surface convection and mixing in many models seems overly strong, leading to overly deep mixed layers; (2) Atlantic Water cyclonic circulation around the continental slopes and ridges of the Arctic Ocean may be strongly influenced in the Canada Basin by the strength of the Beaufort Gyre winds/ice motion (which is important because considerable early AOMIP activity focused on getting a cyclonic circulation in the models, which was then assumed to be correct); and (3) modeled sea ice thickness in most models is generally too low for thick ice and too high for thin ice (Proshutinsky et al., 2011).

An area of strong growth in ice-ocean modeling is data assimilation. Data assimilation is a technique that constrains a model to physical reality by incorporating

observed data. Data assimilation can also fill in gaps in observations and provide better estimates of parameters that are difficult to observed directly (e.g., ice thickness). There are a number of assimilation methods, ranging from the trivial such as “direct replacement” of modeled with observed data (either of ice velocity or concentration) to more sophisticated approaches such as optimal interpolation or Kalman filtering. These account for the error characteristics of both the model and data, as well as the spatial distribution of the data, to minimize error in a statistical sense. Another approach is a variational scheme, where a “cost function” that measures the mismatch between model and data is minimized under the constraint that appropriate model quantities (e.g., mass, momentum, energy) are conserved (see Ghil and Malanotte-Rizzoli, 1991). Data assimilation methods were first developed for atmospheric models to improve weather forecasts (Charney, Hale, and Jastrow, 1969). A good example of the direct replacement method applied to sea ice velocities is the study of Maslanik and H. Maybee (1994). Examples of more sophisticated schemes to assimilate ice velocity include Meier, Maslanik, and Fowler (2000), Meier and Maslanik (2003) and J. Zhang et al. (2003). Assimilation of observed ice concentrations has been addressed by Thomas and Rothrock (1989, 1993) and Thomas et al. (1996).

Perhaps the most notable effort as of this writing is the Pan-Arctic Ice Ocean Modeling and Assimilation System (PIOMAS), developed by the University of Washington Seattle Polar Science Center (Zhang and Rothrock, 2003; Schweiger et al., 2011). PIOMAS provides estimates of Arctic sea ice volume from 1979 onward with regular updates. It consists of a multicategory thickness and enthalpy distribution sea ice model coupled with the Parallel Ocean Program developed at the Los Alamos National Laboratory. Satellite-derived sea ice concentration data are assimilated into the model to improve ice thickness estimates. Sea surface temperature data are assimilated in ice-free areas. Atmospheric forcing of the model, including 10 m winds, near surface air temperature, precipitation, specific humidity, evaporation, sea level pressure, downward longwave radiation, and cloud cover (to compute downward solar radiation) are obtained from the NCEP/NCAR reanalysis. PIOMAS covers the region north of 48°N latitude and is driven at its boundaries with input from a global ocean model (Schweiger et al., 2011). The system is undergoing constant refinement. Results from PIOMAS show a downward trend in sea ice thickness from 1979 to present consistent with the observed downward trend in sea ice extent. Figure 9.11 shows the mean annual cycle in ice volume from PIOMAS for the 1979–2011 period and for selected individual years. For the 1979–2011 average, volume ranges from 28,700 km³ in April to 12,300 km³ in September. The low volume in recent years compared to the long-term average is clear. The estimated ice volume of 3,400 km³ for September 2012 is the lowest in the PIOMAS record.

9.5 Global Climate Models

GCMs represent one of our most valuable tools to both better understand changes in climate that have occurred in the past, changes over the instrumental record, and those that can be expected in the future. The analysis of global climate model

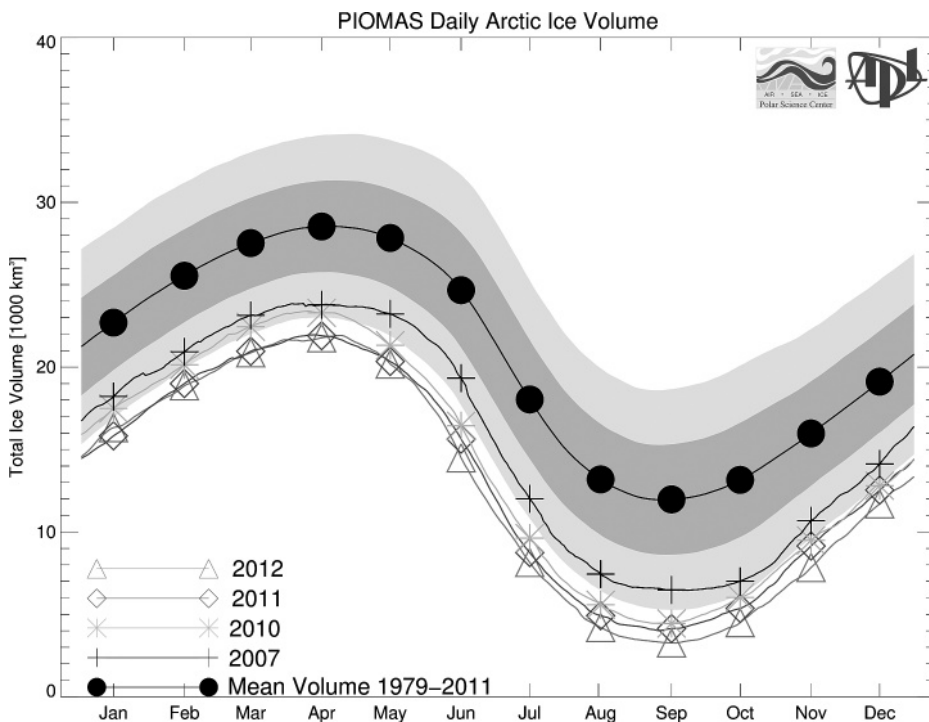


Figure 9.11. Annual cycle of Arctic sea ice volume from PIOMAS for 2007, 2010, 2011, 2012, and for the long-term (1979–2011) mean. Shaded areas indicate one and two standard deviations from the mean (courtesy of A. Schweiger, University of Washington, Seattle WA). (See plate section for color version.)

projections and hindcasts (simulation of past conditions, such as over the twentieth century) has been greatly facilitated by the Intergovernmental Panel on Climate Change (IPCC) series of assessments. The Program for Climate Model Diagnosis and Intercomparison (PCMDI) at the Lawrence Livermore National Laboratories has the mission of developing methods and tools for the diagnosis and intercomparison of output from GCMs contributed by modeling centers around the world. The Coupled Model Intercomparison Project 3 (CMIP3) managed by PCMDI enabled scientists to perform model analyses for the IPCC Fourth Assessment Report (AR4). CMIP5 is the next phase and includes simulations for the Fifth Assessment Report, AR5. It contains simulations to evaluate the veracity of model hindcasts, projections for the near term (out to about 2035) and projections to the end of the twenty-first century and beyond.

Although procedures for generating simulations have evolved through time and details depend on the modeling center, one can broadly view the process as having three steps: (1) one starts with a pre-industrial simulation with climate forcings (e.g., greenhouse gas concentrations, aerosol levels) set to a pre-industrial state; (2) starting from the pre-industrial state, the models are run with the best estimates of historical climate forcings up through the present (hindcasts); and (3) the models

are then run with a series of different assumed greenhouse gas climate forcings (scenarios) out into the future. Although one obtains a series of projections based on different emissions scenarios, as noted in Section 9.1, many modeling centers also provide ensembles – a set of simulations that start from slightly different initial conditions which enable comparisons between the forced component of a climate change with natural climate variability. For example, in the case on the NCAR CESM, the CMIP5 archive contains five historical (1850–2005) ensemble members started on January 1 from years 863, 893, 983, 937, and 1031 of a long-term pre-industrial (pre-1850) spin-up integration.

Simulations for the IPCC AR4 contained in the CMIP3 archive made use of a suite of emissions scenario based on models of economic and population growth and technological development. The A1 group of scenarios describes a future world of rapid economic growth, a global population that peaks in the middle of the century and then declines, and a rapid introduction of new and more efficient technologies. A1 is in turn subdivided into fossil intensive (A1FI), non-fossil energy sources (A1T), or a balance across all energy sources (A1B). Other scenarios include A2, B1, and B2. B1, for example, describes a world like A1 in which global population peaks in mid-century and then declines, but in this case with a rapid change in economic structures toward a service and information economy, with the introduction of clean and resource-efficient technologies. Simulations for the IPCC AR4 contained in the CMIP5 archive by comparison made use of Representative Concentration Pathways (RCPs), which are based on a possible range of radiative forcing in W m^{-2} in the year 2100 (RCP 2.6, RCP 4.5, RCP 6.0, and RCP 8.5). The range covered by the RCPs is wider than that used in earlier IPCC Assessment Reports. In the extreme RCP 8.5 scenario, carbon dioxide levels by the year 2100 reach 1,300 ppm (today's value is a little more than 400 ppm). RCP 2.6 is as modest as RCP 8.5 is extreme, with greenhouse-gas emissions dropping to zero by about 2070, and then continuing to fall, with emissions becoming negative (carbon is removed from the atmosphere).

Figure 9.12 shows projected (2006–2100) and hindcast (1900–2005) anomalies in annual mean surface air temperature for the Arctic (taken here as the region poleward of 65°N) from the CMIP5 models, along with the Arctic time series from the ERA-Interim reanalysis for the 1979–2011 period (see Section 9.7). Anomalies are expressed with respect to the 1986–2005 period. For the hindcasts and projections, the solid line represents the mean from all models and their ensemble members, while the shading indicates the one standard deviation range between the all models and their ensemble members. The top (bottom) of the bars on the right side of the plot represent the average of the +1 (−1) standard deviation values from all models and their ensemble members for the last decade of the twenty-first century. The salient points of the figure are that: (1) for the next couple of decades, projected temperature changes are not strongly dependent on the RCP (there is much overlap between all of the projections); (2) for a given scenario, there is a large range in projected warming by the end of the twenty-first century, but how warm the Arctic becomes depends strongly on human behavior.

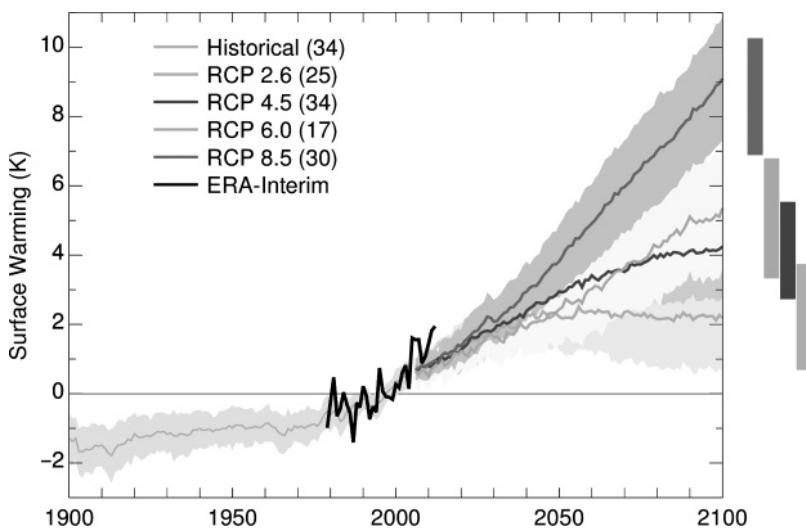


Figure 9.12. CMIP5 hindcasts (1900–2006) and projections (2006–2007) of annual surface air temperature anomalies for the Arctic (the region poleward of 65°N), along with the Arctic record from the ERA-Interim reanalysis. See text for details (courtesy of A.P. Barrett, NSIDC, Boulder, CO). (See plate section for color version.)

GCMs have been widely used to evaluate hindcasts of Arctic sea ice extent and projections out to the year 2100 and beyond. In a widely cited paper, J. Stroeve et al. (2007) examined simulations of September Arctic sea ice extent for September from the CMIP3 model archive, including ensemble members, for the 1900–2100 period. For the twenty-first century, use was made of simulations with the A1B emissions scenario, the most widely examined scenario used in the CMIP3 simulations. The primary conclusions were that: (1) essentially all of the models show declining September ice extent over the period of observations, providing evidence for a role of external forcing on the observed trend; and (2) the simulated trends, viewed as a group, are smaller than the observed trend. In a subsequent effort, Stroeve et al. (2012) examined output from the later generation of models contained in the CMIP5 archive, focusing on the RCP 4.5 scenario for projections. Although there is a wide range in modeled sea ice extents between the various CMIP5 models, the CMIP5 multimodel ensemble mean was found to be more consistent with the historical observations, both in terms of the observed average extent and the rate of decline over the past several decades (Figure 9.13). Trends from most ensemble members and models are nevertheless still smaller than the observed trend. Pointing to strong impacts of internal climate variability, 16 percent of the ensemble member trends as evaluated over the period of satellite observations were statistically indistinguishable from zero. When the analysis was constrained by rejecting those models that do an especially poor job at reproducing the observed climatological mean September ice extent, the spread in projected ice extent throughout the twenty-first century from the CMIP5 and CMIP3 models is similar. Furthermore, a similar number of these ensemble members reach nearly ice-free September conditions (less than $1.0 \times 10^6 \text{ km}^2$)

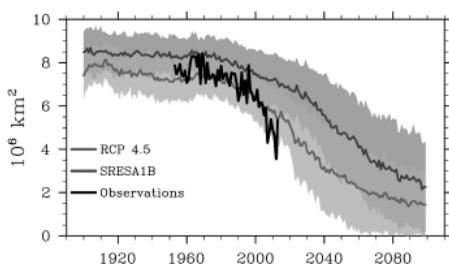


Figure 9.13. Multimodel ensemble mean sea ice extent based on observations (black line), the CMIP5 models (light gray line for the ensemble mean and light gray shading for the ± 1 standard deviation) and the CMIP3 models (dark gray line for the ensemble mean and light gray shading for the ± 1 standard deviation) (courtesy of J. Stroeve, NSIDC, Boulder, CO). (See plate section for color version.)

before the end of the twenty-first century. Viewed in this context, conclusions drawn from CMIP5 are not much different than those from CMIP3. Importantly, the CMIP5 simulations do not appear to have appreciably reduced uncertainty as to when a seasonally ice-free Arctic Ocean will be realized. In a subsequent study, J. Liu et al. (2013) attempted to reduce the spread in the projected timing of a seasonally ice-free Arctic Ocean (ice extent less than $1.0 \times 10^6 \text{ km}^2$) based on both the ability of models to reproduce the observed sea ice climatology and variability since 1979 and the strong and persistent relationships between present and future ice conditions. Both approaches point to a seasonally ice-free state between 2054–2058 assuming a high emissions (RCP 8.5) scenario.

Understanding why different models behave differently, even when driven with the same climate forcings, is a very active area of research. With respect to the tendency for the CMIP3 models to be “conservative” regarding their depiction of the trend in September extent over the period of observations, it appears that at least part of the explanation is that these models do not capture the observed thinning of the ice cover and the acceleration in drift speed that should accompany this thinning (Rampal et al., 2011). With respect to the wide range in projections of sea ice extent, much attention has focused on depictions of mean sea ice thickness and its spatial distribution under the present climate. Differences in mean thickness between different models point, at least in part, to difference in the sea ice energy balance, in turn pointing to issues such as cloud cover as it affects the downward solar and longwave radiation fluxes, or ocean heat fluxes. Differences in the special distribution of ice thickness point to differences in depiction of the surface wind field. Simply put, if a model cannot simulate the mean sea level pressure field over the Arctic Ocean with reasonable fidelity, the spatial pattern of sea ice thickness is likely to be poorly simulated.

Along with considerable scatter in depictions of present-day ice thickness and extent, results from the CMIP5 simulations point to some systematic model biases. Figure 9.14 shows the spatial pattern of observed September sea ice thickness based on the NASA ICESat aircraft missions (aircraft altimetry), the September pattern based on averaging output from all of the CMIP5 models for years corresponding to the ICESat data, and the difference between the modeled and observed thickness. The ICESat data depict the well-known pattern of the thickest ice being located north of the Canadian Arctic Archipelago and Greenland, with thinner ice over the Eurasian side of the Arctic Ocean. The difference field (modeled minus observed thickness) shows clearly that, viewed as a group, the ice cover from the CMIP5

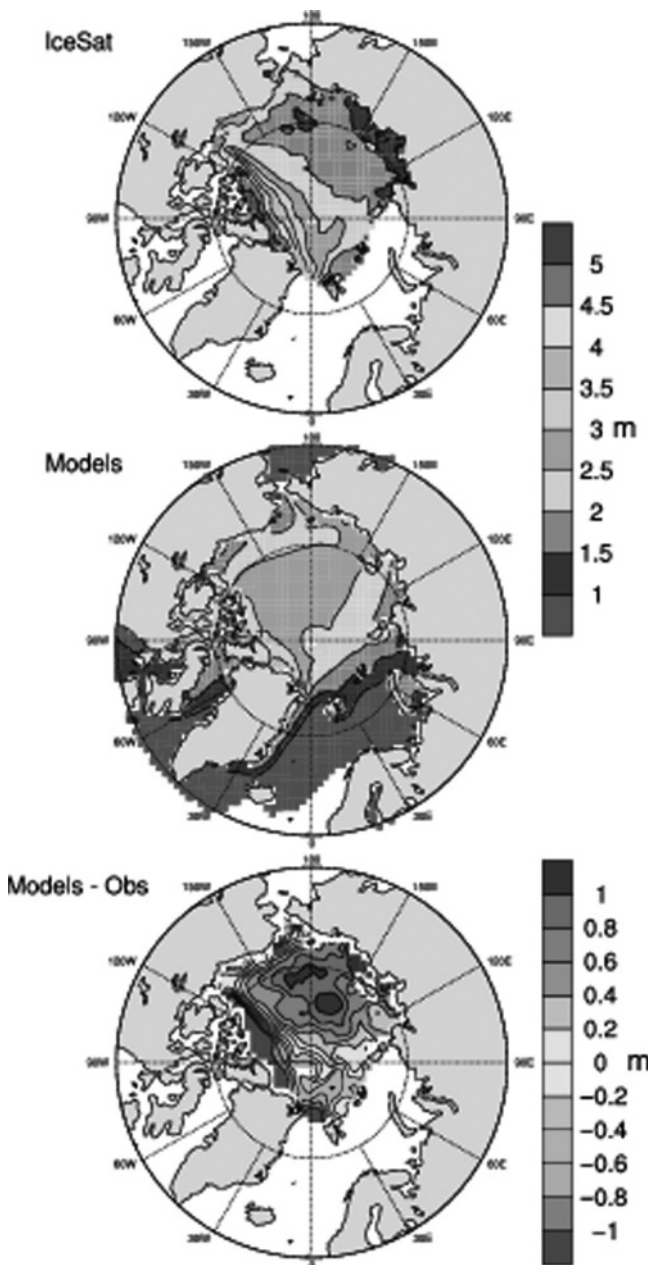


Figure 9.14. Fields of mean September sea ice thickness based on observations from IceSat, the average of all CMIP5 models over the period of ICESat observations and the difference between the modeled and observed values (courtesy of A.P. Barrett, NSIDC, Boulder, CO). (See plate section for color version.)

models is too thin north of the Canadian Arctic Archipelago and Greenland, and too thick elsewhere.

Similarly, as shown by Slater and Lawrence (2012), there are large differences between different CMIP5 models in their depiction of both the present-day

distribution of near-surface Northern Hemisphere permafrost and projected changes through the twenty-first century, even with the same RCP scenario. In their study, near-surface permafrost is taken to be present if the soil at 3.5 m has a temperature of 0°C or less for the present and prior year. The scatter between models reflect both differences in simulated surface climates (e.g., air temperature and surface radiation fluxes) as well as the ability of the land surface models to properly represent permafrost physics. There is a large range in complexity in the land surface models, with soil column depths ranging from 3–47 m, with between three and twenty-three soil layers. Horizontal resolutions in the models are also quite variable. Within these limitations, the models indicate that by the year 2100, for RCP 4.5, near-surface permafrost will retreat from the present day discontinuous permafrost zone, while for RCP 8.5 it may only be found in the Canadian Arctic Archipelago, the Russian Arctic coast, and east Siberian uplands.

As has been addressed in several places in this textbook, recent decades have seen a stronger rise in surface and lower tropospheric air temperatures over the Arctic compared to the globe as a whole, most notable in autumn and winter, a process termed Arctic amplification (Figure 1.5). As introduced in Chapter 2, this outsized warming appears to involve a suite of processes, including reductions in sea ice extent, leading to stronger summer heat gain in the ocean mixed layer, with this heat then released back to the atmosphere in autumn and winter, changes in atmospheric circulation leading to increased atmospheric heat flux convergence, changes in cloud cover and water vapor, and increased concentrations of black carbon aerosols and soot on snow. Arctic amplification is in turn a near universal feature of global climate model projections for the twenty-first century that include rising concentrations of atmospheric carbon dioxide (Holland and Bitz, 2003; Serreze and Barry, 2011). On the basis of averaging all of the CMIP3 simulations with the A1B emissions scenario, by the last two decades of the twenty-first century, surface air temperatures over the Arctic during winter are expected to be 5°C or more above those for the 1980–1999 period, with the largest warming over the Arctic Ocean, in considerable part because of having less sea ice (Figure 9.15). Arctic amplification is by contrast not a prominent feature of summer. However, a closer look at the data again reveals large differences between different models; some show a particularly strong cold-season Arctic amplification, whereas others show it to be weaker.

Figure 9.15 also shows projected changes in precipitation and in sea level pressure across the globe relative to 1980–1999. The pattern of projected precipitation changes is complex and manifests the increased moisture-holding capacity of the warmer atmosphere along with changes in atmospheric circulation. In areas in which there are efficient precipitation-generating mechanisms, precipitation is expected to increase. This includes regions near the equator where there is strong convection, and in middle and Arctic latitudes where ascent and cooling of poleward-moving airmasses linked to extratropical cyclone activity allows water vapor to condense. Increased Arctic precipitation may also result from sea ice loss because the open water provides a regional moisture source. The expected increase in evapotranspiration in the Arctic is more than compensated by the increase in

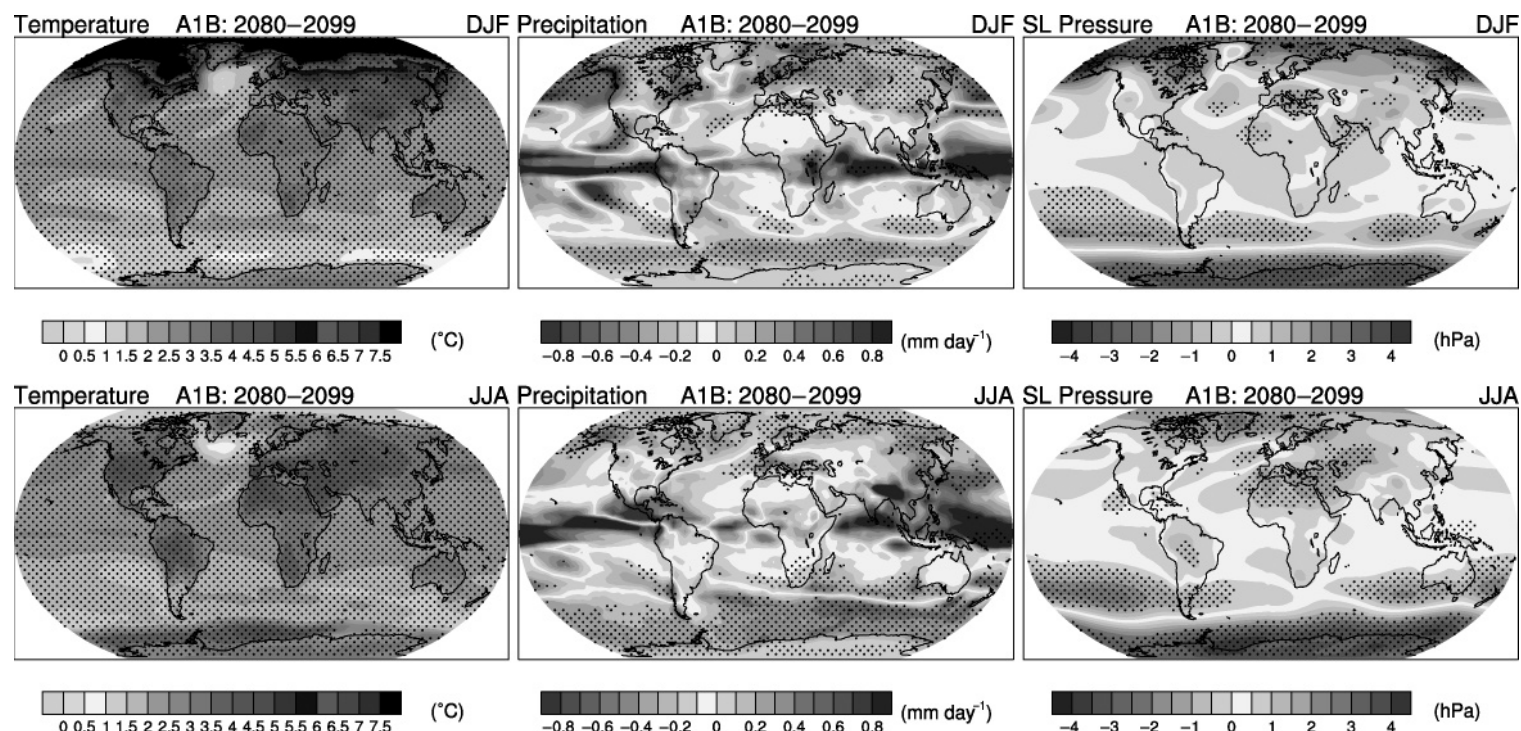


Figure 9.15. Projected changes for winter (DJF) and summer (JJA) of surface temperature, precipitation, and sea-level (SL) pressure for 2080–2099, relative to 1980–1999, based on the CMIP3 models using the A1B emissions scenario (by permission of the IPCC). (See plate section for color version.)

precipitation, leading to an increase in river discharge to the Arctic Ocean. Sea-level pressure is expected to fall in the high latitudes, with compensating increases in parts of the middle latitudes and subtropics, where precipitation amounts are expected to decline. This follows because high pressures at the surface tend to be accompanied by descending air motion unfavorable to condensation. Again, however, projections between different models vary greatly. Changes in precipitation are particularly uncertain.

9.6 Regional Climate Models

There are many regional climate models in existence. Models of the 1990s to early 2000s vintage were evaluated through the Arctic Regional Climate Model Comparison Project (ARCMIP), a coordinated set of simulations of the present-day Arctic climate, focusing on the SHEBA year (October 1997–October 1998). This year was chosen because of the availability of high quality data from the field camp in the Beaufort and Chukchi seas, aircraft observations, as well as data from the Barrow Arctic Radiation Monitoring site and remote sensing. Use was also made of observations from the Mackenzie GEWEX study. At least seven modeling groups participated. Like other MIPs, the simulations employed common initial and boundary conditions for each model. Rinke et al. (2005) summarize performance biases of the ARCMIP models for geopotential height, 2-m temperature, cloud cover, and surface radiation fluxes. Results indicate that the model composite mean biases are on the order of differences between different observations or data analyses. Echoing the GCM comparisons, there is considerable scatter between the simulations for individual models.

Regional climate models in wide use include:

Regional Atmospheric Climate Model (RACMO): RACMO was developed by the Royal Netherlands Meteorological Institute. It has a number of variations and is constantly being improved. The Institute for Marine and Atmospheric Research Utrecht integrated a multilayer snow routine into RACMO that treats snow grain size growth, vertical heat conduction, firn densification, the percolation and refreezing of meltwater, meltwater runoff, snow transport, and other processes, coupled to the atmospheric part of RACMO. It has been widely used in studies of the surface mass balance of the Greenland and Antarctic ice sheets (e.g., Ettema et al., 2009; van den Berg et al., 2011).

Weather Research and Forecasting (WRF) model: WRF was developed to be a next-generation regional model that could be used for both research and operational weather forecasting. In part, WRF was intended as a replacement for the fifth-generation Pennsylvania State University National Center for Atmospheric Research, known as MM5. The WRF was originally developed for mid-latitude applications, but – in modified form – it has been widely used in polar studies. In the Arctic, WRF is the atmospheric component of the Regional Arctic Climate Model

(Cassano, Higgins, and Seefeldt, 2011) and the Arctic System Reanalysis (ASR) (Bromwich et al., 2010), which will be described later.

HIRHAM: In its different versions, HIRHAM has been applied variously to the Arctic, the Antarctic and mid-latitudes. For example, Box and Rinke (2003) used HIRHAM to examine the Greenland Ice Sheet surface climate. HIRHAM draws from both HIRLAM (High Resolution Limited Area Model – designed for short-range weather forecasting) and ECHAM, a constantly evolving CGM developed by the Max Plank Institute for Meteorology. The acronym HIRHAM comes from a combination of HIRLAM and ECHAM4.

A good example of a regional model application to sea ice processes is that of Lynch, Maslanik, and Wu (2001a), who used the Arctic Regional Climate System Model (ARCSyM) to simulate the extremely low ice sea extent and concentration observed over the western Arctic in the summer of 1990. Development of the open-water feature was examined as a case study in Chapter 7 from an observational viewpoint. ARCSyM (Lynch et al., 1995), which has been retired, includes a dynamic-thermodynamic sea ice model. In various simulations, the required driving fields at the model boundaries have been provided from the NCEP/NCAR reanalysis and ECMWF operational analyses.

Lynch et al. (2001a) conducted a control experiment, followed by several sensitivity experiments. The model was initialized on April 15, 1990, and integrated over a six-month period. Sea ice was initialized to an ice area defined by SSM/I data, with thickness initialized from output of a ten-year simulation using a different stand-alone sea ice model. ARCSyM was forced at the lateral boundaries with ECMWF operations analyses. The control run simulation reproduced the observed ice anomaly quite well, along with the major aspects of strong cyclone activity, early opening of leads and polynyas along the Eurasian coast and enhanced ice melt that were important to its development (see Chapter 7). Sensitivity experiments **a** through **e** used the same configuration as for the control run, except that:

- (a) The model was initialized with a uniform 2.0 m ice thickness (PRECON)
- (b) The ice dynamics subroutine was turned off (NODYN)
- (c) The surface albedo for all grid points was fixed to the initial sea ice albedo (NOIALB)
- (d) The latent heat flux from leads and open water was set to the ice latent heat flux from ice (NOLHF)
- (e) Ice area was constrained to a non-anomalous ice area from May through July (NOANOM)

Results from these simulations appear in Figure 9.16 as ice concentrations averaged for September 1990. They are quite instructive in showing the power of the model sensitivity experiments in isolating the key mechanisms of ice loss.

Ice concentrations from the NOLHF are quite similar to those from the control run. This indicates that removing the extra source of moisture represented by open water has little effect. Given that the ice anomaly pattern from NOLHF is very

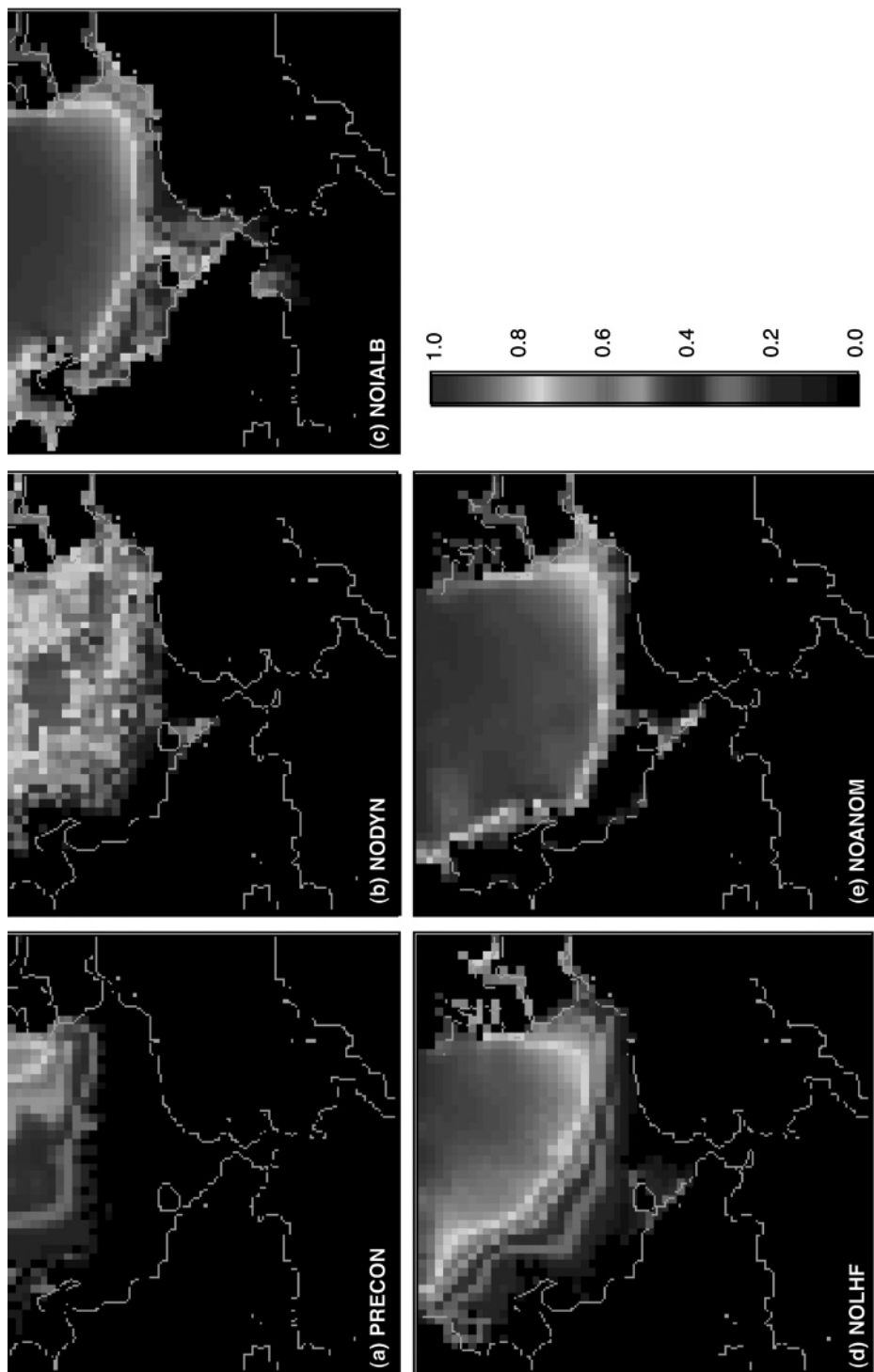


Figure 9.16. Average September ice concentration (percent) from five sensitivity experiments using the ARCSyM model addressing development of the 1990 sea ice anomaly (from Lynch et al., 2001a, by permission of AGU). (See plate section for color version.)

similar to that of the control run (not shown), it can be compared with anomaly patterns from the other experiments. Results from the PRECON experiment point out the importance of specifying the initial ice thickness. In the control experiment, ice is much thicker than 2 m over most of the domain. Starting with an overly thin ice cover in the PRCN experiment leads to an unrealistically large ice loss. The reason is that less total energy is needed to completely melt the thin ice. When the ice dynamics are turned off (NODYN) we see the role of ice motion in the development of the feature. With no dynamics to move the ice offshore, the spatial pattern of observed ice loss cannot be reproduced.

Removing the ice albedo feedback (NOIALB) gives a September ice field that is more extensive and more compact, owing to reduced summer melt. This is in accord with observations, which suggest the importance of unusually early melt and consequent albedo reductions in the development of the ice anomaly. Without the early opening of coastal leads and polynyas seen in the observations (the NOANOM experiment), a smaller ice anomaly is generated, and the ice edge is more compact than for the control experiment.

A good example of an ice sheet application is the study by Ettema et al. (2009), who used RACMO (version RACMO2/GR) to study the surface mass balance of the Greenland Ice Sheet for the 1957–2007 period. The model was run at an 11 km resolution for a domain covering the Greenland Ice Sheet and adjacent seas. For their application, RACMO2 was coupled to a physical snow model. The atmospheric part of the model was forced at the lateral boundaries and the sea surface by ECMWF data. Looking at the ice sheet as a whole, subtracting total modeled mass loss as averaged over the 1958–2007 period represented by runoff (248 Gt yr^{-1}) and evaporation/sublimation (26 Gt yr^{-1}) from total mass gain averaged over the same period from snowfall (697 Gt yr^{-1}) and rainfall (46 Gt yr^{-1}) yields an average positive net surface mass balance for the ice sheet of $469 \pm 41 \text{ Gt yr}^{-1}$. The surface mass balance trend over the 1958–2007 period is positive over the interior and negative along coastal regions (Figure 9.17). Their results suggest that considerably more mass accumulates on the Greenland Ice Sheet than previously thought, adjusting earlier estimates upward by as much as 63 percent. It is stressed that surface mass balance does not include mass loss by iceberg calving. Iceberg calving is a major source of mass loss. As had been discussed in Chapter 8, the total mass balance for the Greenland Ice Sheet is at present decidedly negative.

9.7 Numerical Weather Prediction Models

Almost any study of observed variability of the Arctic atmospheric circulation makes use of output from NWP models. From the preceding discussion, NWP output is also commonly used as lateral forcing for regional climate models or to provide wind forcing for sea ice and coupled ice-ocean models. Output from GCMs is also commonly verified against output from NWP models. We hence tend to think of NWP output as “truth.” The assumption, however, is incorrect. It is better to think

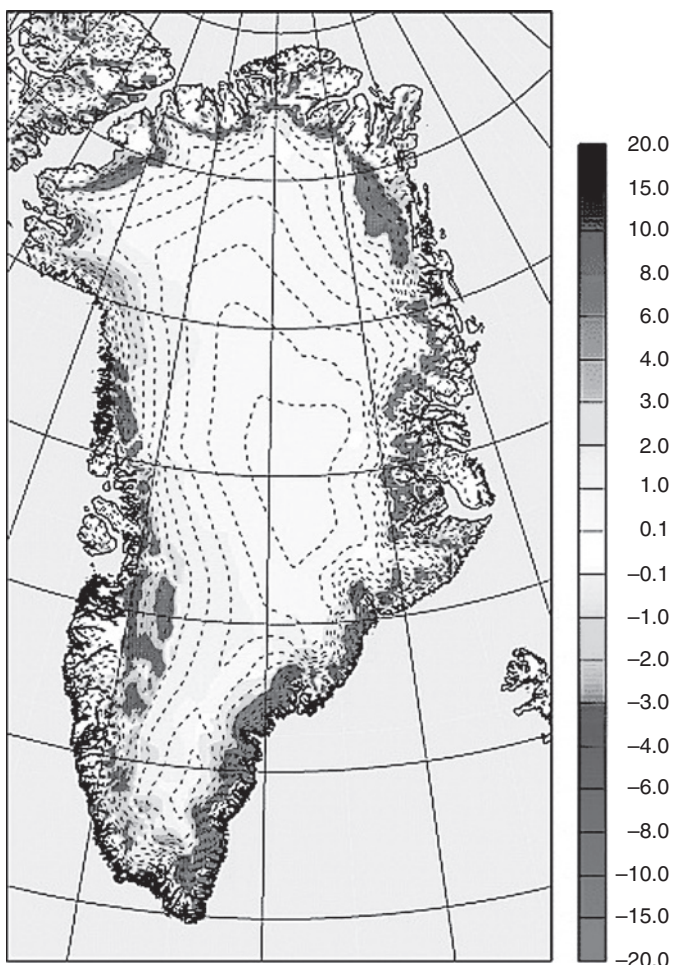


Figure 9.17. Modeled surface mass balance trend (1958–2007) in kg m^{-2} based on a simulation with RACMO2/GR. Thin dashed lines are 250 m elevation contours (from Ettema et al., 2009, by permission of AGU). (See plate section for color version.)

of NWP models as an optimal blend of observations and an AGCM or regional atmospheric model.

In climate simulations, such as for hindcasts or for greenhouse-gas experiments, specification of the initial boundary conditions (e.g., of SST, sea ice distribution, land surface cover, greenhouse gas concentrations) is much more important than the specification of the initial atmospheric state (i.e., the three-dimensional distribution of temperature, winds, and humidity at the start of the model simulation). However, because of the complex and chaotic nature of the atmosphere, predicting the weather at a given time and place depends critically on specification of the initial atmospheric state.

NWP starts with an initial atmospheric state to get a short term (e.g., typically six hours) forecast of the future atmospheric state as well as of various surface

fluxes and variables (e.g., precipitation, evaporation, radiation and SAT). The forecasted atmospheric state will differ from the true atmospheric state because of the inability to perfectly specify the initial atmospheric conditions, as well as shortcomings in the model physics, resolution, and parameterizations. In NWP, there is an ongoing process of restoring the model back toward the true atmospheric state through assimilation of observations. In this process, the forecasts, adjusted by data assimilation (the blended fields generally termed “analyses”), represent the new initial state to generate the next forecast (similar techniques are being applied to sea ice models, see Section 9.4). Assimilation data for NWP models are primarily tropospheric observations of temperatures, pressure height, winds, and humidity obtained from radiosonde profiles and satellite retrievals. Surface variables such as precipitation, evaporation, radiation fluxes, and SAT are typically not assimilated and are simply model forecasts. Surface conditions, such as sea ice cover, sea surface temperatures, snow cover, and vegetation cover are generally prescribed from observations.

Analyses and forecasts from operational numerical weather predictions systems are not ideal for climate studies (e.g., to study year-to-year variability in precipitation or temperature). The reason is that operational systems are constantly being refined so as to get better forecasts. As a result, if one were to look at a time series of outputs from an operational NWP system, one would encounter pseudo-climate signals (jumps) attributed to the frequent changes in these systems. Atmospheric reanalyses are special forms of NWP that are intended to get around this problem by using unchanging (static) versions of the atmospheric model and assimilation system.

The first reanalysis attempted was the NCEP/NCAR effort (Kalnay et al., 1996; Kistler et al., 2001). A number of the figures in this book are based on NCEP/NCAR data. The NCEP/NCAR reanalysis has involved recovery and assembly of numerous atmospheric data sets, which are quality-controlled and then assimilated with the static assimilation and forecast system. It is fair to say that the NCEP/NCAR reanalysis revolutionized climate research. The NCEP/NCAR reanalysis effort is still ongoing, and now provides more than fifty years (continually updated) of global atmospheric analyses and surface fields.

Although a number of more modern reanalyses are now in existence, based on better models and data assimilation approaches, they have all built on lessons learned from the NCEP/NCAR effort. One important lesson is that even with a static model and assimilation system, pseudo-climate signals will still be present owing to changes in the amount and quality of assimilation data. Users of reanalysis data must always be aware of this problem, especially for time series and trend analyses. Prior to 1958, the frequency of radiosonde reports in the Arctic is very low. Radiosonde coverage increased after 1958, and again in the early 1970s. Satellite data (temperature and humidity information) began to be incorporated in the 1970s. Starting in 1979, drifting buoy data from the IABP began to provide regular reports of surface pressure over the Arctic Ocean, helping to constrain the field of atmospheric mass.

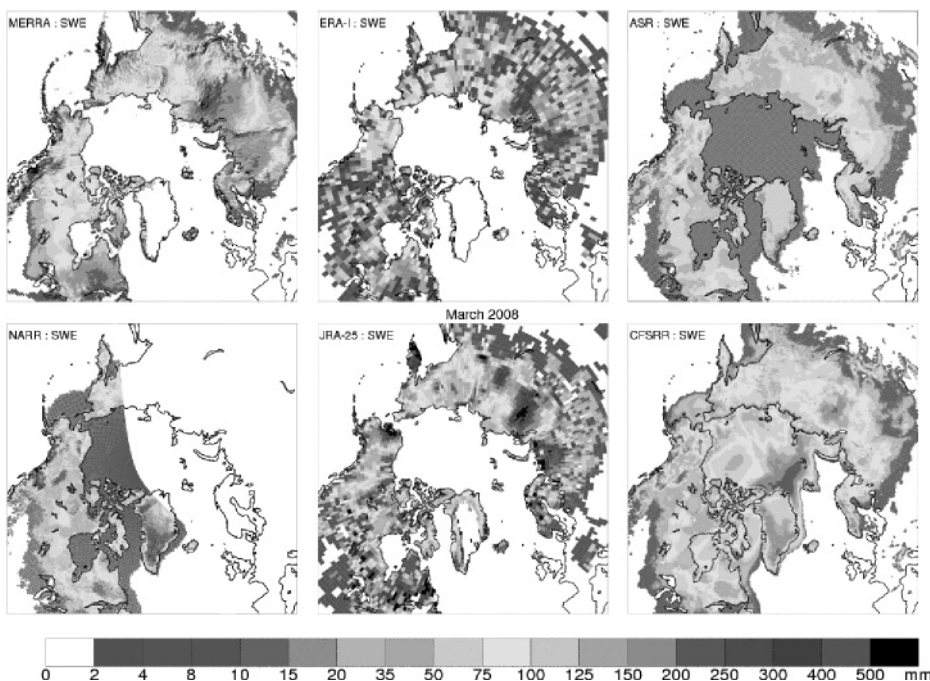


Figure 9.18. Mean snow water equivalent (mm) for March from six atmospheric reanalysis: MERRA, ERA-I, ASR, NARR (the North American Regional Reanalysis), JRA-25 (the Japanese twenty-five-year reanalysis), and CFSR (courtesy of D. Slater, NSIDC, Boulder, CO). (See plate section for color version.)

Examples of modern atmospheric reanalyses include:

Modern Era Retrospective-Analysis for Research and Applications (MERRA):

This reanalysis was developed by the National Aeronautics and Space Administration (NASA) for the satellite era (1979 onward) (Rienecker et al., 2011). MERRA uses the Goddard Earth Observing System Data Assimilation System Version 5. The analysis is performed at a horizontal resolution of 2/3 degree longitude by 1/2 degree latitude at seventy-two vertical levels. Surface data, near surface meteorology, selected upper-air fields and vertically integrated fluxes and budgets are produced at one hour intervals.

NOAA Climate Forecast System Reanalysis (CFSR):

The CFSR (Saha et al., 2010) also extends from 1979 onward. The global atmosphere resolution is about 38 km with sixty-four levels in the vertical. The atmospheric model includes observed variations in carbon dioxide along with changes in aerosols and other trace gases and solar variations. Oceanic and land surface output products are available at a horizontal resolution of 0.33° latitude $\times 0.33^\circ$ longitude and on an hourly basis.

ERA-Interim:

This is an effort by ECMWF to prepare for their next general reanalysis that will replace the discontinued ERA-40 system (Dee et al., 2011). ERA-Interim data are also available from 1979 onward. Compared to ERA-

40, ERA-Interim has increased the number of pressure levels from twenty-three to twenty-seven; uses improved model physics, new humidity analysis, more extensive use of satellite radiances, and improved fast radiative transfer model; and includes additional cloud parameters. Data are available at 0.75° resolution.

Arctic System Reanalysis (ASR): The ASR is intended to provide a high resolution in space (10 km) and time (3 h) data assimilation of the Arctic's atmosphere/sea ice/land system by assimilating observations into Polar WRF. As of this writing, ASR data are available for the years 2000–2010 at a 30 km resolution (Bromwich et al., 2010).

Analyzed fields (fields directly affected by assimilated data), such as 500 hPa height, tend to be depicted quite similarly between different reanalyses. However, because of various factors (including model physics, assimilation approaches, and resolution), forecast surface fields – such as precipitation, evaporation, and radiation fluxes – can be quite different. This is abundantly clear in Figure 9.18, which shows average March snow water equivalent for the north polar region from six atmospheric reanalyses. Consequently, it is now common practice in climate studies to look at output from several reanalyses to establish a range of estimates.

9.8 Ecosystem Models

Terrestrial ecosystems in the Arctic and boreal forest regions are expected to be highly sensitive to climate change and may play a strong role in biospheric feedbacks to global climate (Kittel, Steffen, and Chapin, 2000). This sensitivity arises from complex interactions between ecosystem structure and function, soil and permafrost processes, and regional climate. Biophysical and biogeochemical dynamics of these landscapes in turn impact the global climate system through control over surface-atmosphere exchanges of energy and greenhouse gases. Arctic and boreal ecosystems are characterized by large carbon stocks. Tundra ecosystems contain a significant fraction of the world's soil carbon that might react to near-term climate change. There is strong evidence that recent warming in the Arctic has affected both the structure and function of Arctic ecosystems. Functional responses include changes in the biogeochemical cycling of carbon, nutrients, and water in ecosystems, whereas structural responses represent changes in the species composition across a landscape that may further modify the function of ecosystems (Clein et al., 2000). The observed greening of the Arctic tundra is an example of the latter.

The issues are complex. For example, the analysis of A. Betts (2000) indicates that a change from tundra to boreal forest could increase carbon uptake by trees and help mitigate the warming effects of atmospheric greenhouse gas loading. However, such changes could be offset by the lower albedo of boreal forest as compared to tundra. A substantial amount of carbon and nitrogen from the tundra could be released in inorganic forms. As these soils warm, decomposition rates increase and the growing season lengthens. A large release of carbon dioxide from these soils

could enhance the rate and magnitude of climate warming. On the other hand, a large release of inorganic nitrogen could also result in increased Net Primary Production (NPP), which could buffer carbon loss from the soil or cause Arctic ecosystems to act as a net sink for carbon dioxide (Clein et al., 2000).

NPP is Gross Primary Productivity (GPP) minus plant autotrophic respiration, with a positive NPP representing net plant growth. GPP is the photosynthetic uptake of carbon dioxide by plants and autotrophic respiration is the release of carbon dioxide by plants as they convert simple sugars, the raw products of photosynthesis, into more complex organic matter, such as leaves, roots, and wood. This contrasts with heterotrophic respiration (HR), which is the release of carbon dioxide by animals, microbes, and other organisms that (like the authors of this text book) consume organic matter rather than producing it themselves. Net Ecosystem Production (NEP) is NPP minus HR and represents the net carbon balance of the ecosystem, with a positive NEP representing a net uptake of carbon by the biosphere. Net Ecosystem Exchange (NEE) is HR plus fire and other non-biological carbon dioxide emissions minus NPP, with a positive NEE representing a net release of carbon into the atmosphere. Ignoring fire and other emissions, NEE equals – NEP (see the book by Chapin, Matson, and Mooney, 2000).

It should come as no surprise that modeling Arctic ecosystems and ecosystem change is a vibrant research area. Ecosystem models vary widely in how they represent physical and biological processes and their intended application. Some models focus on agriculture ecosystems and crop yield, others on forest dynamics and timber stocks, and still others estimate surface energy and mass fluxes in fully coupled models of land-ocean-atmosphere dynamics (Earth System Models). Biogeochemistry models represent ecosystem dynamics as the exchange of carbon and nutrients between various “pools,” such as wood, litter, and soil pools. In addition to biogeochemistry, dynamic vegetation models also include competition between plant species to allow simulated grasslands to evolve into forests and back again as climate changes. Ground temperature, water availability, and other aspects of the physical environment strongly influence ecosystem dynamics and many models include representations of soil thermodynamics, surface and soil hydrology, and snow pack development. These models can now simulate how changing climate influences ecosystem dynamics, and how changing ecosystem dynamics influence climate on time scales of minutes to centuries.

These models must address important issues and challenges in the Arctic, such as “woody encroachment” and the northward advance of the tree line into tundra regions driven by higher temperatures and longer growing seasons. Another challenge is how warming will affect wetlands and lakes and the resulting changes in carbon dioxide and methane fluxes. Permafrost or perennially frozen ground underlying much of the tundra in the Arctic is impermeable to water, resulting in innumerable lakes and wetlands. Warming will thaw some portion of the permafrost, changing the number and distribution of lakes in the Arctic. The decay of organic matter in these lakes and wetlands is often anaerobic, producing methane rather than carbon dioxide fluxes to the atmosphere. Because methane is twenty-three

times more effective than carbon dioxide in trapping heat near the surface of the earth, any change in the number and distribution of lakes will affect methane emissions, and thus potentially global climate.

One model used in a number of Arctic studies is the Terrestrial Ecosystem Model (TEM), an ecosystem model that uses biogeochemistry to describe carbon and nitrogen dynamics of plants and soils. It uses spatially referenced information on climate, elevation, soils, vegetation, and water availability as well as soil- and vegetation-specific parameters to estimate monthly fluxes of carbon and nitrogen and pool sizes at high resolution (0.5 degrees latitude/longitude). TEM has greatly evolved through the years to include soil thermodynamic and hydrologic processes. A fairly recent Arctic application is that of Yi et al. (2009), who used TEM to simulate the dynamics of evapotranspiration, soil temperature, active layer depth, soil moisture, and water table depth over the Alaska tundra in response to both climate variability and fire disturbance.

D. McGuire and his colleagues (2010) used TEM as part of a model-based study of the carbon balance for the Arctic as a whole over the 1997–2006 period. They considered a linked framework of carbon dioxide and methane exchange across the Arctic land, ocean, and atmosphere. The study was driven by recognition that the Arctic carbon balance may be influenced by the strong warming being observed there. They concluded that, over the 1997–2007 period, the terrestrial areas of the Arctic were a source of carbon to both the atmosphere and to the ocean (via dissolved carbon in runoff), while – at the same time – the ocean sequestered carbon from both the land and atmosphere, with the ocean sink exceeding the land source by about 30 Tg per year. When exchanges were broken down into carbon dioxide and methane, a more complex picture emerged. Although both the land and ocean were sinks of carbon dioxide, the land sink diminished over the study period because of increased fire disturbance while the ocean sink strengthened because of a stronger phytoplankton uptake linked to diminished sea ice extent. In turn, terrestrial areas were a growing source of methane to the atmosphere. They concluded that the radiative effects of the methane emissions exceeded the radiative effects of the carbon dioxide sink, so that the Arctic was a source of greenhouse gas forcing to the climate system. The key questions from their study are whether carbon dioxide emissions attributed to increased fire frequency will overwhelm the increased ocean uptake as sea ice extent continues to decline, and whether enhanced GPP because of rising atmospheric carbon dioxide will compensate for enhanced climate forcing linked to the methane emissions.

An issue of growing interest is the potential for a permafrost carbon feedback (PCF) on climate. Permafrost regions of the Northern Hemisphere contain about 1,700 Gt of carbon as organic matter, roughly double the amount of carbon in the atmosphere and nearly all of it frozen in the permafrost (Tarnocai et al., 2009). As temperature continue to rise in the Arctic, some of this organic matter will thaw and begin to decay, releasing carbon dioxide and methane into the atmosphere, accelerating climate warming and promoting further permafrost thaw. K. Schaefer et al. (2011) examined the PCF using the Simple Biosphere/Carnegie-Ames-Stanford Approach (SiBCASA) model in simulations of the terrestrial carbon cycle from 1973 to 2200 for regions of continuous and discontinuous permafrost north of 45°N.

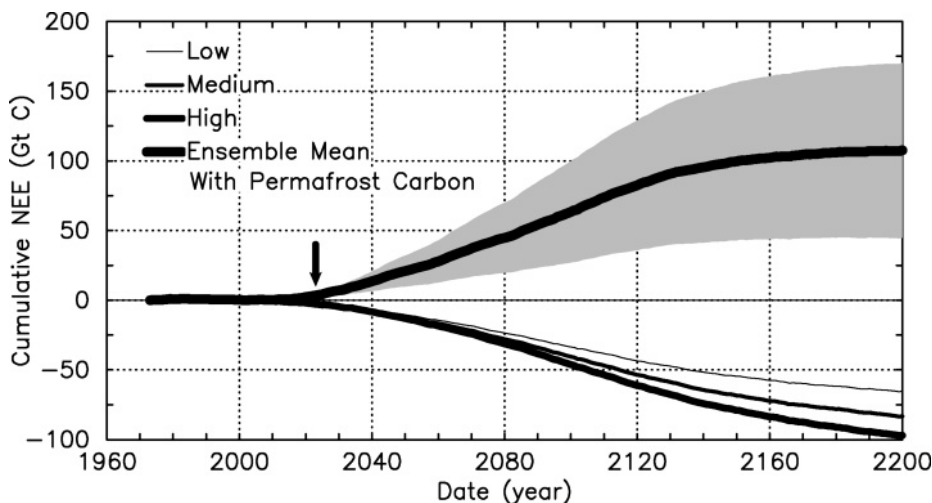


Figure 9.19. Cumulative Net Ecosystem Exchange (NEE) for low, medium, and high warming rates without permafrost carbon and the ensemble mean cumulative NEE with permafrost carbon flux. The grey bar represents uncertainty and the arrow marks the time at which the permafrost carbon flux becomes positive (adapted from Chaefer et al., 2011).

SiB CASA includes biogeochemistry and sophisticated representations of soil thermodynamics, soil hydrology, and snow pack dynamics designed to simulate permafrost dynamics. Details of the model and the experimental design are fully described by Schaefer et al. (2011).

Key results from the study are summarized in Figure 9.19, which shows cumulative NEE summed for the years 1900 through 2200, with a negative NEE representing a net cumulative carbon uptake by the land. Without a PCF (the three lines at the bottom representing low, medium, and high warming rates), the cumulative NEE starts at zero and turns negative, indicating enhanced plant growth in permafrost regions driven by longer growing seasons, higher temperatures, and increased atmospheric carbon dioxide concentrations. In contrast, as shown in the upper line, accounting for the PCF changes the permafrost regions from a net carbon sink to a source relative to the atmosphere. The line shows the ensemble mean of the simulations with the grey shaded area indicating the uncertainty. Their best estimate of PCF strength indicates a cumulative flux of 190 ± 64 Gt of permafrost carbon to the atmosphere by the year 2200, equivalent to an increase in atmospheric carbon dioxide concentration of 87 ± 29 ppm. The subsequent study by A. MacDougall, C. Avis, and A. Weaver (2012), using the University of Victoria Earth System Climate Model (ESCM), comes to broadly similar conclusions.

9.9 Summary of Model Errors

As is evident from preceding discussion, models are prone to errors from a variety of sources. A major thrust of the various MIPs is to examine such errors with the

aim of developing better models. Of special relevance to regional climate models, GCMs, and LSMs (with or without coupling to an atmospheric model) is suboptimal parameterization. For simulations of the Arctic region, the parameterization of snow and sea ice albedo stands out. From Chapter 5, we know that the factors controlling snow and sea ice albedo are quite complex. The level of detail at which albedo is treated can impact strongly on simulated snow and ice mass, the surface energy balance, and hence the strength of ice-albedo feedbacks. For atmospheric models, another problem with first-order impacts on the surface energy budget is the simulation of Arctic cloud cover. Especially for global climate models, the relatively coarse representations of topography, sea ice margins, and coasts can have strong expressions on the simulated atmospheric circulation, such as in the placement of storm tracks. Global and regional models, including coupled ice-ocean models, also vary widely in their treatment of the ocean, which, among other things, will impact sea ice growth and melt. In turn, different assumptions regarding ice interaction may lead to different realizations of ice circulation and ice thickness distributions. Turning back to the land surface, projected future changes in the Arctic's terrestrial carbon budget are dependent on assumptions regarding the function and structure of Arctic ecosystems.

Many of the model types reviewed in this chapter require specified driving fields (e.g., "stand alone" LSMs and sea ice models, active layer thickness models, and regional climate models). The quality of the model output will depend in part on the quality of these driving fields. Some simulations rely on sparse station data or remotely sensed fields (e.g., snow water equivalent) of uncertain quality. However, for many simulations, the driving fields represent output from another model, in particular, from NWP. Outputs from NWP models have their own sources of error, variously from difficulties in specifying the initial atmospheric state to biases in surface fields related to suboptimal parameterization of albedo, evaporation, and convective precipitation. In conclusion, while modeling is one of the most important tools for understanding the Arctic climate system, model output must always be viewed with appropriate caveats.

Focus Questions and Exercises

- 1) A common shortcoming of global climate models is that they cannot properly simulate the observed distribution and radiative properties of Arctic cloud cover. Why should this problem concern us?
- 2) It has sometimes been argued that it is more productive to examine spatio-temporal variability in Arctic precipitation using output from an atmospheric reanalysis like MERRA than using data from the available gauge network. Do you agree or disagree with this argument? Why?
- 3) Even the best land surface model in the world can produce large biases in simulated snow depth, evaporation, latent and sensible heat fluxes, and other variables. Why is this so?

Arctic Paleoclimates

Overview

Global and Arctic climates have varied widely in the past. On time scales of tens to hundreds of millions of years, these changes were at least partly a result of the shifting configurations of land and ocean and mountain-building events associated with continental drift. Even though it appears that the earth has experienced ice ages in many periods of its history, including the Neoproterozoic, 710 and 640 million years before present (hereafter abbreviated as Ma), the Ordovician and Silurian (460 to 430 Ma), and the Carboniferous and Permian (350 to 250 Ma), we know few details about these events. Much more is known of global and Arctic climates during the Quaternary. The Quaternary, comprised of the Pleistocene and Holocene epochs, extends from about 2.6 million years ago to the present.

The Ice Ages of the Pleistocene captivate the imagination. The Pleistocene was characterized by many glacial advances and retreats. Although the climate of the Arctic varied with these glacial cycles, which seem to have been triggered by periodicities in the earth's axial tilt, the eccentricity of its orbit about the sun and the precession of the equinoxes, collectively known as Milankovitch cycles, high-latitude processes, such as ice-albedo feedbacks and deepwater formation in the northern North Atlantic, likely contributed to change. The most complete information on the Pleistocene is for the last glacial cycle, extending from the Holocene back to the Eemian Interglacial, (130,000–115,000 years ago; 130–115 ka). Climates during the last glacial cycle were extremely variable, featuring Dansgaard-Oeschger (D-O) cycles, characterized by rapid

warming, typically occurring over a matter of decades, and then gradual cooling over several centuries. D-O cycles can be stratigraphically related to layers of ice-rafterd detritus released from armadas of melting icebergs calved from the ice sheets, the most pronounced of which are termed Heinrich events. These Heinrich events occur in the cold periods immediately preceding D-O warming. Causes of the D-O cycles are still incompletely understood.

The Last Glacial Maximum (LGM) occurred from 18–25 ka (depending on the region and interpretation). Terrestrial ice extent during the LGM is fairly well known. There were immense ice sheets in North America (the Laurentide, second in size only to the Antarctic Ice Sheet and the Innuitian Ice Sheet over the Canadian Arctic islands) and parts of Eurasia. Along with the major Fennoscandian Ice Sheet, ice sheets covered Svalbard, Franz Josef Land, the Barents Sea, Novaya Zemlya, the Kara Sea, Iceland and part of the British Isles. The process of deglaciation after the LGM was very irregular. Of particular note is the Younger Dryas (YD) event from about 12.8 to 11.5 ka, which represented a temporary return to near glacial conditions. Regional climate expressions of the YD were quite varied.

The Holocene epoch (formally defined as the past 11.7 ka) has been generally warm, and although characterized by a more stable climate than the Pleistocene, has still been quite variable. Especially mild conditions during the first part of the Holocene, known as the Holocene Thermal Maximum, were followed by general cooling, during which the sea ice cover expanded and glacier extent increased. The Little Ice Age (LIA) represents the most recent major cooling. Ice core records from Greenland indicate that temperatures there reached their lowest point in the past millennium between AD 1579 and 1730. Causes of the LIA are still debated. Although solar variability appears to have played a role, new evidence points to effects of an extended period of explosive volcanism and attendant climate feedbacks. The LIA has been followed by general warming extending through the present.

10.1 The Distant Past

The present geography of the Arctic is just a brief snapshot in geologic time (Figure 10.1). In 1912, Alfred Wegner proposed that the earth's continents were once part of a single supercontinent that he named Pangea (meaning “all lands”). Modern theory explaining continental drift, termed plate tectonics, was developed during the 1960s. The earth's crust is divided into a number of continental and oceanic plates. Because of convection currents in the mantle arising from heat generated by radioactive decay, the ocean floors are continually moving, sinking at the edges, spreading from the center, and being regenerated. Convection moves the

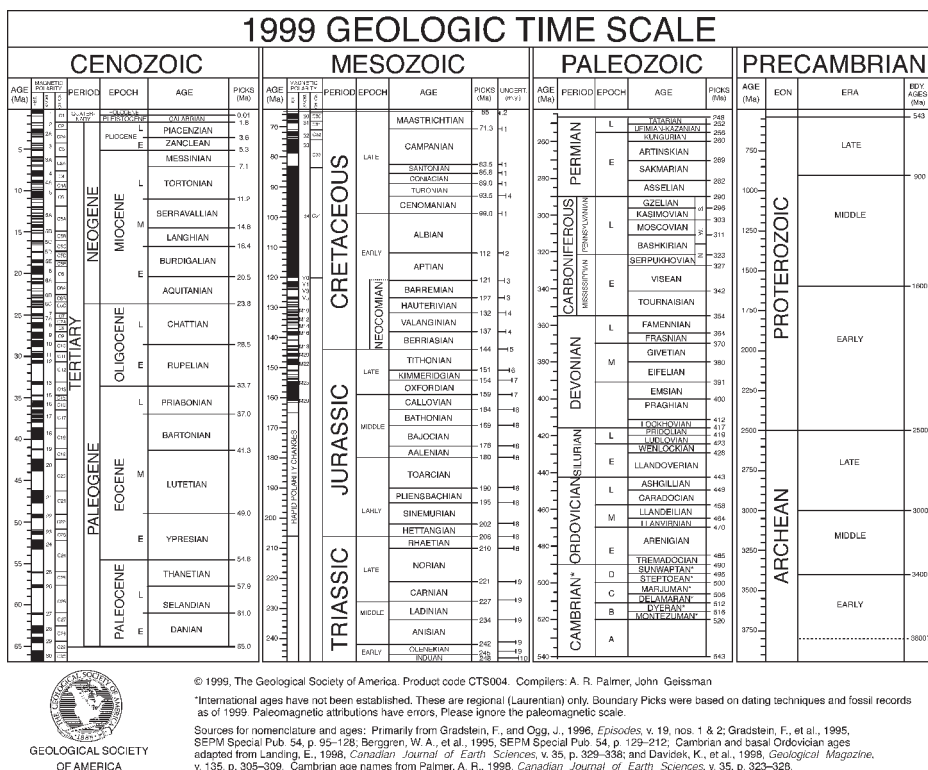


Figure 10.1. The geologic time scale (from the Geological Society of America, product code CTS004, compiled by A.R. Palmer and J. Geissman, by permission of Geological Society of America).

plates in different directions. We now believe that the supercontinent Pangea broke up roughly 200 Ma during the early Jurassic period. Continental drift is of course still occurring, but by about 2 Ma the continents looked largely as they do today.

Just prior to the breakup of Pangea, the present Arctic land masses were located in mid-latitudes. Displacement of the region to north of the Arctic Circle occurred around 100 Ma during the Cretaceous. The Canadian Basin and Makarov Basin seem to have originated during the Cretaceous period. Sea floor spreading increased in the early Tertiary (about 57 Ma) when Greenland separated from Eurasia and the Eurasian and Nordic basins formed (Vogt, 1986). This changing distribution of lands and ocean and mountain-building events (orogenies) had strong impacts on climate. In the Paleocene and Eocene epochs (60–50 Ma), Ellesmere Island seems to have supported many subtropical vertebrate fauna in a swamp-forest environment (McKenna, 1980). Deciduous conifer species grew in west Greenland and Spitsbergen. A deepwater connection to the Nordic Seas via the Fram Strait developed around 35 Ma. This was about the time when temperatures of the global ocean surface and bottom waters began to decrease sharply. Global sea level lowering in the late Miocene (6.5–5.2 Ma) led to isolation of the Arctic Ocean and exposure of the shelf areas (Danilov, 1989). However, a major marine transgression (sea level

rise) followed during the early Pliocene (5–3.5 Ma). Ice-rafterd sediment began to appear in the Nordic Basin at about 4 Ma. The Bering Strait appears to have opened in the Late Miocene and earliest Pliocene, about 5.5 to 4.8 Ma (Marincovich and Gladenkov, 1999).

Progressive cooling during the late Tertiary period is well-documented. Tectonic isolation of the Arctic from the North Atlantic and Pacific occurred during the Pliocene (3.5–3.0 Ma). This promoted cooling and accumulation of land ice in Alaska, Iceland, and Greenland (Harris, 2001). Seasonal freezing of the Arctic Ocean may have begun in the late Pliocene, with a perennial sea cover present by 0.85 Ma (Herman, 1983). The formation of permafrost in the Arctic probably occurred about 1.65 Ma. However, evidence from Fairbanks, Alaska suggests an earlier onset of 2.2–2.5 Ma (Harris, 2001). The time required for ground freezing to the depth observed today, assuming only conductive heat transfer, can be estimated from the long-term geothermal gradient, the paleotemperature history of the upper surface of permafrost, and the soil thermal properties. Calculations by V. Lunardini (1993) for Prudhoe Bay, Alaska, suggest that with a constant surface temperature of -11°C , development of 90 percent of the observed equilibrium thickness of permafrost (600 m) would have been achieved within around 0.5 million years. Alternative temperature histories support more rapid growth. For example, a surface temperature 2.5°C lower would enable permafrost 570 m thick to form in only 120,000 years. Lunardini also calculates that the maximum permafrost thickness of around 1,400 m observed in eastern Siberia (Duchkov and Balobaev, 2001) might have required the complete Quaternary period to form.

10.2 Paleoclimate Records for the Quaternary

10.2.1 Primary Sources

The remainder of this chapter focuses on the Quaternary. As mentioned, the Quaternary started around 2.6 Ma and comprises the Pleistocene (2.6 Ma to 11.7 ka) and Holocene (11.7 ka to present) epochs (Figure 10.1). The Quaternary is recent enough so that many different types of paleoclimate evidence are preserved, especially from the last interglacial onwards.

A wealth of information has been obtained by coring the polar ice sheets, such as from GISP 2, GRIP and Antarctic ice core projects (e.g., the Vostok and EPICA cores). The new North Greenland Eemian Ice Drilling (NEEM) ice core records extend to 130 ka, back to the last interglacial (the Eemian), and Antarctic ice cores extend back much further (430 to 750 ka). Arctic ice cores have also been obtained from smaller ice caps in the Canadian Arctic Archipelago (Devon Island, Ellesmere Island, Baffin Island). Thousands of marine sediment cores have been collected across the world's oceans, many providing records for the complete Quaternary and even longer. Other paleo-environmental information for the Quaternary comes from pollen, diatoms, and plant and animal macrofossils preserved in lake sediments and

peat bogs; loess deposits, tree rings (dendrochronology), speleothems (mineral formations in limestone caves), and geomorphic features such as raised beaches and marine terraces, moraines, and glacial erratics. The Arctic is a rich source of paleoclimate information and some detailed records have come from this area. A remarkable record of Arctic climate extending back 2.8 million years, hence containing the entire Quaternary as well as the late Pliocene, is now available from a core drilled through the bottom sediments of Lake El'gygytgyn in northeastern Russia (Melles et al., 2012). Lake El'gygytgyn is located in a meteorite impact crater that formed 3.58 Ma.

Paleoclimatology is an immense field, and it is beyond the scope of this book to describe in depth the wide variety of climate reconstruction techniques. R. Bradley (1999) provides a comprehensive review. However, we still need to address several issues, such as radiocarbon dating. It is also necessary to come to grips with ice and ocean cores, which provide many of the longest paleoclimate records. Some of our most intriguing insights (as well as questions) regarding past climates have come from these records. It is not only the long time coverage from marine and ice cores that make them so valuable, but also that they are generally continuous and, in the case of ice cores, provide information at high temporal resolution.

10.2.2 ^{14}C Versus Calendar Dates

Although dates in this chapter (as ka or Ma) are cited as estimated calendar years before present (with the present taken as the year 1950), there is still modern literature that reports ages in uncalibrated radiocarbon years (^{14}C years before present). We performed conversions as necessary. Radiocarbon dating is useful back to about 40 ka. Radiocarbon is produced in the upper atmosphere by neutron bombardment of nitrogen atoms. The neutrons are part of the cosmic radiation entering the upper atmosphere. Plants and animals assimilate ^{14}C into their tissues through photosynthesis and respiration, with the ^{14}C content in equilibrium with that of the atmosphere. This equilibrium occurs as there is a constant exchange of new ^{14}C as old cells die and are replaced. When organisms die, exchange and replacement of ^{14}C ends, and the ^{14}C decays to nitrogen as a function of time (radiocarbon has a half-life of 5.73×10^3 years), activating a radioactive "clock." However, for many reasons, including variations in the cosmic ray flux, ^{14}C levels have varied over time. Although ^{14}C age is close to calendar age for the past 2,500 years, before then there is a substantial difference, with ^{14}C underestimating true age (Bradley, 1999). For example, a ^{14}C age of 10 ka corresponds to a calendar age of 11,500 ka; whereas a ^{14}C age of 20 ka corresponds to a calendar age of about 23.9 ka.

10.2.3 Ice Cores

Snow that falls on an ice sheet is compressed by subsequent snowfall, becomes firn, with a density of 550 kg m^{-3} around 10 m depth, and then ice (a density of at least 840 kg m^{-3}), where pore close-off occurs at depths of about 60 m in Greenland.

Seasonality of snow accumulation leads to annual layers of ice that can be identified back to around 40 ka years ago in central Greenland. Researchers drill vertically through the ice to recover cores comprising layer upon layer of “fossil snow.” Among the most valuable records preserved in these cores is the stable isotopic composition of precipitation, both in terms of the concentrations of deuterium (^2H), the naturally occurring heavy isotope of hydrogen, and especially of ^{18}O .

^{18}O is a heavy isotope of oxygen, containing two more neutrons than ^{16}O . During evaporation (which occurs primarily from the oceans which cover most of the planet), water molecules based on the lighter ^{16}O isotope turn to vapor more easily than those based on heavier ^{18}O . Because of this fractionation, the resulting atmospheric water vapor is depleted in ^{18}O compared to the initial water. In equilibrium conditions, atmospheric water vapor contains about 1 percent less ^{18}O than ocean water. When water vapor condenses and precipitation occurs, the heavier H_2^{18}O molecules preferentially fall out, so the precipitation is relatively enriched in ^{18}O compared to the water vapor remaining in the atmosphere. Progressive cooling and condensation, such as when air moves from warm tropical oceans to colder northern lands, results in progressively “lighter” water vapor with less and less ^{18}O . Precipitation will therefore have less and less ^{18}O , as the water vapor becomes increasingly depleted of the heavy isotope. In cold regions, the isotopic composition of precipitation recorded in ice cores is largely a function of condensation temperature; therefore, “fossil snow” frozen in polar ice sheets contains a record of past temperatures. Although other factors are involved, the basic interpretation is that the higher the temperature of condensation, the higher the ^{18}O concentration of glacier ice.

The ^{18}O concentration is measured as the proportion of ^{18}O versus ^{16}O , expressed as $\delta^{18}\text{O}$ values. $\delta^{18}\text{O}$ is the difference in per mil (o/oo) between the observed $^{18}\text{O}/^{16}\text{O}$ ratio in the ice sample and the ratio in a standard sample of ocean water, termed Standard Mean Ocean Water (SMOW). Specifically

$$\delta^{18}\text{O} = \frac{(^{18}\text{O}/^{16}\text{O})_{\text{sample}} - (^{18}\text{O}/^{16}\text{O})_{\text{SMOW}}}{(^{18}\text{O}/^{16}\text{O})_{\text{SMOW}}} \times 10^3 \text{ o / oo} \quad (10.1)$$

The less negative the ratio, the higher the inferred paleotemperature. Values of $\delta^{18}\text{O}$ stored in the GRIP ice core from Summit, Greenland over the last glacial cycle range from about -32 o/oo (relatively warm climates) to -43 o/oo (very cold climates).

Ice cores also yield many other types of information. The thickness of each annual ice layer records past rates of snow accumulation. Impurities in the ice, including wind-blown dust and soluble ions, give information on characteristics of the atmospheric circulation and land surface. The influence of volcanic eruptions is seen in tephra horizons (layers of volcanic ash) and peaks in acidity owing to sulfates. Air bubbles trapped in the ice are samples of past atmospheres, containing information on trace gases, such as concentrations of carbon dioxide and methane (e.g., Petit et al., 1999). Heavy metals in the ice document industrial activity. In recent years, ice cores have recorded radioactive fallout from nuclear bomb tests conducted in the

atmosphere from the mid-1940s through early 1960s and even from the Chernobyl reactor accident. One of the few positive impacts of these testaments to human folly is that the radioactive layers serve as useful stratigraphic markers.

10.2.4 Marine Sediment Cores

Ocean basins accumulate sediments – mixes of continentally derived material and microscopic marine organisms that rain out, or live and die in the sediments and accumulate year after year in layers. Oxygen isotope records are also preserved in ocean cores. These come from the remains of calcareous organisms (planktonic and benthic foraminifera) preserved in sediments.

The oxygen isotopic composition of the bodies of these organisms is determined by two primary factors. The first is the isotopic composition of the ocean water. During the buildup of continental ice sheets, water is transferred via the hydrologic cycle (evaporation, condensation and precipitation) from the oceans to land, where it is stored for long periods as ice. Because the heavier ^{18}O evaporates less readily than ^{16}O , ^{16}O is preferentially removed from the oceans. The oceans hence become enriched in ^{18}O . The isotopic compositions of foraminifera preserved in marine sediments are therefore primary interpreted as records of terrestrial ice volume. The second primary factor influencing foraminifera is the temperature of the water. For every 1°C drop in ocean temperature, there is a relative enrichment in the faunal debris of 0.02 ‰ ^{18}O . A correction for this has to be made so as to infer information about terrestrial ice volume.

Like ice cores, ocean cores contain many different types of information about the past. Different species of planktonic and benthic foraminifera thrive in different types of environmental conditions, so changes in the abundance of different taxa through time record environmental changes in the uppermost and deep ocean, respectively. For example, the relative abundance (as a percentage of all forams present) of left-coiling (sinistral) *N. Pachyderma* (a planktonic foram that lives in cold water) yields information on SST. Ocean cores also yield information from inorganic markers, such as detritus carried and dropped by icebergs.

10.3 Features of the Quaternary

10.3.1 General Timeline

How many major ice advances and retreats occurred over the Quaternary is unclear and there are discrepancies to be resolved between continental and deep-sea chronologies. Ice-rafterd detritus (IRD) in marine sediments dated to around 2.6 Ma marks the initiation of glaciation at sea level in the circum-North Atlantic region (Ehlers and Gibbard, 2003). S. Harris (2001) suggests that four major cold events during the Pliocene and eleven during the Quaternary affected the Cordillera of North America (including those of Alaska and the Yukon). One of the remarkable

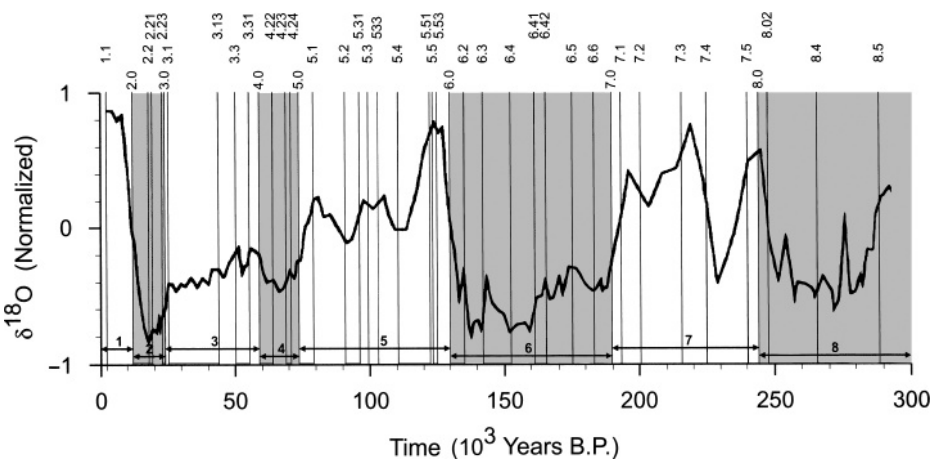


Figure 10.2. The SPECMAP (Spectral Mapping Project) composite chronology for a set of seven stacked (superimposed) $\delta^{18}\text{O}$ records from different ocean basins of the world. Dating involves tuning of the marine isotope records by orbital forcing (from Martinson et al., 1987, by permission of Elsevier).

results from the El'gygytgyn lake core record is evidence for a series of “super interglacials” in the Arctic through the Quaternary, warmer than the Eemian (Melles et al., 2012)

Over the past 400,000 years, which is better known, there have been at least four major global-scale ice advances. During the past 0.9 million years, there were eight ice age cycles with durations of about 100,000 years and these fluctuations appear to have increased in amplitude over the past 430,000 years. Prior to about 0.9 ma, ice age cycles had a 41,000 year duration. The reason for this shift is not understood. The Antarctic ice core from Dome C (EPICA Community Members, 2004) spans eight glacial cycles and clearly shows the increased amplitude of ice volume over the past four cycles. Between 750 and 430 ka, warm intervals were longer (up to 28,000 years duration) but these interglacials had less pronounced warmth than later ones.

The Last Glacial Cycle, which we know most about, started about 124 ka at the peak of the Eemian Interglacial, and extends to the start of the Holocene. The paleoclimate community often refers to history in terms of marine “stages,” based on ^{18}O in benthic foraminifera. Odd-numbered stages correspond to warmer conditions and/or less terrestrial ice, whereas even-numbered stages correspond to colder conditions and/or more terrestrial ice. There are also substages. The Eemian interglacial (Kolfschoten, Gibbard, and Knudsen, 2003; Shackleton et al., 2003) is associated with Marine Isotope Substage 5e (MIS 5e also known as MIS5.5). Figure 10.2 is a composite MIS chronology extending back to 300 ka (in normalized units). In this figure, substages 5a-e correspond to 5.1–5.5. While 5a, 5c and 5e (5.1, 5.3, 5.5) were periods of reduced ice volume and/or higher temperature within stage 5, 5b, and 5d (5.2 and 5.4) were periods of cooler conditions and/or terrestrial ice growth, but on a smaller scale than in stage 4 (Bradley, 1999).

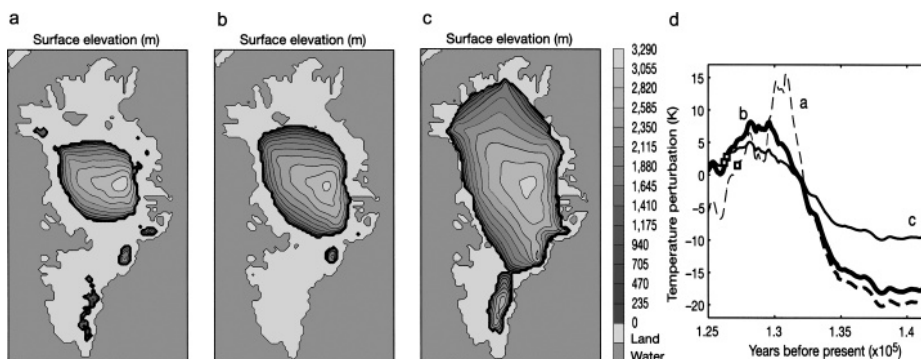


Figure 10.3. Modeled extent and elevation of the Greenland Ice Sheet during the Eemian interglacial (a-c) under three different temperature reconstructions (d) based on the GRIP ice core records (adapted from Cuffey and Marshall, 2000, by permission of Nature).

Kukla et al. (2002a) identify the Eemian with widespread temperate mixed forest cover in Europe and temperatures comparable with the present day or even higher. In January, mean temperatures were 2–3°C higher than now in northwestern Russia and 12°C higher in the lower Lena River basin. In the central Siberian Arctic coastal area, July temperatures were 4–8°C higher than now and the frost-free season was up to 50 percent longer. The Greenland Ice Sheet was reduced in size compared to day, but how much smaller is still unclear. Modeling studies suggest that it may have lost 30–60 percent of its volume. At the peak of the Eemian, global sea level appears to have been 4–7 m higher than today, with the mass loss from the Greenland Ice Sheet contributing to anywhere from 2.2–4.5 m of sea level rise (van Den Berg et al., 2011). Figure 10.3 illustrates the modeled extent and elevation of the Greenland Ice Sheet during the Eemian by K. Cuffey and S. Marshall (2000), on the basis of three different interglacial temperature reconstructions. Although it has long been recognized from ice core data that there was significant melt of the sheet during the Eemian (e.g., Koerner, 1989), analysis of the new NEEM ice core points to a fairly modest decrease in surface elevation of the ice sheet, arguing for a modest 2 m contribution to sea level. This indicates that Antarctica must have contributed strongly to the total Eemian sea level rise (NEEM community members, 2013).

As is evident from Figure 10.2, the Eemian interglacial was followed by a cold glacial, which was itself characterized by fluctuations between periods of extensive ice (stades) and less extensive ice (interstadia). During about 90 percent of the last glacial cycle, global temperatures were substantially lower than those of the Holocene. Temperatures in northern middle and high latitudes dropped in a series of steps between MIS 5 and 2. Ice cover began to build up in northern North America, Scandinavia and the Arctic Archipelagos around 110 ka. Major ice sheets were present over northern North America, and Fennoscandinia by about 90 ka but their extent is poorly known. In northern Europe and northwest Russia, four glacial stades are apparent within the last glaciation. Recent work in northern Russia indicates

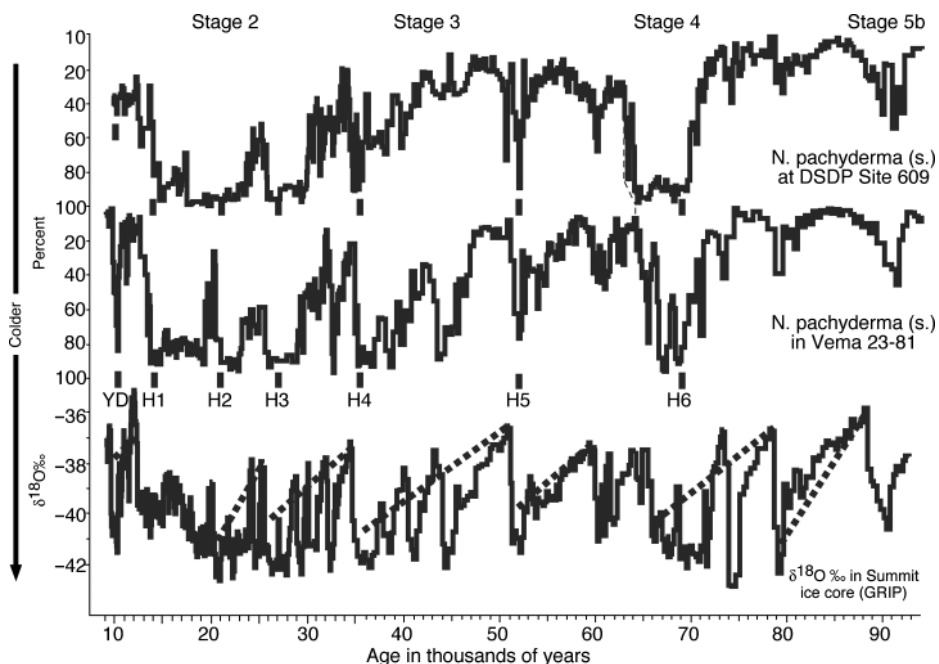


Figure 10.4. Reconstructions from several data sources illustrating climate changes since 93 ka. The top two panels give the abundance of *N. Pachyderma* from two North Atlantic ocean cores (DSDP 609, approximately 50°N, 45°W, Vema 23-81, approximately 54°N, 18°W), and the bottom panel is the $\delta^{18}\text{O}$ record from the GRIP Summit ice core. The dotted lines on the bottom panel illustrate long-term cooling trends. H1-H6 indicate Heinrich Events, and YD indicates the Younger Dryas event. The age scale is approximate (courtesy of G. Bond, Lamont-Doherty Earth Observatory, Palisades, New York).

that the most extensive glaciation there may have been during the so-called Middle Valdai, prior to 40 ka, contrasting with the maximum in global ice volume 25–18 ka, as discussed later.

There were large fluctuations in sea level (marine transgressions and regressions) associated with ice sheet growth and decay. These represent the direct influence of changes in terrestrial ice volume on eustatic sea level, as well as the response of the earth through glacio-hydro-isostatic effects. The latter involve vertical movements of the land induced by varying loads of ice and water and the redistribution of mass. These processes are still occurring today. During the marine regressions and transgressions, zones of frozen ground in the coastal and continental shelf areas of the Arctic, especially Eurasia, underwent successive north–south displacements (Rozenbaum and Shpolyanskaya, 2000).

Figure 10.4, based on the original work of G. Bond et al. (1993), gives a closer focus on climate changes from about 93 ka through the early Holocene on the basis of the relative abundance of left-coiling (sinistral) *N. Pachyderma* in two ocean cores in the North Atlantic and in the $\delta^{18}\text{O}$ record at the GRIP Summit ice core. These records go back to Stage 5b (5.2). Recall that a more negative (i.e., lighter)



Figure 10.5. Extent of Northern Hemisphere glacial ice during the Last Glacial Maximum (from Denton and Hughes (eds.), 1981, by permission of John Wiley and Sons).

$\delta^{18}\text{O}$ in ice cores means colder conditions over Greenland. A higher percentage of left-coiling *N. Pachyderma* (a cold water planktonic foram) is interpreted as lower sea surface temperatures. The scale for the percentage of *N. Pachyderma* is reversed, providing easier comparison with the ice core record. Changes often began and ended rapidly – much faster than indicated in this low-resolution figure. We will return to this issue shortly.

The LGM occurred anywhere from 18–25 ka, depending on the region and interpretation. In Figure 10.2, we see a minimum in $\delta^{18}\text{O}$ (i.e., coldest conditions) at stage 2.2, around 18 ka. Figure 10.5 summarizes the approximate extent of Northern Hemisphere ice sheets during the LGM. Although some aspects of this figure are controversial and some have been revised (see later discussion), it makes the fundamental point that glaciation was widespread. The Laurentide Ice Sheet was the largest after that of Antarctica. It covered most of Canada, merging in the west with the Cordilleran Ice Sheet and the Innuitian Ice Sheet over the Canadian Arctic islands, and reaching into the northern United States. Moraine features such as Cape Cod and Long Island are geomorphological relics of the Laurentide Ice Sheet. In Europe, the Fennoscandian (or Scandinavian) Ice Sheet covered Scandinavia and part of western Russia. Glacial ice covered parts of the ocean shelf areas off northwest Russia but most of Siberia was ice free. During the LGM, sea level was 120–135 m lower than today. The Bering land bridge, connecting eastern Siberia with western Alaska, last emerged at about 70 ka. The land bridge is of great anthropological importance in that it allowed the migration of humans into North America.

Deglaciation – the transition from the LGM to the Holocene, was not a period of uniform warming, but was interrupted by cold events. The most notable was

the Younger Dryas (YD), from about 12.8–11.5 ka, which represented a return to near glacial conditions. The YD is labeled in Figure 10.4. It corresponds clearly to a $\delta^{18}\text{O}$ minimum in the GRIP record as well as a high percentage of sinistral *N. Pachyderma* (implying low sea surface temperatures) at the VEMA 23–81 ocean core site. The YD had variable regional expressions.

The Holocene (starting at MIS 1, 11.5 ka), generally considered to start at the end of the YD, has been a generally warm period, and although more stable than the last glacial, still exhibited strong temperature variability. Reconstructions from many different sources indicate that, during the Holocene Thermal Maximum or Climatic Optimum, global average temperatures were considerably higher than those of the twentieth century. The period at which maximum warmth occurred varied greatly by region. The Holocene Thermal Maximum was followed by general cooling starting around 5 ka. The most notable cooling since the YD is represented by the LIA. Details of the LGM, deglaciation and the Holocene are examined in Sections 10.5 through 10.7.

10.3.2 Causes of the Quaternary Glacial Cycles

It is widely accepted that the major Quaternary glacial cycles, in considerable part, can be related to cyclic variations in earth orbital geometry that cause variations in the amount of radiation received at different parts of the year over different parts of the earth's surface. These Milankovitch cycles are named after astronomer Milutin Milankovitch, who made the first detailed calculations of their effects on the distribution of solar radiation (Milankovitch, 1941). They involve three factors. The first, eccentricity, varies over an approximate 100,000-year cycle. The earth's orbit is not circular, but elliptical. As such, earth-sun distance varies throughout the year. Radiation receipts are greatest at the time of minimum earth-sun distance (perihelion) and least at maximum earth-sun distance (aphelion). Today, perihelion and aphelion are in January and July, respectively, associated with about a 6 percent difference in the amount of total solar radiation received at the surface. When the earth's orbit becomes more elliptical (greater eccentricity), the amount of energy received varies more strongly. The second factor is the obliquity (or tilt) of the earth's axis relative to its orbital plane about the sun. Obliquity varies over a 41,000-year cycle. The earth's axial tilt is presently 23.5° but varies between about 22° and 24° . The tilt affects the summer-winter radiation contrast and is especially important in high latitudes. The third factor is the timing of the perihelion with respect to the seasons (i.e., the precession of the equinoxes), which changes on a 23,000-year cycle owing to wobbling of the earth on its axis.

Using ocean core records, J. Hayes, J. Imbrie, and N. Shackleton (1976) provided some of the first convincing evidence of a climate link with the Milankovitch cycles. This is considered to be a landmark paper. Conventional paradigm identifies global ice volume being tuned to June extraterrestrial solar radiation at $60\text{--}65^\circ\text{N}$. Glacial conditions seem to be favored by small tilt and perihelion in the Northern Hemisphere winter. These conditions lead to a diminished seasonal contrast with

mild winters and cool summers, the latter favoring survival of snow/ice through the summer. Changes in external radiative forcing then bring about additional responses and feedbacks that foster ice sheet growth and decay, notably in the carbon cycle. Orbital forcing can hence be viewed as the “pacemaker” of the Ice Ages (Hayes et al., 1976). Despite the strong explanatory power of the Milankovitch theory, a number of unresolved issues nevertheless remain, both with respect to the relative roles of eccentricity, obliquity and precession in explaining the onset and termination of glaciations and attendant climate feedback processes (e.g., Wunsch, 2004).

As changes in solar radiation alter the latitudinal temperature gradient, they can modify the strength and characteristics of the atmospheric circulation. This will alter patterns of moisture transport and precipitation. A trigger for glaciation may have been an increase in the meridional temperature gradient leading to enhanced poleward moisture transport (Kukla et al., 2002b). This idea was first suggested by J. Tyndall (1872). As cool Northern Hemisphere summers favor the survival of snow/ice cover through the melt season, this can invoke ice-albedo feedbacks and other processes to promote more ice growth, also affecting the circulation. Barry (1966) calculated atmospheric moisture fluxes into northeastern Canada and examine the synoptic patterns that might favor ice buildup.

Along the lines of the ice-albedo feedbacks, J.D. Ives (Ives, 1957, 1962; Ives, Andrews, and Barry, 1975) proposed the idea of “instantaneous glacierization,” by which a small cooling leads to persistence of a snow cover in critical areas at the end of summer. Ives focused on the Labrador-Ungava plateau and Baffin Island, where modest cooling would bring large areas of the plateau above the snowline, so that glaciation could proceed quickly through ice-albedo feedbacks. Given its summer warmth and low precipitation, the buildup of ice over Keewatin (Canada) poses special difficulty (Brinkman and Barry, 1972; Bromwich, Toracinta, and Wang, 2002). A different idea, proposed by R. Flint (1943), is known as “highland origin and windward growth”. Flint argued that the Laurentide Ice Sheet was initiated in the coastal mountains of Labrador-Ungava and Baffin Island. Glaciers formed in these areas were nourished by precipitation on their windward flanks and advanced into western lowlands to ultimately attain ice sheet proportions. Lowering of the snowline initiated the growth of small cirque glaciers in the mountains of Scandinavia. These glaciers expanded, coalesced, and advanced eastward onto Russia. Growth on the seaward flank was checked by calving into the ocean. G. Denton and T. Hughes (1981) applied a marine ice transgression hypothesis to explain the development of ice sheets with large marine-based components (e.g., the Barents Ice Sheet). In this model, glacierization was triggered by an extension of permanent sea ice into interisland channels and embayments. This resulted in the formation of extensive fast ice (see Chapter 7). Albedo increased, dropping the snow line to sea level. The ice thickened and eventually grounded itself to the ocean bottom, allowing development of a marine ice dome. As discussed by R. Souchez (1997), these different hypotheses are not mutually exclusive and have been applied with some success to understanding the geological traces of the last Pleistocene ice sheets. The

mechanisms are examined in more detail by D. Benn and D. Evans (1998) and have been modeled by W. Peltier (2004).

There is close correspondence between paleotemperatures over the major glacial-interglacial cycles of the Quaternary and concentrations of atmospheric carbon dioxide and methane (Petit et al., 1999; Raynaud et al., 2000; Sigman et al., 2010), with lower concentrations during glacials and higher concentrations during interglacials. This points to strong feedback processes, whereby changes triggered by the Milankovitch cycles are amplified, and, because these greenhouse gases are well-mixed in the atmosphere, the ice age cooling and interglacial warming are globalized. The ranges in CO₂ and CH₄ are, respectively, roughly 300 ppmv and 780 ppbv (interglacial) and 180 ppmv and 320 ppbv (glacial) (Petit et al., 1999). This compares with CO₂ and CH₄ values in the year 2013 of about 400 ppmv and 1,750 ppbv, respectively. The mechanisms for changes in trace gas concentrations remain to be completely resolved. The methane variations are viewed as having a link to the terrestrial biosphere – in colder drier conditions, there were fewer wetlands to act as methane sources. Thinking on the carbon dioxide problem has largely solidified on ocean biogeochemistry and interactions with ocean circulation, in which with the high latitude Southern Ocean plays a key role.

As reviewed by Sigman et al. (2010), under the present climate, biologically produced organic matter sinks out of the surface layers into the deep ocean before it can decompose back into CO₂. This lowers the partial pressure of the CO₂ in surface waters, drawing CO₂ out of the atmosphere. The storage of regenerated CO₂ in the deep ocean also focuses acidity there. This reduces the burial of calcium carbonate in seafloor sediments, making the global ocean more alkaline, increasing the solubility of CO₂ in the sea water, acting to further lower the partial pressure of CO₂ in the atmosphere. In the Southern Ocean, the nutrient rich and CO₂-rich waters then ascend to the subsurface before major nutrients (nitrogen and phosphorus) are fully used by photosynthesis for carbon fixation. This allows CO₂ to escape back to the atmosphere. The available evidence suggests that during ice ages, this release of CO₂ back to the atmosphere was reduced. This could occur in a number of ways, including (1) a decrease in the exchange of surface waters in the Southern Ocean with deeper waters, (2) an enhanced consumption of Southern Ocean surface nutrients by phytoplankton, and (3), an increase in the seasonal coverage of sea ice in the Southern Ocean acting as a cap.

10.3.3 Ice Sheet Influences on Atmospheric Circulation

Modeling studies indicate that the Quaternary ice sheets strongly influenced the atmospheric circulation. It is likely that the winter jet stream over North America was split because of the large extent and height of the Laurentide Ice Sheet. One branch of the jet went around the northern edge of the ice sheet, while the other branch curled south of the ice sheet, so that storm tracks were displaced (Kageyama et al., 1999). The LGM ice sheets also seem to have favored an increased tendency for stationary blocking patterns (Roe and Lindzen, 2001). The study of P. Ditlevsen,

H. Svensmark and S. Johnsen (1996) points to a larger atmospheric thermal gradient than now between the equator and the pole, associated with a colder northern North Atlantic. This suggests stormier conditions. Simulated circulation changes are associated with hydrologic changes. It appears that precipitation was reduced over the Laurentide Ice Sheet while it was enhanced along its southern margins.

Regional modeling studies (Bromwich et al., 2004, 2005) indicate that from November through April, there was a split flow at upper levels around a blocking anti-cyclone over the Laurentide Ice Sheet, with the northern branch over the Canadian Arctic and the southern branch impacting southern North America. The split flow transitioned into a single jet stream migrating northward over the Laurentide Ice Sheet in summer. During summer, pronounced low-level thermal gradients along the southern margin of the ice sheet, resulting from the juxtaposition of the ice sheet and the adjacent warm ice-free land surface, facilitated the development of cyclones tracking over the ice sheet, some producing copious precipitation along and south of the ice sheet terminus. Precipitation along the southern margin was orographically enhanced by the presence of the ice sheet.

10.4 D-O Cycles and Heinrich Events

10.4.1 Overview

The Last Glacial Cycle was characterized by pronounced millennial scale changes between warm and cold conditions, known as Dansgaard-Oeschger (D-O) cycles. D-O cycles are named after the investigators who identified them in Greenland ice core records. Twenty-five D-O cycles have been identified over the last glacial cycle, with an interval between warm and cold phases of roughly 1,500 years (Grootes and Stuiver, 1997), or 2,000–3,000 years for a complete cycle. D-O cycles are characterized by rapid warming, typically occurring over a matter of decades, and then more gradual cooling over a period of centuries. D-O cycles can be stratigraphically related to layers of ice-rafterd detritus (IRD) released from armadas of melting icebergs calved from the ice sheets, the most pronounced of which are termed Heinrich events (Heinrich, 1988). Heinrich events occur in the cold periods immediately preceding D-O warmings. Heinrich events occurred about every 6,000–7,000 years and may have lasted around 500 years. They are labeled in Figure 10.4. Note the correspondence with cold conditions. There are also more modest intervening IRD episodes recurring at more frequent intervals of 2,000–3,000 years, on which the Heinrich events are superimposed. Most of these events (the combination of Heinrich and smaller IRD events) follow the pacing of the D-O cycles.

Explanations for D-O cycles largely revolve around various mechanisms by which the northern North Atlantic could be freshened, leading to a reduction in the strength of the Atlantic Meridional Overturning Circulation (the AMOC, see section 7.5.2) and NADW production, fostering widespread cooling of the North Atlantic region. This would then be followed by recovery of the AMOC and rapid warming.

As for the link to Heinrich events, considerable attention has been paid to “binge-purge” behavior of the Laurentide Ice Sheet. The idea is that during cold conditions, the ice sheet built up to a critical point where basal melting occurred (melting at the base of the ice sheet). Basal melting lubricated the base of the ice sheet and initiated a rapid discharge of icebergs via the Hudson Strait Ice Stream (the Hudson Strait lies between northern Labrador and southern Baffin Island). The iceberg discharge then ceased and the ice sheet rebuilt, followed by another surge episode (MacAyeal, 1993). More recent work (Marcott et al., 2011) points to how the floating ice shelf fronting the Hudson Strait Ice Stream could be destabilized by basal melting linked to subsurface ocean warming, with the subsurface warming occurring at the same time that the AMOC became weak. J. Fluckiger, R. Knutti, and J. White (2006) in turn argue that collapse of the AMOC, along with increased oceanic heat uptake after the AMOC collapse, could lead to rises in sea level, destabilizing Northern Hemisphere ice shelves and ice sheets and triggering ice surges. Alley et al. (2006), by contrast, point to the potential for outburst flooding from subglacial reservoirs following climatic cooling.

10.4.2 Processes

Although D-O cycles and Heinrich events are related phenomena, a full accounting of their causes and linkages has remained elusive. As to how the North Atlantic could be freshened, one of the first ideas that was advanced is the “salt oscillator” (Rooth, 1982; Broecker et al., 1990). There were periods when the AMOC and NADW production were relatively strong (albeit weaker than at present), resulting in enhanced discharge of meltwater and icebergs (the warm part of a D-O cycle). This resulted in freshening in the GIN seas. However, the surface freshening then reduced NADW production, causing widespread cooling of the atmosphere (the transition to the cold part of the D-O cycle). This reduced the meltwater and iceberg discharge. Ocean salinities then rebuilt to a critical point at which NADW production recovered, causing warming (the transition from the cold to warm part of a D-O cycle). The process then repeated itself. The salt oscillator as originally conceived stresses interactions with the Fennoscandian Ice Sheet. However, interactions with the Greenland Ice Sheet and Laurentide Ice Sheet could also be involved. The salt-oscillator (associated with “on” and “off” modes of NADW production) finds some support in S. Lehman and L. Keigwin’s (1992) study of climate variability during the last deglaciation.

Other ideas involve “halocline catastrophes.” For example, P. Clark et al. (2001) proposed that when the Laurentide Ice Sheet margin was between about 43 and 49°N, fluctuations in the location of the margin allowed rerouting of the main runoff from the Mississippi River drainage into the North Atlantic via the St. Lawrence River or the Hudson Strait. The massive freshwater inputs to the northern North Atlantic capped the convection and caused widespread cooling. Another possible forcing is the discharge of water into the North Atlantic from the catastrophic drainage of

proglacial lakes (Siegert, 2001). These are large lakes found ahead of the ice sheet margins, such as Lake Agassiz. Drainage of Lake Agassiz is a contender to explain the Younger Dryas cold event (Section 10.6.2).

These ideas provide some explanation as to why the climate of the Holocene has been relatively stable. As land ice has been much more limited during the Holocene (Greenland and Antarctica excepted), it is harder to get the requisite massive freshwater discharges. NADW production under present conditions, although still somewhat variable, hence stays in the “on” mode. In Chapter 7, we examined the Great Salinity Anomaly of the late 1960s and early 1970s and noted an apparent association with reduced NADW production. The Great Salinity Anomaly could be viewed as a small-scale modern example of a NADW-freshwater link, although this event appears to have been associated with freshwater discharge through the Fram Strait.

A problem with the ideas of drainage rerouting or the rapid drainage of proglacial lakes is that, although D-O events are quasi-periodic, catastrophes, by their nature, tend to have a large random component. Regarding the salt oscillator, there is a problem in timing, questioning cause and effect. Whereas one might consider the freshwater input from icebergs associated with IRD events (and attendant direct inputs of meltwater from the ice sheets) as drivers of D-O cycles, as noted, the IRD events occurred during the cold phases of D-O events, not before them. Indeed, five of the six Heinrich events (Figure 10.4) occurred at the culminations of progressive cooling and were then followed by sharp warming to almost interglacial conditions (Bond and Lotti, 1995).

IRD from at least two widely separated sources is present at the same time in the same eastern North Atlantic cores examined by G. Bond and R. Lotti (1995). This indicates nearly synchronous rates of iceberg calving between these distant areas. One explanation for the synchronous iceberg discharge is that different ice sheets exhibited nearly identical “binge-purge” behavior. However, another explanation is that the synchronous calving represents an external climate forcing. In other words, freshwater input did not force the cooling phases of the D-O cycles, but rather followed the cooling. The freshwater input may have subsequently triggered further cooling. However, Bond and Lotti (1995) acknowledge that recurring binge-purge processes in another ice sheet may have discharged enough ice each time to alter NADW production, with the resulting ocean cooling triggering the iceberg discharges they identified.

Bond and Lotti (1995) found that each discharge of detrital carbonate-bearing ice from the Hudson Strait (associated with the Heinrich events) seems to lag slightly behind the discharge from the other two sources. G. Farmer, D. Barber, and J. Andrews (2003) also find that IRD fluxes into the Nordic Seas appear to have been nearly synchronous with Heinrich events recorded elsewhere in the North Atlantic. It may be that the sudden coolings within the D-O cycles triggered the ice discharges in the Hudson Strait at nearly the same time as discharges from the other two sources. An alternative view is that the trigger could have been sea level rises that seem to accompany each 2,000–3,000-year flood of icebergs to the ocean.

Interestingly, modest IRD events have also recurred through the Holocene (Bond et al., 1997), when (excepting Greenland) there was much less continental ice in the Northern Hemisphere. Using high-resolution Holocene data, Bond et al. (2001) found that these IRD events show a rough recurrence on two time scales, the approximate 1,500 +/- 500 year scale seen during glacial periods, but also around 400–500 years. There is a relationship between these cycles and inferred solar variability. Whether the apparent solar relationship seen in the Holocene records can be extended back into the last glacial cycle is not known. This inferred solar variability is not linked with Milankovitch cycles but to forcing such as those associated with sunspot cycles and altered fluxes of ultraviolet radiation.

R. Alley, S. Anandakrishnan, and P. Jung (2001) and S. Rahmsdorf and R. Alley (2002) propose “stochastic resonance” on a 1,500-year time scale. This involves interactions between a weak periodic climate forcing, climate “noise” and a non-linear amplifier. The basic idea is that one has an amplifier, namely the THC, which does not respond to signals below a certain threshold. However, if climate noise (e.g., random fluctuations in freshwater fluxes) combines correctly with a weak periodic forcing, stochastic resonance can occur, seen as a strong response of the THC. The idea finds support in results from a so-called model of intermediate complexity (Ganopolski and Rahmsdorf, 2001). This study showed that in contrast to “on” and “off” modes of the THC, such as associated with the salt oscillator, or catastrophic events such as the draining of proglacial lakes, a more subtle explanation for D-O events is geographical shifts in NADW production. And it seems that such geographical shifts in NADW production can be triggered fairly easily by climate noise. When this model is driven by random noise of realistic amplitude, combined with a weak periodic (1,500-year) climate signal, D-O events emerge that are very similar to those seen in the Greenland ice core records. The origin of the weak periodic 1,500-year climate forcing has not yet been clearly identified, but the solar variability link postulated by Bond et al. (2001) must be considered as a contender.

A final comment regards interhemispheric correlations. The major aspects of the glacial/interglacial cycles as seen in the Greenland ice cores correspond well to those in Antarctic records, pointing to global-scale signals. However, interhemispheric relationships between millennial-scale D-O cycles are more complex. Evidence from ice cores indicates that when the North Atlantic warms abruptly, Antarctic temperatures drop, a phenomenon known as the bipolar see-saw. This see-saw implicates the AMOC because this circulation is known to orchestrate how heat is redistributed between the Northern and Southern hemispheres. The idea is that a reduction in the strength of the AMOC, such as caused by a massive input of freshwater to the North Atlantic, gives rise to a rapid decrease in northward heat transport in the Northern Hemisphere, compensated by an increase in southward ocean heat transport in the Southern Hemisphere. Records examined by S. Barker et al. (2009) indicate that rapid temperature changes in the South Atlantic during the last deglaciation were, within dating uncertainty, instantaneous and of opposite sign to those that occurred over the North Atlantic.

10.5 Regional Aspects of the LGM

10.5.1 Northern Eurasia

The LGM in northern Eurasia occurred at around 27 ka to 15 ka. The LGM is relatively well documented, although uncertainties remain in northwestern Russia and in the Barents and Kara seas. Through the International Union for Quaternary Research, Commission on Glaciation Work Group 5, glacial chronologies from around the world have been assembled to better understand ice sheet volumes and extents at various times, and to compile a digital database for past ice sheet extents. The results are published in three volumes spanning different parts of the globe (Ehlers and Gibbard, 2003).

J. Svendsen et al. (1999) and M. Siegert (2001) provide modern views of ice extent in northern Eurasia during the LGM (Figure 10.6). Along with the major Fennoscandian Ice Sheet, there were ice sheets covering Svalbard, Franz Josef Land, the Barents Sea, Novaya Zemlya, and the Kara Sea. Another covered the northern part of the British Isles, and Iceland was almost completely covered by ice. There was open ocean along the eastern margins of the Norwegian-Greenland Sea providing a local moisture source to feed the Barents Sea Ice Sheet (Hebbeln et al., 1994). Evidence for open water here includes the discovery of remnants of *Globigerina quinqueloba* (which only live in ice-free waters) in sediment cores. This contrasts with earlier views depicting an ice shelf extending from the Barents Sea (Grossvald, 1980; Lindstrom and MacAyeal, 1986).

The Fennoscandian Ice Sheet reached its maximum extent around 22 ka. At this time, the southern and south-eastern margins were in northeast Germany, northern Poland, the Baltic countries, and northwest Russia (Kleman et al., 1997). Numerical modeling indicates that in a maximum scenario, it reached a maximum thickness of about 2,700 m around 15 ka (Siegert, Dowdeswell, and Melles, 1999), whereas over the Barents Sea it was 1,500–1,800 m thick. Ice in the Kara Sea for this scenario decreased from 1,200 m thickness near Novaya Zemlya to a grounded ice margin east of the Kara Sea coastline. In a minimum model scenario, assuming lower temperatures and slow accumulation, the ice over the Kara Sea may have only been 300 m thick (Siegert, 2001). The marine-based ice sheet in the deeper Barents Sea began to break up around 15 ka and disappeared soon after 9 ka. The last remnants persist today on the archipelagos of Svalbard and Franz Josef Land.

Northern Siberia, including the Taymyr Peninsula, is considered to have been largely ice-free during the LGM (termed the Late Valdai or Sartan Glaciation), but glacial materials dated to 40 ka occur on the Yamal Peninsula, indicating more extensive ice here earlier (Siegert, 2001). Radiocarbon dating of massive ice wedges in permafrost in northern Siberia gives basal ages in the 30–40 ka range (Vasil'chuk and Kotlyakov, 2000). The Late Sartan ice cover in the Ural Mountains and over mountain and upland regions of central and northeastern Siberia was limited, with local ice caps in the Ural mountains, the Anadyr Plateau of central Siberia, and the

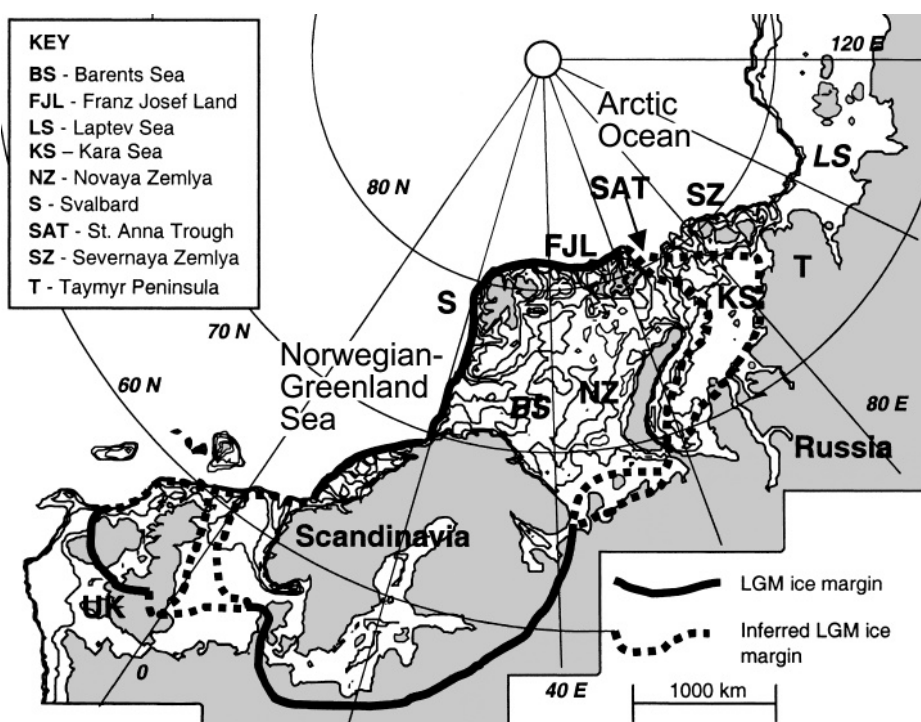


Figure 10.6. Ice extent in northwestern Eurasia during the LGM (adapted by Siegert et al., 2001 from Svendsen et al., 1999, by permission of John Wiley and Sons).

Verkhoyansk, Chersky, and Koryak highlands of northeastern Siberia (Velichko and Spasskaya, 2002; Shahgedanova, 2002).

10.5.2 Arctic Ocean

In general, the Arctic Ocean climate during the LGM featured cold winters, whereas summers were mostly dry and cooler than present. Ice conditions in the Arctic Ocean during the LGM are still poorly known and controversial. One hypothesis is that there were large floating ice shelves, up to 2–3 km thick, over the trans-oceanic ridges. This is evidenced by deep ice scouring on the ridge crests, as discussed later. A contrary hypothesis is that there was thick perennial sea ice, such as occurs off northern Canada at present (Clark, 1982). That sea ice was at least more extensive than at present is well documented. For example, A. de Vernal and C. Hillaire-Marcel (2000) provide evidence of extensive perennial sea ice along the continental margins of eastern Canada.

The idea of an Arctic Ocean ice sheet and large floating ice shelves was first advanced by J. Mercer (1970) and has been restated by Grosswald and Hughes (1999). One piece of supporting evidence is the widespread occurrence of abiotic conditions in the ocean sediments during the LGM. Glacial moulding and scouring of landforms and the fluting or erosion of ridge crests has been identified at 1 km

depth on the Yermask Plateau, Chukchi Borderland and the Lomonosov Ridge by seabed mapping using side-scan sonar (e.g., Polyak et al., 2001). M. Grossvald and T. Hughes (1999) proposed that the collapse of this ice shelf would have eliminated back pressure on ice streams in the Barents-Kara Sea ice sheet allowing fast flow and iceberg calving. They also suggested that in the central Siberian Arctic, where the ice shelf was grounded against the continental shelf, it dammed the Eurasian rivers flowing to the Arctic creating proglacial lakes and periodic flood events to the south (Grossvald, 1999). G. Kriner et al. (2004) show that large ice-dammed lakes in northwest Eurasia around 90 ka could have lessened summer melt on the southern margins of the Barents Sea Ice Sheet, by inducing cooling. A major review of the glacial history of the Arctic Ocean has just been published by M. Jakobsson et al. (2013)

10.5.3 North America and Beringia

As noted, during the last glacial advance (known as the Wisconsin in North America), the major Laurentide Ice Sheet covered most of Canada. It merged in the west with the Cordilleran Ice Sheet and reached into the northern United States. The glacial history of the early Wisconsin is little known as paleoclimate information over land was largely destroyed by the extensive late Wisconsin ice. More problematic is the ice extent in the Canadian Arctic Archipelago. J. England (1999; England et al., 2006) and C. O’Cofaigh et al. (1999) advocated the existence of an ice sheet over the Queen Elizabeth Islands north of Lancaster Sound (termed the Innuitian Ice Sheet, see Figure 10.5) but not all of the evidence is consistent with such an interpretation (Wolfe and King, 1999). Nevertheless, England et al. (2006) show that the Innuitian Ice Sheet was composed of an alpine and a lowland sector. Advance of the alpine sector occurred as recently as about 22.5 ka. Outflow from alpine and lowland divides produced several ice streams, one extending northwestward across the Canadian Arctic Archipelago to the polar continental shelf. Retreat of the ice commenced along its southwest margin around 13.5 ka. However, most of the ice sheet remained on the continental shelf during the Younger Dryas.

The Laurentide Ice Sheet appears to have been multidomed with centers over Quebec-Labrador, northern Keewatin, and Baffin Island (Dyke, Dredge, and Vincent, 1982; Clark, Knight, and Gray, 2000). A model of the ice sheet growth, dynamics, and decay developed by W.Peltier (1994) predicted a 2,500-m thick ice sheet with eastern and western domes and another in the Cordilleran Ice Sheet. S. Marshall et al. (2000) extended this modeling through the Wisconsin glacial cycle, which pointed to phases of growth and decay and the formation of pro-glacial lakes at the southern margin during the deglaciation, leading to melt water outflows, initially to the Gulf of Mexico via the Mississippi, and later to the North Atlantic. In addition, iceberg calving episodes in the Hudson Strait injected sediment into the North Atlantic.

The Cordilleran Ice Sheet extended into southeastern Alaska and westward into the eastern Aleutian Islands, but a separate ice cap covered the Brooks Range. Much

of Alaska was ice-free. In Greenland, the ice sheet during the LGM was somewhat more extensive and thicker than now, mainly in southern Greenland (Siegert, 2001). However, ice also filled the Nares Strait, linking the Innuitian and Greenland ice sheets. Outlet glaciers reached the shelf break.

Steppe-tundra vegetation was thought to have covered Beringia (eastern Siberia and Western Alaska surrounding the Bering land bridge) (Hopkins et al., 1982). There are fossil fauna of large grazing animals including mammoth. This interpretation is based on terrestrial records and is supported for at least the glacial onset (23 ka) in the Yukon, eastern Beringia (Zazula et al., 2002). However studies of marine cores (Elias et al., 1996) show that at least on the former Bering land bridge there was widespread moist shrub tundra. Studies in Alaska point to less widespread steppe/tundra than was formerly proposed. Insect evidence for the full glacial interval points to dry heaths and meadows, shrub tundra, and interspersed marshes and ponds.

10.6 Deglaciation

10.6.1 Fundamental Features

Deglaciation began between 15 ka and 13 ka, depending on the latitude of the area. Ice retreat was accompanied by changes in vegetation and in the atmospheric circulation. For example, before 15 ka, eastern interior Alaska was dominated by cold, very dry conditions (Edwards et al., 2001). After 14 ka, slight warming allowed birch and poplar growth. This interval also saw the northward expansion of the tree line in eastern Siberia. Around 11 ka, the Bering seaway was reestablished and summer temperatures inferred from insect evidence on the Bering shelf were slightly higher than now. However, winter temperatures appear to have been somewhat colder (Elias et al., 1996). The tundra/steppe extended well into Europe at this time (Rochon et al., 1998).

The fundamental driver of the deglaciation was increasing solar radiation. However, deglaciation was by no means uniform, pointing to a strong role of processes within the coupled atmosphere-ocean-ice sheet system. Greenland ice cores document a number of notable events. The Older Dryas (OD) was followed by the Bölling-Allerod (B/A), a warm event starting at about 14.7 ka and ending at about 13 ka (Figure 10.7). The B/A has two parts, the earlier Bölling being the warmest. The subsequent Allerod, although still warm, was somewhat cooler. The B/A ended sharply with the advent of the YD cold interval, which lasted from about 12.8 to 11.5 ka. The YD represented a return to near glacial conditions. The Laurentide and Fennoscandian ice sheets began to re-advance during the YD, as did smaller alpine glaciers at many sites. The onset and termination of the YD were rapid, occurring over years or decades. While the YD was a cold period overall, conditions were nevertheless quite variable both spatially and temporally (Mayewski et al., 1993).

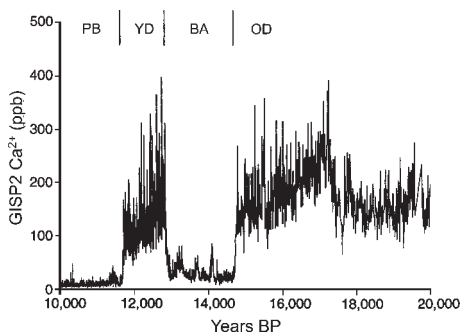


Figure 10.7. Calcium concentrations (ppb) covering the 10–20 ka period, based on GISP2 ice core data. The sample resolution is approximately two years through the Holocene, a mean of 3.48 years within the YD (Younger Dryas) and BA (Bolling/Allerod), and three to fifteen years during the OD (Older Dryas) (from Mayewski et al., 1993, by permission of AAAS).

10.6.2 The Younger Dryas

Figure 10.7 illustrates the YD in terms of high calcium concentrations recorded in the GISP 2 ice core. The YD was also associated with high dust concentrations and high magnesium levels. These features imply an intensified circulation over continental regions and increased aridity. In addition, ammonium, nitrate, sulfate, sodium, chloride and potassium concentrations rose (Mayewski et al., 1993). These large increases cannot be explained by increased windiness alone. Destruction of biomass because of colder conditions during the YD could have caused the observed increase in ammonium.

It appears that NADW formation decreased, associated with cooling in the North Atlantic and equatorward retreat of the ocean Polar Front. SSTs decreased rapidly in the GIN seas by about 6°C, returning to near LGM values (Rochon et al., 1998). However, a sea ice-free corridor persisted along the Norwegian coast. Some of the reconstructed oceanic changes in the GIN seas during the YD are illustrated in Figure 10.8. Dates are ¹⁴C years before present, which appear younger than calendar dates (see Section 10.2.2). The reductions in August SST and the increase in the number of months with sea ice cover are especially notable.

Some high-latitude areas experienced a more extreme YD event than others. The YD was strongly expressed in the North Atlantic and in the Nordic Seas. Western Norway experienced a very severe change, seen by a considerable halt in disintegration of the ice sheet and the development of extensive moraines. In the western Nordic seas, there was a slight increase in IRD input (Hebbeln, Heinrich, and Baumann, 1998). This compares with little or no change in Svalbard (Birks et al., 1994). A cold dry climate in northwest Russia is inferred from pollen records which indicate that steppe/tundra vegetation was present (Subetto, Wohlfarth, and Davydona, 2002). The YD was not well-expressed in the Southern Hemisphere and most of these records point to warm conditions (Siegert, 2001).

The transition out of the cold climate of the YD into the Holocene occurred very quickly (Dansgaard, White, and Johnsen, 1989; Severinghaus et al., 1998). Warming of 7°C occurred in less than fifty years over Greenland. The Greenland climate also became more humid, most likely owing to the reduction in sea ice cover, allowing more evaporation and increased precipitation falling as snow (Alley, 1993). Dust

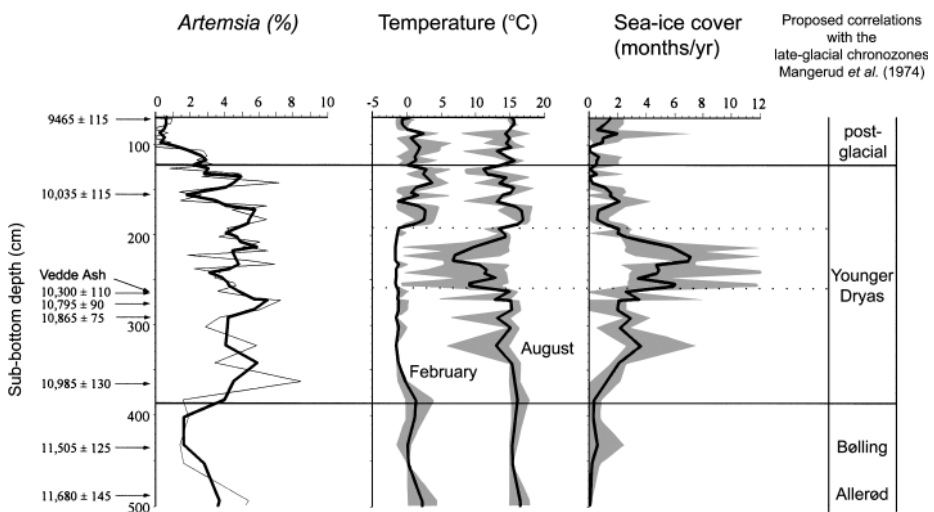


Figure 10.8. Inferred changes in *Artemesia*, sea surface temperature and sea ice cover in the North Sea during deglaciation (from Rochon et al., 1998, by permission of Elsevier).

concentrations in the GRIP ice core decreased by a factor of 3 within a twenty-year period indicating that storminess rapidly decreased.

Like D-O events, the cause of the YD is still uncertain, but evidence again implicates changes in NADW production. One theory (Broecker et al., 1989) involves a large influx of melt water through the St. Lawrence Seaway and into the North Atlantic. This resulted from the drainage of Lake Agassiz, a proglacial lake that formed at the foot of the retreating Laurentide Ice Sheet. The lake had been draining into the Mississippi basin. However, it is argued that just before the start of the YD, there was a catastrophic rerouting into the St. Lawrence seaway, associated with a 40 m drop in the lake level. Drainage was then routed back to the Mississippi (Figure 10.9). As reviewed by Bradley (1999), a number of problems became evident with this view, including indications that the YD occurred at a time when discharge to the world ocean was less than either the preceding or following 1,000 years, and that the melt-water flux from the St. Lawrence was actually reduced during the YD episode. In a subsequent study, Broecker (1990) argued that the period of rapid sea level rise prior to the YD lowered salinity in the surface layer so much that the North Atlantic was already predisposed for a shut down or major cessation in NADW production. A. Fanning and A. Weaver (1997) offer modeling support for this view. An ongoing challenge to the flood hypothesis has been the lack of clear geomorphic evidence for the flood pathway (Broecker, 2006). However, J. Murton et al. (2010) identify a path along the Mackenzie River to the Arctic Ocean that may resolve this problem.

Lehman and Keigwin (1992) give a different perspective. Their study addressed the YD as part of a focus on sudden changes in the North Atlantic circulation during the deglaciation phase. They show that prior to the YD, episodes of freshening, associated with meltwater inputs from the decaying Fennoscandian Ice Sheet,

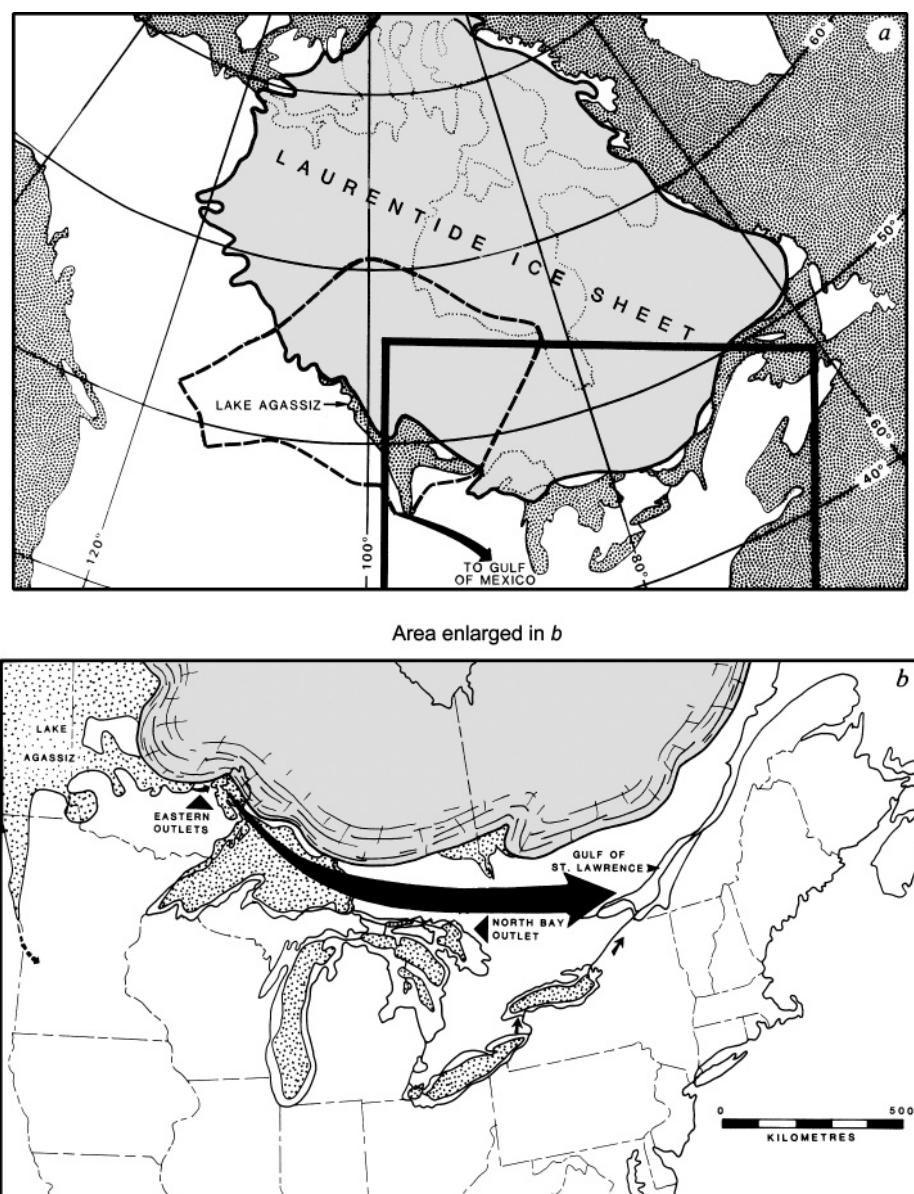


Figure 10.9. The Laurentide Ice Sheet and the routing of overflow from the Lake Agassiz basin (dashed line) to the Gulf of Mexico just before the Younger Dryas (a) and routing of overflow from Lake Agassiz through the Great Lakes to the St. Lawrence and northern North Atlantic during the Younger Dryas (b) (from Broecker et al., 1989, by permission of Nature).

immediately preceded faunal evidence for coolings associated with weakenings of the THC. The THC then recovered. The cause and effect is hence reminiscent of the salt-oscillator model. The more recent of these melting events (~13.4–13.0 ka) may have triggered the much longer and more severe YD. They note a link between

freshening beginning about fifty years after the onset of the YD and initial discharge of stored meltwater from the so-called Baltic Ice Lake. This may have prolonged and intensified suppression of NADW production during the YD. They find another interval of freshening after about 10.4 ka ^{14}C (~12.6 ka calendar) associated with final discharge of the Baltic Ice Lake. The major point is that warming and associated enhanced meltwater input promoted weakening of the THC and cooling, followed by recovery. The intensity of the YD event may have been in part fostered by additional freshwater inputs provided by drainage of the Baltic Ice Lake.

However, as outlined by Lehman and Keigwin (1992), a complete focus on the Fennoscandian Ice Sheet seems insufficient – the Laurentide Ice Sheet must also be involved. It appears that while the melting rates of both the Fennoscandian and Laurentide ice sheets may have been influenced by changes in the THC, their individual meltwater contributions may have had very different effects on the THC. Meltwater from the Laurentide Ice Sheet (e.g., from the drainage of Lake Agassiz) must travel farther to reach areas of convection in the GIN seas, so a greater or prolonged melting of the Laurentide Ice Sheet may have been needed for an equivalent damping effect on the circulation. It may be that the Laurentide Ice Sheet meltwater built up in the Atlantic, leading to a non-linear response of NADW production to ice sheet melting. This may account for the increasingly severe reductions in the THC during the deglaciation period that culminated in the millennial-scale YD.

Another idea involves sea ice. During the LGM, when sea level was much lower, the Arctic Ocean was very isolated, and the Fram Strait was narrower, restricting sea ice transport into the North Atlantic. Very thick sea ice would have built up in the Arctic Ocean, remaining largely immobile until rising sea level, breakup of the Barents Sea Ice Sheet and the return of warmer Atlantic waters to the Arctic Ocean allowed for massive discharge of sea ice into the North Atlantic. A final trigger may have come when sea level rose sufficiently such that the Bering land bridge was covered, allowing throughflow from the Pacific to the Atlantic, flushing out the ice (Bradley, 1999). Dating of terrestrial peats on the Chukchi shelf place this crucial event at about 13 ka, just before the YD (Elias et al., 1996). The processes are hence reminiscent of those that led to the Great Salinity Anomaly.

A hypothesized link between the YD and a large meteorite impact, while initially gaining considerable attention, has not been supported by subsequent studies. A link with volcanic activity remains controversial.

10.7 The Holocene

10.7.1 A Return to Warm Conditions

The Holocene is generally considered to begin at the close of the YD episode. Around 10 ka the perihelion occurred in July as opposed to January at present (and during the LGM). This made Northern Hemisphere summers warmer than today and the winters colder. The tilt of the earth was about 1 degree greater, further adding to increased seasonality and greater summer radiation for the Northern

Hemisphere. July solar radiation at 65°N reached its maximum positive anomaly around 9 ka when it was 7 percent greater than today. The remaining terrestrial ice sheets saw dramatic retreat, with the Laurentide Ice Sheet shrinking to a tiny remnant in Quebec-Labrador by about 6 ka. In Eurasia, northward flowing rivers had formed large proglacial lakes where they were dammed by the ice front, especially in the Ob basin. Their overflow southward during glacial retreat is thought to have caused mega-floods. Grossvald (1999) suggests these events occurred about 12, 10, and 7 ka. However, his model demands a much more extensive ice cover over northern Siberia than recent work would support.

The first half of the Holocene contained the most dramatic increase in temperatures. There was a 9°C increase in SST in the Greenland-Iceland-Norwegian seas causing summer air temperatures to be between 10–14°C and winter air temperatures between 4–9°C. An increased poleward flow of warm Atlantic water reached the Fram Strait by 9.5 ka (Koc, Jansen, and Hafildason, 1993). The influx of warm water affected atmospheric circulation and caused a reduced latitudinal temperature gradient and poleward expansion of the subtropical gyre.

The Holocene Thermal Maximum (HTM) was characterized by warmer than present conditions at many sites. D. Kaufman, T. Ager, and N. Anderson (2004) mapped the onset and termination of the HTM for North America based on a variety of paleoclimate evidence that primarily provide estimates of summer temperatures (Figure 10.10). At the terrestrial sites where quantitative estimates could be obtained, HTM summer temperatures were on average 1.6 C higher than twentieth-century averages. However, both the onset and termination of the HTM varied widely depending on location. Over northwest Canada and Alaska, onset of the HTM was quite early, generally between 11–9 ka, about 4,000 years earlier than for northeastern Canada. The later HTM onset over northeastern Canada is argued to reflect proximity to the chilling effects of the shrinking Laurentide Ice Sheet and influences of atmospheric and oceanic circulation. The pattern for the termination of the HTM over North America largely follows the pattern for onset; over Alaska, the HTM ended quite early, from between 11–9 ka, compared to as late as 3–4 ka over northeastern North America.

Boreal forest was present north of the modern treeline between 10 ka to 5 ka in western Canada, and 5 ka to 4 ka in central Canada but from 4 ka to 2 ka in eastern Canada (McDonald and Gajewski, 1992). However, in Alaska, the Holocene treeline never extended beyond its modern limit (Anderson and Brubaker, 1994). The period from about 6 ka to 4 ka saw the historical maximum amount of driftwood occurrence in the Canadian Arctic. As shown in Figure 10.11, the Aggasiz ice core from Ellesmere Island shows maximum pollen concentrations at about 3.1 ka (Bradley, 1990).

A notable event interrupting the overall warmth of the early- and mid-Holocene was a prominent cooling event dated at about 8.2 ka (Alley et al., 1997; Kobashi et al., 2007). It is generally believed that this was because of a large pulse of meltwater to the North Atlantic from glacial lakes Aggasiz and Ojibway, associated with the final collapse of the Laurentide Ice Sheet. It appears that average

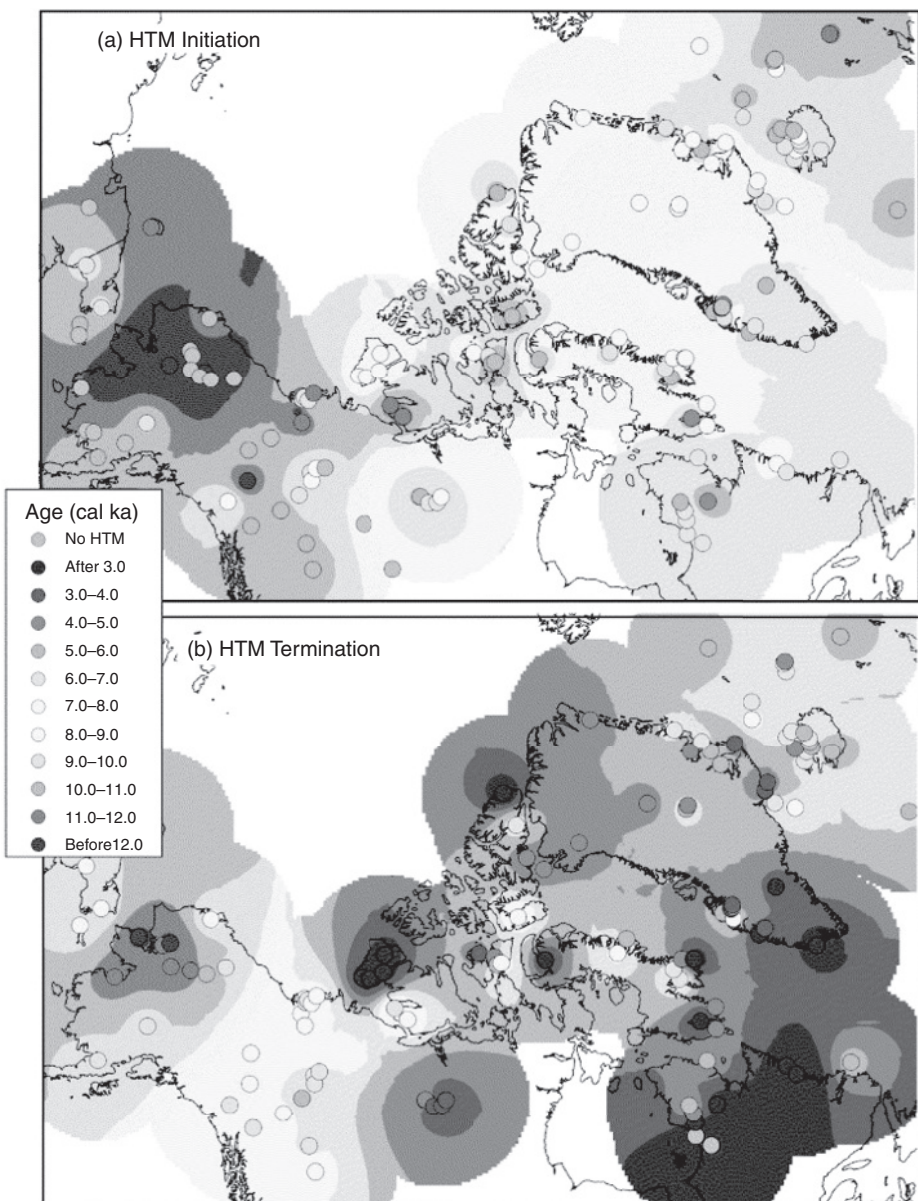


Figure 10.10. Onset (a) and termination (b) of the Holocene Thermal Maximum (ka, calendar years) based on a variety of paleoclimate data (from Kaufman et al., 2004, by permission of Elsevier). (See plate section for color version.)

temperatures in the Greenland region dropped by more than 3°C over a period of twenty years. Cold conditions lasted about 150 years. There is evidence for hemispheric-scale cooling and drying. Pointing again to amplifying climate feedbacks, the event was associated with declines in both global carbon dioxide and methane concentration.

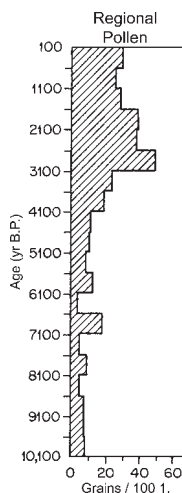


Figure 10.11. Regional pollen concentrations in the Aggasiz Ice Cap ice core A77 (from Bradley, 1990, by permission of Elsevier).

10.7.2 Late Holocene Cooling, Medieval Warm Period and the LIA

While the above evidence points to a generally warm climate in the first half of the Holocene, albeit with a notable 8.2 ka cooling event and a highly variable timing of the HTM depending on the region, conditions by about 5 ka were overall beginning to deteriorate. Atlantic water retreated southward to the central Greenland-Iceland-Norwegian seas and the cold East Greenland current strengthened. Average temperatures continued to drop through 3 ka. The Atlantic ceased to have significant influence on the GIN seas and the sea ice cover expanded (Koc et al., 1993).

Kaufman et al. (2009) synthesized a set of proxy records from lakes, tree rings and ice cores to assess the temperature history of the Arctic region over the past 2,000 years. Figure 10.12, the composite temperature time series for the Arctic as a whole, is representative of summer conditions. The key conclusion from this analysis is that a progressive cooling over the first 1,900 years of the record abruptly reversed during the twentieth century, with four of the five warmest decades occurring between the years 1950 and 2000. The cooling over the first 1,900 years of the temperature record is interpreted as a response to a steady reduction in northern hemisphere summer insolation (Milankovitch forcing) following the HTM. Within this 1,900-year long general cooling trend there are centennial scale fluctuations. Although not pronounced in the Arctic proxy records, there is evidence for both the Medieval Warm Period from about 900 to 1050 and the Little Ice Age (LIA) from about 1600 to 1850. Proxy synthesis for the Northern Hemisphere as a whole do not show the 1,900-year general cooling trend that is prominent in the Arctic analysis. A reconstructed time series of summer Arctic sea ice extent by C. Kinnard et al. (2011) for the past 1,450 years is broadly consistent with the reconstructed temperature record but contains some puzzling features. Notably, ice extent appears to have been reduced during the period of the LIA, which they argue may relate to advection of warm Atlantic water into the Arctic.

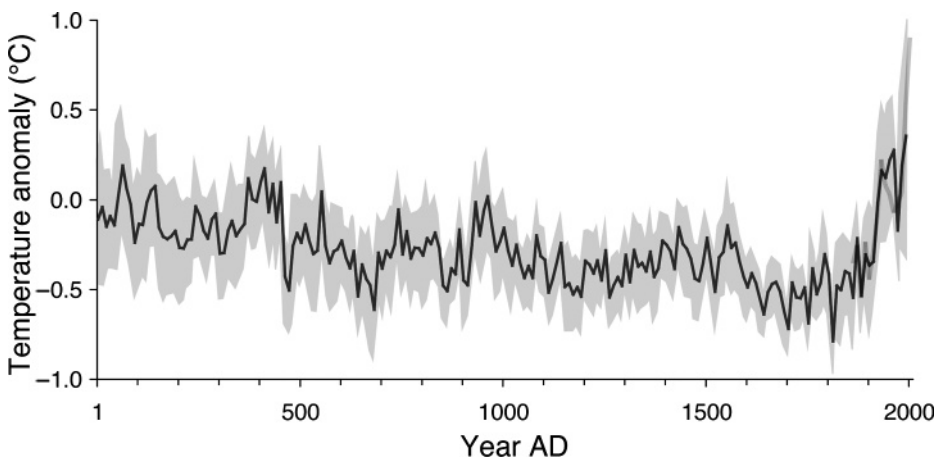


Figure 10.12. Arctic summer temperature anomalies for the past 2,000 years based on a variety of proxy sources. The black line shows a reconstruction of summer Arctic land temperatures over the past 2,000 years, based on a composite of twenty-three proxy records from lake sediments, ice cores, and tree rings relative to the 1961–1990 reference period. The shaded area represents variability among different Arctic sites. The gray line shows Arctic temperatures from the instrumental record (courtesy of D. Kaufman, Northern Arizona University, Flagstaff AZ, based on Kaufman et al. 2009). (See plate section for color version.)

During the Medieval Warm Epoch, surface air temperatures may have been higher than at the start of the twentieth century in some areas, such as Scandinavia and Greenland. Historical evidence includes records of crop planting in more northern latitudes than the present. However, the picture is still unclear. T. Hughes and H. Diaz (1994) give a useful review.

The LIA represents the most recent major cooling (Grove, 2004). Whereas in Figure 10.12, the LIA occurred from about 1600–1850, depending on the region and the analysis, it dated anywhere from AD 1250–1920 to AD 1550–1850 (Christiansen, 1998). It is clearly recorded in Greenland ice cores (Fischer et al., 1998). Records at GISP2 indicate that temperatures reached their lowest point in the past millennium between AD 1579 and 1730 (Kreutz, 1997). Temperatures in the northern to mid-latitudes dropped an average of 0.5 to 1.2°C. In Norway, advance and retreat histories of glaciers during the LIA seem to have varied according to distance of the glaciers from moisture sources (Benn and Evans, 1998).

Causes of the LIA are still somewhat uncertain. Solar variability likely played a role (e.g., Rind et al., 2004). The Maunder Minimum from AD 1680 to 1730 was a period of near absence of sunspots. Although low numbers of sunspots are known to reduce total solar output, changes in the ultraviolet part of the solar spectrum are proportionately much larger, invoking potential responses in both the stratospheric and tropospheric atmospheric circulation, and recent work points to feedbacks in the ocean-atmosphere system that can amplify the response to irradiance variations. J. Lean, J. Beer, and R. Bradley (1995) attribute most of the temperature

variability in the Northern Hemisphere from 1610 to 1800 to irradiance changes. Suspicion that volcanism played a role (e.g., Crowley, 2000) has recently gained additional support. Precisely dated records from Arctic Canada and Iceland show that ice growth began abruptly between the years 1275 and 1300, and intensified between the years 1430 and 1455, coinciding with two periods of intense explosive volcanism. Results from a climate model simulation suggest that while the volcanism itself caused summer cooling (through aerosol loading), cold summers can be maintained long after volcanic aerosols are removed through sea ice/ocean feedbacks (Miller et al., 2012).

10.7.3 The Twentieth Century and Beyond

The pattern of surface air temperature change from the twentieth century onward is widely viewed in terms of an overall upward trend linked to increasing concentrations of atmospheric greenhouse gases with superposed imprints of natural variability operating on a variety of timescales. Considerable attention has been paid to a period of strong Arctic warming that occurred from the 1920s to the 1940s (e.g., Overland et al., 2004; Polyakov et al., 2002; Serreze and Francis, 2006), followed by cooling through about 1970 and then renewed warming. Until recently, the maximum warmth of the 1920s–1940s event was comparable to temperatures observed today. As has been frequently pointed out (e.g., Serreze et al., 2000; Polyakov and Johnson, 2000; Polyakov et al., 2002; Semenov and Bengtsson, 2003, Chylek et al., 2009), such low frequency variability in the Arctic can greatly complicate separating natural fluctuations climate from those attributed to anthropogenic influences.

In being largely isolated to the northern high latitudes (although having a clear expression in the global mean), the earlier twentieth-century event is quite different from more recent warming, which essentially covers all latitudes (Serreze and Francis, 2006). Impacts of changing Atlantic heat transport to the Arctic reducing sea ice extent likely played an important role; this is supported by evidence that the warmth was strongest in the Atlantic sector and that it was most conspicuous during autumn and winter, at which time the effects of reduced ice cover on air temperature would be expected to be most pronounced. This in turn invokes links with altered patterns of atmospheric circulation (Bengtsson, Semenov, and Johannessen, 2004). However, the warming period did not coincide with a strongly positive phase of the NAO (Polyakov et al., 2009), as would be expected based on the conventional paradigm that a positive NAO fosters a stronger ocean heat transport into the Arctic. T.L. Delworth and T.R. Knutson (2000) attempted to explain the phenomenon using a coupled ocean-atmosphere climate model. They included observed, time-varying concentrations of greenhouse gases and sulfate aerosols in six realizations of 135-year duration. These runs were compared to those from a 1,000-year control simulation with a constant atmospheric composition. The warming event was reproduced by only one of the six realizations, suggesting a strong role of natural climate variability. But as warming events of this magnitude

were not seen in the control run, they concluded that greenhouse gases and sulfate aerosols may indeed have played a role.

As is seen in Figure 1.5 and discussed in Chapter 2, warming over past several decades, although largely global in its nature, has been larger in the Arctic as compared to the global or Northern Hemisphere average. This Arctic amplification appears to have several causes, including responses to reduced sea ice cover, altered cloud cover, and changes in atmospheric circulation. As discussed in Chapter 9 (see Figure 9.15) Arctic amplification is expected to become more prominent through the twenty-first century.

Focus Questions and Exercises

- 1) Why is it important to study paleoclimates?
- 2) Should the Younger Dryas be viewed as the last of the Dansgaard-Oeschger cycles? List some arguments for and against this view.
- 3) Why have Dansgaard-Oeschger cycles not been observed during the Holocene?

The Uncertain Future

Overview

The broad picture of Arctic change projected through the twenty-first century is a warming climate, with this warming outsized in comparison to the globe as a whole, and a continued reduction in sea ice extent in all seasons, but especially in summer and early autumn. We are also likely to see warming and thawing of permafrost, gradual replacement of tundra with shrub vegetation, a shorter snow-covered season and a modest increase in precipitation. The Greenland Ice Sheet will continue to lose mass, likely at an accelerating rate, contributing to sea level rise. This picture of the Arctic's future, however, is muddied by unknowns. The Arctic is home to strong natural variability in climate, and it would come as no surprise if the general trend toward warming was interrupted by decadal-scale periods of little temperature change or even cooling. There are unknowns with global or hemispheric-scale ramifications, key among these being the timing and strength of the permafrost carbon feedback, responses of the atmospheric circulation to sea ice loss, future rates of greenhouse gas emissions, and changes in aerosol concentration and type. A massive release of methane from seafloor sediments along the Arctic continental shelves appears to be a remote possibility. As the Arctic becomes more accessible, it is likely to see increased activity linked to development of oil and gas resources, shipping, and tourism, bringing economic benefits along with the danger of environmental degradation and disruption of traditional lifestyles. This brief closing chapter explores some of these issues.

11.1 Natural Climate Variability

Natural climate variations from day-to-day (weather), week-to-week, and within a season, stem largely from the internal dynamics of the atmosphere. This is seen in the passage of baroclinic shortwaves and their associated surface cyclones and anti-cyclones, and variations in the planetary waves. However, as we have seen, there can be low-frequency variability in atmospheric circulation modes (teleconnections) such as the NAO and its hemispheric-scale counterpart, the AO (Figure 4.21), having pronounced effects on Arctic climate (Figure 4.22). An overall trend in the winter behavior of the NAO or the AO, either toward its positive phase (such as occurred from about 1970 through the 1990s) or toward its negative phase (as was the case from about 1950 through 1970) may have strong imprints on spatial patterns of temperature trends through the twenty-first century, either adding to or subtracting from the general background warming expected from rising concentrations of atmospheric greenhouse gases. The same general statement holds for other patterns of atmospheric variability known to strongly affect Arctic climate, such as the PDO.

Aspects of natural atmospheric variability will almost certainly influence the evolution of the Arctic sea ice cover. As discussed in Chapter 7, there is evidence that the strong decline in end-of-summer sea ice extent reflects, in part, processes by which thinning of the ice cover via wind-driven transport of thick ice out of the Arctic through the Fram Strait during winter have worked in the same direction as thinning because of the overall warming. As such, an extended period with positive winter phase of the NAO or AO, which tends to be associated with strong pressure gradient across the Fram Strait (see Chapter 7), is likely to hasten the decline in summer ice extent.

By this reasoning, an extended negative phase should slow the ice loss. Past studies have shown that the wind pattern associated with the negative phase of the winter AO tends to favor retention of sea ice through the subsequent summer melt season. However, there is evidence that the rules are changing. For example, whereas the winter of 2009/2010 was characterized by an extreme negative phase of the AO, September 2010 sea ice extent nevertheless ended up quite low (fifth lowest in the satellite record through 2102). Although this unexpected response in part reflects pronounced differences in atmospheric circulation during the winter of 2009/2010 compared to the mean anomaly pattern based on past negative AO winters, contributing factors include both the reduced ice thickness at the start of the melt season, and that it is now so warm that multiyear ice transported into the southerly reaches of the Beaufort and Chukchi seas via the Beaufort Gyre circulation no longer circulates back into the central Arctic Ocean but rather melts out during summer (Stroeve et al., 2011a). Phrased differently, the Beaufort and Chukchi seas have become a graveyard for multiyear ice.

Recall also from Chapter 7 that, from the 1990s through the first decade of the twenty-first century, there has been an uneven process of increasing ocean heat

transport into the Arctic from Atlantic-layer waters which has been linked to the warm phase of the Atlantic Multidecadal Oscillation. It has been argued (e.g., Polyakov et al., 2010) that this has fueled a substantial additional heat flux to the bottom of the sea ice cover, contributing to thinning, in turn making the ice more vulnerable to disruption by extreme atmospheric events. Although the role of this extra Atlantic-layer heat on the observed evolution of the sea ice cover remains unresolved, the question also remains as to whether this change in ocean circulation represents natural low-frequency ocean variability or contains an anthropogenic influence. Analysis of paleoclimate evidence suggest that the early twenty-first century temperatures of Atlantic water entering the Arctic are unprecedented over the past 2,000 years (Spielhagen et al., 2011). The issue of natural variability versus forced change also holds with respect to evidence for a link between declining sea ice extent and thickness and warmer Pacific Surface Water entering the Arctic Ocean via the Bering Strait (Shimada et al., 2006).

The sun, of course, is the ultimate source of energy to the climate system. Space-borne measurements indicate that the solar constant ($\sim 1361.5 \text{ W m}^{-2}$) is not entirely constant. These data show a variation in the annual mean of about 1 W m^{-2} in total irradiance between the minimum and maximum of the eleven-year sunspot cycle, which has a discernible effect on global average temperatures. However, as discussed, there is evidence of periods with considerably larger changes in solar output, such as during the Maunder Minimum (sunspot minimum) from 1680 to 1730, and it is increasingly recognized that solar influences can be amplified within the climate system through changes in stratospheric and tropospheric atmospheric circulation and feedbacks in the ocean-atmosphere system (Lean, 2009). Although explosive volcanic activity is known to have impacts on climate, a period of volcanic activity working in conjunction with altered solar output and attendant climate feedbacks, could have strong climate influences.

11.2 Greenhouse Gas Growth and Aerosols

Another element of uncertainty surrounding the Arctic's future lies in the growth of greenhouse gas concentrations through the twenty-first century. Looking back to Figure 9.12, in terms of projected changes in surface air temperature, the growth rate scenario over the next twenty years or so is not especially important, the reason being that the spread in projected temperature change attributed to natural climate variability and model-to-model differences in sensitivity are as large as the spread attributed to the differences in climate forcing. The separation in projected temperatures between the scenarios becomes apparent later in the century. The same general statement can be made with respect to sea ice extent, which, as we have seen, responds sensitively to changes in winds linked to shifts in the phase of the NAO and other teleconnection patterns as well as changes in ocean circulation. The future rate of greenhouse gas emissions itself depends on many factors, including population growth, economic growth (particularly in developing countries such as

China and India), and the development and adoption of new technologies. Wild cards include feedbacks involving the release of carbon from terrestrial and subsea reservoirs in the Arctic, discussed in the next section.

Although aerosol forcing is a key uncertainty in climate change science, aerosol loading owing to incomplete combustion of fossil fuels is known, in a globally averaged sense, to be a cooling agent, offsetting some of the warming attributed to increasing greenhouse gas concentrations. As discussed in Chapter 2, aerosols have direct climate effects through scattering and absorption of solar radiation as well as a number of indirect effects linked to cloud albedo, amount, and lifetime that revolve around the role of aerosols as cloud condensation nuclei. Changes in combustion technologies and fuel sources (e.g., a shift from coal to natural gas or nuclear) will alter aerosol concentrations and types, and thereby affect the rate of climate warming. However, Arctic responses may be different than for the globe as a whole. Regarding aerosol direct effects, one must consider potential changes in the concentration of black carbon aerosols, which strongly absorb solar radiation, and hence unlike sulfate aerosols have a warming effect (Shindell and Faluvegi, 2009). A related issue is soot on snow, which reduces the surface albedo. Regarding aerosol indirect effects, it is important to remember that, in contrast to lower latitudes, and except for summer, the net cloud radiative forcing in the Arctic is positive. In other words, in the Arctic, clouds are not cooling agents but rather warming agents. This is because the impact of clouds on reducing the solar flux at the surface through their high albedo is outweighed by the increased longwave flux to the surface. Arctic cloud amount appears to be quite sensitive to a small increase in aerosol loading when aerosol concentrations are low (Mauritzen et al., 2011).

11.3 Feedbacks and Responses

There are questions regarding the nature and strength of climate feedbacks and how different feedbacks will interact with each other. As just discussed, Arctic cloud cover may be influenced by changes in aerosol concentration and type, but warming will also influence cloud amount and radiative properties, as well as the surface albedo because of changes in snow cover and sea ice extent. Whereas general warming will alter the frequency of mixed phase versus water phase clouds, cloud amount and radiative properties will likely themselves also be altered by an increase in open water. Based on analysis of numerous data sets over the 2006–2008 period, J. Kay and A. Gettleman (2009) find that whereas there has been no summer cloud response to declines in Arctic sea ice extent, low clouds do form over newly open water during autumn. They explain this in terms of the low static stability and strong air-sea temperature gradients during early autumn that promote large upward turbulent latent and sensible heat fluxes. This contrasts with summer, when near-surface stability is strong, and air-sea temperature gradients are small.

Cloud cover will also be influenced by changes in atmospheric circulation that represent responses to a warming climate. Although these may be attributed to

events external to the Arctic, there is growing recognition that changes within the Arctic, especially linked to sea ice extent and thickness, may alter patterns of atmospheric circulation both within and beyond the region (e.g., Francis et al., 2009; Overland and Wang, 2010, Francis and Vavrus, 2012). Whether such impacts have actually been observed remains highly controversial.

Albedo feedback has always been part of the Arctic sea ice system. In response to spring warmth, dark melt ponds form and bare ice is exposed, fostering further ice melt because of the reduction in albedo. Dark open water areas that form readily absorb solar energy, fostering melt of surrounding ice. Without this albedo feedback, the amplitude of the seasonal cycle in sea ice extent would be smaller than is observed. The downward trend in September ice extent has in part been attributed to a growing importance of the albedo feedback (e.g., Perovich et al., 2007; Stroeve et al., 2011b). This is because of the transition to an Arctic ice pack dominated by thinner, first-year ice. Thus, open water areas are exposed earlier in the melt season and become more extensive throughout summer, further accentuating summer ice melt.

Concerns have been raised over the existence of a sea ice “tipping point” involving albedo feedback. The idea is that as the climate warms and the spring sea ice cover thins to some critical value, a strong kick from natural climate variability (from either the ocean or the atmosphere) could induce a reduction in sea ice extent sufficiently large to set the albedo feedback process into high gear. As a result, the path of a general downward trend in summer ice cover would be interrupted by sudden plunge, hastening the slide to a seasonally ice-free ocean. S. Tietsche et al. (2011) examined the tipping point argument via a series of coupled global climate model experiments. They started with reference simulations for the twenty-first century using the A1B greenhouse-gas emissions scenario. September ice cover in these simulations was found to typically disappear by the year 2070. They then conducted a new set of runs, whereby every twenty years through the twenty-first century they artificially removed the entire sea ice cover on July 1. Instead of maintaining ice-free conditions, ice extent in September recovered to values typical of the reference simulations within a couple of years, even in the warmer later parts of the century. As expected, with ice-free summers, the ocean picks up a great deal of extra heat, delaying autumn ice growth. They argue that if there was a sea ice tipping point, this summer heat gain would lead to an ice cover the following spring that is thin enough to completely melt out over the following summer. Instead, their simulations showed that so much ocean heat is lost during polar winter that enough ice grows to survive the next summer’s melt. In other words, the strong polar winter cooling acts as a strong negative feedback. Their interpretation of these results is that there is no sea ice tipping point.

What actually transpires in the twenty-first century of course remains to be seen. One issue germane to how the sea ice cover will evolve is the observation that ocean heat gained in summer from the surface from absorption of solar radiation can be stored in the Arctic Ocean in a near surface layer (25–35 m) through the winter season. Via storm-driven winter mixing, it appears that some of this heat can be used

to melt sea ice (Jackson et al., 2010). Other issues include impacts of increased Atlantic layer inflow on winter ice growth and changes in cloud cover that alter the surface radiation budget, all of which are very difficult to model. Interestingly, ocean heat loss in autumn and winter, while representing a negative feedback with respect to the ice loss, is an important part of the observed process of Arctic amplification (the ocean loses heat, which is expressed as an atmospheric heat gain). At issue is the extent to which, via atmospheric circulation, the effects of ice loss on heating of the lower atmosphere are spread beyond the areas of ice loss to inhibit ice growth or to warm surrounding land areas.

An uncertainty with global ramifications is the permafrost carbon feedback discussed in Chapter 9. The rate of anthropogenic carbon emissions through the twenty-first century is of course relevant as this bears on the rate of terrestrial permafrost warming and thaw. As just discussed, the rate of warming over land may also be influenced by the rate of sea ice loss (Lawrence and Slater, 2005). As also discussed in Chapter 9, a common feature of global climate model simulations of the twenty-first century is an increase in precipitation over northern high latitudes. Coupled with warming, it is reasonable to expect more winter snowfall but a shorter snow-covered seasonal overall. Snow cover is an insulator. This implies that permafrost warming will be hastened not only by high surface air temperatures in summer, putting more heat into the soil column, but by a reduction in winter heat loss from the soil column attributed to the increased insulating effect of a deeper winter snowpack. A complicating issue is how reduced sea ice extent will contribute to changes in Arctic precipitation, both through influences on atmospheric circulation patterns and by providing an additional moisture source.

There has been speculation regarding the possibility of a massive and rapid methane release from Arctic submarine sediments along continental shelves that were exposed during past periods of lower sea level. Under the proper temperature and pressure conditions, methane produced by microbial activity can become trapped in these sediments in a solid (hydrate) form (i.e., as an ice). The concern is that with ocean warming, these hydrates will warm, melt, and lead to a release of methane to the atmosphere. As methane is a powerful greenhouse gas, such a release would lead to further climate warming. G. Westbrook et al. (2009) document numerous plumes of gas bubbles of predominantly methane emanating from the seabed of the West Spitzbergen continental margin. Some of the plumes were observed to extend upwards to within 50 m of the surface before dissolving into the water column. They argue that this methane release can be linked to warming of the northward-flowing West Spitzbergen Current over the past several decades that has reduced the extent of the gas hydrate stability zone, which is a function of both pressure and temperature. A subsequent modeling study lends support to this conclusion (Reagan and Moridis, 2009). N. Shakhova et al. (2010) argue that a release to the atmosphere of only a small fraction of methane held in hydrate form along the East Siberian Arctic shelf region (the Laptev, East Siberian, and Russian part of the Chukchi seas) could trigger an abrupt climate warming. They highlight that more than 5,000 at-sea observations collected during six ship cruises between the years

2003 and 2008 point to dissolved methane concentrations in these coastal waters that are supersaturated with respect to the atmosphere, implicating a seabed source. A subsequent observational study (Shakova et al., 2013) lends further credence to the view of the East Siberian shelf as an important region of methane release, but highlights the importance of direct transport to the atmosphere as bubbles. Through mixing processes, the passage of storms appears to enhance the bubble-associated methane release. They argue that as sea ice extent declines and winds have a longer fetch over open water, this storm-induced mixing will become more pronounced.

However, the prevailing view is that an alarmist attitude is unwarranted. Global methane levels increased up until the late 1990s, and then leveled off. Although levels then started to rise again in 2007, there is little evidence that this jump was because of melting hydrates or thawing terrestrial permafrost. Methane stopped increasing in the Northern Hemisphere in 2008. Arctic methane release is likely to happen fairly slowly, as it takes time for the oceans to warm and for that warmth to penetrate into the hydrates. The methane then has to get through the thick sediments (Kerr, 2010).

11.4 Human Responses to a Changing Arctic

The future is likely to see considerable disruption of traditional Arctic lifestyles. The reasons are many, and include impediments to travel because of changing sea ice and snow conditions, changes in the abundance, location, and habits of species harvested by indigenous peoples, and changing economics. Indeed, as marine access improves, the Arctic is likely to become a much busier place than today, with strategic implications for Canada, Denmark, Norway, Russia, and the United States, in particular (AMSA, 2009). The shelf seas of the Arctic Ocean in particular hold considerable reserves of oil and natural gas that remain to be exploited but will become more accessible as the ice-free season in these areas grows in length and winter ice conditions become milder. Milder ice conditions will also make it easier to exploit hard minerals. Supporting these activities will naturally lead to an increase in ship traffic. There has been considerable discussion regarding prospects for increased commercial shipping across the Arctic Ocean via the Northwest Passage or the Northern Sea Route (Figure 1.1) and there have been numerous ship passages in recent years to demonstrate the viability of these routes.

A reliable Arctic Ocean shortcut might attract increased tourism along with commercial shipping, but economic viability is very much open to question. First, for the foreseeable future, there will be substantial winter sea ice, meaning that these passages will be open only on a seasonal basis. Because of strong interannual variability in Arctic climate, for decades to come, these passages are unlikely to be open every year. Second, Arctic maritime infrastructure is at present inadequate and would require substantial investment, including aids to navigation, port facilities, icebreaking escort, ship tracking, oil spill prevention and response, environmental monitoring, and search and rescue capabilities. Another issue is competition – by

the year 2015, the Panama Canal is slated to have a new set of locks and other improvements that will allow it to handle more traffic and larger ships.

11.5 Concluding Remarks

The broad picture of Arctic change through the twenty-first century seems clear. Building on the introduction to this chapter, the Arctic will become warmer than today, and the rate of warming will be larger than that for the globe as a whole, especially in autumn and winter. Sea ice will continue to decline in extent and thickness, helping, along with other processes, to fuel the outsized warming of the Arctic. Like air temperature, the change will not be steady, but will instead appear as an overall trend with strong imprints of natural variability. The Arctic Ocean is likely to become essentially free of sea ice in late summer by sometime in the middle or later part of the century but perhaps earlier. Over land, there will be a gradual replacement of tundra with shrub vegetation, and a shorter snow-covered season. It appears that total precipitation will increase, which will likely be seen as increased river discharge to the Arctic Ocean. The Greenland Ice Sheet will continue to lose mass, likely at an accelerating rate.

However, as we have learned, not just in this chapter, but throughout this book, the future holds many uncertainties. Reducing these uncertainties represents a major challenge. Although coupled global climate models represent one of our most important tools for understanding how the climate system will evolve through the twenty-first century, they still have many shortcomings, particularly with respect to projections on the regional scale. As just one example, although many of the CMIP3 models produce patterns of atmospheric variability that resemble the NAO, AO, PNA, PDO, and ENSO, there are significant biases in the temporal and spatial characteristics of the patterns – many models either under or over represent the strength of the patterns or incorrectly place the location of the teleconnection “centers of action” (Stoner et al., 2009). This is a fundamental problem in the Arctic, where such modes of variability are known to have strong imprints on climate and are likely to strongly shape the evolution of the system. Also at issue are deficiencies in model representations of the surface energy budget, ocean-sea ice-climate interactions, and associated feedbacks. The future of the Greenland Ice Sheet and its contribution to sea level rise is especially difficult to project because changes in climate and oceanic conditions may then lead to changes in ice sheet dynamics involving backpressure effects, basal lubrication, and other factors (Chapter 8).

Better understanding the future course of the Arctic climate system certainly requires improved models, but it is also increasingly necessary to break down traditional disciplinary barriers and develop a more system oriented approach. The Arctic is the home of myriad climate interactions and feedbacks involving the atmosphere, land, ocean, and cryosphere, which are in turn tightly coupled to the global climate system. But it seems that the more we understand how the Arctic

functions, the more questions we raise. Herein lies our continued fascination with the Arctic climate system.

Focus Questions and Exercises

- 1) What do you view as the most important factor driving uncertainty as to when the Arctic Ocean may become seasonally free of sea ice?
- 2) Do you think that Arctic cloud cover will change over the twenty-first century? Why? How would these changes affect other parts of the Arctic climate system?
- 3) It has been argued that increased ship traffic in the Arctic will accelerate loss of the sea ice cover. Is this argument valid?

References

- Aagaard, K. and Carmack, E.C. [1989]. The role of sea ice and other fresh waters in the Arctic circulation. *J. Geophys. Res.* **94**(C10), 14485–14498.
- Abdalati, W. and Steffen, K. [1995]. Passive microwave-derived snow melt regions on the Greenland Ice Sheet. *Geophys. Res. Lett.* **22**, 787–790.
- [1997]. Snowmelt on the Greenland Ice Sheet as derived from passive microwave satellite data. *J. Climate* **10**, 165–175.
- [2001]. Greenland Ice Sheet melt extent: 1979–1999. *J. Geophys. Res.* **106**(D24), 33983–33988.
- Arctic Climate Impact Assessments (ACIA) [2005]. *Impacts of a Warming Climate: Arctic Climate Impact Assessment*. Cambridge: Cambridge University Press.
- Agnew, T.A., Le, H., and Hirose, T. [1997]. Estimation of aggregate-scale sea ice motion from SSM/I 85 Ghz imagery. *Ann. Glaciol.* **25**, 305–311.
- Albright, M. [1980]. Geostrophic wind calculations for AIDJEX. In: R.S. Pritchard (ed.), *Sea Ice Processes and Models*. Seattle: University of Washington Press, pp. 402–409.
- Alexander, M.A., Bhatt, U.S., Walsh, J.E., Timlin, M.S., Miller, J.S., and Scott, J.P. [2004]. The atmospheric response to realistic Arctic sea ice anomalies in an AGCM during winter. *J. Climate* **17**, 890–905.
- Alexandrova, V. [1970]. The vegetation of the tundra zones in the USSR and data about its productivity. In: W.A. Fuller and P.G. Kevan (eds.), *Productivity and Conservation in Northern Circumpolar Lands*. Morges, Switzerland: Int. Union Conserv. Nature Res., IUCN Publication No. 16, pp. 93–114.
- Alexeev, V.A., Ivanov, V.V., Kwok, K., and Smedsrud, L.H. [2013]. North Atlantic warming and declining volume of Arctic sea ice. *The Cryosphere Discussions* **7**, 245–265, doi:10.5194/tcd-7-245-2013.
- Alley, R. B., Anandakrishnan, S., and Jung, P. [2001]. Stochastic resonance in the North Atlantic. *Paleoceanography* **16**, 190–198.

- Alley, R.B., Dupont, T.K., Parizek, B.R. et al. [2006]. Ourburst flooding and the initiation of ice-stream surges in response to climatic cooling: A hypothesis. *Geomorphology* **75**, 76–89, doi:10.1016/j.geomorph.2004.01.011.
- Alley, R.B., Mayewski, P.A., Sowers, T., Stuiver, M., Taylor, K.C., and Clark, P.U. [1997]. Holocene climatic instability: A prominent widespread event 8200 years ago. *Geology* **25**, 483–486.
- Alley, R.B., Meese, D.A., Schuman, C.A. et al. [1993]. Abrupt increase in Greenland snow accumulation at the end of the Younger Dryas event. *Nature* **362**, 527–529.
- Alt, B.T. [1975]. *The Energy Balance Climate of Meighen Ice Cap, N.W.T.* Polar Continental Shelf Project, Energy, Mines and Resources, Canada. Vol. 1.
- Alt, B.T., Labine, C. L., Atkinson, D. E., and Wolfe, P.M. [2000]. Automatic weather station results from Fosheim Peninsula, Ellesmere Island, Nunavut. *Geol. Surv. Canada Bull.* **529**, 37–97.
- Ambaum, M.H.P. and Hoskins, B.J. [2002]. The NAO troposphere-stratosphere connection. *J. Climate* **15**, 1969–1978.
- Ambaum, M.H.P., Hoskins, B.J., and Stephenson, D.B. [2001]. Arctic Oscillation or North Atlantic Oscillation? *J. Climate* **14**, 3495–3507.
- Ananjeva, G.V. [2000]. Study of the distribution of lakes in Russian Arctic with the use of GIS technologies. *Kriosfera Zemli* **4**, 67–73.
- Anderson, D.L. [1961]. Growth rate of sea ice. *J. Glaciol.* **3**, 1170–1172.
- Anderson, P.M. and Brubaker, L.B. [1994]. Vegetation history of North Central Alaska: A mapped summary of Late Quaternary pollen data. *Quatern. Sci. Rev.* **13**, 71–92.
- Anderson, R., Boville, B., and McClellan, D.E. [1955]. An operational frontal contour analysis model. *Quart. J. Roy. Met. Soc.* **81**, 588–599.
- Andreas, E. L., Miles, M. W., Barry, R.G., and Schnell, R. C. [1990]. Lidar-derived particle concentrations in plumes from Arctic leads. *Ann. Glaciol.* **14**, 9–12.
- Andreas, E. L., Paulson, C.S., Williams, R.M., Lindsay, R.W., and Businger, J.A. [1979]. The turbulent heat flux from Arctic leads. *Boundary Layer Meteorol.* **17**, 57–91.
- Andrews, D.G., Holton, J.R., and Leovy, C.B. [1987]. *Middle Atmosphere Dynamics*. Orlando, FL: Academic Press.
- Arbatskaya, M.K. and Vaganov, E.A. [1997]. Long-term variation in fire frequency and radial increment in pine from the middle taiga subzone of central Siberia. *Russian Journal of Ecology* **28**, 291–297.
- Arctic Climatology Project [1997]. *Environmental Working Group Joint U.S.-Russian Atlas of the Arctic Ocean – Winter Period*. L. Timokhov and F. Tanis (eds). Ann Arbor, MI: Environmental Research Institute of Michigan with the National Snow and Ice Data Center, CD-ROM.
- [1998]. *Environmental Working Group Joint U.S.-Russian Atlas of the Arctic Ocean – Summer Period*. L. Timokhov and F. Tanis (eds). Ann Arbor, MI: Environmental Research Institute of Michigan with the National Snow and Ice Data Center, CD-ROM.
- [2000]. *Environmental Working Group Arctic Meteorology and Climate Atlas*. F. Fetterer and V. Radionov (eds.) National Snow and Ice Data Center, Boulder CO, CD-ROM.
- Arctic Marine Shipping Assessment (AMSA) [2009]. *Arctic Marine Shipping Assessment 2009 Report*. Arctic Council, April 2009, second printing.

- Armstrong, T.E. [1952]. *The Northern Sea Route. Soviet Exploitation of the Northeast Passage*. Cambridge: Cambridge University Press.
- [1984]. In search of a northern sea-route to Siberia, 1553–1619. *Arctic* **37**, 429–440.
- [1995]. The Soviet Northern Sea Route. *Geogr. Rev.* **121**, 136–148.
- Arnell, N.W. [1995]. Grid mapping of river discharge. *J. Hydrol.* **167**, 39–56.
- Badgley, R. I. [1966]. Heat budget at the surface of the Arctic Ocean. In: J.O. Fletcher (ed.), *Proceedings of the Symposium on the Arctic Heat Budget and Atmospheric Circulation, Memo. RM-5233-NSF*. Santa Monica, CA: Rand Corp., pp. 267–277.
- Baer, K.E. [1838]. On the ground ice or frozen soil of Siberia. *J. Roy. Geog. Soc.* **8**, 210–213.
- Baldwin, M.P. and Dunkerton, T.J. [1999]. Propagation of the Arctic Oscillation from the stratosphere to the troposphere. *J. Geophys. Res.* **104**, 30937–30946.
- [2001]. Stratospheric harbingers of anomalous weather regimes. *Science* **294**, 581–584.
- Bales, R.C., McConnell, J.R., Mosley-Thompson, E., and Csatho, B. [2001]. Accumulation over the Greenland Ice Sheet from historical and recent records. *J. Geophys. Res.* **106**(D24), 33813–33825.
- Ballinger, T.J., Schmidlin, T.W., and Steinhoff, D.F. [2013]. The polar marine climate revisited. *Journal of Climate* **26**, 3935–3952.
- Bamber, J.L., Layberry, S.F., and Gogineni, S.P. [2001]. A new ice thickness and bed data set for the Greenland Ice Sheet. *J. Geophys. Res.* **106**(D24), 33773–33780.
- Barker, S., Diz, P., Vautravers, M.J. et al. [2009]. Interhemispheric Atlantic seesaw response during the last glaciation.
- Nature* **457**, 1097–1103, doi:10.1038/nature07770.
- Barnston, A.G. and Livezy, R.E. [1987]. Classification, seasonality and persistence of low-frequency atmospheric circulation patterns. *Mon. Wea. Rev.* **115**, 1083–1126.
- Barr, W. [1978]. The voyage of the *Sibiryakov*, 1932. *Polar Record* **19**, 253–266.
- [1985]. *The Expeditions of the First International Polar Year*. Tech. Paper No. 29. Calgary: Arctic Institute of North America.
- [1991]. The Arctic Ocean in Russian History to 1945. In: L.W. Brigham (ed.), *The Soviet Maritime Arctic*. Annapolis, MD: Naval Institute Press, pp. 11–32.
- Barrie, L.A., Bottenheim, J.W., Schnell, R.C., Crutzen, R.C., and Rasmussen, R.A. [1988]. Ozone destruction and photochemical reactions at polar sunrise in the lower Arctic atmosphere. *Nature* **334**, 138–141.
- Barrow, J. [1818]. *A Chronological History of Voyages into the Arctic Regions* (1818). London: John Murray (reprinted 1971, New York: Barnes and Noble).
- Barry, R.G. [1966]. Meteorological aspects of the glacial history of Labrador-Ungava with special reference to vapor transport. *Geogr. Bull.* **8**, 319–340.
- [1967]. Seasonal location of the Arctic front over North America. *Geogr. Bull.* **9**, 79–95.
- [1996]. The parameterization of surface albedo for sea ice and its snow cover. *Progress in Physical Geography* **20**, 63–79.
- [2008]. *Mountain Weather and Climate*. New York: Cambridge University Press.
- Barry, R.G. and Carleton, A.M. [2001]. *Synoptic and Dynamic Climatology*. London: Routledge.

- Barry, R.G. and Gan, T.Y. [2011]. *The Global Cryosphere: Past, Present and Future*. Cambridge: Cambridge University Press.
- Barry, R.G., Courtin, G.M., and Labine, C. [1981]. Tundra climates. In: L.C. Bliss, A.W. Heal, and J. Moore (eds.), *Tundra Ecosystems: A Comparative Analysis*. Cambridge: Cambridge University Press, pp. 81–114.
- Barry, R.G., Crane, R.G., Schweiger, A., and Newell, J. [1987]. Arctic cloudiness in spring from satellite imagery. *Int. J. Climatol.* **7**, 428–451.
- Barry, R.G. and Jackson, C.I. [1969]. Summer weather conditions at Tanquary Fiord, N.W.T. 1963–67. *Arct. Alp. Res.* **1**, 169–180.
- Barry, R.G. and Kiladis, G.N. [1982]. Climatic characteristics of Greenland. In: U. Radok (ed.), *Climatic and Physical Characteristics of the Greenland Ice Sheet*, Vol. 1. Boulder: Cooperative Institute for Research in Environmental Sciences, University of Colorado, pp. 7–33.
- Barry, R.G., Moritz, R.E., and Rogers, J.C. [1979]. The fast ice regimes of the Beaufort and Chukchi Sea coasts, Alaska. *Cold Regions Sci. Technol.* **1**, 129–152.
- Barry, R.G., Serreze, M.C., Maslanik, J.A., and Preller, R.H. [1993]. The Arctic sea-ice climate system: Observations and modeling. *Rev. Geophys.* **31**, 397–422.
- Beesley, J.A. and Moritz, R.E. [1999]. Toward an explanation of the annual cycle of cloudiness over the Arctic Ocean. *J. Climate* **12**, 395–415.
- Belkin, I.M., Levitus, S., Antonov, J., and Malmberg, S.A. [1998]. The “Great Salinity BEDMAP 2.” <http://www.bbc.co.uk/news/science-environment-21692423>
- Belov, M.I. [1969]. *Istoriya Otkrytiya Osvoyeniya Severnogo Morskogo Puti*.
- IV. 1933–1945. (History of the Discovery and Exploitation of the Northern Sea Route. IV. 1933–1945). Leningrad: Gidrometeoizdat.
- Bender, G. [1984]. *The Distribution of Snow Accumulation on the Greenland Ice Sheet, M.S. Thesis*. Fairbanks, AK: Geophysical Institute, University of Alaska. [Available from Geophysical Institute, University of Alaska, P.O. Box 7555780, Fairbanks, AK 99775–5780].
- Bengtsson, L., Semenov, V.A., and Johannessen, O.M. [2004]. The early twentieth-century warming in the Arctic – a possible mechanism. *J. Climate* **17**, 4045–4057.
- Benn, D.I. and Evans D.J.A. [1998]. *Glaciers and Glaciation*. London: Arnold.
- Benson, C.S. [1969]. *The Seasonal Snow Cover of Arctic Alaska*. Arctic Institute of North America Technical Report No. 51. Calgary, Alberta: Arctic Institute of North America.
- [1970]. *Ice Fog. Low Temperature Air Pollution Defined with Fairbanks, Alaska as Type Locality*. CRREL Research Report 121. US Army, Cold Regions Research and Engineering Laboratory, Hanover, New Hampshire.
- Benson, C.S. and Bowling, S.A. [1975]. The sub-Arctic heat island as studied at Fairbanks, Alaska. In: Weller and Bowling, S.A. (eds.), *Climate of the Arctic*, Fairbanks, Alaska: Geophysical Institute, University of Alaska, pp. 309–311.
- Beringer, J., Tapper, N.J., McHugh, I. et al. [2001]. Impact of Arctic treeline on synoptic climate. *Geophys. Res. Lett.* **28**, 4247–4250.
- Betts, A.K. [2000]. Offset of the potential carbon sink from boreal forestation by decreases in surface albedo. *Nature* **408**, 187–190.

- Bhatt, U.S., Walker, D.A., Reynolds, M.K. et al. [2010]. Circumpolar Arctic tundra vegetative change is linked to sea ice decline. *Earth Interactions* **14**, 1–20.
- Bilello, M.A. [1957]. A survey of Arctic snow-cover properties as related to climatic conditions. *Res. Rep. 39*. Hanover, New Hampshire: U.S. Army CRREL.
- Birks, H.H., Paus, A., Svendsen, J.I., Alm, T., Mangerud, J., and Landvik, J.Y. [1994]. Late Weichselian environmental change in Norway, including Svalbard. *J. Quatern. Sci.* **9**, 133–145.
- Bitz, C.M., Battisti, D.S., Moritz, R.E., and Beesley, J.A. [1996]. Low-frequency variability in the Arctic atmosphere, sea ice and upper-ocean climate system. *J. Climate* **9**, 394–408.
- Blanchet, J-P., and Girard, E. [1995]. Water vapour-temperature feedback in the formation of continental Arctic air: Implication for climate. *Sci. Total. Environ.* **160/161**, 793–802.
- Bliss, L.C. [1997]. Arctic ecosystems of North America. In: F.E. Wielgolaski (ed.), *Polar and Alpine Tundra, Ecosystems of the World*, Vol. 3. Amsterdam: Elsevier, pp. 551–683.
- Blyth, J.D.M. [1951]. German meteorological activities in the Arctic, 1940–1945. *Polar Record* **6**, 185–226.
- Bojkov, R.D. and Fiolotov, V.E. [1995]. Estimating the global ozone characteristics during the last 30 years. *J. Geophys. Res.* **100**(D8), 16537–16551.
- Bonan, G.B. [1995]. Sensitivity of a GCM simulation to inclusion of inland water surfaces. *J. Climate* **8**, 2691–2704
- [2008]. Forests and climate change: Forcings, feedbacks, and the climate benefits of forests. *Science* **320**, 1444–1449, doi:10.1126/science.1155121.
- Bonan, G.B., Chapin, F.S. III, and Thompson, S.L. [1995]. Boreal forest and tundra ecosystems as components of the climate system. *Climatic Change* **29**, 145–167.
- Bonan, G.B., Pollard, D., and Thompson, S.L. [1992]. Effects of boreal forest vegetation on global climate. *Nature* **359**, 716–718.
- Bond, G., Broecker, W., Johnsen, S. et al. [1993]. Correlations between climate records from North Atlantic sediments and Greenland ice. *Nature* **365**, 143–147.
- Bond, G.C., Kromer, B., Beer, J. et al. [2001]. Persistent solar influence on North Atlantic climate during the Holocene. *Science* **294**, 2130–2136.
- Bond, G. C. and Lotti, R. [1995]. Iceberg discharges into the North Atlantic on millennial time scales during the last glaciation. *Science* **267**, 1005–1010.
- Bond, G.C., Showers, W., Cheseby, M. et al. [1997]. A pervasive millennial-scale cycle in North Atlantic Holocene and glacial climates. *Science* **278**, 1257–1266.
- Borisov, A.A. [1975]. *Klinaty SSSR v Proshlom, Nastoyashchimi i Budushchimi*. (Climates of the USSR, Past, Present and Future). Leningrad: Leningrad University.
- Borodachev, B.E. and Shil'nikov, V. I. [2002]. *Istoriya L'dovoi Aviatsionnoi Razvedki v Arktike na Zamerzayushchikh Moryakh Rossii (1914–1993 gg.)*. (The History of Aerial Ice Reconnaissance in the Arctic and Ice-covered Seas of Russia, 1914–1993). St. Petersburg: Gidrometeoizdat.
- Bourgeois, Q. and Bey, I. [2011]. Pollution transport efficiency toward the Arctic: Sensitivity of aerosol scavenging and source regions. *J. Geophys. Res.* **116**, D08213, doi: 10.1029/2010JD015096.

- Bourke, R.H. and Garrett, R.P. [1987]. Sea ice thickness distribution in the Arctic Ocean. *Cold Reg. Sci. Technol.* **13**, 259–280.
- Bourke, R.H. and McLaren, A.S. [1992]. Contour mapping of Arctic Basin ice draft and roughness parameters. *J. Geophys. Res.* **97**(C11), 17715–17728.
- Boville, B.W., MacFarlane, M.A. and Steiner, H.A. [1959]. An Atlas of Stratospheric Circulation, October 1958 – March 1959. In: *Arctic Meteorology Research Group, Publication in Meteorology* No. 37. Montreal, Canada: McGill University, Defense Research Board, Department of National Defense.
- Bovis, M.J. and Barry, R.G. [1974]. A climatological analysis of north polar desert areas. In: T.L. Smiley and J.H. Zumberge (eds.), *Polar Deserts and Modern Man*. Tucson, AZ: University of Arizona Press, pp. 23–31.
- Bowling, L.C., Lettenmaier, D.P., and Matheussen, B.V. [2000]. Hydroclimatology of the Arctic drainage basin. In: E.L. Lewis et al. (eds.), *The Freshwater Budget of the Arctic Ocean*. Dordrecht, the Netherlands: Kluwer Academic Publishers, pp. 57–90.
- Bowling, L.C., Lettermaier, D.P., Nijssen, B. et al. [2003]. Simulation of hydrologic responses in the Torne-Kalix basin: PILPS Phase 2(e) 1: Experiment description and summary intercomparisons. *Global and Planetary Change* **38**, 1–30.
- Bowling, S.A. [1986]. Climatology of high-latitude air pollution as illustrated by Fairbanks and Anchorage, Alaska. *J. Clim. Appl. Meteor.* **25**, 22–34.
- Box, J.E. and Rinke, A. [2003]. Evaluation of Greenland Ice Sheet surface climate in the HIRHAM regional climate model using automatic weather station data. *J. Climate* **16**, 1302–1319.
- Box, J.E. and Steffen, K. [2001]. Sublimation on the Greenland Ice Sheet from automated weather station observations. *J. Geophys. Res.* **106**(D24), 33965–33981.
- Bradley, R.S. [1990]. Holocene paleoclimatology of the Queen Elizabeth Islands, Canadian High Arctic. *Quatern. Sci. Rev.* **9**, 365–384.
- Bradley, R.S., [1999]. *Paleoclimatology: Reconstructing Climates of the Quaternary*. San Diego, CA: Academic Press.
- Bradley, R.S. and Serreze, M.C. [1987]. Topoclimate studies of a high Arctic plateau ice cap. *J. Glaciol.* **33**, 149–158.
- Bridgman, H.A., Schnell, R.C., Kahl, J.D., Herbert, G.A., and Joranger, E. [1989]. A major haze event near Point Barrow, Alaska: Analysis of probable source regions and transport pathways. *Atmos. Environ.* **23**, 2537–2549.
- Brinkman, W. and Barry, R.G. [1972]. Paleoclimatological aspects of the synoptic climatology of Keewatin, Northwest Territories, Canada. *Paleogeogr., Paleoclimatol., Paleoecol.* **11**, 87–91.
- Broecker, W.D. [1990]. Salinity history of the northern Atlantic during the last glaciation. *Paleoceanography* **5**, 459–457.
- Broecker, W.S. [2006]. Was the Younger Dryas triggered by a flood? *Science* **312**, 1146–1148, doi:10.1126/science.1123253.
- Broecker, W.S., Bond, G., Klas, M. Bonani, G., and Wolfi, W. [1990]. A salt oscillator in the glacial North Atlantic? 1. The concept. *Paleoceanography* **5**, 469–477.
- Broecker, W.S., Kennett, J.P., Flower, B.P. et al. [1989]. Routing of meltwater from the Laurentide Ice Sheet during the Younger Dryas episode. *Nature* **341**, 318–321.

- Bromwich, D., Kuo, Y-H., Serreze, M. *et al.* [2010]. Arctic System Reanalysis: Call for community involvement. *Eos Trans. Amer. Geophys. Union* **91**, 13, doi:10.1029/2010EO020001.
- Bromwich, D.H., Chen Q-S., Bai, L-S., Cassano, E.N., and Li, Y. [2001b]. Modeled precipitation variability over the Greenland Ice Sheet. *J. Geophys. Res.* **106**(D24), 33891–33908.
- Bromwich, D. H., Keen, R.A., and Bolzan, J.F. [1993]. Modeled variations of precipitation over the Greenland Ice Sheet. *J. Climate* **6**, 1253–1268.
- Bromwich, D.H., Toracinta, E.R., Oglesby, R.J., Fastook, J.L., and Hughes, T.J. [2005]. LGM summer climate on the southern margin of the Laurentide Ice Sheet: Wet or dry? *J. Climate* **18**, 3317–3338, doi: <http://dx.doi.org/10.1175/JCLI3480.1>.
- Bromwich, D.H., Toracinta, E.R., and Wang, S-H. [2002]. Meteorological perspectives on the initiation of the Laurentide Ice Sheet. *Quaternary International* **95–96**, 113–124.
- Bromwich, D.H., Toracinta, E.R., Wei, H., Oglesby, R.J., Fastook, J.L., and Hughes, T.J. [2004]. Polar MM5 simulations of the winter climate of the Laurentide Ice Sheet at the LGM. *J. Climate* **17**, 3415–3433, doi: [http://dx.doi.org/10.1175/1520-0442\(2004\)017<3415:PMSOTW>2.0.CO;2](http://dx.doi.org/10.1175/1520-0442(2004)017<3415:PMSOTW>2.0.CO;2).
- Brooks, C.E.P. [1931]. The vertical temperature gradient in the Arctic. *Meteorology Magazine* **66**, 267–268.
- Brown, J., Ferrians, O.J. Jr., Heginbottom, A.J. and Melnikov, S.E. [1997]. *Circum-Arctic Map of Permafrost and Ground-Ice Conditions*. U.S. Geological Survey Circum-Pacific Map Series, CP-45.
- Brubaker, K.L., Entekhabi, D., and Eagleson, P.S. [1993]. Estimation of continental-scale precipitation recycling. *J. Climate* **6**, 1077–1089.
- Bryan, K. [1969]. Climate and the ocean circulation, III, The ocean model. *Mon. Weather Rev.* **97**, 806–827.
- Bryson, R.A. [1966]. Air masses, stream lines, and the boreal forest. *Geogr. Bull.* **8**, 228–269.
- Bulatov, V. and Popov, G. [1996]. Novaya Zemlya: Myfy I real'nost'. In: V.F. Tolkachev (ed.), *Terra Incognita Arktik*. Archangelsk: Pomorskogo Mezhdunarodnogo Pedagogicheskii Universitet, pp. 5–68.
- Busch, N., Ebel, U., Kraus, H., and Schaller, E. [1982]. The structure of the subpolar inversion-capped ABL. *Arch. Met. Geophys. Bioklim.* **31A**, 1–18.
- Businger, S. and Reed, R.J. [1989]. Cyclogenesis in cold air masses. *Weather and Forecasting* **4**, 133–156.
- Carleton, A.M. [1996]. Satellite climatological aspects of cold air mesocyclones in the Arctic and Antarctic. *Global Atmos. Ocean. Syst.* **5**, 1–42.
- Carmack, E.C. [1990]. Large-scale physical oceanography of polar oceans. In: W.O. Smith Jr. (ed.), *Polar Oceanography, Part A, Physical Science*. San Diego, CA: Academic Publishers, pp. 171–222.
- Carroll, J.J. and Fitch, B.W. [1981]. Effects of solar elevation and cloudiness on snow albedo at the South Pole. *J. Geophys. Res.* **86**, 5271–5276.
- Cassano, J. J., Higgins, M.E., and Seefeldt, M.W. [2011]. Performance of the Weather Research and Forecasting (WRF) model for month-long pan-Arctic simulations. *Mon. Wea. Rev.* **139**, 3469–3488, <http://dx.doi.org/10.1175/MWR-D-10-05065.1>.
- Cassau, C. and Terray, L. [2001]. Dual role of Atlantic and Pacific SST anomalies on the North Atlantic/Europe winter climate. *Geophys. Res. Lett.* **30**, 3195–3198.
- Catchpole, A.J.W. and Faurer, M.A. [1983]. Summer sea ice severity in Hudson

- Strait, 1751–1850. *Climatic Change* **5**, 115–139.
- Central Intelligence Agency (CIA) [1978]. *Polar Regions Atlas*. Produced by National Foreign Assessment Center, Central Intelligence Agency.
- Chapin, F.S. III, Matson, P.A., and Mooney, H.A. [2000]. *Principles of Terrestrial Ecosystem Ecology*. New York: Springer Verlag.
- Charlier, R.H. [1969]. The geographic distribution of polar desert soils in the northern hemisphere. *Geol. Soc. Amer. Bull.* **80**, 1985–1996.
- Charney, J., Hale, M., and Jastrow, R. [1969]. Use of incomplete historical data to infer the present state of the atmosphere. *J. Atmos. Sci.* **26**, 1160–1163.
- Chartrand, D.J., de Grandpere, J., and McConnell, J.C. [1999]. An introduction to stratospheric chemistry. *Atmosphere-Ocean* **37**, 309–367.
- Chase, T.N., Herman, B., Peilke, R.S. Sr., Zeng, X., and Leuthold, M. [2002]. A proposed mechanism for the regulation of minimum midtropospheric temperatures in the Arctic. *J. Geophys. Res.* **107**(D14), doi: 10.1029/2001JD001425.
- Chen, Q.S., Bromwich, D.H., and Bai, L. [1997]. Precipitation over Greenland retrieved by a dynamic method and its relation to cyclonic activity. *J. Climate* **10**, 839–870.
- Chernov, Y.I. and Matveyeva, N.V. [1997]. Arctic Ecosystems in Russia. In: F.E. Wielgolaski (ed.), *Polar and Alpine Tundra Ecosystems of the World*, Vol. 3. Amsterdam: Elsevier, pp. 361–507.
- Choudhury, B.J. and Chang, A.T.C. [1981]. The albedo of snow for partially cloudy skies. *Boundary Layer Meteorol.* **20**, 371–389.
- Christiansen, H.H. [1998]. ‘Little Ice Age’ nivation activity in northeast Greenland. *The Holocene* **8**, 719–728.
- Chylek, P., Folland, C.K., Lesins, G., Dubey, M.K., and Wang, M.-Y. [2009]. Arctic air temperature change amplification and the Atlantic Multidecadal Oscillation. *Geophys. Res. Lett.* **36**, L14801, doi:10.1029/2009GL038777.
- Clark, C.D., Knight, J.K., and Gray, J.T. [2000]. Geomorphological reconstruction of the Labrador sector of the Laurentide Ice Sheet. *Quatern. Sci. Rev.* **19**, 1343–1366.
- Clark, D.L. [1982]. Origin, nature and world climate effect of the Arctic Ocean ice cover. *Nature* **300**, 321–325.
- Clark, D.L. and Grantz, A. [2002]. Piston cores improve understanding of deep Arctic Ocean. *Eos Trans. Amer. Geophys. Union* **83**, 417, 422–423.
- Clark, P.U., Marshall, S.J., Clarke, G.K., Hostettler, S.W., Liccardi, J.M., and Teller, J.T. [2001]. Freshwater forcing of abrupt climate change during the last Glaciation. *Science* **293**, 283–287.
- Clark, P.U., Pisias, N.G., Stocker, T.F., and Weaver, A.J. [2002]. The role of the thermohaline circulation in abrupt climate change. *Nature* **415**, 863–869.
- Clein, J.S., Kwiatkowski, B.L., McGuire, A.D. et al. [2000]. Modeling carbon responses of tundra ecosystems to historical and projected climate: A comparison of a plot-and global-scale ecosystem model to identify process-based uncertainties. *Global Change Biology* **6** (Supplement 1), 127–140.
- Cohen, J. and Entekhabi, D. [1990]. Eurasian snow cover variability and Northern Hemisphere climate predictability. *Geophys. Res. Lett.* **26**, 345–348.
- Cohen, J., Saito, K. and Entekhabi, D. [2001]. The role of the Siberian High in Northern Hemisphere climate variability. *Geophys. Res. Lett.* **28**, 299–302.

- Colony, R., Radionov, V., and Tanis, F.L. [1998]. Measurements of precipitation and snow pack at the Russian North Pole drifting stations. *Polar Record* **34**, 3–14.
- Compo, G.P., Whitaker, J.S., Sardeshmukh, P.D. et al. [2011]. The Twentieth Century Reanalysis Project, *Quart. J. Roy. Meteor. Soc.*, **137**, 1–28, doi: 10.1002/qj.776.
- Cook, E.R., D'Arrigo, R.D., and Briffa, K.R. [1998]. A reconstruction of the North Atlantic Oscillation using tree-ring chronologies from North America and Europe. *Holocene* **8**, 9–17.
- Courtin, G.H. and Labine, C.L. [1977]. Microclimatological studies of the Truelove Lowland, Devon Island, Northwest Territories. In: L.C. Bliss (ed.), *Truelove Lowland, Devon Island, Canada, a High Arctic Ecosystem*. Edmonton: University of Alberta Press, pp. 73–106.
- Crowley, T.J. [2000]. Causes of climate change over the past 1000 years. *Science* **289**, 270–276.
- Cuffey, K.M. and Marshall, S.J. [2000]. Substantial contribution to sea-level rise during the last interglacial from the Greenland Ice Sheet. *Nature* **404**, 591–594.
- Cullather, R.I., Bromwich, D.H., and Serreze, M.C. [2000]. The atmospheric hydrologic cycle over the Arctic basin from reanalyses. Part I: Comparison with observations and previous studies. *J. Climate* **13**, 923–937.
- Cullather, R.I. and Lynch, A.H. [2003]. The annual cycle and interannual variability of atmospheric pressure in the vicinity of the North Pole. *Int. J. Climatol.* **23**, 1161–1183.
- Curry, J. [1983]. On the formation of polar continental air. *J. Atmos. Sci.* **40**, 2278–2292.
- Curry, J.A. and Ebert, E.E. [1992]. Annual cycle of radiation fluxes over the Arctic Ocean: Sensitivity to cloud optical properties. *J. Climate* **5**, 1267–1280.
- Curry, J.A., Ebert, E.E., and Herman, G.F. [1988]. Mean and turbulent structure on the summertime Arctic cloudy boundary layer. *Quart. J. Roy. Met. Soc.* **114**, 715–746.
- Curry, J. A., Meyer, F.G., Radke, L.F., Brock, C.A., and Ebert, E.E. [1990]. Occurrence and characteristics of lower tropospheric ice crystal in the Arctic. *Int. J. Climatol.* **10**, 749–764.
- Curry, J. A., Rossow, W.B., Randall, D., and Schramm, J.L. [1996]. Overview of Arctic cloud and radiative characteristics. *J. Climate* **9**, 1731–1764.
- Curry, J.A., Schramm, J.L., and Ebert, E.E. [1995]. On the ice albedo climate feedback mechanism. *J. Climate* **8**, 240–247.
- Cushman, S.A. and Wallin, D.O. [2002]. Separating the effects of environmental, spatial and disturbance factors on forest community structure in the Russian Far East. *Forest Ecology and Management* **168**, 201–215.
- Danielsen, E.F. [1968]. Stratospheric-tropospheric exchange based on radioactivity, ozone and potential vorticity. *J. Atmos. Sci.* **25**, 502–518.
- Danilov, I.D. [1989]. Geological and paleoclimatic evolution of the Arctic during Late Cenozoic time. In: Y. Herman (ed.), *The Arctic Seas. Climatology, Oceanography, Geology, and Biology*. New York: Van Nostrand, Reinhold, pp. 759–760.
- Danilov, I.L. [2000]. Arkticheckii Okean kak faktor globalnykh klimaticheskikh izmenenii. (The Arctic Ocean as a factor in global climate). In: *Global Variations of the Environment (Climate and Water Regime)* (in Russia). Moscow: Nauchny Mir, pp. 91–121.

- Dansgaard, W., Johnsen, S.J., Clausen, H.B., and Langway, C.C., Jr., [1971]. Climatic record revealed by the Camp Century ice core. In: K.K. Tuckian (ed.), *The Late Cenozoic Glacial Age*. New Haven, CT: Yale University Press, pp. 37–56.
- Dansgaard, W., White, J.W.C., and Johnsen, S.J. [1989]. The abrupt termination of the Younger Dryas event. *Nature* **339**, 532–534.
- Dawson, H.P. [1886]. *Observations of the International Polar Expedition, Fort Rae*. London: Eyre and Spottiswoode.
- Dee, D. P., Uppala, S.M., Simmons, A.J. et al. [2011]. The ERA-Interim reanalysis: Configuration and performance of the data assimilation system. *Quart. J. Roy. Meteor. Soc.* **137**, 553–597, doi: 10.1002/qj.828.
- Defant, F. and Taba, H. [1957]. The threefold structure of the atmosphere and the characteristics of the tropopause. *Tellus* **9**, 259–274.
- Delworth, T.L. and Knutson, T.R. [2000]. Simulation of early 20th century global warming. *Science* **287**, 2246–2250.
- Denton, G.H. and T. Hughes (eds.) [1981]. *The Last Great Ice Sheets*. New York: John Wiley and Sons.
- Derksen, C. and Brown, R. [2012]. Spring snow cover extent reductions in the 2008–2012 period exceeding climate model projections. *Geophys. Res. Lett.* **39**, L19504, doi:10.1029/2012GL053387.
- Dery, S.J. and Wood, E.F. [2005]. Decreasing river discharge in northern Canada. *Geophys. Res. Lett.* **32**, L10401, doi: 10.1029/2005GL022845.
- Desborough, C.E. [1999]. Surface energy balance complexity in GCM land surface models. *Clim. Dynam.* **15**, 389–403.
- Deser, C. [2000]. On the teleconnectivity of the “Arctic Oscillation.” *Geophys. Rev. Lett.* **27**, 779–782.
- Deser, C., Magnusdottir, G., Saravanan, R., and Phillips, A. [2004]. The effects of North Atlantic SST and sea ice anomalies on the winter circulation in CCM3. Part II: Direct and indirect components of the response. *J. Climate* **17**, 877–889.
- Deser, C., Walsh, J.E., and Timlin, M.S. [2000]. Arctic sea ice variability in the context of recent atmospheric circulation trends. *J. Climate* **13**, 617–633.
- DeVeer, G. [1876]. *The Three Voyages of Willem Barents to the Arctic Regions*. London: Hakluyt Society.
- de Vernal, A. and Hillaire-Marcel, C. [2000]. Sea ice cover, sea surface salinity and halo-1 thermocline structure of the northwest North Atlantic: modern values versus full glacial conditions. *Quatern. Sci. Rev.* **19**, 65–85.
- Dickson, R.R., Meincke, J., Malmberg, S.A., and Lee, A.J. [1988]. The “Great Salinity Anomaly” in the northern North Atlantic, 1968–1982. *Progress in Oceanography* **20**, 103–151.
- Dickson, R.R., Osborn, T.J., Hurrell J.W. et al. [2000]. The Arctic Ocean response to the North Atlantic Oscillation. *J. Climate* **13**, 2671–2696.
- Ding, Y-H. [1990]. Build-up, air mass transformation and propagation of the Siberian High and its relation to cold surges in East Asia. *Met. Atmos. Phys.* **44**, 281–292.
- Dingman, S.L., Barry, R.G., Weller, G., Benson, C., LeDrew, E., and Goodwin, C. [1980]. Climate, snow cover, microclimate and hydrology. In: J. Brown et al. (eds.), *An Arctic Ecosystem: the Coastal Tundra at Barrow, Alaska*. Stroudsburg, PA: Dowden, Hutchinson and Ross, pp. 30–65.
- Ditlevsen, P.D., Svensmark, H., and Johnsen, S. [1996]. Contrast in atmospheric and climate dynamics of the last-glacial and Holocene periods. *Nature* **379**, 810–813.

- Dong, X., Baike, Xi, Crosby, K., Long, C.N., Stone, R.S., and Shupe, M.D. [2010]. A 10 year climatology of Arctic cloud fraction and radiative forcing at Barrow, Alaska. *J. Geophys. Res.* **115**, D17212, doi: 10.1029/2009JD013489.
- Dorsey, H.G. Jr., [1945]. Some meteorological aspects of the Greenland Ice Cap. *J. Meteor.* **2**, 135–142.
- Doyle, J.D. and Shapiro, M.A. [1999]. Flow response to large-scale topography: The Greenland tip jet. *Tellus* **51**, 728–748.
- Duchkov, A.D. and Balobaev, V.T. [2001]. Geothermal studies of permafrost response to global natural changes. In: R. Paeppe and V. Melnikov (eds.), *Permafrost Response on Economic Development, Environmental Security and Natural Resources*. Dordrecht, the Netherlands: Kluwer Academic Publishers, pp. 317–332.
- Dukhovsky, D.S., Johnson, M.A., and Proshutinsky, A. [2004]. Arctic decadal variability: An auto-oscillatory system of heat and fresh water exchange. *Geophys. Res. Lett.* **31**, L03302, doi: 10.1029/2003GL019023.
- Dunbar, M. and Dunbar, M.J. [1972]. The history of the North Water. *Proc. Roy. Soc. Edinburgh* **B72**, 231–241.
- Dyke, A.S., Dredge, L.A., and Vincent, J-S. [1982]. Configuration and dynamics of the Laurentide Ice Sheet during the late Wisconsin maximum. *Geogr. Phys. Quaternaire* **36**, 5–14.
- Dymond, J. and Wales, W. [1770]. Observations on the state of the air, winds, weather, etc. made at Prince of Wales Fort, on the North-West coast of Hudson Bay. *Phil. Trans.* **60** (Royal Society, London) 137–177.
- Dyurgerov, M.B. and Meier, M.F. [1997]. Year-to-year fluctuation of global mass balance of small glaciers and their contribution to sea level changes. *Arctic and Alpine Research* **29**, 392–402.
- Dzerdzevskii, B.L. [1945]. *Tsirkulatsionnye skhemy v troposfere Tsentralnoi Arktike*. (Circulation Schemes for the Central Arctic Troposphere) Izdat. Akad. Nauk SSSR (Transl. In Sci, Rep. No.3, Contract AF 19 (122)-128, Meteorology Dept., University of California, Los Angeles).
- Eastman, R. and Warren, S.G. [2010a]. Interannual variations of Arctic cloud types in relations to sea ice. *J. Climate* **23**, 4216–4232, doi:10.1175/2010JCLI3492.1.
- [2010b]. Arctic cloud changes from surface and satellite observations. *J. Climate* **23**, 4233–4241, doi: 10.1175/2010JCLI3544.1.
- Edwards, M.E., Mock, C.J., Finney, B.P., Barber, V.A., and Bartlein, P.J. [2001]. Potential analogues for paleoclimatic variations in eastern interior Alaska during the past 14,000 yr: Atmospheric circulation controls of regional temperature and moisture responses. *Quatern. Sci. Rev.* **20**, 189–202.
- Ehlers, J. and Gibbard, P.L. [2003]. Extent and chronology of glaciations. *Quatern. Sci. Rev.* **22**, 1561–1568.
- Elias, S.A., Short, S.K., Nelson, C.H., and Birks, H.H. [1996]. Life and times of the Bering Land Bridge. *Nature* **382**, 60–63.
- Elk, M.B., Mitchell, K.E., Lin, Y. et al. [2003]. Implementation of NOAH land surface model advances in CEP operational Eta model. *J. Geophys. Res.* **108**, 8851, doi:10.1029/2002JD003296.
- Elliott-Fisk, D.L. [1983]. The stability of the northern Canadian tree limit. *Ann. Assoc. Amer. Geogr.* **73**, 560–576.
- Eltahir, E.A.B. and Bras, R.L. [1996]. Precipitation recycling. *Rev. Geophys.* **34**, 367–378.
- Emanuel, K.A. and Rotunno, R. [1989]. Polar lows as Arctic hurricanes. *Tellus* **41A**, 1–17.

- Emery, W.J., Fowler, C.W., and Maslanik, J.A. [1997]. Satellite-derived maps of Arctic and Antarctic sea ice motion: A new multi-year record of ice transport. *Geophys. Res. Lett.* **24**, 897–900.
- England, J. [1999]. Coalescent Greenland and Innuitian ice during the Last Glacial Maximum: Revising the Quaternary of the Canadian High Arctic. *Quatern. Sci. Rev.* **18**, 421–456.
- England, J., Atkinson, N., Bernardsk, J., Dyke, A.S., Hodgson, D.A. and Cofaigh, C.O. [2006]. The Innuitian Ice Sheet: Configuration, dynamics and chronology. *Quatern. Sci. Rev.* **25**, 689–703.
- European Project for Ice Coring in Antarctica (EPICA) Community Members [2004]. Eight glacial cycles from an Antarctic ice core. *Nature* **429**, 623–628.
- Ettema, J., van den Broeke, M.R., van Meijgaard, E. et al. [2009]. Higher surface mass balance of the Greenland Ice Sheet revealed by high-resolution climate modeling. *Geophys. Res. Lett.* **36**, L12501, doi:10.1029/2009GL038110.
- Ezer, T., Mellor, G.L., and Greatbatch, R.G. [1995]. On the interpentadal variability of the North Atlantic Ocean: Model simulated changes in transport, meridional heat flux, and coastal sea level between 1955–1959 and 1970–1974. *J. Geophys. Res.* **100**, 10559–10566.
- Fanning, A.F. and Weaver, A.J. [1997]. Temporal-geographical meltwater influences on the North Atlantic conveyor: implications for the Younger Dryas event. *Paleoceanography* **12**, 307–320.
- Farmer, G.L., Barber, D.C., and Andrews, J.T. [2003]. Provenance of late Quaternary ice proximal sediments in the North Atlantic: Nd, Sr and Pd isotopic evidence. *Earth Planet. Sci. Lett.* **209**, 227–243.
- Field, W.O. (ed.) [1975]. *Mountain Glaciers of the Northern Hemisphere* (2 Vols.). Hanover, NH: U.S. Army CRREL.
- Fischer, H., Werner, M., Wagenbach, D. et al. [1998]. Little Ice Age clearly recorded in northern Greenland ice cores. *Geophys. Res. Lett.* **25**, 1749–1752.
- Fisher, R.H. [1984]. The early cartography of the Bering Strait region. *Arctic* **37**, 574–589.
- Fisheries and Environment Canada [1978]. *Hydrological Atlas of Canada*. Ottawa, Canada: Fisheries and Environment Canada, Minister of Supply and Services.
- Flato, G. M. and Hibler, W.D. III [1992]. Modeling pack ice as a cavitating fluid. *J. Phys. Oceanogr.* **22**, 626–651.
- Fleming, G. H. and Semtner, A.J. Jr. [1991]. A numerical study of interannual forcing on Arctic ice. *J. Geophys. Res.* **96**(C3), 4589–4603.
- Fleming, J.A. (ed.) [1907]. *The Ziegler Polar Expedition 1903–1905: Scientific Results Obtained Under the Direction of William J. Peters*. Washington, DC: National Geographic Society (Section C, pp. 369–487).
- Flint, R.F. [1943]. Growth and decay of the North American Ice Sheet during the Wisconsin age. *Bull. Amer. Geol. Soc.* **54**, 325–362.
- Fluckinger, J., Knutti, R., and White, J.W.C. [2006]. Oceanic processes as potential trigger and amplifying mechanisms for Heinrich events. *Paleoceanography* **21**, PA2014, doi:10.1029/2005PA001204.
- Foley, J.A., Kutzbach, J.E., Coe, M.T., and Levis, S. [1994]. Feedbacks between climate and boreal forests during the Holocene Epoch. *Nature* **371**, 52–54.
- Francis, J.A., Chan, W-H., Leathers, D.J., Miller, J.R., and Veron, D.E. [2009]. Winter Northern Hemisphere weather patterns remember summer.

- Geophys. Res. Lett.* **36**, L07503, doi:10.1029/2009GL037274.
- Francis, J.A. and Hunter, E. [2006]. New insight into the disappearing Arctic sea ice. *Eos Trans. Amer. Geophys. Union* **87**, 509–524.
- Francis, J.A. and Vavrus, S.J. [2012]. Evidence linking Arctic amplification to extreme weather in mid-latitudes. *Geophys. Res. Lett.* **39**, L06801, doi:10.1029/2012GL051000.
- Franklin, J. [1828]. *Narrative of a Second Expedition to the Shores of the Polar Sea in the Years 1825, 1826 and 1827*. London: John Murray (reprinted Rutland, Vermont, 1971).
- French, H.M. [2007]. *The Periglacial Environment*, 3rd edition. New York: J. Wiley.
- Frey, K.E., Perovich, D.K., and Light, B. [2011]. The spatial distribution of solar radiation under a melting Arctic sea ice cover. *Geophys. Res. Lett.* **38**, L22501, doi:10.1029/2011GL049421.
- Fyfe, J.C. [2003]. Separating extratropical zonal wind variability and mean change. *J. Climate* **16**, 863–874.
- Gadbois, P. and Laverdiere, C. [1954]. Esquisse geographique de la region de Floeberg Beach, nord de l'isle Ellesmere. *Geogr. Bull.* **6**, 17–44.
- Gaigerov, S.S. [1967]. *Aerology of the Polar Regions* (Moscow, 1964). Jerusalem: Israel Program of Scientific Translations.
- Gakkel, Y.Y. and Chernenko, M.B. [1959]. *Sovetskoye Arkitckoye Moreplavaniye 1917–1932 gg. Istoryya Otkrytiya I. Osvoyeniya Severnogo Morskogo Puti, III*. (Soviet Arctic Navigation 1917–1932. History of the Discovery and Exploitation of the Northern Sea Route, Vol. 3). Leningrad: Morsko Transport.
- Galloway, J.L. [1958]. The three-front model: Its philosophy, nature, construction and use. *Weather* **13**, 395–403.
- Ganopolski, A. and Rahmsdorf, S. [2001]. Rapid changes of glacial climate simulated in a coupled climate model. *Nature* **409**, 153–158.
- Garrett, T.J. and Verzella, L.L. [2008]. Looking back: An evolving history of Arctic aerosols. *Bull. Amer. Meteorol. Soc.* **89**, 299–302, doi:10.1175/BAMS-89-3-299.
- Gavrilov, A.V. [2001]. Geocryological mapping of Arctic shelves. In: R. Paepe and V. Melnikov (eds.), *Permafrost Response on Economic Development, Environmental Security and Natural Resources*. Dordrecht, the Netherlands: Kluwer Academic Publishers, pp. 69–86.
- Gerrard, A.J., Kane, T.L., Thayer, J.P., Duck, T.J., Whiteway, J.A., and Fielder, J. [2002]. Synoptic scale study of the Arctic polar vortex's influence on the middle atmosphere. 1. Observations. *J. Geophys. Res.* **107**(D16), doi:10.1029/2001JD000681.
- Ghil, M. and Malanotte-Rizzoli, P. [1991]. Data assimilation in meteorology and oceanography. *Adv. Geophys.* **33**, 141–266.
- Glazovsky, A.F. 2003. Glacier changes in the Russian Arctic. In: *Papers and Recommendations: Snow Watch 2002 Workshop and Assessing Global Glacier Recession. Glaciol. Data Report GD-32*. NSIDC/WDC for Glaciology, Boulder, pp. 78–82.
- Golubchikov, Y.N. [1996]. *Geografiya Gornykh i Polyarnikh Stran. (The Geography of Mountain and Polar Lands)*. Moscow: Moscow University Press.
- Goodrich, L.E. [1982]. Efficient numerical technique for one-dimensional thermal

- problems with phase change. *Int. J. of Heat and Mass Transfer* **21**, 615–621.
- Govorukha, L.S. [1988]. *Sovremennoe Nazemnoe oledenie Sovyetskoi Arktiki. (Modern Terrestrial Glaciation of the Soviet Arctic)*. Leningrad: Gidrometeoizdat.
- Gow, A.J. and Tucker, W.B. III [1987]. Physical properties of sea ice discharge from Fram Strait. *Science* **236**, 236–439.
- Greatbatch, R.J., Fanning, A.F., Goulding, A.D., and Levitus, S. [1991]. A diagnosis of interpentadal circulation changes in the North Atlantic. *J. Geophys. Res.* **96**, 22009–22023.
- Greely, A.W. [1896]. *Three Years of Arctic Service. An Account of the Lady Franklin Bay Expedition of 1881–84 and the Attainment of the Farthest North* vols. 1 and 2. New York: Charles Scribner's Sons.
- Groisman, P.Y., Koknaeva, V.V., Belokrylova, T.A., and Karl, T.R. [1991]. Overcoming biases of precipitation: A history of the USSR experience. *Bull. Amer. Meteorol. Soc.* **72**, 1725–1733.
- Grønæs, S. and Kvamstø, N.G. [1995]. Numerical simulations of the synoptic conditions and development of Arctic outbreak polar lows. *Tellus* **47A**, 797–814.
- Grootes, P.M. and Stuiver, M. [1997]. Oxygen 18/16 variability in Greenland snow and ice with 103-to-105 year time resolution. *J. Geophys. Res.* **102**, 26455–26470.
- Grossvald, M.G. [1980]. Late Weichselian Ice Sheet of northern Eurasia. *Quatern. Res.* **13**, 1–32.
- [1999]. *Evraziiskie Gidrosvernye Katastrofy I Oledenie Arktiki (Eurasian Hydrospheric Catastrophes and the Glaciation of the Arctic)*. Moscow: Nauchnu Mir.
- Grossvald, M.G. and Hughes, T.J. [1999]. The case for an ice shelf in the Pleistocene Arctic Ocean. *Polar Geog.* **23**, 23–54.
- Grove, J.M. [2004]. *The Little Ice Ages: Ancient and Modern*. 2nd Edition. London/New York: Routledge.
- Gyakum, J.R. [2000]. Moisture transports to Arctic drainage basins relating to significant precipitation events and cyclogenesis. In: E.P. Jones, P. Lemke, T.D. Prowse, and P. Wadhams (eds.), *The Freshwater Budget of the Arctic Ocean. NATO Science Series 2. Environmental Security – Vol. 70*. Dordrecht, the Netherlands: Kluwer Academic Publishers, pp. 1978–2008.
- Hagglund, M.G. and Thompson, H.A. [1964]. *A Study of Sub-zero Canadian Temperatures*. Memoir No. 16, Meteorological Branch, Department of Transport, Canada.
- Hahn, C.J., Warren, S.G., and London, J. [1995]. The effect of moonlight on observations of cloud cover at night and application to cloud climatology. *J. Climate* **8**, 1429–1446.
- Häkkinen, S. [1993]. An Arctic source for the Great Salinity Anomaly: A simulation of the Arctic ice-ocean system for 1955–1975. *J. Geophys. Res.* **98**(C9), 16397–16410.
- [1999]. A simulation of thermohaline effects of a Great Salinity Anomaly. *J. Climate* **12**, 1781–1795.
- Hansen, J. and Nazarenko, L. [2003]. Soot climate forcing via snow and ice albedo. *Proc. Nat. Acad. Sci.*, www.pnas.org/doi/10.1073/pnas.2237157100.
- Hammer, C., Mayewski, P. A., Peel, D., and Stuiver, M. [1997]. Preface. Greenland Summit ice cores. Greenland Ice Sheet Project 2/Greenland Ice Core Project. *J. Geophys. Res.* **102** (C12), 26315–26316.

- Hare, F.K. [1958]. Weather and Climate. In: G.H. Kimble and D. Good (eds.), *Geography of the Northlands*. New York: The American Geographical Society and John Wiley and Sons, Inc., pp. 58–83.
- [1960a]. The disturbed circulation of the Arctic stratosphere. *J. Meteor.* **17**, 36–51.
- [1960b]. The summer circulation of the Arctic stratosphere below 30 km. *Quart. J. Roy. Met. Soc.* **86**, 127–146.
- [1961]. *The Circulation of the Stratosphere*. Publication in Meteorology No. 43. Montreal, Canada: Arctic Meteorology Research Group, McGill University.
- [1968]. The Arctic. *Quart. J. Roy. Met. Soc.* **94**, 439–459.
- Hare, F.K. and Orvig, S. [1958]. *The Arctic Circulation: A Preliminary View*. Arctic Meteorology Research Group, Publication in Meteorology, No. 12. Montreal, Canada: McGill University.
- Hare, F.K. and Ritchie, J.C. [1972]. The boreal microclimates. *Geog. Rev.* **62**, 333–365.
- Hare, S.R. and Mantua, N.J. [2000]. Empirical evidence for North Pacific regime shifts in 1979 and 1989. *Progress in Oceanography* **47**, 103–145.
- Harris, J.M. and Kahl, J.D. [1994]. An analysis of ten-day isentropic flow patterns for Barrow, Alaska. *J. Geophys. Res.* **99**, 25845–25856.
- Harris, S.A. [2001]. Sequence of glaciations and permafrost events. In: R. Paepe and V. Melnikov (eds.) *Permafrost Response on Economic Development, Environmental Security and Natural Resources*. Dordrecht, the Netherlands: Kluwer Academic Publishers, pp. 227–252.
- Hartmann, B.H. and Wendler, G. [2003]. The significance of the 1976 Pacific climate shift on the climatology of Alaska. *J. Climate* **18**, 4824–4839.
- Hartmann, D.L., Wallace, J.M., Limpasuvan, V., Thompson, D.W.J., and Holton, J.R. [2000]. Can ozone depletion and global warming interact to produce rapid climate change? *Proc. Nat. Acad. Sci.* **97**, 1412–1417.
- Hastings, A.D. Jr. [1961]. *Atlas of the Arctic Environment*. Natick, MA: U.S. Army Rep. R-33, HQ Quartermaster Res. Eng. Command.
- Hattersley-Smith, G. [1974]. *North of Latitude Eighty. The Defense Research Board in Ellesmere Island*. Ottawa, Canada: Defense Research Board.
- Hattersley-Smith, G., Crary, A.P., and Christie, R.L. [1955]. Northern Ellesmere Island, 1953 and 1954. *Arctic* **8**, 2–36.
- Hayes, J.D., Imbrie, J., and Shackleton, N.J. [1976]. Variations in the earth's orbit: Pacemaker of the ice ages. *Science* **194**, 1121–1132.
- Hebbeln, D., Dokken, T., Andersen, E.S., Hald, M., and Elverhoi, A. [1994]. Moisture supply for northern ice-sheet growth during the Last Glacial Maximum. *Nature* **370**, 357–360.
- Hebbeln, D., Heinrich, R., and Baumann, K.H. [1998]. Paleoceanography of the last interglacial/glacial cycle in the polar North Atlantic. *Quatern. Sci. Rev.* **17**, 125–153.
- Heinemann, G. and Klein, T. [2002]. Modeling and observations of the katabatic flow dynamics over Greenland. *Tellus* **54A**, 542–554.
- Heinrich, H. [1988]. Origin and consequences of cyclic ice rafting in the northeast Atlantic Ocean during the past 130,000 years. *Quatern. Res.* **29**, 142–152.
- Herber, A., Thomason, L.W., Gernandt, H. et al. [2002]. Continuous day and

- night aerosol optical depth observations In the Arctic between 1991 and 1999. *J. Geophys. Res.* **107**(D10), doi: 10.1029/2002JD002079.
- Herman, G. and Goody, R. [1976]. Formation and persistence of summertime Arctic stratus clouds. *J. Atmos. Sci.* **33**, 1537–1553.
- Herman, G.F. and Curry, J.A. [1984]. Observational and theoretical studies of solar radiation in Arctic stratus clouds. *J. Climate Appl. Meteor.* **23**, 5–24.
- Herman, Y. [1983]. Arctic Ocean paleoceanography in late Neogene time and its relationship to global climate. *Oceanology* **23**, 81–87.
- Herschel, J.F.W. (ed.) [1851]. *Admiralty Manual of Scientific Enquiry: Prepared for the Use of Officers in Her Majesty's Navy; and Travellers in General*. London: 2nd edition (reprinted Dawson, Folkestone, 1974).
- Hewson, T.D. [1998]. Objective fronts. *Meteorological Applications* **5**, 37–63.
- Hibler, W.D. III [1979]. A dynamic thermodynamic sea ice model. *J. Phys. Oceanogr.* **9**, 815–846.
- [1980]. Modeling a variable thickness sea ice cover. *Mon. Wea. Rev.* **108**, 1943–1973.
- [1986]. Ice dynamics. In: N. Untersteiner (ed.), *The Geophysics of Sea Ice, NATO ASI Ser., Ser. B Phys.*, vol. 146. New York: Plenum Press, pp. 577–640.
- Hibler, W.D. III and Bryan, F. [1987]. A diagnostic ice-ocean model. *J. Phys. Oceanogr.* **17**, 987–1015.
- Hibler, W.D., Heil, P., and Lytle, V.I. [1998]. On simulating high-frequency variability in Antarctic sea-ice dynamics models. *Ann. Glaciol.* **27**, 443–448.
- Hibler, W.D. and Schulson, E.M. [2000]. On modeling the anisotropic failure and flow of flawed sea ice. *J. Geophys. Res.* **105**(C7), 17105–17120.
- Highwood, E.J., Hoskins, B.J., and Berrisford, P. [2000]. Properties of the Arctic tropopause. *Quart. J. Roy. Met. Soc.* **226**, 1515–1532.
- Hinkel, K.M., Nelson, F.E., Klene, A.E., and Bett, J.H. [2003]. The urban heat island in winter at Barrow, Alaska. *Int. J. Climatol.* **23**, 1889–1905.
- Hinzman, L.D., Kane, D.L., Bensen, C.S., and Everett, K.R. [1996]. Energy balance and hydrological processes in an Arctic watershed. *Ecological Studies* **120**, 131–154.
- Hobbs, W.H. [1910]. Characteristics of the inland ice of the Arctic regions. *Amer. Phil. Soc.* **49**, 57–129.
- [1926]. *The Glacial Anticyclones, the Poles for the Atmospheric Circulation*. New York: MacMillan.
- [1945]. The Greenland glacial anticyclone. *J. Meteor.* **2**, 143–153.
- [1948]. The climate of the Arctic as viewed by explorer and meteorologist. *Science* **108**, 193–201.
- Hoerling, M.P., Hurrell, J.W., and Xu, T. [2001]. Tropical origins for recent North Atlantic climate change. *Science* **292**, 90–92.
- Hoerling, M.P., Hurrell, J.W., Xu, T., Bates, G.T., and Phillips, A. [2004]. Twentieth century North Atlantic climate change. Part II: Understanding the effect of Indian Ocean warming. *Clim. Dynam.* **23**, 395–405, doi: 10.1007/s00382-004-0433-x.
- Hoinka, K.P. [1998]. Statistics of the global tropopause pressure. *Mon. Wea. Rev.* **126**, 3303–3325.
- Holland, M.M. and Bitz, C.M. [2003]. Polar amplification of climate change in coupled models. *Clim. Dynam.* **21**, 221–232.

- Holland, M.M., Bitz, C.M., Eby, M., and Weaver, A.J. [2001]. The role of ice-ocean interactions in the variability of the North Atlantic thermohaline circulation. *J. Climate* **14**, 656–675.
- Holloway, G. and Sou, T. [2002]. Has Arctic sea ice rapidly thinned? *J. Climate* **15**, 1691–1701.
- Holmgren, B. [1971]. *Climate and energy exchange on a sub-polar ice cap in summer. Part E. Radiation Climate*. Meteorologiska Institutionen, Uppsala Universitet, Meddelande Nr. 111.
- Holton, J.R. [1992]. *An Introduction to Dynamic Meteorology*. Third Edition. San Diego, California: Academic Press.
- Hopkins, D.M., Matthews, J.V. Jr., Schweger, C.L., and Young, S.B. [1982]. *Paleoecology of Beringia*. New York: Academic Press.
- Hubberten, H-W. and Romanovskii, N.N. [2001]. Terrestrial and offshore permafrost evolution of the Laptev Sea region during the last Pleistocene-Holocene glacial – eustatic cycle. In: R. Paepe and V. Melnikov (eds.), *Permafrost Response on Economic Development, Environmental Security and Natural Resources*. Dordrecht, the Netherlands: Kluwer Academic Publishers, pp. 43–60.
- Huffman, G.J., Alder, R.F., Arkin, P.A. et al. [1997]. The Global Precipitation Climatology Project (GPCP) Combined Precipitation Data Set. *Bull. Amer. Meteorol. Soc.* **78**, 5–20.
- Huffman, G.J., Alder, R.F., Morrissey, M.M. et al. [2001]. Global precipitation at one-degree daily resolution from multisatellite observations. *J. Hydrometeorology* **2**, 36–50.
- Hughes, M.K. and Diaz, H.F. [1994]. Was there a “Medieval Warm Period”? *Climatic Change* **26**, 109–142.
- Hurrell, J.W. [1995]. Decadal trends in the North Atlantic Oscillation: Regional temperatures and precipitation. *Science* **269**, 676–679.
- [1996]. Influence of variations in extratropical wintertime teleconnections on Northern Hemisphere temperature. *Geophys. Res. Lett.* **23**, 665–668.
- Hurrell, J.W., Hoerling, M.P., Phillips, A., and Xu, T. [2004]. Twentieth century North Atlantic climate change. Part I: Assessing determination. *Clim. Dynam.* **23**, 371–389, doi: 10.1007/s00382-004-0432-y.
- Hurrell, J.W., Kushnir, Y., Ottersen, G., and Visbeck, M. [2003]. An overview of the North Atlantic Oscillation. In: *The North Atlantic Oscillation: Climate Significance and Environmental Impact*. Geophysical Monograph 134, American Geophysical Union, pp. 1–35.
- Hurrell, J.W. and van Loon, H. [1997]. Decadal variations in climate associated with the North Atlantic Oscillation. *Climatic Change* **36**, 301–326.
- Huybrechts, P., Kuhn, M., Lambeck, K. et al. [2001]. Changes in Sea Level. In: *Climate Change 2001, The Scientific Basis*. Cambridge: Contribution of Working Group I to the Third Assessment Report of the Intergovernmental Panel on Climate Change, Cambridge University Press, pp. 639–693.
- Intrieri, J.M., Fairall, C.W., Shupe, M.D. et al. [2002]. Annual cycle of Arctic surface cloud forcing at SHEBA. *J. Geophys. Res.* **107**(C10), doi: 10.1029/2000JC000439.
- Intrieri, J.M. and Shupe, M.D. [2004]. Characteristics and radiative effect of diamond dust over the western Arctic Ocean region. *J. Climate* **17**, 2953–2960.

- Ives, J.D. [1957]. Glaciation in the Torngat Mountains, northern Labrador. *Arctic* **10**, 67–87.
- [1962]. Indications of recent extensive glacierization in north-central Baffin Island. *J. Glaciol.* **4**, 197–205.
- [1974]. Permafrost. In: J.D. Ives and R.G. Barry (eds.), *Arctic and Alpine Environments*. London: Methuen, pp. 159–194.
- Ives, J.D., Andrews, J.T., and Barry, R.G. [1975]. Growth and decay of the Laurentide Ice Sheet and comparisons with Fennoscandia. *Die Naturwissenschaften* **62**, 118–125.
- Jackson, C.I.J. [1959a]. *Operation Hazen: The Meteorology of Lake Hazen, N.W.T., Based on Observations Made During the International Geophysical Year 1957–58*. Montreal, Canada: Arctic Meteorology Research Group, McGill University, Publication in Meteorology No. 15–16. McGill University, Montreal, Parts I–IV.
- [1959b]. Coastal and inland weather contrasts in the Canadian Arctic. *J. Geophys. Res.* **64**, 1451–1455.
- Jackson, J.M., Carmack, E.C., McLaughlin, F.A., Allen, S.E., and Ingram, R.G. [2010]. Identification, characterization, and change of the near-surface temperature maximum in the Canada Basin, 1993–2008. *J. Geophys. Res.* **115**, C05021, doi:10.1029/JC005265.
- Jacobs, J.D., Barry, R.G., and Weaver, R.L. [1975]. Fast ice characteristics with special reference to the eastern Canadian Arctic. *Polar Record* **17**, 521–536.
- Jakobsson, M., Andreassen, K., Bjarnadottir, L.R., et al. [2013]. Arctic Ocean glacial history. *Quatern. Sci. Rev.* In press.
- Jeffries, M.K. [1992]. Arctic ice shelves and ice islands: Origin, growth and disintegration, physical characteristics, structural stratigraphic variability, and dynamics. *Rev. Geophys.* **30**, 245–267.
- Jiang, Y., Dixon, T.H., and Wdowinski, S. [2010]. Accelerating uplift in the North Atlantic region as an indicator of ice loss. *Nature Geoscience* **3**, 404–407, doi:10.1038/NGEO845.
- Johnson, G.L., Pogrebinsky, J., and Macnab, R. [1994]. Arctic structural evolution: Relationship to Paleoceanography. In: O.M. Johannessen, R.D. Muench, and J.E. Overland (eds.), *The Polar Ocean and their Role in Shaping the Global Environment. Geophys. Monogr.* 85. Washington, DC: American Geophysical Union, pp. 285–294.
- Jones, P.D. [1987]. The twentieth century Arctic high – fact or fiction? *Clim. Dynam.* **1**, 63–75.
- Kageyama, M., Valdes, P.J., Ramstein, G., Hemitt, C., and Wyputta U. [1999]. Northern Hemisphere storm tracks in present day and Last Glacial Maximum climate simulations: A comparison of the European PMIP models. *J. Climate* **12**, 742–760.
- Kahl, J.D. [1990]. Characteristics of the low-level temperature inversion along the Alaskan Arctic coast. *Int. J. Climatol.* **10**, 537–548.
- Kalnay, E., Kanamitsu, M., Kistler, R., et al. [1996]. The NCEP/NCAR 40-year re-analysis project. *Bull. Amer. Meteorol. Soc.* **77**, 437–471.
- Kane, D.L., Hinzman, L.D., Bensen, C.S., and Liston, G.E. [1991]. Snow hydrology of a headwater Arctic basin, I. *Water Resources Research* **27**, 1099–1109.
- Kane, D.L., Hinzman, L.D., Woo, M., and Everett, K. [1992]. Arctic Hydrology and Climate Change. In: *Arctic Ecosystems in a Changing Climate*. San Diego, CA: Academic Press, pp. 35–57.
- Kane, E.K. [1856]. *Arctic Explorations: The Second Grinnell Expedition in*

- Search of Sir John Franklin, 1853, '54, '55.* Vol. 1 and Vol. 2. Philadelphia, PA: Childs and Peterson.
- Kaufman, D.S., Ager, T.A., Anderson, N.J. et al. [2004]. Holocene thermal maximum in the Western Arctic (0–180° W). *Quatern. Sci. Rev.* **23**, 629–660, <http://dx.doi.org/10.1016/j.quascirev.2003.09.007>.
- Kaufman, D.S., Schneider, D.P., McKay, N.P. et al. [2009]. Recent warming reverses long-term Arctic cooling. *Science* **325**, 1236–1239, doi: 10.1126/science.1173983.
- Kay, J.E. and Gettleman, A. [2009]. Cloud influence and response to seasonal Arctic sea ice loss. *J. Geophys. Res.* **114**, D128204, doi: <http://dx.doi.org/10.1029/2009JD011773>.
- Keegan, T.J. [1958]. Arctic synoptic activity in winter. *J. Meteor.* **15**, 513–521.
- Kellogg, W.W. [1973]. Climatic feedback mechanisms involving the polar regions. In: G. Weller and S.A. Bowling (eds.), *Climate of the Arctic*. Fairbanks, AK: Geophysical Institute, University of Alaska, pp. 111–116.
- Kerr, R.A. [2010]. “Arctic Armageddon” needs more science, less hype. *Science* **329**, 620–621.
- Key, J.R. and Intrieri, J. [2000]. Cloud particle phase determination with AVHRR. *J. Appl. Meteor.* **36**, 1797–1805.
- Kinnard, C., Zdanowicz, Fisher, D.A., Isaksson, E., de Vernal, A., and Thompson, L.G. [2011]. Reconstructed changes in Arctic sea ice over the past 1,450 years. *Nature* **479**, 509–512, doi: 10.1038/nature10581.
- Kirwan, L.P. [1962]. *A History of Polar Exploration*. London: Penguin Books.
- Kistler R., Kalnay, E., Collins, W. et al. [2001]. The NCEP-NCAR 50-year reanalysis: Monthly means CD-ROM and Documentation. *Bull. Amer. Meteorol. Soc.* **82**, 247–267.
- Kittel, T.G., Steffen, W.L., and Chapin, F.S. III [2000]. Global and regional modeling of Arctic-boreal vegetation distribution and its sensitivity to altered forcing. *Global Change Biology* **6** (Supplement 1), 1–18.
- Klein, T. and Heinemann, G. [2002]. Interaction of katabatic winds and mesocyclones near the eastern coast of Greenland. *Meteorological Applications* **9**, 407–422.
- Kleeman, J., Hätterstrand, C., Borgström, I., and Stroeve, A. [1997]. Fennoscandian paleoglaciology reconstructed using a glacial-geological inversion model. *J. Glaciol.* **43**, 283–299.
- Knight, J.R., Allan, R.J., Folland, C.K., Vellinga, M., and Mann, M.E. [2005]. A signature of persistent natural thermohaline cycles in observed climate. *Geophys. Res. Lett.* **32**, L20708, doi: 10.1029/2005GL024233.
- Kobashi, T., Severinghaus, J.P., Brook, E.J., Barnola, J-M., and Grachev, A.M. [2007]. Precise timing and characterization of abrupt climate change 8200 years ago from air trapped in polar ice. *Quatern. Sci. Rev.* **26**, 1212–1222, doi: 10.1016/j.quascirev.2007.01.009.
- Koc, N., Jansen, E., and Hafildason, H. [1993]. Paleoceanographic reconstructions of surface ocean conditions in the Greenland, Iceland and Norwegian seas through the last 14ka based on diatoms. *Quatern. Sci. Rev.* **12**, 115–140.
- Koch, D. and Hansen, J. [2005]. Distant origins of Arctic black carbon: A Goddard Institute for Space Sciences Model Experiment, *J. Geophys. Res.* **110**, D04204, doi: 10.1029/2004JD005296.
- Koch, K.R. [1891]. History of the supplementary expedition under

- K.R. Koch to Labrador. In: G. von Neumayer (ed.), *Die Deutschen Expeditionen und ihre Ergebnisse. Band I. Geschichtlicher Theil*, Berlin: A. Asher, pp. 145–188.
- Kodera, K. and Chiba, M. [1995]. Tropospheric circulation changes associated with stratospheric sudden warming: A case study. *J. Geophys. Res.* **100**(D6), 11055–11068.
- Koenig, L.S., Greenaway, K.R., Dunbar, M., and Hattersley-Smith, G. [1952]. Arctic Ice Islands. *Arctic* **5**, 62–102.
- Koerner, R.M. [1970]. Weather and ice observations of the British Trans-Arctic Expedition 1968–69. *Weather* **25**, 218–228.
- [1989]. Ice core evidence for extensive melting of the Greenland Ice Sheet in the last interglacial. *Science* **244**, 964–968.
- Kolfschoten, T. van., Gibbard, P.L. and Knudsen, K-L. [2003]. The Eemian Interglacial: a global perspective. Introduction. *Global Planet. Change* **36**, 17–49.
- Konzelmann, T. and Ohmura, A. [1995]. Radiative fluxes and their impact on the energy balance of the Greenland Ice Sheet. *J. Glaciol.* **41**, 490–502.
- Korotkevich, E.S. [1972]. *Polarnye pustyni (Polar Deserts)*. Leningrad: Gidrometeoizdat.
- Koryakin, V.S. [1990]. Ledniki Novoi Zemli i klimat. (Glaciers of Novaya Zemlya and climate). *Priroda* (No. 1), 23–29.
- Koster, R.D. and Suarez, M.J. [1992]. Modeling the land surface boundary in climate models as a composite of independent vegetation stands. *J. Geophys. Res.* **97**(D3), 2697–2715.
- Kotlyakov, V.M. (ed.) [1997]. *World Atlas of Snow and Ice Resources*. Moscow: Russian Academy of Sciences.
- Kovaks, A. and Mellor, M. [1974]. Sea ice morphology and ice as a geological agent in the Southern Beaufort Sea. In: J.C. Reed and J.E. Sater (eds.), *The Coast and Shelf of the Beaufort Sea*. Arlington, Virginia: AINA, pp. 113–124.
- Krebs, S.J. and Barry, R.G. [1970]. The Arctic front and the tundra-taiga boundary in Eurasia. *Geogr. Rev.* **60**, 548–554.
- Krenke, A.N. [1961]. The ice dome with firm nourishment in Franz Josef Land (translated in 1997). In: V.M. Kotlyakov (ed.), *34 Selected Papers on Main Ideas in Soviet Glaciology, 1940s–1980s*. Moscow: Institute of Geography, R.A.S., pp. 132–144.
- Kreutz, K.J., Mayewski, P.A., Meeker, L.D., Twickler, M.S., Whitlow, S.I., and Pittalwala I.I. [1997]. Bipolar changes in atmospheric circulation during the Little Ice Age. *Science* **277**, 1294–1296.
- Kriner, G., Mangerud, J., Jacobsson, M., Crucifix, M., Ritz, C., and Svendsen, S. [2004]. Enhanced ice sheet growth in Eurasia owing to adjacent ice-dammed lakes. *Nature* **427**, 429–432.
- Kristjánsson, J.E. and McInnes, H. [1999]. The impact of Greenland on cyclone evolution in the North Atlantic. *Quart. J. Roy. Met. Soc.* **125**, 2819–2834.
- Kukla, G.J., Clement, A.C., Cane, M.A., Gavin, J.E., and Zebiak, S.E. [2002b]. Last Interglacial and early glacial ENSO. *Quatern. Res.* **58**, 27–31.
- Kukla, G.J., Michael L., Bender, J-L. de Beaulieu et al. [2002a]. Last Interglacial climates. *Quatern. Res.* **58**, 2–13.
- Kurashima, A. [1968]. Studies on the summer and winter monsoons in east Asia based on dynamic concept. *Geographical Magazine* (Tokyo) **34**, 145–236.
- Kutzbach, J.E. [1970]. Large-scale features of monthly mean Northern Hemisphere

- anomaly maps of sea level pressure. *Mon. Wea. Rev.* **98**, 708–716.
- Kwok, R., Cunningham, G.F., and Pang, S.S. [2004]. Fram Strait sea ice outflow. *J. Geophys. Res.* **109**, C01009, doi:10.1029/2003JC001785.
- Kwok, R. and Rothrock, D.A. [1999]. Variability of Fram Strait ice flux and North Atlantic Oscillation. *J. Geophys. Res.* **104**(C3), 5177–5189.
- Labitzke, K. [1968]. Midwinter warmings in the upper stratosphere in 1966. *Quart. J. Roy. Met. Soc.* **94**, 279–291.
- [1981]. Stratospheric-mesospheric midwinter disturbances: A summary of observed characteristics. *J. Geophys. Res.* **86**, 9665–9678.
- Lafleur, P.M. and Rouse, W.R. [1995]. Energy partitioning at treeline forest and tundra sites and its sensitivity to climate change. *Atmosphere-Ocean* **33**, 121–133.
- Lammers, R.B., Shiklomanov, A.I., Vorosmarty, C.J., Fekete, B.M., and Peterson, B.J. [2001]. Assessment of contemporary Arctic river runoff based on observational records. *J. Geophys. Res.* **106** (D4), 3321–3334.
- Larsen, J.A. [1974]. Ecology of the northern forest border. In: Ives, J.D. and Barry, R.G. (eds.), *Arctic and Alpine Environments*. London: Methuen, pp. 341–368.
- Laursen V. [1959]. The Second International Polar Year. *Annals Int. Geophys. Year* (Pergamon) **1**, 211–234.
- Laursen, V. [1982]. The Second International Polar Year (1932/33). *WMO Bull.* **31**, 214–226.
- Lawrence, D.M. and Slater, A.G. [2005]. A projection of near-surface permafrost degradation during the 21st century. *Geophys. Res. Lett.* **32**, L24401, doi:10.1029/2005GL025080.
- Lazier, J.R.N. [1980]. Oceanographic conditions at weather station Bravo, 1960–1974. *Atmosphere-Ocean* **18**, 18227–18238.
- Lean, J. [2009]. Cycles and trends in solar irradiance and climate. *Wiley Interdisciplinary Reviews: Climate Change* **1**, 111–122.
- Lean, J., Beer, J., and Bradley, R.S. [1995]. Reconstructions of solar irradiance since 1610: Implications for climate change. *Geophys. Res. Lett.* **22**, 3195–3198.
- Lebedev, V.V. [1938]. Rost l'do v arkticheskikh rekakh I moriakh v zavisimosti ot otritsatel'nykh temperatur vozdukha. (Growth of ice in Arctic rivers and seas and its dependence on negative air temperature). *Problemy Arktiki* **5**, 9–25.
- LeDrew, E.F. [1984]. The role of local heat sources in synoptic activity in the Arctic Basin. *Atmosphere-Ocean* **22**, 309–327.
- [1988]. Development processes for five depression systems within the Polar Basin. *J. Climatol.* **8**, 125–153.
- [1989]. Modes of synoptic development within the Polar Basin. *Geojournal* **18**, 79–85.
- Legates, D.R. and Willmott, C.J. [1990]. Mean seasonal and spatial variability in gauge-corrected, global precipitation. *Int. J. Climatol.* **10**, 111–127.
- Lehman, S.J. and Keigwin, L.D. [1992]. Sudden changes in North Atlantic circulation during the last deglaciation. *Nature* **356**, 757–762.
- Levere, T.H. [1993]. *Science and the Canadian Arctic. A Century of Exploration 1818–1918*. Cambridge: Cambridge University Press.
- Levi, B.G. [1992]. Arctic measurements indicate chilly prospect of ozone depletion. *Physics Today* **45**, 17–19.

- L'Heureux, M.L., Kumar, A., Bell, G.D., Halpert M.S., and Higgins, R.W. [2008]. Role of the Pacific-North American (PNA) pattern in the 2007 Arctic sea ice decline. *Geophys. Res. Lett.* **35**, L20701, doi: 10.1029/2008GL035205.
- Liang, X., Lettenmaier, D.P., Wood, E.F., and Burges, S.J. [1994]. A simple hydrologically based model of land surface water and energy fluxes for GSMS. *J. Geophys. Res.* **99**(D7), 14415–14428.
- Limpasuvan, V., Thompson, D.W.J., and Hartmann, D.L. [2004]. On the lifecycle of Northern Hemisphere sudden stratospheric warming. *J. Climate* **17**, 2584–2596.
- Lindstrom, D.R. and MacAyeal, D.R. [1986]. Paleoclimatic constraints on the maintenance of possible ice-shelf cover in the Norwegian and Greenland seas. *Paleoceanography* **1**, 313–337.
- Liu, J., Song, M., Hortin, R.M., and Hu, Y. [2013]. Reducing spread in climate model projections of a September ice-free Arctic. *Proc. Nat. Acad. Sci.*, www.pnas.org/cgi/doi/10.1073/pnas.1219716110.
- Loewe, F. [1936]. The Greenland Ice Cap as seen by a meteorologist. *Quart. J. Roy. Met. Soc.* **62**, 359–377.
- [1963]. On the radiation economy. Particularly on ice and snow-covered regions. *Beiträge F. Geophysik* **72**, 371–376.
- Lorenz, E.N. [1951]. Seasonal and irregular variations of the northern hemisphere sea-level pressure profile. *J. Meteor.* **8**, 52–59.
- Lotz, J.R. and Sagar, R.B. [1963]. Northern Ellesmere Island – an Arctic desert. *Geogr. Annal.* **A44**, 366–377.
- Lunardini, V. J. [1993]. Permafrost formation time. In: *Permafrost, Sixth International Conference Proceedings*, Vol. 1. South China University of Technology Press, pp. 420–425.
- Lydolph, P.E. [1977]. *World Survey of Climatology, Vol. 7, Climates of the Soviet Union* (H.E. Landsberg, ed. in chief). Amsterdam: Elsevier.
- Lynch, A.H., Bonan, G.B., Chapin III, F.S., and Wu, W. [1999a]. Impact of tundra ecosystems on the surface energy budget and climate of Alaska. *J. Geophys. Res.* **106**(D6), 6647–6660.
- Lynch, A.H., Chapin, F.S. III, Hinzman, L.D. et al. [1999b]. Surface energy balance on the Arctic tundra: Measurements and models. *J. Climate* **12**, 2585–2606.
- Lynch, A.H., Chapman, W.L., Walsh, J.E., and Weller, G. [1995]. Development of a regional climate model of the western Arctic. *J. Climate* **8**, 1555–1570.
- Lynch, A.H., Maslanik, J.A. and Wu, W. [2001a]. Mechanisms in the development of anomalous sea ice extent in the western Arctic: A case study. *J. Geophys. Res.* **106**(D22), 28097–28105.
- Lynch, A.H., Slater, A.G., and Serreze, M. [2001b]. The Alaskan frontal zone: Forcing by orography, coastal contrast and the boreal forest. *J. Climate* **14**, 4351–4362.
- MacAyeal, D.R. [1993]. Binge/purge oscillation of the Laurentide Ice Sheet as a cause of the North Atlantic Heinrich events. *Paleoceanography* **8**, 775–784.
- MacDougall, A.H., Avis, C.A., and Weaver, A.J. [2012]. Significant contribution to climate warming from the permafrost carbon feedback. *Nature Geoscience* **5**, 719–721, doi: 10.1038/NGE01573.
- Magee, N., Curtes, J., and Wendler, G. [1999]. The urban heat island effect at Fairbanks, Alaska. *Theoretical and Applied Climatology* **64**, 39–47.

- Mahoney, Eicken, H., Gaylord, A.G., and Shapiro, L. [2007]. Alaska landfast sea ice: Links with bathymetry and atmospheric circulation. *J. Geophys. Res.* **112**, C02001, doi: 10.1029/2006JC003559.
- Mhoover, Z.M. [1983]. *Klimatologiya Tropopauzy* (Climatology of the Tropopause). Leningrad: Gidrometeoizdat.
- Makshtas, A.P. [1984]. *The Heat Budget of Arctic Ice in Winter* (in Russian). St. Petersburg, Russia: Gidrometeoizdat (English translation, E. L Andreas, International Glaciological Society, Cambridge, England, 1991).
- Manabe, S. [1969]. Climate and the ocean circulation. 1. The atmospheric circulation and the hydrology of the earth's surface. *Mon. Wea. Rev.* **97**, 739–774.
- Manabe, S. and Stouffer, R.J. [1999]. The role of thermohaline circulation in climate. *Tellus* **51A-B**, 91–109.
- Manney, G.L., Santee, M.L., Rex, M. et al. [2011]. Unprecedented Arctic ozone loss in 2011. *Nature* **478**, 469–475, doi:10.1038/nature10556.
- Mansir, A.R. [1989]. *Quest for the Northeast Passage*. Montrose, CA: Kittiwake Publ.
- Mantua, N.J., Hare, S.R., Zhang, Y., Wallace, J.M., and Francis, R.C. [1997]. A Pacific interdecadal climate oscillation with impacts on salmon production. *Bull. Amer. Meteorol. Soc.* **78**, 1069–1079.
- Marcott, S.A., Clark, P.U., Padman, L. et al. [2011]. Ice shelf collapse from subsurface warming as a trigger for Heinrich events. *Proc. Nat. Acad. Sci.*, www.pnas.org/cgi/doi/10.1073/pnas.1104772108.
- Marincovich, L. Jr. and Gladkov, A. Yu. [1999]. Evidence for an early opening of the Bering Strait. *Nature* **397**, 149–151.
- Marshall, S.J., Tarasov, I., Clarke, G.K.C., and Peltier, W.R. [2000]. Glaciological reconstruction of the Laurentide Ice Sheet: physical processes and modeling challenges. *Can. J. Earth Sci.* **37**, 769–793.
- Martin, C. [1988]. William Scoresby Jr. (1789–1857) and the Open Polar Sea – myth and reality. *Arctic* **41**, 39–47.
- Martinson, D.G., Pisias, N.G., Hayes, J.D., Imbrie, J., Moore, T.C., and Shackleton, N.J. [1987]. Age dating and the orbital theory of the ice ages: development of a high-resolution 0–300,000 year chronostratigraphy. *Quatern. Res.* **27**, 1–29.
- Maslanik, J.A., Fowler, C., Key, J., Scambos, T., Hutchinson, T., and Emery, W. [1997]. AVHRR-based Polar Pathfinder products for modeling applications. *Ann. Glaciol.* **25**, 388–392.
- Maslanik, J.A., and Maybee, H. [1994]. Assimilating remotely-sensed data into a dynamic-thermodynamic sea ice model. In: *Proc. International Geosci. Remote Sens. Symp.*, Pasadena, CA, pp. 1306–1308.
- Maslanik, J.A., Serreze, M.C., and Agnew, T. [1999]. On the record reduction in 1998 western Arctic sea-ice cover. *Geophys. Res. Lett.* **26**, 1905–1908.
- Maslowski, W., Marble, D.C., Walczowski, W., and Semtner, A.J. [2001]. On large-scale shifts in Arctic Ocean and sea ice conditions. *Ann. Glaciol.* **33**, 545–550.
- Maslowski, W., Newton, B., Schlosser, P., Semtner, A., and Martinson, D. [2000]. Modeling recent climate variability in the Arctic Ocean. *Geophys. Res. Lett.* **27**, 3743–3746.
- Matthes, F.E. [1946]. The glacial anticyclone theory examined in light of recent meteorological data from

- Greenland. Part I. *Trans. Amer. Geophys. Union* **27**, 324–341.
- Matthes, F.E. and Belmont, A.D. [1946]. The glacial anticyclone theory examined in light of recent meteorological data from Greenland. Part II. *Trans. Amer. Geophys. Union* **27**, 324–341.
- Mauritzen, C., Sedlar, J., Tjernstrom, M. et al. [2011]. An Arctic CNN-limited cloud aerosol regime. *Atmos. Chem. Phys.* **11**, 165–173, doi:10.5194/acp-11–165–2011.
- Mayewski, P.A., Meeker, L.D., Whitlow, S. et al. [1993]. The atmosphere during the Younger Dryas. *Science* **261**, 195–198.
- Maykut, G.A. [1978]. Energy exchange over young sea ice in the central Arctic. *J. Geophys. Res.* **83**(C7), 3646–3658.
- [1982]. Large-scale heat exchange and ice production in the central Arctic. *J. Geophys. Res.* **87**, 7971–7984.
- [1985]. *An Introduction to Ice in the Polar Oceans*. Seattle, WA: Applied Physics Laboratory, University of Washington, APL-UW 8510, September 1985.
- [1986]. The surface heat and mass balance. In: N. Untersteiner (ed.), *The Geophysics of Sea Ice. NATO ASI Ser., Ser. B Phys.*, Vol. 146. New York: Plenum, pp. 395–464.
- Maykut, G.A. and Untersteiner, N. [1971]. Some results from a time dependent, thermodynamic model of sea ice. *J. Geophys. Res.* **76**, 1550–1575.
- McClelland, J.W., Dery, S.J., Peterson, B.J., Holmes, R.M., and Wood, E.F. [2006]. A pan-arctic evaluation of river discharge during the latter half of the 20th century. *Geophys. Res. Lett.* **33**, L06715, doi:10.1029/2006GL025753.
- McClelland, J.W., Holmes, R.M., Peterson, B.J., and Stieglitz, M. [2004]. Increasing river discharge in the Eurasian Arctic: consideration of dams, permafrost thaw, and fires as potential agents of change. *J. Geophys. Res.* **109**, D18102, doi:10.1029/2004JD004583.
- McClintock, F.L. [1862]. Meteorological Observations in the Arctic Seas by Sir Francis Leopold McClintock, R.N., Made on Board the Arctic Searching Yacht “Fox” in Baffin Bay and Prince Regent’s Inlet in 1857, 1858, and 1859. Reduced and Discussed by Charles A Schott. *Smithsonian Contrib. to Knowledge*, 13, art. 2.
- McConnell, A. [1986]. The scientific life of William Scoresby Jr. with a catalogue of his instruments and apparatus in the Whitby Museum. *Annals of Science* **43**, 257–286.
- McDonald, G. and Gajewski, K [1992]. The northern treeline of Canada. In: D.G. Janelle, (ed.), *Geographical Snapshots of North America*. New York: Guilford Press, pp. 34–37.
- McGuire, A.D., Hayes, D.J., Kicklighter, D.W. et al. [2010]. An analysis of the carbon balance of the Arctic Basin from 1997 to 2006. *Tellus* **62B**, 455–474, doi:10.1111/j.1600–0889.2010.00497.x.
- McIntyre, D.P. [1958]. The Canadian three-front, three jetstream model. *Geophysica (Helsinki)* **6**, 309–324.
- McKenna, M.C. [1980]. Eocene paleolatitude, climate and mammals of Ellesmere Island. *Paleogeog., Paleoclimatol., Paleoecol.* **30**, 349–362.
- McLaren, A.S. [1989]. The under-ice thickness distribution of the Arctic Basin as recorded in 1958 and 1970. *J. Geophys. Res.* **94**(C4), 4971–4983.
- McPhee, M.G. [1980]. An analysis of pack ice drift in summer. In: R.S. Pritchard (ed.), *Sea Ice Processes and Models*. Seattle, WA: University of Washington Press, pp. 339–394.

- McPhee, M.G., Stanton, T.P., Morison, J.H., and Martinson, D.G. [1998]. Freshening of the upper ocean in the central Arctic: Is perennial ice disappearing? *Geophys. Res. Lett.* **25**, 1729–1732.
- Meier, W.N. and Maslanik, J.A. [2003]. Effect of environmental conditions on observed, modeled, and assimilated sea ice motion errors. *J. Geophys. Res.* **108**(C5), 3152, doi: 10.1029/2002JC001333.
- Meier, W.N., Maslanik, J.A., and Fowler, C.W. [2000]. Error analysis and assimilation of remotely sensed ice motion within an Arctic sea ice model. *J. Geophys. Res.*, **105**(C2), 3339–3356.
- Mekis, E. and Hogg, W.D. [1999]. Rehabilitation and analysis of Canadian daily precipitation time series. *Atmosphere-Ocean* **37**, 53–85.
- Melles, M., Brigham-Grette, J., Minyuk, P.S. et al. [2012]. 2.8 millions years of Arctic climate change from Lake El'gygytgyn, NE Russia. *Science* **337**, 315–320, doi: 10.1126/science.1222135.
- Mercer, J.H. [1970]. A former ice sheet in the Arctic Ocean. *Palaeogeogr., Paleoclimatol., Palaeoecol.* **8**, 19–27.
- Meteorological Council [1879–1888]. *Contributions to our Knowledge of the Meteorology of the Arctic Regions*. London: Meteorological Council, Official, No. 34. Her Majesty's Stationery Office, Part 1, (1879), pp. 1–39. Part 2, (1880), pp. 40–254. Part 3 (1882), pp. 255–414. Part 4 (1885), pp. 413–495. Part 5 (1888), pp. 1–37.
- Milankovitch, M. [1941]. *Kanon der Erdbestrahlung und seine Abwendung auf das Eiszeitproblem (Canon of Insolation and the Ice-Age Problem)*, Royal Serbian Academy, Special Publication, Vol. 132, Translation [1969], Israel Program for Scientific Translation, Jerusalem.
- Miles, M.W. and Barry, R.G. [1989]. Large-scale characteristics of fractures in multi-year Arctic pack ice. In: K.B.E. Axelsson and L.A. Fransson (eds.), *Proceedings, 10th International Conference on Port and Ocean Engineering Under Arctic Conditions (POAC 89), Vol 1*. Lulea, Sweden: Department of Engineering, Lulea University of Technology, 103–112 pp.
- Miller, G.H., Geirsdottir, A., Zhong, Y. et al. [2012]. Abrupt onset of the Little Ice Age triggered by volcanism and sustained by sea-ice/ocean feedbacks. *Geophys. Res. Lett.* **39**, L02708, doi:10.1029/2011GL050168.
- Mirny, J. [1934]. *To the North. The Story of Arctic Exploration from Earliest Times to the Present*. New York: Viking Press.
- Mirrless, S.T.A. [1934]. Meteorological Results of the British Arctic Air Route Expedition, 1930–31. *Geophysical Memoirs* 7. London: Meteorological Office.
- Mitchell, J.M., Jr. [1957]. Visual range in the polar regions with special reference to the Alaskan Arctic. *J. Atmos. Terr. Phys. Spec. Suppl.*, 195–211.
- Mohn, H. [1905]. Meteorology, XVII. In: F. Nansen (ed.), *The Norwegian North Polar Expedition, 1893–1896. Scientific Results, Vol. 6*. New York: Greenwood Press (reprinted 1969).
- [1907]. Meteorology. In: *Report of the Second Norwegian Expedition in the "Fram" 1898–1902. Vol. 1 (4)*. Kristiana: A.W. Brøgger, Videnskabs., pp. 1–399.
- Montgomery, M.R. [1952]. Further notes on ice islands in the Canadian Arctic. *Arctic* **5**, 183–187.
- Moore, G.W.K., [2003]. Gale force winds over the Irminger Sea to the east of Cape Farewell, Greenland. *Geophys. Res. Lett.* **30**, 1894, doi:10.1029/2003GL018012.

- Moore, G.W.K. [2012]. A new look at Greenland flow distortion and its impacts on barrier flow, tip jets and coastal oceanography. *Geophys. Res. Lett.* **39**, L22806, doi:10.1029/2012GL054017.
- Moore, G.W.K. and Pickart, R.S. [2012]. Northern Bering Sea tip jets. *Geophys. Res. Lett.* **39**, L08807, doi:10.1029/2012GL051537.
- Moritz, R.E. [1979]. *Synoptic climatology of the Beaufort Sea coast*. Occasional Paper No. 30. Boulder, CO: Institute of Arctic and Alpine Research, University of Colorado.
- [1988]. The ice budget of the Greenland Sea. *Tech. Rep. APL-UW TR 8812*. Seattle, WA: Appl. Phys. Lab., University of Washington.
- Mote, T.L. [2007]. Greenland surface melt trends 1973–2007: Evidence of a large increase in 2007. *Geophys. Res. Lett.* **34**, L22507, doi: 10.1029/2007GL031976.
- Mueller, D.R., Vincent, W.F., and Jeffries, M.O. [2003]. Break-up of the largest Arctic ice shelf and associated loss of an epishelf lake. *Geophys. Res. Lett.* **30**, doi: 10.1029/2003GLO1731.
- Müller, F. and Roskin-Sharlin, N. [1967]. *A High Arctic Climate Study on Axel Heiburg Island, Canadian Archipelago, Summer 1961. Part I, General Meteorology*. Axel Heiburg Island Reports on Meteorology 3. Montreal, Canada: McGill University.
- Murgatroyd, R.J. [1969]. The structure and dynamics of the stratosphere. In: G. A. Corby (ed.), *The Global Circulation of the Atmosphere*. London: Royal Meteorological Society, pp. 159–195.
- Murton, J.B., Bateman, M.D., Dallimore, S.R., Teller, J.T. and Yang, Z. [2010]. Identification of Younger Dryas outburst flood path from Lake Agassiz to the Arctic Ocean. *Nature* **464**, 740–743, doi: 10.1038/nature08954.
- Mynemi, R.B., Keeling, C.D., Tucker, C.J., Asrar, G., and Nemani, R.R. [1997]. Increased plant growth in the northern high latitudes from 1981–1991. *Nature* **386**, 698–702.
- Mysak, L.A. and Huang, F.I. [1992]. A latent- and sensible-heat polynya model for the North Water, northern Baffin Bay. *J. Phys. Oceanogr.* **22**, 596–608.
- Nagurny, A.P. [1998]. Climatic characteristics of the tropopause over the Arctic Basin. *Annal. Geophysicae* **16**, 110–115.
- Nakamura, N. and Oort, A.H. [1988]. Atmospheric heat budgets of the polar regions. *J. Geophys. Res.* **93**(D8), 9510–9524.
- Nansen, F. [1898]. *Farthest North*. London: George Newnes, vols. 1 and 2.
- [1902]. *The Norwegian Polar Expedition, 1893–1896, Scientific Results*. Oslo: Jacob Dybwad, 6 vols.
- Nemani, R.R., Keeling, C.D., Hashimoto, H. et al. [2003]. Climate-driven increases in global terrestrial net primary production from 1982–1999. *Science* **300**, 1560–1562.
- Nghiem, S.V., Hall, D.K., Mote, T.L. et al. [2012]. The extreme melt across the Greenland Ice Sheet in 2012. *Geophys. Res. Lett.* **39**, L20502, doi:10.1029/2012GL053611.
- Nichols, H. [1976]. Historical aspects of the Canadian forest tundra-ecotone. *Arctic* **29**, 38–47.
- Nolin, A.W. and Liang, S. [2000]. Progress in bidirectional reflectance modeling and applications for surface particulate media: snow and soils. *Remote Sensing Review* **18**, 307–342.
- North Greenland Eemian Ice Drilling (NEEM) Community Members [2013]. Eemian interglacial reconstructed from a Greenland folded ice core, *Nature* **493**, 489–494, doi:10.1038/nature11789.

- NSIDC (National Snow and Ice Data Center) [1996]. *Arctic Ocean Snow and Meteorological Observations from the North Pole Drifting Stations: 1937, 1950–1991*. Boulder, CO: National Snow and Ice Data Center, CD-ROM.
- O’Cofaigh, C., Lemmen, D.S., Evans, D.J.A., and Benarski, J. [1999]. Glacial landform-sediment assemblages in the Canadian High Arctic and their implications for late Quaternary Glaciation. *Ann. Glaciol.* **28**, 195–201.
- Oelke, C., Zhang, T., Serreze, M., and Armstrong, R. [2003]. Regional-scale modeling of soil freeze/thaw over the Arctic drainage basin. *J. Geophys. Res.* **108**(D10), doi:10.1029/2002JD002722.
- Ogi, M. and Wallace, J.M. [2007]. Summer minimum Arctic sea ice extent and the associated summer atmospheric circulation, *Geophys. Res. Lett.* **34** L12705, doi: 10.1029/2007GL029897.
- Ogi, M., Yamazaki, K., and Tachibana, Y. [2004]. The summertime annular mode in the Northern Hemisphere and its linkage to the winter mode. *J. Geophys. Res.* **109**, D20114, doi: 10.1029/2004JD004514.
- Ohmura, A. [1984]. Comparative energy balance study for Arctic tundra, sea surface, glaciers and boreal forest. *GeoJournal* **8**, 221–228.
- Ohmura, A., Calanca, P., Wild, M., and Anklin, M.A. [1999]. Precipitation, accumulation and mass balance of the Greenland Ice Sheet. *Zeitschr. Gletscherk. Glazialgeol.* **35**, 1–20.
- Oke, T.R. [1987]. *Boundary Layer Climates*. Second Edition. New York: Routledge.
- Okhuizen, E. [1995]. The cartography of the Northern Sea Route, 15th–19th centuries. In: H. Kitagama (ed.), *Northern Sea Route; Future and Perspective*. (The Proceedings of INSROP Symposium, Tokyo ‘95).
- Tokyo: Ship and Ocean Foundation, pp. 567–576.
- Oleson, K. W., Lawrence, D.M., Bonan, G.B. et al. [2010]. *Technical Description of Version 4.0 of the Community Land Model (CLM)*. NCAR Tech. Note NCAR/TN-478 +STR. Boulder, CO: National Center for Atmospheric Research.
- Oltmans, S.J., Schnell, R.C., Sheridan, P.J. et al. [1989]. Seasonal surface ozone and filterable bromine relationship in the high Arctic. *Atmos. Environ.* **23** 2431–2441.
- Orvig, S. [1954]. Glacial meteorological observations on ice-caps in Baffin Island. *Geogr. Annal.* **36**, 193–318.
- Outten, S.D., Renfrew, I.A., and Petersen, G.N. [2009]. An easterly tip jet off Cape Farewell, Greenland, II: Simulations and dynamics. *Quart. J. Roy. Met. Soc.* **135**, 1934–1949.
- Overland, J.E., Francis, J.A., Hanna, E., and Wang, M. [2012]. The recent shift in early summer atmospheric circulation. *Geophys. Res. Lett.* **39**, L19804, doi:10.1029/2012GL053268.
- Overland, J.E. and Guest, P.S. [1991]. The snow and air temperature budget over sea ice during winter. *J. Geophys. Res.* **96**(C3), 4651–4662.
- Overland, J.E., McNutt, S.L., Groves, J., Saio, S., Andreas, E.L., Persson, P., and Ola G. [2000]. Regional sensible and radiative heat flux estimates for the winter Arctic during the Surface Heat Budget of the Arctic Ocean (SHEBA) experiment. *J. Geophys. Res.* **105**(C6), 14093–14102.
- Overland, J.E., Miletta Adams, J., and Bond, N.A. [1997]. Regional variation of winter temperatures in the Arctic. *J. Climate* **10**, 821–837.
- Overland, J.E., Spillane, M.C., Percival, D.B., Wang, M., and Mofjeld, H.O. [2004]. Seasonal and regional variation

- of pan-Arctic surface air temperature over the instrumental record. *J. Climate* **15**, 3263–3282.
- Overland, J.E. and Turet, P. [1994]. Variability of the atmospheric energy flux across 70°N computed from the GFDL data set. In: O.M. Johannessen, R.D. Muench and J.E. Overland (eds.), *The Polar Oceans and Their Role in Shaping the Global Environment, The Nansen Centennial Volume*. Geophys. Monogr. 85, American Geophysical Union, pp. 313–325.
- Overland, J.E., Turet, P., and Oort, A.H. [1996]. Regional variations of moist static energy flux into the Arctic. *J. Climate* **9**, 54–65.
- Overland, J.E. and Wang, M.-Y. [2010]. Large-scale atmospheric circulation changes are associated with the recent loss of Arctic sea ice. *Tellus* **62A**, 1–9.
- Palmén, E. [1951]. The role of atmospheric disturbances in the general circulation. *Quart. J. Roy. Met. Soc.* **77**, 337–354.
- Palmén, E. and Newton, C.W. [1969]. *Atmospheric Circulation Systems. Their Structure and Physical Interpretation*. San Diego, CA: Academic Press.
- Parish, T.R. and Cassano, J.J. [2003]. Diagnosis of the katabatic wind influence on the wintertime Antarctic surface wind field from numerical simulations. *Mon. Wea. Rev.* **131**, 1128–1139.
- Parkinson, C.L., Comiso, J.O., Zwally, H.J., Cavalieri, D.J., Gloersen, P., and Campbell, W.J. [1987]. *Arctic Sea Ice, 1973–1976: Satellite Passive Microwave Observations*. Washington, DC: NASA SP-489, NASA Scientific and Technical Information Branch.
- Parkinson, C.L. and Washington, W.M. [1979]. A large-scale numerical model of sea ice. *J. Geophys. Res.* **84**(C1), 311–337.
- Parry, W.E. [1821]. *Journal of a Voyage for the Discovery of a Northwest Passage from the Atlantic to the Pacific: Performed in the Years 1819–1820, in Her Majesty's Ships Hecla and Griper, With an Appendix, Containing the Scientific and Other Observations*. London: John Murray (reprinted New York, 1968).
- Passarge, S. [1920]. *Die Grundlagen der Landschaftskunde*. Hamburg: L. Friedericken and Company.
- Pawson, S. and Kubitz, T. [1996]. Climatology of planetary waves in the northern stratosphere. *J. Geophys. Res.* **101** (D12), 16987–16996.
- Peltier W.R. [1994]. Ice age paleotopography. *Science* **265**, 195–201. [2004]. Global glacial isostacy and the surface of the Ice Age earth: The ICE-5G(VM2) model and GRACE. *Ann. Rev. Earth. Planet. Sci.* **32**, 111–150.
- Penner, C.M. [1955]. A three-front model for synoptic analyses. *Quart. J. Roy. Met. Soc.* **81**, 89–91.
- Perlitz, J. and Harnik, N. [2003]. Observational evidence of a stratospheric influence on the troposphere by planetary wave refraction. *J. Climate* **16**, 3011–3026.
- Perovich D.K., Light B., Eicken H., Jones K.F., Runciman K., and Nghiem, S.V. [2007]. Increasing solar heating of the Arctic Ocean and adjacent seas, 1979–2005: Attribution and role in the ice-albedo feedback. *Geophys. Res. Lett.* **34**, L19505, doi:10.1029/2007GL031480.
- Persson, P., Ola, G., Fairall, C.W., Andreas, E.L., Guest, P.S., and Perovich, D.K. [2002]. Measurements near the Atmospheric Surface Flux group tower at SHEBA: Near-surface conditions and surface energy budget. *J. Geophys. Res.* **107**(C10), doi: 10.1029/2000JC000705.

- Peterson, B.J., Holmes, R.M., McClelland, J.W. et al. [2002]. Increasing river discharge to the Arctic Ocean. *Science* **298**, 2171–2173.
- Petit, J.R., Jouzel, J., Raynaud, D. et al. [1999]. Climate and atmospheric history of the past 420,000 years from the Vostok ice core, Antarctica. *Nature* **399**, 429–436.
- Pettersen, S. [1950]. Some aspect of the general circulation of the atmosphere. *Centenary Proc. of the Royal Meteorological Society, London*, 120–155.
- Petzold, D.E. [1977]. An estimation technique for snow surface albedo. *Climatological Bulletin* **26**, 1–11.
- Pickart, R.S., Spall, M.A., Ribergaard, M.H., Moore, G.W.K., and Miliff, R.F. [2003]. Deep convection in the Irminger Sea forced by the Greenland tip jet. *Nature* **424**, 152–156, doi:10.1038/nature01729.
- Pielke, R.A. and Vidale, P.L. [1996]. The boreal forest and the polar front. *J. Geophys. Res.* **100**(D12), 25755–25758.
- Polyak, L., Edwards, M.H., Coakley, B.J., and Jaobsson, M. [2001]. Ice shelves in the Pleistocene Arctic Ocean inferred from glaciogenic deep-sea bedforms. *Nature* **410**, 453–457.
- Polyakov, I.V., Alekseev, G.V., Bekryaev, R.V. et al. [2002]. Observationally based assessment of polar amplification of global warming. *Geophys. Res. Lett.* **29**, doi: 10.1029/2001GL011111.
- Polyakov, I.V., Alexeev, V.A., Bhatt, U.S., Polyakova, E.I., and Zhang, X. [2009]. North Atlantic warming: patterns of long-term trend and multidecadal variability. *Climate Dynamics* **34**, 439–457, doi: 10.1007/s00382-008-0522-3.
- Polyakov, I.V., Beszczynska, A., Carmack, E.C. et al. [2005]. One more step toward a warmer Arctic. *Geophys. Res. Lett.* **32**, L17605, doi:10.1029/2005GL023740.
- Polyakov, I.V. and Johnson, M.A. [2000]. Arctic decadal and interdecadal variability. *Geophys. Res. Lett.* **27**, 4097–4100.
- Polyakov, I.V., Timokhov, L.A., Alexeev, V.A. et al. [2010], Arctic Ocean warming contributes to reduced polar ice cap. *J. Phys. Oceanogr.*, **40**, 2743–2756, doi: 10.1175/2010JPO4339.1.
- Pomeroy, J.W. and Essery, R.L.H. [1999]. Turbulent fluxes during blowing snow: field tests of model sublimation predictions. *Hydrological Processes* **13**, 2963–2975.
- Pomeroy, J.W., Gray, D.M., and Landine, P.G. [1993]. The Prairie Blowing Snow Model: Characteristics, validation, operation. *J. Hydrol.* **144**, 165–192.
- Porter, D.F., Cassano, J.J., Serreze, M.C., and Kindig, D.N. [2010]. New estimates of the large-scale Arctic energy budget. *J. Geophys. Res.* **115**, D08108, doi: 10.1029/2009JD012653.
- Portis, D.H., Walsh, J.E., El Hambly, M., and Lamb, P. [2001]. Seasonality of the North Atlantic Oscillation. *J. Climate* **14**, 2069–2078.
- Post, A. and Mayo, L.R. [1971]. Glacier dammed lakes and outburst floods in Alaska. *Hydrological Investigations Atlas HA-455*. Washington, DC: U.S. Geological Survey.
- Proshutinsky, A., Aksenov, Y., Clement Kinney, J. et al. [2011]. Recent advances in Arctic Ocean studies employing models from the Arctic Ocean Intercomparison Project. *Oceanography* **24**, 102–113, <http://dx.doi.org/10.5670/oceanog.2011.61>.
- Pryzbylak, R. [2003]. *The Climate of the Arctic*. Dordrecht, the Netherlands: Kluwer Academic Publishers.

- Putnins, P. [1969]. The climate of Greenland. In: S. Orvig (ed.), *Climates of the Polar Regions, World Survey of Climatology*, Vol. 14. Amsterdam: H.E. Landsberg, (ed. in chief), Elsevier, pp. 3–128.
- Raatz, W.E., Schnell, R.C., Shapiro, M.A., Oltmans, S.J., and Bodhaine, B.A. [1985]. Intrusions of stratospheric air into Alaska's troposphere. *March 1983, Proc. Third Symp. Arctic Air Chemistry, Downsview*, 2153–2158.
- Radok, U. [1968]. Deposition and erosion of snow by the wind. *Res. Rep. 230*. Hanover, NH: U.S. Army CRREL.
- Rahmsdorf, S. and R. Alley [2002]. Stochastic resonance in glacier climate. *EOS, Transactions, American Geophysical Union*, **83**, 129, 135.
- Ramanathan, V., Cess, R.D., Harrison, E.F. et al. [1989]. Cloud-radiative forcing and climate: Results from the Earth Radiation Budget Experiment. *Science* **243**, 57–63.
- Rampal, P., Weiss, J., Dubois, C., and Campin, J.-M. [2011]. IPCC climate models do not capture Arctic sea ice drift acceleration: Consequences in terms of projected sea ice thinning and decline. *J. Geophys. Res.* **116**, C00D07, doi:10.1029/2011JC007110.
- Rasmusson, E. [1979]. The polar low as an extratropical CISK disturbance. *Quart. J. Roy. Met. Soc.* **105**, 531–549.
- Rasmusson, E. and Turner J. [2002]. *Polar Lows. Mesoscale Weather Systems in the Polar Regions*. Cambridge: Cambridge University Press.
- Rawlins, M.S., Serreze, M.C., Schroeder, R., Zhang, X., and McDonald, K.C. [2009]. Diagnosis of the record discharge of Arctic-draining Eurasian river in 2007. *Env. Res. Lett.* **4**, doi:10.1088/1748–9326/4/4/045011.
- Ray, P.H. [1885]. *Report of the International Polar Expedition to Point Barrow, Alaska*. Washington, DC: Arctic Publications, U.S. Signals Office, Govt. Printing Office.
- Raynaud, D., Barmola, J-M, Chappellaz, J., Blunier, T., Indermuhle, A., and Stauffer, B. [2000]. The ice record of greenhouse gases; a view in the context of future changes. *Quatern. Sci. Rev.* **19**, 9–18.
- Reagan, M.T. and Moridis, G.J. [2009]. Large scale simulation of methane hydrate disassociation along the West Spitzbergen Margin. *Geophys. Res. Lett.* **36**, L23612, doi:10.1029/2009GL041332.
- Reed, R.J. [1960]. Principal frontal zones of the Northern Hemisphere in winter and summer. *Bull. Amer. Meteorol. Soc.* **41**, 591–598.
- [1962]. *Arctic Forecast Guide*. Norfolk, VA: U.S. Navy Weather Research Facility 16–0462–058.
- Reed, R.J. and Kunkel, B.A. [1960]. The Arctic circulation in summer. *J. Meteorol.* **17**, 489–506.
- Reiter, E.R. [1975]. *The Natural Stratosphere of 1974*. CIAP Monograph 1. Washington, DC: Dept. of Transportation DOT-TST-75-51.
- Renfrew, I.A. [2003]. Polar Lows. In: J.R. Holton, J.A. Curry and J.A. Pyle (eds.), *Encyclopedia of Atmospheric Sciences*. London and San Diego, CA: Academic Press, pp. 1761–1768.
- Riedlinger, S.H. and Preller, R.H. [1991]. The development of a coupled ice-ocean model for forecasting ice conditions in the Arctic. *J. Geophys. Res.* **96**(C9), 16955–16978.
- Rienecker, M.M., Suarez, M.J., Gelaro, R. et al. [2011]. MERRA – NASA's Modern-Era Retrospective Analysis for Research and Applications. *J. Climate*, **24**, 3624–3648, doi:10.1175/JCLI-D-00015.1.

- Rignot, E., Box, J.E., Burgess, E., and Hanna, E. [2008]. Mass balance of the Greenland Ice Sheet from 1958–2007. *Geophys. Res. Lett.*, **35**, L20502, doi: 10.1029/2008GL035417.
- Rignot, E. and Kanagaratnam, P. [2006]. Changes in the velocity structure of the Greenland Ice Sheet. *Science*, **311**, 986–990.
- Rigor, I.G., Colony, R.L., and Martin, S. [2000]. Variations in surface air temperature in the Arctic, 1979–97. *J. Climate* **13**, 896–914.
- Rigor, I.G. and Wallace, J.M. [2004]. Variations in the age of Arctic sea-ice and summer sea-ice extent. *Geophys. Res. Lett.* **31**, L09401, doi:10.1029/2004GL019492.
- Rigor, I.G., Wallace, J.M., and Colony, R.L. [2002]. Response of sea ice to the Arctic Oscillation. *J. Climate* **15**, 2648–2663.
- Rind, D., Shindell, D., Perlitz, J. et al. [2004]. The relative importance of solar and anthropogenic forcing of climate change between the Maunder Minimum and the present. *J. Climate* **17**, 906–929.
- Rinke, A., Dethloff, K., Cassano, J. et al. [2005]. Ensemble performance in ARCMIP1 experiments: Spatial patterns and height profiles. *Clim. Dynam.* **26**, doi:10.1007/s00382-005-0095-3.
- Rochon, A., de Vernal, A., Sejrup, H.P., and Hafnidason, H. [1998]. Palynological evidence of climate and oceanographic changes in the North Sea during the last deglaciation. *Quatern. Res.* **49**, 197–207.
- Rodewell, M.J., Rowell, D.P., and Folland, C.K. [1999]. Oceanic forcing of the wintertime North Atlantic Oscillation and European climate. *Nature* **398**, 320–323.
- Roe, G.H. and Lindzen, R.S. [2001]. The mutual interaction between continental-scale ice sheets and atmospheric stationary waves. *J. Climate* **14**, 1450–1465.
- Rogers, A.N., Bromwich, D.H., Sinclair, E.N., and Cullather, R.I. [2001]. The atmospheric hydrologic cycle over the Arctic Basin from reanalyses Part 2. Interannual variability. *J. Climate* **14**, 2414–2429.
- Rogers, J.C. [1978]. Meteorological factors affecting interannual variability of summertime ice extent in the Beaufort Sea. *Mon. Wea. Rev.* **106**, 890–897.
- [1984]. Association between the North Atlantic Oscillation and the Southern Oscillation in the Northern Hemisphere. *Mon. Wea. Rev.* **112**, 1999–2015.
- Romanov, I.P. [1991]. *Ledyanoi Pokrov Arkticheskogo Basseina* (Ice Cover of the Arctic Basin, in Russian). St. Petersburg, Russia: Arctic and Antarctic Research Institute.
- [1995]. *Atlas of ice and snow of the Arctic Basin and Siberian Shelf Seas* (Second edition of atlas and monograph). New York: Backbon Publishing Company.
- Romanov, I.P., Konstantinov, Yu. B., and Kornilov, N.A. [2000]. North Pole Drifting Stations (1937–1991). *The Arctic Climatology Project Arctic Meteorology and Climate Atlas*. Boulder, CO: National Snow and Ice Data Center, CD-ROM.
- Romanovsky, V.E., Drozdov, D.S., Oberman, N.G. et al. [2010a]. Thermal state of permafrost in Russia. *Permafrost and Periglacial Processes* **21**, 136–155.
- Romanovsky, V.E., Smith, S.L., and Christiansen, H.H. [2010b]. Permafrost thermal state in the polar Northern Hemisphere during the International Polar Year 2007–2009 – a synthesis. *Permafrost and Periglacial Processes* **21**, 106–116.
- Rooth, C. [1982]. Hydrology and ocean circulation. *Progress in Oceanography* **11**, 131–149.

- Ross, Sir John. [1835]. *Narrative of a Second Voyage in Search of a North-West Passage: And of a Residence in the Arctic Regions during the Years 1829, 1830, 1831, 1832, 1833*. London: A.W. Webster.
- Rossow, W. and Schiffer, R.A. [1991]. ISCCP cloud data products. *Bull Amer. Meteorol. Soc.* **72**, 2–20.
- Rothrock, D.A. and Thomas, D.R. [1990]. The Arctic Ocean multiyear ice balance. *Ann. Glaciol.* **14**, 252–255.
- Rothrock, D.A., Yu, Y., and Maykut, G.A. [1999]. Thinning of the Arctic sea ice cover. *Geophys. Res. Lett.* **26**, 3469–3472.
- Rothrock, D.A., Zhang, J., and Yu, Y. [2003]. Arctic ice thickness anomaly of the 1990s: A consistent view from observations and models. *J. Geophys. Res.* **108**(C3), 3083, doi:10.1039/2001JC001208.
- Rozenbaum, G.E. and Shpolyanskaya, N.A. [2000]. *Pozdnekainozoiskaya Istoryya Kriolitozony Arktiki I Tendentsii ee Budushchego Razvitiya. (Late Cainozoic History of the Cryolithozones of the Arctic and Tendencies of their future Development)*. Moscow: Nauchnyi Mir.
- Ryder, C. [1896]. *Isforholdene I Nordhavet, 1877–1892*. Kobenhaven: Tidsskr. f. Sovaesen.
- Saha, S., Moorthi, S., Pan, H-L. et al. [2010]. The NCEP Climate Forecast System Reanalysis. *Bull. Amer. Meteorol. Soc.*, **91**, 1015–1057, doi: 10.1175/2010BAMS3001.1.
- Sahsamanoglou, H.S., Makrogianis, T.J., and Kallimopolous, P.P. [1991]. Some aspects of the basic characteristics of the Siberian anticyclone. *Int. J. Climatol.* **11**, 827–839.
- Saladin d'Anglure, B. [1984]. The route to China: Northern Europe's Arctic delusions. *Arctic* **37**, 446–452.
- Sampe, T. and Xie, S.P. [2007]. Mapping high sea winds from space: A global climatology. *Bull. Amer. Meteorol. Soc.* **88**, 1965–1978, doi:10.1175/BAMS-88-12–1965.
- Sater, J.E. (Coordinator) [1968]. *Arctic Drifting Stations. A Report on Activities Supported by the Office of Naval Research: Proceedings of the Symposium*. Washington, DC: Arctic Institute of North America.
- Savours, S.A. [1984]. “A very interesting point in geography”: The 1773 Phipps expedition towards the North Pole. *Arctic* **37**, 402–428.
- Schaefer, K., Zhang, T., Bruhwiler, L., and Barrett, A.P. [2011]. Amount and timing of permafrost carbon release in response to climate warming. *Tellus* **63B**, 165–180, doi: 10.1111/j.1600–0889.2011.00527.
- Scherhag, R. [1960]. Stratospheric temperature changes and the associated changes in pressure distribution. *J. Meteorol.* **17**, 575–582.
- Schlesinger, M.E. [1985]. Analysis of results from energy balance and radiative-convective models. In: M.C. MacCracken and F.M. Luther (eds.), *Projecting the Climatic Effects of Increasing Carbon Dioxide*. Washington, DC: U.S. Dept. Energy, DOE/ER-0237, pp. 81–147.
- Schnell, R.C., Barry, R.G., Miles, M.W., Abndreas, E.L., Radke, L.F., Brock, C.A., McCormick, P.J., and Moore, J.L. [1989]. Lidar studies of leads in Arctic sea ice. *Nature* **339**, 530–532.
- Schweiger, A.J. and Key, J.R. [1992]. Arctic cloudiness comparison of ISCCP-C2 and Nimbus –7 satellite derived cloud products with a surface-based cloud climatology. *J. Climate* **5**, 1514–1527.
- Schweiger, A.J., Lindsay, R.W., Key, J.R., and Francis, J.A. [1999]. Arctic clouds

- in multiyear satellite data sets. *Geophys. Res. Lett.* **26**, 1845–1848.
- Schweiger, A., Lindsay, R., Zhang, J., Steele, M., Stern, H., and Kwok, R. [2011]. Uncertainty in modeled Arctic sea ice volume. *J. Geophys. Res.* **116**, C00D06, doi:10.1029/2011JC007084.
- Scoresby, W. [1811–1816]. On the Greenland or Polar ice. *Mem. Wernerian Soc. Natural History (Edinburgh)* **2**, 261–338.
- [1820]. *An Account of the Arctic Regions with a History and Description of the Northern Whale-Fishery. Vol. The Arctic.* New York: A.M. Kelley Publishers.
- Selinger, F. and Glen, A. [1983]. Arctic meteorological operations and counter-operations during World War II. *Polar Record* **21**, 559–567.
- Semenov, V.A. and Bengtsson, L. [2003]. Modes of wintertime Arctic temperature variability. *Geophys. Res. Lett.* **30**, 1781, doi: 10.1029/2003GLO17112.
- Semtner, A.J. [1987]. A numerical study of sea ice and ocean circulations in the Arctic. *J. Phys. Oceanogr.* **17**, 1077–1099.
- Serreze, M.C. [1995]. Climatological aspects of cyclone development and decay in the Arctic. *Atmosphere- Ocean* **33**, 1–23.
- Serreze, M.C. and Barrett, A.P. [2008]. The summer cyclone maximum over the central Arctic Ocean. *J. Climate* **21**, 1048–1065, doi:10.1175/2007JCLI1810.1.
- [2011]. Characteristics of the Beaufort Sea High. *J. Climate* **24**, 159–182, doi:10.1175/2010JCLI3636.1.
- Serreze, M.C., Barrett, A.P., Slater, A.G. et al. [2006]. The large-scale freshwater cycle of the Arctic. *J. Geophys. Res.* **111**, C11010, doi:10.1029/2005JC003424.
- Serreze, M.C., Barrett, A.P., Slater, A.G., Steele, M., Zhang, J., and Trenberth, K.E. [2007]. The large-scale energy budget of the Arctic. *J. Geophys. Res.* **112**, D11122, doi:10.1029/2006JD008230.
- Serreze, M.C., Barrett, A.P., and Stroeve, J. [2012]. Recent changes in tropospheric water vapor over the Arctic as assessed from radiosondes and atmospheric reanalyses. *J. Geophys. Res.* **117**, D10104, doi: 10.1029/2011JD017421.
- Serreze, M.C. and Barry, R.G. [2011]. Processes and impacts of Arctic amplification: A research synthesis. *Global and Planetary Change* **77**, 85–96.
- Serreze, M.C., Barry, R.G., and McLaren, A.S. [1989]. Seasonal variations in sea ice motion and effects on sea ice concentration in the Canada Basin. *J. Geophys. Res.* **94**(C8), 10955–10970.
- Serreze, M.C., Barry, R.G., and Walsh, J.E. [1995a]. Atmospheric water vapor characteristics at 70°N. *J. Climate* **8**, 719–731.
- Serreze, M.C. and Bradley, R.S. [1987]. Radiation and cloud observations on a high Arctic plateau ice cap. *J. Glaciol.* **33**, 162–168.
- Serreze, M.C., Bromwich, D.H., Clark, M.P., Etringer, A.J., Zhang, T., and Lammers, R. [2003a]. The large-scale hydro-climatology of the Arctic drainage. *J. Geophys. Res.* **108**(D2), doi: 10.1029/2001JD000919.
- Serreze, M.C., Carse, F., Barry, R.G., and Rogers, J.C. [1997]. Icelandic Low cyclone activity: Climatological features, linkages with the NAO, and relationships with recent changes in the Northern Hemisphere circulation. *J. Climate* **10**, 453–464.
- Serreze, M.C., Clark, M.P., and Bromwich, D.H. [2003b]. Monitoring precipitation over the Arctic terrestrial drainage system: Data requirements, shortcomings and applications of atmospheric reanalysis. *J. Hydrometeorology* **4**, 387–407.

- Serreze, M.C. and Etringer, A.J. [2003]. Precipitation characteristics of the Eurasian Arctic drainage system. *Int. J. Climatol.* **23**, 1267–1291.
- Serreze, M.C. and Francis, J. [2006]. The Arctic amplification debate. *Climatic Change* **76**, 241–264, doi: 10.1007/s10584-005-9017-y.
- Serreze, M.C., Kahl, J.D., Andreas, E. L., Maslanik, J. A., Rehder, M.C., and Schnell, R.C. [1992a]. Theoretical heights of buoyant convection above open leads in the winter Arctic pack ice cover. *J. Geophys. Res.* **97**(C6), 9411–9422.
- Serreze, M.C., Kahl, J.D., and Schnell, R.C. [1992b]. Low-level temperature inversions of the Eurasian Arctic and comparisons with Soviet drifting station data. *J. Climate* **5**, 615–629.
- Serreze, M.C., Lynch, A.H., and Clark, M.P. [2001]. The Arctic frontal zone as seen in the NCEP-NCAR reanalysis. *J. Climate* **14**, 1550–1567.
- Serreze, M.C., Maslanik, J.A., and Key, J.R. [1997]. *Atmospheric and Sea Ice Characteristics of the Arctic Ocean and the SHEBA Field Region in the Beaufort Sea*. Special Report – 4, National Snow and Ice Data Center. Boulder, CO: National Snow and Ice Data Center.
- Serreze, M.C., Maslanik, J.A., Key, J.R., Kokaly, R.F., and Robinson, D.A. [1995b]. Diagnosis of the record minimum in Arctic sea ice area during 1990 and associated snow cover extremes. *Geophys. Res. Lett.* **22**, 2183–2186.
- Serreze, M.C., Walsh, J.E., Chapin, F.S. III et al. [2000]. Observational evidence of recent change in the northern high latitude environment. *Climatic Change* **46**, 159–207.
- Severinghaus, J.P., Sowers, T., Brook, E.J., Alley, R.B., and Bender, M.L. [1998]. Timing of abrupt climate change at the end of the Younger Dryas interval from thermally fractionated gases in polar ice. *Nature* **391**, 141–146.
- Shackleton, N.J., Fernanda Sanchez- Goni, M., Pailler, D., and Lancelot, Y. [2003]. Marine isotope substage 5e and the Eemian Interglacial. *Global Planet. Change* **36**, 151–155.
- Shahgedanova, M. (ed.) [2002]. *The Physical Geography of Northern Eurasia*. Oxford: Oxford University Press.
- Shahgedanova, M., Perov, V., and Mudrow, Y. [2002]. The mountains of northern Russia. In: M. Shahgedanova (ed.), *The Physical Geography of Northern Russia*. Oxford: Oxford University Press, pp. 284–313.
- Shakhova, N., Semiletov, I., Salkuk, A., Yusupov, V., Kosmach, D., and Gustavson, O. [2010]. Extensive methane venting to the atmosphere from sediments of the East Siberian Arctic Shelf. *Science* **327**, 1246–1250, doi: 10.1126/science.1182221.
- Shakhova, N., Semiletov, I., Leifer, I., Sergienko, V., Salyuk, A., Kosmach, D. et al. [2013]. Ebullition and storm-induced methane release from the East Siberian Arctic shelf. *Nature Geoscience*, doi: 10.1038/NGE02007.
- Shapiro, M.A. [1985]. Dropwinsonde observations of an Icelandic low and a Greenland mountain-lee wave. *Mon. Wea. Rev.* **113**, 680–683.
- Shapiro, M.A., Fedor, L.S., and Hampel, T. [1987a]. Research aircraft measurements of a polar low over the Norwegian Sea. *Tellus* **39A**, 272–306.
- Shapiro, M.A., Hampel, T., and Krueger, A.J. [1987b]. The Arctic tropopause fold. *Mon. Wea. Rev.* **115**, 444–454.
- Shapiro, M.A., Schnell, R.C., Parungo, F.P., Oltmans, S.J., and Bodhaine, B.A.

- [1984]. El Chichon volcanic debris in an Arctic tropopause fold. *Geophys. Res. Lett.* **11**, 421–424.
- Shepherd, A., Ivins, E.R., Valentina, G.A. et al. [2012]. A reconciled estimate of ice-sheet mass balance. *Science* **338**, doi: 10.1126/science.1228102.
- Shiklomanov, I.A., Shiklomanov, A.I., Lammers, R.B., Peterson, B.J., and Vorosmarty, C.J. [2000]. The dynamics of river water inflow to the Arctic Ocean. In: E.L. Lewis, E.P. Jones, P. Lemke, T.D. Prowse, and P. Wadhams (eds.), *The Freshwater Budget of the Arctic Ocean. NATO Science Series 2. Environmental Security – Vol. 70*. Dordrecht, the Netherlands: Kluwer Academic Publishers, pp. 281–296.
- Shimada, K., Kamoshida, T., Itoh, M. et al. [2006]. Pacific inflow: Influence on catastrophic reduction of sea ice cover in the Arctic Ocean. *Geophys. Res. Lett.* **33**, L08605, doi:10.1029/2005GL025624.
- Shindell, D. and Faluvegi, G. [2009]. Climate response to regional radiative forcing during the twentieth century. *Nature Geoscience* **2**, 294–300, doi: 10.1038/NGE0473.
- Shine, K.P. [1984]. Parameterization of shortwave flux over high albedo surfaces as a function of cloud thickness and surface albedo. *Quart. J. Roy. Met. Soc.* **110**, 747–764.
- Shulski, M. and Wendler, G. [2007]. *The Climate of Alaska*. Fairbanks, AK: University of Alaska Press.
- Siegent, M.J. [2001]. *Ice Sheets and Late Quaternary Environmental Change*. Chichester, England: John Wiley and Sons.
- Siegent, M.J., Dowdeswell, J.A., and Melles, M. [1999]. Late Weichselian glaciation of the Eurasian High Arctic. *Quatern. Res.* **52**, 273–285.
- Sigman, D.M., Hain, M.P., and Haug, G.H. [2010]. The polar ocean and glacial cycles in atmospheric CO₂ concentration, *Nature* **466**, doi: 10.1038/nature09149.
- Slater, A.G., Bohn, T.J., McCreight, J.L., Serreze, M.C., and Lettenmaier, D.P. [2007]. A multimodel simulation of pan-Arctic hydrology. *J. Geophys. Res.* **112**, G04S45, doi:10.1029/2006JG00303.
- Slater, A.G. and Lawrence, D.M. [2012]. Diagnosing present and future permafrost in climate models. *J. Climate* **26**, 5608–5622, doi:10.1175/JCLI-D-12-00341.1.
- Slater, A.G., Schlosser, C.A., Desborough, C.E. et al. [2001]. The representation of snow in land surface schemes; results from PILPS 2(d). *J. Hydrometeorology* **2**, 7–25.
- Smith, E.H., Soule, F.M., and Mosby, O. [1937]. *The “Marion” and “General Green” Expeditions to Davis Strait and Labrador Sea, Under Direction of the United States Coast Guard, 1928–1931–1933–1934–1935: Part 2: Scientific Results*. Washington, DC: Bulletin U.S. Coast Guard.
- Smith, S. D., Anderson, R.O., den Hartog, G., Topham, D.R., and Perkin, R.G. [1983]. An investigation of a polynya in the Canadian Archipelago, 2, Structure of turbulence and sensible heat flux. *J. Geophys. Res.* **88**(C5), 2900–2910.
- Solomon, S. [1999]. Stratospheric ozone depletion: A review of concept and history. *Rev. Geophys.* **37**, 275–316.
- Souchez, R. [1997]. The buildup of the ice sheet in central Greenland. *J. Geophys. Res.* **102**(C12), 26317–26323.
- Spielhagen, R.F., Werner, K., Sorensen, S.A. et al. [2011]. Enhanced modern heat transfer to the Arctic by warm Atlantic water. *Science* **331**, 450–453, doi:10.1126/science.1197397.

- Srokosz, M., Baringer, M., Bryden, H. et al. [2012]. Past, present, and future changes in the Atlantic Meridional Overturning Circulation. *Bull. Am. Meteorol. Soc.* **93**, 1663–1676, doi: <http://dx.doi.org/10.1175/BAMS-D-11-00151.1>.
- Stamnes, K.H., Tsay, S-C., Wiscombe, W., and Jayaweera, K. [1988]. Numerical stable algorithm for discreet-ordinate radiative transfer in multiple scattering and emitting layered media. *Appl. Opt.* **27**, 2502–2509.
- Steele, M. and Boyd, T. [1998]. Retreat of the cold halocline layer in the Arctic Ocean. *J. Geophys. Res.* **103**, 10419–10435.
- Steele, M., Ermold, W., Hakkinen, S. et al. [2001]. Adrift in the Beaufort Gyre: A model comparison. *Geophys. Res. Lett.* **28**, 2935–2938.
- Steele, M., Thomas, D., and Rothrock, D. [1996]. A simple model study of the Arctic Ocean freshwater balance, 1979–1985. *J. Geophys. Res.* **101**(C9), 20833–20848.
- Steffen, K. [1985]. Warm water cells in the North Water, northern Baffin Bay during winter. *J. Geophys. Res.* **90**(5), 9129–9136.
- Steffen, K. and Box, J.E. [2001]. Surface climatology of the Greenland Ice Sheet: Greenland Climate Network 1995–1999. *J. Geophys. Res.* **106**(D24), 33951–33964.
- Steffen, K., Box, J.E., and Abdalati, W. [1996]. Greenland Climate Network: GC-Net. In: S.C. Colbeck (ed.), *CRREL 96–27 Special Report on Glaciers, Ice Sheets and Volcanoes (tribute to M. Meier)*. Hanover, NH: US Army, pp. 98–103.
- Stern, H.L. and Moritz, R.E. [2002]. Sea ice kinematics and surface properties from RADARSAT synthetic aperture radar during the SHEBA drift. *J. Geophys. Res.* **107**(C10), 8028, DOI: 10.1029/2000JC000472.
- Stigebrandt, A. [2000]. Oceanic freshwater fluxes in the climate system. In: E.L. Lewis, E.P. Jones, P. Lemke, T. Prowse, and P. Wadhams (eds.), *The Freshwater Budget of the Arctic Ocean. NATO Science Series 2. Environmental Security – Vol. 70*. Dordrecht, the Netherlands: Kluwer Academic Publishers, pp. 1–20.
- Stone, R.S., Herber, A., Mazzola, M. et al. [2010]. A three-dimensional characterization of Arctic aerosols from airborne sun photometer observations: PAM-ARCMIP, April 2009. *J. Geophys. Res.* **115**, D13203, doi: 10.1029/2009JD013605.
- Stoner, A.M.K., Hayoe, K., and Ruebbles, D.J. [2009]. Assessing general circulation model simulations of atmospheric teleconnection patterns. *J. Climate* **22**, 4348–4372, doi:10.1175/2009JCLI2577.1.
- Stroeve, J., Holland, M.M., Meier, W., Scambos, T., and Serreze, M. [2007]. Arctic sea ice decline: Faster than forecast. *Geophys. Res. Lett.* **34**, doi: 10.1029/2007GL029703.
- Stroeve, J.C., Kattsov, V.K., Barrett, A., Serreze, M., Pavlova, T., Holland, M., and Meier, W.M. [2012]. Trends in Arctic sea ice extent from CMIP5, CMIP3 and observations. *Geophys. Res. Lett.* **39**, L16502, doi:10.1029/2012GL052676.
- Stroeve, J.C., Maslanik, J., Serreze, M.C., Rigor, I., Meier, W.M., and Fowler, C. [2011a]. Sea ice response to an extreme negative phase of the Arctic Oscillation during winter 2009/2010. *Geophys. Res. Lett.* **38**, L02502, doi:10.1029/2010GL045662.
- Stroeve, J.C., Serreze, M.C., Holland, M.M., Kay, J.E., Maslanik, J. and Barrett, A.P. [2011b]. The Arctic's rapidly

- shrinking sea ice cover: a research synthesis. *Climatic Change*, doi:10.1007/s10584-011-0101-1.
- Sturm, M., Racine, C., and Tape, K. [2001]. Climatic change: Increasing shrub abundance in the Arctic. *Nature* **411**, 546–547.
- Sturm, M.M., Holmgren, J., and Liston, G. E. [1995]. A seasonal snow cover classification system for local to global application. *J. Climate* **8**, 1261–1283.
- Su, F., Adam, J.C., Trenberth, K.E., and Lettenmaier, D.P. [2006]. Evaluation of surface water fluxes of the pan-Arctic land region with a land surface model and ERA-40 reanalysis. *J. Geophys. Res.* **111**, D05110, doi:10.1029/2005JD006387.
- Subetto, D.A., Wohlfarth, B., Davydona, N.N. et al. [2002]. Climate and environment on the Karelian Isthmus, northwestern Russia, 13000–9000 cal. yrs BP. *Boreas* **31**, 1–19.
- Svendsen, J.I., Astakhov, V.I., Bolshiyanov, D.Y. et al. [1999]. Maximum extent of the Eurasian ice sheets in the Barents and Kara Sea region during the Late Weichselian. *Boreas* **28**, 234–242.
- Sverdrup, H.U. [1933]. *The Norwegian North Polar Expedition with the "Maud", 1918–1925, Volume II: Meteorology*. Bergen: John Griegs, Boktrykkeri.
- Tape, K., Sturm, M., and Racine, C. [2006]. The evidence for shrub expansion on northern Alaska and the Pan-Arctic. *Global Change Biol.* **12**, 686–702.
- Tarnocai, C., Canadell, J.G., Schuur, E.A.G., Kuhry, P., Mazhitova, G., and Zimov, S. [2009]. Soil organic carbon pools in the northern circumpolar permafrost region. *Global Biogeochemical Cycles* **23**, GB2023, doi: 10.1029/2008GB003327.
- Tedesco, M., Fettweis, X., van den Broeke, M.R. et al. [2010]. The role of albedo and accumulation in the 2010 melting record in Greenland. *Environmental Research Letters* **6**, 014005, doi: 10.1088/1748-9326/6/1/014005.
- Thomas, D.R., Martin, S., Rothrock, D.A., and Steele, M. [1996]. Assimilating satellite concentrations into an Arctic mass balance model: 1979–1985. *J. Geophys. Res.* **101**(C9), 20849–20868.
- Thomas, D.R. and Rothrock, D.A. [1989]. Blending sequential Scanning Multichannel Microwave Radiometer and buoy data into a sea ice model. *J. Geophys. Res.* **94**(C8), 10907–10920.
- [1993]. The Arctic Ocean ice balance: A Kalman smoother estimate. *J. Geophys. Res.* **98**(C6), 10053–10067.
- Thomas R.H. [2004]. Force-perturbation analysis of recent thinning and acceleration of Jakobshavn Isbrae, Greenland. *J. Glaciol.* **50**, 57–66, doi:10.3189/172756504781830321.
- Thomas, R.N. [2001]. Program for Arctic Regional Climate Assessment (PARCA): Goals, key findings, and future directions. *J. Geophys. Res.* **106**(D24), 33691–33705.
- Thompson, D.W.J. and Wallace, J.M. [1998]. The Arctic Oscillation signature in the wintertime geopotential height and temperature fields. *Geophys. Res. Lett.* **25**, 1297–1300.
- Thompson, D.W.J. and Wallace, J.M. [2000]. Annular modes in the extratropical circulation. Part I: Month-to-month variability. *J. Climate* **13**, 1000–1016.
- Thompson, D.W.J., Wallace, J.M., and Hegerl, G. [2000]. Annular modes in the extratropical circulation. Part II: Trends. *J. Climate* **13**, 1018–1036.
- Thorndike, A.S. [1986]. Kinematics of sea ice. In: N. Untersteiner (ed.), *The Geophysics of Sea Ice, NATO ASI Ser.*,

- Ser. B Phys.*, Vol. 146. New York: Plenum Press, pp. 489–549.
- Thorndike, A.S. and Colony, R. [1982]. Sea ice motion in response to geostrophic winds. *J. Geophys. Res.* **87**(C8), 5845–5852.
- Tietche, S., Notz, D., Jungclaus, J.H., and Marotzke, J. [2011]. Recovery mechanisms of Arctic summer sea ice. *Geophys. Res. Lett.* **38**, L02707, doi:10.1029/2010GL045698.
- Trenberth, K.E. [1998]. Atmospheric moisture residence times and cycling: implications for rainfall rates and climatic change. *Climatic Change* **39**, 667–694.
- Trenberth, K.E. and Caron, J.M. [2001]. Estimates of meridional atmosphere and ocean heat transports. *J. Climate* **15**, 3433–3443.
- Trenberth, K.E., Caron, J.M., and Stepaniak, D.P. [2001]. The atmospheric energy budget and implications for surface fluxes and ocean heat transports. *Clim. Dynam.* **17**, 259–276.
- Trenberth, K.E. and Paolino, D.A. [1980]. The Northern Hemisphere sea-level pressure data set: Trends, errors and discontinuities. *Mon. Wea. Rev.* **108**, 855–872.
- Trenberth, K.E. and Stepaniak, D.P. [2003]. Co-variability of components of poleward atmospheric energy transports on seasonal and interannual timescales. *J. Climate* **16**, 3706–3722.
- Tsukernik, M., Chase, T.N., Serreze, M.C. et al. [2004]. On the regulation of minimum mid-tropospheric temperatures in the Arctic. *Geophys. Res. Lett.* **31**, L06112, doi: 10.1029/2003GLO18831.
- Tsukernik, M., Kindig, D.N., and Serreze, M.C. [2007]. Characteristics of winter cyclone activity in the northern North Atlantic: Insights from observations and regional modeling. *J. Geophys. Res.* **112**, D03101, doi: 10.1029/2006JD007184.
- Tumel, N. [2002]. Permafrost. In: M. Shahgedanova (ed.), *The Physical Geography of Northern Eurasia*. Oxford: Oxford University Press, pp. 149–168.
- Tyndall, J. [1872]. *The Forms of Water in Clouds and Rivers, Ice and Glacier*. Akron, OH: The Werner Co.
- Uttal, T., Curry, J.A., McPhee, M.G. et al. [2002]. Surface heat budget of the Arctic Ocean. *Bull. Amer. Meteorol. Soc.* **83**, 255–275.
- Vage, K., Spengler, T., Davies, H., and Pickart, R. [2009]. Multi-event analysis of the westerly Greenland tip jet based upon 45 winters in ERA-40, *Quart. J. Roy. Met. Soc.*, **135**, 1999–2011.
- van den Berg, W.J., van den Broeke, M., Etteme, J., van Meijgaard, E., and Kaspar, F. [2011]. Significant contribution of insolation to Eemian melting of the Greenland Ice Sheet. *Nature Geoscience* **4**, 679–683, doi:10.1038/NGE01245.
- van den Broeke, M., Bamber, J., Etteme, J. et al. [2009]. Partitioning recent Greenland mass loss. *Science* **326**, 984–986, doi:10.1126/science.1178176.
- van der Veen, C.J., Bromwich, D.H., and Castello, C.K. [2001]. Trend surface analysis of Greenland accumulation. *J. Geophys. Res.* **106**(D24), 33909–33918.
- van Kolfschoten, T., Gibbard, P.L., and Knudsen, K-L. [2003]. The Eemian Interglacial: A global perspective. Introduction. *Global Planet. Change* **36**, 17–49.
- van Loon, H. [1967]. The half –yearly oscillation in middle and high southern latitudes and the coreless winter. *J. Atmos. Sci.* **24**, 472–486.
- van Loon, H. and Rogers, J.C. [1978]. Seesaw in winter temperatures between Greenland and Northern Europe. Part I: General description. *Mon. Wea. Rev.* **106**, 296–310.

- Vasil'chuk, Yu. K. and Kotlyakov, V.M. [2000]. *Osnovy Izotopnoi Geokriologii I Glaciologii (Principles of Isotope Geocryology and Glaciology)*. Moscow: Moscow University Press.
- Vaughan, R. [1999]. *The Arctic: A History*. Stroud, England: Sutton Publishing.
- Velitchko, A.A. and Spasskaya, I. [2002]. Climate change and the development of landscapes. In: Shahgedanova, M. (ed.), *The Physical Geography of Northern Eurasia*. Oxford University Press, pp. 36–69.
- Verseghy, D.L. [1991]. CLASS: A Canadian Land Surface Scheme for GCMs. I. Soil model. *Int. J. Climatology* **11**, 111–133.
- Verseghy, D.L., McFarlane, K.A., and Lazar, M. [1993]. CLASS: A Canadian Land Surface Scheme for GCMs. II. Vegetation model and coupled runs. *Int. J. Climatology* **13**, 347–370.
- Vinje, T. [2001]. Fram Strait ice fluxes and atmospheric circulation: 1950–2000. *J. Climate* **14**, 3508–3517.
- Vinje, T., and Finnekasa, O. [1986]. The ice transport through Fram Strait. *Rep. NR* 186. Oslo: Norsk Polarinstitut.
- Vinje, T., Nordlund, N., and Kvambekk, A. [1998]. Monitoring ice thickness in Fram Strait. *J. Geophys. Res.* **103**, 10437–10449.
- Viterbo, P. and Beljaars, A.C.M. [1995]. An improved land surface parameterization scheme in the ECMWF model and its validation. *J. Climate* **8**, 2716–2748.
- Vogt, P.R. [1986]. Seafloor topography, sediments and paleoenvironments. In: B.G. Hurdle (ed.), *The Nordic Seas*. New York: Springer Verlag, pp. 237–410.
- von Helmholtz, H. [1888]. Ueber Atmosphaerische Bewegungen. *Meteor. Zeit.* **5**, 329–340.
- von Neumayer, G. and Boergen, C.N.J. (eds.) [1886]. *Die Internationale Polarforschung 1882–1883. Die Beobachtungs Ergebnisse der Deutschen Stationen, Vol. 1, Kingua-Fjord und die meteorologischen Stationen. Vol. 2, Ordnung in Labrador, Hebron, Okak, Nain, Zoar, Hoffenthal, Rama, sowie die magnetischen Observatorien in Breslau und Goettingn*. Berlin.
- Vorusmarty, C.J., Fekete, B., Meybeck, M., and Lammers, R.B. [2000]. The global system of rivers: Its role on organizing continental landmass and defining land-to-ocean linkages. *Global Biogeochemical Cycles* **14**, 599–621.
- Vowinkel, E., and Orvig, S. [1967]. The inversion layer over the polar ocean. *World Meteorological Organization Tech. Note No. 87*. Geneva: Polar Meteorology: Proc. of the WMO/SCAR/ICPM Symp. on Polar Meteorology.
- Vowinkel, E. and Orvig, S. [1970]. The climate of the North Polar Basin. In: S. Orvig (ed.), *World Survey of Climatology, Vol. 14: Climates of the Polar Regions*. Amsterdam: Elsevier, pp. 129–226.
- Wadhams, P. [1980]. Ice characteristics in the seasonal ice zone. *Cold Reg. Sci. Technol.* **2**, 37–87.
- [1983]. Sea ice thickness distribution in Fram Strait. *Nature* **305**, 108–111.
- [2000]. *Ice in the Ocean*. London: Taylor and Francis.
- Walker, D.A., Gould, W.A., Maier, H.A., and Reynolds, M.K. [2002]. The Circumpolar Arctic Vegetation Map. AVHRR-derived base maps, environmental conditions, and integrated mapping procedures. *Int. J. Rem. Sensing* **23**, 4551–4570.
- Walker, G.T. and Bliss, E.W. [1932]. World weather. *V. Mem. Roy. Meteor. Soc.* **103**, 29–64.
- Walker, J.M. [1967]. Subterranean isobars. *Weather* **22**, 296–297.

- Wallace, J.M. [1983]. The climatological mean stationary waves: Observational evidence. In: B. Hoskins and R. Pearce (eds.), *Large Scale Dynamical Processes in the Atmosphere*. San Diego, CA: Academic Press, pp. 27–53.
- [2000]. North Atlantic Oscillation/annular mode: Two paradigms – one phenomenon. *Quart. J. Roy. Met. Soc.* **126**, 791–805.
- Wallace, J.M. and Gutzler, D.S. [1981]. Teleconnections in the geopotential height field during the Northern Hemisphere winter. *Mon. Wea. Rev.* **109**, 784–812.
- Walland, D.J. and Simmonds, I. [1997]. Modeled atmospheric response to change in Northern Hemisphere snow-cover. *Clim. Dynam.* **13**, 25–34.
- Wallis, H. [1984]. England's search for the Northern Passages in the sixteenth and early seventeenth centuries. *Arctic* **37**, 453–472.
- Walsh, J.E. and Chapman, W.L. [1990]. Arctic contribution to upper-ocean variability in the North Atlantic. *J. Climate* **3**, 1462–1473.
- Walsh, J.E., Hibler, W.D. III, and Ross, B. [1985]. Numerical simulation of northern hemisphere sea ice variability, 1951–1980. *J. Geophys. Res.* **90**(C3), 4847–4865.
- Walsh, J.E., Zhou, X., Portis, D., and Serreze, M.C. [1994]. Atmospheric contributions to hydrologic variations in the Arctic. *Atmosphere-Ocean* **32**, 733–755.
- Wang, J., Zhang, J., Watanabe, E. et al. [2009]. Is the dipole anomaly a major drier to record lows in Arctic summer sea ice extent? *Geophys. Res. Lett.* **36**, L05706, doi:10.1029/2008GL036706.
- Warneke, C., Froyd, K.D., Brioude, J. et al. [2010]. An important contribution to springtime Arctic aerosol from biomass burning in Russia. *Geophys. Res. Lett.* **37**, L01801, doi:10.1029/2009GL041816.
- Warren, B.A. [1983]. Why is no deep water formed in the North Pacific? *J. Mar. Res.* **41**, 327–347.
- Warren, S.G. [1982]. Optical properties of snow. *Rev. Geophys. Space Phys.* **2**, 67–89.
- Warren, S.G., Hahn, C.J., London, J., Chervin, R.M., and Jenne, R. [1988]. Global distribution of total cloud cover and cloud type amounts over the ocean. *NCAR Tech. Note, TN – 317+STR*. Boulder, CO: NCAR.
- Watkins, H.G. [1932]. The British Arctic Air Route Expedition. *Geogr. J.* **79**, 353–367; 466–501.
- Weaver, A.J., Bitz, C.M., Fanning, A.F., and Holland, M.M. [1999]. Thermohaline circulation: High-latitude phenomena and the difference between the Pacific and Atlantic. *Ann. Rev. Earth Planet. Sci.* **27**, 231–285.
- Webber, P.J. [1974]. Tundra primary productivity. In: J.D. Ives and R.G. Barry (eds.), *Arctic and Alpine Environments*. London: Methuen, pp. 445–473.
- Weeks, W.F. and Ackley, S.F. [1986]. The growth, structure and properties of sea ice. In: N. Untersteiner (ed.), *The Geophysics of Sea Ice, NATO ASI Ser., Ser. B Phys.*, Vol. 146. New York: Plenum Press, pp. 9–164.
- Weller, G., Cubley, S., Parker, S., Trabant, D., and Benson, C. [1972]. The tundra microclimate during snow melt at Barrow, Alaska. *Arctic* **24**, 291–300.
- Weller, G. and Holmgren, B. [1974]. The microclimates of the Arctic Tundra. *J. Appl. Meteor.* **11**, 854–862.
- Welsh, J.P., Ketchum, R.D. Jr., Lohanick, A.W., Farmer, L.D., Eppler, D.T., Burge, R.E., and Radl, C.J. [1986]. *A Compendium of Arctic Environmental*

- Information. Naval Ocean Res. Dev. Activity Report* 138. Michigan: NSTL.
- Wendler, G.W., Easton, F.D., and Ohtake, T. [1981]. Multiple reflection effects on irradiance in the presence of Arctic stratus clouds. *J. Geophys. Res.* **86**(C3), 2049–2057.
- Westbrook, G.K., Thatcher, K.E., Rohling, E.J. et al. [2009]. Escape of methane gas from the seabed along the West Spitzbergen continental margin. *Geophys. Res. Lett.* **36**, L15608, doi:10.1029/2009GL039191.
- Wexler, H. [1936]. Cooling in the lower atmosphere and the structure of polar continental air. *Mon. Wea. Rev.* **64**, 122–136.
- Weyl, P.K. [1968]. The role of the oceans in climatic change: A theory of the ice ages. *Meteorological Monographs* **8**, 38–62.
- Wielicki, B.A., Barkstrom, B.R., Harrison, E.F., Lee III, R.B., Louis Smith, G., and Cooper, J.E. [1996]. Clouds and the Earth's Radiant Energy System (CERES): An Earth observing system experiment, *Bull. Am. Meteorol. Soc.*, **77**, 853–868.
- Williams, R. S. and Ferrigno, J.G. (eds.) [2002]. *Satellite Image Atlas of Glaciers of the World*. North America, Washington DC: U.S. Geol. Survey, Professional paper, 1386-J.
- Wilson, C.V. [1958]. Synoptic regimes of the lower Arctic troposphere during 1955. *Arctic Meteorology Research Group, Publication in Meteorology No. 8*. Montreal, Canada: McGill University.
- Wilson, C.V. and Godson, W.L. [1962]. The stratospheric temperature field at high latitudes. *Arctic Meteorology Research Group Publication in Meteorology No. 46*. Montreal, Canada: McGill University.
- [1963]. The structure of the Arctic winter stratosphere over a 10-year period. *Quart. J. Roy. Met. Soc.* **89**, 205–224.
- Wilson, L.D., Curry, J.A., and Ackerman, T.P. [1993]. Satellite retrieval of lower-tropospheric ice crystal clouds in the polar regions. *J. Climate* **6**, 1467–1472.
- Wiscombe, W.J. and Warren, S.G. [1980]. A model for the spectral albedo of snow. I. Pure snow. *J. Atmos. Sci.* **37**, 2712–2733.
- Wohlleben, T.M.H. and Weaver, A.J. [1995]. Interdecadal climate variability in the subpolar North Atlantic. *Clim. Dynam.* **11**, 459–467.
- Wolfe, A.P. and King, R.H. [1999]. A palaeoclimatological constraint to the extent of the last glaciation on northern Devon Island, Canadian high Arctic. *Quatern. Sci. Rev.* **18**, 1563–1568.
- Woo, M-K., Heron, R., Marsh, P., and Steer, P. [1983]. Comparison of weather station snowfall with winter snow accumulation in high Arctic basins. *Atmosphere-Ocean* **21**, 312–325.
- World Meteorological Organization [1989]. *WMO Sea-Ice Nomenclature, Terminology, Codes and Illustrated Glossary*. Geneva: WMO/OMM/BMO, 259, TP 145, Secretariat WMO, Vol. 1.
- Wright, J.K. [1953]. The open polar sea. *Geogr. Rev.* **63**, 338–365.
- Wunsch, C. [2004]. Quantitative estimate of the Milankovitch-forced contribution to observed Quaternary climate change. *Quatern. Sci. Rev.* **23**, 1001–1012, <http://dx.doi.org/10.1016/j.quascirev.2004.02.014>.
- Xie, P. and Arkin, P.A. [1997]. Global precipitation: A 17-year monthly analysis based on gauge observations, satellite estimates and numerical model outputs. *Bull. Amer. Meteorol. Soc.* **78**, 2539–2558.
- Yang, D. [1999]. An improved precipitation climatology for the Arctic Ocean. *Geophys. Res. Lett.* **26**, 1525–1528.

- Yang, D., Goodison, B., Metcalfe, J. et al. [2001]. Compatibility evaluation of national precipitation gauge measurements. *J. Geophys. Res.* **106**(D2), 1481–1491.
- Yang, D., Kane, D.L., Hinzman, L.D., Zhang, X., Zhang, T., and Ye, H. [2002]. Siberian Lena river hydrologic regime and recent change. *J. Geophys. Res.* **107**(D23), doi: 10.1029/2002JD002542.
- Ye, B., Yang, D., and Kane, D. [2003]. Changes in Lena River streamflow hydrology: Human impacts versus natural variations. *Water Resources Research* **39**, doi: 10.1029/2003WR001991.
- Yi, S., McGuire, A.D., Harden, J. et al. [2009]. Interactions between soil thermal and hydrological dynamics in the response of Alaska ecosystems to fire disturbance. *J. Geophys. Res.* **114**, G02015, doi: 10.1029/2008JG000841.
- Zangl, G. and Hoinka, K.P. [2001]. The tropopause in the polar regions. *J. Climate* **14**, 3117–3139.
- Zazula, G.D., Froese, D.G., Telka, A.M., Mathewes, R.W., and Westgate, J.A. [2002]. Plants, bugs and giant mammoth tusk: Paleoenvironment of Last Chance Creek, Yukon Territory. In: *Yukon Exploration and Geology, 2002*, Government of Canada Publications, pp. 251–258.
- Zhang, J.L. and Rothrock, D.A. [2003]. Modeling global sea ice with a thickness and enthalpy distribution model in generalized curvilinear coordinates. *Mon. Wea. Rev.* **131**, 845–861.
- Zhang, J., Rothrock, D.A., and Steele, M. [2000]. Recent changes in Arctic sea ice: The interplay between ice dynamics and thermodynamics. *J. Climate* **13**, 3099–3114.
- Zhang, T., Stammes, K., and Bowling, S.A. [2001]. Impact of atmospheric thickness on the atmospheric downwelling longwave radiation and snowmelt under clear-sky conditions in the Arctic and subarctic. *J. Climate* **14**, 920–939.
- Zhang, T-J., Barry, R.G., Knowles, K., Heginbottom, J.A., and Brown, J. [1999]. Statistics and characteristics of permafrost and frozen ground ice distribution in the Northern Hemisphere. *Polar Geog.* **23**, 147–169.
- Zhang, T-J., Heginbottom, J.A., Barry, R.G., and Brown, J. [2001]. Further statistics on the distribution of permafrost and frozen ground in the Northern Hemisphere. *Polar Geog.* **24**, 14–19.
- Zhang, X., He, J., Zhang, J. et al. [2012]. Enhanced poleward moisture transport and amplified northern high-latitude wetting trend. *Nature Climate Change*, doi:10.1038/NCLIMATE1631.
- Zhang, X., Walsh, J.E., Zhang, J., Bhatt, U.S., and Ikeda, M. [2004]. Climatology and interannual variability of Arctic cyclone activity, 1948–2002. *J. Climate* **15**, 2300–2317.
- Zhou, L., Tucker, C.J., Kaufmann, R.K., Slayback, D., Shabanov, N.V., and Myneni, R.B. [2001]. Variations in northern vegetation activity inferred from satellite data of vegetation index during 1981 to 1999. *J. Geophys. Res.* **106**(D17) 20069–20083.
- Zhu, Y. and Newell, R.E. [1998]. A proposed algorithm for moisture fluxes from atmospheric rivers. *Mon. Wea. Rev.* **126**, 725–735.
- Zubenok, Z.T. [1976]. Isparenie sushi vodosbornogo basseina Severnogo Ledovitogo Okeana. (Evaporation from the basins draining into the Arctic). *Trudy Arkt. Antarkt. Nauchno.-issled. Inst.* **323**, 87–100.

- Zubov, N. N. [1945]. *L'dy Arktiki*. Moscow: Glavsevmorputi. English translation: [1963]. *Arctic Sea Ice*. Suitland, MD: U.S. Nav. Hydrogr. Office. Available as AD426972 from Natl. Tech. Inf. Serv., Springfield, VA.
- Zwally, J., Abdalati, W., Herring, T. et al. [2002]. Surface melt-induced acceleration of Greenland Ice-Sheet flow. *Science* **297**, 218–222, doi:10.1126/science.1072708. PMID 12052902.
- Zwally, J. and Giovinetto, M.B. [2001]. Balance mass flux and ice velocity across the equilibrium line in drainage systems of Greenland. *J. Geophys. Res.* **106**(D24), 33717–33728.

Index

- active layer, *See* permafrost
aerological approach, *See* precipitation minus evapo-transpiration (P-ET)
aerosols, *See also* energy balance – surface
 Arctic haze, 54–55, 144
 climate impacts, 55–56, 144, 346
 sources, 54–55
air temperature
 Arctic amplification, 20, 53, 297
 extremes at surface, 51, 263–264
 inversions, 53, 139, 168–172
 kernlose pattern in troposphere, 103–104
 projected changes, 297
 regional variations at surface, 24, 51–53
 seasonal variations at surface, 24, 51–53,
 139
 trends at surface, 20, 53, 341–342
Alaska, 2, 6, 7, 164–167, 269, 271
albedo, *See also* energy balance – surface
 clouds, 138–139
 definition, 147–148
 ice-albedo feedback, 172–174
 influence on cloud radiative forcing, 158
 major surface types, 148
 planetary, 67, 77, 79
 regional variations at surface, 138, 140, 152–153,
 156, 269
 scale issues, 151
 sea ice, 150–151
 SHEBA observations, 160–162
 snow, 148–150
 spectral reflectance, 149
Aleutian Low, *See* atmospheric circulation
Amundsen, Roald, 9, 10
annual cycles of climate elements
 cloud cover, 58–60, 255, 267, 268
 energy budget terms, 161, 163
 precipitation, 195–197, 265, 267, 268
 runoff, major watersheds, 204
 temperature, 265, 267, 268, *See also* air
 temperature
 anticyclones, *See* atmospheric circulation
 Arctic “back door”, 210, 245–247
 Arctic Climate Impact Assessment (ACIA), 21
 Arctic climate regimes
 central Arctic Ocean, 250, 268
 Greenland, 249–261
 maritime Arctic, 250, 264–266
 mountains and uplands, 269–270
 polar desert, 40–41, 250, 262–264
 Arctic, definition, 23, 26
 Arctic Dipole Anomaly, *See* atmospheric circulation
 modes and their impacts
 Arctic exploration, 1–14
 Arctic frontal zone, *See* atmospheric circulation
 Arctic haze, *See* aerosols
 Arctic lands, topography, 37–38
 Arctic Observing Network (AON), 18–19
 Arctic Ocean
 Atlantic inflow, 20, 32–33, 241–242, 345
 Atlantic layer, 20, 33, 213, 241–242
 bathymetry, 25, 27
 circulation, 32–33, 36
 definition, 25–26
 freshwater budget, 32, 34–37, 177
 halocline, 31–32, 212, 241
 marine access, 22, 349–350
 mixed layer, 31, 212–213

- Arctic Ocean (*cont.*)
 Pacific inflow, 242
 pycnocline, 32, 212–213
 salinity, surface, 32
 sea ice cover, *See* sea ice characteristics; sea ice zones
 sea level gradients, 246
 vertical temperature and salinity structure, 31–33
- Arctic Ocean Intercomparison Project (AOMIP), 289–290
- Arctic Oscillation (AO), *See* atmospheric circulation modes and their impacts
- Arctic Regional Climate Model Comparison Project (ARCMIP), 299
- Arctic stratus, *See* cloud cover
- Arctic System Reanalysis (ASR), 306
- Arctic terrestrial drainage, *See also* water budgets – major watersheds, 32–33, 35
- Arctic treeline, 41
- Atlantic inflow, *See* Arctic Ocean
- Atlantic layer, *See* Arctic Ocean
- Atlantic Meridional Overturning Circulation (AMOC), 245, 325–326, 328
- atmospheric circulation, *See also* atmospheric circulation modes and their impacts
 Aleutian Low, 86–87, 105–106
 Beaufort Sea High (anticyclone), 104
 centers of action, 87, 104–106
 circumpolar vortex and planetary waves, 86, 93, 101–103, 108
 cyclogenesis and deepening, 106–110
 cyclone activity, 69, 86, 88, 106–110, 123, 125
 frontal activity, 86, 89–90, 110–116
 Icelandic Low, 86–87, 105, 107–109
 impacts of sea ice loss on, 125–126, 347
 jet streams, 91, 92, 114–115
 mid-troposphere, 86, 101–104
 North Atlantic storm track, 105, 109, 126
 Polar Lows, 117–120
 sea level pressure distribution, 85, 104–106
 Siberian High (anticyclone), 86–87, 104–105
 stratosphere, 85, 90–95
 atmospheric circulation modes and their impacts, *See also* atmospheric circulation
 Arctic Dipole Anomaly (DA), 87, 133–135, 241
 Arctic Oscillation (AO), 86, 128–131, 192–194, 238–240
 El-Nino Southern Oscillation (ENSO), 123–131
 North Atlantic Oscillation (NAO), 86–87, 120–128, 192–194, 238–240, 288–289, 344
 Northern Annular Mode (NAM), *See* Arctic Oscillation (AO)
 Pacific Decadal Oscillation (PDO), 87, 131–133
 Pacific North American (PNA) teleconnection, 87, 135–137
 atmospheric energy budget, *See* energy budget – Arctic column view
 atmospheric moisture balance, *See* precipitation minus evapo-transpiration (P-ET)
- Atmosphere Ocean Global Climate Models (AOGCMs), *See* models – types and applications
- atmospheric reanalyses, *See* models – types and applications
- automatic weather stations, Greenland, 16, 252
- aufeis, 44
- Baffin Bay, 2
- Baffin Island, 2, 15
- Baffin, William, 4
- Barents Sea, 3, 25
- Barents, Willem, 4
- Barrow, Alaska, 158, 267
- Barrow, John, 6
- Beaufort Sea
 Beaufort Gyre, *See* sea ice circulation
 Beaufort Sea High, *See* atmospheric circulation location, 2
 sea ice conditions, 236–237
- Beringia, 322
- Bering land bridge, 321, 332, 336
- Bering Sea, 2
- Bering Strait, 2, 5
- Bering, Vitus, 1, 5
- bipolar seesaw, 328
- blowing snow, 64
- Bølling-Allerød (B-A), 232
- boreal forest, 41
- brine rejection, *See* sea ice growth and melt
- British Trans-Arctic expedition, 15
- Brooks Range, 269
- Brunei, Oliver, 4
- Camp Century, 16
- Canadian Arctic Archipelago, 4
- Canadian Land Surface Scheme (CLASS), 283
- carbon budget, 306–309
- carbon dioxide and methane concentrations, 309, 324, 345–346, *See also* IPCC emission scenarios
- centers of action, *See* atmospheric circulation
- central Arctic Ocean (climate), *See* Arctic climate regimes
- central Arctic Ocean, definition, 25
- CFSR (atmospheric reanalysis), 19, 304
- CHASM (CHAmeleon Surface Model), 282
- Chersky-Momsky Mountains, 270
- Chukchi Sea, 2, 25
- circumpolar vortex, *See* atmospheric circulation
- clear-sky transmittance, *See* solar radiation
- climate change and variability – past, *See also* paleoclimate records; atmospheric circulation modes and their impacts
- Cordilleran Ice Sheet, 321, 331–332
- Daangsaaard Oeschger (DO) cycles, 311–312, 325–328
- distant past, 311–314
- Eemian Interglacial, 311, 318–319

- Fennoscandian Ice Sheet, 321, 329
Heinrich events, 325–326
Holocene, 311, 322, 337–341
Holocene Thermal Maximum (HTM), 337
Ice Rafted Detritus (IRD), 325, 327–328
Innuitian Ice Sheet, 321–331
instrumental record, 20–22, 341–342
last glacial cycle, 318–322
last Glacial Maximum (LGM), 312, 321, 329–332
late Holocene cooling, 339
Laurentide Ice Sheet, 321, 324–325, 331
Little Ice Age (LIA), 339–341
Medieval Warm Epoch, 339–340
Milankovitch cycles, 322–324, 332, 336–337, 339
Quaternary, general timeline, 317–322
sea level changes, 319, 321
Younger Dryas (YD), 312–322, 332–336
climate change and variability – projections for 21st century and beyond
carbon cycle, 308–309
permafrost, 296–297
sea ice, 294–296
temperature, 293
uncertainties, 293, 294–297, 309–310, 343–351
climate models, *See* models – types and applications
cloud condensation nuclei, 55, 59
cloud cover
 albedo, 138–139, 144
 amount, 24–25, 56–60, 61
 Arctic stratus, 58–59, 144
 cloud-radiation feedback, 174–175
 cloud radiative forcing (or effect), 60, 139, 157–159
 convective, 56, 81
 influence of aerosols, 55
 longwave absorption and emission, 138–139, 154
 noctilucent, 56
 polar stratospheric clouds (PSCs), 98–99
 relative transmission, 145
 trends, 60
 types, 56, 145
clouds, *See* cloud cover
cold air lakes, 51
Community Land Model (CLM), 282
condensate plumes, 164
conditional instability of the second kind (CISK), 117–118
conduction, *See* energy balance – surface
continental shelf, 25
Cook, James, 5
cooling effect of an ice cap or glacier, 267
Cordilleran Ice Sheet, *See* climate change and variability – past
Coupled Model Intercomparison Project (CMIP3 and CMIP5), 3, 19, 292–299
coupled models, *See* models – types and applications
Crocker Land, 9
cyclone activity, *See* atmospheric circulation
cyclogenesis and deepening, *See* atmospheric circulation
Dansgaard-Oeschger (D-O) cycles, *See* climate change and variability – past
data assimilation, 291, 304
Davis Strait, 2
daylength, 23–24
deglaciation, 332
depth hoar, 47
diamond dust, 56, 171
discharge and runoff, *See also* water budgets – major watersheds
gauging stations, 197–199
hydrographs, 203
major watersheds, 198–199, 201–208
modeled, 284–285
projected changes, 297–298
runoff surface, 199–201
trends, 207–208
variability, 203–206
Distant Early Warning Line (DEWLINE), 14
divergence, *See* sea ice deformation
drainages (watersheds), major, 32–33, 198–199
drainage of proglacial lakes, 334, 337
dynamic vegetation models, 276
Earth System Models, 275–276, *See also* models-types and applications
East Greenland Current, 33
East Siberian Sea, 3, 25
ECMWF land surface model, 283
ecosystem models, *See* models – types and applications
eddy correlation approach, 141–142
Eemian interglacial, *See* climate change and variability – past
Eliassen-Palm (EP) flux, 95–96
Ellesmere Island, 2
El-Niño Southern Oscillation (ENSO),
 See atmospheric circulation modes and their impacts
energy balance – surface
 annual cycle from SHEBA observations, 159–164
 bulk heat gain, 75, 140, 142
 conductive flux, 75, 138–140, 142–143, 162–163
 emissivity, longwave, 140–141, 154
 equations, 139–140
 feedbacks involving, 172–176
 latent heat flux, 74, 139–142, 162–164, 165–166
 longwave radiation, 140–141, 152–155, 160–162
 melt term, 75, 139–140, 142
 net radiation, 138–140, 155–157, 160–162, 165–166
 net surface heat flux, 71–72, 73–79, 82–84, 139–140, 165–166
 regional contrasts, 164, 166–167

- energy balance – surface (*cont.*)
 sensible heat flux, 74, 138–142, 162–164,
 165–166
 shortwave (global) radiation, 140, 143–147,
 160–162
 sublimation, 141, 258–259
 tundra, 165–166
 energy budget – global view
 poleward energy transports, 68–70
 radiation budget, global average, Top of
 Atmosphere (TOA), 66–67
 radiation budget, TOA, latitudinal
 distribution, 67–68
 energy budget – Arctic column view
 Arctic ocean domain, annual cycle,
 82–84
 framework and equations, 65–66, 70–76
 polar cap domain, annual cycle, 76–79
 polar cap domain, annual mean, 82
 polar cap, longitudinal dependence of horizontal
 energy transports, 80–81
 equilibrium line altitude, 270
 ERA-15 (atmospheric reanalysis), 69
 ERA-40 (atmospheric reanalysis), 19
 ERA-Interim (ERA-I) (atmospheric reanalysis),
 305
 evaporation and evapo-transpiration (ET),
See also energy balance – surface
 conversion from latent heat flux, 187
 major watersheds, 194
 measurement approaches, 187
 spatial and seasonal patterns, 188–189
- Fairbanks, Alaska, 271
 fast ice zone, *See* sea ice zones
 feedbacks – climate
 carbon cycle, 324
 cloud-radiation, 174–175
 ice-albedo, 172–174, 323–324
 permafrost carbon feedback, 308–309
 water vapor, 175–176
 fell fields, 40
 Fennoscandian Ice Sheet, *See* Climate change and
 variability – past
 first year ice, *See* sea ice types
 floeberg, 9
 foehn, 263–264
 forest-tundra boundary or ecotone, 41, 115–116, 262
Fram, 2, 11
 Fram Strait, *See also* Arctic Ocean
 ice export, *See also* sea ice circulation, 242–244
 liquid water export, 36
 role in Arctic Ocean freshwater budget, 36
 Franklin, John, 1, 6, 7–8
 Franz Josef Land, 3, 10, 12, 15, 270
 frazil ice, *See* sea ice types
 freshwater budget, *See* Arctic Ocean
 freshwater capping, 247–248, 325–328
 Frobisher, M., 1, 6
- frontal activity and frequency, *See* atmospheric
 circulation
 frozen ground, *See* permafrost
- gauge undercatch, *See* precipitation
 geologic time scale, 313
Georgy Sedov, 14
Gjoa, 9
 glaciations, *See* paleoclimate records
 global climate models (GCMs), *See* models – types
 and applications
 Global Energy and Water Exchanges (GEWEX)
 project, 18
 global radiation, *See* energy balance – surface
 grease ice, *See* sea ice types
 Great Salinity Anomaly, 211, 247–248
 Greely, Adolphus, 11
 greenhouse gas growth, 309, 345–346,
See also IPCC emission scenarios
 Greenland, *See also* Greenland Ice Sheet
 influence on cyclogenesis, 108–109
 katabatic winds, 254–255
 location, 2
 precipitation, 183–184, 249, 257–258
 sublimation, 258–259
 temperature regime, 252–253
 tip jets, 249, 255–257
 Greenland glacial anticyclone theory, 87–88
 Greenland Ice Core Project (GRIP), 16
 Greenland Ice Sheet, *See also* Greenland
 Eemian extent, 319
 early exploration, 8
 early meteorological studies, 13
 general features, 250–252
 ice cores, 16, 314–317
 mass balance, 20, 262–262
 radiation regime, 144, 254
 sea level equivalent, 39, 251
 surface melt extent, 20, 39, 259–261
 “Zwally effect”, 262
 Greenland Ice Sheet Project (GISP), 16
 gross primary production (GPP), 307–308
- Hall, Charles, 8
 halocline, *See* Arctic Ocean
 heat islands, 270–271
 Heinrich events, *See* climate change and
 variability – past
 Henson, Matthew, 9
 heterotrophic respiration (HR), 307
 high Arctic, 40
 HIRHAM regional climate model, 300
 historical exploration, *See* Arctic exploration
 Holocene Thermal Maximum, *See* climate change
 and variability – past
 Hudson Bay, 2, 4, 6
 Hudson, H., 1, 4
 Hudson’s Bay Company, 4, 6
 human alterations of river hydrology, 199–200

- humidity, 53–54
hydrographs of Arctic-draining rivers, *See* discharge and runoff
hydrologic impacts of atmospheric modes, *See* atmospheric circulation modes and their impacts

ice ages, *See* climate change and variability – past
ice-albedo feedback, *See* feedbacks, climate
icebergs, 250
ice caps, 24, 39
ice content of permafrost, *See* permafrost
ice cores, *See* paleoclimate records
ice crystal plumes, *See* condensate plumes
ice crystals, 47, 56, 59, 164, 171
“ice factory” of the Arctic Ocean, 223
ice fog, 271
ice formation in fresh water, 212
ice island T-3, 15, 40
ice jams, 206
Iceland, 2
Icelandic Low, *See* atmospheric circulation
ice-rafterd detritus (IRD) events, *See* climate change and variability – past
ice sheet influences on atmospheric circulation, 324–325
Innuitian Ice Sheet, *See* climate change and variability – past
instantaneous glacierization, 323–324
International Arctic Buoy Program (IABP), 16, 217
International Geophysical Year (IGY), 15
International Ice Patrol Service, 12
International Permafrost Association (IPA), 42–43
International Polar Year (IPY), 11, 13–14, 18
international science programs, 18
International Satellite Cloud Climatology Project (ISCCP), 57
IPCC emission scenarios, 293
isotopic composition, ice and ocean cores, 316–317

Jan Mayen, 262–265
Jeanette, 10, 11
jet streams, *See* atmospheric circulation

Kara Sea, 3, 25
katabatic winds, *See* Greenland
kernlose pattern in troposphere, *See* air temperature
Koch, J.P., 9
Kotzebue, Otto von, 6

Lake Aggasiz, 334–337
Lake El’gytgyn, 314, 318
Lake Hazen, 263
lakes, distribution, 44–45
landfast ice, *See* sea ice types
land surface models (LSMs), *See* models – types and applications
Laptev Sea, 3, 5, 25

Last glacial cycle, *See* climate change and variability – past
Last Glacial Maximum (LGM), *See* climate change and variability – past
Laurentide Ice Sheet, *See* climate change and variability – past
leads, *See* sea ice deformation
Lena River, 32–33, *See also* water budgets – major watersheds
Little Ice Age, *See* climate change and variability – past
Lomonosov, M.V., 6
longwave radiation at the surface, *See* energy balance – surface
longwave radiative equilibrium, 53, 170–172, *See also* air temperature
Low Arctic, 40

Mackenzie, Alexander, 6
Mackenzie River, 32–33, *See also* water budgets – major watersheds
Manhattan, 14
Marginal Ice Zone (MIZ), *See* sea ice zones
marine sediment cores, *See* paleoclimate records
maritime Arctic, *See* Arctic climate regimes
M’Clure, R., 8
Maud, 12–13
Maunder Minimum, *See* climate change and variability – past
Medieval Warm Epoch, *See* climate change and variability – past
melt ponds, *See* sea ice growth and melt
melt season, *See* sea ice growth and melt
MERRA (atmospheric reanalysis), 19, 305
methane in submarine sediments, 348–349
Milankovitch cycles, *See* climate change and variability – past
model errors, 309
models – types and applications
 atmospheric reanalyses, 19, 273, 276
 ecosystem models, 276, 306–309
 global climate models (GCMs, AOGCMs, ESMs), 275, 291–299
 land surface models (LSMs), 274, 280–286
 numerical weather prediction (NWP) models, 276, 302–306
 regional climate models, 299–302
 sea ice and coupled ice/ocean models, 274–275, 286–291
 single column models (SCMs), 274, 276–280
modes of variability, *See* atmospheric circulation modes and their impacts
Mohn, Henrik, 9, 10
moisture budget of an atmospheric column, *See* precipitation minus evapo-transpiration (P-ET)
moisture transports, horizontal
 longitudinal variations, 54, 80–81
related to the NAO and AO, 192–194

- momentum balance, *See* sea ice circulation
 mountains and uplands, 269–270
 multiple reflection and scattering, 144, 150
 multiyear ice, *See* sea ice types
- Nansen, Fridtjof, 1, 8, 11, 13, 54
 Nares, G., 1, 9, 11–12
 National Ice Center (NIC), 222
 National Science Foundation (NSF) projects, 18, 19
 NCEP/NCAR (atmospheric reanalysis), 19, 304
 net precipitation (P-ET), *See* precipitation minus evapo-transpiration (P-ET)
 net ecosystem exchange (NEE), 307
 net ecosystem production (NEP), 307
 net primary production (NPP), 307
 net radiation, *See* energy balance – surface
 net surface heat flux, *See* energy balance – surface
 NOAH Land Surface Model, 282
 noctilucent clouds, *See* cloud cover
 normalized difference vegetation index (NDVI), 20
 North Atlantic Deepwater (NADW) production, 245–248, 326–328, 333–336
 North Atlantic Oscillation (NAO), *See* atmospheric circulation modes and their impacts
 North Atlantic storm track, *See* atmospheric circulation
 Northeast Passage, *See* Northern Sea Route
 Northern Annular Mode (NAM), *See* atmospheric modes and their impacts
 Northern Sea Route, 3, 4, 5, 11
 North Pole Drifting Stations, 14–15
 North Water Polynya, 8
 Northwest Passage, 2, 4, 7, 8, 9
 Norwegian Sea, 3, 104
 Novaya Zemlya, 3, 4
 numerical weather prediction (NWP) models, *See* models – types and applications
- Ob River, 32–33; *See also* water budgets – major watersheds
 ocean circulation, *See* Arctic Ocean
 orbital variations, *See* Milankovitch cycles
 ozone
 absorbtion by, 91, 143
 boundary layer, 170
 column totals, 98
 hole, 98
 measurements, 98–99
- Pacific Decadal Oscillation (PDO), *See* atmospheric circulation modes and their impacts
 Pacific inflow, *See* Arctic Ocean
 Pacific North American (PNA) teleconnection, *See* atmospheric circulation modes and their impacts
 paleoclimate records, *See also* climate change and variability – past
 ice cores, 16, 314–317
 ocean cores, 314
- pollen, 314
 radiocarbon dating, 315
 tree rings, 315
- Pan-Arctic Ice Ocean Modeling and Assimilation System (PIOMAS), 291
- pancake ice, *See* sea ice types
 Pangea, 313
 Parry, William, 7
 patterned ground, 40
 Peary, Robert, 1, 8, 9
 Perennial Ice Zone (PIZ), *See* sea ice zones
 permafrost
 active layer, 42, 280
 continuous, 42–43
 definition, 42
 discontinuous, 43
 extent, 24, 42–44
 ice content, 44
 permafrost carbon feedback, *See* feedbacks, climate
 sporadic, 43
 submarine, 43–44
 thickness, 42–44
 warming, 20–21, 44
- Project for Intercomparison of Land Surface Schemes (PILPS), 283–285
- planetary albedo, *See* albedo
 planetary waves, *See* atmospheric circulation
 polar desert, *See* Arctic climate regimes
 Polar Lows, *See* atmospheric circulation
 Polar MM5, 299
 polar night jet stream, *See* atmospheric circulation
 polar stratospheric clouds (PSCs), *See* cloud cover
 poleward energy transports, *See* energy budget – global view
 polynyas, *See* sea ice characteristics
 potential vorticity, 94–95, 100
 precipitable water, 53–54
 precipitation
 Arctic frontal zone, 181–182
 central Arctic Ocean, 179, 185–186
 convective, 181
 frequency and phase, 184–186
 Greenland, 183–184
 major watersheds, 194
 maritime Arctic, 265
 measurement difficulties, 62, 178
 polar desert, 264
 projected changes, 62–63, 297
 recycling ratio, 194–196
 seasonality, 62, 177–182
 spatial patterns, 24, 62, 177–182
 station network, 60–61, 180
- precipitation minus evapo-transpiration (P-ET)
 aerological approach, 189–190
 impacts of NAO and AO, 193–194
 major watersheds, 35, 194
 ocean, 35
 seasonality, 191–192

- spatial patterns, 177–178, 191–192
Program for Arctic Regional Climate Assessment (PARCA), 252
Project for Intercomparison of Land Surface Parameterization Schemes (PILPS), 283–285
pycnocline, *See* Arctic Ocean
- Quaternary, *See* Climate change and variability – past
- radiative boundary layer, 167–168
radiative transfer models, 58, 144, 152, 297–299
radiocarbon dating, *See* paleoclimate records
radiosondes, 168–169, 190
Rae, Dr. John, 7–8
rafting, *See* sea ice deformation
recycling ratio, *See* precipitation
Regional Atmospheric Climate Model (RACMO), 299
regional climate models, *See* models – types and applications
remote sensing
 clouds, 57–58, 59–60, 61
 Greenland Ice Sheet, 261
 important systems, 17–18
 precipitation, 61
 radiation budget, 68, 76, 145–147, 153–157, 159–160
 sea ice, 21, 27, 224–225, 227, 232, 243, 295–296, 300
 snow, 21, 279–280
Resolute Bay, 264
ridging, *See* sea ice deformation
river discharge, *See* discharge and runoff
Ross, John, 7
Royal Society, 7
runoff, *See* discharge and runoff
- salinity
 effect on temperature of maximum density, 212
 surface, 31–32
 vertical structure, 31–33, *See also* Arctic Ocean
“salt oscillator” concept, 326
sastrugi, 47–48
Scoresby Jr., William, 6, 8
sea ice characteristics
 concentration, 27, 222–223
 extent, 26–27, 28
 polynyas, 27
 salinity, 29
 snow on sea ice, 49–51
 thickness and draft, 29, 223–225, 295–296
sea ice circulation
 Beaufort Gyre, 210, 218, 223
 Fram Strait ice export, 36, 239, 241, 242–244
 general characteristics, 28, 210
 momentum balance, 226–227
 Transpolar Drift Stream (TPDS), 208–219, 210
 variability, 227, 235–241
- sea ice deformation
 differential velocity, 228–232
 divergence and convergence, 28, 210, 228–232
 leads, 28, 223
 rafting and ridging, 28, 210, 223, 228, 230–231
 shear, 210, 229–230
sea ice growth and melt
 brine rejection, 213–214
 equilibrium ice growth, 209–210, 216–217
 general characteristics, 28–29, 209–210
 ice age, 214–215
 melt ponds, 151
 thick ice growth, 216–217
 young ice growth, 214–215
sea ice types
 firstyear ice (FYI), 213–214, 224–225
 frazil ice, 214
 pancake ice, 214
 multiyear ice 29 (MYI), 29, 213–214, 224–225
sea ice variability and trends
 anomalies, causes of, 234–242
 observed trends, 20–21, 232, 234
 projected changes, 294–295
sea ice zones
 fast ice, 219, 222
 Marginal Ice Zone (MIZ), 210, 220, 222
 Perennial Ice Zone (PIZ), 210, 219, 222
 Seasonal Ice Zone (SIZ), 210, 219
 shear zone, 219–220
 sea ice and coupled ice/ocean models, *See* models – types and applications
sea level pressure, *See* atmospheric circulation
Seasonal Ice Zone (SIZ), *See* sea ice zones
sensible heat flux, *See* energy balance – surface
Severnaya Zemlya, 3, 270
Seward, William T., 7
shear, *See* sea ice deformation
shear zone, *See* sea ice zones
SHEBA, 18, 159–162
Siberian High (anticyclone), *See* atmospheric circulation
Sibiryakov, 14
single column models (SCMs), *See* models – types and applications
skin temperature, 167–168
snow cover
 albedo, 45
 classes, 46–47
 density, 47–50
 depth, 47–51
 duration, 46
 extent, 46
 melt, 48
 trends, 20–21, 49
 water equivalent, 51, 284–285, 306
snow line altitude, 51
snow on sea ice, *See* sea ice characteristics

- solar radiation, *See also* energy balance – surface
 attenuation, clear sky, 143
 clear sky transmittance, 144
 definition, 67
 solar zenith angle, 143
 spectral reflectance, *See* albedo
 Spitsbergen, 14
St Roch, 14
 stochastic resonance, 328
 stratosphere, *See* atmospheric circulation
 stratospheric circulation, *See* atmospheric circulation
 Stefansson, Vilhjamar, 9
 sublimation, *See* energy balance – surface;
See also Greenland
 Submarine Arctic Science Program (SCICEX), 15–16
 submarine permafrost, *See* permafrost
 sudden stratospheric warmings,
See also atmospheric circulation, 95–98, 130
 Summit, Greenland, 16
 surface air temperature, *See* air temperature
 surface albedo, *See* albedo; energy balance – surface
 surface energy balance, *See* energy
 balance – surface
 surface net radiation budget, *See* energy
 balance – surface
 Svalbard, 3, 266
 Sverdrup, Otto, 1, 8, 9, 12
 Swiss Camp, 255
 systematic observations, beginning of, 11–14
 taiga, 41
 temperature, *See* air temperature
 temperature of water density maximum, 211
 temperature versus density, fresh water, 212
 temperature versus density, salt water, 212
Tethergoff, 9–10
 thermal conductivity, *See* energy balance – surface
 Thermal Front Parameter (TFP), 110–111
 thermocline, *See* Arctic Ocean
 thermohaline circulation, 244–248, 325–328, 335
 Torne-Kalix river system, 283
 Transpolar Drift Stream (TPDS), *See* sea ice motion
 tropopause, 100–101
 tropospheric circulation, *See* atmospheric circulation
 tundra, 40
 upward-looking sonar (ULS), 243
 Ural mountains, 270
 urban modifications of climate, 270–271
 USS *Nutilus*, 15
 USS *Queenfish*, 15
 Variable Infiltration Capacity (VIC) model, 280–282
 vegetation and climate change, 20, 41–42
 velocity derivatives, *See* sea ice deformation
 Ward Hunt Ice Shelf, 15, 39
 warming of permafrost, *See* permafrost
 water budgets – major watersheds, 194–196,
 198–199, 201–208
 water molecule, 211
 watersheds (drainages), major, 32–33, 198–199
 water vapor, 53–54, *See also* precipitation minus
 evapo-transpiration (P-ET)
 Weather Research and Forecasting (WRF) model, 299–300
 Wegener, Alfred, 1, 13
 wetlands, 202
 Weyprecht, Lt. Karl, 9–10, 11
 wind induced surface heat exchange (WISHE), 118–120
 wind speed and direction, *See also* atmospheric circulation; Greenland, 63–64
 World Climate Research Programme (WCRP), 18
 Wrangel Island, 6, 10
 Wrangel, F., 5
 Yenisey River, 32–33, *See also* water
 budgets – major watersheds
Yermak, 10–11
 Younger Dryas (YD), *See* climate change and
 variability – past

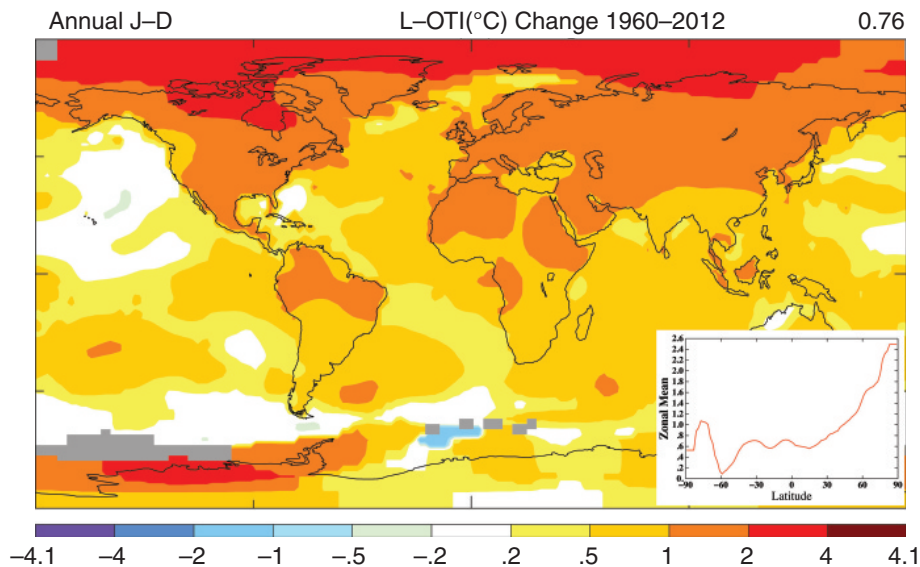


Figure 1.5. Linear trends in annual averages surface air temperature over the 1960–2012 period. The inset shows linear trends averaged by latitude. The larger trends over the Arctic region (Arctic amplification) are obvious (based on the National Aeronautics and Space Administration Goddard Institute for Space Sciences [NASA GISS] temperature analysis) (<http://data.giss.nasa.gov/gistemp>).

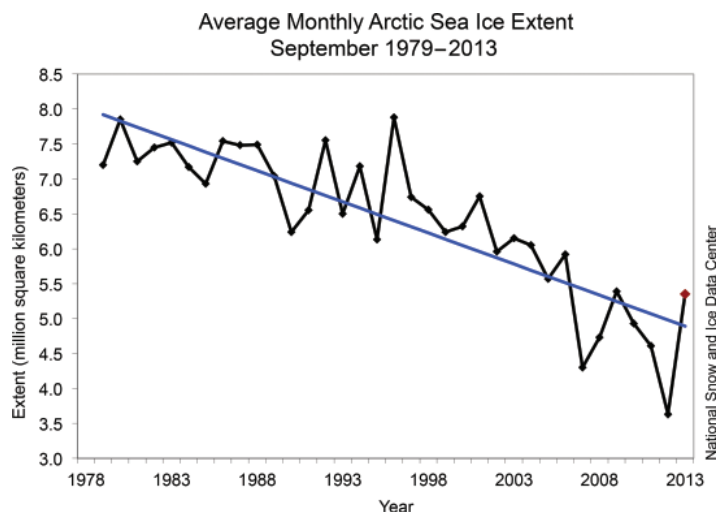


Figure 1.6. Time series and linear trend in September Arctic sea ice extent over the 1979–2013 period (from NSIDC, Boulder, CO).

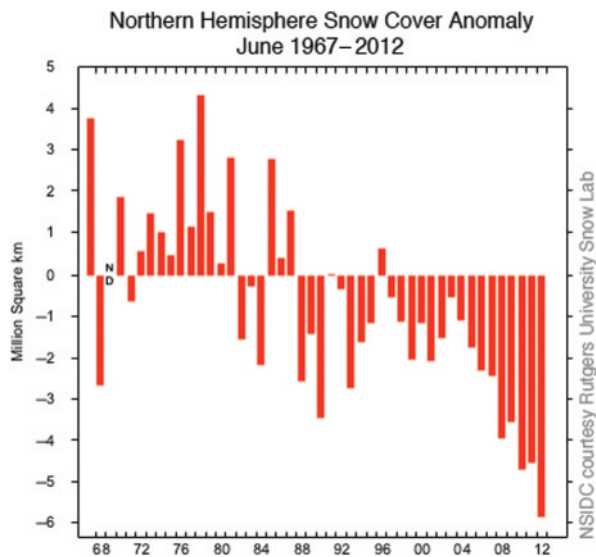


Figure 1.7. Anomalies in satellite-derived snow cover extent for the Northern Hemisphere over the 1967–2012 period (from NSIDC, courtesy Rutgers University Snow Laboratory).

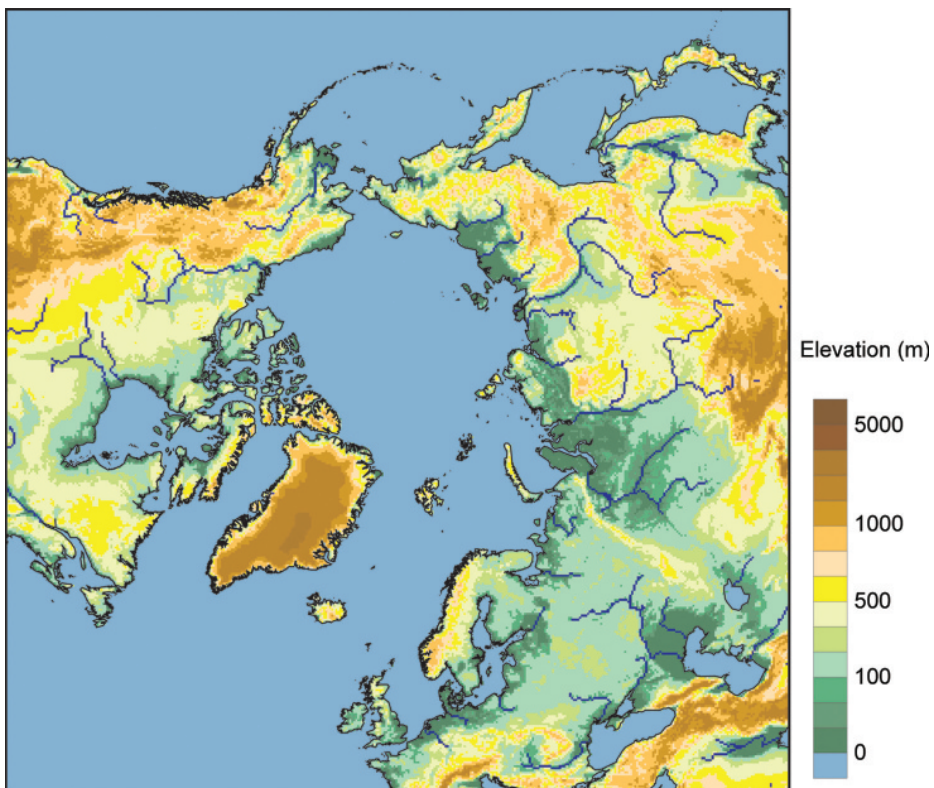


Figure 2.13. Physiography of the Arctic lands, showing topography and major river systems (courtesy of R. Lammers, University of New Hampshire, Durham, NH).

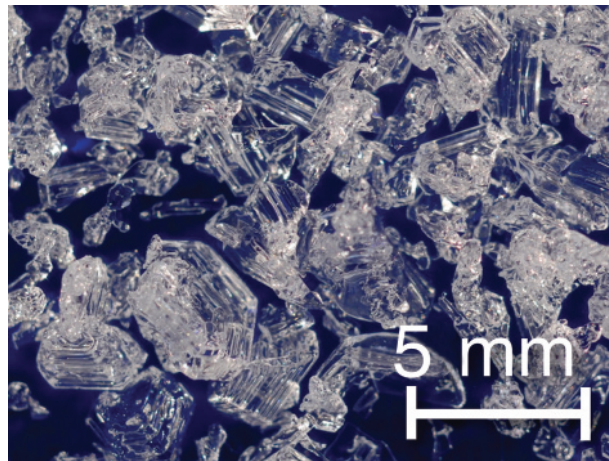


Figure 2.18. Depth hoar crystals collected from the base of a tundra snowpack on the North Slope of Alaska (courtesy of Kelly Elder, USDA Forest Service).



Figure 2.19. Sastrugi on the North Slope of Alaska (courtesy of Matthew Sturm, University of Alaska, Fairbanks, AK).

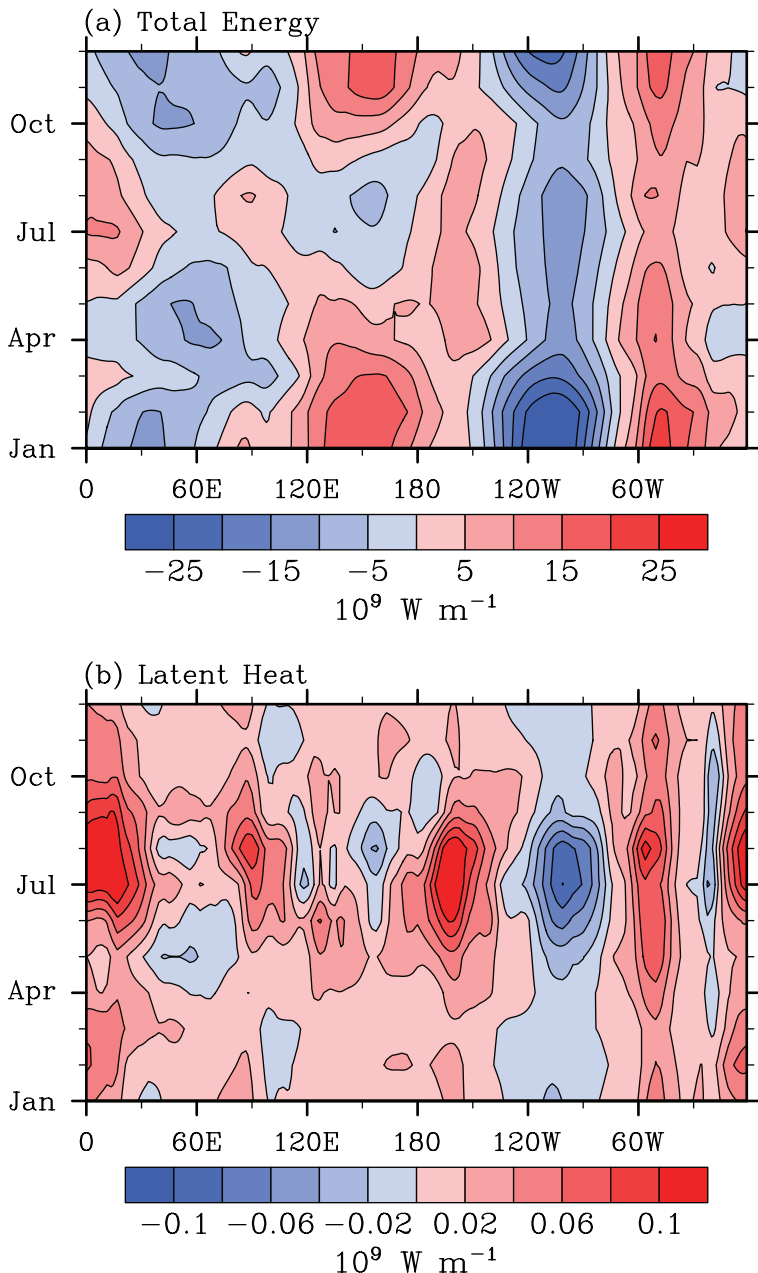


Figure 3.9. Annual cycle of the vertically integrated flow of: (a) total atmospheric energy; and (b) latent heat energy from ERA-40 across 70°N by longitude in units of Gigawatts per meter ($\text{GW m}^{-1} = 10^9 \text{ W m}^{-1}$) (from Serreze et al., 2007, by permission of AGU).

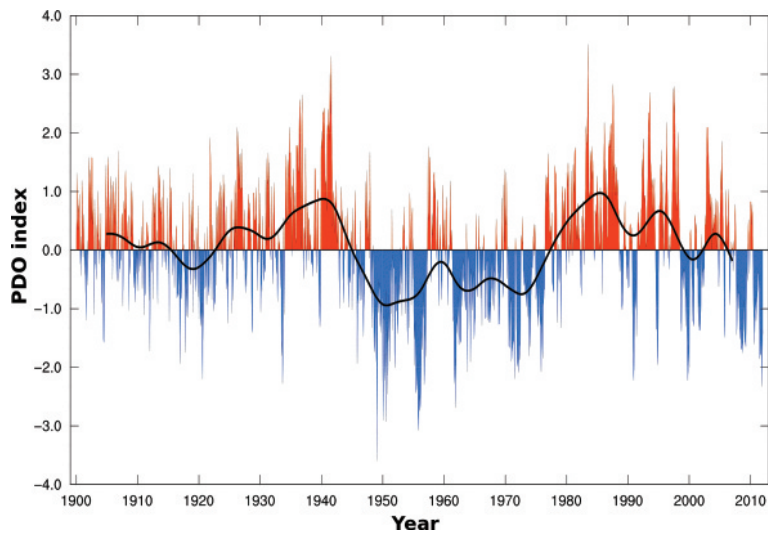


Figure 4.23. Monthly values of the Pacific Decadal Oscillation (PDO) index for the 1900–2011 period, the bold line shows the index values smoothed with a 121-month running average (by permission of Creative Commons Attribution-Share Alike 3.0 Unreported license (CC BY-SA 3.0), data from <http://jisao.washington.edu/pdo/PDO.latest>).

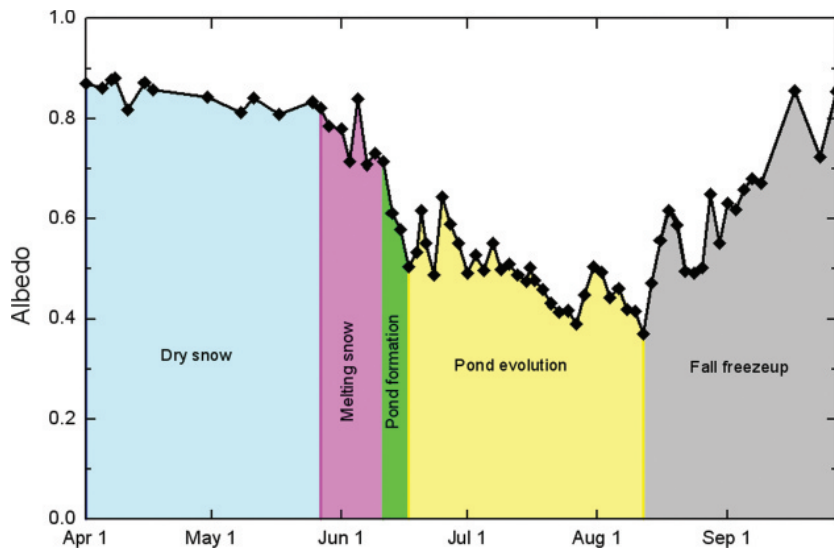


Figure 5.3. Seasonal cycle of surface albedo as measured based on data collected during the SHEBA experiment (courtesy of Donald Perovich, USA CRREL).



Figure 5.4. Summer melt ponds on the sea ice surface (courtesy of Donald Perovich, USA CRREL).

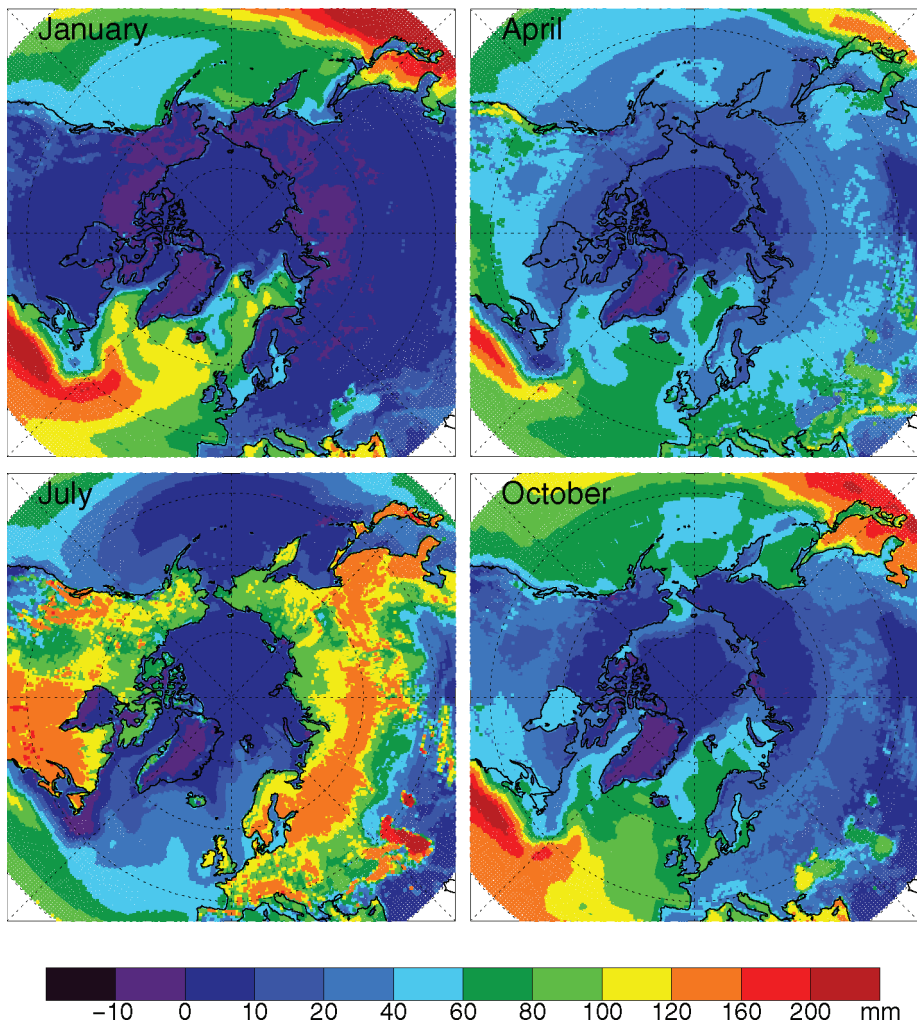


Figure 6.8. Evapotranspiration (mm, taken as positive upwards) for the four mid-season months based on MERRA data over the 1979–2009 period (courtesy D. Slater, NSIDC).

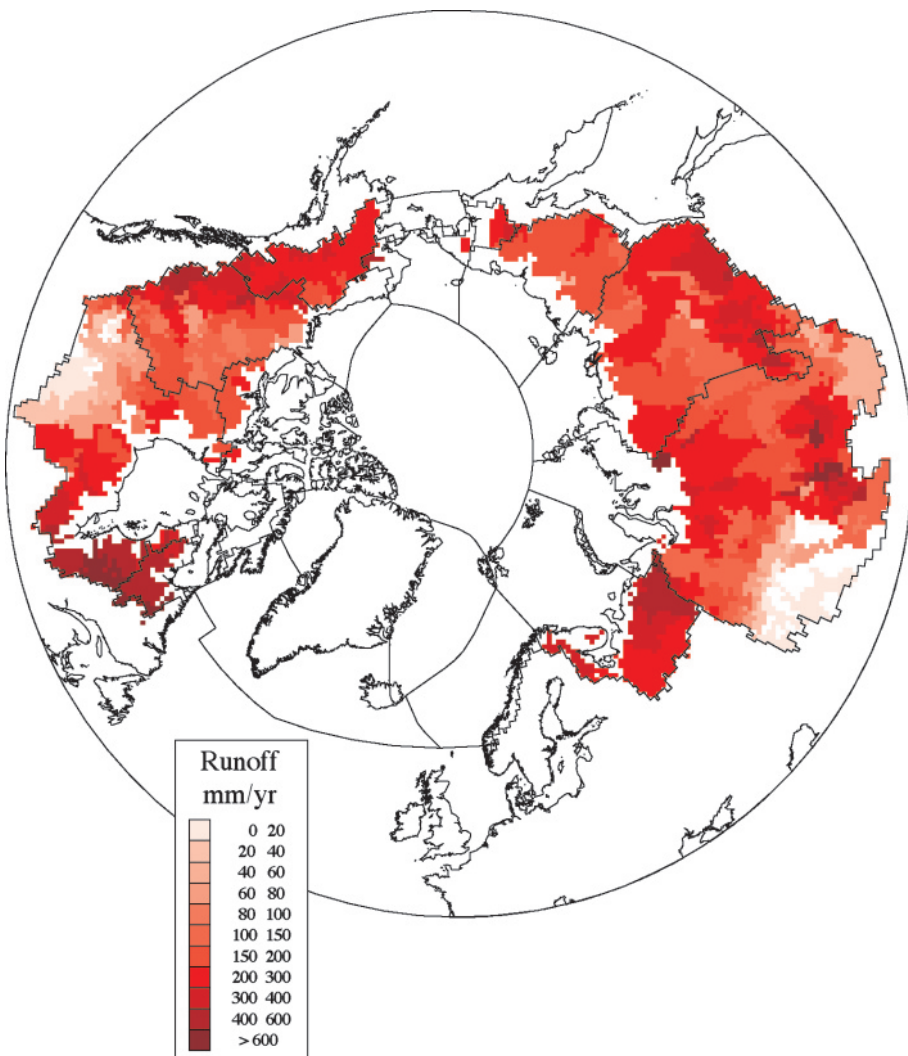


Figure 6.16. Mean annual runoff surface for the Arctic Drainage over the January 1960–December 1989 period. White areas within the southern Ob basin represent internal drainage basins. Large areas along the Arctic Ocean coast and the Canadian Arctic Archipelago (shown as white) are ungauged (from Lammers et al., 2001, by permission of AGU).

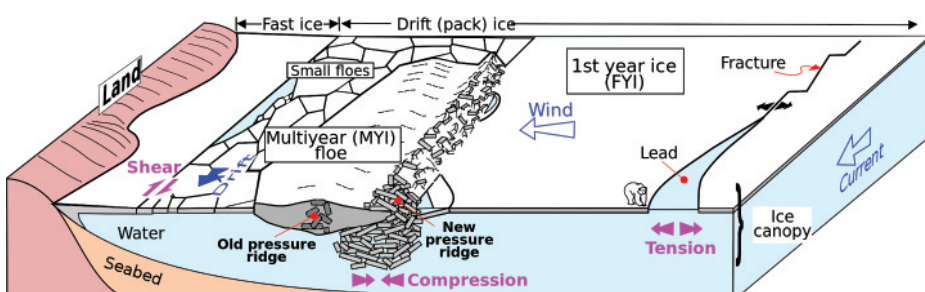
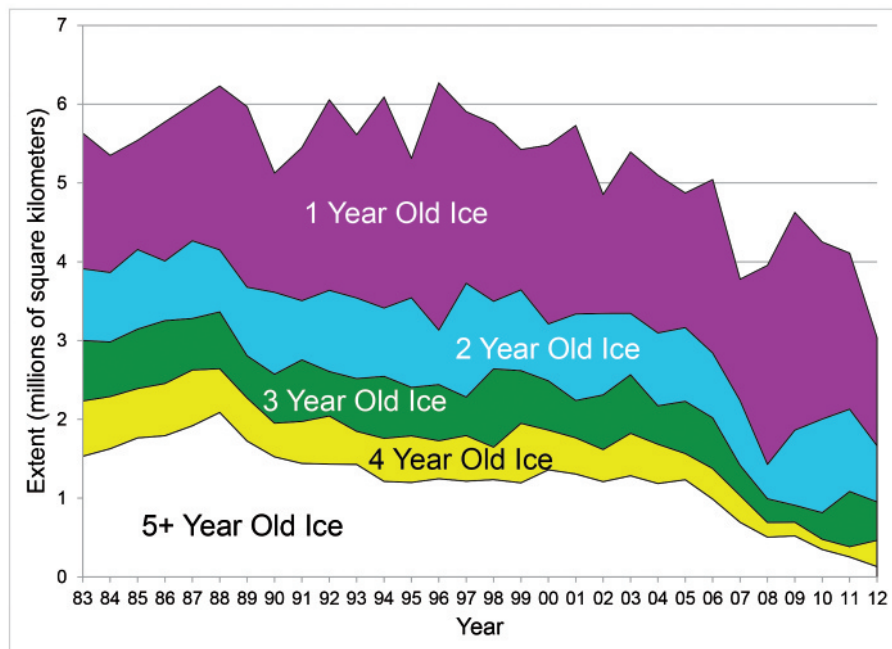
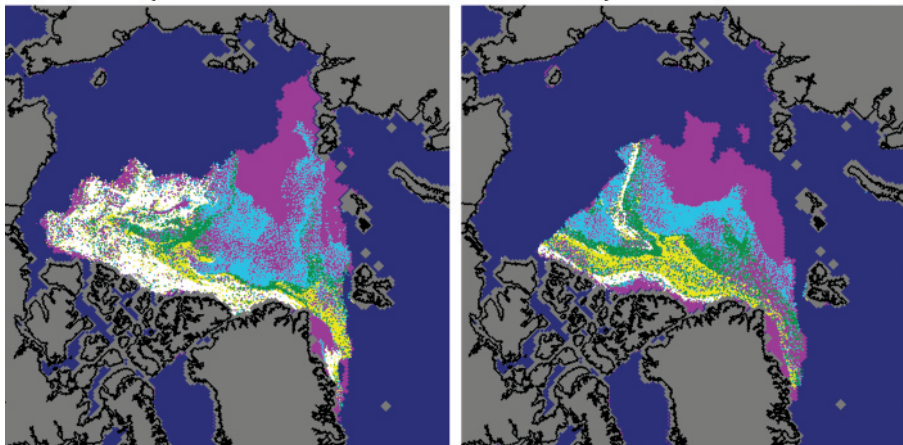


Figure 7.1. Schematic of basic sea ice types, morphology, and processes (Wikimedia Commons, author Lusilier, licensed under the Creative Commons Attribution-Share Alike 3.0 unported license).

Arctic Sea Ice Age

September 2007

September 2012



NSIDC courtesy M. Tschudi and J. Maslanik, University of Colorado Boulder

Figure 7.4. Ice age based on a tracking algorithm applied to satellite data. The top panel shows the spatial pattern of ice age classes for September 2012 and September 2007; the bottom panel shows the time history of September age classes for the Arctic Ocean as a whole back to 1983 (from NSIDC, courtesy of J. Maslanik and M. Tschudi, University of Colorado Boulder).



Figure 7.6. Highly deformed sea ice near Barrow, Alaska, during the spring of 2008 (photograph by M.C. Serreze).

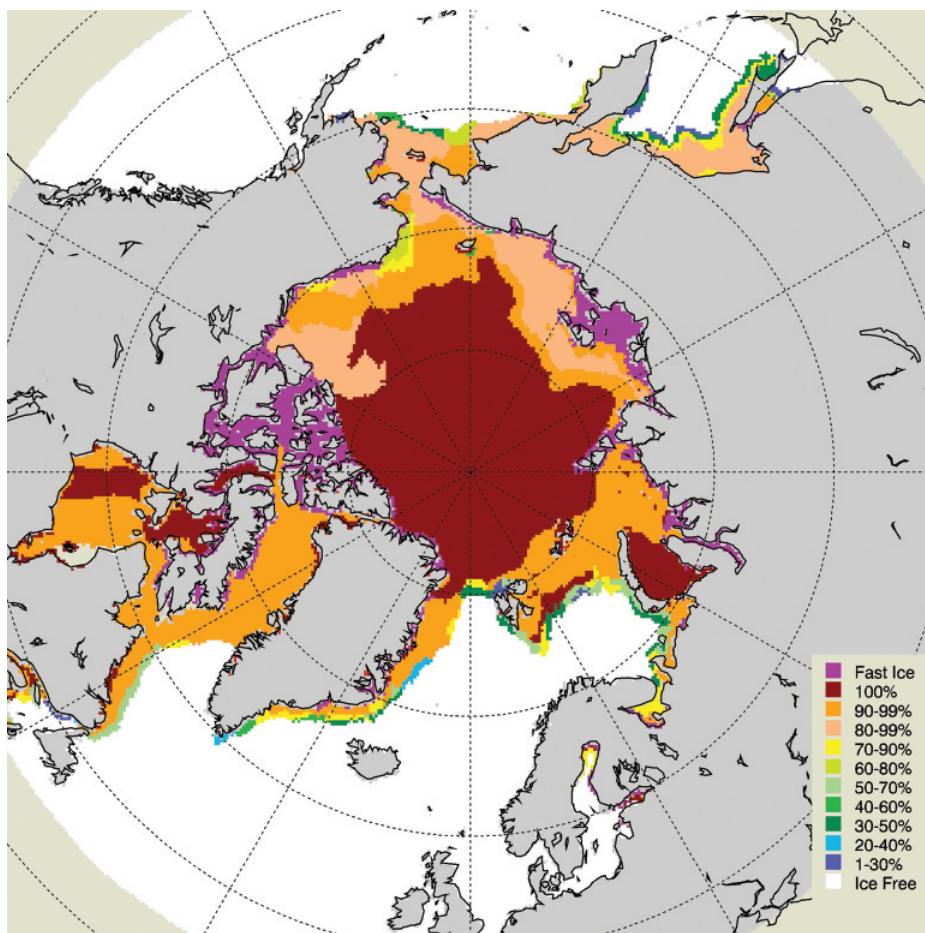
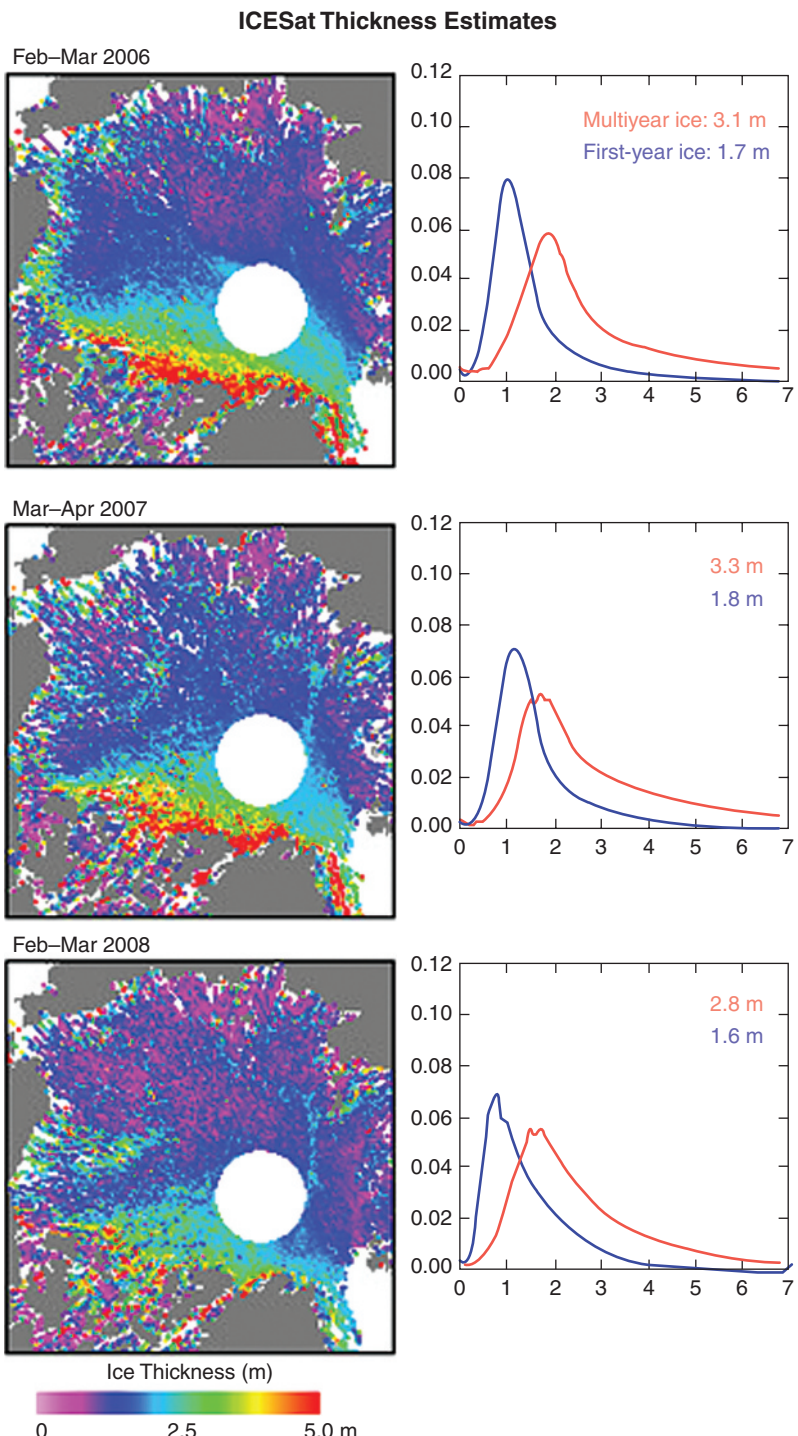


Figure 7.8. Ice concentration for the Arctic and peripheral seas (see color bar) for the January 5–11, 1994 period, based on the analysis of the National Ice Center (courtesy of K. Knowles, NSIDC, Boulder, CO).



National Snow and Ice Data Center courtesy Ronald Kwok, NASA Jet propulsion Laboratory

Figure 7.10. Spatial fields of estimated sea ice thickness and probability density functions (PDFs) (probability given on the y-axis) based on ICESat retrievals for February–March 2006, March–April 2007, and February–March 2008. PDFs are given from both multiyear ice and first-year ice. The white circle indicates the region north of satellite coverage (from NSIDC, courtesy of R. Kwok, NASA, JPL).

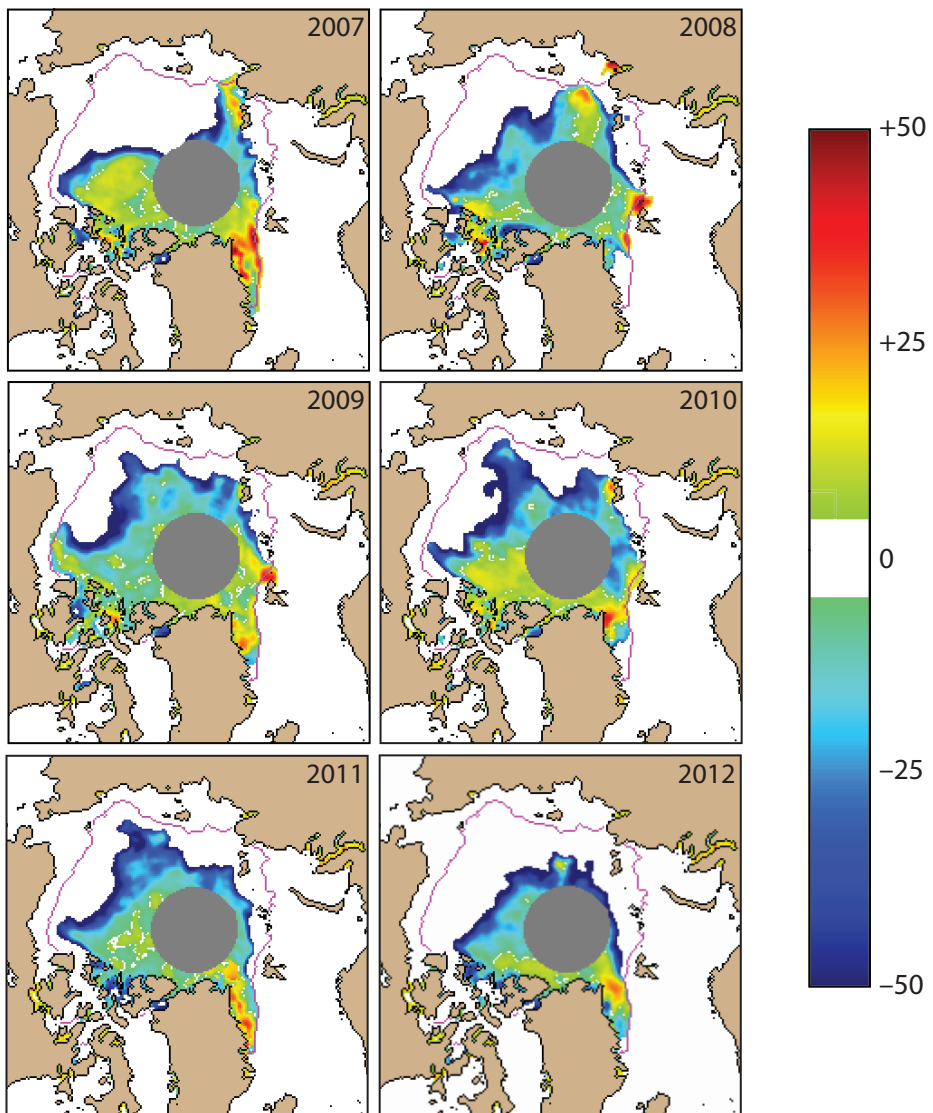


Figure 7.16. Mean September ice extent (all colored regions) and anomalies in ice concentration (in %, see color bar) for the years 2007 through 2012, based on satellite passive microwave data. The median September ice extent is shown by the purple line. Concentration anomalies and median extent are both referenced to the 1979–2000 period, which includes data from SMMR. This accounts for the larger “polar hole” of no data coverage compared to the SSM/I SSMIS period 1987–present (courtesy of W. Meier, NSIDC, Boulder, CO).

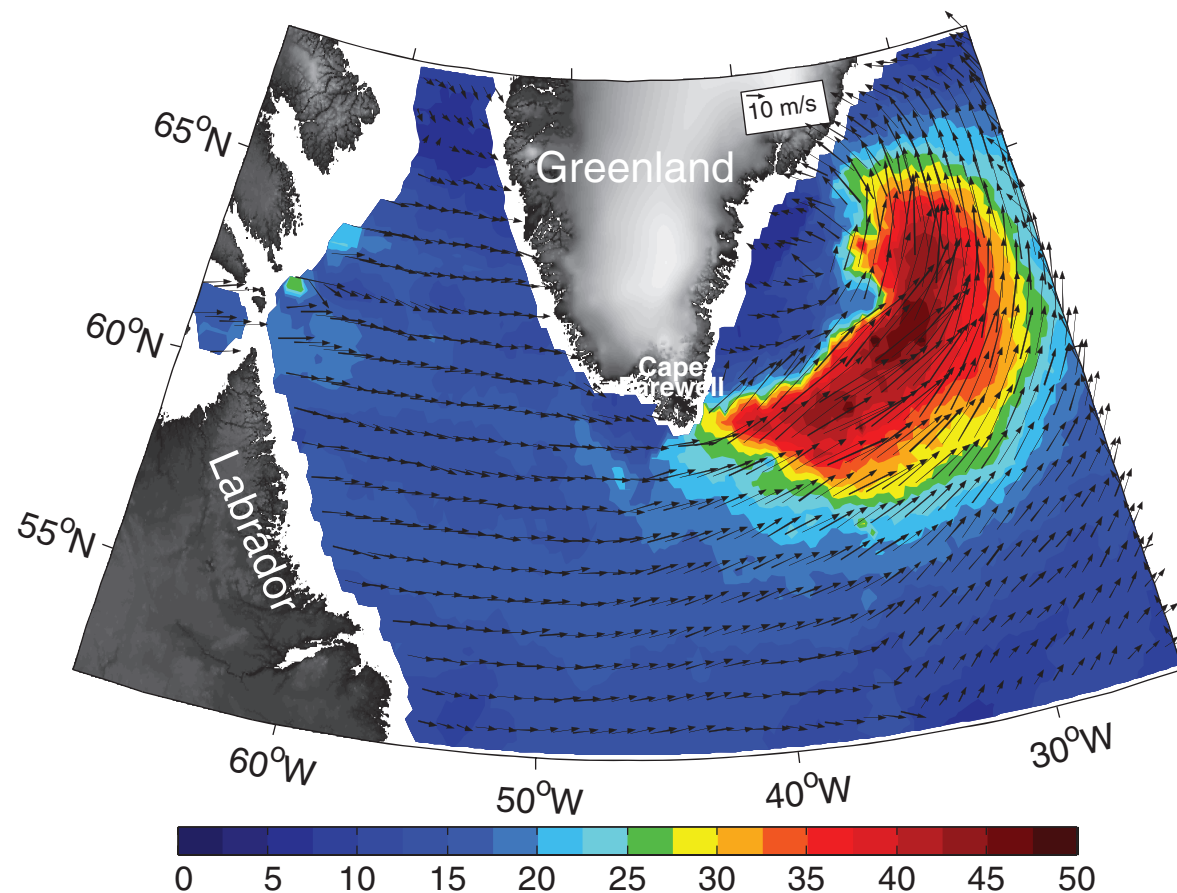


Figure 8.3. Winds speeds in m s^{-1} (see color bar) and wind direction (vectors) for a forward Greenland tip jet event that occurred on December 5, 2002, based on data from the NOAA QuikSCAT satellite (courtesy of Kjetil Våge, Woods Hole Oceanographic Institute, Woods Hole, MA).

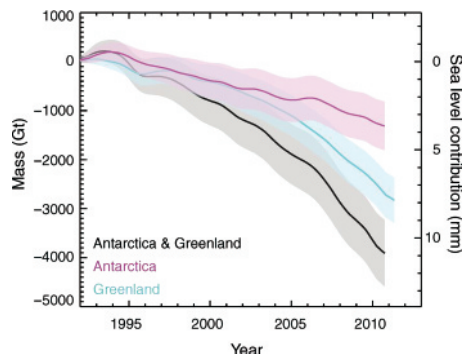


Figure 8.6. Cumulative annual mass balance (Gigatonnes and equivalent sea level rise) over the 1992–2011 period for Greenland, Antarctica, and Greenland and Antarctica combined (adapted from Shepherd et al., 2012, by permission of AAAS).



Figure 8.8. Maritime Arctic environment in summer, Kings Bay, Svalbard (courtesy of M.C. Serreze, NSIDC, Boulder, CO).

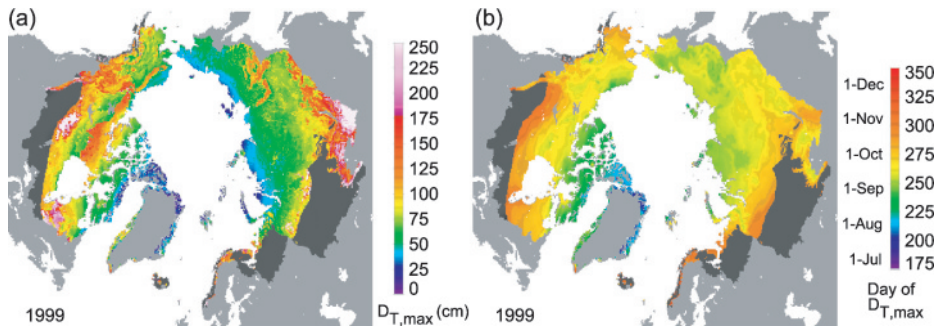


Figure 9.4. Modeled maximum depth of active layer (a) and the date of maximum thaw depth (b) for 1999 over the Arctic terrestrial drainage. Areas with no permafrost in the drainage and the Greenland Ice Sheet are indicated by dark grey shading (from Oelke et al., 2003, by permission of AGU).

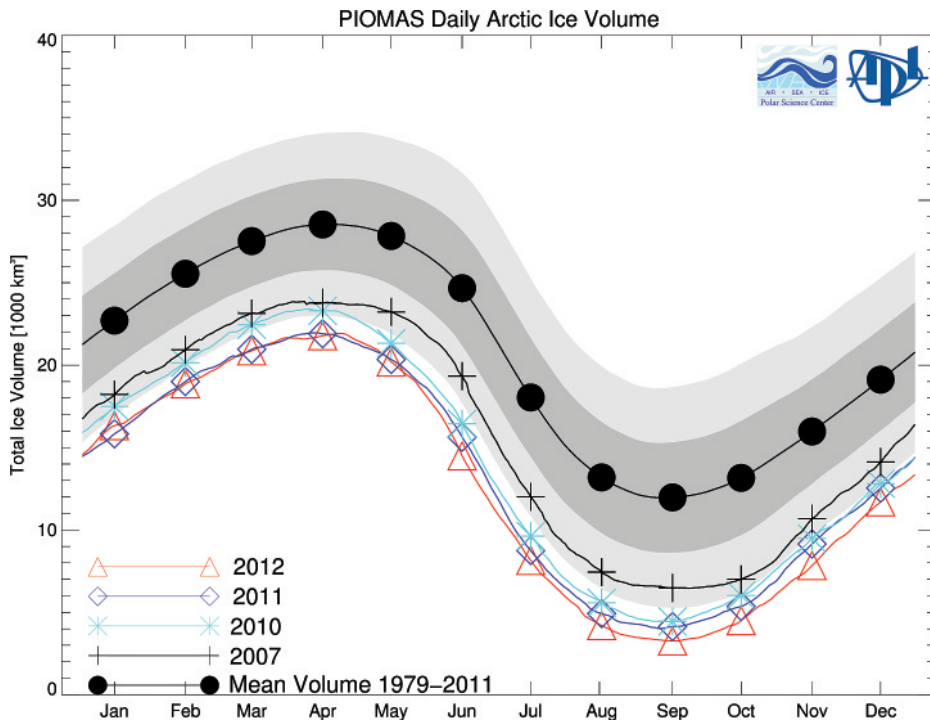


Figure 9.11. Annual cycle of Arctic sea ice volume from PIOMAS for 2007, 2010, 2011, 2012, and for the long-term (1979–2011) mean. Shaded areas indicate one and two standard deviations from the mean (courtesy of A. Schweiger, University of Washington, Seattle WA).

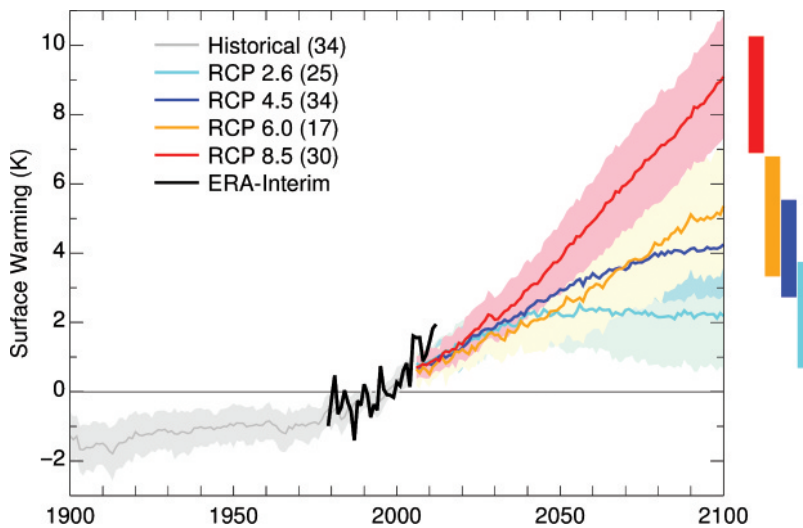


Figure 9.12. CMIP5 hindcasts (1900–2006) and projections (2006–2007) of annual surface air temperature anomalies for the Arctic (the region poleward of 65°N), along with the Arctic record from the ERA-Interim reanalysis. See text for details (courtesy of A.P. Barrett, NSIDC, Boulder, CO).

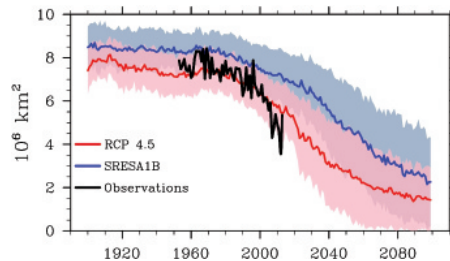


Figure 9.13. Multimodel ensemble mean sea ice extent based on observations (black line), the CMIP5 models (red line for the ensemble mean and red shading for the ± 1 standard deviation) and the CMIP3 models (blue line for the ensemble mean and red shading for the ± 1 standard deviation) (courtesy of J. Stroeve, NSIDC, Boulder, CO).

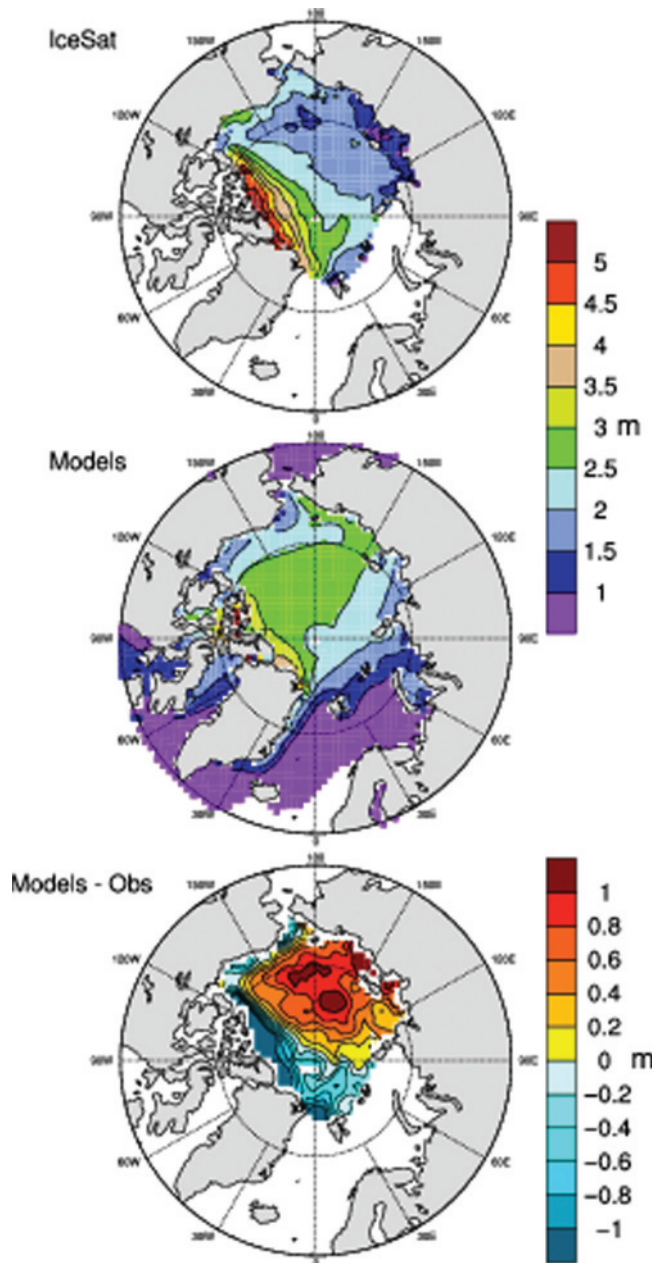


Figure 9.14. Fields of mean September sea ice thickness based on observations from IceSat, the average of all CMIP5 models over the period of ICES at observations and the difference between the modeled and observed values (courtesy of A.P. Barrett, NSIDC, Boulder, CO).

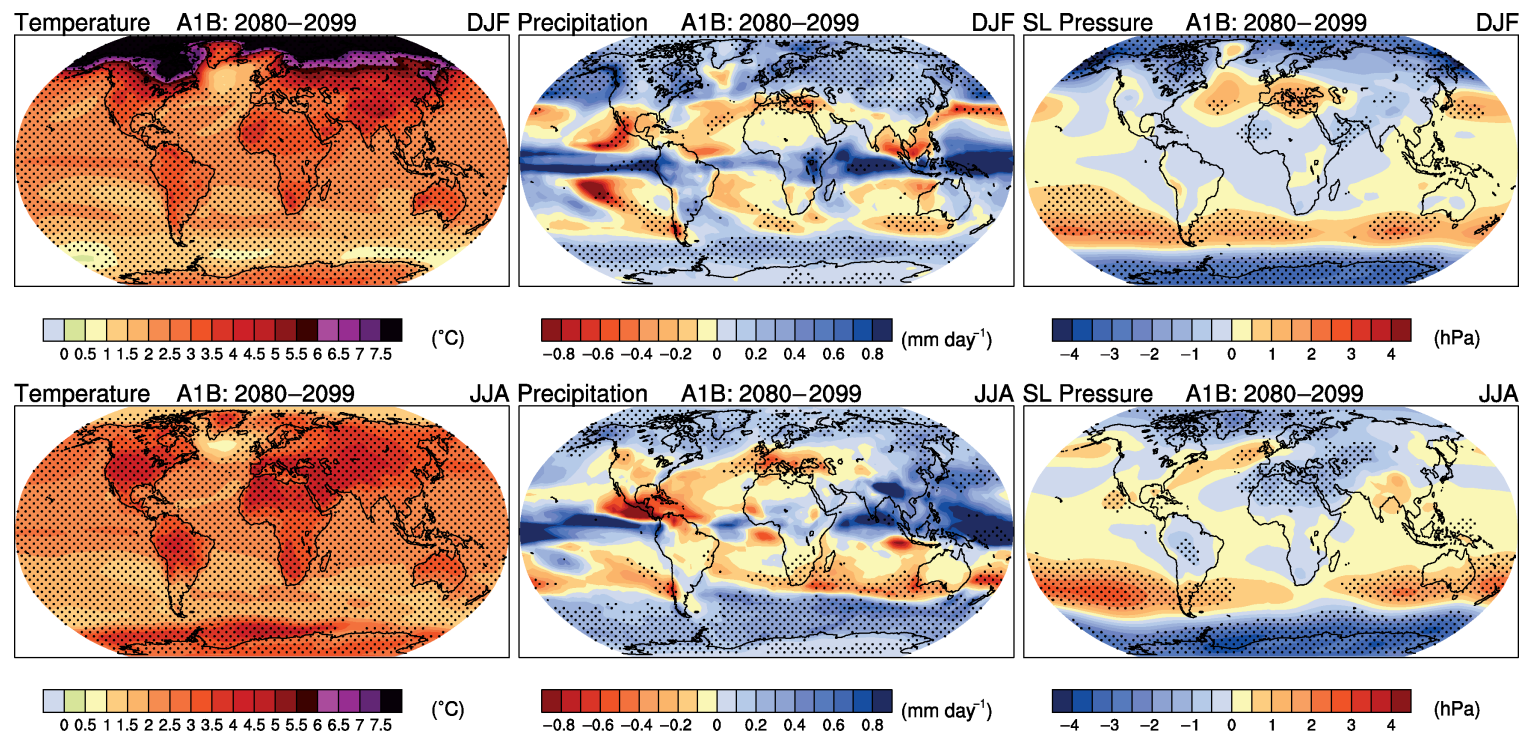


Figure 9.15. Projected changes for winter (DJF) and summer (JJA) of surface temperature, precipitation, and sea-level (SL) pressure for 2080–2099, relative to 1980–1999, based on the CMIP3 models using the A1B emissions scenario (by permission of the IPCC).

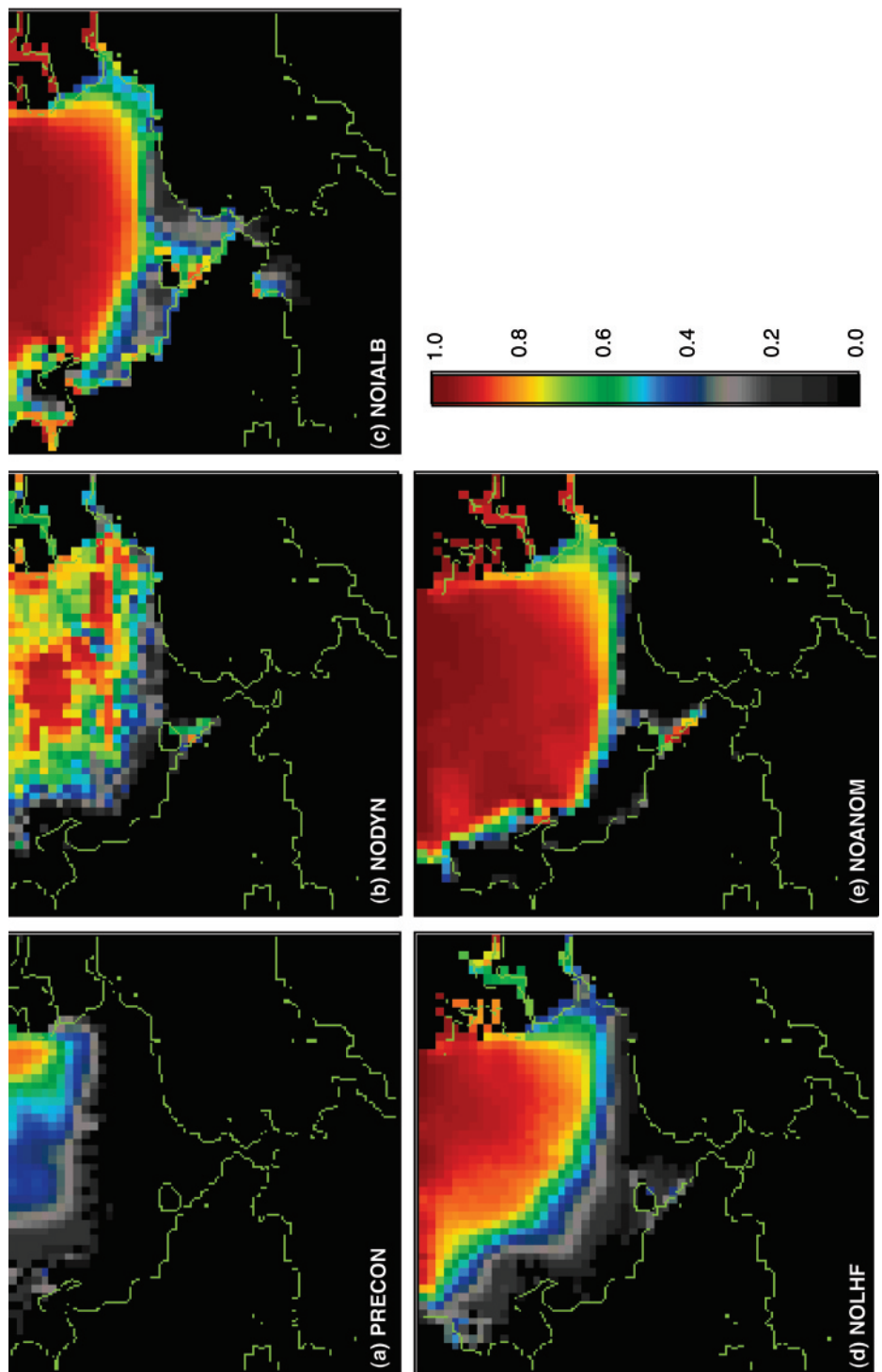


Figure 9.16. Average September ice concentration (percent) from five sensitivity experiments using the ARCSyM model addressing development of the 1990 sea ice anomaly (from Lynch et al., 2001a, by permission of AGU).

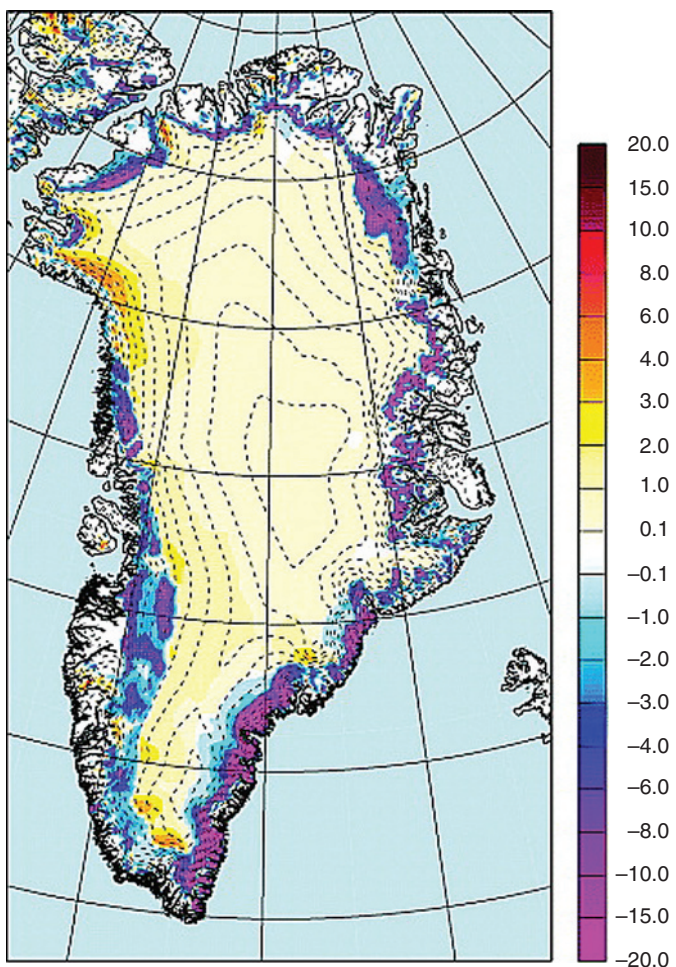


Figure 9.17. Modeled surface mass balance trend (1958–2007) in kg m^{-2} based on a simulation with RACMO2/GR. Thin dashed lines are 250 m elevation contours (from Ettema et al., 2009, by permission of AGU).

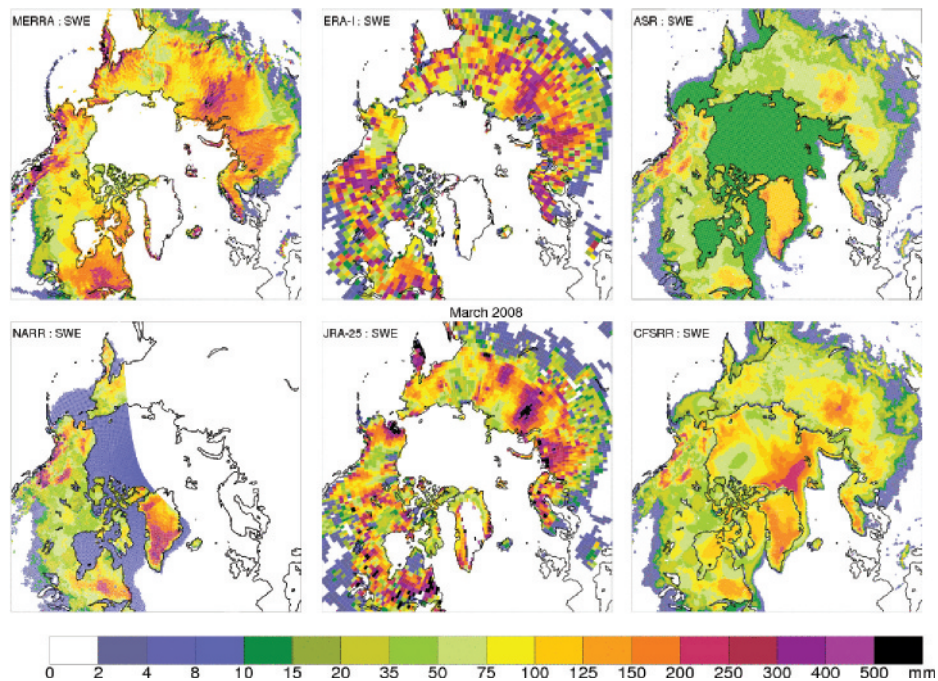


Figure 9.18. Mean snow water equivalent (mm) for March from six atmospheric reanalysis: MERRA, ERA-I, ASR, NARR (the North American Regional Reanalysis), JRA-25 (the Japanese twenty-five-year reanalysis), and CFSR (courtesy of D. Slater, NSIDC, Boulder, CO).

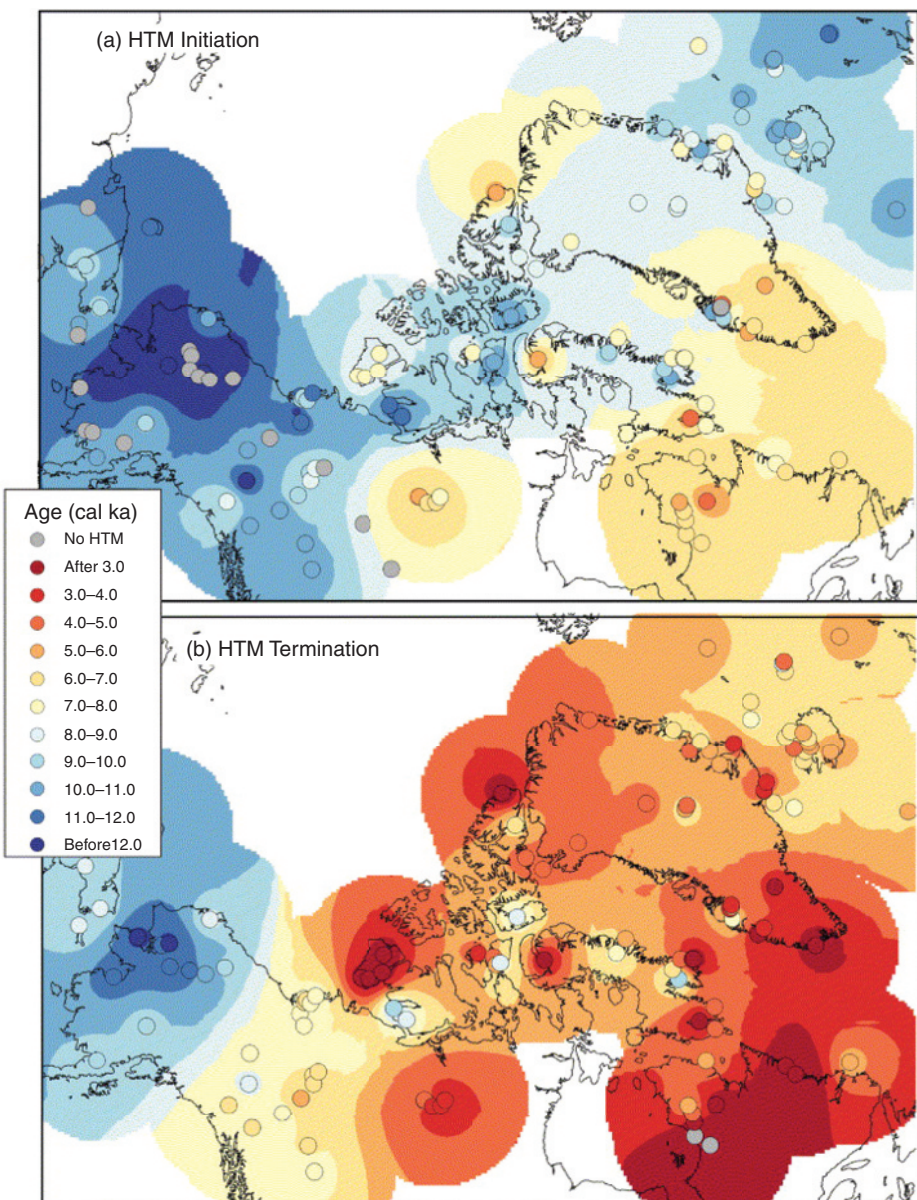


Figure 10.10. Onset (a) and termination (b) of the Holocene Thermal Maximum (ka, calendar years) based on a variety of paleoclimate data (from Kaufman et al., 2004, by permission of Elsevier).

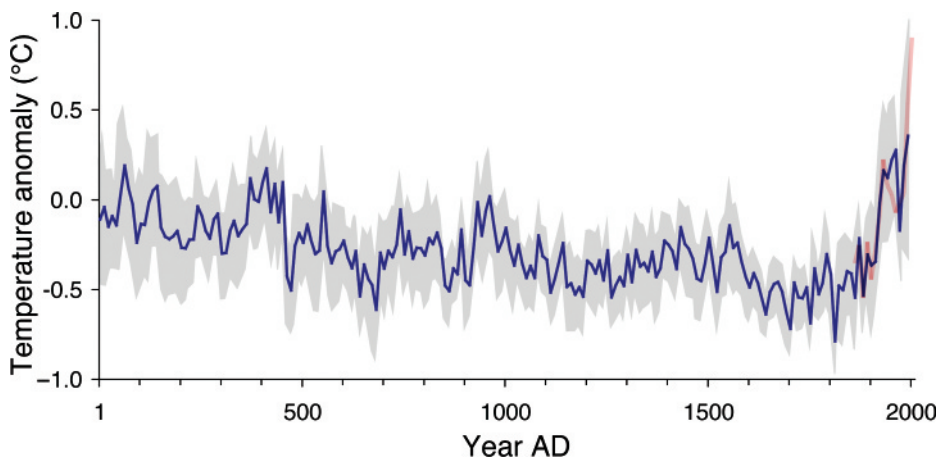


Figure 10.12. Arctic summer temperature anomalies for the past 2,000 years based on a variety of proxy sources. The blue line shows a reconstruction of summer Arctic land temperatures over the past 2,000 years, based on a composite of twenty-three proxy records from lake sediments, ice cores, and tree rings relative to the 1961–1990 reference period. The shaded area represents variability among different Arctic sites. The red line shows Arctic temperatures from the instrumental record (courtesy of D. Kaufman, Northern Arizona University, Flagstaff AZ, based on Kaufman et al. 2009).